

GDANSK UNIVERSITY OF TECHNOLOGY
FACULTY OF OCEAN ENGINEERING AND SHIP TECHNOLOGY
SECTION OF TRANSPORT TECHNICAL MEANS
OF TRANSPORT COMMITTEE OF POLISH ACADEMY OF SCIENCES
UTILITY FOUNDATIONS SECTION
OF MECHANICAL ENGINEERING COMMITTEE OF POLISH ACADEMY OF SCIENCE

ISSN 1231 – 3998
ISBN 83 – 900666 – 2 – 9

Journal of POLISH CIMAC

**SELECTED PROBLEMS
OF DESIGNING
AND OPERATING
TECHNICAL SYSTEMS**

Vol. 6

No. 3

Gdansk, 2011

Science publication of Editorial Advisory Board of POLISH CIMAC

Editorial Advisory Board

J. Girtler (President) - *Gdansk University of Technology*
L. Piaseczny (Vice President) - *Naval Academy of Gdynia*
A. Adamkiewicz - *Maritime Academy of Szczecin*
J. Adamczyk - *University of Mining and Metallurgy of Krakow*
J. Blachnio - *Air Force Institute of Technology*
C. Behrendt - *Maritime Academy of Szczecin*
P. Bielawski - *Maritime Academy of Szczecin*
T. Chmielniak - *Silesian Technical University*
R. Cwilewicz - *Maritime Academy of Gdynia*
T. Dąbrowski - *WAT Military University of Technology*
Z. Domachowski - *Gdansk University of Technology*
C. Dymarski - *Gdansk University of Technology*
M. Dzida - *Gdansk University of Technology*
J. Gardulski - *Silesian University of Technology*
J. Gronowicz - *Maritime University of Szczecin*
V. Hlavna - *University of Žilina, Slovak Republic*
M. Idzior - *Poznan University of Technology*
A. Iskra - *Poznan University of Technology*
A. Jankowski - *President of KONES*
J. Jaźwiński - *Air Force Institute of Technology*
R. Jedliński - *Bydgoszcz University of Technology and Agriculture*
J. Kiciński - *President of SEF MEC PAS, member of MEC*
O. Klyus - *Maritime Academy of Szczecin*
Z. Korczewski - *Gdansk University of Technology*
K. Kosowski - *Gdansk University of Technology*
L. Ignatiewicz Kowalczyk - *Baltic State Maritime Academy in Kaliningrad*
J. Lewitowicz - *Air Force Institute of Technology*
K. Lejda - *Rzeszow University of Technology*

J. Macek - *Czech Technical University in Prague*
Z. Matuszak - *Maritime Academy of Szczecin*
J. Merksiz - *Poznan University of Technology*
R. Michalski - *Olsztyn Warmia-Mazurian University*
A. Niewczas - *Lublin University of Technology*
Y. Ohta - *Nagoya Institute of Technology*
M. Orkisz - *Rzeszow University of Technology*
S. Radkowski - *President of the Board of PTDT*
Y. Sato - *National Traffic Safety and Environment Laboratory, Japan*
M. Sobieszczanski - *Bielsko-Biala Technology-Humanistic Academy*
A. Soudarev - *Russian Academy of Engineering Sciences*
Z. Stelmasiak - *Bielsko-Biala Technology-Humanistic Academy*
M. Ślęzak - *Ministry of Scientific Research and Information Technology*
W. Tarelko - *Maritime Academy of Gdynia*
W. Wasilewicz Szczagin - *Kaliningrad State Technology Institute*
F. Tomaszewski - *Poznan University of Technology*
J. Wajand - *Lodz University of Technology*
W. Wawrzyński - *Warsaw University of Technology*
E. Wiederuh - *Fachhochschule Giessen Friedberg*
M. Wyszyński - *The University of Birmingham, United Kingdom*
S. Żmudzki - *West Pomeranian University of Technology in Szczecin*
B. Żółtowski - *Bydgoszcz University of Technology and Life Sciences*
J. Żurek - *Air Force Institute of Technology*

Editorial Office:

GDANSK UNIVERSITY OF TECHNOLOGY
Faculty of Ocean Engineering and Ship Technology
Department of Ship Power Plants
G. Narutowicza 11/12 80-233 GDANSK POLAND
tel. +48 58 347 29 73, e – mail: sek4oce@pg.gda.pl
www.polishcimac.pl

This journal is devoted to designing of diesel engines, gas turbines and ships' power transmission systems containing these engines and also machines and other appliances necessary to keep these engines in movement with special regard to their energetic and pro-ecological properties and also their durability, reliability, diagnostics and safety of their work and operation of diesel engines, gas turbines and also machines and other appliances necessary to keep these engines in movement with special regard to their energetic and pro-ecological properties, their durability, reliability, diagnostics and safety of their work, and, above all, rational (and optimal) control of the processes of their operation and specially rational service works (including control and diagnosing systems), analysing of properties and treatment of liquid fuels and lubricating oils, etc.

All papers have been reviewed

@Copyright by Faculty of Ocean Engineering and Ship Technology Gdansk University of Technology

All rights reserved

ISSN 1231 – 3998

ISBN 83 – 900666 – 2 – 9

Printed in Poland



Introduction

In contemporary science we can observe more and more specialization in various scientific disciplines. This specialization makes that research is conducted with not proper consideration of the knowledge of other scientific disciplines even if they belong to the same field of knowledge. Thus, the specialists dealing with the theme that belongs to the „Machine Building and Operating” discipline, are reluctant to study achievements of the related disciplines such as: „Automation and Robotics”, „Electronics”, „Electrical Engineering”, „Energetics”, „Computer Science”, „Mechanics” or “Transport”. Much more unconcerned is the knowledge of such disciplines as: „Biocybernetics & Biomedical Engineering” and „Biotechnology”, although they are classified to the field of knowledge defined as „technical sciences”. The situation is understandable. It follows from the anxiety that study of developments in other scientific disciplines may cause falling behind with developments in the discipline practiced by the given scientist. In consequence, making a Doctoral Thesis can be admittedly easier but making a Habilitation Thesis – much more difficult. Habilitation can be achieved among others when a candidate in his/her research output can prove application for the first time the knowledge of any other discipline, e.g. „Mathematical Sciences”.

In each scientific discipline, independently which field of knowledge it belongs to, the science is being developed in result of applying proper scientific methods. However, regardless of application of the specific methods, in each scientific discipline there are also used deductive and inductive methods if the created knowledge is supposed to have essential cognitive properties. Deductive methods are used when it is necessary to prove a thesis statement (statements). When a hypothesis (hypotheses) is (are) to be verified then the inductive or deductive methods are applied. As a rule, underestimated is the method called analogy. The analogy, however, enables searching for a common *reason (rationale, cause)* characterizing different research objects (specific for particular scientific disciplines), while deduction consists in matching *consequence (result, conclusion)* to *reason*, and induction – *reason to consequence*.

For this reason it might be of interest to many scientists and also beneficial for development of technical sciences to present in the *Journal of POLISH CIMAC* designed for publication of articles concerning the knowledge enclosed in the „Machine Building and Operating” discipline, also these works which are classified to other mentioned scientific disciplines belonging to the field of knowledge - „technical sciences”, although they are not directly related to the theme being the mainstream of this journal. This volume contains precisely this kind of publications. I remain with the conviction that such an approach to the dissemination of knowledge comprising both cognitive properties (important for science) and utilitarian properties (important in practice of designing, manufacturing and operating technical equipment), will contribute to accelerating the development of the technical sciences.

Editor-in-Chief
prof. Jerzy Girtler

CONTENTS

Bochat A., Zastempowski M.: MODELLING OF THE CUTTING PROCESS BY THE DRUM CUTTING UNIT	9
Ciechacki K., Szykowny T.: APPLICATION OF GTAW METHOD FOR SURFACE REMELTING OF COOPER DUCTILE CAST IRON	15
Domanowski P., Wocianiec R., Bujnowski S., Zdrojewski J.: AUTOMATIC DRILLED HOLES POSITION CORRECTION FOR A SHIP WINDOW	23
Domanowski P., Nowak B.: NUMERICAL AND EXPERIMENTAL STUDY ON ALUMINIUM PIPE BENDING PROCESS	33
Holka H.: STABILITY CONDITION OF THE TRACTOR TRAILER VIBRATION	43
Kaminski P.: COMPUTER-AIDED SYSTEM TO ALLOTMENT OF THE OPERATING TASKS IN THE SHIP ENGINE ROOM	49
Kostek R., Landowski B.: A SIMULATION STUDY OF MIXING GRANULAR MATERIALS	57
Kostek R., Landowski B.: SIMULATION OF THE GRANULAR FLOW OF GRINDING MEDIA INSIDE A BALL MILL	65
Kukliński M.: INFLUENCE OF VOIDS AND LAYERS NUMBER ON MECHANICAL PROPERTIES OF HAND LAY-UP BENDED LAMINATES	69
Landowski B. Pawlikowski A.: ANALYSIS OF THE WORKING PROCESS OF AN AUTOMATED HIGH BAY RACKING SYSTEM	75
Leppert T.: SURFACE LAYER MICROSTRUCTURE AND MICROHARDNESS AFTER TURNING IN DIFFERENT COOLING AND LUBRICATING CONDITIONS	87
Leppert T.: INFLUENCE OF COOLING AND LUBRICATION ON CHIP FORMATION AND ITS FORM IN TURNING	97
Lipski A., Mroziński S.: APPROXIMATE DETERMINATION OF A STRAIN- CONTROLLED FATIGUE LIFE CURVE FOR ALUMINUM ALLOY SHEETS	107
Lipski A., Mroziński S., Lis Z.: EVALUATION OF THE RIVET HOLE SIZING DEGREE EFFECT ON THE FATIGUE LIFE	119
Ławrynowicz Z.: AFFECT OF DECARBURIZATION TIMES OF BAINITIC FERRITE LATHS ON THE MICROSTRUCTURE IN FE-CR-C STEEL	127
Ławrynowicz Z.: INFLUENCE OF CEMENTITE PRECIPITATION ON THE EXTENT OF BAINITE REACTION IN FE-CR-SI-C STEEL	137
Marchewka A., Wocianiec R, Zdrojewski J.: FILM AND PANEL TWO-DIMENSIONAL RELATIVE POSITION OPTIMIZATION	145
Mikołajczyk T., Polasik R.: NON-CONVENTIONAL MILLING USING INDUSTRIAL ROBOT	159

Mroziński S., Pepliński J.: THE INFLUENCE OF THE BUTT WELD ON FATIGUE LIFE	165
Mroziński S., Skocki R.: SOFTENING OF MARTENSITIC CAST IRON	173
Paczkowski T.: THE ELECTRODE VIBRATIONS SYNCHRONIZATION IN ELECTROCHEMICAL MACHINING	181
Paczkowski T., Zdrojewski J.: BOUNDARY CONDITIONS ANALYSIS OF ECM MACHINING FOR CURVILINEAR SURFACES	193
Pejkowski Ł., Skibicki D.: ANALYSIS OF ACCELERATED METHODS FOR DETERMINATION OF FATIGUE CURVE	199
Pepliński K., A.Mozer.: ANSYS POLYFLOW SOFTWARE USE TO OPTIMIZE THE SHEET THICKNESS DISTRIBUTION IN THERMOFORMING PROCESS	215
Pepliński K., A.Mozer.: DESIGN OF EXTRUSION DIE FOR PLASTIC PROFILE USING ANSYS POLYFLOW SOFTWARE	221
Pepliński K.: SELECT TECHNICAL ASPECT OF ENERGY USING AND MANAGEMENT IN INJECTION MOLDING PROCESS	227
Piątkowski T., Sempruch J.: RANGES OF APPLICATION OF SORTING MANIPULATORS	235
Ranatowski E.: ANALYSIS OF THE HETEROGENEOUS WELD JOINTS IN ASPECT OF FRACTURE MECHANICS	245
Ranatowski E.: THE ASPECTS OF DIMENSIONING OF THE CONSTRUCTIONS WITH USE OF THE FRACTURE MECHANICS	253
Ranatowski E.: RELATION BETWEEN STRESS STATE AND FRACTURE RESISTANCE IN MISMATCHED WELD JOINTS	261
Sawicki J.: ANALYSIS OF INFLUENCE OF ELECTROLYTE FLOW VOLUME RATE IN INTERELECTRODE GAP ON PHYSICAL AND GEOMETRIC PARAMETERS OF ELECTRO-CHEMICAL MACHINING	269
Sempruch J. Tomaszewski T.: APPLICATION OF MINI SPECIMENS TO HIGH-CYCLE FATIGUE TESTS	279
Strzelecki P. Sempruch J.: MODYFICATION OF SELECTED METHODS OF RAPID DETERMINATION OF FATIGUE CHARACTERISTICS IN THE RANGE OF LIMITED FATIGUE LIFE	289
Styp-Rekowski M., Mańka E.: FACTORS DETERMINING HOISTING SHAFT ROPE DURABILITY	297
Szala G.: COMPARATIVE ANALYSIS OF CYCLIC PROPERTIES OF METALS OBTAINED IN CONDITIONS OF STRESS AND STRAIN RANGE DIVERSIFICATION CONTROL ON THE EXAMPLE OF C45 STEEL	305
Szczutkowski M.: COMPUTER AIDED LABORATORY ACCREDITATION PROCESS. MEASUREMENT DATABASE AS AN INITIAL STAGE OF SOFTWARE APPLICATION	313
Szykowny T., Ciechacki K.: SURFACE HARDENING OF PLAIN DUCTILE CAST IRON	319

Tomporowski A., Mroziński A.: MODIFICATION OF GRINDERS OF BIOMATERIALS USED FOR ENERGY PURPOSES	327
Tomporowski A.: THE PROCESS OF MODELLING CURVE OF AN INEQUALITY GRINDING RICE GRAINS	339
Tomporowski A.:DESIGN CONSIDERATIONS FOR SHREDDER FEED CONVEYORS USED IN FARM AND FOOD INDUSTRY	347
Topoliński T., Wirwicki M.: METHODOLOGY OF FATIGUE TESTS FOR GLUED DENTAL SAMPLES	355



MODELLING OF THE CUTTING PROCESS BY THE DRUM CUTTING UNIT

Andrzej Bochat, Marcin Zastempowski

*University of Technology and Life Sciences in Bydgoszcz
Faculty of Mechanical Engineering
ul. Kaliskiego 7, 85-796 Bydgoszcz, Poland
e-mail: zastemp@utp.edu.pl*

Abstract

This paper presents developed mathematical models of parameters that characterize the vegetable material cutting process using a drum cutting unit, including: elementary cutting resistance model, elementary cutting work referred to the cutting area and elementary cutting work model referred to the weight of the cut material. The models describe the relationships between key design features and parameters of the drum cutting unit as well as selected properties of the cut material.

Keywords: cutting drum, modelling, vegetable material

1. Introduction

The drum cutting unit is the main working unit of self-propelled, trailer type and stationary chaff-cutters [1, 2, 3, 4]. The drum cutting unit is designed to cut vegetable material (stalks or blades) into parts of defined length (chaff). Thanks to the use of such unit in chaff-cutters it is possible to obtain required degree of the material size reduction. Whereas to get desired feeding results, uniform length chaff is required. However the length depends on individual animal features and feeding method.

Cutting drums can be of open or closed design [1]. An open type drum consists of the shaft, where perforated disks are mounted. The disks are fitted with cutter holders. And the cutter holders hold cutters. Depending on the drum design, it is equipped with straight or helical cutters.

Moreover, cutters may be monolithic or sectional. The cutting drum is fixed with bearings mounted in side plates of the chaff-cutters.

While the shaft of the closed type cutting drum is fitted with the closed cylinder structure (instead of several disks) with brackets holding the cutters, mounted on cylinder side surface.

The cutting drum rotation causes the cutters to move as well. As the cutters move relative to fixed cutter, they press the vegetable material first and then cut it.

Vegetable material is fed between the cutter cutting edge and counter-cutting edge thanks to rotation of pulling-and-squeezing drums, which pre-shape and pre-compact the vegetable material.

The idea of the vegetable material feeding and cutting process using the cutting drum is shown in Fig. 1.

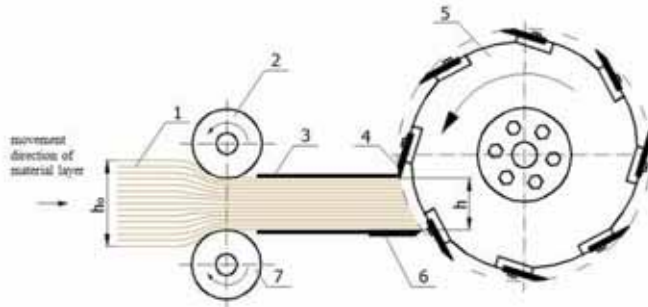


Fig. 1. The vegetable material feeding and cutting process using the cutting drum [1]:
 1 – material layer, 2 – top pulling-and-squeezing drum, 3 – pressure plate, 4 – cutter, 5 – cutting drum,
 6 – fixed cutter, 7 – bottom pulling-and-squeezing drum,
 h_0 – height of the material layer before compaction, h – height of the material layer after compaction

The aim of this paper is to develop mathematical models that characterize the vegetable material cutting process using a drum cutting unit, including:

- unit cutting resistance model p_c ,
- elementary cutting work model referred to the cutting area L_{js} ,
- elementary cutting work referred to the weight of the cut material L_{JM} .

2. Mathematical models

Based on the analysis of the pressed vegetable material layer cutting process using the drum cutting unit, authors proposed mathematical model of the process.

Figure 2 shows the force system acting on the cutter during vegetable material layer cutting process.

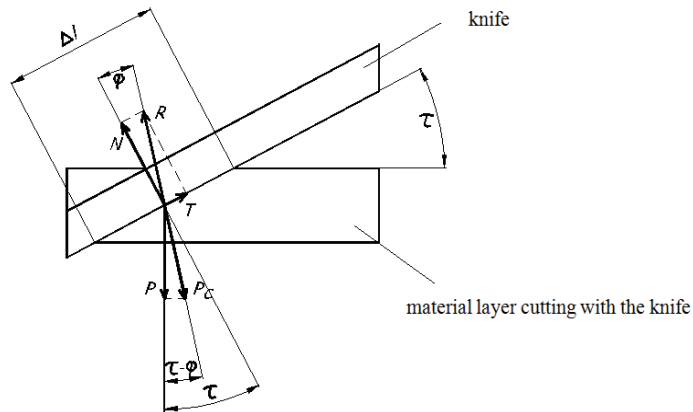


Fig. 2. The force system acting on the drum cutter during vegetable material layer cutting process

The objective of the circumferential force P shown in Fig. 2 is to overcome the resultant cutting resistance, consisting of: normal force N and friction force T generated as a result of the impact of the material layer on the cutter. The value of the normal force N depends on the unit cutting resistance p_c as well as effective length of the cutter Δl :

$$N = p_c \Delta l. \quad (1)$$

The friction force T depends on the friction angle φ and it is expressed by the formula:

$$T = N \tan \varphi = p_c \Delta l \tan \varphi. \quad (2)$$

The resultant cutting resistance P_c originating from the normal force and the friction force shall thus be expressed with the following formula:

$$P_c = \frac{p_c \Delta l}{\cos \varphi}. \quad (3)$$

The circumferential force P is the vertical component of the cutting resistance force P_c and it is expressed by the formula:

$$P = P_c \cos(\tau - \varphi) = \frac{p_c \Delta l}{\cos \varphi} \cos(\tau - \varphi). \quad (4)$$

After conversions of the formula (4) and taking into account that: $\tan \tau = \mu$, where μ is the friction factor between the cutter and the material layer, we get the formula of the circumferential force P :

$$P = \frac{p_c \Delta l}{\cos \varphi} \cos \tau \cos \varphi (1 + \mu \tan \tau) = p_c \Delta l \cos \tau (1 + \mu \tan \tau). \quad (5)$$

As a result of the analysis of rectangular vegetable material cutting, the authors divided the process into 3 stages, with the following assumptions:

- the layer is cut only with one cutter each time,
- the height of the material layer being cut is equal to the distance travelled by a given point of the cutter that passes through that layer.

STAGE I

At that stage the cutter is sinking into the material layer (the effective cutter length Δl is increasing).

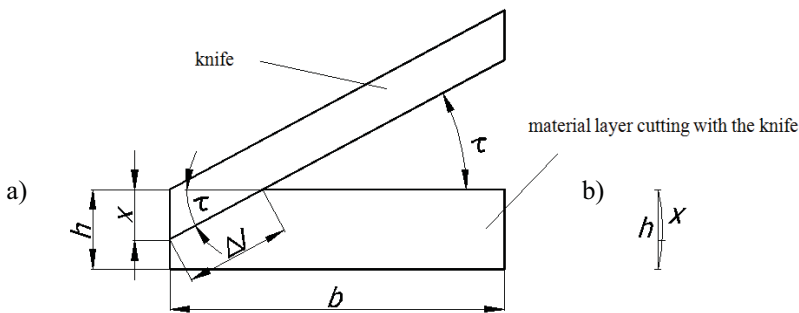


Fig. 3 Cutter sinking into the material layer (Stage I)
a) cross-section of the layer, b) comparison of the arc length and the layer height h

According to Fig. 3a, the difference between the length of the arc drawn by any point of the cutter from the top to the bottom edge of the material layer being cut is approximately equal the

height of the layer h , which results from the fact that for small angles $h \approx h \frac{\Psi}{\sin \Psi}$, because $\sin \Psi \approx \Psi$. Using the trigonometric relationship $\frac{x}{\Delta l} = \sin \tau$, we get: $\Delta l = \frac{x}{\sin \tau}$. Whereas for $x = h$, we get: $\Delta l = \frac{h}{\sin \tau}$. Hence the cutting work L_{nl} at Stage I of the cutter movement can be expressed with the relationship:

$$L_{nl} = \frac{1}{r} \int_0^h M_c(x) dx, \quad (6)$$

where:

$M_c(x)$ – moment of cutting.

Taking into account that $M_c = C \frac{x}{\sin \tau}$, the cutting work within the range $0 \leq x \leq h$ can be expressed with the following relationship:

$$L_{nl} = \frac{C}{r} \int_0^h \frac{x}{\sin \tau} dx = \frac{C}{r} \left[\frac{x^2}{2 \sin \tau} \right]_0^h = \frac{C}{r} \frac{h^2}{2 \sin \tau}, \quad (7)$$

where:

$C = p_c r \cos \tau (1 + \mu \tan \tau)$ – the constant occurring in the remaining relationships.

STAGE II

At that stage the cutter is cutting the layer of material (the effective cutter length Δl does not change).

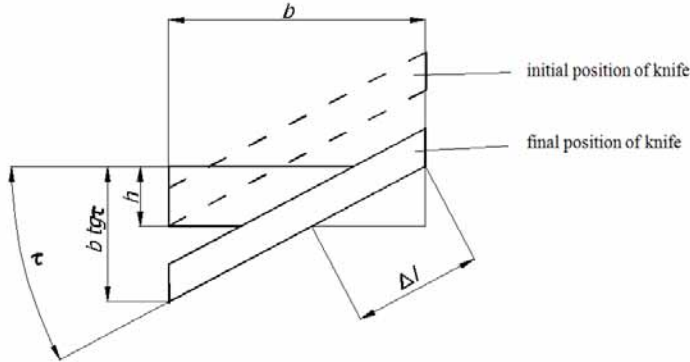


Fig. 4. Cutting of the material layer (Stage II)

According to Fig. 4, cutting process at stage II concerns the range $h \leq x \leq b \tan \tau$. The value of Δl is constant within the range $h \leq x \leq b \tan \tau$, and it is expressed by the following relationship: $\Delta l = \frac{h}{\sin \tau}$.

Hence the cutting work is defined by the formula:

$$L_{nII} = \frac{C}{r} \int_h^{btg\tau} \frac{h}{\sin \tau} dx = \frac{C}{r} \frac{h}{\sin \tau} (btg\tau - h). \quad (8)$$

STAGE III

At that stage the cutter is coming out of the material layer (the effective cutter length Δl is decreasing).

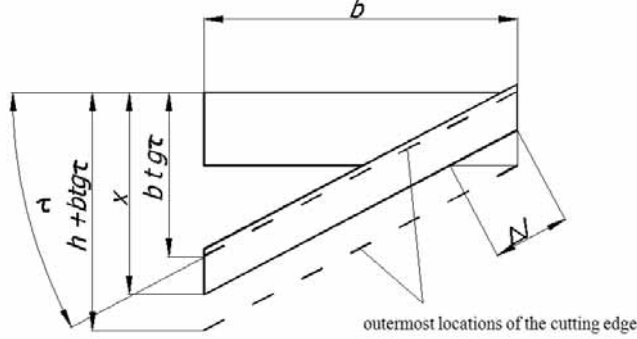


Fig. 5 Cutter coming out of the material layer (Stage III)

According to Fig.5, cutting process at stage III concerns the range $btg\tau \leq x \leq h + btg\tau$, i.e. it takes place over the same length as in stage I.

Within the range $btg\tau \leq x \leq h + btg\tau$, the value $\Delta l = \frac{x - btg\tau}{\sin \tau}$.

Hence the cutting work is denominated by the formula:

$$L_{nIII} = \frac{C}{r} \int_{btg\tau}^{h+btg\tau} \frac{(x - btg\tau)}{\sin \tau} dx = L_{nI} = \frac{C}{r} \frac{h^2}{2 \sin \tau}.$$

As a result, the total work made by the cutter when passing through the vegetable material layer being cut shall be expressed with the formula:

$$L_n = L_{nI} + L_{nII} + L_{nIII} = \frac{C}{r} \left(\frac{h^2}{2 \sin \tau} + \frac{hbtg\tau}{\sin \tau} - \frac{h^2}{\sin \tau} + \frac{h^2}{2 \sin \tau} \right) = \frac{C}{r} \frac{hb}{\cos \tau}. \quad (9)$$

Considering that:

$$(M_c)_{sr} = \frac{L_n z}{2\pi}, \quad (10)$$

where:

z - number of cutters taking part in the cutting process.

Hence, after conversions, we get:

$$(M_c)_{sr} = \frac{z h b p_c (1 + \mu g \tau)}{2\pi}. \quad (11)$$

Thus the unit cutting resistance is defined by the formula:

$$p_c = \frac{2\pi (M_c)_{sr}}{z h b (1 + \mu g \tau)} = \frac{2\pi J_b \frac{d\omega}{dt}}{z h b (1 + \mu g \tau)}, \quad (12)$$

where:

J_b - moment of inertia of the cutting drum,

$\frac{d\omega}{dt}$ - angular acceleration of the cutting drum.

While the elementary cutting work referred to the cutting area can be calculated based on the following relationship:

$$L_{js} = \frac{L_n}{h b} = p_c (1 + \mu g \tau), \quad (13)$$

and the elementary cutting work referred to the weight m_j of the cut material can be determined based on the formula:

$$L_{jM} = \frac{L_n}{m_j} = \frac{z \omega h b p_c (1 + \mu g \tau)}{2\pi W}, \quad (14)$$

where:

$m_j = W \frac{2\pi}{z \omega}$; W - the cutting unit throughput.

3. Summary

The developed mathematical models are of significant scientific importance as they explain the essence of the vegetable material cutting process using a drum cutting unit. No studies on that subject can be found in the professional literature. Moreover, after positive experimental verification, they can be used for simulations at the design stage of new drum cutting units. It is very important as agricultural works are of seasonal nature. Due to that nature it was impossible to create "data base" sufficient to facilitate quick design of working units of that type, despite of sometimes long-years experiments.

References

- [1] Bochat A., *Teoria i konstrukcja zespołów tnących maszyn rolniczych*, Wydawnictwo Uniwersytetu Technologiczno-Przyrodniczego, Bydgoszcz, 2010.
- [2] Bochat A., Błaszczczyk M., Problematyka badawcza procesu cięcia warstwy źdźbeł i łodyg, *Inżynieria i Aparatura Chemiczna* 46, nr 1, 2007, s. 28-29.
- [3] Haffert A., Harms H.H., *Schnittvorgang im Feldhäckslern*, *Landtechnik* 2, 2002, 106-107.
- [4] O'Dogherty M.J., Gale G.E., *Laboratory studies of the cutting of grass stems*. *Journal of Agricultural Engineering Research* Vol. 35, 1986, s.115-129.



APPLICATION OF GTAW METHOD FOR SURFACE REMELTING OF COPPER DUCTILE CAST IRON

Krzysztof Ciechacki, Tadeusz Szykowny*

*University of Technology and Life Sciences
al. Prof. S. Kaliskiego 7, 85-789 Bydgoszcz, Poland
tel.: +48 52 3408719, fax: +48 52 3408796
e-mail: krzysztof.ciechacki@utp.edu.pl

Abstract

The GTAW method was employed for surface remelting of copper ductile cast iron of 0.48 or 0.95 % copper content by mass and pearlitic/ferritic or pearlitic structure. The cold remelting or multiple remelting technique was adopted to harden the cast iron. The remelted layers underwent tests of hardness, tests of micro-hardness of individual structural components and microscopic tests (LEM). The tests focused on the presence of macro- and micro-cracks within the hardened layer.

Keywords: *copper ductile cast iron, surface hardening, GTAW method*

1. Introduction

The presence of copper in cast iron favours the creation of a pearlitic matrix during the eutectoid reaction and slightly increases hardenability of cast iron. The copper content in cast iron usually does not exceed 2% [10].

Copper ductile cast iron of pearlitic structure is characterized with high tensile strength (grades with strength exceeding 600 MPa), increased hardness and relatively low plasticity [11]. Many applications require cast iron of improved abrasive wear resistance. In such cases, it is necessary to surface harden surfaces subjected to abrasive wear and contact load. The required high abrasive and contact wear resistance of castings may be ensured by surface hardening. The most frequently used methods for cast iron hardening include: casting method, induction or flame surface hardening [1,5]. As an alternative to those methods, hardening techniques using concentrated energy sources may be used, e.g. GTA welding [2-4, 6-8, 12-14].

Study [9] showed that depending on the cast iron grade and remelting parameters, macro- and micro-cracks of various intensity occur in the remelted layer. Their presence, especially in case of contact stresses may cause accelerated wear of the hardened layer through flaking and pitting.

The direct purpose of the research described herein was to obtain, with the surface remelting method, a layer with hardness and macro- and micro-structure ensuring optimum tribological properties of copper cast iron.

2. Material, programme and research object

Two grades of copper ductile cast iron with chemical composition given in table 1 were used for the tests.

Table 1. Chemical composition of cast iron, % mass

Cast iron identification	C	Si	Mn	P	S	Cr	Cu	Ti	Mg
A	3.76	3.07	0.35	0.07	0.02	0.04	0.48	0.024	0.06
B	3.66	2.63	0.29	0.09	0.015	0.03	0.95	0.016	0.07

The cast iron identified with letter A has a pearlitic/ferritic structure (approx. 15% of ferrite) and is classified as EN-GJS-600-3. The cast iron identified with letter B, as-cast, has a pearlitic structure and is classified as EN-GJS-700-2 (fig.1).

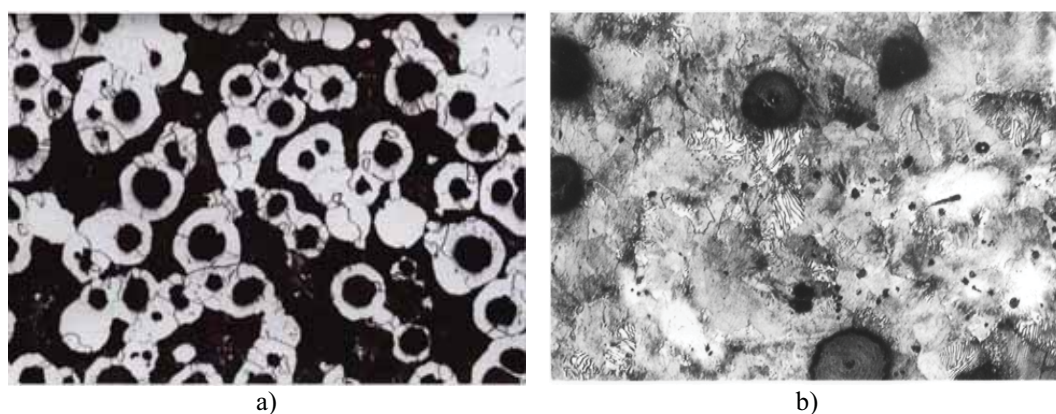


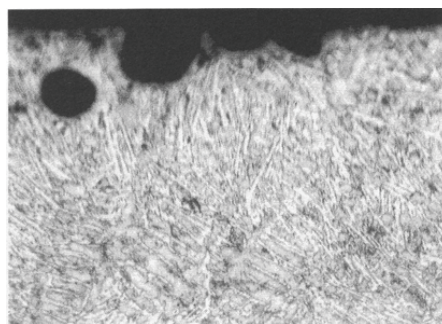
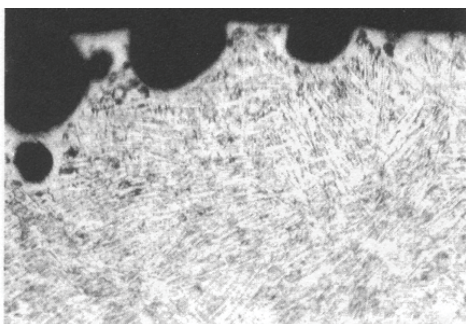
Fig.1. Cast iron micro-structure, a) pearlitic/ferritic cast iron – A, b) pearlitic cast iron – B, microscope magnification 170x, etching with 2% HNO₃

For the purpose of surface remelting of A and B cast iron, the GTAW method was applied with a 2.4 mm diameter tungsten electrode. Argon 4.0 was used as shielding gas. Travel speed of a nonconsumable electrode was 200 mm/min. Cast iron A was remelted once with 80; 120; 160 or 200A current and repeatedly with 160A current. Cast iron B was remelted once and repeatedly only with 160A current.

The phase composition of the remelted layer was determined by X-ray diffraction. Micro-hardness measurements were made for individual structural and phase components using Hanneman tester. Measurements of hardness on the remelted surface were performed using the Rockwell method, C scale. The structure of remelted layers was evaluated on lateral metallographic microsections etched with nital.

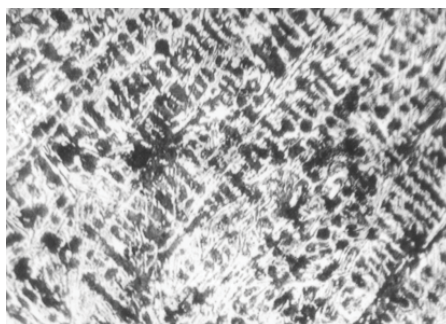
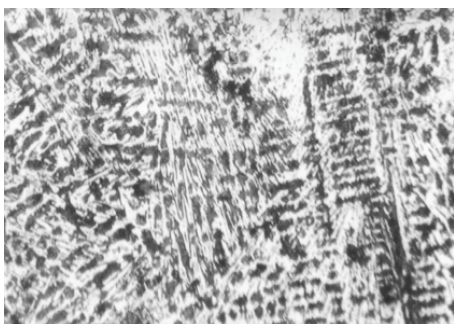
3. Research results and analysis of the results

The structure of cast iron A and B remelted once includes, in the surface zone, cementite and martensite (fig.2), whereas in case of repeated remelting – transformed ledeburite (fig.3).



*Fig. 2. Structure of the surface-adjacent layer of cast iron remelted once
a) cast iron A b) cast iron B, magnification 400x, etching with 2% HNO_3*

Regardless of the cast iron grade and current parameters of the melting process, the phase composition of the remelted layer remained the same.



*Fig. 3. Micro-structure of the surface-adjacent layer of cast iron remelted four times
a) cast iron A, b) cast iron B, magnification 400x, etching with 2% HNO_3*

Regardless of the copper content in cast iron and the number of times remelting is repeated, the intermediate layer (heat affected zone) is characterized with the same type and distribution of structural components. In the micro-area directly adjacent to transformed ledeburite (melted area), there are globular graphite precipitates surrounded by ledeburite and martensite. In that area, partial remelting occurred in the process (fig.4).

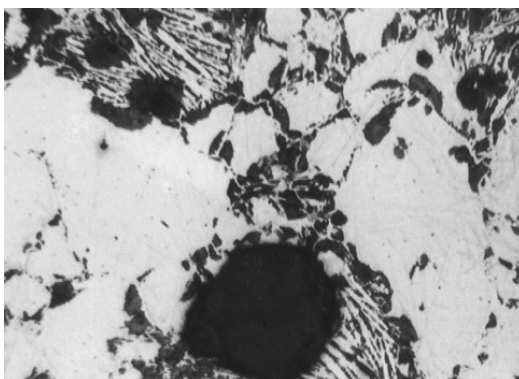


Fig. 4. Micro-structure of the partial remelting zone of cast iron B, remelted 6 times, magnification 400x, etching with 2% HNO_3

Further away from the partial remelting surface, there is a solid layer of martensite. In that layer, there are cracks perpendicular to the remelted surface that are orientated parallel to the remelting direction (fig.5).

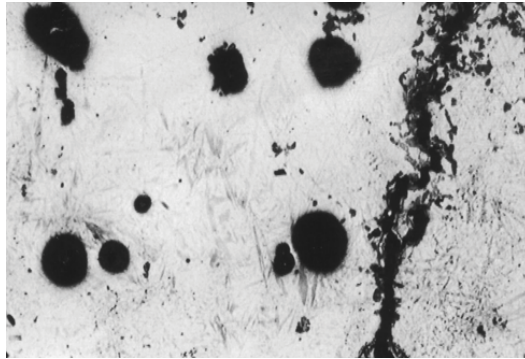


Fig. 5. Micro-structure of the martensitic zone of cast iron B, remelted 6 times, magnification 70x, etching with 2% HNO₃

It must be emphasized that cracks occur only in the martensitic structure zone. They do not continue into the adjacent areas. Further deep, there is a mix of martensite grains against the pearlitic background (fig.6).

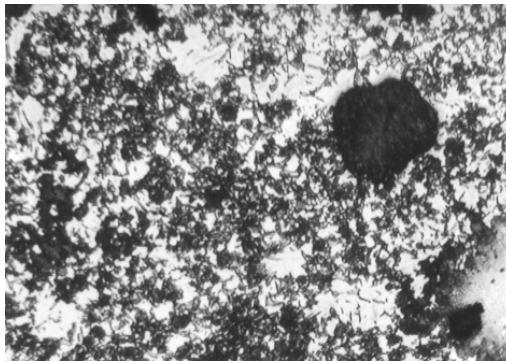


Fig. 6. Micro-structure of the partial martensitic transformation zone of cast iron B, remelted 6 times, magnification 170x, etching with 2% HNO₃

Further away from the surface, there is a fine-grained mix of light martensite grains against the pearlitic background (fig.7). The base material is coarse pearlite (fig.8).

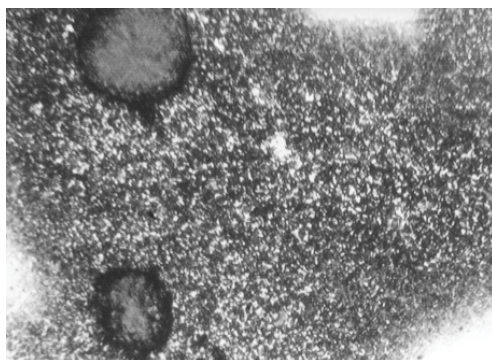


Fig. 7. Micro-structure of the fine-grained martensitic/pearlitic mix of cast iron B, remelted 6 times, magnification 170x, etching with 2% HNO_3

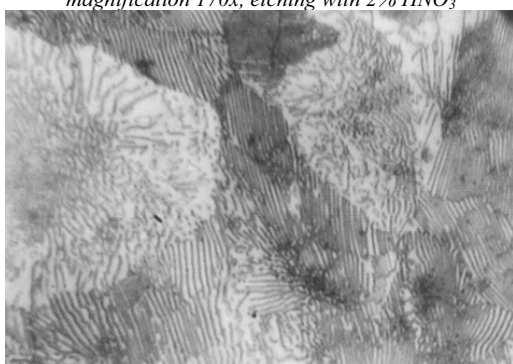


Fig. 8. Micro-structure of the base material, magnification 170x, etching with 2% HNO_3

The width of the remelted layer of cast iron B depends to a small extent on the number of remelting operations so that for the material remelted 6 times it is 13mm and for the material remelted 4 times – 11mm. The thickness of the remelted layer of the ledeburitic structure is greater in case of remelting repeated 6 times – 1.9mm and 1.3mm for remelting repeated 4 times. The width of the martensitic layer under the ledeburite layer is significantly greater for remelting repeated 6 times – 1.3mm, while for remelting repeated 4 times it is 0.8mm.

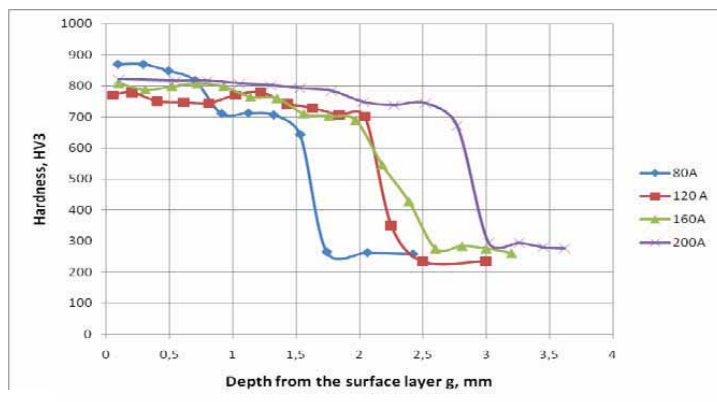


Fig. 9. Distribution of hardness in the hardened layer of cast iron A

The analysis of distribution of hardness HV3 of cast iron A measured along the remelting axis from the surface into the material enables estimation of thickness of specific zones of the remelted layers (fig.9). As the current increases from 80 to 200 A, the thickness of the remelting zone changes from approx. 1.5 to 2.5 mm, while the thickness of the heat affected zone – from 0.4 to 0.6 mm.

Micro-hardness $\mu\text{HV}0.1$ of individual structural or phase components in the layer remelted four or six times of cast iron B is as follows: for remelting repeated 4 times, micro-hardness of ledeburite is 841 μHV and micro-hardness of martensite – 859 μHV , while for remelting repeated 6 times, micro-hardness is respectively 737 and 903 μHV . Micro-hardness of martensite grains in the partial martensitic transformation zone is 702 μHV . Micro-hardness of the fine-grained mix of pearlite and martensite is 373 μHV .

Hardness of cast iron B remelted 4 times measured on the surface is 59HRC, while hardness of cast iron remelted 6 times – 57HRC.

4. Conclusion

When copper cast iron, with both lower (0.48% Cu) and higher copper content (0.95% Cu) is remelted only once, hardness measured on the surface of the material within 66÷68 HRC, which results from the martensitic/cementitic structure of its surface-adjacent layer. Repeated remelting results in the ledeburitic structure of the outer zone. Hardness of the transformed ledeburite is by about 10 HRC lower than hardness of the cementitic/martensitic mix. Hardness and micro-hardness of ledeburite is affected by the number of remelting operations. Fewer remelting operations result in greater hardness and micro-hardness of ledeburite, due to a smaller spacing of cementite in ledeburite. The number of remelting operations has no significant influence on geometric parameters of the remelted material (depth, width of zones). The parameters used for the research did not eliminate micro-cracks within the remelted layer. Whenever the cast iron was remelted repeatedly, micro-cracks in the intermediate layer (martensitic structure) occurred between the remelted material and the base material. Cast iron B with higher copper content has a thicker martensitic layer due to its greater hardenability. In general, the GTAW-based premelting process is an effective method for surface hardening by creating structures of fine tribological properties. Cracks should be eliminated by optimizing remelting conditions for specific chemical composition of cast iron.

References

- [1] Klimpel A., *Metal welding and cutting – technologies*, WNT, Warsaw 1999.
- [2] Orłowicz W. et al.: *Surface hardening of cast iron*, 8th International Conference „Development trends in manufacturing processes”, Section III, p. 65, Zielona Góra 1997.
- [3] Orłowicz W., Trytek A., *Performance aspects of quick crystallization of the outer layer of ductile cast iron castings*, R8, p. 301, 2002.
- [4] Orłowicz W., Trytek A., *Application of GTAW process for surfacing of cast iron castings*, Acta Metallurgica Slovaca, R7, p. 9, 2001.
- [5] Piaskowski J., Jankowski A., *Ductile cast iron*, WNT, Warsaw 1974.
- [6] Trytek A., *Ductile cast iron castings surface hardened with electric arc plasma*, Foundry Review, no. 12, p. 431, 1998.
- [7] Szykowny T., Ciechacki K., *Improving properties of cast iron as tool material through plastic forming and heat treatment*, 7th National Conference, Tool issues in plastic treatment, Bydgoszcz-Venice. p. 145, 2001.
- [8] Szykowny T., Ciechacki K., *Structure and hardness of layers remelted with the GTAW method of ductile cast iron*, Foundry Archives, annual volume 6, no. 18 (2/2), p 195, 2006.

- [9] Wrotny L., *Machining tool design basics*, WNT, Warsaw 1973
- [10] Podrzucki Cz., *Cast iron-structure, properties, application*. ZG STOP, Volume I and II, Cracow 1991.
- [11] Kosowski A., Podrzucki Cz., *Alloy cast iron, AGH course book*, no. 825, Cracow, 1981.
- [12] Orłowicz W., Trytek A., *Ductile cast iron elements surface hardened using the GTAW method*. Naukovi Wisti, National Technical University of Ukraine, Nacionalnyj Transportnij Universitet, Kijiv, No 10, p.21-26, 2005
- [13] Orłowicz W., Mróz M., *Influence of welding parameters on thermal efficiency and melting efficiency of the GTAW process*. Foundry Archives, 2003, vol. 3, no. 10, 74-80.
- [14] Orłowicz W., Trytek A., *Application of the GTAW method for surface hardening of cast iron castings*. Welding Institute Bulletin, vol. 48, book 5, p.63-71, 2004.



AUTOMATIC DRILLED HOLES POSITION CORRECTION FOR A SHIP WINDOW

Piotr Domanowski, Ryszard Wocianiec, Sławomir Bujnowski, Jarosław Zdrojewski

Uniwersytet Technologiczno-Przyrodniczy w Bydgoszczy
al. Prof. S. Kaliskiego 7, 85-789 Bydgoszcz, Poland
e-mail: piotr.domanowski@utp.edu.pl

Abstract

The article presents how to measure and correct the position of the holes on the example of the ship window frame. Ship window frame is manufactured from welded blank and then bent on the bending machine and welded. In order to minimize shape deformation the frame is straightened by hand. Linear dimensions of the frame are about three times larger than the dimension of the location of the holes relative to the edge of the frame. The quality criterion for ship window requires all drilled holes to be located in a straight line. To reach this goal a special procedure was developed to distribute holes in the frame on the base of the window frame shape deviations measured first before drilling. In the following section design of a special machine tool– coordinate drill equipped with a measuring head, as a unit being able to measure and drill automatically. It allows to shuttle processing of frames and to simplify their identification. Construction of the drive and control machining is also presented. The machine has been implemented in a local company, which is a global leader in the production of ship windows.

Keywords: position correction, ship window, shape deviations

1. Introduction

Production of marine equipment, carried out by specialized companies, is characterized by a not very large series of windows of differing geometric features. This forces the use of flexible production, which can quickly be adapted to new products. Ship windows are the outer structure of marine equipment and aesthetic factors are very important. Windows mounted in the hull of the vessel must hold dimensions of the frame for their proper assembly. The windows often have other features too, such as translucency in various weather conditions, fire and radiation protection, and others. The requirements and economic balance of shipowners, enforces automation for this kind of production.

2. Frame manufacturing technology and sources of frame shape errors

Ship windows consist of a frame window and glass package with elements attaching it to the frame. A exemplary window is shown in Fig. 1, the frame cross section elements of the package

mounting shaft is shown in Fig. 2. The technological process of manufacturing marine window frames consists of the following steps:

- generate a workpiece in a T-profile form. It is obtained by linear welding of a structural steel flat bar with a stainless steel rod of square section. Due to the unbalanced position of the rod relative to flat profiles during bonding the workpiece will get large plastic deformation in two planes. To compensate deformation, the rolling mill or if necessary the hydraulic press is used, to improve straightening,
- bending frame corners on CNC bending machine,
- closing the frame with butt welding unit,
- weld treatment on a special CNC milling [1],
- straightening of selected frame parts,
- machining of the holes,
- painting,
- assembly of the window.

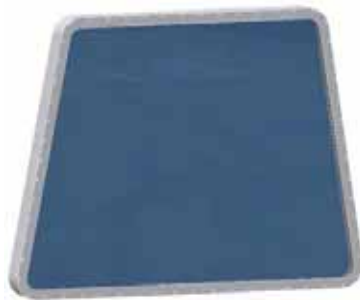


Fig. 1. Design form of ship window

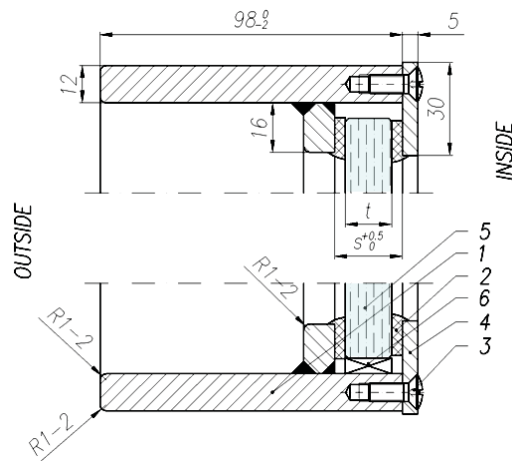


Fig. 2. Window ship cross section: 1 - window frame, 2 - rubber seal, 3 - screw cap, 4 - windows fixing package overlay, 5 - windows pack, 6 - spacing insert

An important component of the technological process is to implement a package of shaft holes. These holes are made simultaneously in frame 1 and overlay 4 and serve to attach the glass package 5 with gaskets 2 and spacers 6 by means of fixing package 4 and screw caps 3. The design documentation specifies the number and location of the holes relative to the edges of the frame. Due to the large dimensions of the frame and the class of accuracy adopted for machining, we are dealing with shape errors of the same order of the dimensions determining the position of the hole in the transverse direction to the frame (the frame in cross section). In practical realization the location of the hole was obtained by measuring the distance from the edge of the frame to the drilled hole. Holes were made to the mid-thickness of the frame. Because for all the holes that distance was the same, the location of the holes relative to the external frame of reference had errors similar to the shape errors of the window frame. Tab. 1 shows the frame shape errors occurred, in the example of a rectangular frame, these errors also occur for frames in the shape of a parallelogram, trapezoid, and others.

3. Theoretical background to hole position correction

The task to improve the visual geometric features consisted on the distribution of the position of the holes in a way that they lied on one line and at the same time that their outline didn't reach the edge of the frame by a distance shorter than 0.5 mm. Efficient was to carry out measurements of the frame attached to the machine tool table and then adjusting the position of the holes. Measurements carried out in the holes framework are presented in Fig. 3:

- in the corner of the frame, in the middle of the arc,
- at points distant by a fixed amount from the end of the arc corner of the frame,
- in a certain number of points equally spaced on the straight parts of the frame.

To carry out framework measurements measuring sensors adapted for this purpose were used in the tip. Foray to the measuring point was carried out in a direction perpendicular to the theoretical position of the frame. The observed deviations of the dimensions correspond to the 13 accuracy class curved window frame. For a window with a length of 3000 mm it corresponds to a tolerance of 3.3mm. Hole spacing with constant distance is not possible: the holes located on the edge of the sheet metal would exceed the 12mm thickness. Thus, their location must be designated for each processing case individually, Fig. 3.

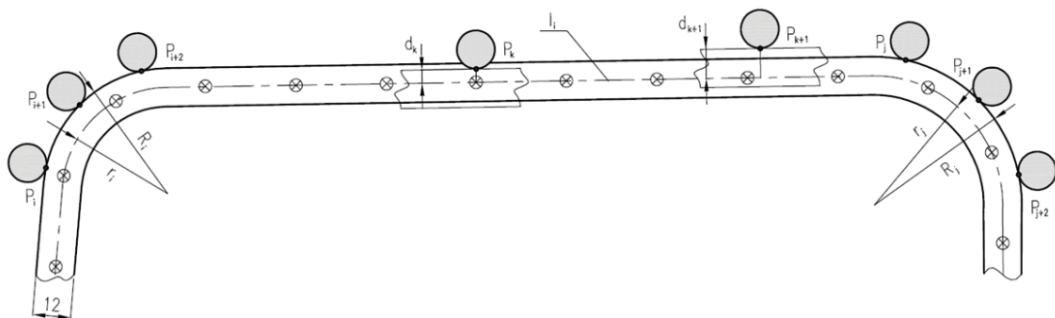
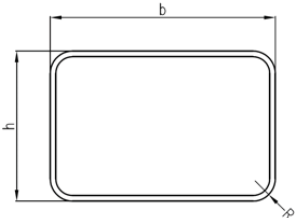
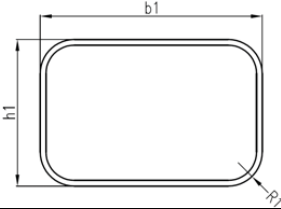
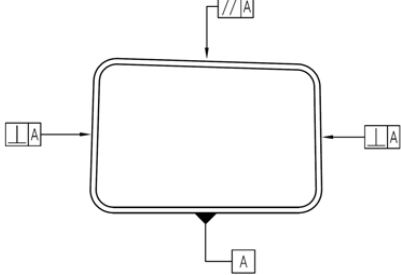
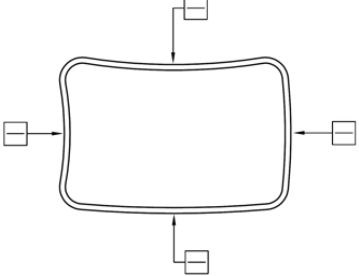
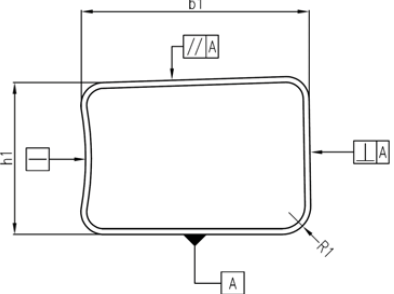


Fig. 3. Determining the line of holes

Tab.1. The most common errors in the shape of the window frames

Original frame shape	Common errors description
	Correct frame
	Errors in the linear dimensions of the frame: width and height, radius values errors
	Parallelism and squareness errors of the window frame sides
	Frame sides straightness errors
	<p>Superposition errors:</p> <ul style="list-style-type: none"> • frame linear dimensions: width and height, radius, values errors, • parallelism and perpendicularity of the sides of the window frame, • frame side straightness.

A drilling procedure starts with the designation of hole centre i and the corner-rays R_i and spacing of the holes arc $r_i = R_i - 6$ mm. The line of openings between successive corners l_i will be tangent between them. To determine the possibility of a correct implementation of the holes is sufficient to calculate the distance d_k of the measuring points P_k made on the straight parts of the frame to the corresponding tangents l_i [2]. The distances satisfying the condition $3.5 \leq d_k \leq 8.5$ are the basis for analysis termination. It's then possible to determine the coordinates of the desired number of holes evenly spaced on the holes line. Distances not meeting the above condition for the M6 thread used disqualify performed calculations, but are however the basis for further search for a correct solution. They generally consist in modifying the position of the line of holes l_i depending on the condition of not meeting the acceptable values of d_k and the position of a particular "defective" point relative to the radius corner. The modification consists in the rotation of the line corresponding to the center of the radius of the right corner and its offset. Such a case requires correction of the position of the holes on the line of the corner holes arc. It comes down to the calculation of the spacing distance of the measurement points of the new corner holes line and verifying the condition of correctness of the position of the hole.

4. Construction of a machine tool to drill holes with automatic placement correction

For the practical implementation of the automatic position correction in terms of production, construction of a special CNC drilling unit equipped the measuring system was economically justified. Following design assumptions were specified, they were the basis for constructing a technical project:

- frame radiuses measurement,
- frame sides measurement,
- frame height measurement in the corners and on the frame straight sides,
- tool length measurement,
- uniform distribution of the holes,
- correction of position holes in a direction perpendicular to the frame,
- automatic tool change,
- performed operations: pre- drilling, drilling, post- drilling, counter boring, threading,
- generating g-code file compliant with a ISO code,
- archiving actual shape of the frame and the position of all drilled holes.

Drilling machine is presented in Fig. 4 and 5. Drilling machine consists of guides 1, where portal 2 moves in the X direction. On the portal there are guides 3, where support 4 moves in the Y-axis direction. Support is equipped with head 5 moving in the Z axis direction. Drilling machine is equipped with two work tables 7, built on the guides 6, which allow you to work interchangeable. The workpiece is fixed to the machining table with lever handles and then the table is moved in the area of machining and then is set and fixed in the base position. The second table at this time is in the outer position which allows the secure exchange of the workpiece. After starting a job cycle the frame at the characteristic points is measured. At the frame measuring cycle is pushed (by the cylinder) out of the enclosure, and moves at the measuring points in the perpendicular to the frame direction. After the measurement at the given point, and probe tip is

moving away, and measuring head will move to the next measuring point. Measuring tip is coupled to the sensor using magnetic clutch that allows disconnection in case of collision at crossings – Fig. 6. To machine holes in the frame special sequence of tools will be used: countersinking, $\varnothing 5$, $\varnothing 6.5$ drill, countersink and tapered with tap M6 holder for threading.

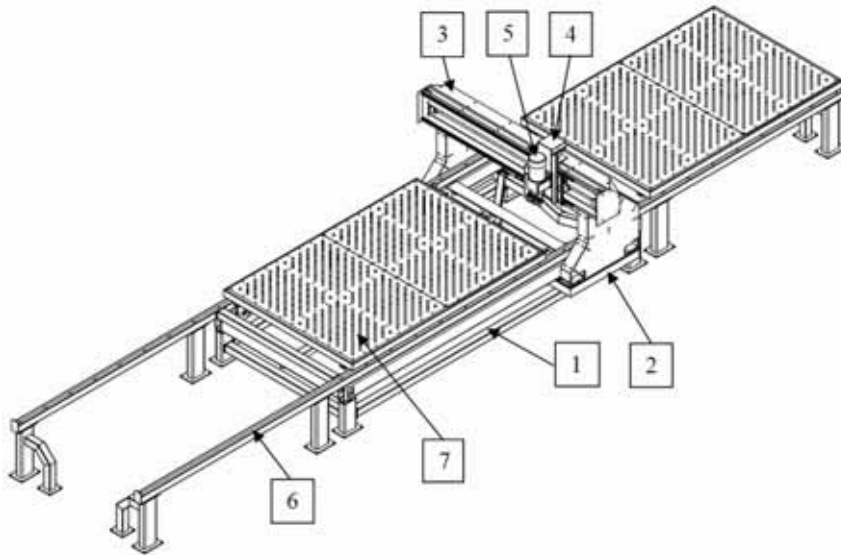


Fig. 4. Main elements of the drilling machine



Fig. 5. View of drilling machine specialized for ship frames



Fig. 6. Automatic measuring cycle of the ship frame

5. Machine tool drive and control

Control of the machine tool has been designed using Mitsubishi elements: FX3U driver [3] with positioning module, and MRJ3 series servos. These servos allow to work with a resolution of 18 bits which gives 262,144 pulses per screw revolutions. Positioning module allows independent work of both axes on the interpolation work and we have choice here, among other things, linear interpolation, circular, etc. For spindle motor control the inverter from Mitsubishi [4] was used, which is attached to the PLC driver. Control system block diagram is shown in Fig. 7 and the practical implementation we used in Fig. 8.

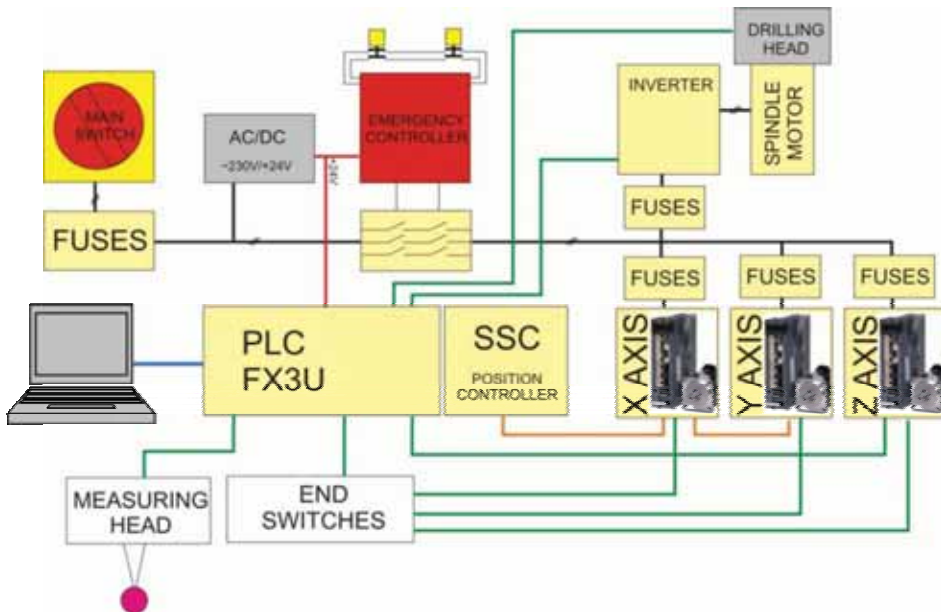


Fig. 7. Block diagram of the drilling machine control system

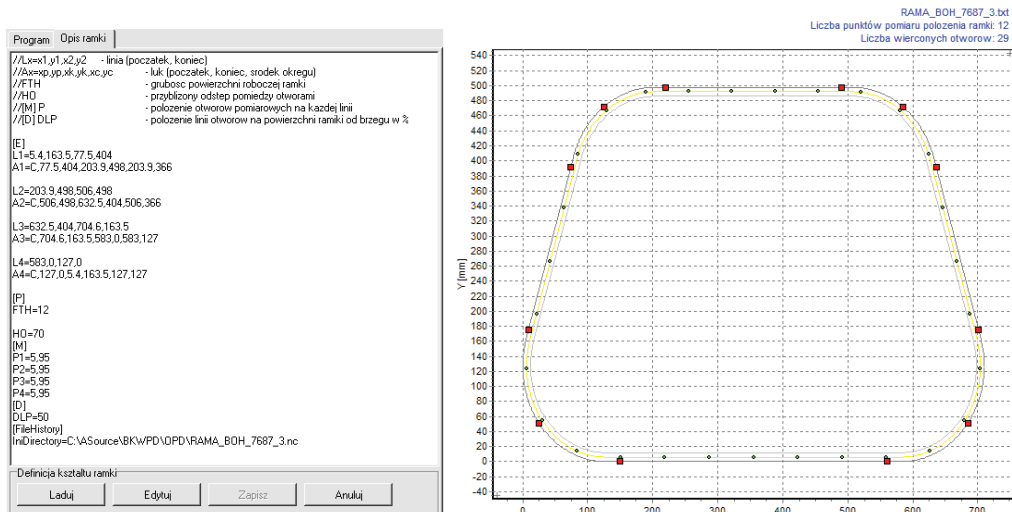
The controller has functions to change the position of the drilling head so it can: pick the right tool, execute cycle of the Z-axis with the specified parameters (feed rate, target position, starting position, along with an adjustable movement speed in each passage), has been implemented. Special functions are associated with the measurement in any direction you choose, spindle speed, initialization of each axis, have been programmed. For each axis there are two pairs of limit switches attached. Internally they are supported by an external controller and they belong to appropriate servo for a given axle. On each axis there also is a SW limit switch responsible for the estimating the zero position of axis, and it also is attached to the appropriate servo. PLC driver communicates with the industrial computer on the 232 link with the Mitsubishi corporate protocol, which allows to read and save any of the flags and registers, and allows the controlling software to run specific procedures in the PLC drivers and to read the status and many other values.



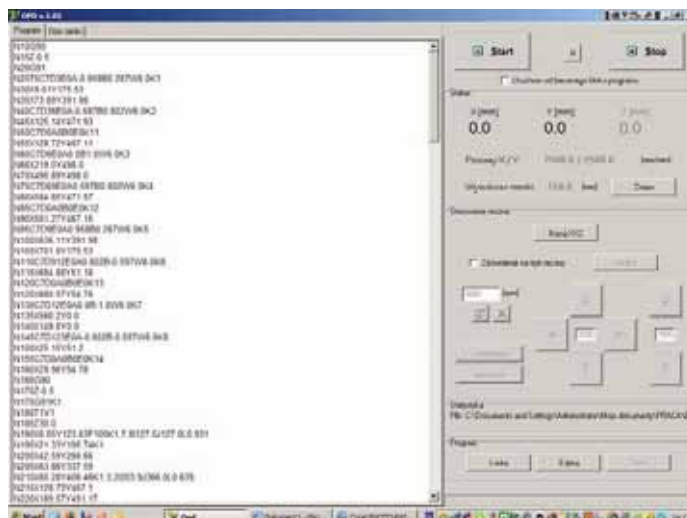
Fig. 8. Control system: a) operator panel, b) interior of the control panel

6. Program to control the machine tool

The developed program to handle the drill allows to load the frame's geometrical features, the number of holes done, to load the number and the location of measurement points data, to generate the ISO for the machine tool controlling, to measure and calculate an adjustment position of each hole, data logging for identified frameworks. The geometry of the ship frame has the characteristic that between straight sections appear corners in the form of arcs. Within the frame description there is the data set describing all arcs and straight sections. Arcs describe the coordinates of the start and end points while the arcs describe the coordinates of the starting and ending points and the coordinates of the center of the arc.



This data can easily be read from executive frame – Fig. 9, or analyze specially for this purpose developed macro used in the CAD program in the company. Almost all types of windows manufactured in the shape of a rectangle, parallelogram and trapezium and ship porthole (round windows) can be described this way. After loading the geometry window and technological data the program generates a g-code controlling the machine tool according to ISO standards – Fig. 10. Code also includes instructions responsible for changing tools and serving functions such as coolant addition for a tool.



Operator's task is to choose a program in the form of g-code or in the text form containing parametric description of the frame and desired settings for the holes placement. If a text form was selected it has to be converted additionally into a ISO code. Generating ISO code, we can decide to:

- enable measurement cycle preceding drilling,
- enable measurement at the corners of the frame (measured in the XY and /or Z),
- the type of strategy for holes position correction (linear, adaptive),
- disable some cycles used when drilling the frame.

Having established the g-code program, after fitting the frame, the operator by pressing the "GO" button runs the machine tool. Based on the initial measurement cycle, data for given correctors is determined. Correctors during drilling cycle enable to calculate the given hole position offset $\langle dx_i, dy_i \rangle$, taking into account the measured deviation of the frame shape and its location on the work table. Correctors can be of two kinds. The first one have a impact on the location of the holes on the straights (sides of the frame), the other - on the arcs (corners). This division is associated with changes in the geometry of arcs, affecting not only the location of its center, but also changes of its radius. When drilling, every frame is labeled and data containing drilled holes position including applied corrections will be saved into the file. This data can be easily used in the future for the service purpose to restore defective or damage ship frame.

7. Summary

Completed theoretical studies have enabled the practical implementation of automated ship windows manufacturing for hole drilling in frames and overlays. The resulting increase in terms of work quality during the process, comparable to manual processing justifies the costs for the construction of machine tool. In addition a window elements identifying was inserted, especially for the frame, the windows and the overlay package, which allows you to restore these elements if they are damaged during the operation. Further work should include optimization of measurement procedures and machine productivity increasing.

References

- [1] Domanowski P., Wocianiec R., *Recykling półfabrykatu profili stalowych*, Inżynieria i Aparatura Chemiczna, No 05/2010, Vol. 10, str. 150-151.
- [2] Jakubiec J., Malinowski J., *Metrologia wielkości geometrycznych*, WNT Warszawa, 2004.
- [3] *Instruction Manual Melservo J3 Series*, Mitsubishi Electric Corporation, 2009.
- [4] *Instruction Manual Inverter FR-A700*, Mitsubishi Electric Corporation, 2009.



NUMERICAL AND EXPERIMENTAL STUDY ON ALUMINIUM PIPE BENDING PROCESS

Piotr Domanowski*, Bartosz Nowak**

* *University of Technology and Life Sciences in Bydgoszcz*
al. Prof. S. Kaliskiego 7, 85-789 Bydgoszcz, Poland
e-mail: piotr.domanowski@utp.edu.pl

** *Kazimierz Wielki University in Bydgoszcz*
ul. Chodkiewicza 30, 85-064 Bydgoszcz, Poland

Abstract

In this paper the analysis of cold working bending process of the aluminum pipe was presented based on both numerical simulations and experimental tests. The parameters such as wall thickness above and below bending axis were compared and discussed for both numerical simulations and experimental tests. The numerical simulations were performed in Abaqus 6.9/CAE computational environment on the basis of finite element method while the bending machine was designed and constructed for the purpose of tests. The usefulness of numerical simulations was also discussed.

Keywords: *bending process, numerical simulations*

1. Introduction

Bending is a process in which metal can be deformed by plastic deformation. This results in changes in both its dimension and its shape. In the bending process material is stressed beyond the yield strength but below the ultimate tensile strength [2, 7]. Bending process is performed on machines called benders.

The aim of this study was to perform the analysis of the bending process on the basis of numerical simulations and of technological process. The study was focused on the changes of cross-sectional dimensions of the pipe which took place during the process.

To fulfilled the aim of the study experimental tests conducted on bending machine in technological process were performed as well as the numerical simulations of the bending process.

The outcomes and the conclusions presented in this paper were used in improving of the design of the automatic bending machine constructed for the purpose of the service in industry [6].

2. Materials and methods

The object of the analysis was the pipe made out of aluminum type WA6060. The pipe belongs to the fuel supply system of the car produced in Poland. The initial diameter of the pipe was 8 mm and initial wall thickness 1 mm. The pipe is bent during bending process. The final shape and dimensions of the bent pipe are shown in Fig. 1.

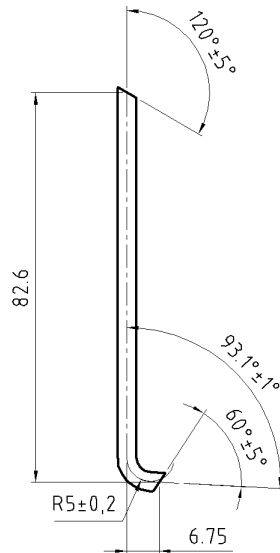


Fig. 1. The main dimensions of the pipe

The material of the pipe consists of aluminum and other additives such as magnesium, silicone and iron. This type of aluminum alloy was designated as EN WA 6060. Material properties of aluminum alloy WA 6060 are presented in Tab. 1. The properties of aluminum alloy were based on literature investigations [4-7] and data given by the producer of pipes. The main material's features includes good strength for tensile stresses and moderate fatigue strength. The material possesses high ability to forming profiles with complicated shapes.

Tab. 1. Mechanical properties of aluminum alloy WA 6060

Property	Symbol	Value
Young modulus	E	70GPa
Poisson's ratio	ν	0.30
Yield strength	R_{p02}	160MPa
Ultimate tensile strength	R_m	190MPa
Elongation	A	0.16

The process of pipe bending is performed in room temperature. The pipe is wrapped around the rotating roller. The geometry of the roller (rotating bending die) is presented in Fig. 2.

Numerical calculations were performed in computational environment Abaqus/CAE 6.9 with the use of finite element method. The graphical preprocessor of that environment was used for

preparation of geometry of numerical model. Processor of computational environment was used to perform calculations based on Newton-Rawson procedure [3, 8]. The results of performed calculations were gathered and presented with use of post-processor of Abaqus/CAE 6.9 computational environment.

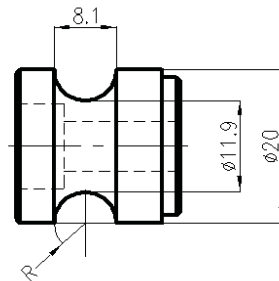


Fig. 2. The main dimensions of the roller

The geometry of the numerical model of the pipe consisted of: pipe, upper holder of bending head, lower holder of bending head integrated with rotational die, upper holder of the feeding head and lower holder of the feeding head. The geometry and the orientation of the elements mentioned above are presented in Fig. 3.

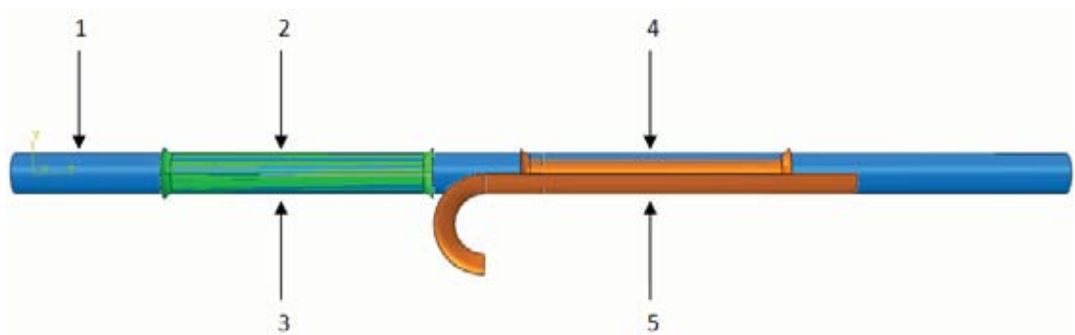


Fig. 3. Geometry of numerical model; 1- pipe, 2- upper holder of the feeding head, 3 - lower holder of the feeding head, 4 - upper holder of the bending head, 5 - lower holder of the bending head integrated with rotational die

Nonlinear model of aluminum material was used in calculations. Properties of aluminum material WA 6060 supplied by the producer were mentioned in the previous section of the text. Modeling of aluminum material was based on linear elastic-plastic model of material with linear hardening elaborated on the basis Tab. 1. Isotropic hardening was defined on the basis of yield stress and yield strain. Material that was taken into account was isotropic and homogenous. The characteristics of stress-strain relations for simplified aluminum material model based on technical data delivered by producer of material and full stress-strain relation in extension test are presented in Fig. 4.

In the numerical analysis the contact between the following surfaces was defined: upper holder of the feeding head - pipe, lower holder of the feeding head - pipe, upper holder of the bending head - pipe, lower holder of the bending head integrated with rotational die - pipe. In numerical procedure the value of static friction coefficient was $\mu_s = 0.2$ and kinematic friction coefficient $\mu_k = 0.05$. The following boundary conditions were applied to the numerical model:

upper holder of the bending head - full fixation (all degrees of freedom restrained) only rotations in Y-Z plane allowed, lower holder of the bending head integrated with rotational die - full fixation (all degrees of freedom restrained) only rotations in Y-Z plane allowed, upper holder of the feeding head - rectilinear movement along Z axis with the velocity equaled to angular velocity of roller, lower holder of the feeding head - full fixation (all degrees of freedom restrained).

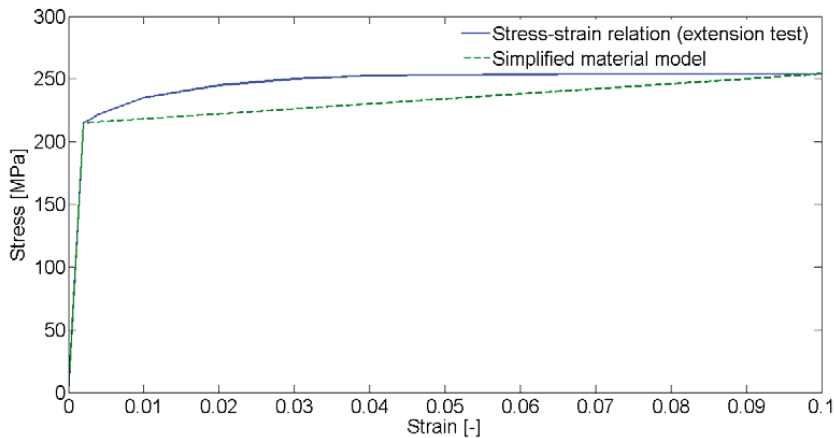


Fig. 4. Characteristics of stress-strain relations

Rotation was realized by revolution of lower holder of bending head integrated with rotational die and upper holder of the bending head by angle 90° . Translations and rotations are shown in Fig. 5. Boundary conditions and kinematics of used in numerical simulations were similar to those in experimental tests.

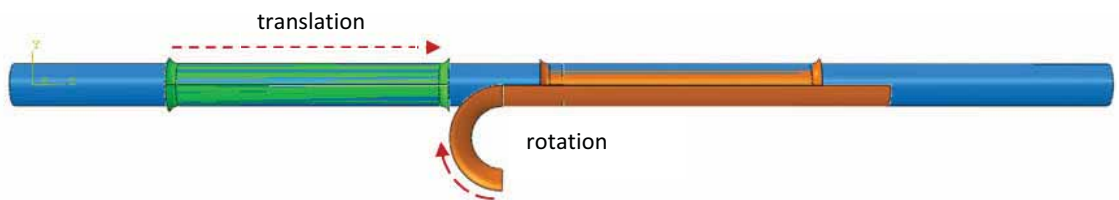


Fig. 5. View and description of boundary conditions

Discretization of the pipe with the use of finite element method was performed by use of continuum hexahedral finite elements with linear shape function. Eight nodes were located in the corners of each element. Each node had three translational degrees of freedom. The finite elements were labeled according to [1] as C3D8R. The number of finite elements equalled for pipe was 8388. Discretization of the upper holder of bending head, lower holder of bending head integrated with rotational die, upper holder of the feeding head and lower holder of the feeding head was done by use of rigid non-deformable shell finite elements. Those finite elements were labeled according to [1] as R3D4. The number of finite elements was as follows: the upper holder of bending head 1560, lower holder of bending head integrated with rotational die 1896, upper holder of the feeding head 1560 and lower holder of the feeding head 1560.

The total number of finite elements was 15 650, while total number of nodes was 21 209. Due to symmetry of the numerical model only half of the model was taken into account.

The view of mesh of the pipe and holders are presented in Fig. 6.

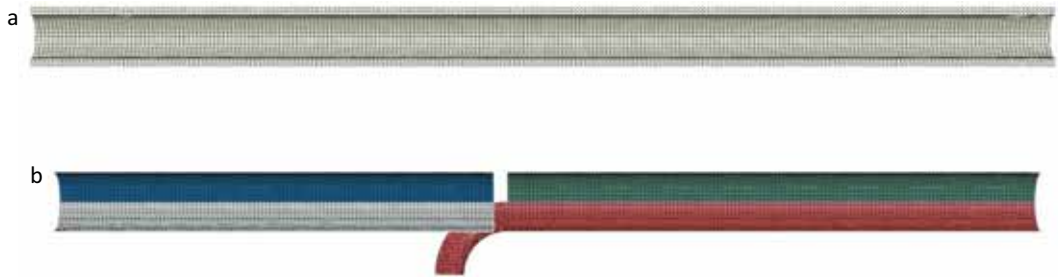


Fig. 6. Finite element mesh; a - pipe, b - holders (tools)

In numerical simulations the problem was described by the following equation: (1):

$$\mathbf{M}\ddot{\mathbf{u}} + \mathbf{C}\dot{\mathbf{u}} + \mathbf{K}\mathbf{u} = \mathbf{P} \quad (1)$$

where:

\mathbf{M} – mass matrix,

\mathbf{C} – damping matrix,

\mathbf{K} – stiffness matrix,

\mathbf{P} – vector of external forces,

\mathbf{u} – vector of nodal displacements,

$\dot{\mathbf{u}}$ – vector of nodal velocities,

$\ddot{\mathbf{u}}$ – vector of nodal accelerations.

Direct integration method was used for solving equation:

$$\dot{\mathbf{u}}_{(i+\frac{1}{2})}^N = \dot{\mathbf{u}}_{(i-\frac{1}{2})}^N + \frac{\Delta t_{(i+\frac{1}{2})} + \Delta t_{(i-\frac{1}{2})}}{2} \ddot{\mathbf{u}}_{(i)}^N \quad (2)$$

$$\mathbf{u}_{(i+1)}^N = \mathbf{u}_{(i)}^N + \Delta t_{(i+1)} \dot{\mathbf{u}}_{(i+\frac{1}{2})}^N \quad (3)$$

where:

i – iteration,

N – degree of freedom.

The machine for automatic pipe bending was constructed for purpose of realising the bending process. It consists of the following devices: material feeder, bender (bending device), unit of semi-finished products and unit of finished products. Scheme of the bending device is presented in Fig. 7. The bending device consists of: upper holder of the feeding head, lower holder of the feeding head, upper holder of the bending head, lower holder of the bending head integrated with rotational die.

The upper holder of the feeding head is connected to force actuator equipped with adjustable pressure force in range 0 - 300 N. The machine is equipped with feeder of the material which includes holder and force actuator. The machine is designed for running in automatic cycle. The elements responsible for automatization of the process are not shown in Fig. 7. Pneumatic actuators and servo-motors were used in engineering of power transmission. Power drive of rotation holder was realized by motoreducer, which consists of servo-motor and planetary gear with velocity ratio of 1:100. The planetary gear used in construction of the power drive of rotation holder had circumferential backlash smaller than $5'$.

The bending process is realized on the bending machine in the following way. The pipe is loaded to bender device from semi-finished products unit and secured firmly in pneumatic holders. The pressure force of the holders is set to ensure the secure fixation of the pipe. Then the rotation pneumatic holder rotates about the angle of 90° and makes the pipe to be bent. When the bending is finished rotation pneumatic holder rotates back about the angle of 90° and the pipe is pushed forward to the jaw of the saw. The desired length of bent pipe is cut. After that process starts again.

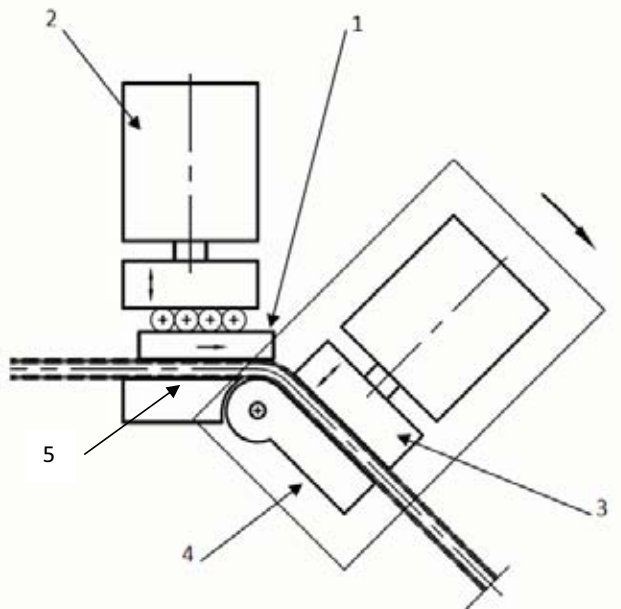


Fig. 7. Scheme of the bending device; 1- upper holder of the feeding head, 2 - lower holder of the feeding head, 3 - upper holder of the bending head, 4 - lower holder of the bending head integrated with rotational die, 5 - pressure force actuator

3. Results and discussion

The results consist of outcomes obtained on the basis of numerical simulations and experimental tests. They include: pipe's diameter measured in the bending plane, thickness of the pipe's wall above bending axis and thickness of the pipe's wall below bending axis. Measurements were done on selected fragment of the pipe, which is shown in Fig. 8. It represents wrapped

around the roller die fragment of the pipe in range $0^\circ - 90^\circ$. The measurements were performed every 5° .

The results of numerical simulations were obtained with use of pre-processor of Abaqus/CAE computational environment. Measurements in experimental tests were conducted on the basis of computer aided measurements of pipe's micro- section. The scheme for experimental measurements of pipe's parameters after bending process is presented in Fig. 9.

The cross-section of the pipe with the distribution of pipe's thickness wall and the magnitude of equivalent plastic strains were presented in Fig. 10 while cross-section of the pipe for experimental tests in Fig. 11.



Fig. 8. The measuring length of the pipe after deformation

In discussion the results obtained from numerical simulations and experimental tests have been compared. It can be observed that during bending process the cross-sectional area of bending material was changed. It was caused by changing of transversal dimensions of compressed and tensioned layers of the material. The differences between numerical and experimental results were in range 1% - 26% for all parameters on the measuring length.

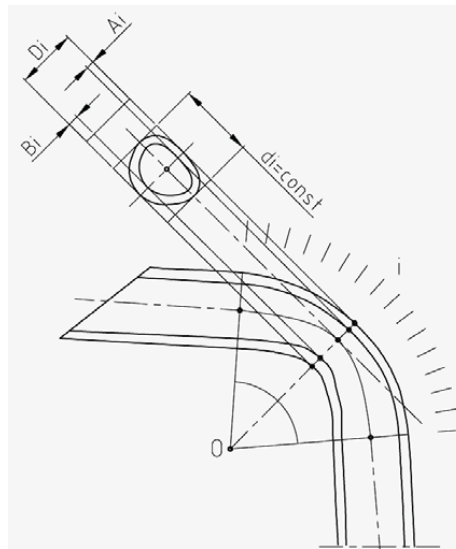


Fig. 9. Measuring of pipe's thickness

The comparison of distribution of the pipe's diameter on the measuring length of the pipe for numerical simulations and experimental tests was shown in Fig. 12. It can be noticed that the pipe's diameter decreases in the plane of bending. The smallest value obtained in numerical simulations was 5.11 mm while in experimental tests was 5.92 mm. The difference between these values results 16 %. It must be stated that the position of the smallest value in experimental tests is shifted by 1° comparing to numerical simulations. However experimental and numerical results are in good qualitative agreement.

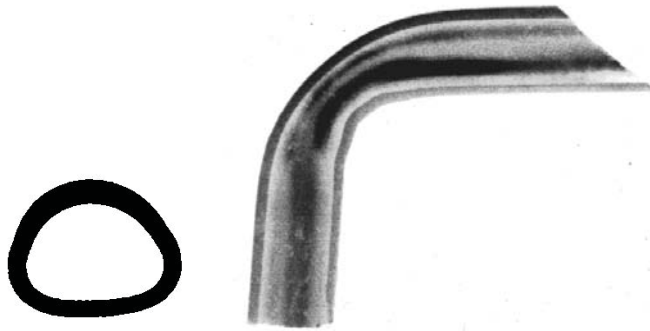


Fig. 10. Section of the pipe - experimental test

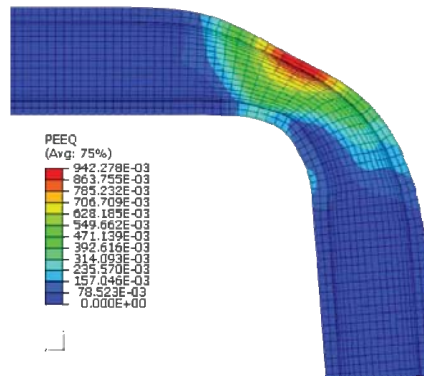


Fig. 11. Distribution of pipe's thickness wall and the magnitude of equivalent plastic strains

The comparison of distribution of the pipe's thickness above the bending axis on the measuring length of the pipe for numerical simulations and experimental tests was shown in Fig. 13. The smallest value obtained in numerical simulations was 0,56 mm while in experimental tests was 0.71 mm. The difference between these values results 26 %. It must be stated that the position of the smallest value in experimental tests is shifted by 2° comparing to numerical simulations. However experimental and numerical results are in good qualitative agreement.

The comparison of distribution of the pipe's thickness below the bending axis on the measuring length of the pipe for numerical simulations and experimental tests was shown in

Fig. 14. The smallest value obtained in numerical simulations was 0,84 mm while in experimental tests was 0.98 mm. The difference between these values results 17 %. It must be stated that the position of the smallest value in experimental tests is shifted by 5° comparing to numerical simulations. However experimental and numerical results are in good qualitative agreement.

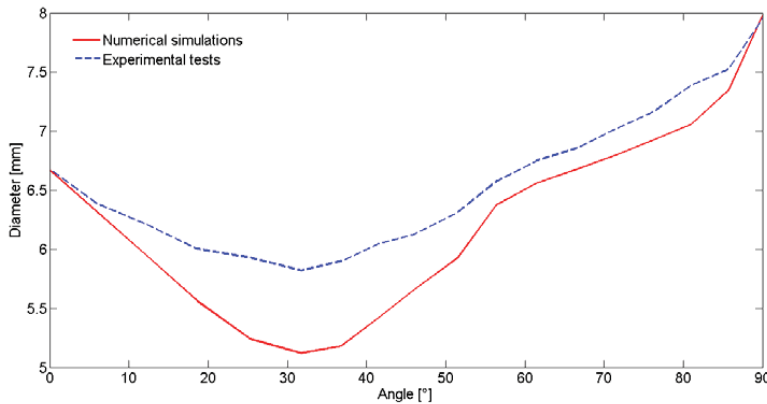


Fig. 12. The comparison of distribution of pipe's diameter on measuring length for experimental and numerical results

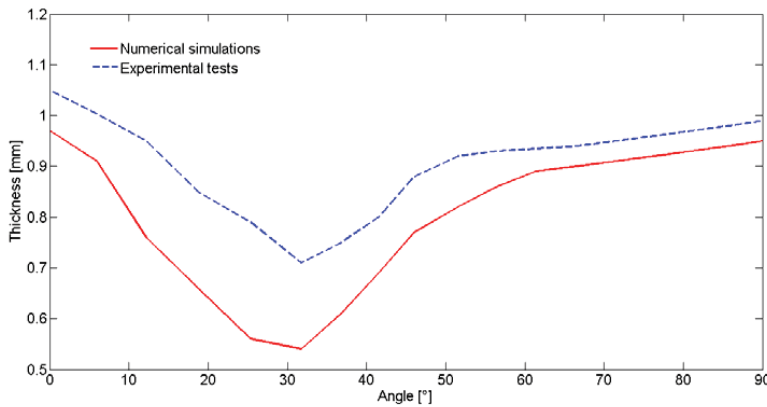


Fig. 13. The comparison of distribution of pipe's thickness above neutral axis of bending on measuring length for experimental and numerical results

4. Conclusions

It can be seen from the analysis presented above that the results of computer simulations and experimental tests are in good qualitative agreement, even though application of simplified material model in numerical analysis. In some cases the values of numerical and experimental results were different. This discrepancy could be caused by application of aluminum material model which was based on linear elastic-plastic model with linear hardening, which in fact was a significant simplification. However the technical data of the material supplied by the producer

often includes only parameters such as Young modulus, Poisson ratio, Yield stress, Ultimate stress which are not sufficient to obtain full stress-strain relation.

Results improvements could be obtain by application of more sophisticated model of the material.

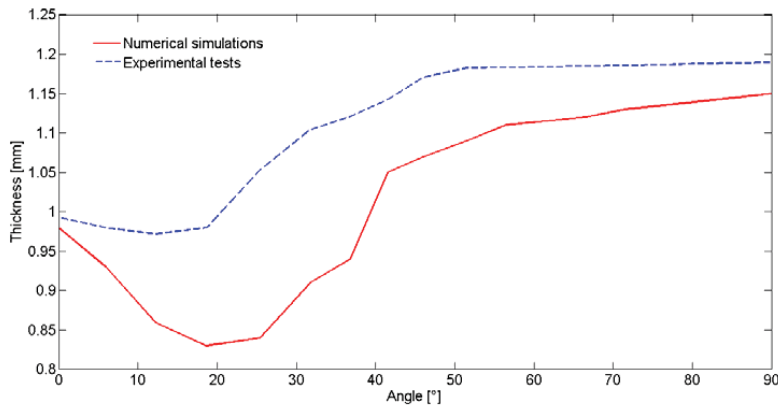


Fig. 14. The comparison of distribution of pipe's thickness below neutral axis of bending on measuring length for experimental and numerical results

References

- [1] ABAQUS. *Abaqus manuals*. Inc. Providence, 2005.
- [2] Altan T, *Metal forming handbook*. Springer Verlag Berlin Heidelberg, 1998.
- [3] Bathe K. *Finite Element Procedures*. Prentice Hall, 1996.
- [4] Boyer H E. *Atlas of strain-stress curves*. ASM International, 1987.
- [5] Dixit U M, Dixit U S. *Modeling of metal forming and machining processes by finite element and soft computing methods*. Springer Verlag London, 2006.
- [6] Domanowski P, Wocianiec R. *Structure Design and Numerical Control System of Automatic Pipe Bending Machine*, 13th International Conference on Developments in Machinery Design and Control, Bydgoszcz, Poland 2009.
- [7] Wogoner R. H, Chenot U. S. *Fundamentals of metal forming*, Wiley, 1996.
- [8] Zienkiewicz O. C., Taylor R. L. *The Finite Element Method Vol. 1*. Butterworth-Heinemann, 2000.



STABILITY CONDITION OF THE TRACTOR TRAILER VIBRATIONS

Henryk Holka

University of Technology and Life Sciences, Faculty of Mechanical Engineering,

Al. Prof. S. Kaliskiego 7, Pl – 85-789 Bydgoszcz, Poland

e-mail: holka@utp.edu

Abstract

An important problem connected with the dynamics of vehicles are transverse vibrations of transport aggregates such as tractor, truck-trailer. This is of big importance as the discussed units are achieving higher and higher speeds, thereby posing hazard to traffic safety, besides, it is worth knowing the nature of these vibration, that is, whether they are forced or self- excited. The above mentioned issue was given much attention, in the former Soviet Union countries, and also later, [1], [2], [4]. In work [5], vibrations of a trailer whose connection to the truck or tractor by a rotary joint with one degree of freedom, was studied. However, it was a certain simplification of the real system, therefore, in this work a connection with two degrees of freedom has been introduced. The equation of motion have been derived and then the influence of the system parameters on the trailer vibration have been analyzed. The investigation showed that stability of the system is determined mostly by the damping.

Keywords: transfers vibration, tractor trailer, stability, damping

1. Motion equation model

The system presented in Fig.1 will be studied.

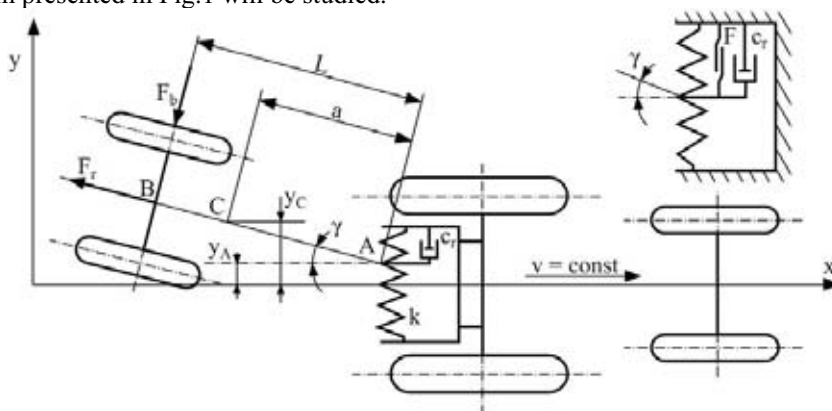


Fig. 1. Two degree of freedom model of a trailer

In order to examine all the effects, which occur during the motion, it was assumed that the unit is moving along a straight and horizontal road with the constant speed v .

Assuming $\sin\gamma \approx \gamma$, $\cos\gamma = 1$ $F = f_r \cos\gamma$, $F_f = fG_k$, the equation of motion has the form;

$$\begin{aligned} m \left(\ddot{y} + a \ddot{\gamma} \right) &= -C r_o \dot{y}_A - k y_A - f_r F_f + F_f \gamma - F_b; \\ a m \ddot{y} + J_A \ddot{\gamma} &= -L F_b, \end{aligned} \quad (1)$$

where:

- m [kg] - body mass,
- J [kgm²] - moment of inertia,
- k [Nm⁻¹] - spring stiffness,
- c_r [Nsm⁻¹] - damper rate,
- F [N] - force of dry friction,
- F_r - coefficient of dry friction,
- F_b [N] - side force,
- F_f [N] - force of rolling friction,
- f - coefficient of friction,
- G_k [N] - gravity force of wheel section.

The unknown side force can be obtained from the form [1],

$$F_b = k_y \Psi, \quad \text{and } \Psi = \gamma + \frac{\dot{y}_A + L \dot{\gamma}}{v} \quad (2)$$

where: k_y N deg⁻¹ - resisting coefficient.

Now the equation (1) can be written as:

$$\begin{aligned} m \ddot{y}_A + \left(c_r + \frac{k_y}{v} \right) \dot{y}_A + k y_A + a m \ddot{\gamma} + \frac{k_y L}{v} \dot{\gamma} + (k_y - F_f) \gamma &= -f_r F_f, \\ a m \ddot{y}_A + \frac{k_y L}{v} \dot{y}_A + J_A \ddot{\gamma} + \frac{k_y L}{v} \dot{\gamma} + k_y L \gamma &= 0. \end{aligned} \quad (3)$$

A stability condition can be investigated from the characteristic equation

$$\begin{vmatrix} ms^2 + \left(c_r + \frac{k_y}{v} \right) \lambda + k & ams^2 + \frac{k_y L}{v} \lambda + (k_y - F_f) \\ ams^2 + \frac{k_y L}{v} \lambda & J_A s^2 + \frac{k_y L^2}{v} \lambda + k_y L \end{vmatrix} = 0 \quad (4)$$

and from above, equation (4) can be written as: a

$$a_o \lambda^4 + a_1 \lambda^3 + a_2 \lambda^2 + a_3 \lambda + a_4 = 0 \quad (5)$$

where :

$$\begin{aligned} a_o &= m J_A; \\ a_1 &= \left(k_r + \frac{k_y}{v} \right) J_A + (L - 2a) \frac{m k_y L}{v}, \\ a_2 &= (L - a) m k_y + a m F_f + c J_A + k_r \frac{k_y L^2}{v}, \\ a_3 &= \left(k_r v + c L + F_f \right) \frac{k_y L}{v}, \\ a_4 &= c k_y L. \end{aligned}$$

The equation (4) has a stable solution if:

$$a_i > 0 \text{ and} \quad (6a)$$

$$a_3 (a_1 a_2 - a_3 a_0) - a_1^2 a_4 > 0. \quad (6b)$$

Since the coefficient of dry friction is a not component of coefficient a_1 and characteristic equation, it can be concluded that it does not affect on the stability system. Let us analyze the influence of the system parameters on the trailer vibration stability.

Coefficient a_0 always positive;

Coefficient $a_1 > 0$ if $v > 0$ hence we receive:

$$a < \left(k_r + \frac{k_y}{v} \right) \frac{J_{Av}}{2mk_y L} + 0,5L. \quad (7)$$

For the trailer speed $v > 0$, the distance of mass center from the center of connection should be :

$$a < 0,5L + \frac{J_A}{2mL}. \quad (8)$$

If this condition is not fulfilled there occur conditions for transverse vibrations.

If $a_1 > 0$, then the remaining coefficients (a_2, a_3, a_4) with $v > 0$ have also positive values which can not be said about inequality (6b). With positive values of all coefficients, the above mentioned inequality can be negative.

2. Example

For determination of the negative influence of vibrations on the trailer stability, an example for the following data: $m=3522$ kg, $J_c=3453$ kg m², $L=2,5$ m $a=2,15$ m, $k_y=80000$ N deg⁻¹, $k=5886$ N/m, $c_r=2452$ N sm⁻¹, $v=8,6$ m/s will be analyzed.

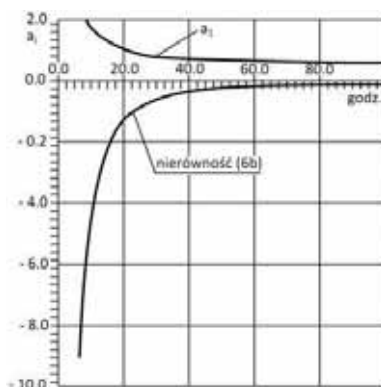


Fig. 2. Dependence of coefficient a_1 and inequality (6b) on the speed

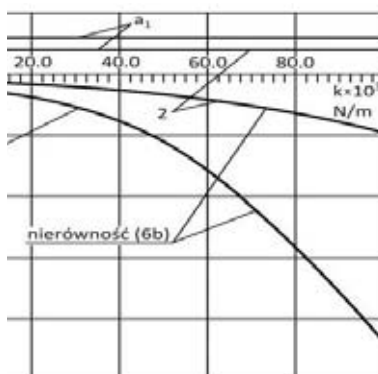


Fig. 3. Dependence of coefficient a_1 and inequality (6b) on stiffness k : 1 - asphalt, $v=30\text{km/h}$, 2 - unpaved road, $v=14\text{km/h}$

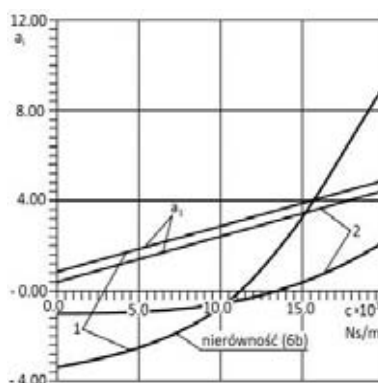


Fig. 4. Dependence of coefficient a_1 and inequality (6b) on damping c , 1- $v=14\text{km/h}$, 2- $v=30\text{km/h}$

In figure 2, there has been presented a dependence of a_1 coefficient and inequality (6b) on the trailer speed. The figure shows that for all speeds $a_1 > 0$, whereas, inequality (6b) is negative. However, for speeds higher than 40km/h , inequality (6b) and vibration amplitudes are insignificant.

Fig.3 shows a dependence of a_1 coefficient and (6b) inequality on the connection stiffness for two speeds and different road surfaces. For all the values of coefficient $a_1 > 0$, inequality (6b) is negative. However, it can be noted that the absolute value of inequality (6b) increases along with k stiffness value rise.

Fig.4 demonstrates the dependence of coefficient a_1 and inequality (6b) on the connection damping. From the chart it can be seen that with $c > 10 \cdot 10^3$, both curves are positive and the vibrations decrease rapidly.

3. Conclusions

1. Increasing the trailer connection makes the vibrations become unstable.
2. Damping in the connection has the largest influence on the trailer vibrations.
3. Being familiar with the impact of stiffness and damping is of great importance for constructors.

References

1. Guskov V. V.: Tractor trains. Mashinostrojenie, 1982.
2. Guskov V. V.: Tractors. Theory. Mashinostrojenie, 1988.
3. Borkowski W.: Dynamika maszyn roboczych. Warszawa, WNT, 1996.
4. Holka H.: Obciążenie i drgania agregatów traktorowych. Praca habilitacyjna, Mińsk, Białoruś, 1998.
5. Holka H., Peszyński K.: Modelling and analysing of transfers vibration of the tractor trailer. Engineering Mechanics 2001, Svratka, Czech Republic, 2001.



COMPUTER-AIDED SYSTEM TO ALLOTMENT OF THE OPERATING TASKS IN THE SHIP ENGINE ROOM

Piotr Kaminski

Gdynia Maritime University,

Morska Str. 83,

81-226 Gdynia,

E-mail: pkam@am.gdynia.pl

Abstract

The frequent causes of ships' detentions by port authorities are abnormalities of ship power plant functioning. Each extended ship lay time in port results in a waste of ship operating time thus costs rise to ship owners. This is connected with improper ship power plant management. In order to avoid this, a ship engineer should have at his disposal computer aided system supporting him in the managing of the ship power plant. The prototype of a computer-aided system of operational and maintenance task assignation in ship engine room has been presented in this paper. This system contains three modules that respond of decision-making process for three stages: collecting essential information about operating tasks, selecting of operational and maintenance tasks, generating of the optimal schedule for the set of the determined conditions. For allotment problem was formulated, in the most substantial operating states of a ship like lay time in harbour and sea voyage, the knapsack algorithm' was applied. The mathematical model uses two-criterions optimization for operational and maintenance task assignation in the ship engine room.

Keywords: *Ship engine room, tasks scheduling, AHP method*

1. Introduction

According to many experts to reach correct management of ship power plant involves great difficulties to decision-making persons, i.e. ship chief engineers. This is caused i.e. by:

- increasing number of automated ship systems,
- multiple number of operational processes executed in parallel,
- lack of appropriate information making it possible to quickly master systems and task planning,
- frequent changes of staff members,
- increasing number of requirements for safety of persons, ship and environment.

Moreover changing international maritime law imposes many additional tasks dealing not only with new procedures connected with safety at sea but also with their detail documentation. Such state leads to a situation in which decision-making is more and more difficult and knowledge and experience of ship engineers may appear insufficient. In such conditions making a decision dealing with power plant management may be incorrect or irrational and in consequence causing various losses, e.g. loss of ship service time leading this way to increasing overall cost of ship operation. In order to eliminate such situations ship engineers should have at his disposal a software which could be a „tool” aiding him in organizing ship power plant management process. Such system would collect information concerning realization of all operations in power plant or make use of data bases of already functioning information systems, analyse any limitations associated with

their realization and finally advising ship engineer on which tasks and in which sequence they have to be realized.

In ship power plant a team often consisted of several persons performs operations resulting from realization of many tasks of different time horizons, realized in parallel. This requires, from chief engineer, to make rational decisions concerning a.o. determination of a kind, range, sequence and executors of operations. To make such decisions it is necessary to collect and process suitable information. Among other, the following can serve as their sources:

- technical and operational documentation of machines and installations, requirements associated with safety at sea and marine environment protection (conventions, codes, rules of classification societies, rules of maritime administrations, ship owner's regulations etc.),
- data bases of information systems used in ship power plant,
- assessment of technical state of ship power plant machines and systems,
- assessment of state of provisions (fuels, lubricants, spare parts etc.),
- occurrence of a destructive event, e. g. machine failure,
- assessment of feasibility of appropriate actions, e.g. expected time of port staying, deadline of subsequent shipyard's repair etc.,
- assessment of accessibility of an external service in a given shipping region,
- assessment of capability of crew to realize planned operations,
- assessment of crew experience associated with carrying out given kinds of operations [2].

2. Solution of the chief engineer decision-making problem

The main problem to be solved by ship chief engineer within the scope of ship power plant management can be formulated as follows: *„Knowing a set of tasks to be realized as well as taking into account available means (technical, personnel and time resources), operational requirements concerning ship, as well as limitations of different kind, one should make choice of appropriate operations and integrate them into one ordered set of actions”*. In other words the thing is that a decision should be taken as to such above mentioned operations whose realization would be most effective from the point of view of ship service.

The decision problem of ship power plant technical management is defined as the following triple:

- the set of decision variables, (i.e. the set of all operations to be executed),
- the set of operators to which appropriate operations should be assigned,
- as well as that of the relations r understood as the relationships between elements of the sets and also containing some features of the elements.

In the process of decision making by ship engineer dealing with assigning the operational tasks to engine room staff the following three main phases should be distinguished:

- collecting and processing all available and necessary data (those earlier mentioned and those presented in [1]),
- selecting the tasks whose realization is constrained by all possible operational limitations as well as ambient conditions in which a given decision is made [3],
- assigning the earlier selected tasks to power plant crew members, in compliance with their competences so as to obtain the best schedule from the operational point of view [2].

3. The data collection module

To generate the appropriate operating tasks schedule it is necessary to use essential information. Such information are collected on a ship in a different form: on the new ships in the computer databases, on the older ships mostly in the paper documentation form.

The data collection module of prototype computer-aided system to support operating tasks scheduling in engine room as an interface is presented on Figure 1. It contains a list of the example-tasks for the selected unit from the engine room systems structure and attributed to each the number of parameters. These parameters are: the area of operation (operating, maintenance, safety, provision), type of the task (planned, emergency, etc.), execution time, frequency of task repetition, the ship's operating stage, the engine room's operating stage in which the task performance can be achieved, the operator executed this task (according to the duties), etc. Data collected by this module are stored in external database created in MS Access. This allows to other systems or programs used the data by SQL. This also permitted to use the databases of other computer systems used in the engine room by the presented system. On the Fig.1 is presented the graphical interface of the computer system consists of two main parts. The first of them, shown on the right-hand side, is characteristic for systems applied in engine room and it demonstrates of power plant structure.

Engine Room Structure: SIŁOWNIA OKRĘTOWA

Tasks

Lp.	Zadanie
1.	Badanie awaryjnej pompy pożarowej
2.	Analiza oleju obiegowego silnika głównego
3.	Badanie pianowej instalacji gaśniczej
4.	Czyszczenie lub wymiana filtra powietrza
5.	Kontrola / naprawa sprzęgła pompy rezerwowej oleju o napędzie elektrycznym

Tasks Parameters: BADANIE AWARYJNEJ POMPY POŻAROWEJ

PARAMETERS	SPARE PARTS AND SPECIAL TOOLS	TASK DESCRIPTION	
Operating area Bezpieczeństwa	Frequency repetition (absolute time) 31	Completion date 29-11-2007	Completion time 5
Type of task Awaryjne	Frequency repetition (work time) 10	Operator IV mechanik	
When the task can be executed <input type="checkbox"/> Working <input checked="" type="checkbox"/> Not working	Ship Operating Stage <input checked="" type="checkbox"/> Port <input checked="" type="checkbox"/> Voyage <input checked="" type="checkbox"/> Shipyard <input checked="" type="checkbox"/> Anchor	Engine Room Operating Stage <input checked="" type="checkbox"/> All machinery in Engine Room working <input checked="" type="checkbox"/> Only Main Engine shout down <input checked="" type="checkbox"/> All machinery in Engine Room shout down	
<input type="checkbox"/> Influence atmosphere conditions <input type="checkbox"/> Special tools <input type="checkbox"/> istnieje możliwość zastąpienia urządzenia	<input type="checkbox"/> Spare Parts <input type="checkbox"/> Outside service		

Fig. 1. An example screen of the graphical interface of the computer-aided prototype system for allotment of the operation tasks in ship power plant. Ship power plant structure – in polish (on left hand side), operating task parameters defining (on right hand side)

4. The selection and hierarchy tasks module

Next module of the prototype computer-aided system to support of operating tasks scheduling is designed to stages:

- selection and elimination of the tasks which, cannot be executed in given conditions, due to various circumstances,
- hierarchization of importance the remaining tasks in operational point of view.

In the first stage the chief engineer have to determines the conditions in which the schedule of operating tasks will be done:

- operating stage of ship and operating stage of engine room in which the task performance can be achieved,
- operators, which has at disposal,
- weather conditions,
- time that is available to tasks execution, etc.

After approved these conditions the decision-maker can also limits additionally the tasks because of another reason not involve in computer system i.e. the availability of special tools, etc. Such list of selected operating tasks are automatically give in to hierarchy process because of the importance (coefficient wg_i in equation1) of each tasks in the engine room operation process, which consider for example:

- what kind of task is: planned, forced by breakdown or administration, etc.
 - planned time of the maintenance task execution,
 - number of the same devices and their technical condition, etc.
- So hierarchically list of operating tasks is essential to generate optimal schedule.

Siłownia okrętowa

- Instalacja balastowa
- Instalacja chłodnicza
 - Sprężarka nr 1
 - Sprężarka nr 2
 - Sprężarka nr 3
 - Skraplacz nr 1
 - Skraplacz nr 2
 - Chłodnia (mięso)
 - Parownik
 - Zawór rozprężny
 - Wentylator
 - Chłodnia (ryby)
 - Chłodnia (nabiał)
 - Chłodnia (warzywa)
- Instalacja klimatyzacyjna
- Instalacja żezowa
 - Pompa żezowa
 - Odolejacz
 - Pompa odolejacza
 - Zbiorniki separujące
 - Czujnik oleju
 - Filtry na ssaniu studzienek z
- Instalacja ścieków sanitarnych
- Instalacja śludge
- Instalacja przeciwpożarowa
- Instalacja sprężonego powietrza
- Instalacja wody sanitarnej
- Maszyna sterowa
- Wentylatory siłowni
- Silnik Główny
- Zespół Agregatów Prądowórczych
- Instalacja paliwowa
 - Pompa transportowa HFO nr
 - Pompa transportowa HFO nr

LISTA ZADAŃ DO REALIZACJI

All tasks	Planned	Damages	Other tasks
TASKS			
Lp.	Nazwa		
1.	Analiza oleju obiegowego silnika głównego		
2.	Badanie awaryjnej pompy pożarowej		
3.	Badanie instalacji wykrywczej dymu		
4.	Badanie pianowej instalacji gaśniczej		
5.	Badanie silnika łodzi ratunkowej		
6.	Czyszczenie / przedmuchanie poziomowskazu wody kotła pomocniczego		
7.	Czyszczenie filtra ndśrodkowego		

WARUNKI PODJĘCIA DECYZJI

Engine Room Operating Stage
 Cała siłownia pracuje

Ship Operating Stage
 Port

Atmosphere conditions
 Dobre

Define start time
 01-03-2011 16:21

Define ending time
 02-03-2011 11:40

Accessible operators

- ☒ Chief Engineer
- ☒ 2nd. Engineer
- ☒ 3rd. Engineer
- ☒ 4th. Engineer
- ☐ Fitter
- ☐ Motorman
- ☐ wiper

Outside operators

- ☐ Outside service
- ☐ Shipyard operators
- ☐ Others operator

APPROVE VALUES

Fig. 2. An example screen of the graphical interface for determine the conditions for which the schedule is generated - selecting and hierarchization module.

5. Module of generating the optimal solution of the schedule

The operating tasks scheduling problem in the engine room is an optimization problem, which like many issues of this type has been implemented as a transportation problem (otherwise also known as: knapsack problem). That is a special case of binary (0-1) issues of combinatorial optimization [5]. In this problem has been defined two criteria for their selection and allocation:

- the most important tasks should be realized, i.e. the schedule should consist of the lists of the tasks assigned to every operator, and having the importance index wg_i of the possible largest value,
- the time of realization of the tasks should be close to the available time for their realization, in other words to obtain the best use of the available time.

In accordance with the way of formulation of optimization function, described in [4], in the presented problem such function can be assumed to be a combination of assessment criteria of scalar form, generally defined as a weighed sum of:

- task importance indices,
- time intervals for their realization.

In the case of the so formulated objective function one has to do with two-criterion optimization. By introducing to it the coefficients ρ_1, ρ_2 called the criterion weighing factors, a choice on which criterion would be more important, becomes possible. Such choice is made by the decision maker, i.e. chief engineer, depending on needs appearing in a given instant. The coefficients ρ_1, ρ_2 can take values from the interval $<0, 1>$, and their sum should be always equal to 1.

Therefore the best schedule, out of all allowable solutions, is that for which the sum of the weighed sums of two presented criteria, for all considered operators, reaches a maximum. The general form of the objective function is as follows:

$$F_j = \max \sum_{j=1}^o \left(sk \cdot \rho_1 \cdot \sum_{i=1}^n wg_i x_{ij} + \rho_2 \frac{\sum_{i=1}^n t_i x_{ij}}{T_s} \right) \quad (1)$$

where:

- $i = 1, 2, 3, \dots, n$ – number of tasks,
- $j = 1, 2, 3, \dots, o$ – number of operators,
- ρ_1, ρ_2 – weighing factor of the criterions,
- x_{ij} – factor which determines the assignment of i -th task to j -th operator,
- sk – scale (a coefficient so selected as to obtain balanced values of sum components),
- wg_i – task importance index,
- T_s – the time available for realization of tasks staying in port, sea voyage time).

In the process of generating the best solutions of the problem takes into account four main constraints:

- total time of the tasks assigned to each of the operators cannot be greater than the available time T_s intended to proceed,
- the task can be assigned only once in the schedule,
- each task is performed by only one of the operators
- way of assigning tasks to individual operators determined,

There are the following assumptions adopted too:

- each operator can perform only one task in a given interval of time,
- each task has a number of attributes stored in a database, or defined in earlier stages (the elimination of impossible tasks to performing in the given conditions, prioritizing tasks) [1], [2],
- allocation of tasks to individual operators to be implemented in accordance with the hierarchy of professional.

The standard knapsack problem consists in filling the “knapsack” of a given limited volume by using elements (blocks) of various dimensions and values in such a way as to fill the knapsack so as to make its value the greatest. In the same way can be formulated the problem faced by ship

chief engineer in some specific situations (e.g. short stay in port or short sea voyage), who must assign operational tasks to power plant crew members so as to make the best use of available time and simultaneously to realize the most important tasks out of the set of the tasks whose realization cannot be performed during the available time interval. For solving the problem of optimization of the schedule of operational tasks in ship power plant the last of the presented method, i.e. the method of indirect searching, called also the searching with reversals. The method was selected due to its simplicity, as it contains basic steps of almost all searching methods and simultaneously is one of the quickest among them [4]. In order to check the above presented mathematical model as well as the method of solving of the decision problem usually faced by chief engineers, a prototype computer software for aiding in planning the operational tasks in ship power plant in some definite conditions, was elaborated. In Fig.3 shows the interface of system, which demonstrates solution of the chief engineer scheduling problem for the sample data (sample tasks). The top bar shows two important parameters of the problem: 'Maximum time', i.e. the time interval for which the schedule is considered (e.g. port staying time, sea voyage time etc.), 'Criterion weighing factor' (the parameter p in equation.1) i.e. that determining which choice is of a greater importance: that of the most important tasks or that of the most effective use of the available time. There are a few additional option to choose for the user to presenting the solutions of optimization process. On the remaining parts of window shows the results of the optimal schedule generating process. On the left side, in the area 'Schedule variants', is shown the schedules in the text form, on the right graphic form called. Gantt chart, where the height of each row represented each operator skills and the assigned operating tasks are represented by rectangle (different colour and size).

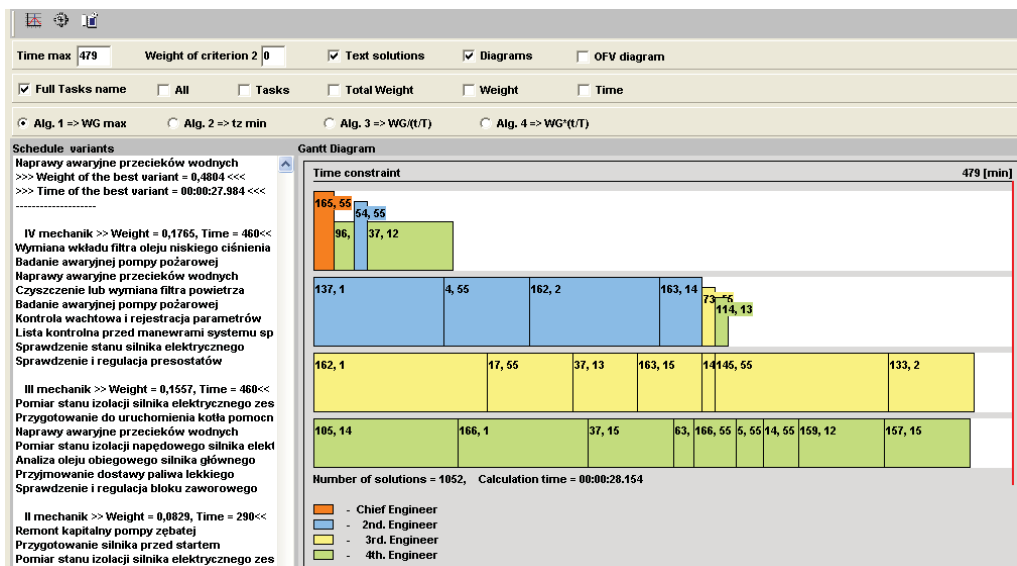


Fig. 3. An example screen of the graphical interface of the operation tasks allotment system Gantt chart – schedule generating module.

6. Conclusion

In this paper has been presented an approach to solving the decision problem associated with scheduling of operational tasks realized by staff in ship power plant, with making into account different conditions. The prototype system consists of three modules corresponding to the stages of decision-making process of operating tasks allotment in engine room and there could be draw the following conclusions:

- the problem formulation as a 'many-knapsack' problem seems to be a natural responding to task allocation process in the ship power plant,
- objective function which takes into account the crucial elements considered by chief engineer in scheduling the operational tasks in ship power plant: i.e. importance of a given task, competences of each of the operators, time available for realization of necessary tasks, has been elaborated.
- advantages of the solution searching method, especially: simplicity, the basic steps of nearly all review methods, convinced to use it for scheduling optimization in the ship engine room.

References

- [1] Kamiński, P., *Formulation objective function of the decision - making problem in ship power plant*, Proceedings of Conference – Engineering design in integrated product development, pp. 205-212, Zielona Góra 2006.
- [2] Kamiński, P., *Identification of elements of decision problem of ship power plant management*, Proceedings of Polyoptimization & CAD Conference, Mielno 2006
- [3] Kamiński, P., *Wybrane zagadnienia związane z zarządzaniem eksploatacją siłowni okrętowej*, Materiały konferencyjne – Projektowanie i zarządzanie realizacją produkcji, pp. 95-102, Zielona Góra 2005.
- [4] McDiarmid, C.J.H., *The Solution of a Timetabling Problem*. Journal Institute Mathematics Applications 9, pp. 23-34, 1972.
- [5] Smutnicki C.: *Algorytmy szeregowania*, Wydawnictwo Exit, Warszawa 2002.



A SIMULATION STUDY OF MIXING GRANULAR MATERIALS

Robert Kostek, Bogdan Landowski

*University of Technology and Life Sciences
Faculty of Mechanical Engineering
ul. Kaliskiego 7, 85-796 Bydgoszcz, Poland
tel.: +48 52 3408495, fax: +48 52 3408495
e-mail: robertkostek@o2.pl, e-mail: lbogdan@utp.edu.pl*

Abstract

Mixing the granular materials is a critical process in many industries, especially in pharmaceutical one, where homogeneous blends of ingredients are required. The homogenisation process is time and energy consuming, thus this article is focused on the process. The mixing process has been simulated with the discrete element method – DEM, which gives an opportunity to study the granular flow of mixed ingredients. Following stages of the mixing process have been presented for various shapes of blenders and analysed, which gives an opportunity to understand the process and mechanisms of homogenisation. Apart from the three basic mechanisms of homogenisation: diffusion, convection and shear, one more has been found.

Key words: discrete element methods, blender, mixing

1. Introduction

Blenders are applied in: pharmaceutical [4, 15, 27], cosmetic, food [32] and detergent industries, to name a few. The mixing process influences both quality of products and their cost, thus there is a need to describe the process. The mixing process is a result of diffusion, convection and shear, which are the main mechanisms of the homogenisation described in the literature [1, 4, 27]. The mechanisms can be observed during simulation of the granular flow with DEM. The mixing process has been described in two books [1, 27], which are basic ones for this subject. Apart from the theoretical analysis, and experimental results the authors presented there some practical advice. Nevertheless recommended parameters of the mixing process, and results of simulation obtained with DEM have not been presented [1, 27].

The discrete element method (DEM) is a numerical method dedicated for computing motion of a large number of particles. The discrete element method is closely related to molecular dynamics (MD), particle method (PM), multibody systems (MBS) and smooth particle method (SPM). The fundamental assumption in the discrete element method is that material consists of large assemblies of separate particles. The number of the discrete particles can be a few millions [29] and even billions [2, 18, 24]. The basic idea of modelling bodies, as large assemblages of separate-discrete elements, makes the method very universal; because each body can be modelled as an assemblage of separate atoms, or groups of atoms. Materials like gases, liquids, solids (powder, sand or rock) can be simulated with the method. The particles may have different shapes and properties. Complex non-linear interactions between bodies, and within bodies, are simulated with a numerical method. Next, the motion of particles, which is described by differential non-linear

equations, is computed. Finally, the motion of a large number of particles, like molecules or grains of sand, is presented as a movie and analysed [8, 11, 17, 19, 28, 29]. The discrete element methods are applied to solve a wide range of engineering and scientific problems in: mineral processing, rock blasting, crushing, powder technology, laser processing, granular flow of stones, blow up of building and many more areas [23].

Particles in DEM can be modelled with: points, polygons, circles, ellipses, polyhedral [19] or with spheres [10]. A discrete element can represent: a stone, a grain of sand, a seed, a grain of powder, or a molecule. In the case of modelling solid bodies the elements can represent rigid or deformable bodies (primitives). If bodies are modelled with FEM primitives, then both elastoplastic distortion of bodies and their fragmentation (cracking) can be simulated. The phenomena can be simulated with so called combined finite-discrete element method [23]. More details about DEM have been published in literature [5, 6, 22, 23, 25, 33].

The considered problem of mixing granular materials is studied with rigid discrete elements. Three forces act on particles: terrestrial gravity force Q , normal contact force F_n and friction force F_t (Fig. 1). The normal force is usually described by simple models, which reflects restitution phenomena [16, 20, 23], while the friction force is described with Coulomb's model. Motion of each element is described by three differential equations:

$$\ddot{x} = m^{-1} \sum F_x, \quad (1)$$

$$\ddot{y} = m^{-1} \sum F_y, \quad (2)$$

$$\ddot{\alpha} = I^{-1} \sum M, \quad (3)$$

where:

x denotes x -component of displacement,

y y -component of displacement,

F_x x -component of acting force,

F_y y -component of acting force, m mass of element,

α angular displacement of element,

I moment of inertia,

M moment of acting force.

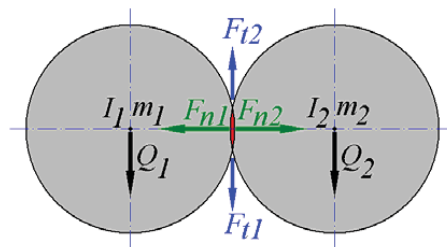


Fig. 1. Forces acting on two discrete elements during their collision

The discrete element method (DEM) gives an opportunity to model mixing the granular materials [21, 23] and consider various: shapes of blenders, values of speeds and fill levels, which are the key factors. An analysis of the factors can be done at a very early stage, at the stage of conception and designing. This gives an opportunity to improve construction of blenders, and to make them more efficient. Moreover, DEM makes an easier understanding of the mixing process.

Thus this article presents results of simulation obtained with DEM and their interpretation. The simulations have been done with Algodoo [12].

2. Simulation of the mixing process

One of the most common technique of mixing the granular ingredients is to rotate a container with the ingredients [15]. This type of blenders are: double cone, IBC and drum blender, which are widely used in the pharmaceutical industry [1, 9, 15, 27]. The ingredients are well mixed after making - from 200 to 700 rotations [1], or after fifteen minutes [27]. The mixing process takes place in the space near the surface, where following layers of particles slide down. Deep under the surface the mixing process does not exist [21]. The layers near the surface move quicker, than the ones deeper under the surface, which in turn introduce the shear. The diffusion process is coupled with collisions between particles, chaotic behaviour [7, 26], and the butterfly effect. The butterfly effect is a part of chaotic dynamics, which are result of non-linear interactions. The collisions are particularly intensive in the space, where the sliding particles reach a wall of a container (Fig. 4b). The convection is coupled with shear, and is observed when particles of one ingredient are displaced by particles of a second ingredient (Fig. 2e). Summarising the mixing process, we can say that, the grains of ingredients are periodically brought into the mixing zone, near the surface, where chaotic dynamics appear, and next after sliding down, they are covered by the following layers of particles. That makes the blend more homogenous.

This section presents results of the simulation. The computations have been done for three blenders: double cone, IBC and drum blender, the two dimensional models of which are presented in the Figs. 2-3. The simulation has been computed for 2400 particles, and the following values of parameters: radius of particles $r=0,01\text{m}$, the restitution coefficient $C_R=0,05$ and coefficient of Coulomb friction $\mu=0,5$. The polygons (Figs. 2-4) are inscribed in a circle, the centre of which defines the centre of rotation. The circle determines the radius $R=1\text{m}$, which has been adopted to calculate the dimensionless Froude number. The Frode number is relationship between centrifugal and gravitational acceleration, it can be treated as a dimensionless rotating frequency [30]. It is dimensionless number of mixing, which reflects flow condition. The Frode number is expressed by the following formula [1]:

$$Fr=\omega^2 Rg^{-1}, \quad (4)$$

where:

Fr - denotes the Frode number,
 ω - angular speed [rad/s],
 R - radius of the circle [m], and
 g - acceleration of gravity [m/s^2].

The Frode number equals one, when the angular speed ω reaches the critical value ω_{kr} . The presented calculations (Figs. 2-4) have been done for $Fr = 0,3025$ and fill level close to 50%, which are typical for industrial blenders (e.g. [9, 13,14]).

The obtained results show that the border between red and blue ingredients becomes longer and more sophisticated (Figs. 2b, 3b, 4b) after one rotation. Next rotations make the border more and more sophisticated. The process, which can be observed, is baker's transformation. The ingredient is stretched and folded, which leads to a spiral shape -"vortex" (Figs. 2ef, 3f, 4d). The spiral structures have been observed previously in cylindrical blenders [3, 26, 31]. The spiral structures, which are a result of baker's transformation, are finally destroyed by diffusion, which is a result of chaotic dynamics. The two processes - baker's transformation and diffusion lead to a mixed state

(Figs. 2a-o, 3a-o, 4a-o). The spiral structures are sensitive to the speed of blenders, that is an interesting problem.

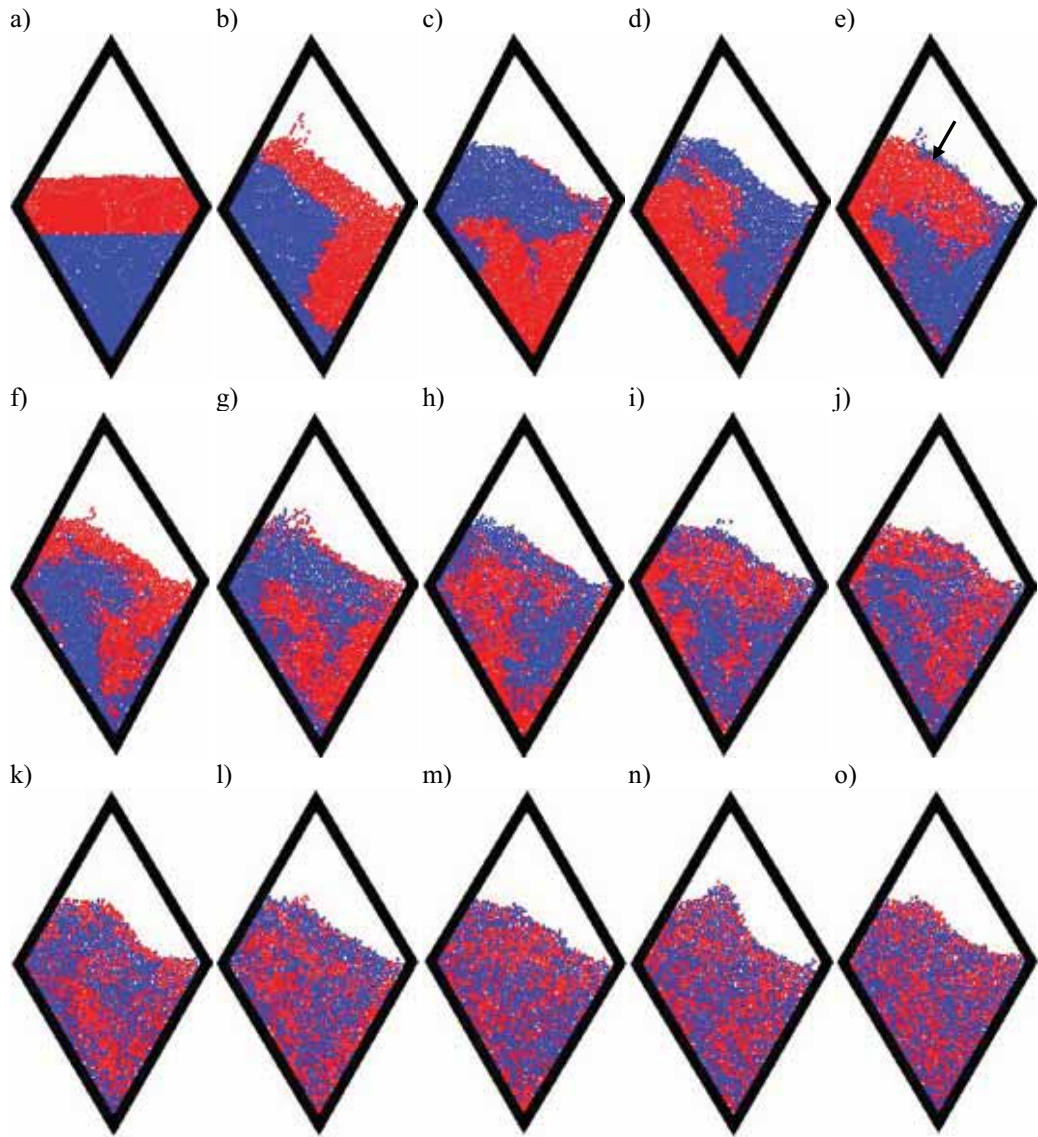


Fig. 2. The consecutive stages of the mixing process calculated for the double cone blender, the pictures present particles after: 0 a), 1 b), 2 c), 3 d), 4 e), 5 f), 6 g), 7 h), 8 i), 9 j), 10 k), 11 l), 12 m), 13 n) and 14 o) rotations

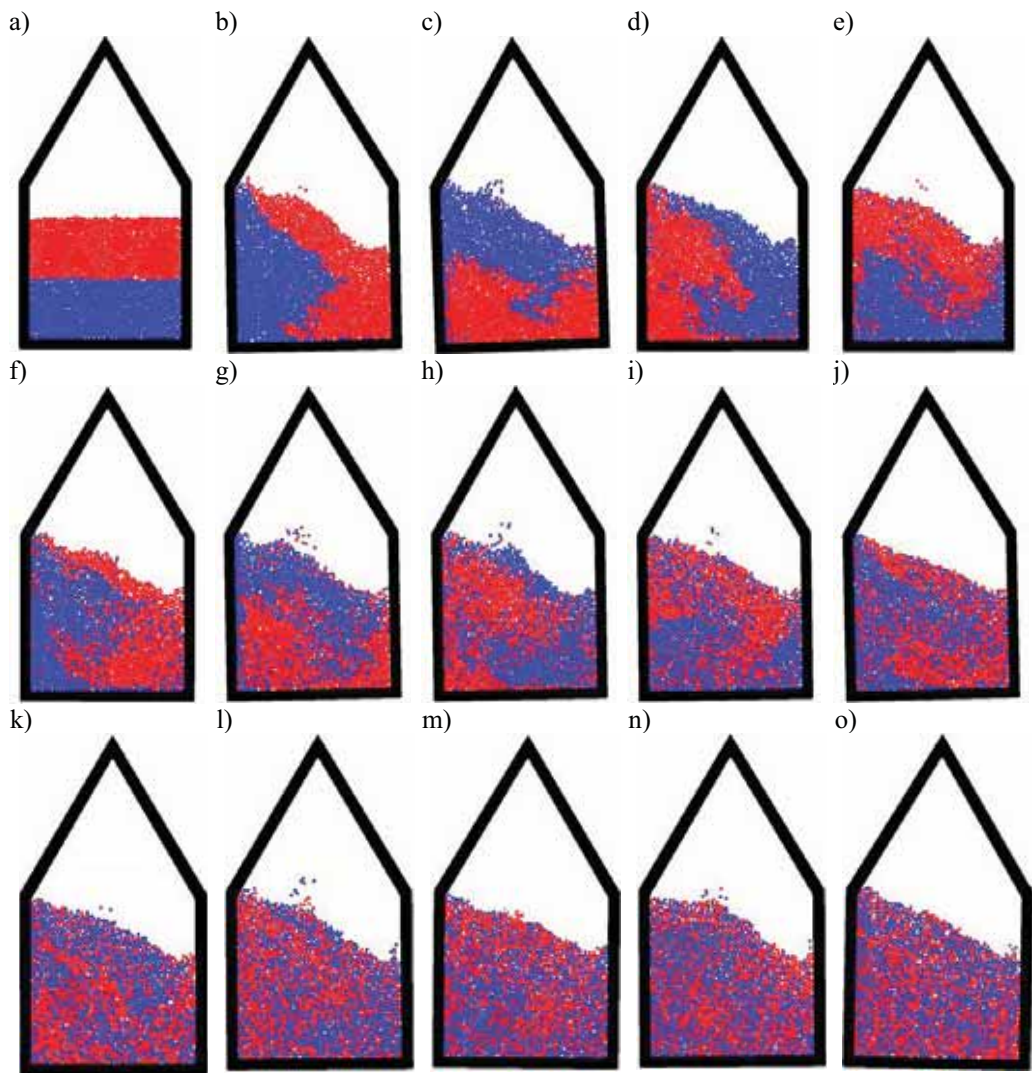


Fig. 3. The consecutive stages of the mixing process calculated for the IBC blender, the pictures present particles after: 0 a), 1 b), 2 c), 3 d), 4 e), 5 f), 6 g), 7 h), 8 i), 9 j), 10 k), 11 l), 12 m), 13 n) and 14 o) rotations

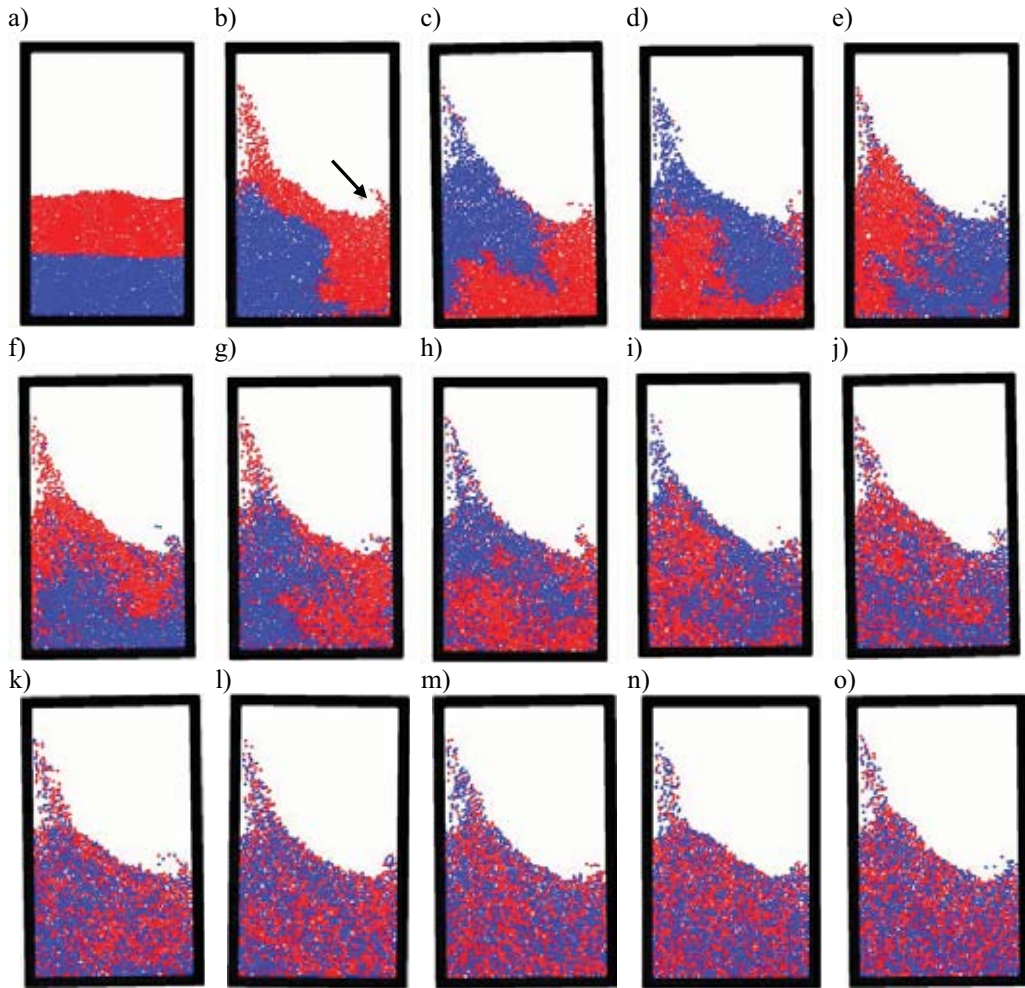


Fig. 4. The consecutive stages of the mixing process calculated for the drum blender, the pictures present particles after: 0 a), 1 b), 2 c), 3 d), 4 e), 5 f), 6 g), 7 h), 8 i), 9 j), 10 k), 11 l), 12 m), 13 n) and 14 o) rotations

The diffusion process can be observed in Figs. 2f, 3f, 4f. An analysis of the results tends to conclusion that the diffusion process is the most intensive in drum blender, while the diffusion process in IBC blender is slightly less intensive. At the same time the diffusion process in double cone blender is less intensive than in IBC blender. After nine rotations blend in drum blender, is the most homogeneous comparing with IBC and double cone blenders; it is difficult to find the spiral shape (Fig. 4j). That is a result of the intensive diffusion process and chaotic dynamics. Finally after fourteen rotations blends in drum blender and IBC blender are homoheneus and a progress of the mixing process is not as significant, as has been observed on the early stage (Figs. 3o, 4o). While in in double cone blender, sets of blue and red particles are observed (Fig. 2o).

Results of simulation obtained with DEM has been compared against experinental results published previously [34]. A good agerrement between results tends to conclusion, that discrete element method can provide a valid information about mixing process.

3. Conclusions

The presented computational results show mixing process of two granular ingredients within three blenders. Apart from the three basic mixing mechanisms: diffusion, convection and shear, one more mechanism has been observed. The mechanism is the baker's transformation and diffusion. The baker's transformation leads to a spiral shape of ingredients. Then the diffusion process finally destroys the spiral shape, which makes a blend more homogeneous. That is the point of mixing. The diffusion process can be coupled with the butterfly effect, which is typical for chaotic systems. The mixing process is the most intensive on the early stage; while after some period of time the progress of the mixing process is not significant. The phenomenon has been observed experimentally and described in literature.

Summarising this, the mixing process can take less time if the diffusion process is more intensive - granular flow is more chaotic, and the baker's transformation - "vortex" is faster; that is practical conclusion. Moreover designers can use the discrete element method to improve blenders.

References

- [1] Boss J., *Mieszanie materiałów ziarnistych*, PWN, Warszawa 1987.
- [2] Chatelaina P., Curionib A., Bergdorfa M., Rossinellia D., Andreonib W., Koumoutsakos P., *Billion vortex particle direct numerical simulations of aircraft wakes*, Computer Methods in Applied Mechanics and Engineering, vol. 197, no 13-16, pp. 1296-1304, 2008.
- [3] Chaudhuria B., Mehrotraa A., Muzzioa F.J., Tomassone M.S., *Cohesive effects in powder mixing in a tumbling blender*, Powder Technology, vol. 165, no 2, pp. 105-114, 2006.
- [4] Choldrich R., *Fundamentals of particle technology*, Midland Information Technology and Publishing, Loughborough, 2002.
- [5] Cleary P.W., Ha J., *Three-dimensional SPH simulation of light metal components*, Journal Light Metals, vol. 2, no 3, pp. 16-183, 1993.
- [6] Cundall P.A., *A computer model for simulating progressive large scale movements in blocky rock systems*, ISRM Symp., Nancy, France, Proc. 2, pp. 129-136, 1971.
- [7] Doucet J., Bertrand F., Chaouki J., *Experimental characterization of the chaotic dynamics of cohesionless particles: application to a V-blender*, Granular Matter, vol. 10, no 2, pp. 133-138, 2008.
- [8] Fraige F.Y., Langston P.A., Chen G.Z., *Distinct element modelling of cubic particle packing and flow*, Powder Technology, vol. 186, no 3, pp. 224-240, 2008.
- [9] Fuller W.O., Abbe P.O., *Mixing up a batch: batch mixer types and selection tips*, available from:
<http://www.pauloabbe.com/productLines/doubleArmSigmaBladeMixers/batchMixingTips.html>
- [10] Garcia X., Latham J.P., Xiang J., Harrison J.P., *A clustered overlapping sphere algorithm to represent real particles in discrete element modelling*, Geotechnique, vol. 59, no 9, pp. 779-784, 2009.
- [11] Hoover Wm. G., *Computational Physics with Particles – Nonequilibrium Molecular Dynamics and Smooth Particle Applied Mechanics*, Computational Methods in Science and Technology, vol. 13, no 2, pp. 83-93, 2007.
- [12] <http://www.algoryx.se>.
- [13] <http://www.consumasz.pl/mbs.htm>.
- [14] <http://www.khodiyaarind.com/industrial-mixer.html>.
- [15] <http://www.pharmaceuticalonline.com>.

- [16] Hunt K.H., Crossley F.R.E., *Coefficient of restitution interpreted as damping in vibroimpact*, Transactions of the ASME, Journal of Applied Mechanics, vol. 42, no 2, pp. 440-445, 1975.
- [17] Kostek R., Munjiza A., *Visualization of results received with the discrete element method*, Computational Methods in Science and Technology (CMST), vol. 15, no 2, pp. 151-160, 2009.
- [18] Koumoutsakos P., *Multiscale flow simulations using particles*, Annual Review of Fluid Mechanics, vol. 37, pp. 457-487, 2005.
- [19] Latham J.P., Munjiza A., Garcia X., Xiang J., Guises R., *Three-dimensional particle shape acquisition and use of shape library for DEM and FEM/DEM simulation*, Minerals Engineering, vol. 21, no 11, pp. 797-805, 2008.
- [20] Michalczyk J., *Phenomenon of force impulse restitution in collision modelling*, Journal of theoretical and applied mechanics, vol. 46, no 4, pp. 897-908, 2008.
- [21] Moakher M., Shinbrot T., Muzzio F.J., *Experimentally validated computations of flow, mixing and segregation of non-cohesive grains in 3D tumbling blenders*, Powder Technology, vol. 109, no 1-3, pp. 58-71, 2000.
- [22] Mohammadi S., *Discontinuum Mechanics*, Wit Press, 2003.
- [23] Munjiza A., *The combined finite-discrete element method*, Wiley, 2005.
- [24] ParaView, <http://www.paraview.org>.
- [25] Shi G., *Discontinuous deformation analysis – A new numerical model for the statics and dynamics of deformable block structures*, 1st U.S. Conf. on Discrete Element Methods, Golden. CSM Press: Golden, CO, pp. 16, 1989.
- [26] Shinbrot T., Alexander A., Muzzio F.J., *Spontaneous chaotic granular mixing*, Nature, vol. 397, no 6721, pp. 675-678, 1999.
- [27] Stęk F., *Mieszanie i mieszalniki*, WNT, Warszawa 1981.
- [28] The Scientific Computing and Imaging (SCI) Institute web site <http://www.sci.utah.edu>
- [29] Tsuji T., Yabumoto K., Tanaka T., *Spontaneous structures in three-dimensional bubbling gas-fluidized bed by parallel DEM-CFD coupling simulation*, Powder Technology, vol. 184, no 2, pp. 132-140, 2008.
- [30] Weinekötter R., Gericke H., *Mixing of solids*, Kluwer, 2000.
- [31] Weiss P., *Mastering the mixer the frustrating physics of cake mix and concrete*, Science News, vol. 164, no 4, pp. 56, 2003.
- [32] Węgrzyn M., *Energochłonność procesu mieszania materiałów sypkich mieszadłem łopatkowym*, Inżynieria Rolnicza, no 7 (82), pp. 439-447, 2006.
- [33] Williams J.R., Hocking G., Mustoe G.G.W., *The theoretical basis of the Discrete Element Method*, NUMETA 1985, Numerical Methods of Engineering, Theory and Applications, A.A. Balkema, Rotterdam, January 1985.
- [34] Kostek R., Landowski B. *Simulation of the granular flow of grinding media, inside a ball mill*, Polish CIMAC, accepted.



SIMULATION OF THE GRANULAR FLOW OF GRINDING MEDIA, INSIDE A BALL MILL

Robert Kostek, Bogdan Landowski

*University of Technology and Life Sciences,
Faculty of Mechanical Engineering
ul. Kaliskiego 7, 85-796 Bydgoszcz, Poland
e-mail: robertkostek@o2.pl, e-mail: lbogdan@utp.edu.pl*

Abstract

The ball mills are often applied in mineral processing, they are e.g. an important part of the cement industry. A key factor, which influences the milling process, is the granular flow of grinding media. The flow determines: energy consumption, time of milling and capacity; thus there is a need to describe the phenomenon. The discrete element method - DEM is a computational method, which allows to simulation of the granular flow, thus it has been applied in this article. The received results of simulation have been compared with experimental results.

Keywords : DEM, ball mill

1. Introduction

The ball mills are widely used machines. They are mainly used to powder minerals, that is their typical application. The powdering takes place between balls, due to normal and tangent forces. The forces determine interaction between the balls, thus they have an influence on the granular flow of the grinding media. In the considered case, the interaction between the balls has been described with Coulomb friction, and restitution coefficient.

At the stage of conception and designing, various: shapes of liners, values of speed and fill levels can be considered. That gives an opportunity to analyse, the dynamics of grinding balls, acting forces and power consumption, at the very beginning stage. This is the reason why the discrete element method, has been applied in mineral processing [1, 2, 3, 4].

The basic concept of the discrete element methods (DEM) is to model the bodies with large assemblages of particles (discrete elements), which is a very general and practical approach. The discrete elements can represent: atoms, groups of atoms, grains of sand, stones or FEM primitives. That approach gives an opportunity to model: gases, fluids and solids, thus DEM is used to solve a wide range of engineering and scientific problems [5]. Motion of the discrete elements, which is described by the second order ordinary differential equations, is computed, and finally the motion is presented as a movie and analysed [1, 2, 5, 6, 7].

2. The granular flow of grinding balls inside a ball mill

As it has been mentioned above - shape of liners, values of speed and fill levels influence the

milling process. Liners are designed in the way, that impedes rolling balls on the liners, and makes an easier lifting the grinding balls. The values of speed of the mills n are in the range from $n=0,55n_{kr}$ to $n=0,85n_{kr}$, but the typical value is $n=0,75n_{kr}$ (e.g. [8]). The critical speed n_{kr} is reached when centripetal acceleration of any liner, is equal to the gravity acceleration. While the fill levels are in the range from 0,3 to 0,55 - which is the maximum value.

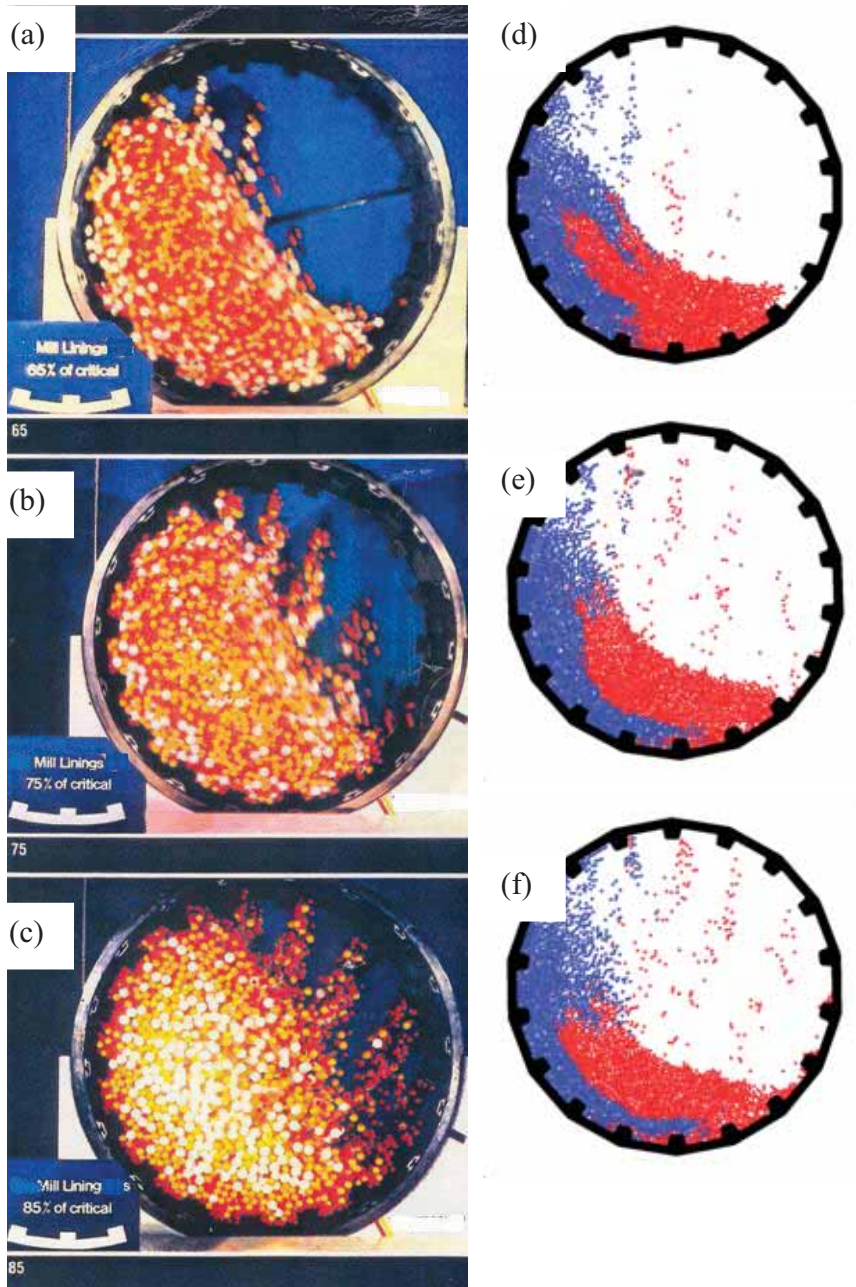


Fig. 1 Comparison of the experimental results (a-c) [9] with the results of simulation (d-f), for the following speeds:
 $n=0,65 n_{kr}$ (a,d), $n=0,75 n_{kr}$ (b,e), $n=0,85 n_{kr}$ (c,f)

Some experimental results have been published on Internet [9], which gives an opportunity to compare them with the results of simulation (Fig.1). The simulation has been computed for 3702 particles, and the following values of parameters have been adopted to perform the simulation: the restitution coefficient $C_R=0,05$ and coefficient of Coulomb friction $\mu=0,5$. In spite of the fact that, the values of the parameters have not been published on the web site [9], the computational results show good agreement with the experimental results. The number of balls falling down seems to be bigger in the experiment, but it results from the fact that: the simulated model is two-dimensional, while experiment was three-dimensional, moreover the particles used in experiment are bigger than these in the simulation. The presented results show good agreement with the results of simulations, which have been published previously in literature as well [4,10]. The considered granular flow of grinding media, inside a ball mill has been simulated with program algodo [11].

3. Summary

The presented results show granular flow of the grinding media, inside the ball mill, for three values of speed. The computational results have been received with DEM, and have been validated against the experimental results. The comparison shows good agreement between them, which suggests that the study should be continued. It shows that, DEM provides valid information, which can be used by the designers. Summarising DEM is a useful tool in future modification of the ball mills.

References

- [1] Cleary P.W., Commonwealth Scientific and Industrial Research Organisation - http://www.cmis.csiro.au/cfd/dem/ballmill_3D/index.htm.
- [2] http://www.metso.com/miningandconstruction/mm_wear.nsf/WebWID/WTB-080528-2256F-33C82?OpenDocument&mid=B63338D07460BCB4C22575BB004636A3.
- [3] Cleary P.W., *Ball motion, axial segregation and power consumption in a full scale two chamber cement mill*, Minerals Engineering, vol 22, no 9-10, pp 809-820, 2009.
- [4] Cleary P.W., *Charge behaviour and power consumption in ball mills: sensitivity to mill operating conditions, liner geometry and charge composition*, International Journal of Mineral Processing, vol 63, no 2, pp 79-114, 2001.
- [5] Munjiza A., *The combined finite-discrete element method*, Wiley 2005.
- [6] Latham J. P., Munjiza A., Garcia X., Xiang J., Guises R., *Three-dimensional particle shape acquisition and use of shape library for DEM and FEM/DEM simulation*, Minerals Engineering, vol 21, no 11, 2008, pp 797-805.
- [7] Kostek R., Munjiza A., *Visualization of results received with the discrete element method*, Computational Methods in Science and Technology (CMST), vol 15, no 2, 2009, pp. 151-160.
- [8] Błasiński H., Młodzieński B., *Aparatura przemysłu chemicznego*, WNT, Warszawa 1976.
- [9] <http://www.miningbasics.com/effect-ball-mill-charge-pressure-and-impact-grinding>.
- [10] Cleary P.W., *Axial transport in dry ball mills*, Applied Mathematical Modelling, vol 30, no 11, pp 1343-1355, 2006.
- [11] www.algodoo.com.



INFLUENCE OF VOIDS AND LAYERS NUMBER ON MECHANICAL PROPERTIES OF HAND LAY-UP BENDED LAMINATES

Mariusz Kukliński

University of Technology and Life Sciences in Bydgoszcz
Al. Prof. S. Kaliskiego, 85-796 Bydgoszcz, Poland
tel.: +48 52 3408268, fax.: +48 52 340825
e-mail: mariusz.kuklinski@utp.edu.pl

Abstract

Composite materials are broadly used in industry. In maritime industry composite materials with great success supersede conventional materials as steel and wood. Engine foundations and power-transmitting shafts belong to the newest applications of composite materials in maritime industry. Composite shafts are fabricated predominantly by rowing method but for engine foundations hand lay-up method is still used. One of the greatest disadvantages of hand lay-up (contact) method is hazardous distribution of resin matrix and voids or air blisters that remain in bulk resin matrix or may stick to reinforcement fibres. This hazardous distribution of resin may cause inaccuracies in calculation of voids percentage in laminate. If an air blister sticks to a fibre its prejudicial influence on laminate resistance is greater than if it remains in bulk resin. Number of layers that constitute a laminate influences the maximum bending stress in specimen. This relation however is different from that in tensile tests.

Keywords: composite materials, laminates, hand lay-up method, fibreglass reinforcement, voids percentage, layers number

1. Introduction

Composite materials with layered structure are being used broadly in many branches of industry. Automotive, rail, maritime and aerospace industry are the most distinctive fields where composite materials continuously broaden their applications [1]. Laminates and sandwich composites offer to constructors technological latitude in planning wide scope of material properties and make possible fabricating parts of complex shape. Resistance to corrosion and amagnetic properties are also their significant trump cards. Sandwich composites with foam or honeycomb core due to their high stiffness to mass ratio are frequently used for building yacht and ship hulls. Ultimately composite materials are used for constructing engine foundations and shafts transmitting power from engine to propeller. Such shafts may transmit the power even of one megawatt. Composite shafts are not only about 80% lighter then steel ones, but also save on complexity. Steel shafts which may not distort in operation have limited length. Conventional transmission line is therefore made up of multiple shafts along with pedestal bearings and other elements. Composite shafts, because of their less mass, can be made longer, that results in fewer transmission arrangements. Composite shafts do not corrode and run more quietly.

The basic method used for mass-produced and reliable composite products is called Resin Transfer Moulding (RTM). This method consists in impregnating with resin a preform placed in rigid, hermetic mould. This method is applicable for products that must be characterized by significant smoothness on both sides and is restricted to elements of small and medium

dimensions. The costs of moulds, especially the heated ones, costs of pressure-circuits and instrumentation used in this method are significant. Other, less expensive method, especially suitable for mass-produced elements of extensive surfaces e.g. plates and long profiles is called Resin Film Infusion (RFI) [2,3]. In this method one-sided mould is used for impregnating the preform with resin. The other side is hermetically protected with a flexible polymer cover. While extracting the air from beneath the cover, it presses the preform and the resin is being distributed evenly through the preform, ensuring very good impregnation of the preform and high percentage of reinforcing fibres in the product. This method is successfully used in production of aircraft wings, fuselages and boat hull sheathings.

Major part of composite products is still produced manually (contact method). This technology is applicable for fibre-reinforced laminates formed by process of applying alternately reinforcing layers and resin matrix. This paper presents influence of voids percentage and number of layers on mechanical properties of laminate subjected to bending.

2. Material characteristics of laminate matrices and reinforcements

Laminates under consideration were made of two kinds of polyester resins: orthophthalic and isophthalic one. The polyester orthophthalic resin used was a A105 - thixotropic and preaccelerated, unsaturated, general purpose resin, that is suitable for spray-up and hand lay-up methods for manufacturing numerous moldings and is especially recommended for manufacturing of boats. The polyester isophthalic resin we used was a K530 - thixotropic, preaccelerated, special purpose resin with good mechanical properties combined with high temperature resistance. K530 is a medium reactive polyester resin with relatively long geltime, suitable for spray-up and hand lay-up application for manufacturing different types of composites, exposed to a corrosive environment and/or composites where good mechanical properties are important e.g. tanks, pipes, silos, boats, etc. Comparison of mechanical properties of these two matrices is shown in Tab. 1.

Tab. 1. Comparison of mechanical properties of K 530 and M 105 resin matrices

Property at 23 °C	K 530	A 105	Units	Method
Density	1,1	1,1	[kg/dm ³]	ISO 2811
Tensile strength	65	55	[MPa]	ISO 527
Tensile modulus	4100	3600	[MPa]	ISO 527
Flexural strength	125	90	[MPa]	ISO 178
Flexural modulus	3700	4100	[MPa]	ISO 178

The aim of carried out tests was to find out relations between voids percentage, number of layers that constitute certain laminate and its mechanical properties in bending. Each laminate consist of a certain sequence of layers. Its structure is described by the following relation:

$$Wch + x(M450 + R600) + M450 + V30, \quad (1)$$

where:

Wch – chemo-resistant layer: V30+M300+2(M450),

x – number of coupled layers (M450+R600),

M450 - E-glass mat of 450 [g/m²] specific weight,

M300 – E-glass mat of 300 [g/m²] specific weight,

R600 – E-glass woven rowing of 600 [g/m²] specific weight,

V30 – E-glass veil of 30 [g/m²] specific weight.

So we deal with a laminate of asymmetric layer sequence. The mats M300 and M450 are of the same type of chopped strand mats for hand lay-up which homogeneity doesn't exceeds the range of $\pm 10\%$. The mat's glass fibres combine the electrical and mechanical properties of traditional E-glass with the acid corrosion resistance of E-CR glass. It is made of randomly oriented chopped glass strands bonded together using an emulsion binder. The emulsion binder uniquely bonds the mat so that it conforms rapidly to highly contoured moulds. The emulsion binder produces superior handling properties compared to powder bonded mats. The typical laminate properties of applied mats in an orthophthalic polyester resin with 31% weight glass content, moulded by hand lay-up method shows Tab. 2. The veil V30 is a type of very thin mat of 30 [g/m²] specific weight, so we assume that its mechanical properties in a laminate layer are that of given in Tab. 2.

Tab. 2. Mechanical properties of M300, 450 mats in orthophthalic polyester resin with 31% weight glass content

Tensile Strength	Tensile Elongation	Tensile Modulus	Flexural Modulus	Flexural Strength	Flexural Elongation
108 [MPa]	1.8 [%]	7800 [MPa]	6770 [MPa]	204 [MPa]	3.4 [%]

In another Type Approval Certificate we find similar values for laminas made of M 300 and M 450 mats with less weight glass content (Tab. 3):

Tab. 3. Mechanical properties of M300, 450 and 600 mats in orthophthalic polyester resin

Property	300 [g/m ²]	450 [g/m ²]	600 [g/m ²]	Units	Method	
Glass content	29	28	29	[%]	ISO 1172	mean
Tensile strength	105/88	112/88	105/83	[MPa]	ISO 3268	mean/msmv
Tensile modulus	7404	7182	7045	[MPa]	ISO 3268	msv (mean)
Flexural strength	166/155	206/128	179/128	[MPa]	ISO 178	mean/msmv
Flexural modulus	6195	6095	6425	[MPa]	ISO 178	msv (mean)

where:

mean – mean of type test results,

msv – manufacturer's specified value, verified to be within $\pm 10\%$ of mean of type test results,

msmv – manufacturer's specified minimum value, verified to be below mean – $2 \times$ standard deviation of type test results.

We notice that the strength characteristics of the mats in laminas are specific weight dependent. The ultimate glass reinforcement type utilized in specimens preparation was R600 i.e. E-glass woven roving in the form of plain weave fabric which specifications according to a quality certificate are given in Tab. 4.

Tab. 4. Selected properties of R600 E-glass woven roving

Property	Value	Units	Method
Density (warp x weft)	2.6 x 2.25	[ends/cm]	GB/T 18370-2001
Tex (warp x weft)	1200 x 1200	[g/km]	ISO 1889
Weight	585	[g/m ²]	ISO 3374

Specimens were cut out of laminates prepared by contact method using rollers. Fabrication process was carried out conserving weight proportions of reinforcement to matrix as 3 to 4. Assuming that E-glass density equals $2.58 \text{ [g/cm}^3\text{]}$ and utilizing data given in Tab. 1. we calculate a volumetric enforcement ratio of laminates [4]:

$$f_f = \frac{V_f}{V_m + V_f}, \quad (2)$$

where:

f_f – volumetric enforcement ratio,
 V_f – volume of reinforcement material,
 V_m – volume of matrix material.

Subsequently we calculate theoretical density of specimen according to the given formula [5]:

$$\rho_{ct} = \rho_f \cdot f_f + \rho_m(1 - f_f), \quad (3)$$

where:

ρ_{ct} – theoretical density of laminate,
 ρ_f – density of reinforcement,
 ρ_m – density of matrix.

The main disadvantage of contact method constitute air blisters or voids that remain in the resin matrix when the rolling is not performed carefully. In this paper we demonstrate also the influence of voids in resin matrix on mechanical properties of fabricated laminates. Having measured the real specimen's density we calculate the voids percentage using following formula:

$$f_v = \frac{\rho_{ct} - \rho_{cp}}{\rho_{ct}} \cdot 100\%, \quad (4)$$

where:

f_v – voids percentage,
 ρ_{cp} – real density of laminate.

Ultimately, four kinds of laminates were used for testing which properties are tabulated beneath:

Tab. 5. Properties of tested laminates

Symbol	Matrix	Number of coupled layers: x in (1)	Total number of layers	Theoretical density
C1	A105	1	8	$1.46 \text{ [g/cm}^3\text{]}$
C2	A105	2	10	$1.46 \text{ [g/cm}^3\text{]}$
D1	K530	1	8	$1.46 \text{ [g/cm}^3\text{]}$
D2	K530	2	10	$1.46 \text{ [g/cm}^3\text{]}$

3. Testing procedure, results and interpretation

Bending tests were carried out according to the procedures described in adequate standards: PN-EN ISO 14125 for three point bending on machine INSTRON 8774 with 0.5% precision range. Comparison of results is shown in Fig. 1. We notice predictable relation, that maximum bending stress increases alongside with decrease of voids percentage. Considering laminate types marked as C1 and C2 we see that the maximum bending stress is greater for laminate consisting of 10 layers then for that of 8 layers. Taking into account that laminates C1 and C2 are of similar quality, this relation is different from the relation between maximum tensile stress and number of layers published in [5]. The relation between maximum bending stress and number of layers is inverse in case of laminates D1 and D2. In this case the laminate made up of 8 layers reveals greater maximum bending stress then that of 10 layers. This fact has its reason in quality differences. Laminates under consideration were made by contact method, so comparing D1 and D2 laminates we discover that laminate D2 was defectively impregnated and demonstrates tendency to delamination.

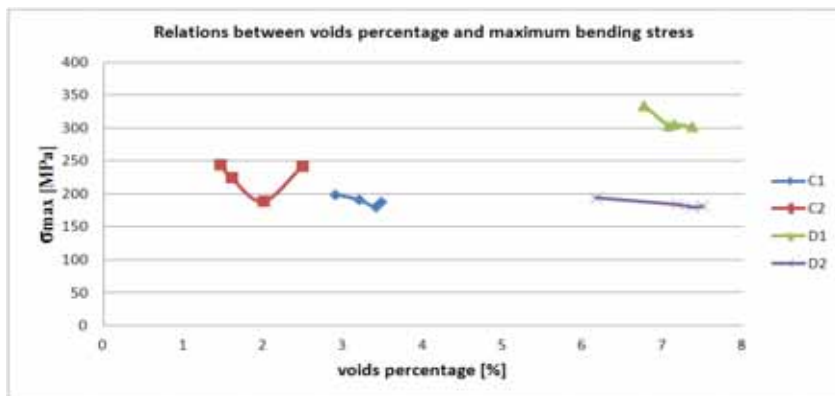


Fig. 1. The relation between voids percentage and maximum bending stress

The Fig. 2 and Fig. 3 reveal differences in fabrication quality of D1 and D2 laminates. Evaluating graphs of bending tests we notice that D1 laminate ruptures consistently in consequence of proper fabrication method while D2 laminate shows tendency to delamination.

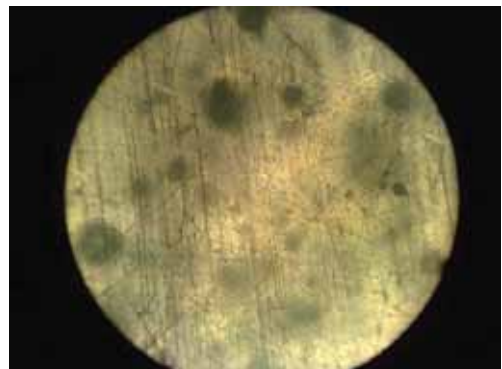
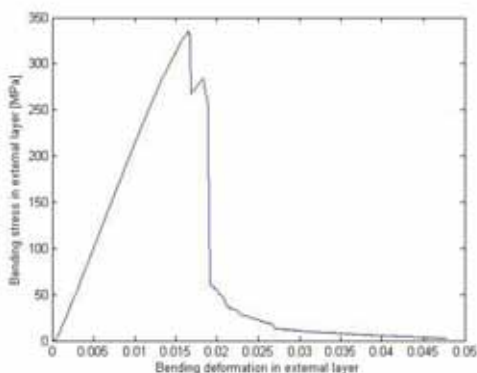


Fig. 2. The graph of bending test and structure of D1 laminate

The graph of bending test of D2 laminate (Fig. 3) shows clearly laminar form of crack. The quality of contact method of fabrication we may also evaluate comparing visible structure of laminate. We see that the D1 laminate has visible voids, but in structure of the D2 laminate we may see fibres of reinforcement. It reveals that impregnation of reinforcement is worse in D2 laminate than in D1 laminate.

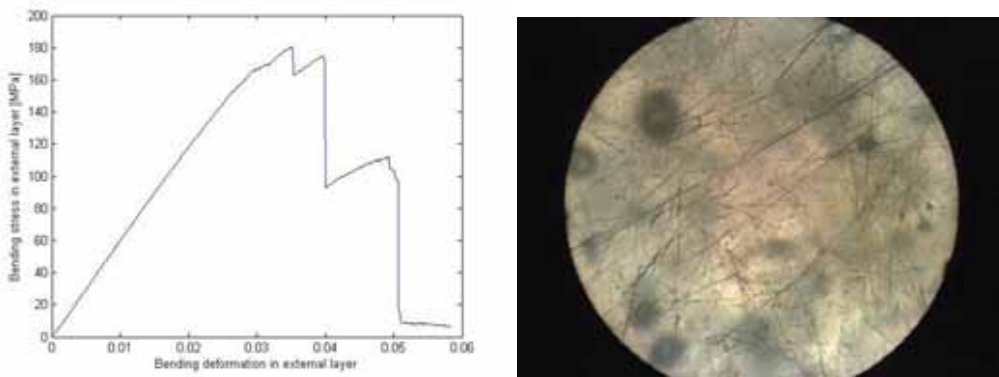


Fig. 3. The graph of bending test and structure of D2 laminate

Another case that needs an explanation is the increase of maximum bending stress in specimens having greater voids percentage. This is clearly visible in 4th specimen of the C1 laminate. This phenomenon may have two reasons. First, the technique of calculating voids percentages consists in measuring real density of specimens. If the local weight proportion of reinforcement to matrix is other then 3 to 4 it will cause the change in real density. The other possibility is that the voids situated in proximity of reinforcement fibres are more harmful for mechanical properties of laminate than voids situated in bulk resin matrix.

5. Conclusions

Analyzing the influence of voids percentage on maximum bending stress we conclude that its influence is harmful and in case of contact method of fabrication the local weight proportion of reinforcement to matrix may differ that influences calculation of voids percentages.

Maximum bending stress depends on number of layers that constitute the laminate and this relation is different from that in tensile loading.

References

- [1] www.compositn.net
- [2] Qi B., Ness R., Tong L., *A Stitched Blade-Stiffened RFI Composite Panel under Shear Loading*, Journal of Reinforced Plastics and Composites 2002, 21, pp. 255-276.
- [3] Kozioł M., Myalski J., Bogdan A., *Wytwarzanie kompozytów warstwowych metodą RFI*, Kompozyty 9:3(2009), pp. 265-270.
- [4] Wilczyński A.P., *Polimerowe kompozyty włókniste*, WNT, Warszawa 1996.
- [5] Ochelski S., *Metody doświadczalne mechaniki kompozytów konstrukcyjnych*, WNT, Warszawa 2004.



ANALYSIS OF THE WORKING PROCESS OF AN AUTOMATED HIGH BAY RACKING SYSTEM

Bogdan Landowski

*University of Technology and Life Sciences,
Faculty of Mechanical Engineering
ul. Kaliskiego 7, 85-796 Bydgoszcz, Poland
tel.: +48 52 3408495, fax: +48 52 3408495
email: lbogdan@utp.edu.pl*

Andrzej Pawlikowski

*Jabil Global Services Poland
ul. Fordońska 248G, 85-766 Bydgoszcz, Poland
email: apawlikowski_ando@wp.pl*

Abstract

This paper analyses selected aspects of effectiveness and reliability of one of the supply chain links, i.e. an automated high bay racking system (a stacker crane). The primary purpose of the research was to determine and analyse reliability indicators as well as to assess and analyse characteristics of changes of the working process being carried out. The research was performed according to the passive experiment method in natural operating conditions. The stacker crane and the individual operations of the working process were decomposed for the needs of the research. Identification of the object and subject of the research made it possible to identify significant (for the purposes of the paper) operational states of the investigated stacker crane. The working process being carried out was identified, a model of the working process was built and the performed operations were decomposed within the extent of the research. The paper presents selected results of the research performed.

Keywords: *automated high bay racking system, effectiveness, supply chain*

1. Introduction

This paper analyses selected aspects of effectiveness and reliability of one of the supply chain links, i.e. an automated high bay racking system hereinafter referred to as the stacker crane. The stacker crane (made by EGEMiN, Breadabaan 1201 B-2900 Schoten) is one of the material supply chain links for the storage areas of the enterprise under investigation. The object of the research is a service enterprise, specialised in repairing electronic devices (laptops, printers, scanners, switches, solar panels, AC adapters, computer screens, digital cameras, DVD players etc.). The enterprise deals with guarantee repairs, and it offers post-guarantee repairs, too.

The logistics processes in so called storage management, covering flow of material goods, creation of reserves as well as creation and processing related information require to have a specified technical infrastructure, consisting of [1, 7]:

- storage structures,
- on-site handling equipment (to transport cargo and manipulate the cargo),
- storage equipment,
- product packaging,
- computation and information technology devices as well as appropriate software.

Short series of products (i.e. laptops, screens), variety of models (about two thousand models), extensive variety of components (about six thousand) with simultaneous necessity to reduce stocks make the enterprise to use automated storage systems. The necessity to optimise personal costs (salary) and storage costs (rate of return of 1 m² of the warehouse) make it necessary to apply automated distribution of material, picking and packing orders.

According to the data presented by SSI SCHAFFER [9] the cost of storing materials in a warehouse may reach about 40% of the total storage costs. Shortening the time to move the materials according to the principle “a product to an employee” increases productivity. Automated storage equipment may be a crucial element in the cost optimised logistics chain. This equipment is used, among other things, in the logistics subsystems in which short access time to the material being stored is required. The primary tasks of such a warehouse is to receive materials from a supplier, periodic storage, and then successive deliveries of them to satisfy the needs of the service part of the enterprise.

The primary goal was to determine and analyse selected reliability indicators as well as to assess and analyse characteristics of changes of the working process being carried out.

The stacker crane and the individual operations of the working process being carried out were decomposed for the needs of the research. The analysis of the space of the operational states of the stacker crane and the analysed working process made it possible to identify the significant (for the purposes of the paper) operational states of the investigated stacker crane.

The next stage was to perform operational investigations of the stacker crane. The obtained source data concerning the states and operational events were entered into a computer system. The statistical analysis as well as the necessary calculations and data processing were performed by applying the MS Excel programme. The paper presents selected results of the research, calculations and analyses.

2. Research object

The research object is an electronic sector enterprise which provides comprehensive design, production and services for various industrial sectors. The primary place of business of the analysed enterprise is located in St. Petersburg, Florida, USA.

The analysed division of the enterprise employs some 650 people now. The area of the facility is about 21,500 square meters, divided into halls designated as A, B, C, D. Each of them is equipped with an incoming warehouse, a service hall, an outgoing warehouse. Logistics solutions:

1. Automated warehouse of components for all the projects.
2. Separated incoming warehouse and outgoing warehouse (finished goods) for the specific project.
3. Access to the warehouses through loading docks.
4. Global storage programme – Xelus Parts Planning (planning the components for 1 to 3 months; preparing the stock of components for new models with appropriate advance).
5. Advanced IT system, integrated service, storage and accounting programme enables to check the repair status in real time via WWW site.
6. Global agreement with the courier company UPS, DHL:
 - a) all the parcels are insured,
 - b) simplified complaint procedure,

- c) fixed time of deliveries of parcels to the division: at 8:00 a.m., collection of parcels at 8:00 p.m. (road transport / air transport),
- d) guaranteed time of delivering parcels, at the latest within 24 hours.

The investigated stacker crane is an automatically controlled, single aisle rail guided stacker crane, intended to store small components.

A typical rail guided stacker crane is made of the following parts:

- a beam connected with the traction assembly to move the stacker crane along the racks and power rail fixed to the warehouse flooring,
- a post connected with the traction beam and equipped with the parts fixing it to the rack structure in its upper part,
- trolley moving vertically with a catch (tray) for cargo (container),
- electric driving and controlling system.

The stacker crane (Fig. 1, Fig. 2) consists of a working aisle in which a single-mast trolley moves guided by steel rails, and on both side of the aisle racks are installed. The order picking and packing as well as the container handling area, equipped with conveyors, is positioned at the beginning of the racking system. The stacker crane leaves the cargo taken from the rack at this place. Then the conveyor takes a container to the operator (warehouse operative) and after completing the operator's task (for instance taking one item of the order) the container, after scanning the code, is moved back the rack place. The equipment is controlled by the computer programme based on the WMS (Warehouse Management System) which registers location of all the materials in the warehouse, and records them on real time basis.

The structure of the equipment is designed to handle cardboard boxes, steel trays or containers as cargo carriers. Materials (electronic components) are stored in containers. The stacker crane is equipped with a set of sensors allowing, from the operator's place, to interact with the environment – performance of a transport task. The executive elements are motors: for the X axis (along the movement aisle), for the Z axis (vertical movement – lifting the tray) and for the Y axis (trolley with the tray – inserting a container into the racking system). The operator controls, by means of the computer system, the operations "Bring", "Send back" (this operation consists of scanning the tray code and sending the tray back) as well as the operation "Transport" (organizational changes in the warehouse), however picking and packing all the product groups takes place according to the ABC rule (the operator in the electronic register finds an index of the component ordered by a technician).

The basic task of the stacker crane is to receive materials from a supplier, periodic storage, and then successive deliveries of them from the warehouse to satisfy the needs of the service part of the enterprise.



Fig. 1. View of the stacker crane from the operator's side (own work)



Fig. 2. View of the telescopic platform (own work)

3. Selected research results

The research was performed according to the passive experiment method in natural operating conditions.

The selected results of the research presented herein refer to 17 selected exemplary so called working days. The working process being carried out was identified, a model of the working process was built and the performed operations were decomposed within the extent of the research. The following operations of the working process were distinguished and analysed:

- Bring (Fig. 3 shows decomposition of the operation),
- Send back – including scanning the tray number,
- Transport,
- Reject.

The selected research results presented herein refer mainly to the random variables denoting:

- the number of the analysed primary operations and their components,
- the duration of the distinguished operational states of the stacker crane.

The sum of all the correct and incorrect operations, within the time interval under investigation, was 11,448, of which wrong operations amounted to 3,978 and represent about 35% of all the operations.

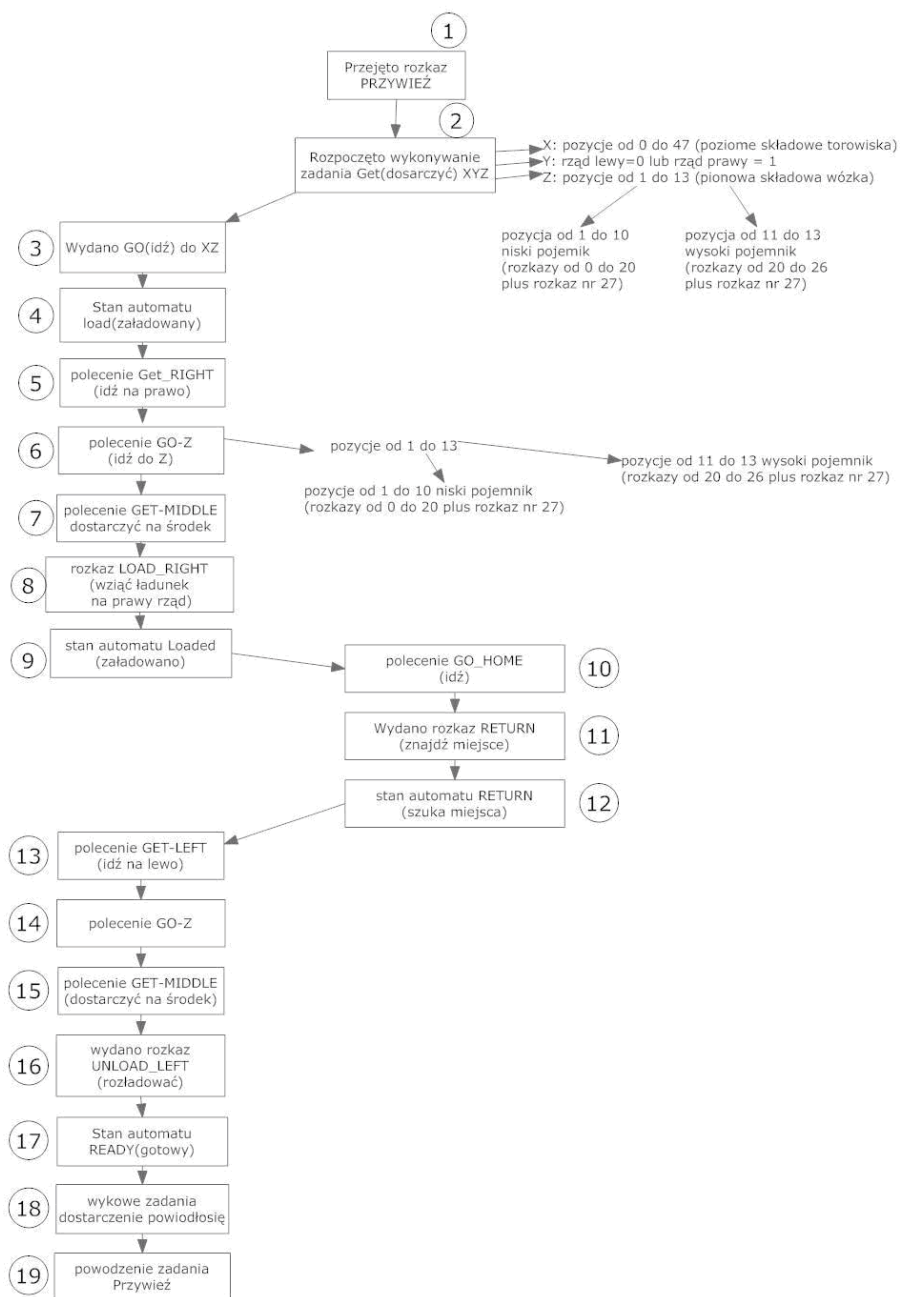


Fig. 3. Decomposition of the command Bring (own work)

The codes and abbreviations used later on in the paper (including the ones in the tables and on the diagrams) stand for:

- B1 – error code: Error! Performance of the command Bring,
- B2 – error code Error! Coordinates XYZ outside the range,
- B3 – error code Error! Number of the tray outside the range,

- B4 – error code Error! Failed to read the file with the shelf base,
- B5 – error code Error! Performance of the command MAN,
- B6 – error code Error! Performance of the command Send back,
- O-1 – code of the operator 1,
- O-2 – code of the operator 2,
- O-3 – code of the operator 3,
- O-4 – code of the operator 4.

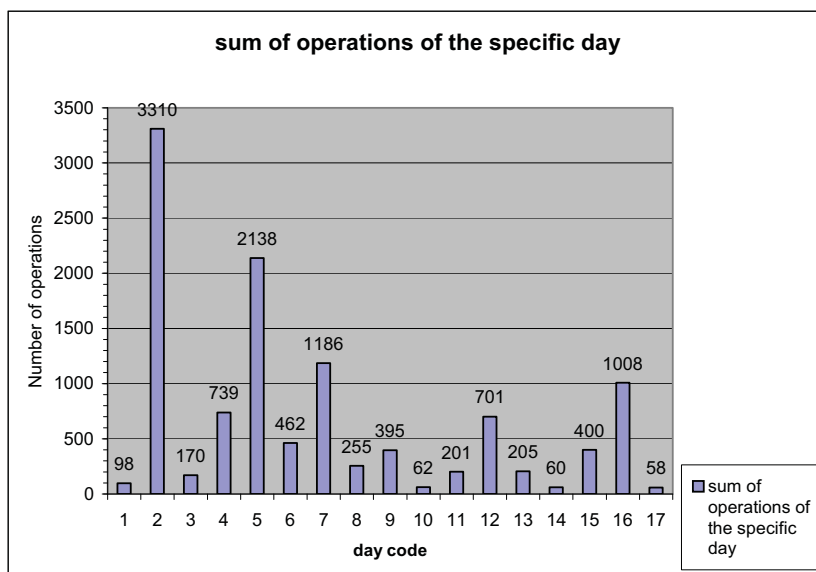


Fig. 4. Number of operations (own work)

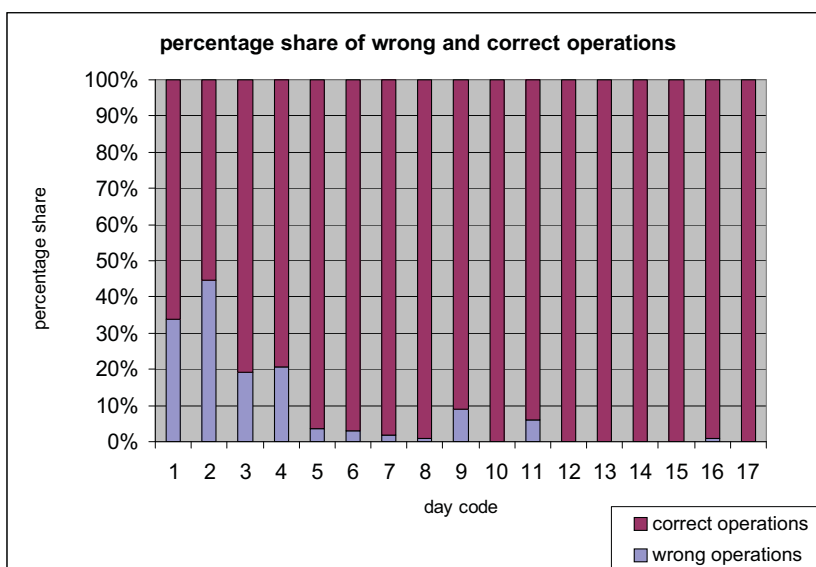


Fig. 5. Percentage share of wrong and correct operations in total number of the operations (own work)

The paper presents selected results of the research concerning duration of the analysed operations of the working process and their components later on. The following designations were applied:

- T_1 – duration of wrong operations (duration of the state S_1 – operational state, in which the object wrongly performs the working process operations),
- T_2 – duration of correct operations, (duration of the state S_2 – operational state, in which the object correctly performs the working process operations),
- $T_{2/1}$ – duration of the operations correctly performed, designated as “others” – starting the controller work, initiation of the object work, changing the server status, ending the controller work (duration of the state S_{21} – operational state (sub-state of the state S_2), in which the object correctly performs the working process operations designated as “others”),
- $T_{2/2}$ – duration of correctly performed operation Scanning the tray (duration of the state S_{22} – operational state (sub-state of the state S_2), in which the object correctly performs the operation Scanning the tray of the working process),
- $T_{2/3}$ – duration of correctly performed operation Send back (duration of the state S_{23} – operational state (sub-state of the state S_2), in which the object correctly performs the operation Send back of the working process)
- $T_{2/4}$ – duration of correctly performed operation Bring (duration of the state S_{24} – operational state (sub-state of the state S_2), in which the object correctly performs the operation Bring of the working process)
- $T_{2/5}$ – duration of correctly performed operation Transport (duration of the state S_{25} – operational state (sub-state of the state S_2), in which the object correctly performs the operation Transport of the working process)
- $T_{2/6}$ – duration of correctly performed operation Reject (duration of the state S_{26} – operational state (sub-state of the state S_2), in which the object correctly performs the operation Reject of the working process),

where:

$$T_2 = \sum_{i=1}^6 T_{2/i} \quad (1)$$

- T_3 – waiting time to perform the task (duration of the state S_3 – operational state, in which the object waits for performance of the task).

Moreover, values of the following indicators were determined:

W_1 – effectiveness indicator:

$$W_1 = T_2 / (T_2 + T_3) \quad (2)$$

W_2 – readiness indicator:

$$W_2 = (T_2 + T_3) / (T_1 + T_2 + T_3) \quad (3)$$

The selected results of the research are presented in the figures from 4 to 6 and in the tables from 1 to 3.

Tab. 1. Percentage share of duration of the analysed states (own work)

Day code	State code		
	S ₁	S ₂	S ₃
1	0.099	0.077	0.825
2	0.077	0.232	0.691
3	0.004	0.227	0.769
4	0.002	0.159	0.841
5	0.021	0.680	0.299
6	0.122	0.063	0.815
7	0.021	0.087	0.892
8	0.000	0.046	0.954
9	0.068	0.034	0.898
10	0.000	0.005	0.995
11	0.005	0.076	0.919
12	0.000	0.081	0.919
13	0.000	0.022	0.978
14	0.000	0.005	0.995
15	0.000	0.053	0.947
16	0.021	0.047	0.932
17	0.000	0.991	0.009
Sum	0.025	0.145	0.83

Tab. 2. Types of errors (own work)

Day code	Error code						Sum
	B1	B2	B3	B4	B5	B6	
1	34				16		50
2	709	41	2156				2906
3	76		1	8			85
4	372	1					373
5	102		4	2		48	156
6					100		100
7	42				9		51
8			2				2
9	35				102	21	158
10							
11	16				35		51
12							
13							
14							
15							
16	20				26		46
17							
Sum	1406	42	2163	10	288	69	3978

Tab. 3. Values of the selected indicators (own work)

Day code	State code				Indicator code		State code					
	S1	S2	S3				S2/1	S2/2	S2/3	S2/4	S2/5	S2/6
	Summary duration						Summary duration					
	T1	T2	T3	Suma			T2/1	T2/2	T2/3	T2/4	T2/5	T2/6
	hours:minutes:seconds				W1	W2	hours:minutes:seconds					
1	0:07:34	0:05:53	1:03:12	1:16:39	0,09	0,90	0:05:53	0:00:00	0:00:00	0:00:00	0:00:00	0:00:00
2	0:36:17	1:49:51	5:27:08	7:53:16	0,25	0,92	1:49:51	0:00:00	0:00:00	0:00:00	0:00:00	0:00:00
3	0:01:16	1:20:02	4:30:42	5:52:00	0,23	1,00	1:20:02	0:00:00	0:00:00	0:00:00	0:00:00	0:00:00
4	0:00:59	1:13:45	6:30:58	7:45:42	0,16	1,00	1:13:45	0:00:00	0:00:00	0:00:00	0:00:00	0:00:00
5	0:08:33	4:33:08	2:00:08	6:41:49	0,69	0,98	3:54:08	0:03:32	0:17:59	0:15:15	0:01:21	0:00:53
6	0:47:06	0:24:27	5:14:28	6:26:01	0,07	0,88	0:15:27	0:00:44	0:03:10	0:05:06	0:00:00	0:00:00
7	0:08:33	0:36:14	6:10:56	6:55:43	0,09	0,98	0:00:44	0:00:38	0:02:57	0:31:55	0:00:00	0:00:00
8	0:00:00	0:07:34	2:35:59	2:43:33	0,05	1,00	0:00:00	0:00:11	0:00:52	0:06:31	0:00:00	0:00:00
9	0:12:19	0:06:14	2:43:54	3:02:27	0,04	0,93	0:00:20	0:00:24	0:02:39	0:02:51	0:00:00	0:00:00
10	0:00:00	0:01:47	5:25:13	5:27:00	0,01	1,00	0:00:00	0:00:05	0:00:27	0:01:15	0:00:00	0:00:00
11	0:01:16	0:20:00	4:01:15	4:22:31	0,08	1,00	0:16:52	0:00:27	0:00:59	0:01:42	0:00:00	0:00:00
12	0:00:00	0:18:06	3:24:02	3:42:08	0,08	1,00	0:00:03	0:01:26	0:07:22	0:09:15	0:00:00	0:00:00
13	0:00:00	0:05:19	3:55:37	4:00:56	0,02	1,00	0:00:00	0:00:25	0:02:08	0:02:46	0:00:00	0:00:00
14	0:00:00	0:01:44	5:43:30	5:45:14	0,01	1,00	0:00:00	0:00:05	0:00:29	0:01:10	0:00:00	0:00:00
15	0:00:00	0:23:59	7:04:59	7:28:58	0,05	1,00	0:06:12	0:00:48	0:04:53	0:12:06	0:00:00	0:00:00
16	0:13:29	0:30:12	9:57:15	10:40:56	0,05	0,98	0:05:42	0:02:00	0:10:25	0:12:05	0:00:00	0:00:00
17	0:00:00	1:13:29	0:00:42	1:14:11	0,99	1,00	1:12:26	0:00:05	0:00:25	0:00:33	0:00:00	0:00:00
Sum	2:17:22	13:11:44	75:49:58	91:19:04	---	---	10:21:25	0:10:50	0:54:45	1:42:30	0:01:21	0:00:53

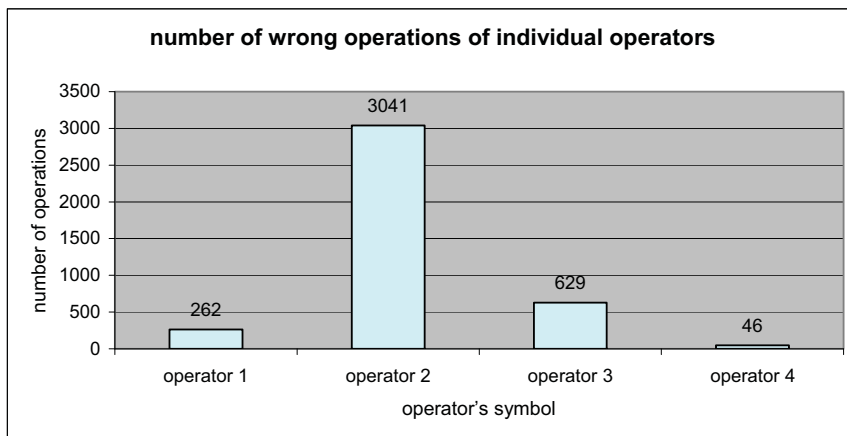


Fig. 6. Number of wrong operations, split into the specific operator (own work)

4. Summary and final conclusions

A stacker crane and the working processes being performed in a real operating system were decomposed for the needs of the paper. On the basis of the research it was found that the EGEMiN

post stacker crane was characterised by the following values of duration of the analysed states during the time interval under investigation:

- S_1 – 2 hours 17 minutes 22 seconds (performance time of wrong operations), which represents 3% of the total working time of the stacker crane;
- S_2 – 13 hours 11 minutes 44 seconds (performance time of correct operations), which represents 14% of the total working time of the stacker crane;
- S_3 – 75 godzin 49 minutes 58 seconds (waiting time to perform the task), which represents 83% of the total working time of the stacker crane.

The sum of all the correct and incorrect operations, during the time interval under investigation, was 11,448, of which wrong operations amounted to 3,978, which represents about 34.7% of all the operations. The nominal time of the operator's work (warehouse operative) is 136 hours, the actual time of work of the stacker crane is 91 hours 19 minutes 4 seconds, which represents about 67.1% of the nominal time of the operator's work.

The total duration of the operations Bring, Send back (including the tray scanning), Transport, Reject as well as other operations (changing the server state, starting the controller work, ending the controller work, etc.), represents 14% of the working time of the equipment. The duration of the state of the object waiting to perform the tasks Bring, Send back (including the tray scanning), Transport, Reject represents 83%, and of the wrongly performed operations is 3% of the object working time. The average value of the analysed effectiveness indicator W_1 of the stacker crane in the time interval under investigation was 17%.

It was observed that the operator designated with the code O1, performed wrong operations much more frequently than the other operators. The percentage share of the errors caused during the work of the operator designated with the code O1, in the total number of wrongly performed operations is 76.4% of wrong operations for the time interval under investigation. Additional investigation of the reasons for performing wrong operations by the operator designated with the code O1 should be considered.

Liquidation of the investigated fixed asset (the EGEMiN stacker crane) should be considered due to low level of use (the ratio of the effective working time of the stacker crane to the time of the operator's work <the shift duration>).

It seems that the elaborated method to analyse the operation and maintenance process of the analysed stacker crane, performed in the research object, the element of which is the compiled set of the patterns of the spreadsheets (containing, among other things, calculation formulas for automatic determination of values of the analysed indicators) is a useful tool to assess effectiveness and readiness of the investigated EGEMiN stacker crane. By using the created pivot tables of the MS Excel programme it is possible to obtain data from the files of the controlling programme of the stacker crane (Log module) and process them automatically in order to obtain results in the form of a set of the indicators and a presentation of the results in a graphical form. The results of the performed work as well as the remarks and observations made when identifying the research object and subject and when performing the research work were handed over to the decision makers of the analysed enterprise. Their effect was an introduction of changes to the work organisation, modification of the operating process of the investigated stacker crane and modification in the enterprise management subsystem.

References

- [1] Abt S., *Systemy logistyczne w gospodarowaniu. Teoria i praktyka logistyki*, Wydanie II, Wydawnictwo Akademii Ekonomicznej, Poznań 1997.
- [2] Aldag R. J., Stearns T. M., *Management*, South Western Publishing Co., Cincinnati 1987.
- [3] Blokus-Roszkowska A., Kołowrocki K., Kwiatkowska-Sarnecka B., Soszyńska J., *Modelowania niezawodności i bezpieczeństwa złożonych systemów i procesów*, Problemy

- niezawodności systemów XXXV Zimowa szkoła niezawodności, Wydział Transportu Politechniki Warszawskiej, Szczyrk 2007.
- [4] Bukowski L., *Prognozowanie niezawodności i bezpieczeństwa systemów zautomatyzowanych*, Problemy niezawodności systemów XXXI Zimowa Szkoła Niezawodności, Wydział Transportu Politechniki Warszawskiej, Szczyrk 2003.
 - [5] Coyle J. J., Bardi E., Calvinato J. L., *Transportation*, West Publ. Co., New York 1990.
 - [6] Dokumentacja techniczno-ruchowa CRC, EGEMIN, Holandia 1993.
 - [7] Fijałkowski J., *Transport wewnętrzny w systemach logistycznych - wybrane zagadnienia*, Oficyna Wydawnicza Politechniki Warszawskiej, Warszawa 2000.
 - [8] Krawczyk S., *Zarządzanie procesami logistycznymi*, PWE, Warszawa 2001.
 - [9] Malanowska I., Fajfer P., *Zastosowanie nowoczesnych technologii dla zwiększenia efektywności zarządzania magazynem*, E-mentor nr 2 (39)/2011 (www.e-mentor.edu.pl/artykul/index/numer/39/id/833).
 - [10] Woropay M., Knopik L., Landowski B., *Modelowanie procesów eksploatacji w systemie transportowym*, Biblioteka Problemów Eksploatacji, Bydgoszcz-Radom 2001.



SURFACE LAYER MICROSTRUCTURE AND MICROHARDNESS AFTER TURNING IN DIFFERENT COOLING AND LUBRICATING CONDITIONS

Tadeusz Leppert

University of Technology and Life Sciences
ul. Prof. S. Kaliskiego 7, 85-789 Bydgoszcz, Poland
e-mail: tleppert@utp.edu.pl

Abstract

The cooling and lubricating liquids widely used in metal machining are more and more often considered to be harmful to the natural environment and human health. For economic and ecological reasons the industry and research institutions are searching for methods and measures to limit or eliminate them. This is naturally determined by the conditions that the quality of machined surfaces has to be the same or at least comparable to that obtained with conventional cooling methods. The article presents the results of research into the influence of cooling and lubrication on surface layer physical properties -microhardness and microstructure changes, after turning the C45 and X2CrNiMo 17-12-2 steel dry, with minimal quantity lubrication (MQL) and emulsion in a wide range of cutting parameters. Significant differences in the microhardness parameter $HV_{0.02}$ and surface layer microstructure depending on the cutting zone cooling and lubrication conditions have been observed. The research has also shown that despite difficulty in turning X2CrNiMo 17-12-2 steel, properly selected cutting parameters help to limit or eliminate fluids used in conventional cooling and lubrication and still obtain comparable or even better surface layer quality.

Keywords: surface layer microhardness, microstructure; dry, MQL, wet turning

1. Introduction

Eliminating or limiting the application of cutting fluids is related to changes in the interaction between the thermal and mechanical factor in the process of constituting the surface layer. As a result, the phenomena occurring in the turning process cause changes in the surface layer which, compared to the core material, can be characterized by highly differentiated microhardness and metallographic microstructure [2,3,13]. This has a considerable influence on the application-related properties of the surface produced. The significant changes in the structure of the surface layer appear in dry turning of difficult-to-machine steels e.g. titanium alloys or corrosion and temperature resistant steels [1,2,7,9]. Low thermal conductivity and high chemical reactivity of these alloys with many tool materials result in a higher temperature in the cutting zone and material increased plastic deformations. This, on the other hand, leads to an increased tool wear, greater surface roughness and strong chip-tool adhesion and surface texture deformations [1,11,13]. Additionally, the high temperature causes microstructure changes and phase

transformations which can take the form of changed microhardness and metallurgical alterations in the surface layer [4]. Depending on the employed cutting parameters a white layer can be created, which causes the hardness of the surface layer to be higher or lower than that of the bulk material [2,4,5,7,8,11,12]. Surface layer properties after turning carbon and difficult to machine steels in various cooling and lubrication conditions have not been adequately investigated and remain still the subject of scientific interest.

The aim of the conducted research was to determine the influence of cooling and lubrication conditions on the surface layer microhardness and microstructure alteration in turning carbon steel C45 and austenitic stainless steel X2CrNiMo 17-12-2 dry, with MQL and emulsion in a wide range of cutting parameters.

2. Experimental procedure

Turning tests were carried out on a lathe TUD 50 for which carbon C45 and austenitic stainless steel X2CrNiMo 17-12-2 rods with 15 mm length segments for each cutting test were prepared. In advance of turning experiments, the test specimens were pre-machined with 1 mm depth of cut. The workpiece chemical composition and mechanical properties are presented in table 1.

Tab. 1. Chemical composition and mechanical properties

Steel	Chemical composition, %								
	C	Si	Mn	P	S	N	Cr	Mo	Ni
X2CrNiMo 17-12-2	<0,03	≤1,0	<2,0	≤0,045	≤0,015	≤0,011	16,5-18,5	2-2,5	10-13
C45	0,42-0,50	0,17-0,37	0,5 - 0,8	≤ 0,04	≤ 0,04	-	≤ 0,30	≤ 0,10	≤0,30
Mechanical properties									
	R _e , MPa		R _m , MPa		A ₅ , %		HB		
X2CrNiMo 17-12-2	200		500-700		40		215		
C45	340		620		16		207		

The sintered carbide inserts SNMG 120408TF grade IC907 with a TF chip breaker covered using the PVD method with a (TiAlSi)N coating (produced by ISCAR) were used. They were fixed in a tool holder MSS 2525-12-EB (produced by Mircona AB) with cooling channels for an internal lubrication system. The tool point had the following geometry: the orthogonal rake angle $\gamma_0=5^\circ$, orthogonal clearance angle $\alpha_0=10^\circ$, cutting edge angle $\kappa_r=45^\circ$, cutting inclination angle $\lambda_s=0^\circ$ and corner radius $r_\epsilon=0,8$ mm. Each set of turning experiments was conducted using a new insert edge.

The cooling and lubrication methods included:

D - dry cutting,

MQL - minimum quantity lubrication, carried out by an Accu-Lube Minibooster II applicator which produced a mixture of lubricant (biodegradable vegetable oil Accu-Lube LB 8000) and air in the form of fine aerosol, targeting the rake face and principal and auxiliary flank. The oil utilization by the MQL system was $0,014 \text{ mm}^3/\text{s}$.

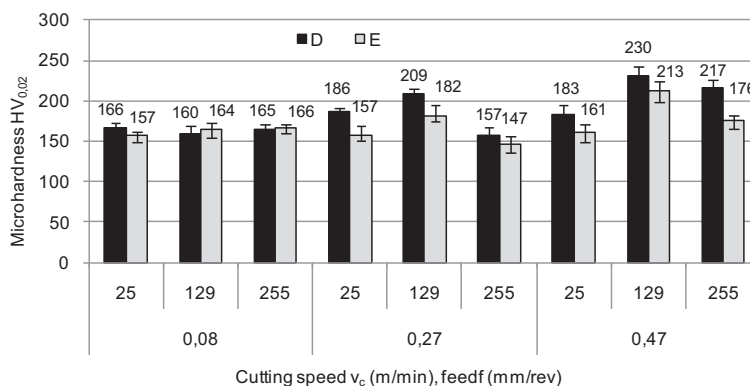
E - application of 6% emulsion with $0,07 \text{ dm}^3/\text{s}$ flow volume.

The experiments were conducted in two steps. The preliminary tests were carried out in dry and with emulsion turning using C45 steel. For austenitic stainless steel X2CrNiMo 17-12-2 the experiments were performed in turning dry, with MQL and emulsion.

The microhardness measurements were made on metallographic specimens of the surface layer cross-sectioned perpendicularly to the machined surface. The microhardness (Vickers' method) of the external cylindrical surface as well as inside the surface layer was measured with a Hanemann-type hardness tester under a load of 0,2 N. For each set of results a mean value and standard variation were calculated. The measurement of depth of plastic deformations in the surface layer and pictures of the metallographic structure were made with an optical microscope Epityp 2 (Carl Zeiss Germany) at a 400x magnification.

3. Results and discussion

Microhardness and metallographic structure are crucial parameters which describe physical properties of the surface layer. The results of microhardness measurements of the surface layer of C45 steel specimens presented in Fig. 1 prove that the influence of the cooling and lubrication mode in the cutting zone on the surface layer microhardness is highly diversified, without a clearly visible tendency. The existing differences in the surface layer hardness depend on the employed cutting parameters. Eliminating cooling and lubricating liquids from the process of machining of the C45 steel in the range of the used cutting speeds and feed rates causes an increase in the surface layer microhardness. At low cutting speeds (25m/min), increasing the feed rate from 0,08 to 0,47 mm/rev does not significantly influence the microhardness. When the cutting speed increases up to 129 m/min, increasing the feed rate results in a greater microhardness of the surface layer. After turning at a speed of 255 m/min, as the feed rate increases from 0,08 to 0,27 mm/rev, the surface layer microhardness becomes lower both in dry machining and in machining with emulsion. When the feed rate is increased to 0,47 mm/rev, the microhardness becomes bigger. In addition, the difference in microhardness between dry turning and turning with emulsion becomes clearer, the values for dry turning are higher by approximately 23% than those for turning with emulsion and equal to 217 and 176 HV_{0,02} respectively. In many combinations of cutting speeds and feed rates, the presented results of the measurements for dry turning and turning with emulsion do not differ significantly. This may mean that a change of conditions in the chip formation zone was not significant enough to have any impact on the microhardness of the surface layer.



Rys. 1. Influence of cooling and lubricating mode on surface layer microhardness (steel C45)

The pictures of metallographic structures of the surface layer taken perpendicularly to the machined surface are presented in Fig. 2. They show plastically deformed grain of the

metallographic structure created in dry turning and turning with emulsion of steel C45. The texturized grains, an effect of mechanical loads during machining, are also visible.

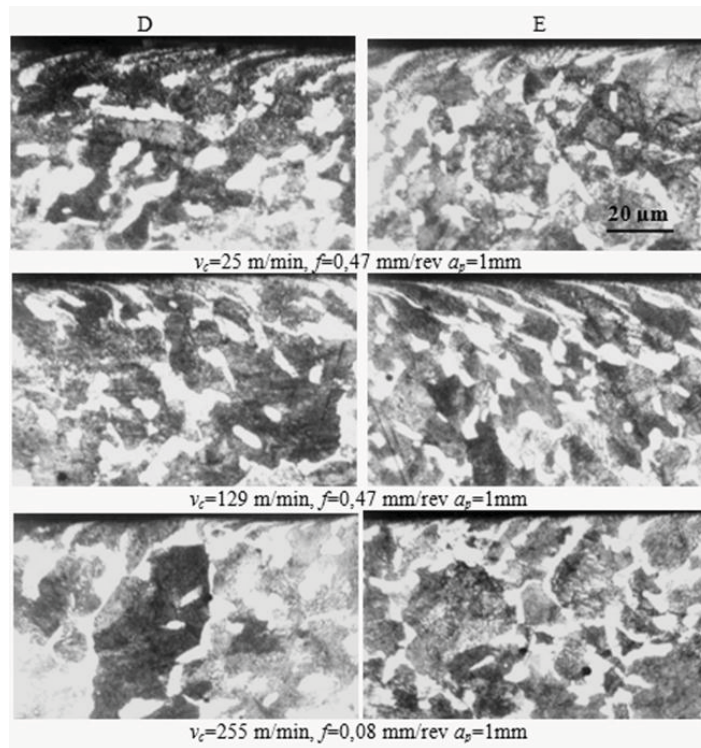


Fig. 2. Metallographic structure of the surface layer after turning dry and with emulsion, depending on the cutting speed and feed rate (steel C45)

The depth of the deformed surface layer determined on the measurements of the plastically deformed grains of the metallographic structure in the range of the used cutting parameters varies from 5 to 24 μm (Fig. 3). Eliminating emulsion from the process of machining contributes to an increased depth of deformations in the surface layer at low cutting speeds (25 m/min). As the depth increases, so does the depth of plastically deformed layer after turning with emulsion, which can be attributed to lower material hardness at a higher temperature of machining and material's increased tendency to undergo plastic deformations [6]. Out of the technological parameters of machining, the greatest influence on the depth of plastic deformations in the surface layer is exerted by the feed rate: increasing it leads to deeper plastic deformations. The impact of the cutting speed depends on the used mode of cooling and lubrication and on the feed rate. Increasing the cutting speed from 25 to 255 m/min at a fixed feed rate of 0,08 mm/rev causes deeper plastic deformations both in dry machining and machining with emulsion. The depth of plastic deformations in the former is higher.

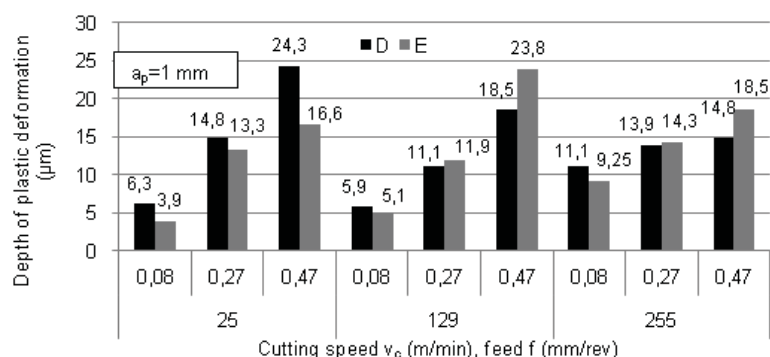


Fig. 3. Influence of cooling and lubrication mode on the depth of plastic deformations in the surface layer (steel C45)

When the feed rate is increased to 0,27 mm/rev, the influence of the increased cutting speed on the depth of plastic deformations is lower, and at a feed rate of 0,47 mm/rev it can be seen that the depth of plastic deformations in the surface layer in the function of the cutting speed after dry turning is lower as well. This is a result of the cutting temperature becoming higher, which reduces cutting resistance. In machining with emulsion, the depth values are similar. The resultant changes of the thickness of the plastically deformed surface layer depend on the strength of the mechanical and thermal factor [4]. At the same time the deformation of the metallographic structure proves that the mechanical factor plays a crucial role in turning with emulsion.

The results of the measurements of the surface layer microhardness after dry turning of the X2CrNiMo17-12-2 steel, turning with MQL and turning with emulsion reveal significant differences in microhardness values both on external surfaces and deeper into the workpiece (fig. 4). As the depth of the surface layer increases, the variation of microhardness disappears or becomes insignificant (Fig. 4b). The change of the surface layer microhardness value compared to the core hardness (M point) ranges from 326 to 248 HV_{0,02} and appears at a depth of 0,13 mm. In the range of the used modes of cooling and lubrication as well as cutting parameters, the lowest values of microhardness were recorded after turning with MQL (281 HV_{0,02}), and the highest after turning with emulsion (358 HV_{0,02}). This can be justified by a tendency of this steel to become hardened as a result of plastic deformations when the action of a cooling medium is intensified [9]. The increase of the temperature in dry turning caused greater plasticization of the material in the chip formation zone, which negatively affected the cutting force and work piece hardening in the surface layer. The impact of MQL caused a larger decrease in microhardness in turning with emulsion than was the case in dry turning, especially at a low feed rate (0,08 mm/rev). The action of the lubricating medium in oil aerosol, despite lowered friction between the moving surfaces of the tool edge and machined workpiece, had a limited influence on the decrease of surface layer microhardness as compared to dry turning.

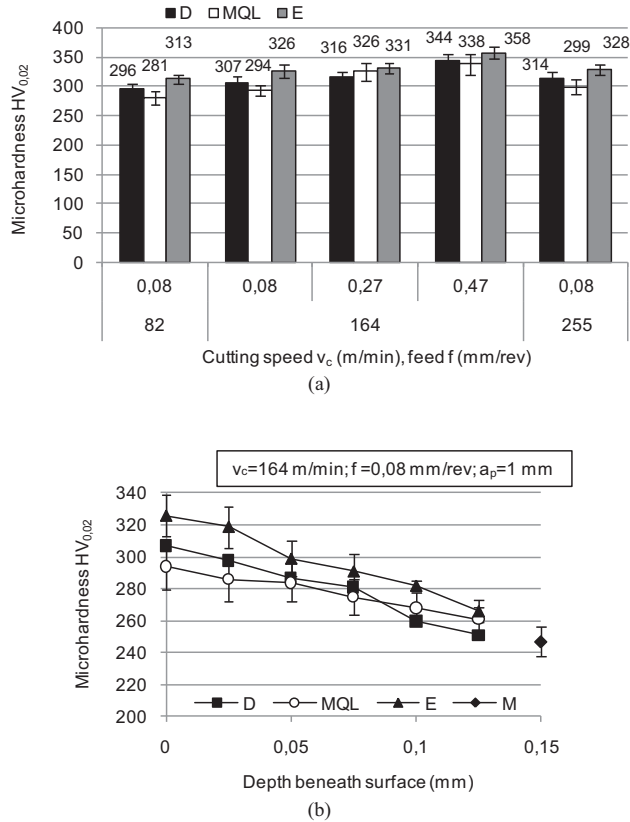


Fig. 4. Influence of cooling and lubrication mode on surface layer microhardness (a) and inside the surface layer (b) (steel X2CrNiMo17-12-2)

The influence of the cutting parameters on the surface layer microhardness measured on external surface of the machined sample is presented in Fig. 5. The measurement results revealed a significant impact of the cutting speed (ranging from 82 to 164 m/min) on the surface layer microhardness after turning with MQL and with emulsion (Fig. 5a). A further increase in the cutting speed up to 255 m/min influenced the surface layer microhardness to a lesser degree. In dry turning and in turning with MQL it increased by app. 2% whereas in turning with emulsion the increase equaled to 0,6%. A greater increase in the surface layer microhardness was caused by the feed rate and depth of cut. However, similarly to the cutting speed, the two parameters do not change the impact of the cooling and lubricating mode. After dry turning and turning with emulsion a greater increase of the surface layer microhardness was observed when the feed rate increased from 0,27 to 0,47 mm/rev than when it increased from 0,08 to 0,27 mm/rev and equaled to app. 28 $HV_{0.02}$ (Fig. 5b). In the case of MQL machining, the greatest increase of the surface layer microhardness (45 $HV_{0.02}$) was recorded when the feed rate ranged from 0,08 to 0,27 mm/rev. As the depth of cut increased from 0,5 to 2 mm, the values of the surface layer microhardness became higher both in dry and MQL turning as well as in turning with emulsion (Fig. 5c). The greatest increase (from 284 to 312 $HV_{0.02}$) was observed in MQL turning. The increase in value of these parameters means a larger cross-section of undeformed chip and greater machining resistance, both of them influencing the action and level of plastic deformations in the cutting zone, which cause greater hardness of the surface layer [10]. The observed differences in these values may be attributed to the influence of cooling and lubricating conditions of the cutting

zone and to their impact on thermal and mechanical factors.

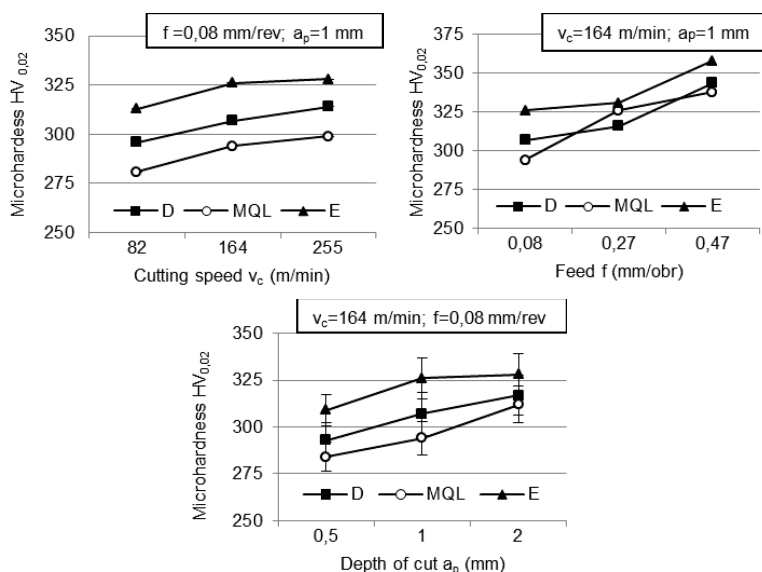


Fig. 5. Influence of cutting speed (a), feed rate (b), depth of cut (c) on surface layer microhardness in used cooling and lubrication conditions (steel X2CrNiMo17-12-2)

The pictures of metallographic structures after turning X2CrNiMo17-12-2 steel at a feed rate of 0,08 mm/rev do not show any clear changes of grains, depending on the cooling and lubrication mode in the cutting zone (Fig. 6). The change of the cutting speed from 82 to 255 m/min did not cause any change in the shape of the grain in the metallographic structure of the surface layer. Increasing the feed rate to 0,47 mm/rev caused slight texturizing of the grain at a depth of app. 4 μ m in turning with emulsion and in dry turning.

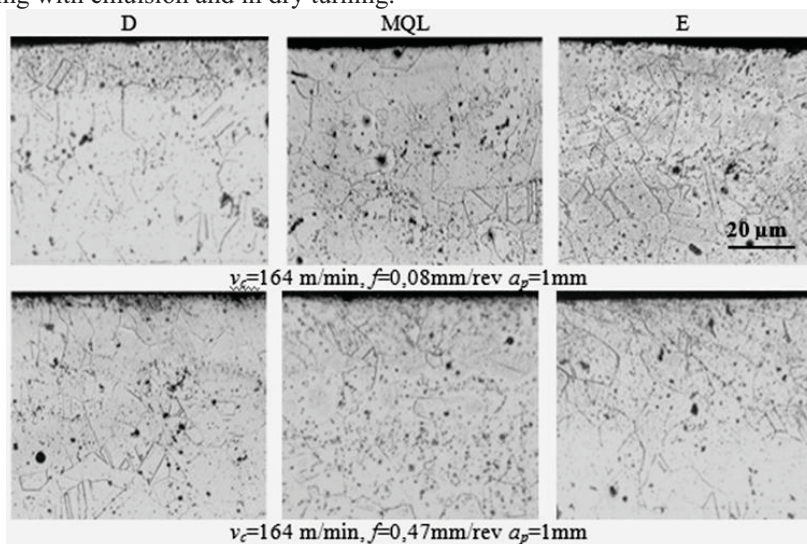


Fig. 6. Metallographic structure of the surface layer after turning dry, with MQL and with emulsion (steel X2CrNiMo17-12-2)

The application of oil fog, depending on the cutting parameters, limits plastic deformations. This is a result of lower friction and cutting force which, on the other hand, is caused by the presence of a lubricant between the moving surfaces of the tool edge and machined work piece with lower material strength in higher temperatures in dry turning, as compared to turning with emulsion.

4. Conclusions

The research has shown that the diversified influence of the cooling and lubricating mode of the cutting zone on the surface layer microhardness depends on the type of machined materials and cutting parameters.

Eliminating emulsion from the process of turning steel C45 causes increased the microhardness of the surface layer. In the range of the used cutting parameters, the values of the microhardness ranged from 157 to 230 HV_{0,02}, and it was the feed rate that influenced it to the largest extent..

The microhardness after turning austenitic stainless steel X2CrNiMo17-12-2 is lower after dry turning and turning with MQL than that after machining with emulsion. The differences in the surface layer microhardness depending on the cooling and lubricating mode disappear as the distance from the external surfaces increases. The greatest variation in the surface layer microhardness compared to the core hardness was observed after turning with emulsion. It ranged from 326 to 248 HV_{0,02}.

When the cutting speed, feed rate and depth of cut increase, so does the microhardness of the surface layer. The greatest influence on the increase in microhardness is exerted by the feed rate and depth of cut.

The cooling and lubrication mode in the cutting zone has a considerable influence on the depth of a plastically deformed surface layer of the C45 steel, whose value was app. 0,13 mm. Eliminating emulsion from the cutting process leads to higher values of the depth of plastic deformations in the surface layer at a low cutting speed (25 m/min). As its value increased, a higher value of the thickness of the plastically deformed layer was recorded after turning with emulsion.

The conditions of cooling and lubricating of the cutting zone and cutting speed in turning steel X2CrNiMo17-12-2 did not reveal any significant variation of the grain shape in the metallographic structure when the feed rate equaled to 0,08 mm/rev. Increasing the value of this parameter to 0,47 mm/rev caused a slight texturizing of the surface layer grain at a depth of up to 4 μm, in dry turning and turning with emulsion.

In the conditions of properly selected cutting parameters, the values of the analyzed indicators of surface texture after dry and MQL turning proved comparable to those achieved in emulsion turning. This means that an effort to eliminate or limit the application of cutting fluids in turning of the C45 and X2CrNiMo17-12-2 steel without quality deterioration is fully justified.

References

- [1] Akasawa, T., Sakurai H., Nakamura M., Tanaka T., Takano K., *Effects of free-cutting additives on the machinability of austenitic stainless steels*, Journal of Materials Processing Technology, Elsevier 143–144, pp. 66–71, 2003.
- [2] Che-Haron, C.H., Jawaid A., *The effect of machining on surface integrity of titanium alloy Ti–6% Al–4% V*, Journal of Materials Processing Technology, Elsevier, 166, pp. 188–192, 2005.

- [3] Che-Haron, C.H., Jawaaid A., *The effect of machining on surface integrity of titanium alloy Ti-6% Al-4% V*, Journal of Materials Processing Technology, Elsevier, 166, pp. 188–192, 2005.
- [4] Chou, Y.K., *Surface hardening of AISI 4340 steel by machining: a preliminary investigation*, Journal of Materials Processing Technology, Elsevier, 124, pp. 172–177, 2002.
- [5] Ezugwu, E.O., Tang S.H. *Surface abuse when machining cast iron (G17) and nikel-base superalloy (Inconel 718) with ceramic tools*, Journal of Materials Processing Technology, Elsevier, 55, pp. 63–69, 1995.
- [6] Han, S., Melkote S.N., Haluska M.S., T.R. Watkins, *White layer formation due to phase transformation in orthogonal machining of AISI 1045 annealed steel*, Materials Science and Engineering A, Elsevier, 488, pp. 195–204, 2008.
- [7] Ibrahim, G.A., Che Haron C.H., Ghani J.A., *The effect of dry machining on surface integrity of titanium alloy Ti-6Al-4V ELI*, Journal of Applied Sciences, Asian Network for Scientific Information, 9 (1), pp. 121–127, 2009.
- [8] Kompella, S., Moylan S.P., Chandrasekar S., *Mechanical properties of thin surface layers affected by material removal processes*, Surface and Coatings Technology, Elsevier, 146 – 147, pp. 384–390, 2001.
- [9] M'Saoubi, R. M., Outeiro J.C., Chandrasekaran H., Dillon O.W., Jawahir I.S., *A review of surface integrity in machining and its impact on functional performance and life of machined products*, International Journal of Sustainable Manufacturing, Inderscience Publishers, 1 (1/2) pp. 203–236, 2008.
- [10] Machado, A.R., Wallbank J., *The effect of extremely low lubricant volumes in machining*, Wear, Elsevier, 210, pp. 76–82, 1997.
- [11] Orrego, D.F., Jimenez L.B.V., Atehortua J.D.E., Ochoa D.M.L., *Effect of the variation of cutting parameters in surface integrity in turning processing of an AISI 304 austenitic stainless steel*, First Brazilian Conference on Tribology, pp. 434–446, 2010.
- [12] Tonshoff, H.K., Brinksmeier E., *Determination of the mechanical and thermal influences on machined surface by microhardness and residual stress analysis*, Annals CIRP, Elsevier, 29(2), pp. 519–530, 1980.
- [13] Wienert, K., Inasaki I., Sutherland J.W., Wakabayashi T., *Dry machining and minimum quantity lubrication*, CIRP, Elsevier, 53 (2), pp. 511–537, 2004.



INFLUENCE OF COOLING AND LUBRICATION ON CHIP FORMATION AND ITS FORM IN TURNING

Tadeusz Leppert

University of Technology and Life Sciences
ul. Prof. S. Kaliskiego 7, 85-789 Bydgoszcz, Poland
e-mail: tleppert@utp.edu.pl

Abstract

Machining with the use of cooling and lubrication liquids (called wet machining) is still the primary method of shaping constructional materials. However, economic and ecological factors cause that wet machining is being replaced by processes which use minimal quantities of cooling and lubrication liquids (MQL machining) or do not use them at all (dry machining). Eliminating cooling and lubrication from cutting processes results in higher temperatures during the cutting process and worse tribological conditions around the moving surfaces between the tool and workpiece. This, on the other hand, causes changes of the conditions in which the chip is formed and a different form of the chips. Another consequence is problems related to hot chips and difficulty measuring hot workpieces. The form of the chip is an important factor particularly noticeable in automated part manufacturing lines, where the chip has to be easily removable from the cutting zone - especially if the parts are made of difficult-to-machine materials. This paper presents results of an investigation into the conditions of chip formation and its form in dry, MQL turning as well as in turning with emulsion. The machined materials include constructional steel C45 and austenitic stainless steel X2CrNiMo 17-12-2. The obtained results confirm a significant role of cooling and lubrication conditions which, however, depends on the selected cutting parameters and the properties of the workpiece material. The results also helped to select cutting conditions which are most suitable for automated machining.

Keywords: cutting chip formation, form, turning dry, MQL, emulsion

1. Introduction

Machining with the use of cooling and lubrication liquids, called wet machining, is still the primary method of shaping constructional materials. However, economic and ecological factors cause that this type of machining is being replaced by processes which use minimal quantities of cooling and lubrication liquids (MQCL) or do not use it at all (dry machining) [1,10,12,15]. Eliminating cooling and lubrication liquids from the cutting process means that their basic functions such as cooling, lubricating and chip removal from the cutting zone are not performed. This fact constitutes the primary drawback of such methods. In practice it means that the cutting temperature is higher and the tribological conditions on the moving surfaces of the tool and workpiece are highly unfavorable. This further leads to quicker tool wear, uneven distribution of the surface layer properties and worse dimensional and shape accuracy of the part. It also changes the conditions of chip formation and its form as well as causing problems related to hot chips and measurements of a hot part. The high temperature melts the chips which stick to the cutting edge and the machined workpiece. The lack of lubrication means increased friction on the tool and flank faces and greater adhesion of the chip to the tool. This causes adhesion and blockage of the chip

area and, in consequence, difficulty removing the chip. Higher temperatures of the cutting process also result in the chip being more prone to deformations, assuming a ribbon-like, snarled form [3,5,6,7,9]. That is why one of the conditions of a successful implementation of dry and MQCL cutting is obtaining acceptable chips in terms of their form and easiness of removal from the cutting zone.

The conditions of chip formation and its shape have a significant influence on cutting efficiency and reliability as well as operators' safety. In terms of chip removal possibilities, uninterrupted machine operation, machine operator's safety and machined surface quality, chips can be divided into acceptable (ribbon-shaped short, helical, tubular, conical and washer type short, arc, connected, loose) and unacceptable (ribbon shaped long, helical, tubular and conical long) [8,13]. The form of the chip is strictly connected with the state of deformations and stresses in the chip formation zone. The factors influencing it include material strength and hardness, which contribute to the state of deformations and stresses in the chip formation zone and its form [4,7]. Apart from the properties of the machined material also the cutting parameters and cooling and lubrication conditions play a crucial role in determining the conditions for chip formation and its form [2,4,9,16].

The research and industrial practice show that eliminating entirely cooling and lubrication liquids from machining processes of certain materials or from certain types of machining requires an appropriate selection of cutting conditions - ones which will result in an acceptable form of the chip and will not cause difficulty in unattended removal from the cutting zone [7]. This problem is especially important in machining difficult-to-machine materials such as e.g. austenitic stainless steels.

The first aim of the research presented in this paper was to determine the impact of the cooling and lubrication mode and cutting parameters on chip formation conditions as well as its form in machining constructional steel C45 and austenitic stainless steel X2CrNiMo 17-12-2. Secondly, it was attempted to determine which cutting conditions will lead to formation of the chips which are acceptable in automated machining.

2. Experimental procedure

Cylindrical turning tests were carried out on carbon C45 and austenitic stainless steel X2CrNiMo 17-12-2 bars. The chemical composition and mechanical properties is presented in table 1.

The sintered carbide inserts SNMG 120408TF grade IC907 with a TF chip breaker covered by PVD method with (TiAlSi)N coating (produced by ISCAR) were employed. They were fixed in a tool holder MSS 2525-12-EB (produced by Mircona AB) with cooling channels for an internal lubrication system (Fig. 1). The following cutting point geometry was applied: the orthogonal rake angle $\gamma_0=5^\circ$, orthogonal clearance angle $\alpha_0=10^\circ$, cutting edge angle $\kappa_r=45^\circ$, cutting inclination angle $\lambda_s=0^\circ$ and corner radius $r_\epsilon=0,8$ mm. The quoted inserts were recommended for machining of stainless steel as well as soft steels machined with medium cutting speeds.

The following cooling and lubrication techniques and their designations were used in the experiments:

D - dry cutting, without cooling or lubrication,

MQL - minimum quantity lubrication, executed by a Minibooster II applicator (produced by Accu-Lube Manufacturing GmbH) for coolant fed tools (Fig.2). Biodegradable vegetable oil Accu-Lube LB 8000 was used as a lubrication medium. The oil consumption by the MQL system was adjusted at a level of $0,014 \text{ mm}^3/\text{s}$.

E - overhead flood application of 6% emulsion with $0,07 \text{ dm}^3/\text{s}$ flow volume, made on the basis of emulsifying oil ARTEsol Super EP (produced by W.O.P. ARTEFAKT).

Tab. 1. Chemical composition and mechanical properties

Steel	Chemical composition, %								
	C	Si	Mn	P	S	N	Cr	Mo	Ni
X2CrNiMo 17-12-2	<0,03	≤1,0	<2,0	≤0,045	≤0,015	≤0,011	16,5-18,5	2-2,5	10-13
C45	0,42-0,50	0,17-0,37	0,5 - 0,8	≤ 0,04	≤ 0,04	-	≤ 0,30	≤ 0,10	≤0,30
Mechanical properties									
	R _e , MPa		R _m , MPa		A ₅ , %		HB		
X2CrNiMo 17-12-2	200		500-700		40		215		
C45	340		620		16		207		

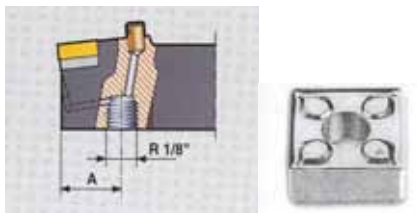


Fig. 1. Tool holder Mircona AB MSS 2525-12-EB and cutting insert SNMG 120408TF grade IC907
The experiments were carried out with the cutting parameters presented in table 2.

Tab. 2. Experimental cutting parameters

X2CrNiMo 17-12-2									
v_c (m/min)	82			164			255		
f (mm/rev)	0,08	0,27	0,47	0,08	0,27	0,47	0,08	0,27	0,47
a_p (mm)	1								
C45									
v_c (m/min)	76			190			237		
f (mm/rev)	0,08	0,27	0,47	0,08	0,27	0,47	0,08	0,27	0,47
a_p (mm)	1								

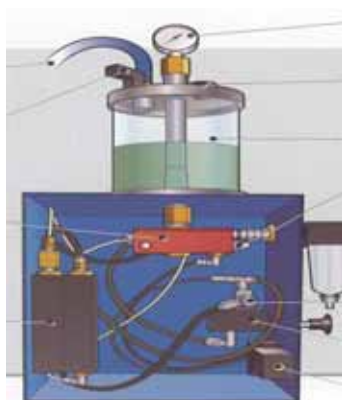


Fig. 2. Accu-Lube Minibooster II




























The chips generated in the process of turning were studied with an optical microscope MWP manufactured by PZO Warsaw, under 10x magnification.

3. Results and discussion

The form of the chips after turning C45 steel dry, with minimal cooling and lubrication in the cutting zone and with a conventional supply of emulsion in the range of employed cutting parameters was presented in table 3. Assessing it for the needs of automated machining systems, it can be concluded that the most desired chip form is loose arcs and short helical pieces [13]. The formation of helical tubular chips or washer type long and snarled is less acceptable because of the problems with removing them from the cutting zone or unacceptable because they may wrap around the tool and machined workpiece, which makes the elimination of the cooling and lubrication liquid impossible.

The interaction of cooling and lubrication conditions of the cutting zone largely depends on the applied cutting parameters. In the range of low and medium feed rates (0,08 and 0,27 mm/rev), the influence of cooling and lubrication in the cutting zone on changes in the chip form is limited. In turning steel C45, the most common are helical tubular long chips or ribbon snarled chips which are, however, difficult to remove. An increase in the feed rate causes a change of the chip form into one that is easier to remove from the cutting zone.

Table. 3. Chip forms after turning C45 steel (PL-ISO 3685)

Cutting parameters			Chip form		
v_c (m/min)	f (mm/rev)	a_p (mm)	D	MQL	E
76	0,08	1			
	0,27				
	0,47				
190	0,08	1			
	0,27				
	0,47				
237	0,08	1			
	0,27				
	0,47				

Elimination or reduction of the cooling and lubricating liquid results in a higher cutting temperature [11] and the friction between the chip and tool edge causes increased compression and curling of the chip [2,9]. In dry and MQL turning, at a feed rate of 0,47 mm/rev, the helical tubular long or helical washer type snarled chip changes its form into a helical tubular short or elemental one. The increase of the feed rate leads to a larger cross-section of the chip and, in consequence, its greater stiffness. This, in connection with a higher cutting speed, renders the chip more breakable. An application of a minimal quantity of a lubricating liquid changes the conditions for chip formation and its removal along the tool face. The penetration of the oil fog onto the chip contact surfaces prevents adhesion and changes the character of the chip-tool contact: rubbing turns into plastic flow, which results in lower compression and curling of the chip. As a result, the length of the chip-tool face contact surface decreases [2,4,9]. The obtained chip is characterized by lower

pulverization, compared to that after dry machining. An increase of the cutting speed at a low feedrate (0,08 mm/rev) causes the chip to be longer and snarled.

A microscopic analysis of the surfaces of the obtained chips performed at a 10x magnification shows that depending on the cooling and lubrication mode, elimination of the emulsion causes larger compression of the chip as a result of greater friction and adhesion between chip surface and the rake face of the tool (Fig. 3). This has also been confirmed in the study [14]. The back surface of the chip after dry turning is rough and dull, with clear signs of discontinuity of the chip material. It is dark blue in color, which clearly points to a high cutting temperature. The chip surfaces after MQCL machining are smoother and lighter, which is a result of a lower cutting temperature and lower chip compression as well as better chip flow conditions.


































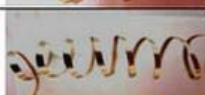








Cutting parameters			Chip form		
v_c (m/min)	f (mm/rev)	a_p (mm)	D	MQCL	E
76	0,08	1			
237	0,27				
	0,47				

Fig. 3. Influence of cooling and lubrication on the chip form (C45 steel)

Eliminating a cooling and lubricating liquid from the machining of the X2CrNiMo17-12-2 steel does not influence the change of the chip form as much as it does in machining the C45 steel. Upon analysis it can be seen that both in dry machining and in machining with emulsion in a wide range of the used cutting parameters, the chips look similar and are more readily removable than these after MQCL machining. The desired form (for the needs of unattended machine operation) includes: arc loose or connected chips as well as helical conical short chips. Replacing the emulsion with oil fog causes that machining generates undesired chip forms: instead of arc loose or connected chips, they are helical conical long and snarled or helical tubular long (tab. 4). Based on the obtained chip forms, it can be concluded that similar conditions of chip formation are also present in dry turning and in turning with emulsion, whose penetration of the chip-tool face contact area is limited - it is proved by a similar structure of the back part of the chips which come in contact with the tool rake (Fig. 4). The tendency of stainless steels to become hardened during machining causes greater compression of the chip, which means that at a lower feed rate (0,27 mm/rev) the obtained chip is arc loose or helical conical short in form.

Similarly to the C45 steel, it is the feed rate that has the greatest influence on the chip form. With its increase the chip form changes favorably in all the used modes of cooling and lubrication of the cutting zone. The cutting speed and depth of cut influence the chip form to a smaller extent. The analysis confirmed the results of the work [14], which pointed that the influence of the cutting speed on the chip form at large feed rates is negligible.

Table. 4. The forms of chips after turning X2CrNiMo17-12-2 steel (PL-ISO 3685)

Cutting parameters			Chip form		
v_c (m/min)	f (mm/rev)	a_p (mm)	D	MQL	E
82	0,08	1			
	0,27				
	0,47				
164	0,08	1			
	0,27				
	0,47				
	0,08	0,5			
		2			
255	0,08	1			
	0,27				
	0,47				


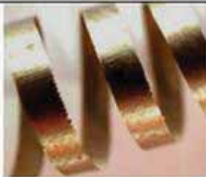
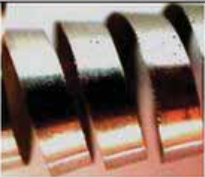

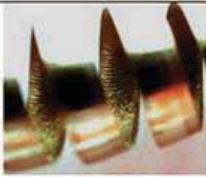




Cutting parameters			Chip form		
v_c (m/min)	f (mm/rev)	a_p (mm)	D	MQL	E
82	0,08	1			
255	0,27				
255	0,47				

Fig. 4. Influence of cooling and lubrication on the chip form (X2CrNiMo17-12-2 steel)

Conclusions

The analysis of chips after turning C45 and X2CrNiMo17-12-2 steels showed a large influence of the cooling and lubrication mode on their form and, in consequence, on the conditions in which they were formed and removed from the machining zone.

Eliminating or minimizing the application of cooling and lubricating liquids in the cutting process may favorably influence the chip form and cannot hinder the practical implementation of dry and MQL turning of the C45 steel. However, reaching an optimal form of the chip requires increased feed rates and cutting speeds.

Dry cutting of the X2CrNiMo17-12-2 steel facilitates achieving the chip form which is very similar to that after cutting with emulsion. A higher cutting zone temperature in dry turning causes lower strength and hardness of the machined material, which is connected with better conditions of chip formation. Reaching a satisfactory chip form in MQL turning requires increased cutting speeds and most of all, higher feed rates.

In the case of finishing turning of aforementioned steel in dry conditions at a low feed rate (0,08 mm/rev), eliminating or minimizing the use of cooling and lubrication media does not significantly influence the chip form, as compared to turning with emulsion. The analysis of the topography of back side of the chips obtained in dry and MQL turning as well as in turning with emulsion indicates on large plastic deformations, which become more intense as the feed rate increases as well as making the chip more brittle.

References

- [1] Avila, R.F., Abrao A.M., *The effect of cutting fluids on the machining of hardened AISI 4340 steel*, Journal of Materials Processing Technology, Elsevier, 119, pp. 21-26, 2001.

- [2] Dhar, N.R., Ahmed M.T., Islam S., *An experimental investigation on effect of minimum quantity lubrication in machining AISI 1040 steel*, Int. Journal of Machine Tools & Manufacture, Elsevier, 47, pp. 748–753, 2007.
- [3] Feldshtein, E., Maruda J., *Changes of some cutting process parameters when MQCL turning*, Advances in Manufacturing Science and Technology, Wyd. PAN, 30(3), pp. 55-64, 2006.
- [4] Feldshtein, E., Maruda J., *Poprawa skrawalności wybranych gatunków stali węglowych w warunkach minimalnego przepływu środka chłodząco-smarującego*, [W:] Obróbka skrawaniem T.3 Zaawansowana technika, Wyd. Uczeln. UTP w Bydgoszczy, pp. 139-146, 2009.
- [5] Feldshtein, E., Maruda J., *Wpływ sposobu chłodzenia i smarowania strefy skrawania na proces tworzenia i łamania wióra*, Archiwum Technologii Maszyn i Automatyzacji, Wyd. Politechniki Poznańskiej 25(2), pp. 9-18, 2005.
- [6] Islam, N.R., Islam M.W., Mithu S., *The influence of minimum quantity of lubrication (MQL) on cutting temperature, chip and dimensional accuracy in turning AISI-1040 steel*, Journal of Materials Processing Technology, Elsevier, 171 pp. 93–99, 2006.
- [7] Jawahir, I.S., Luttervelt C.A., *Recent developments in chip control research and applications*, Annals CIRP, Elsevier, 46 2, pp. 659-693, 1993.
- [8] Kaldor, S., Ber A., Lenz E., *On the mechanism of chip breaking*, Journal. of Engineering for Industry, Transactions ASME, 101, pp. 241–248, 1979.
- [9] Khan, M.M.A., Mithu M.A.H., Dhar N.R., *Effects of minimum quantity lubrication on turning AISI 9310 alloy steel using vegetable oil-based cutting fluid*, Journal of Materials Processing Technology, Elsevier, 209, pp. 5573–5583, 2009.
- [10] Klocke, F., Eisenblaetter G., *Dry Cutting*, Annals CIRP, Elsevier, 46 2, pp. 519 – 526, 1997.
- [11] Sales F.W., Diniz A.E., Machado Á.R., *Application of cutting fluids in machining processes*, Journal of the Brazilian Society of Mechanical Sciences 23(2), pp. 227-240, 2001.
- [12] Sreejith, P.S., Ngoi B.K.A., *Dry machining: Machining of the future*, Journal of Materials Processing Technology, Elsevier, 101, pp. 287-291, 2000.
- [13] *Tool-life testing with single-point turning tools*, ISO3685: 1993
- [14] Varadarajan, A.S., Philip P.K., Ramamoorthy B., *Investigations on hard turning with minimal cutting fluid application (HTMF) and its comparison with dry and wet turning*, Int. Journal of Machine Tools & Manufacture, Elsevier, 42, pp. 193–200, 2002.
- [15] Wienert, K., Inasaki I., Sutherland J.W., Wakabayashi T., *Dry machining and minimum quantity lubrication*, Annals CIRP, Elsevier, 53 (2), pp. 511-537, 2004.
- [16] Wójcik, R., Stachurski W., Górecki G., *Wpływ sposobu chłodzenia i smarowania na przebieg tworzenia wióra*, [W:] Obróbka skrawaniem T.3 Zaawansowana technika, Wyd. Uczeln. UTP w Bydgoszczy, 131-138, 2009.



APPROXIMATE DETERMINATION OF A STRAIN-CONTROLLED FATIGUE LIFE CURVE FOR ALUMINUM ALLOY SHEETS

Adam Lipski, Stanisław Mroziński

University of Technology and Life Sciences in Bydgoszcz
Faculty of Mechanical Engineering

Al. Prof. S. Kaliskiego 7, 85-789 Bydgoszcz, Poland

tel.: +48 52 3408220, fax: +48 52 3408271

e-mail: adam.lipski@utp.edu.pl, stanislaw.mrozinski@utp.edu.pl

Abstract

This paper deals with selected methods of approximate determination of a strain-controlled fatigue life curve for aluminium alloy sheets used in aircraft structures first of all. Authors based their analysis of those methods on the results of own research of 2024-T3 alloy and its Russian equivalent D16CzATW. The approximate strain-fatigue life curves were compared with the experimental curves. The influence of inconsistencies between those curves on the calculation results was analyzed on computational examples by means of the Palmgren-Miner's rule.

Keywords: aluminium alloy, fatigue properties, fatigue life curve, estimation method, monotonic tensile test

List of major symbols and abbreviations

$2N_f$ - reversals to failure (2 reversals = 1 cycle)

b - fatigue strength exponent

c - fatigue ductility exponent

E - Young's modulus, MPa

N_{cal} - calculating fatigue life obtained on the basis of the approximate strain-controlled fatigue life curve, cycles

N_{exp} - calculating fatigue life obtained on the basis of the experimental strain-controlled fatigue life curve, cycles

RA - reduction in area

S_u - ultimate tensile strength, MPa

ε_f - true fracture ductility

ε'_f - fatigue ductility coefficient

$\Delta\varepsilon$ - total strain range

$\Delta\varepsilon_e$ - elastic strain range

$\Delta\varepsilon_p$ - plastic strain range

σ_f - true fracture strength, MPa

σ'_f - fatigue strength coefficient, MPa

FPCM - Four-Point-Correlation Method

USM - Universal Slopes Method
 MUSM - Modified Universal Slopes Method
 UMLM - Uniform Material Law
 MFPCM - Modified Four-Point-Correlation Method
 MMM - Modified Mitchell's Method
 MM - Median Method

1. Introduction

Fatigue curves serve as the basis for the calculation of fatigue strength [7, 17]. As fatigue tests are characterised by high labour and time consumption and are very costly, it is not always possible to perform full range fatigue tests or, for comparison purposes, it is sufficient to approximately determine the fatigue curve based e.g. on relatively simple and quick monotonic tensile tests or on available literature data. Such approach has been introduced, among others, to expert systems used to estimate fatigue properties [5].

A strain-controlled fatigue life curve is characterized by the following relationship:

$$\frac{\Delta \varepsilon}{2} = \frac{\Delta \varepsilon_e}{2} + \frac{\Delta \varepsilon_p}{2} = \frac{\sigma'_f}{E} \cdot (2N_f)^b + \varepsilon'_f \cdot (2N_f)^c. \quad (1)$$

One of the first methods for approximate determination of the relationship (1) based on the monotonous tensile test was proposed by Manson [8]. The first of them - Four-Point-Correlation Method has been later modified by Ong [13]. The second of them - Universal Slopes Method – has been modified by Muralidharan and Manson [11].

Socie, Mitchell and Caulfield [16] presented relationships designed to determine factors of the formula (1) for steel. Another method, intended particularly for steel grades with hardness value below 500 HB, was proposed by Mitchell [10]. Bäuml and Seeger [2] presented Uniform Material Law Method which is suitable for metals. Its coefficients are very similar to those of the Modified Universal Slopes Method. Roessle and Fatemi [15] proposed the method used for steel and based on the hardness value and the Young's modulus only. Whereas Hatscher, Marquardt and Zenner presented the Variable Slopes Method empirically verified for steel sheet [4]. Whereas as regards Polish literature, we can mention the study by Flasińska and Łagoda that includes attempts to find the relationship between selected static and fatigue properties [3].

Studies by Ong [12] (for 49 steel grades) as well as Kim, Chen, Han and Lee [6] (for 8 steel grades) also include empirical analysis of methods for approximate determination of a strain-controlled fatigue life curve. Park and Song [14] analysed several methods used for 138 types of material (116 steel grades, 16 aluminium alloys and 6 titanium alloys) and they concluded that methods proposed by Bäuml and Seeger [2], Muralidharan and Manson [11] as well as by Ong [13] provide better approximation of experimental data than the remaining ones. Song and Park [18] analysed 6 methods used for 5 groups of materials and they found out that universal slopes method seems to be the best for steel whereas the method developed by Bäuml and Seeger gives satisfactory results when monotonous properties exclude necking [2]. They also proposed a new method (a modified Mitchell's method) which better estimates fatigue properties of aluminium alloys [10]. Whereas Meggiolaro and Castro presented Medians Method based on statistical analysis of parameters used in the relationship (1) performed for 724 steel grades and 81 aluminium alloys [9].

2. Selected methods of fatigue curve determination for aluminium alloys

2.1. Four-Point-Correlation Method (FPCM) - (Manson, 1965)

The Four-Point-Correlation Method proposed by Manson [8] is based on plastic strain and elastic strain values represented by lines $\Delta\varepsilon_p$ and $\Delta\varepsilon_e$. Those lines are determined upon the basis of two points.

Coefficients used in the formula (1) for this method can be characterised by the following relationships:

$$\sigma'_f = \frac{E}{2} \cdot 10^{b \cdot \log 2 + \log \left[\frac{2,5 S_u \cdot (1 + \varepsilon_f)}{E} \right]}, \quad (2)$$

$$\varepsilon'_f = \frac{1}{2} \cdot 10^{c \cdot \log \frac{1}{20} + \log \left(\frac{1}{4} \cdot \varepsilon_f^{3/4} \right)}, \quad (3)$$

$$b = \frac{\log \left[\frac{2,5 \cdot (1 + \varepsilon_f)}{0,9} \right]}{\log \left(\frac{1}{4 \cdot 10^5} \right)}, \quad (4)$$

$$c = \frac{1}{3} \log \left(\frac{0,0132 - \Delta\varepsilon_e^*}{1,91} \right) - \frac{1}{3} \log \left[\frac{1}{4} \cdot \varepsilon_f^{3/4} \right], \quad (5)$$

where ε_f is dependent on reduction in the RA area of the specimen

$$\varepsilon_f = \ln \left(\frac{1}{1 - RA} \right), \quad (6)$$

whereas $\Delta\varepsilon_e^*$ is the range of the elastic strain for 10 000 load cycles and it can be characterised by the following relationship

$$\Delta\varepsilon_e^* = 10^{b \cdot \log(4 \cdot 10^4) + \log \left[\frac{2,5 S_u (1 + \varepsilon_f)}{E} \right]}. \quad (7)$$

2.2. Universal Slopes Method (USM) - Manson (1965)

Universal Slopes Method [8] assumes that inclination of lines $\Delta\varepsilon_p$ and $\Delta\varepsilon_e$ characterised by exponents b and c does not depend on material type. The fatigue strength coefficient as well as the fatigue ductility coefficient used in the formula (1) take the following form:

$$\sigma'_f = 1,9018 \cdot S_u, \quad (8)$$

$$\varepsilon'_f = 0,7579 \cdot \varepsilon_f^{0,6}, \quad (9)$$

where ε_f is determined according to the relationship (6), whereas exponents $b = -0,12$ and $c = -0,6$ assume constant values.

2.3. Modified Universal Slopes Method (MUSM) - Muralidharan and Manson (1988)

Like the original one, the Modified Universal Slopes Method [11] assumes that the exponents b and c do not depend on the material type. Coefficients used in the formula (1) can be calculated based on the following relationships:

$$\sigma'_f = E \cdot 0,623 \cdot \left(\frac{S_u}{E} \right)^{0,832}, \quad (10)$$

$$\varepsilon'_f = 0,0196 \cdot \varepsilon_f^{0,155} \cdot \left(\frac{S_u}{E} \right)^{-0,53}, \quad (11)$$

where ε_f is determined according to the relationship (6), whereas the exponents assume constant values: $b = -0,09$ and $c = -0,56$.

2.4. Uniform Material Law Method (UMLM) - Bäuml and Seeger (1990)

Uniform Material Law Method [2] assumes that the value of exponents b and c as well as the coefficient ε'_f is constant for the whole group of materials. Only the coefficient σ'_f depends on the material properties. Coefficients used in the formula (1) for this method for aluminium alloys can be characterised by the following relationships:

$$\sigma'_f = 1,67 \cdot S_u, \quad (12)$$

whereas constants value is assumed by: $b = -0,095$, $\varepsilon'_f = 0,35$, $c = -0,69$.

2.5. Modified Four-Point-Correlation Method (MFPCM) – Ong (1993)

Modified Four Point Correlation method (MFPC) proposed by Ong [13] differs slightly from the original method proposed by Manson [8]. According to Modified Four Point Correlation method, a strain-controlled fatigue life curve is determined by calculating the elastic strain amplitude at the load reversal level of 10^0 and 10^6 and the plastic strain amplitude at the load reversal level of 10^0 and 10^4 . In this method, coefficients used in the formula (1) assume the following form:

$$\sigma'_f = S_u \cdot (1 + \varepsilon_f), \quad (13)$$

$$\varepsilon'_f = \varepsilon_f, \quad (14)$$

$$b = \frac{1}{6} \cdot \left[\log \left(0,16 \cdot \left(\frac{S_u}{E} \right)^{0,81} \right) - \log \left(\frac{\sigma_f}{E} \right) \right], \quad (15)$$

$$c = \frac{1}{4} \cdot \log \left(\frac{0,00737 - \frac{\Delta \varepsilon_e^*}{2}}{2,074} \right) - \frac{1}{4} \cdot \log \sigma_f, \quad (16)$$

where ε_f is determined according to the relationship (6), whereas the elastic strain range $\Delta \varepsilon_e^*$ for $2N_f = 10\,000$ reversals is calculated using the formula:

$$\frac{\Delta \varepsilon_e^*}{2} = \frac{\sigma_f}{E} \cdot 10^{\frac{2}{3} \left[\log \left(0,16 \cdot \left(\frac{S_u}{E} \right)^{0,81} \right) - \log \left(\frac{\sigma_f}{E} \right) \right]}. \quad (17)$$

2.6. Modified Mitchell's Method (MMM) - Song and Park (1996)

Song and Park modified Mitchell's method [10] by adapting it specially for aluminium alloys. This method assumes that coefficients used in the formula (1) can be calculated based on the following relationship:

$$\sigma'_f = S_u + 335, \quad (18)$$

$$b = -\frac{1}{6} \cdot \log\left(\frac{S_u + 335}{0,446 \cdot S_u}\right), \quad (19)$$

$$\varepsilon'_f = \varepsilon_f, \quad (20)$$

where ε_f is determined based on the relationship (6), whereas the fatigue ductility exponent assumes constant value $c = -0,664$.

2.7. Median Method (MM) - Meggiolaro and Castro (2004)

Based on properties of 81 aluminium alloys, it was assumed that only fatigue strength coefficient depends on strengths properties [9]:

$$\sigma'_f = 1,9 \cdot S_u, \quad (21)$$

whereas constant value is assumed by: $b = -0,11$, $c = -0,66$ and $\varepsilon'_f = 0,28$.

3. Strength properties of the selected aluminium alloys used for aircraft purposes

Strength properties of the selected aluminium alloys for aircraft purposes were determined in the Institute Laboratory for Material and Structure Testing at the University of Technology and Life Sciences in Bydgoszcz accredited by Polish Centre for Accreditation (Accreditation Certificate No. AB 372). The scope of accreditation includes, but is not limited to research methods used in this study, such as: static tension tests (monotonic properties) and low-cycle fatigue tests for metals.

Tests of both alloy grades, 2024-T3 and D16CzATW, were performed using samples cut from 4 mm thick steel sheets. Basic mechanical properties for both alloy grades were determined in accordance with the norm ASTM E 8M - 04 Standard Test Methods for Tension Testing of Metallic Materials. Table 1 presents selected strength parameters that serve as the base for aforementioned methods of approximate determination of fatigue curves. Low-cycle tests of aluminium alloy grades were performed in accordance with the norm ASTM E 606 - 04 Standard Practice for Strain-Controlled Fatigue Testing. Parameters of fatigue curves determined experimentally were shown in the table 1. Achieved parameters are within the range specified in the literature [1].

4. Approximate fatigue curves determined using methods described herein

Figure 1 shows approximate fatigue curves determined according to abovementioned methods compared to experimental curve for analysed aluminium alloys. Whereas parameters of those curves are presented in Table 2.

All the presented approximate fatigue curves are shifted with regards to the experimental curve. The shape of approximate curves is similar to the experimental curve in the high-cycle range, where elastic component of the total deformation prevails.

However, in the low-cycle range, where plastic strain prevails, the curves are characterized by quite a different shape. The above is also confirmed by the analysis of coefficients in the relationship (1) which were determined using abovementioned methods.

Figure 2a shows the value of the fatigue strength coefficient σ'_f depending on the method used to determine the fatigue curve. Values of that coefficient are within the range $\pm 20\%$ of the value achieved based on experimental tests. Values obtained using the method proposed by Bäuml and Seeger as well as using the modified Mitchell's Method correspond to the largest extent to experimental results.

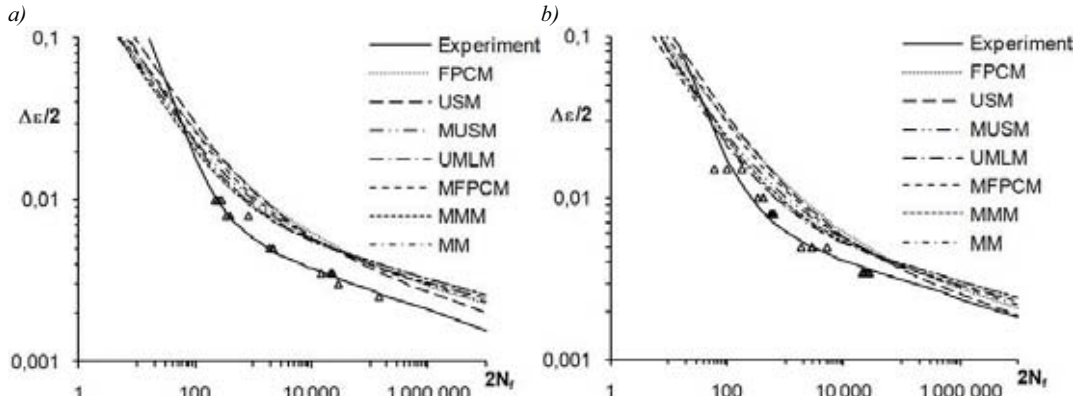


Fig. 1. Approximate fatigue curves determined according to abovementioned methods compared to experimental curve for aluminium alloy grades 2024-T3 (a) and D16CzATW (b)

Tab. 1. Monotonic and fatigue properties of aluminium alloys for aircraft purposes

Aluminium alloy	Monotonic properties				Fatigue properties			
	E	S_u	σ_f	RA	σ'_f	b	ε'_f	c
2024-T3	67 560 MPa	488 MPa	616 MPa	0,233	777 MPa	-0,1234	2,002	-1,1203
D16CzATW	68 402 MPa	460 MPa	613 MPa	0,287	791 MPa	-0,1142	1,456	-1,0718

Table 2. List of coefficients for approximate fatigue curves

Fatigue curve parameters	2024-T3				D16CzATW			
	σ'_f , MPa	b	ε'_f	c	σ'_f , MPa	b	ε'_f	c
FPCM	721,6	-0,0974	0,2153	-0,5141	717,1	-0,1018	0,2690	-0,5272
USM	928,6	-0,12	0,3416	-0,6	874,8	-0,12	0,3955	-0,6
MUSM	696,4	-0,09	0,2176	-0,56	664,0	-0,09	0,2348	-0,56
UMLM	815,5	-0,095	0,35	-0,69	768,2	-0,095	0,35	-0,69
MFPCM	617,6	-0,0817	0,2649	-0,5631	615,6	-0,0846	0,3383	-0,5832
MMM	823,3	-0,0963	0,2649	-0,664	795,0	-0,0980	0,3383	-0,664
MM	927,8	-0,11	0,28	-0,66	874,0	-0,11	0,28	-0,66

Whereas for the fatigue strength exponent b , calculated values are higher than the value achieved experimentally (fig. 2b). The value calculated using the universal slope method best corresponds to the experimental curve in that case.

There are significant differences between calculated values and values determined experimentally for both materials, either in case of fatigue ductility coefficient ε'_f (fig 2c), as well as fatigue ductility exponent c (fig 2d). The biggest differences occur for ε'_f : i.e. values calculated

for the alloy grade 2024-T3 are 6 times lower than the experimental ones (obtained using Bäumel and Seeger's Method) and 9 times lower (achieved using Four-Point-Correlation Method and Modified Universal Slopes Method), whereas for the alloy grade D16CzATW they are 4 times lower (for Universal Slopes Method) and 6 times lower (for Modified Universal Slopes Method). The differences between calculated and experimental values are much lower for c : i.e. values calculated for the alloy grade 2024-T3 are about 1,6 times lower than the experimental ones (obtained using Bäumel and Seeger's Method) and almost 2,2 times lower (achieved using Four-Point-Correlation Method), whereas for the alloy grade D16CzATW they are 1,6 times lower (for Bäumel and Seeger's method) and 2 times lower (for Four-Point-Correlation Method).

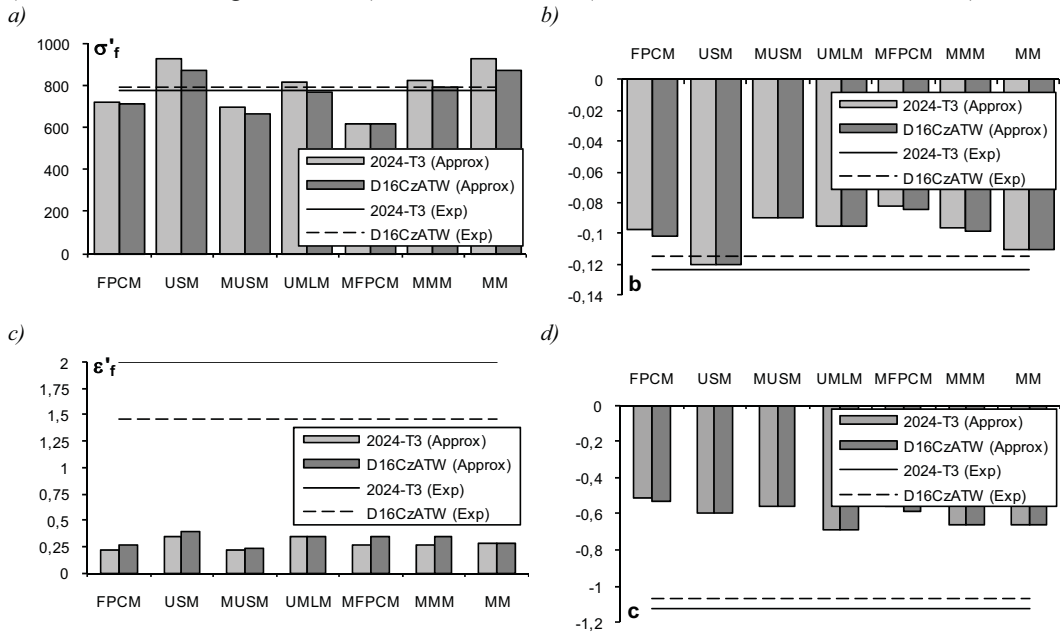


Fig. 2. The value of the fatigue strength coefficient σ'_f , the fatigue strength exponent b , the fatigue ductility coefficient ϵ'_f as well as the fatigue ductility exponent c depending on the method used to determine the fatigue curve

Relatively high conformity between the fatigue ductility coefficient and exponent determines similar shape of the curves in the high-cycle range. Whereas too small values of the fatigue ductility coefficient and exponent cause insufficient inclination of the curves in the low-cycle range.

It should be noted that in most methods the coefficient ϵ'_f and the exponent c are associated with the necking of RA sample and thus the measurement error for this quantity, which is particularly difficult to determine for sheet samples, significantly influences the form of approximate fatigue characteristics.

5. Application of approximate curves to fatigue life analysis

Taking into account the abovementioned differences between the curve determined based on experimental data and approximate curves, authors evaluated suitability of individual approximate curves for determination of fatigue life. This evaluation was performed on the basis of results of fatigue life calculations for programmed load, the example of which is provided in the figure 3.

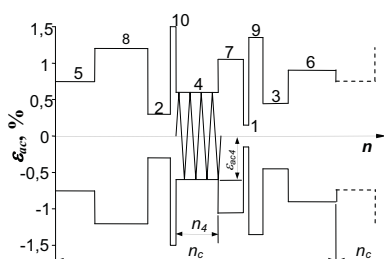


Fig. 3. Load program

This load is characterised by the value of maximum amplitude of the total strain ε_{acmax} as well as the spectrum modulation coefficient ζ referred to the amplitude of the total strain as follows:

$$\zeta = \sum_{j=1}^k \frac{\varepsilon_{acj}}{\varepsilon_{acmax}} \cdot \frac{n_j}{n_c}, \quad (22)$$

where j is the number of the load level, k – number of levels in the load block, n_c – total number of cycles in the load block. All cycles of the programmed load block are alternating cycles ($R=-1$). The fatigue life determined by calculations based on the experimental curve was assumed as the reference level. The calculations were performed using the Palmgren-Miner linear cumulative damage rule.

Figure 4 presents the difference between the values of fatigue life N_{cal} calculated by means of approximate fatigue curves determined using different methods. The analytical fatigue life N_{exp} determined based on experimental curve was assumed as the reference level.

As it can be noted, the lower the ε_{acmax} value in the load block, the higher the errors of the fatigue life approximation. This results from the fact that approximate curves are shifted to the right in relation to the experimental curve in that range (fig. 1). In most cases, the lower the ζ value the higher the calculation error. This results from the fact that load block of lower ζ value is characterised by more cycles with low strain amplitude. The calculation error decreases as the ε_{acmax} value grows, whereas the fatigue life determined based on approximate fatigue curves N_{cal} assumes lower value than the fatigue life determined on the basis of the experimental curve N_{exp} . The experimental curve matches the curve determined using the Four-Point-Correlation Method worst of all. Approximate curves better match the experimental curve for the alloy grade D16CzATW than 2024-T3.

6. Summary

The fatigue strength coefficient σ'_f and the fatigue strength exponent b of either approximate and experimental curves sufficiently conform to each other for both analysed alloys. This conformity determines similar shape of curves in the range where elastic strain prevails. Significant difference between the value of fatigue ductility coefficient ε'_f and the fatigue ductility exponent c determines different shapes of curves in the range of high plastic strain. However, the elastic part of the equation (1), especially exponent b , shall be responsible for a very large error in the fatigue life approximation results in the range of low strain values because of the shift of approximate curves towards higher fatigue life values (fig. 5).

If there is no experimental data, approximate curves provide some information on fatigue properties of a given material. However, use of approximate curves can lead to very big errors, particularly in fatigue life calculations for variable amplitude load.

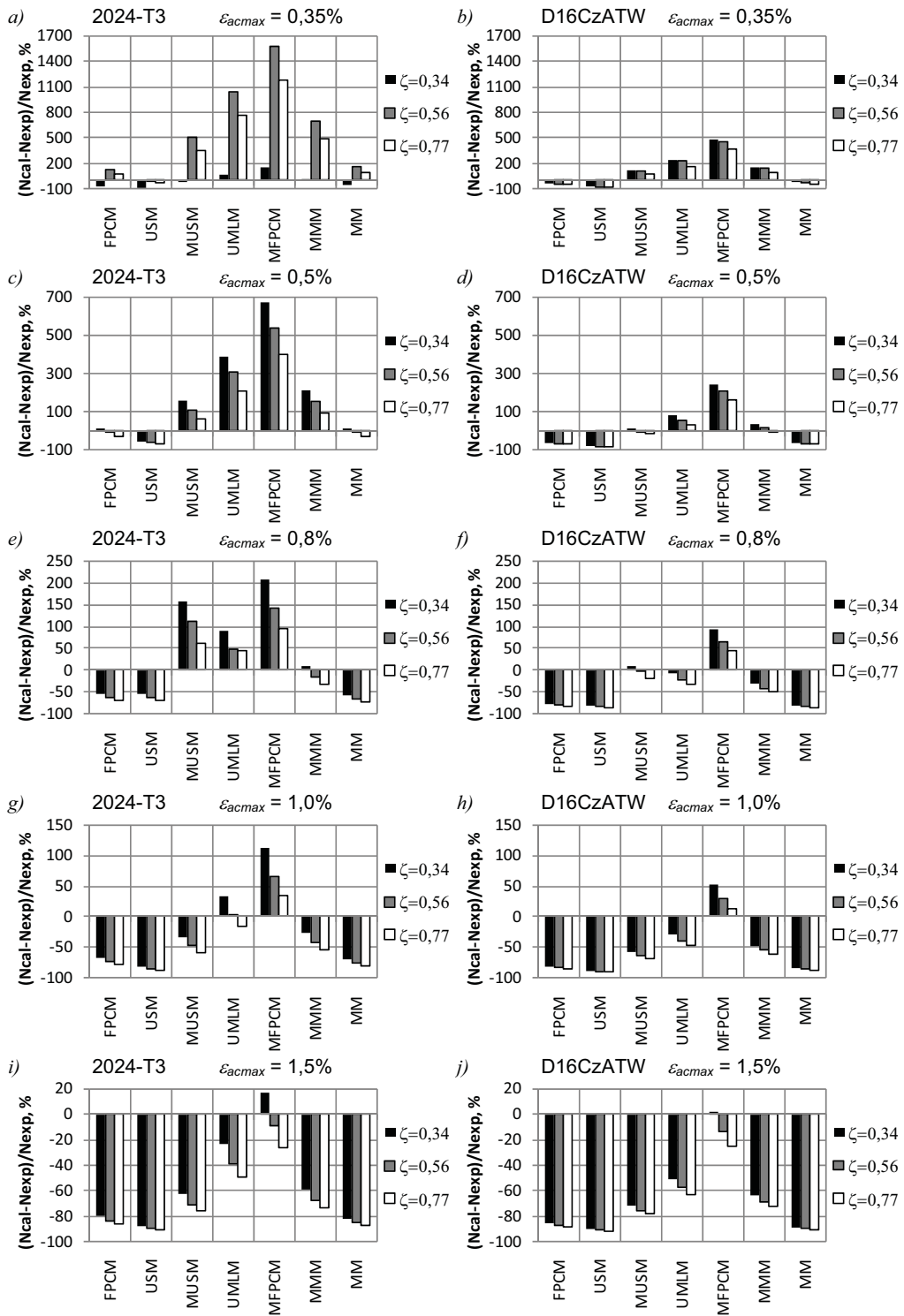


Fig. 4. Differences between values of fatigue life N_{cal} calculated using approximate fatigue curves determined by means of different methods as compared with the analytical fatigue life N_{exp} determined on the basis of the experimental curve

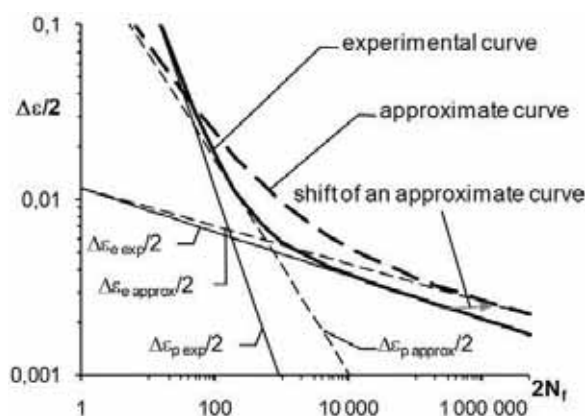


Fig. 5. Shift of approximate curve as a source of calculation error

References

- [1] *ASM Metals Handbook, Fatigue and Fracture*, Vol. 19, 2nd Printing, ASM International, 1997.
- [2] Bäumel A. Jr., Seeger T., *Materials data for cyclic loading*, Elsevier Science Publishers, Amsterdam, 1990.
- [3] Flasińska K., Łagoda T., *The relationship between selected static and cyclic properties of aluminum alloys*, X Polish Fracture Mechanics Conference, Vol. 1, Scientific Papers of Technical University of Opole, Nr 304/2005, z. 82, 2005, pp. 279-288 (in Polish).
- [4] Hatscher A., Marquardt C., Zenner H., *Estimation of fatigue material properties for the lifetime prediction of sheet metal structures*, LCF 5 2003, Berlin, Germany, 2003, pp. 409-414.
- [5] Jeon W.-S., Song J.-H., *An expert system for estimation of fatigue properties of metallic materials*, International Journal of Fatigue, 2002, Vol.24, No. 6, pp. 685–698.
- [6] Kim K.S., Chen X., Han C., Lee H.W., *Estimation methods for fatigue properties of steels under axial and torsional loading*, International Journal of Fatigue, 2002, Vol. 24, pp. 783-793.
- [7] Kocańda S., Szala J., *Basics of the fatigue calculations*, PWN, Warsaw, 1997, 288 ps (in Polish).
- [8] Manson S. S., *Fatigue: A Complex Subject – Some Simple Approximations*, Experimental Mechanics, 1965, Vol. 5, No. 7, 193-226.
- [9] Meggiolaro M.A., Castro J.T.P., *Statistical evaluation of strain-life fatigue crack initiation predictions*, International Journal of Fatigue, 2004, Vol. 26, No. 5, pp. 463–476.
- [10] Mitchell M.R., *Fundamental of modern fatigue analysis for design. Fatigue and Microstructure*, American Society for Metals, Metals Park, Ohio, 1979, pp. 385-437.
- [11] Muralidharan U., Manson S.S., *Modified universal slopes equation for estimation of fatigue characteristics*, Journal of Engineering Materials and Technology, Transactions of the ASME, 1988, Vol. 110, No. 1, pp. 55–58.
- [12] Ong J. H., *An evaluation of existing methods for the prediction of axial fatigue life from tensile data*, International Journal of Fatigue, 1993, Vol. 15, No. 1, pp. 13-19.
- [13] Ong J. H., *An improved technique for the prediction of axial fatigue life from tensile data*, International Journal of Fatigue, 1993, Vol. 15, No. 3, pp. 213-219.
- [14] Park J., Song J., *Detailed evaluation of methods for estimation of fatigue properties*, International Journal of Fatigue, 1995, Vol. 17, No. 5, pp. 365-373.
- [15] Roessle M.L., Fatemi A., *Strain-controlled fatigue properties of steels and some simple approximations*, International Journal of Fatigue, 2000, Vol. 22, No. 6, pp. 495–511.

- [16] Socie D.F., Mitchell M.R., Caulfield E.M., *Fundamentals of modern fatigue analysis*, Fracture Control Program Report, No. 26, University of Illinois, USA, 1977.
- [17] Szala J., *Fatigue damage accumulation hypothesis*, University of Technology and Agriculture in Bydgoszcz, 1998, 175 ps (in Polish).
- [18] Song J.H., Park J.H., *New Proposal or Estimation of Fatigue Characteristics of Metals*, FATIGUE'96, 6th International Fatigue Congress, Vol. II, Berlin, Germany, 1996, pp. 1359-1364.

Scientific work financed from the funds of Polish Ministry of Science and Higher Education in the years 2006-2010 as a research project No. 61/EUR/2006/02. Investigations of the D16CzATW aluminum alloy were realized with the support of Polish Ministry of Science and Higher Education as a research project No. 7 T07B 01018.



EVALUATION OF THE RIVET HOLE SIZING DEGREE EFFECT ON THE FATIGUE LIFE

Adam Lipski, Stanisław Mroziński, Zbigniew Lis

*University of Technology and Life Sciences in Bydgoszcz
Faculty of Mechanical Engineering*

Al. Prof. S. Kaliskiego 7, 85-789 Bydgoszcz, Poland

tel.: +48 52 3408220, fax: +48 52 3408271

e-mail: adam.lipski@utp.edu.pl, stanislaw.mrozinski@utp.edu.pl, zbigniew.lis@utp.edu.pl

Abstract

This paper presents results of research on improvement of riveted joints fatigue life. That improvement was achieved using the rivet hole sizing process. The diagrams of sizing forces as the function of the hole sizing degree were analysed. Results of fatigue tests performed by the authors confirmed that the rivet hole sizing degree significantly influences fatigue life, and the improvement is proportional to the sizing degree.

Keywords: *riveted joints, fatigue life, rivet hole sizing*

1. Introduction

The fatigue strength of riveted joints is influenced by a number of design, process and material-related factors. Design factors include e.g. the type of the connection, size of the riveted joint, thickness of the connected metal plates, the rivet diameter and type or applied pitch of the joint [2]. Fatigue strength is also significantly influenced by rivet holes preparation process. This results from the fact that rivet holes are areas where local stress concentration occur. It is the place where fatigue cracks are initiated which may subsequently develop and lead to disasters.

Rivet holes may be subjected to special processing in order to increase their resistance to fatigue cracking. The most important processes of that kind include reaming and sizing. Reaming reduces the scatter of hole diameters and increases hole surface smoothness. While sizing introduces compressive stress to internal layers of the material. This stress hinders initiation of fatigue cracks on the hole surface. Holes may be sized using special burnishing heads. But this technology can only be used for sizing holes of 3 mm diameter and bigger. Such small holes can, however, be sized using mandrels of appropriate diameter. Achieved surface cold work degree depends on the difference between the diameter of the sized hole and the diameter of the sizing mandrel.

The aim of this study is to analyse the course of rivet hole sizing process using sizing mandrels and to evaluate the impact of the rivet hole sizing degree on the fatigue life. The research described in the study concerned improvement of the fatigue life of riveted joints as a result of local strain hardening of the rivet hole by the sizing process, which also results in the hole surface polishing.

2. Test samples

Samples for tests were made of 1.27 mm thick non-clad plates of aluminium grade 2024-T3. Rivet holes were prepared assuming that they shall be used for 3mm nominal diameter oval head solid rivets for aviation-related purposes [6]. According to [5], finished holes for such rivets should be of 3.1 mm diameter with positive tolerance of +0,1 mm. Holes of such diameter were achieved by two operations. The first one was drilling the hole and the second one – sizing the hole to the diameter of 3.1 mm. The research covered several degrees of hole sizing. In this study, the sizing degree k means the following relationship:

$$k = \left(\frac{d_k - d_w}{d_w} \right) \cdot 100\%, \quad (1)$$

where:

d_k – hole diameter after sizing,

d_w – hole diameter after drilling.

Samples with holes made in conventional way (drilling or drilling and reaming) were also prepared for comparison purposes.

Different sizing degrees were achieved by drilling holes of different diameters in the samples followed by sizing process using sizing mandrel of the same diameter. Holes in the test samples were drilled using special device ensuring appropriate quality and repeatability of the holes. Figure 1a shows the profile of the test samples and the hole diameters. Based on preliminary tests it was concluded that 3.15 mm nominal diameter mandrel is necessary to size the holes to the diameter of 3.1 mm. The shape of the used sizing mandrel is shown in Figure 1b. Five different sizing degrees were achieved by means of five drills of different diameters for preliminary holes and one sizing mandrel. $k = 6.9\%$ ($d_w = 2.9$ mm), $k = 5.08\%$ ($d_w = 2.95$ mm), $k = 3.33\%$ ($d_w = 3.0$ mm), $k = 1.64\%$ ($d_w = 3.05$ mm), $k = 0.30\%$ ($d_w = 3.1$ mm).

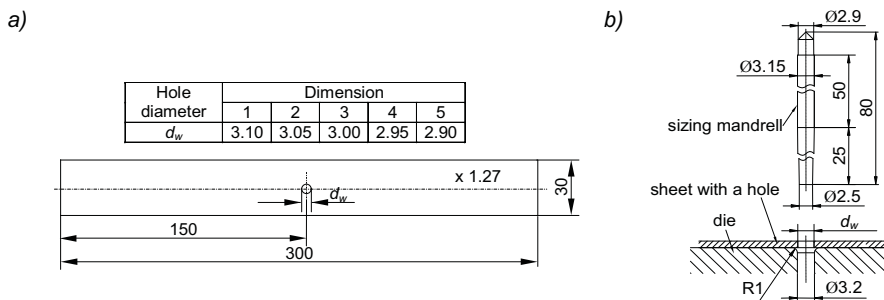


Fig. 1. Samples for fatigue tests (a) and the sizing mandrel (b)

3. Hole sizing tests

Holes were sized using the testing machine INSTRON 8501. To reduce sample deformation in its thickness direction during sizing process, the diameter of the hole in the die supporting the sample was ($\varnothing 3,2$ mm) slightly bigger than the mandrel diameter ($\varnothing 3,15$ mm). Momentary values of the force applied on the mandrel and the mandrel displacement in the hole were recorded during the sizing process.

Sample graph of 2.9 mm hole sizing force as a function of the mandrel displacement was shown in the figure 2. To better illustrate the hole sizing process, the sizing mandrel diagram with three characteristic sample positions with reference to the mandrel were provided under the graph. As expected, the loading force value depends on the position of the mandrel relative to the sample. The mandrel loading force increases linearly when the conical part of it mates with the hole and the force is maximum upon entry of the cylindrical part of the mandrel into the hole. The sizing force is decreasing during gradual displacement of the edge of the cylindrical part in the tapered hole and then, as expected, it remains approximately unchanged by the end of the sizing mandrel displacement.

Figure 2b shows mandrel loading force functions obtained when sizing the holes of different diameters. As the main process of the hole sizing takes place only in the initial stage of sizing (when forcing the tapered part of the mandrel into the hole), the diagrams focus only on that stage. As expected, maximum values of the force applied to the mandrel were observed when forcing the mandrel through the holes drilled using the smallest drill ($d_w=2.9$ mm, $k=6.9\%$). Moreover, based on the achieved graphs, one can also find that they are qualitatively similar. This applies to the shape of prepared sizing mandrel load graphs in their section regarding the tapered part of the mandrel.

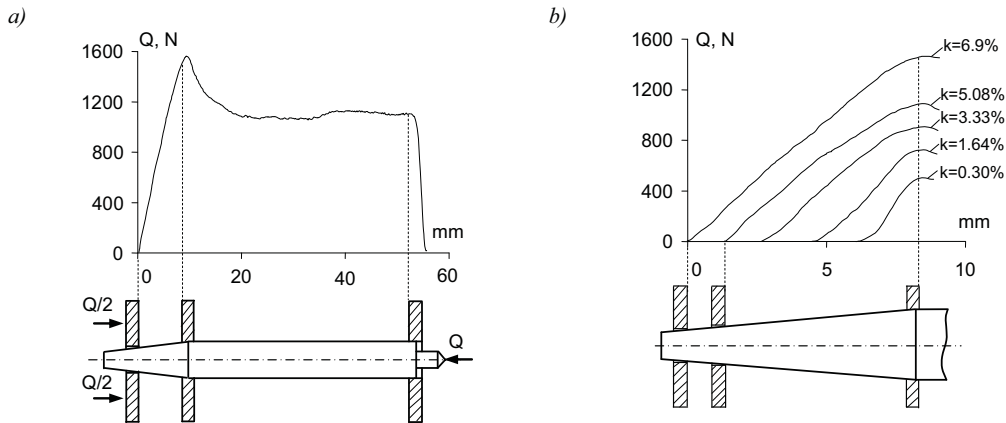


Fig. 2. Hole sizing: a) function of the force for 2.9 mm hole sizing process, b) force functions for sizing holes of different diameters

Hole diameters were measured after sizing. The measurement results were presented in form of a graph (Fig. 3), where hole diameters measured after drilling were additionally presented. Based on the prepared graphs, it can be noted that the machining-related deviation of the diameter depends on the diameter of the hole. The bigger the drill diameter, the smaller the deviation. One can conclude, that despite additional drill guide used during hole drilling, the holes are enlarged due to radial run-out.

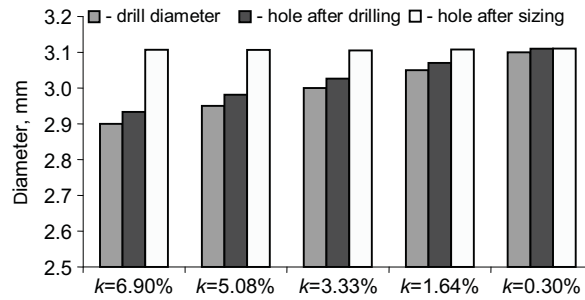


Fig. 3. The results of diameter measurement of holes in samples, acquired after drilling and after sizing

Apart from experimental tests, the sizing process simulation was also performed with finite element method (FEM) using ABAQUS software, version 6.6-4 - Standard module [1]. Dimensions of the sizing mandrel used for experimental test and the simulation as well as dimensions of the sized hole made in the metal plate and die dimensions were shown in the Figure 1b. Due to the type of the system geometry, axially symmetrical 2D model was used for calculations. Both the sizing mandrel and the die were modelled as rigid elements, while the drilled metal plate as a deformable element for which non-linear material characteristics was assumed, achieved by discretization of the monotonous tension graph. As large deformation gradients were expected, the metal plate was discretized using axially symmetrical, 8-node, quadrangle finite element CAX8R. The number of elements was increased around the hole.

Figure 4 shows numerically determined, sample graph of the force necessary to size 3.03 mm hole from a hole drilled with 3.0 mm drill (sizing degree $k = 3.33\%$) as a function of the mandrel displacement. Performed simulations of the process for different values of the friction between the sizing mandrel and the hole indicate that it is one of the major factors influencing the hole sizing force, which does not, however, change, the nature of the process. Properly selected value of the friction factor in the digital model allowed to achieve high compliance with the results of experimental tests of the sizing force as well as the maximum hole sizing force.

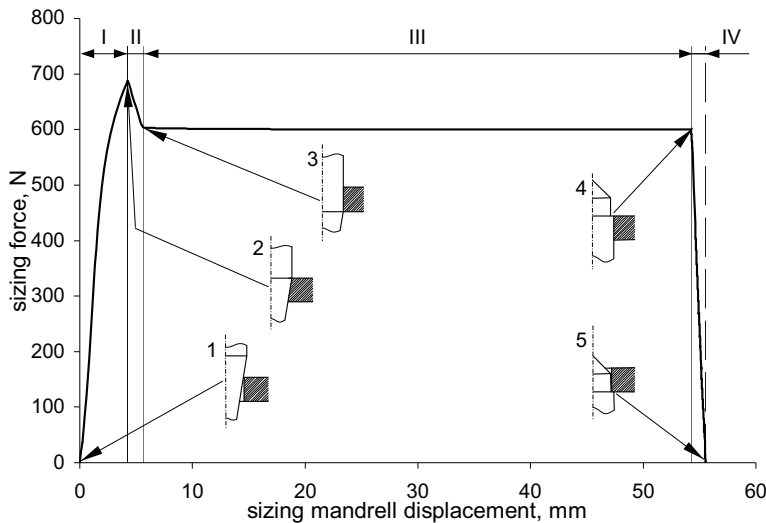


Fig. 4. The graph of the hole sizing force as a function of the sizing mandrel displacement, determined using FEM

Several characteristic stages can be distinguished in the sizing force graph, based on the FEM analysis. Stage I starts with contact between the sizing mandrel and the top edge of the hole and ends when the cylindrical part of the sizing mandrel is aligned with that edge. The sizing force is maximum at that moment. The force starts to decrease gradually from that moment (stage II) by the time, when the tapered part of the mandrel completely leaves the hole. At stage III, when the cylindrical part of the mandrel is forced through the hole, the sizing force virtually does not change. Stage IV begins when the end of the cylindrical part of the sizing mandrel is aligned with the top edge of the hole. The sizing force starts to decrease gradually from that moment down to zero, at which time the cylindrical part of the mandrel is totally outside the hole.

Almost the entire course of the sizing force at the stage III indicates that it is possible to significantly reduce the cylindrical part of the mandrel, which should shorten the process duration.

Results of numerical calculations indicate that maximum radial and axial deformations occur at the hole edge from the sizing mandrel entry side – at the initial stage of the sizing process (stage I), the tapered part of the mandrel is in point contact with the hole edge, which result in high gradient of stress in that area. This has significantly lower effect on the distribution of the circumferential deformations. Relief (stage IV - point 5) has little effect on the character of strain distribution in the hole area. While there are important differences in stress distribution. Load relief practically eliminates radial compressive stress resulting from sizing process. Whereas sizing process introduces high circumferential compressive stress in the material.

4. Fatigue tests

The samples with holes of different sizing degree were subject to fatigue tests. The tests were performed under zero-tension cycle conditions (cycle asymmetry factor $R=0$) with load frequency of 5 Hz. The tests were performed for three levels of the maximum load of the cycle $S_{max} = 150, 175$ and 200 MPa (three samples for each load level). Like sizing of the holes, fatigue tests were also performed using the testing machine INSTRON 8501.

Results obtained during fatigue tests were presented in Figure 5 in bilogarithmic coordinate system, in form of fatigue graphs determined assuming S_{max} as the independent variable of the stress and the fatigue life N as the dependant variable. Results of the fatigue life tests acquired for drilled holes (W) as well as drilled and reamed holes (R) were also added in the figure for comparison. Figure 6 includes the summary of average fatigue life ratio of samples with sized holes to samples with drilled holes, presented for individual load levels.

Based on the achieved results, one can conclude that the lowest fatigue life characterised samples with drilled holes and drilled and reamed holes. The fatigue life of riveted joints improved (by 50 to 74%, depending on load level) even as a result of the hole surface polishing only. This improvement was obtained for samples with $d_w=3.1$ mm ($k=0.30\%$) holes. While two-fold growth of the fatigue life was achieved for $d_w=3.05$ mm hole with slight sizing degree of $k=1.64\%$.

Further significant increase of the fatigue life was achieved by cold work of the hole surface and, based on the position of obtained fatigue life graphs (Fig. 5) and achieved fatigue life values (Fig. 6), it may be concluded that the higher the sizing degree, the higher the fatigue life growth. The growth is also proportional to the mandrel load level. For example, five-fold fatigue life increase (for the load level of 200 MPa) and eight-fold increase (for the load level of 150 MPa) were achieved for samples with $d_w=3.0$ mm ($k=3.33\%$) sized holes. Maximum improvement of fatigue life was obtained for samples with $d_w=2.9$ mm ($k=6.90\%$) sized holes, but the results were characterised by the highest dispersion. Nine-fold improvement of fatigue life was achieved for those samples comparing with drilled hole for the load level of $S_{max} = 200$ MPa and nearly twelve-fold increase for the load level of $S_{max} = 150$ MPa.

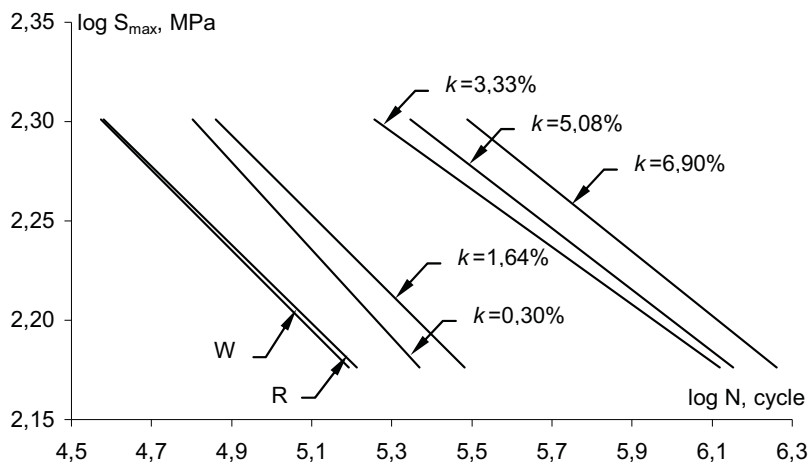


Fig. 5. Fatigue life graphs obtained for samples with holes of different sizing degree

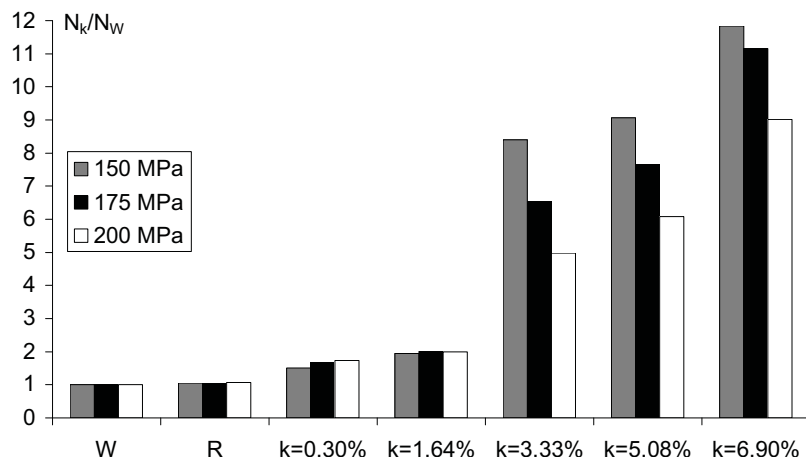


Fig. 6. Average fatigue life ratio of samples with sized holes N_k to samples with drilled holes N_W

5. Summary

Fatigue life of riveted joints improves thanks to additional preparatory operations performed prior to riveting, such as hole sizing. Results obtained in this research confirm information available in the professional literature, concerning positive effect of hole sizing on fatigue life [3]. Cold work and polishing of the hole surface by the sizing mandrel hinders initiation of micro-cracks. It should be emphasized that a number of factors influence fatigue life of the sample with riveted hole. The most important of them include the rivet upset (squeezing) degree or the clearance between the rivet and the hole [4]. Those issues are subject of research works performed in the Institute Laboratory for Research on Materials and Structures of the Faculty of Mechanical Engineering at the University of Technology and Life Sciences in Bydgoszcz, as part of the Eureka IMPERJA project. Those works have, among other things, proven positive effect of hole sizing on fatigue life of riveted pairs used in aviation industry structures.

References

- [1] ABAQUS Version 6.6 PDF Documentation. ABAQUS Inc., 2006.
- [2] Jachimowicz J., Szymczyk E., Sławiński G., *Analiza wpływu technologii nitowania na stan przemieszczeń, odkształceń i naprężeń wokół nitu*, Mechanik Nr 4/2008, ss. 332-337.
- [3] Larouche S. at all, *Influence of Cold Working and Interference Fit on Fatigue Life of 7475-T7351 Aluminum Alloy Fastener Hole*, Design for Durability in the 21th Symposium of the International Committee on Aeronautical Fatigue, 27-29 June 2001, Toulouse, France, Ed. J. Rouchon Cepadues, pp. 681-698.
- [4] Szymczyk E., Jachimowicz J., Sławiński G., *Analiza wpływu luzów technologicznych na pole naprężeń własnych w otoczeniu nitu stożkowego*, Mechanik Nr 7/2008, ss. 629-632.
- [5] Norma branżowa BN-70/1120-03 *Nity lotnicze. Dobór długości, wymiary zakuwek i średnice otworów na nity*.
- [6] Norma branżowa BN-70/1121-03 *Nity lotnicze ze łbem kulistym*.

Scientific work financed from the funds of Polish Ministry of Science and Higher Education in the years 2006-2010 as a research project No. 61/EUR/2006/02.



AFFECT OF DECARBURISATION TIMES OF BAINITIC FERRITE LATHS ON THE MICROSTRUCTURE IN Fe-Cr-C STEEL

Zdzisław Ławrynowicz

*University of Technology and Life Sciences, Mechanical Engineering Faculty
Department of Materials Science and Engineering
av. Kaliskiego 7, 85-789 Bydgoszcz, Poland, e-mail: lawry@utp.edu.pl*

Abstract

The purpose of the present paper is to demonstrate how a thermodynamic method can be used for solving a problem of the decarburisation of bainite laths. The paper presents an investigation of the time required for the diffusion of carbon out of supersaturated laths of ferrite into the retained austenite. This should in principle enable to examine the partitioning of carbon from supersaturated ferrite laths into adjacent austenite and the carbon content in retained austenite using analytical method. The obtained results illustrates that the estimated times are not capable of decarburising the sheaf of ferrite included thick laths of bainitic ferrite during the period of austempering. A consequence of the precipitation of cementite from austenite during austempering is that the growth of bainitic ferrite can continue to larger extent and that the resulting microstructure is not an ausferrite but it is a mixture of bainitic ferrite, retained austenite and carbides.

Keywords: carbon diffusion, decarburisation

1. Introduction

The attractive properties of carbide free bainitic steel are related to its unique microstructure that consists of ferrite and high carbon austenite. Because of this microstructure, the product of austempering reaction is often referred to as “ausferrite” rather than bainite [4,6,13]. If bainite is formed by a shear mechanism it is supposed that bainitic ferrite is supersaturated with carbon and any excess carbon is soon rejected into the residual austenite. It is supposed that the decarburisation time of ferrite lath is a function of lath width and increases with decreasing temperature because the diffusion coefficient of carbon also decreases with temperature. The decarburisation time also increases as the thickness of the ferrite laths increases.

The purpose of the present paper is to demonstrate how a thermodynamic method can be used for solving a problem of the decarburisation of bainite laths and this should in principle enable to examine the possibility of carbides precipitation in Fe-0.38C-0.93Cr steel during bainite reaction.

2. Material and methods

The chemical composition of the steel is listed in Table 1. The concentration of alloying elements is obtained from the chemical analysis.

Tab. 1. Chemical composition and calculated B_S and M_S temperatures of the steel used in the present study.* All concentrations are given in wt. %

Steel	C	Si	Mn	P	S	Cr	Ni	B_S , °C	M_S , °C
Fe-0.38C-0.93Cr	0.38	0.29	0.63	0.01	0.025	0.93	0.11	505	320

*The B_S and M_S temperatures are calculated by using methods developed by Bhadeshia [4]

A high-speed Adamel Lhomargy LK-02 dilatometer was used to establish change of length ($\Delta L/L$) during isothermal bainitic transformation. In order to ensure rapid cooling (300 K s^{-1}) from austenitising temperature, the specimens were 13mm in length and 1.1mm in diameter. The temperature was measured with a 0.1mm diameter NiCr-Ni thermocouple welded to the sample. Cooling was carried out by blowing a helium gas directly onto the surface of the sample. Determination of the linear expansion coefficients was carried out in the UBD Leitz-Wetzlar dilatometer. Thin foils for transmission electron microscopy were prepared from discs slit from heat-treated specimens. The discs were mechanically thinned to 50 μm and were electropolished until perforation occurred in a twin jet polishing unit containing an electrolyte of 5% perchloric acid, 25% glycerol and 70% ethyl alcohol mixture solution. The electrolyte temperature was maintained around -10°C , the polishing potential was 55 V at a current of 30 mA. The foils were examined in a Tesla BS-540 transmission electron microscope operated at 120 kV.

3. Phase diagram

The phase diagram of Fe-0.38C-0.93Cr steel (Fig. 1) was calculated as in Ref. [2,3,10] using a model developed by Bhadeshia [1,16], based on the McLellan and Dunn quasi-chemical thermodynamic model [15]. The bainite B_S and martensite M_S start temperatures were also calculated using the same method [1,16]. The determined carbon concentration of residual austenite x' at the points where the formation of bainite terminate were compared against the extrapolated T_0 , T_0' , and A_3' phase boundaries for Fe-0.38C-0.93Cr steel. In presented diagram (Fig. 1) the reaction is found to stop when the average carbon concentration of the residual austenite is between the T_0 and T_0' lines and in some cases beyond the T_0 line (black circles in Fig. 1). Carbon concentration in retained austenite at the cessation of reaction is close to the T_0' line and supports formation of bainitic ferrite by a shear mechanism. Since diffusionless transformation is not possible beyond the T_0 curve, the obtained results need explanation. This might be explained by the fact that the T_0' line accounts for 400 J/mol of stored energy in the bainite. If this energy is reduced by plastic deformation of the surrounding austenite then a higher volume fraction of bainite should be able to form. Secondly, when carbide precipitation accompanies the development of bainitic ferrite laths as a secondary process, it reduces the carbon content in the austenite and allows the bainitic reaction to proceed to a larger extend.

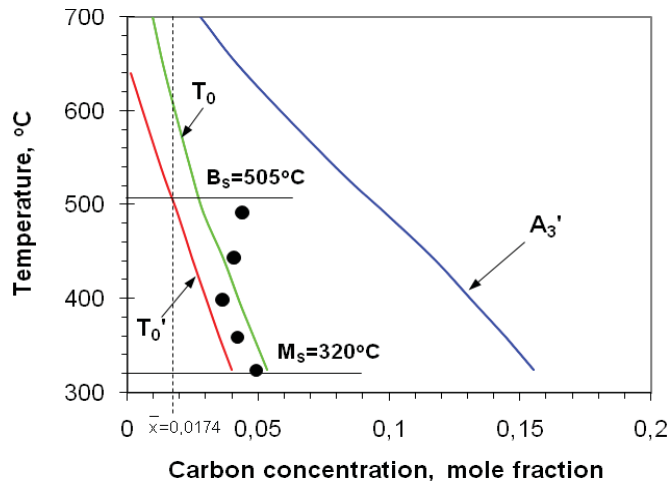


Fig. 1. The calculated phase boundaries A_3' , T_0 and T_0' for the investigated Fe-0.38C-0.93Cr steel together with all the experimental data of the measured carbon contents of the untransformed austenite (black circles)

4. Microstructural analysis

Microstructure of typical upper bainite after holding the Fe-0.38C-0.93Cr steel at 480°C for 2h is seen in Fig. 2. Retained austenite films exist between the ferrite laths. Because carbides were not observed in the ferrite it means that the excess carbon in these ferrite laths partitions into the residual austenite soon after the growth event. The isolated films of austenite can accumulate carbon concentration beyond T_0' line (Fig. 1). Because the austenite is greatly enriched in carbon they cannot transform to bainite once the T_0' line is exceeded. Furthermore, these thin films of the residual austenite are stable to martensitic transformation on cooling to ambient temperature.

Fig. 3 shows microstructure obtained by isothermal transformation at 350°C for 60 seconds. Transmission electron microscopy revealed that the sheaves were composed of much smaller laths of ferrite and the microstructure contain only bainitic ferrite and carbon enriched residual austenite films. In Fig. 2 and 3 it is seen that the morphology of bainitic ferrite is lath rather than plate. Bainitic ferrite laths of thickness about $0.2 \div 0.3 \mu\text{m}$ form separately one from another. Retained austenite was present between the ferrite laths as thin films. The ability to retain such films of austenite is due to partitioning of carbon into residual austenite following the formation of supersaturated bainitic ferrite. Carbides were not observed in ferrite laths of thickness thinner than $0.2 \mu\text{m}$. In this case films of residual austenite can accumulate all the excess carbon from supersaturated ferrite laths of thickness less than $0.2 \mu\text{m}$. It is a possibility that in the later stage of transformation, the carbon concentration of untransformed austenite is decreased by the carbide formation and then the reaction can proceed to a larger extent. The determined microstructural parameters of Fe-0.38C-0.93Cr steel after isothermal transformation are listed in Table 2.

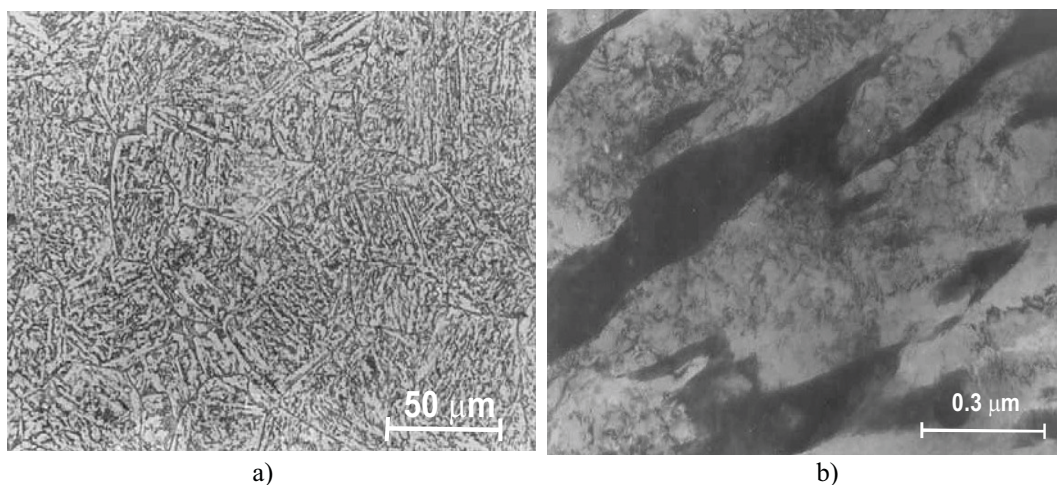


Fig. 2. Microstructure of Fe-0.38C-0.93Cr steel after isothermal transformation at 480°C for 2h, a) light microscopy, etched with 2% nital, b) TEM, thin foil

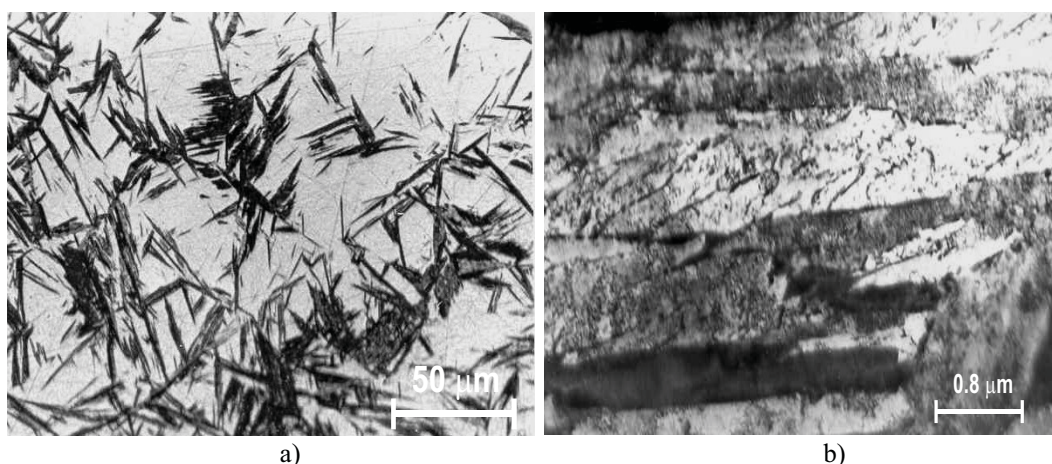


Fig. 3. Microstructure of Fe-0.38C-0.93Cr steel after isothermal transformation at 350°C for 60 seconds, a) light microscopy, etched with 2% nital, b) TEM, thin foil

Tab. 2. Microstructural parameters of Fe-0.38C-0.93Cr steel

Microstructural parameters	Transformation temperature, °C	
	350	480
Average austenite grain size, μm	30	30
Volume of bainite in the form of packets, %	74	41
Average packet length, μm	26	21
Average packet width, μm	17	19
Average width of bainite lath, μm	0.2	0.3
Morphology of retained austenite	thin films, also irregular islands	irregular islands and thin films

5. Method used in estimating the decarburising time of the bainitic ferrite laths

Kinsman and Aaronson [7] first considered the kinetics of the partitioning of carbon from bainitic ferrite of the same composition as the parent phase. For a plate of thickness w_α the flux of carbon is defined along a coordinate z normal to the α/γ interface, with origin at the interface and z being positive in the austenite (Fig. 4).

The method used to calculate the time of decarburising of bainitic ferrite laths is based on the hypothesis that transformation to bainite can only occur in regions of austenite where $x_\gamma \leq x_{T_0}$, where x_γ is the carbon concentration in austenite and x_{T_0} is the carbon concentration corresponding to the T_0 curve. As a lath of bainitic ferrite forms it partitions its excess carbon into the retained austenite. This creates a carbon diffusion field around the lath. Another parallel lath (of the same sheaf) which forms subsequently can only approach the original lath to a point where $x_\gamma \leq x_{T_0}$. The method assumes that the interval between laths formations is larger than the time required to decarburise each lath.

The time t_d needed to decarburise the ferrite is intuitively expected at least to be comparable to that required for a lath to complete its growth. If t_d is small relative to the time required to relieve the carbon supersaturation by the precipitation of carbides within the ferrite, then upper bainite is obtained, otherwise lower bainite forms [5,8,11].

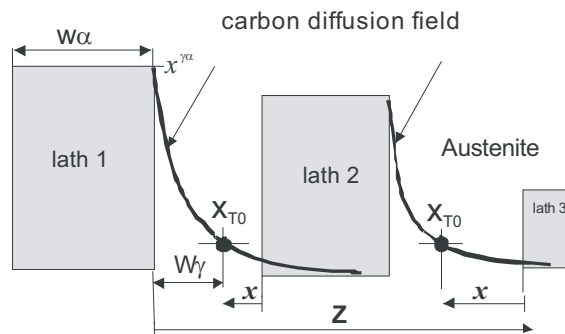


Fig. 4. Schematic diagram of method used in estimating the time of decarburising the bainitic ferrite laths. Lath 1 forms first and lath 2 and 3 and next is allowed to approach it to point where $x_\gamma \leq x_{T_0}$ (distance of this point from lath 1 is denoted w_γ). This is in fact the thickness of the retained austenite film. The mean thickness of the retained austenite films is almost tenfold thinner (0.01-0.02 μm) than the average thickness of the bainitic ferrite laths ($\sim 0.2\mu\text{m}$).

6. The calculation of decarburisation times of supersaturated bainitic ferrite laths

The problem therefore becomes a calculation of the decarburisation times of all bainite laths that exist in all bainite packets inside austenite grains (Fig. 5). The time needed to decarburize the ferrite laths within bainite sheaves, t_{dz} :

$$t_{dz} = \sum_i t_{di} \quad (1)$$

where t_{di} is the time required to decarburise individual supersaturated bainitic ferrite lath of specific thickness w_{ai} .

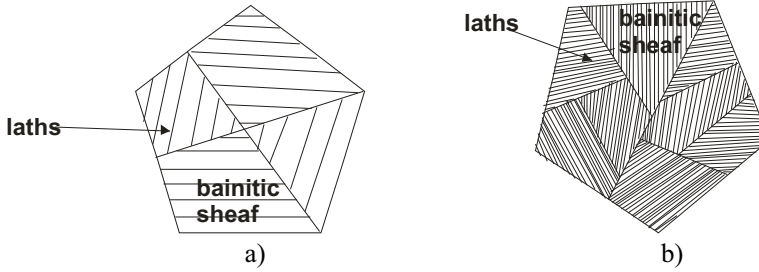


Fig. 5. Schematic illustration of bainite packets size and lath size (width) formed at higher (a) and lower (b) transformation temperature with different thickness of bainitic ferrite laths

Because of the inhomogeneous distribution of carbon and other solutes in the matrix after transformation to bainite the retained austenite is enriched to a greater extent in the immediate vicinity to bainite platelets than in the regions between the bainitic sheaves (Fig. 4, 5) while those regions contain relatively poor carbon [12,14]. Martensite is usually found to be in the blocky regions of untransformed austenite [3]. It indicates that the blocky regions of austenite between bainitic sheaves are less enriched with carbon, and therefore are thermally unstable.

From the mass balance for carbon it follows that [2]:

$$(0.5w_{\alpha})(\bar{x} - x^{\alpha\gamma}) = \int_{z=0}^{\infty} [x_{\gamma}\{z, t_d\} - \bar{x}] dz \quad (2)$$

where \bar{x} is the average mole fraction of carbon in the alloy and $x^{\alpha\gamma}$ and $x^{\gamma\alpha}$ are the paraequilibrium carbon concentration in ferrite and austenite respectively. Since the diffusion rate of carbon in austenite is slower than in ferrite the rate of decarburization will be determined by the diffusivity in the austenite and the concentration of carbon in austenite at the interface remains constant for times $0 < t < t_d$ after which it steadily decreases as the austenite becomes homogeneous in composition. The function x_{γ} is given by:

$$x_{\gamma} = \bar{x} + (x^{\gamma\alpha} - \bar{x}) \operatorname{erfc}\{z / 2(Dt_d)^{0.5}\} \quad (3)$$

This assumes that for $t < t_d$, the concentration of carbon in the austenite at the interface is given by $x^{\gamma\alpha}$.

The diffusion coefficient of carbon in austenite $D\{x\}$, is very sensitive to the carbon concentration and this has to be taken into account in treating the large concentration gradients that develop in the austenite. It is clearly necessary to know $D\{x\}$ at least over a range $\bar{x} \rightarrow x^{\gamma\alpha}$, although experimental determinations of $D\{x\}$ do not extend beyond $x = 0.06$. The value of D was calculated as discussed in Ref. [1]. The good approximation of the dependent diffusivity of carbon in austenite can be a weighted average diffusivity \bar{D} [3,15]. Taking into account carbon concentration gradients it has been demonstrated that for most purposes a weighted average diffusivity \bar{D} can adequately represent the effective diffusivity of carbon [3,9]. Weighted average

diffusivity \bar{D} is calculated by considering the carbon concentration profile in front of the moving ferrite interface as given by the following equation:

$$\bar{D} = \int_{\bar{x}}^{x^{\gamma\alpha}} \frac{Ddx}{(x^{\gamma\alpha} - \bar{x})} \quad (4)$$

On carrying the integration, the time required to decarburise a supersaturated bainitic ferrite lath of thickness w_α is given by [2,3]:

$$t_d = \frac{w_\alpha^2 \pi (\bar{x} - x^{\alpha\gamma})^2}{16 \bar{D} (x^{\gamma\alpha} - \bar{x})} \quad (5)$$

where: \bar{x} is the average carbon concentration in the alloy, $x^{\alpha\gamma}$ and $x^{\gamma\alpha}$ are the carbon concentrations in ferrite and austenite respectively, when the two phases are in paraequilibrium. The calculated diffusion coefficients of carbon in austenite and carbon concentration in austenite $x^{\gamma\alpha}$ and ferrite $x^{\alpha\gamma}$ after isothermal transformation at 350 and 480°C of Fe-0.38C-0.93Cr steel are listed in Tab. 3.

Tab. 3. The calculated diffusion coefficients of carbon in austenite $D\{x\}$ and a weighted average diffusivity \bar{D} and carbon concentration in austenite $x^{\gamma\alpha}$ and ferrite $x^{\alpha\gamma}$ after austempering at 350 and 480°C of Fe-0.38C-0.93Cr steel

Diffusion coefficients	Austempering temperature, °C	
	350	480
$D, \text{m}^2/\text{s}$	0.1856×10^{-16}	0.2172×10^{-14}
$\bar{D}, \text{m}^2/\text{s}$	0.2462×10^{-15}	0.6638×10^{-14}
Carbon concentration, mol		
in austenite, $x^{\gamma\alpha}$	0.1310	0.0809
in ferrite, $x^{\alpha\gamma}$	0.5426×10^{-3}	0.6920×10^{-3}

Calculated decarburisation times (t_d) of distance 30 μm (average austenite grain size) consisted of laths with thickness: 0.05, 0.1, 0.2, 0.3, 0.5, 1.0, 5.0 and 10 μm in Fe-0.38C-0.93Cr steel are shown in Tab. 4.

Tab. 4. Decarburisation times (t_d) of distance 30 μm consisted of laths with thickness: 0.05, 0.1, 0.2, 0.3, 0.5, 1.0, 5.0 and 10 μm in Fe-0.38C-0.93Cr steel

$T_i, ^\circ\text{C}$	Decarburisation times (t_d) of distance of 30 μm in seconds							
	3x10 μm	6x5 μm	30x1 μm	60x0.5 μm	100x0.3 μm	150x0.2 μm	300x0.1 μm	600x0.05 μm
350	5202	2601	520.2	260.1	156.1	104.0	52.0	26.0
480	604.8	302.4	60.5	30.2	18.1	12.1	6.0	3.0

The calculated times of partitioning are shown in Fig. 6 for different thickness of bainitic ferrite phase (for $w_o=0.1, 0.2, 0.5, 1.0, 10, 50,$ and $100\ \mu\text{m}$) and austempering temperatures. For investigated Fe-0.38C-0.93Cr steel calculations show that t_d increases sharply as temperature decreases.

The decarburisation time t_d is a function of lath width and increases with decreasing temperature of isothermal transformation (480 and 350°C) because the diffusion coefficient of carbon also decreases with temperature (Table 3).

Furthermore, it is generally observed that the width of ferrite laths is highly diverse (Fig. 2 and 3) in different packets. This reflect the possibility that cementite can precipitate in thicker bainite laths (when t_d is a long period of time) and in thinner laths has not during isothermal transformation. If the decarburisation process dominates it leads to the formation of upper bainite.

It is also consistent with the fact that upper and lower bainite often form at the same temperature in a given steel or ductile iron [2,3,11]. The decarburisation time also increases as the thickness of the ferrite phase increases (Fig. 6).

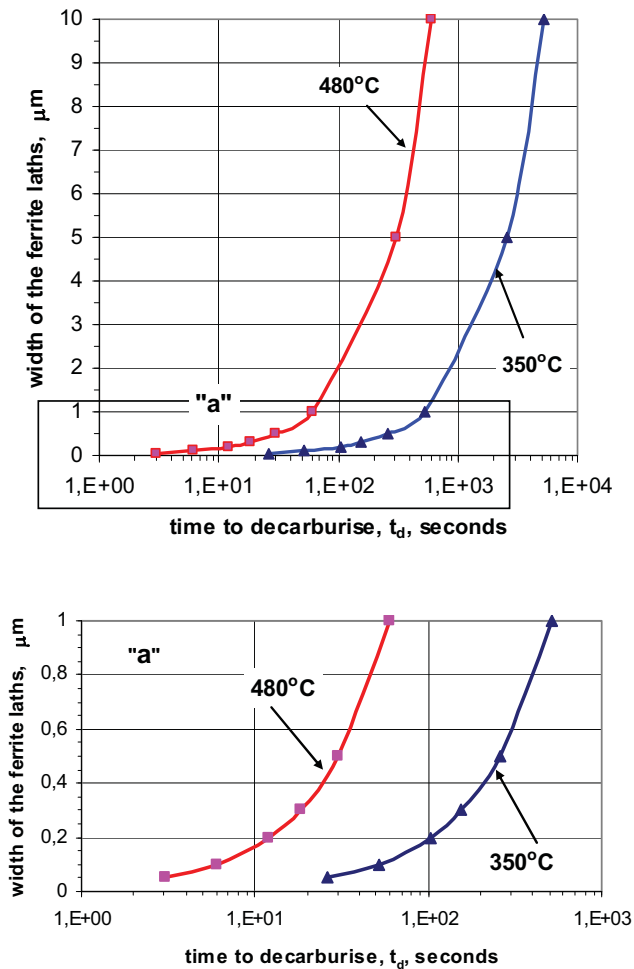


Fig. 6. The calculated decarburisation times for a given width of ferrite phase in investigated Fe-0.38C-0.93Cr steel after austempering at 480 and 350°C . The relationship (5) has been used for calculations

The obtained results illustrates that the estimated times are not capable of decarburising the sheaf of ferrite included thick laths during the period of isothermal holding. A consequence of the precipitation of cementite from austenite during austempering is that the resulting microstructure is not an ausferrite but it is a mixture of bainitic ferrite, retained austenite and carbides.

Conclusions

As a result the following conclusions are reached:

1. Analytical calculations of the time required for the diffusion of carbon out of supersaturated laths of ferrite into the retained austenite indicate that there is a necessity of carbides precipitation from ferrite or/and austenite.
2. A consequence of the precipitation of cementite from ferrite or/and austenite during austempering is that the growth of bainitic ferrite can continue to larger extent and that the resulting microstructure is not an ausferrite but is a mixture of bainitic ferrite, retained austenite and carbides.

References

- [1] Bhadeshia, H.K.D.H., *Diffusion of carbon in austenite*, Metal Science, vol. 15, 477-479, 1981.
- [2] Bhadeshia, H.K.D.H., Christian, J.W., *Bainite in Steels*, Metallurgical Transactions A, 21A, 767-797, 1990.
- [3] Bhadeshia, H.K.D.H., *Bainite in Steels*, Institute of Materials, 1-458, London, 1992.
- [4] Chang, L.C., *Carbon content of austenite in austempered ductile iron*, Scripta Materialia, vol. 39, No 1, 35-38, 1998.
- [5] Christian, J.W., *Theory of transformations in metals and alloys*, p. 778, Oxford, Pergamon Press, 1965.
- [6] Guzik, S.E., *Austempered cast iron as a modern constructional material*, Inżynieria Materiałowa, vol. 6, 677-680, 2003.
- [7] Kinsman, K.R., Aaronson, H.I., *The transformation and hardenability in steels*, Climax Molybdenum Company, Ann Arbor, MI, p.39, 1967.
- [8] Kutsov, A. et al., *Formation of bainite in ductile iron*, Materials Sci. and Engineering, A273-275, 480-484, 1999.
- [9] Ławrynowicz, Z., *Criticism of selected methods for diffusivity estimation of carbon in austenite*, Zeszyty Naukowe ATR, nr 216, Mechanika, vol. 43, 283-287, 1998.
- [10] Ławrynowicz, Z., *Mechanism of bainite transformation in Fe-Cr-Mo-V-Ti-C steel*, International Journal of Engineering, vol. 12, 81-86, 1999.
- [11] Ławrynowicz, Z., *Transition from upper to lower bainite in Fe-Cr-C steel*, Materials Science and Technology, vol. 20, 1447-1454, 2004.
- [12] Ławrynowicz, Z., *A discussion on the mechanism of bainite transformation in steels*, Technology and Materials, Gdańsk, Politechnika Gdańska, vol. 4, pp. 149-155, 2006.
- [13] Pietrowski, S., *Nodular cast iron of bainitic ferrite structure with austenite or bainitic structure*, Archives of Materials Science, vol. 18, No.4, 253-273, 1997.
- [14] Shiflet, G.J., Hackenberg, R.E., *Partitioning and the growth of bainite*, Scripta Materialia, vol. 47, 163-167, 2002.
- [15] Siller, R.H., McLellan, R.B., *The Application of First Order Mixing Statistics to the Variation of the Diffusivity of Carbon in Austenite*, Metallurgical Transactions, vol. 1, 985-988, 1970.

- [16] Takahashi, M., Bhadeshia, H.K.D.H., *A Model for the Microstructure of Some Advanced Bainitic Steels*, Materials Transaction, JIM, vol. 32, 689-696, 1991.



INFLUENCE OF CEMENTITE PRECIPITATION ON THE EXTENT OF BAINITE REACTION IN Fe-Cr-Si-C STEEL

Zdzisław Ławrynowicz

*University of Technology and Life Sciences in Bydgoszcz, Mechanical Engineering Faculty
Department of Materials Science and Engineering,
av. Kaliskiego 7, 85-789 Bydgoszcz, Poland
e-mail address: lawry@utp.edu.pl*

Abstract

The paper presents an investigation of the extend of bainite reaction in the case of cementite precipitation. Experimental measurements of volume fraction of bainitic ferrite and volume of the untransformed austenite indicate that there is a necessity of carbides precipitation from austenite. Carbon concentration in the residual austenite was calculated using volume fraction data of austenite and a model developed by Bhadeshia based on the McLellan and Dunn quasi-chemical thermodynamic model. The comparison of experimental data with the T_0 , T_0' and A_3' phase boundaries suggests the likely mechanism of bainite reaction in Fe-Cr-Si-C steel is displacive rather than diffusional. A consequence of the precipitation of cementite from austenite during austempering is that the growth of bainitic ferrite can continue to larger extent and that the resulting microstructure is not an ausferrite but it is a mixture of bainitic ferrite, retained austenite and carbides.

Keywords: bainite transformation, carbide precipitation, carbon diffusion

1. Introduction

The attractive properties of bainitic steels without carbides are related to its unique microstructure that consists of ferrite and high carbon austenite. Because of this microstructure, the product of bainitic reaction is often referred to as “ausferrite” rather than bainite [5,11,12]. The mixture of bainitic ferrite and untransformed austenite is an ideal combination from many points of view. If the bainitic ferrite-austenite microstructure is held for long time periods, the blocks of high carbon austenite will eventually undergo a transformation to bainite, the two phase ferrite and carbide ($\alpha + \text{Fe}_3\text{C}$). Carbides can be suppressed by alloying with elements such as Si and Al. Once the ausferrite has been produced, the components are cooled to room temperature. The cooling rate will not affect the final microstructure as the carbon content of the austenite is high enough to lower the martensite start temperature to a temperature significantly below room temperature.

The purpose of the present paper is to demonstrate how a thermodynamic method can be used for determination of the carbon concentration in the retained austenite in Fe-Cr-Si-C steel. The method takes into consideration the precipitation of cementite from ferrite or/and austenite during bainite reaction.

2. Experimental procedures

A high-speed Adamel Lhomargy LK-02 dilatometer was used to establish change of length ($\Delta L/L$) during isothermal bainitic transformation. In order to ensure rapid cooling ($\sim 300\text{Ks}^{-1}$) from austenitising temperature (1000°C , 10 minutes), the specimens were 13mm in length and 1.1mm in diameter. Lattice parameter measurements were carried out using a X-ray diffractometer with Fe-filtered CoK_α radiation. The precision ferrite lattice parameter determination included a knowledge of the angular positions of the (110), (200), (211) and (220) peaks. The data were analysed using a Taylor-Sinclair function to extrapolate the values of the ferrite parameter to angular position of $\Theta = 90^\circ$.

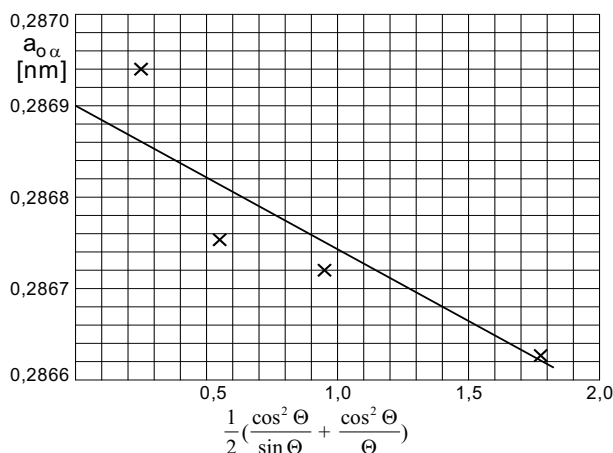


Fig. 1. Extrapolated parameter of ferrite $a_{0\alpha}$ in Fe-Cr-Si-C steel using extrapolation function of Taylor-Sinclair

The linear expansion coefficient of ferrite (e_α) was determined by annealing a specimen at 650°C for 30 minutes to decompose any retained austenite and then recording the change of length during slow cooling. The linear expansion coefficient of austenite (e_γ) was measured after cooling from temperature of 1100°C while the specimen was in the single γ phase field. Determination of the linear expansion coefficients was carried out in a UBD Leitz-Wetzlar dilatometer. The chemical composition of the experimental steel is listed in Table 1.

Tab. 1. Chemical composition of the steel used in this study. All concentrations are given in wt.% and at.% ($\times 10^2$)

Steel		C	Si	Cr	Mn	Ni	P	S
Fe-Cr-Si-C	wt.%	0.36	1.25	1.25	0.95	0.30	0.018	0.008
	at.% (x_i^α)	1.63	2.42	1.31	0.94	0.28	-	-

Lattice parameters, expansion coefficients of ferrite and austenite and parameters for determination of volume fractions of transformation and the carbon concentration of the residual austenite in Fe-Cr-Si-C steel are listed in Tables 2 and 3.

Tab. 2. Lattice parameters and expansion coefficients of ferrite and austenite

Steel	Lattice parameter of ferrite a_{α} , nm	Lattice parameter of austenite a_{γ} , nm	Ferrite e_{α} , $^{\circ}\text{C}^{-1} \times 10^{-5}$	Austenite e_{γ} , $^{\circ}\text{C}^{-1} \times 10^{-5}$
Fe-Cr-Si-C	0.2868 0.2869 *	0.3591	1.589	2.475

* The ferrite lattice parameters determined using a X-ray diffractometer

Tab. 3. Parameters for determination of volume fractions of transformation a residual austenite in Fe-Cr-Si-C steel

Transformed at $^{\circ}\text{C}$	a_{γ} , nm	a_{α} , nm	$\Delta L/L \times 10^{-3}$ *	V_{α}
352	0.3619	0.2882	2.70	0.79
380	0.3622	0.2884	2.25	0.66
414	0.3625	0.2885	1.70	0.50
442	0.3627	0.2886	1.21	0.35
475	0.3630	0.2888	0.25	0.07

* measured values of the dimensional changes accompanying the transformation of austenite to bainitic ferrite at transformation temperature

V_{α} - measured volume fraction of bainitic ferrite

The dilatometry results show that the relative length change during the formation of bainite increases as the isothermal transformation temperature decreases below the B_s temperature (Fig. 2), then the amount of bainite formed is dependent on the transformation temperature.

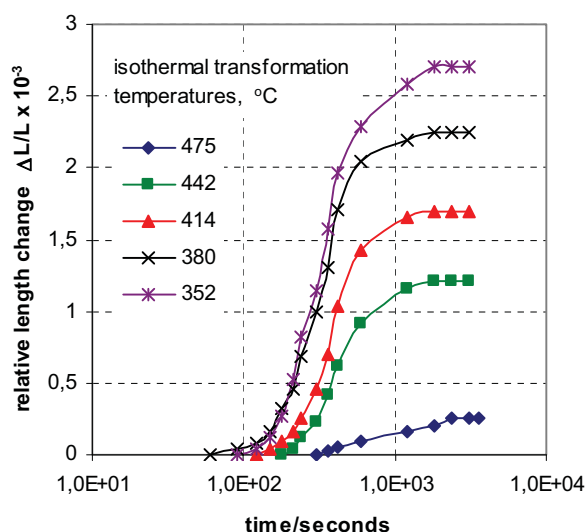


Fig. 2. The relative length change ($\Delta L/L$) observed by dilatometer during isothermal transformation below B_s temperature

3. Phase diagram of austempered Fe-Cr-Si-C steel

It is usually assumed that the point where the microstructure of austempered steel ceases to change represents full transformation. But in case of bainitic transformation, reaction ceases before

the parent phase (austenite) has completely transformed. It means that at any temperature below B_S and in the absence of any interfering secondary reactions only a limited quantity of bainitic ferrite forms before the reaction terminates.

The determined carbon concentrations of the residual austenite at the different temperatures of transformation of bainite are compared with the T_0 , T_0' and A_3' phase boundaries (Table 4) for investigated steel in Figure 3.

Tab. 4. Calculated details for phase diagram of the Fe-Cr-Si-C steel and the carbon concentration in austenite, x_γ at selected temperatures

Reaction temperature, °C	A_3' , mol	x_{T_0} , mol	$x_{T_0'}$, mol	x_γ , mol
475	0.0990	0.0282	0.0184	0.068
442	0.1104	0.0324	0.0221	0.054
414	0.1198	0.0359	0.0246	0.036
380	0.1308	0.0400	0.0283	0.028
352	0.1397	0.0436	0.0317	0.018

A_3' - $x^{\gamma\alpha}$ - paraequilibrium carbon concentration of austenite in mole fraction,

x_{T_0} - T -zero carbon concentration in mole fraction

$x_{T_0'}$ - the same but allowing for the 400J/mol stored energy

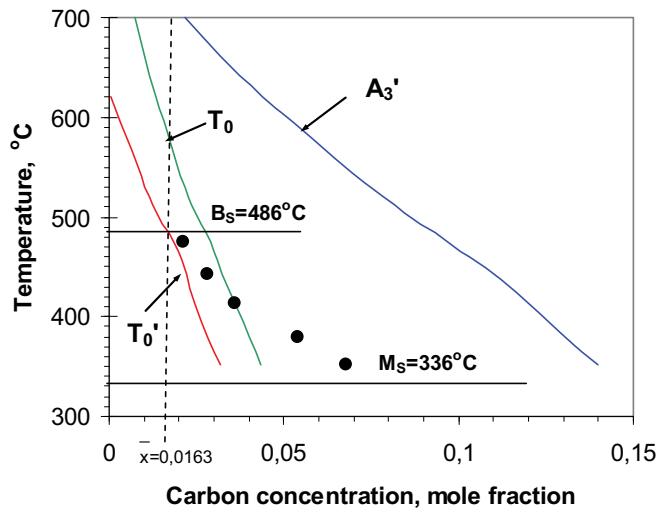


Fig. 3. The calculated phase boundaries A_3' , T_0 and T_0' for the investigated Fe-Cr-Si-C steel together with all the experimental data of the measured carbon contents of the untransformed austenite (black circles)

The diagram was calculated as in Ref. [1-3,8] using a model developed by Bhadeshia [3] based on the McLellan and Dunn quasi-chemical thermodynamic model [13,14]. The martensite and bainite reaction starts temperatures, M_S and B_S are also marked on this diagram. The paraequilibrium phase boundary is chosen because no substitutional alloying element partitioning occurs during bainite formation.

In presented diagram the reaction at temperatures 475, 442 and 414°C is found to stop when the average carbon concentration of the residual austenite is closer to the T_0 and T_0' curves than the A_3' boundary. The maximum extent to which the bainite reaction can proceed is therefore determined by the composition of the residual austenite.

Thus, it is found experimentally that the transformation to upper bainite in Fe-Cr-Si-C steel does indeed stop close to the T_0 boundary (Fig. 3). Similar results have previously obtained by Bhadeshia and Christian [2,4] and by Ławrynowicz and Barbacki for other alloys [6-10].

In Figure 3 the reaction to lower bainite at 352 and 380°C seems to stop when carbon concentration of austenite exceeds the T_0' boundary. This might be explained by the fact that the T_0' line accounts for 400J/mol of stored energy in the bainite. If this energy is reduced by plastic deformation of the surrounding austenite then a higher volume fraction of bainite should be able to form. Furthermore, the measured carbon contents of the austenite after reaction to lower bainite at 352 and 380°C may indicate on the possibility of cementite precipitation from austenite or ferrite.

When the microstructure of Fe-Cr-Si-C steel consists of ausferrite, thus:

$$V_\gamma + V_\alpha = 1 \quad (1)$$

and the permitted fraction of bainite (V_α) can be determined from Lever rule applied to the T_0 curve, Figure 4. The maximum volume fraction of retained austenite (V_γ) will then equal $1 - V_\alpha$.

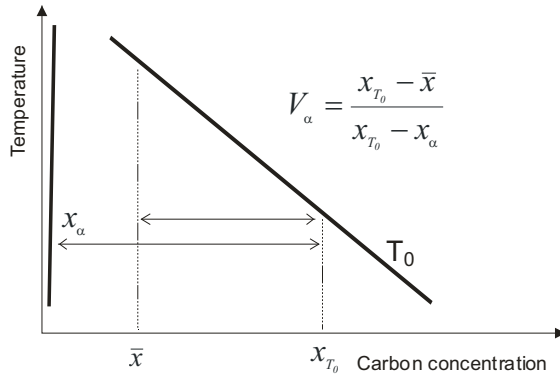


Fig. 4. Application of the Lever-rule to the T_0 curve allows the estimation of the permitted fraction of bainite V_α at any temperature

In case of carbides precipitation the maximum volume fraction of bainitic ferrite (V_α) can be calculated using the following equation [6,15]:

$$V_\alpha = \frac{x_{T'_0} - \bar{x}}{x_{T'_0} - x_\alpha - x_C} \quad (2)$$

where V_α is volume fraction of bainitic ferrite, \bar{x} is the average carbon concentration in the matrix of the alloy, x_α is the paraequilibrium carbon concentration in the bainitic ferrite (0.03 wt.%), $x_{T'_0}$ is the carbon concentration of the austenite corresponding to the T'_0 curve, x_C is the amount of carbon, which is tied up as carbides (cementite).

Thus, the maximum volume fraction of bainite taking into account cementite precipitation can be calculated using the relationship (2), see Fig. 5.

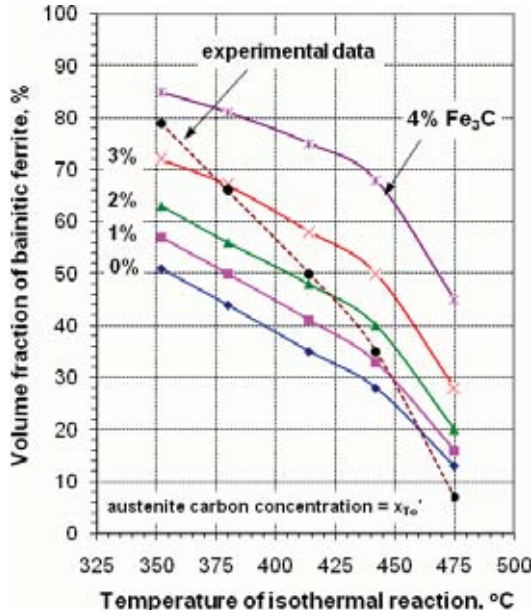


Fig. 5. Experimentally determined and calculated the maximum volume fraction of bainite in investigated Fe-Cr-Si-C steel taking into account cementite precipitation in the range from 0% to 4 wt % Fe_3C . Assumed austenite carbon concentration at the cessation of bainite transformation $x_\gamma = x_{T_0}$

It is seen in Figure 5 that precipitation of cementite leads to an increase of volume fraction of bainitic ferrite. Carbides locally reduce the carbon content of the parent austenite and increase the driving force for further ferrite growth. A consequence of the precipitation of cementite from austenite is that its carbon concentration drops below x_{T_0} , so that the growth of bainitic ferrite can continue to an extent larger than would be otherwise possible.

4. Conclusions

The paper presents an investigation of the extend of bainite reaction in the case of cementite precipitation.

The following conclusions were reached:

1. Experimental measurements of volume fraction of bainitic ferrite and volume of the untransformed austenite indicate that there is a necessity of carbides precipitation during transformation.
2. The carbon concentration of the residual austenite reaches the critical value represented by the T_0 curve and renders the displacive bainite reaction to cease.
3. The extent of transformation to bainite decreases when increasing the isothermal transformation temperature towards the bainite start temperature (B_S). This is because the austenite can only transform to bainite if its carbon concentration is less than a value x_{T_0} given by the T_0 curve.
4. The carbon concentration of the residual austenite increases during bainitic transformation as a consequence of the increasing volume fraction of bainitic ferrite.

5. Precipitation of cementite leads to an increase of volume fraction of bainitic ferrite. Carbides locally reduce the carbon content of the parent austenite and increase the driving force for further ferrite growth.
6. A consequence of the precipitation of cementite from ferrite or/and austenite during bainite reaction is that the resulting microstructure is not a pure ausferrite but is a mixture of bainitic ferrite, retained austenite and carbides.

References

- [1] Bhadeshia, H.K.D.H., *Diffusion of carbon in austenite*, Metal Science, vol. 15, pp. 477-479, 1981.
- [2] Bhadeshia, H.K.D.H., Christian J.W., *Bainite in Steels*, Metallurgical Transactions A 21A, pp. 767-797, 1990.
- [3] Bhadeshia, H.K.D.H., *Bainite in Steels*, Institute of Materials, 1-458, London, 1992.
- [4] Christian, J.W., *Theory of transformations in metals and alloys*, 778, Oxford, Pergamon Press, 1965.
- [5] Guzik, S. E., *Austempered cast iron as a modern constructional material*, Inżynieria Materiałowa, vol. 6, pp. 677-680, 2003.
- [6] Ławrynowicz, Z., Barbacki, A., *The mechanism of bainite transformation in Fe-Cr-Mn-Si-C steel*, Proc. of the Scientific Con. AMTECH'95, Rousse, Bułgaria, pp. 1-8, 19-21 April 1995.
- [7] Ławrynowicz, Z., Barbacki, A., *Analiza mechanizmu izotermicznej przemiany bainitycznej w stali Cr-Mn-Si*, Archiwum Nauki o Materiałach, vol. 17, pp. 127-147, 1996.
- [8] Ławrynowicz, Z., *Mechanism of bainite transformation in Fe-Cr-Mo-V-Ti-C steel*, International Journal of Engineering, 12, pp. 81-86, 1999.
- [9] Ławrynowicz, Z., *Carbon partitioning during bainite transformations in low alloy steels*, Materials Science and Technology, vol. 18, pp. 1322-1324, 2002.
- [10] Ławrynowicz, Z., *Transition from upper to lower bainite in Fe-Cr-C steel*, Materials Science and Technology, vol. 20, pp. 1447-1454, 2004.
- [11] Ławrynowicz, Z., Dymski, S., *Application of the mechanism of bainite transformation to modelling of processing window in ductile iron ADI*, Archives of Foundry Engineering, vol. 6, pp. 177-182, 2006.
- [12] Ławrynowicz, Z., Dymski, S., Giętka, T., *Zastosowanie sieci neuronowych do szacowania zawartości austenitu szczątkowego i własności mechanicznych żeliwa ADI*. PAN-Katowice. Monografia pt.: „Tendencje optymalizacji systemu produkcyjnego w odlewniach”, s. 135-142, 2010.
- [13] McLellan, R.B., Dunn, W.W., J. Phys. Chem. Solids. vol.30, 2631, 1969.
- [14] Siller, R.H., McLellan, R.B., *The Application of First Order Mixing Statistics to the Variation of the Diffusivity of Carbon in Austenite*, Metallurgical Transactions, vol.1, pp. 985-988, 1970.
- [15] Takahashi, M., Bhadeshia, H.K.D.H., *A Model for the Microstructure of Some Advanced Bainitic Steels*, Materials Transaction, JIM, vol. 32, pp. 689-696, 1991.



FILM AND PANEL TWO-DIMENSIONAL RELATIVE POSITION OPTIMIZATION

Adam Marchewka*, Ryszard Wocianiec**, Jarosław Zdrojewski*

University of Technology and Life Sciences
Prof. Kaliski Av. 7, 85-789 Bydgoszcz

*Institute of Telecommunication, Digital Electronic Department

email: adam.marchewka@utp.edu.pl

email: jaroslaw.zdrojewski@utp.edu.pl

*Faculty of Mechanical Engineering

email: ryszard.wocianiec@utp.edu.pl

Abstract

The article presents automatic films registration system for printed circuit board exposure units with a new proposed processing method, based on the Radon transformation. The conditions and criteria of alignment deviation evaluation for selected registration marks were defined. Proposition of a mechatronic unit built on a base images from 2 or 4 movable cameras and 6-axis films positioning device is designed. Align film and panel for a solder mask targets images processing method, based on the Radon transformation, was used. Rules for 2- and 4-point films position optimization were created, as well as marks and registration algorithms. Experimental results showing capability and limits of the registration system were presented.

1 Introduction

The manufacturing process of printed circuit boards (PCB) is complex. It consists of a sequence of complex operations. The PCB nevertheless it is single-sided, double sided or multilayer, is a base for electronic components assembly and it realizes electrical connections between them. Manufacturing cycle is conducted in a technological process consisting of following stages: exposure, development, etching, building assembly, lamination (for multilayer circuits), drilling, plating, solder mask applying and label printing. The whole process gets even more complicated when some connections in the multilayer printed circuit board are made using buried or blind holes. The majority of these stages require continuous control, which is in most cases conducted automatically in optical measuring devices. Geometry and electrical parameters of constructed circuit is measured to keep observed deviations within defined tolerance limits in order to reach the quality of the final product through applying required corrections to the technological process. Currently [1] the requirements for High Density Interconnect circuit boards are defined by an increased number of connections per area unit in comparison with traditional circuits. HDI technology reduces dimensions, weight and improves electrical qualities. Both minimal track width and minimal space width begins from 75 μm , minimal vias diameter from 150 μm , capture pads diameter from 400 μm and soldering pads density above 20/cm². Complexity of printed circuit boards can be defined using following equation [3]:

$$ComplexityIndex = \frac{(Area) \left(\frac{No. OfHoles}{UnitArea} \right)^2 (No.OfLayers)^3}{(MinTraceWidth)(MinAnnularRing)(MinHoleDiameter)}$$

Parameters presented above are exemplary. They describe environment and requirements for circuit boards and also define conditions for the alignment system, which is the subject of this paper. In an exposure machine operation of transferring image from film onto a requested place of resist layer which covers a copper laminated plate, can be conducted in 3 modes:

- outer layer,
- inner layer,
- solder mask.

Each of these modes differently defines the term of optimal position of the film in accordance to the board and/or the second film. Film to film relation is especially important for the double-sided exposure, which is mostly used for its productivity.

For the outer layers drilled holes in the board are used as a reference, and the transferred image must relate to their position. The goal is defined very simply: a hole in the board, and an element from the picture on the film belonging to that given hole should be positioned with the smallest possible deviation in relation to each other during exposure process. For quantity criteria we'll take position deviation defined like on Fig. 1, where as we see we can consider this as two deviations in the direction of OX and OY axes of Cartesian coordinate system, respectively dX and dY , or geometrical sum dPD called process deviation for positioning procedure and representing distance between the center of the hole and the center of the corresponding element on the film.

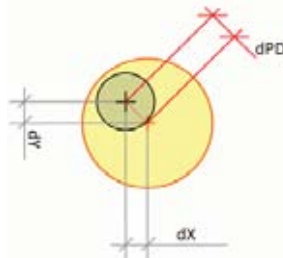


Fig.1 Position evaluation of the elements of the film (circle with bigger diameter) and the hole in the board (circle with smaller diameter) with shown deviations dX , dY , and process deviation dPD .

Since the minimal thickness of the ring surrounding the drilled holes in the board is one of the most important quality conditions, the position of the film has to be strictly related to the position of the drilled holes in the board during the exposure of outer layers. Taking into consideration the following plating process, reaching the limits of the acceptable deviation can lead to breakage of the surrounding ring and disqualification of a circuit board. It is important to note direct relations between total deviation and the size of the circuit components on the film. If the total deviation is smaller, then the sizes of all elements also can be smaller. In this place it would be right to mention that even though our considerations are placed on the area of registration and exposure process, the total geometrical deviations of the final product can also be harmed by: geometry of the films, etching, lamination, drilling and other more detailed steps. In fact, registration process is only one of the several factors that have a direct influence on the final quality of the product, namely the circuit board.

In most cases, for the inner layers we have to deal with a panel on both sides covered with copper and resist (dry or liquid). Also, inner layer mostly does not have any drilled holes and in this case registration has to be made only between the films. For this type of boards, it is required

to have top and bottom film in relation to each other given by specification, what in the end makes elements of one film match elements of the other. In the case of films' only registration we can use the same criteria for evaluating deviations, and, like it was defined on the Fig. 1, we have to consider three values dX , dY and dPD .

Exposing solder mask is one of the final operations for the already assembled multilayer circuit board, when outer layers are already exposed, registration for the films has to be made in relation to what was previously exposed, developed and etched on the panel. Solder mask has a task to leave open only soldering points for electronic assembly: placing and soldering. If all elements of the PCB construction are minimized then also place for the mask has to match existing pattern on the outer layer and follow precisely conditions defined in the specification.

It is evident, from the analysis presented above, that regardless of the mode of exposure the proper location of the film panel and / or second film is required. Evaluation of the registration process can be done by measuring the parameters of dX , dY , dPD (deviations). Activities taken to minimize deviation values always will refer to the whole panel and in fact never to a single selected point. It is possible to define the following criterion (1):

$$\exists dx, dy, d\alpha \forall (x, y) \in PCB, \min(dX(x, y), dY(x, y), dPD(x, y)) \quad (1)$$

Presented criterion (1) describing conditions to evaluate registration process shows film position referring to the whole board area. It takes into account all the points lying on the surface of the circuit. Nevertheless, we will analyze only critical locations from the standpoint of technology and board quality requirements. So, instead of an infinite set of points to analyze we will always use a discrete set with contents depending on design and technological conditions.

2 Proposed system

In order to design system, criterion (1) was taken as a starting point. At the stage of registration we have to deal with deviations depending on different sources:

- Changes of the film geometry depending on the imprecision of the laser plotter, changing line into curve and rectangle into polygon – all this is minimized by the proper calibration of the plotter,
- Changes of the film geometry depending on their thermal stability. Exposure process may lead to film temperature increase and cooling process to temperature decrease. As a consequence, we will observe expanding or shrinking of the film and potential dimensional instability. Typically, dimensional deviations are limited to a given, defined value,
- Random position deviations of drilled holes in the panel that depend on the precision restrictions of a numerically controlled drilling machine and tool (drill bits bending on the laminated surface of the panel).

For the sake of our analysis we assume that the films registration process has to minimize deviations, with no dependence on the source that they are coming from. Measured deviations will be compensated by applying corrections to the film position in a way to minimize their impact within the predefined tolerances.

The registration system should be a compromise between the number of measurement points on the board, the number of cameras used and the time needed to evaluate input data – images from all sources. Taking into account on one hand requirements and on the other the experience of production techniques for manual registration, two solutions were considered. The first uses two cameras and two marks on the board layout and films. In this case the marks are located centrally in the symmetry axis of two shorter sides of the panel. The second solution assumes the use of four cameras and appropriate marks located in the corners of the board.

Regardless of the number of marks and number of used cameras, film positioning is aimed at optimization. Optimization has a task of minimizing the position deviations, which depend on both instable film size and variable location of the panel holes used as registration marks.

We assumed that the system can operate in two different tolerance modes, respectively: dimensional deviations (film to board) and alignment deviation. The basic mode is the mode of DA (Dimensions / Alignment), in which dimensional tolerance (2) and the alignment tolerance (3) are defined separately. In this mode, the measuring system will calculate position of the registration marks on the basis of processed input images from the cameras, and using this data will calculate separately dimensional deviations for both the films and the alignment deviations film to board or film to film. All calculated values will be compared with given tolerance values. If the dimensional deviation is greater than the dimensional tolerance (DT), system will stop registration procedure and an error message describing the reason will be presented to the operator. In the case of crossing the tolerance limit for the alignment deviations (AT), the registration process will be repeated and new deviations will be compared once more with the given tolerance values.

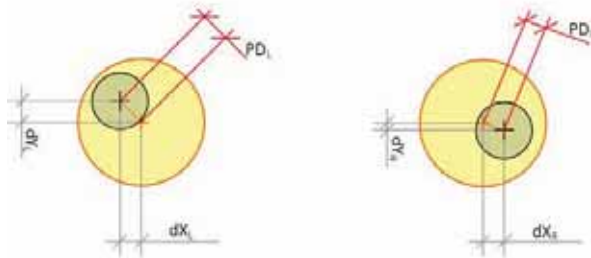


Fig. 2. Dimensional deviation and alignment deviation [dX , dY – alignment deviations (L – Left camera, R – right camera), PD – process deviation]

Beside basic tolerances mode we have also a second one, which is in fact simplified, using just one value of tolerance called PDT (4) (process deviation tolerance). In this mode the value of PDT has a task to define a border for all values of PD (Fig. 2) calculated for the every camera separately. We compare measured distances (PDL , PDR) between the center of the hole in the board and center of the mark on the film (both or single one, depending on the mode), and also distance between mark on both films, with a predefined value of PDT . In the PD mode we do not check separately the tolerances for dimensions and alignment, unlike the DA mode. Formally, the principle of tolerance rules with the use of DA , AT , PDT can be described in the following way (meaning of parameters shown on Fig. 2):

- DA – dimensional tolerance

$$|dXL - dXR| \leq DT \quad (2)$$

- AT – alignment tolerance

$$\max\left(\left|\frac{dXL + dXR}{2}\right|, |dYL|, |dYR|\right) \leq AT \quad (3)$$

- PDT – process deviation tolerance

$$\max(PDL, PDR) \quad (4)$$

where \max - function to get maximum value from the comma delimited list of values.

In the four point (marks) registration mode, the basic rule and optimization condition (5) is still valid. We proceed with an alignment of the film in a way that minimizes the value of $\max(PD)$, measured using images from all used cameras, described as CQ_1, CQ_2, CQ_3, CQ_4 , where symbols CQ_1, \dots, CQ_4 are representing corresponding 4 quadrants of the XOY coordinate system. Every camera CQ_i belongs to the corresponding corner of the board with associated reference hole and film marks.

$$\max(PDQ_1, PDQ_2, PDQ_3, PDQ_4) \quad (5)$$

where PDQ_i is a value of PD measured in the corner of the board belonging to the quadrant i .

Movements of the films can be described by parameters of a flat displacement, represented by offset and rotation value, corresponding respectively to movement along the OX axis, movement along the axis OY and rotation round the zero point of XOY system. Modified and generalized optimization criterion can be written as:

$$\exists(dx, dy, d\alpha), \min(\max(PDQ_1, PDQ_2, PDQ_3, PDQ_4)) \quad (6)$$

As we can see we search for the value of $(dx, dy, d\alpha)$ that minimizes the maximum deviation PD (6) at all points where the position has to be verified. This criterion also fits into the system with two sets of targets as well. In such case in the optimal position appropriate deviations will have following values (7):

$$dXL = -dXR, dYL = 0, dYR = 0 \quad (7)$$

Proposed arrangement to allow the positioning of films and plate is shown below in Fig. 3. illustrating the concept of the device for carrying out this idea.

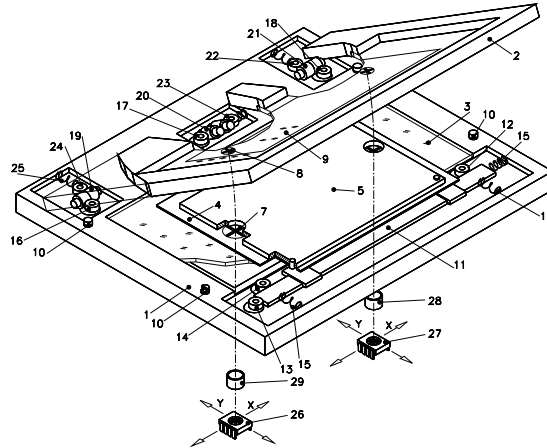


Fig. 3. Concept of the frame to position films and panel before exposure, equipped with cameras to check registration target location and critical deviations

It consists (Fig. 3) of two frames, the lower /1/ and upper /2/, containing glass /3/. Top film /5/ and bottom /4/ has marks placed in the technological margin on the axis of symmetry of the panel's short side for 2 target registration or in the panel corners for 4 targets registration. Eccentric rollers /18, 17, 16/ move top frame. Springs /25/ and rollers /19, 22, 20, 23, 24/ provide play less drive and roller bearings for vertical movement of the frame /2/. Panel /5/ is attached to the panel holder bar 11, also driven by eccentric rolls/12, 13, 14/ supported with a backlash springs /15/. Image with film targets and holes in the panel is projected thru an optical path /28, 29/ to image sensors /26, 27/ – CMOS cameras. Depending on the type and location of targets on the panel cameras with optical system moving in the directions x, y .

Alignment of the films is a very important operation in the exposure process, but not the only one which has to be done to get a ready exposed panel. Usually before alignment films has to be loaded into the frame. During exposure and alignment they are fixed to the glass with a dedicated vacuum, also, they must be pre-aligned in relation to the initial panel location when loaded. Switching the unit into the proper mode can be done by selecting the given job. Job is defining not only a mode for alignment but also the type, count and location for targets, all

tolerances and tolerance mode, and other not alignment related parameters like: limits for the vacuums, time and the way how the panel must be exposed. Basic operations belonging to the exposure unit cycle are shown in Fig. 4.

```
//high level representation for the exposure machine activities
//Job is representing data defining task to do and all needed parameters
int ExposureUnitCycle(){

    InitializeUnit();
    //N will represent number of exposures to do
    int N = SelectJobToDo();

    LoadFilms();
    for (int i = 0; i < N; i++){
        LoadPanel();
        RunRegistrationForCurrentPanelAndFilms();

        if (Max(SetOfDeviations())<ProcessTolerance){
            ExposePanel();
        }
        UnloadPanel();
        if (UserBreak) return;
    }
    UnloadFilms();
}
```

Fig. 4. Exposure unit cycle showing basic operations performed during run

Exposure unit cycle Fig. 4 can be terminated as a result of positioning and exposing assumed number of panels or by the action of the operator depending on external conditions, or by equipment, taking into account the control parameters like, for example, thermal stability of films described above. Because the system automatically verifies the critical tolerances, the need to interrupt the process of alignment or exposure tasks can be transferred to the operator with a corresponding message describing exceptional conditions.

From the side of film positioning application, it is important *RunRegistrationForCurrentPanelAndFilms* function Fig. 4. Detailed activities belonging to this action are shown in Fig. 5. It is assumed that before registration the camera will move automatically to the position of marks according to the selected job. Since each camera is equipped with two axes driven by *DC* motors, a change in their location is done just by specifying the coordinates (x_c, y_c) for the new target position.

```
//high level representation for panel to films alignment
int RunRegistrationForCurrentPanelAndFilms(){
    int counter = 0;
    MeasureTargets();
    if (RepositionCamerasIfNeeded())
        MeasureTargets();
    do {
        SetFilmsToTheStartPosition();
        for (int i = 1; i < NumberOfSteps; i++){
            MeasureTargets();
            MoveFilmsToNewLocation(i,NumberOfSteps);
        }
        MeasureTargets();
        StartContactVacuum();
        MeasureTargets();
        done = (Max(SetOfDeviations())<ProcessTolerance);
        while (!done && (++counter < MaxRepetitionCounter));
        return 0;
    }
}
```

Fig. 5. Alignment cycle to optimize films position

The target measurement process is described as *MeasureTargets* and is performed using the cameras. The calculated location of marks is used to evaluate the parameters, for each film separately. These values are the basis for determining the displacement for every of 6 axis used to

move films. The initial deviation is divided inside the function *MoveFilmsToNewLocation* using the variable "i" representing the next iteration and the parameter *NumberOfSteps* defining how many steps the system should take from a starting point the optimal position. Iterative approaching the optimal location is used to reduce the impact of hysteresis, backlash and stiffness of the mechanical system.

The cycle of positioning shown on Fig.5 may be repeated if after turning on the contact vacuum inside the function *StartContactVacuum* (), required during exposure, the resulting position of the films or panel will be disturbed and final verification will measure deviations being bigger then defined tolerances. Contact vacuum is created in a sealed space between both glasses and includes films and panel (Fig. 3). Contact vacuum has a potentially negative impact on positioning result. In the exposure process it has a very important function – it provides direct contact between the resist and film. Direct contact is necessary to eliminate the effect of undercutting or shade, being a side effect of non parallel rays from UV lamp when exposing.

To carry forward the process of alignment, system based on information from images obtained from cameras observing films and plate at a given location must be able to determine the values of relative displacements, using marks on the films and the hole in the plate. To do so, films and plate must be adequately represented in the image from the camera [7].

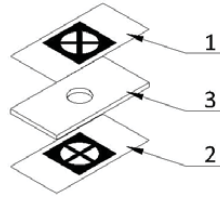


Fig. 6. A sample set of marks: 1 - for the upper film, 2 - for the bottom film, 3 - for the panel

A sample set of marks is shown in Fig.6. At the same location like the hole in the panel, the bottom film has a mark in the form of a "+" and the upper film mark in the form of an 'x'. Sample sizes are: a hole diameter of 3mm, the thickness of the line marks "+" and "x" is 0.254 mm. The form of marks usually is matching the mode of operation and the type of panels.

2.1 Image based marks position

To read detailed information from each single camera is essential for the proper function of the alignment device. Therefore, for this purpose a modified image processing technique based on Radon transform, allowing rapid and accurate determination of straight lines in the image, was used

The Radon transform (TR) is defined as [6]:

$$R_{\theta}(\rho) = \int_{-\infty}^{+\infty} f(x' \cos \theta - y' \sin \theta, x' \sin \theta + y' \cos \theta) dy' \quad (8)$$

where

$$\begin{bmatrix} x' \\ y' \end{bmatrix} = \begin{bmatrix} \cos \theta & \sin \theta \\ -\sin \theta & \cos \theta \end{bmatrix} \begin{bmatrix} x \\ y \end{bmatrix} \quad (9)$$

The Radon operator maps the spatial domain $f(x, y)$ to the projection domain (ρ, θ) , in which θ is the angle and ρ the smallest distance to the origin of the coordinate system. The discrete Radon transform is a useful tool in image processing for detecting of lines in digital images.

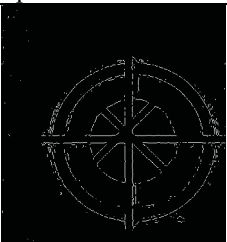
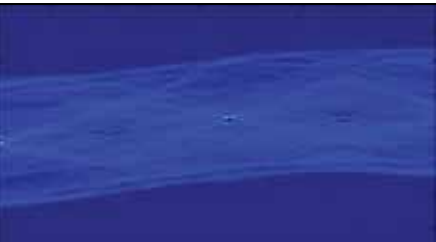


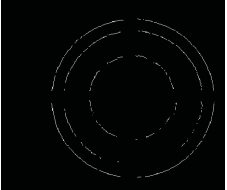
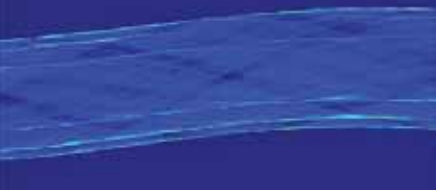

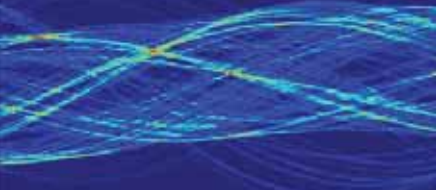
Major key properties of the Radon transform is that a line in an image is transformed into a peak in the parameter domain, where the position of the peak corresponds the line parameter [4,6,9].

Analyzed class of images is characterized by regular shapes such as lines and circles (several of them with a common axis of symmetry). All of them will include the possibility of noise captured directly from images sources, the electronic camera, which have potentially negative effects on parameters values in the field of RT. Studied class of images can be described as a sum of the individual components:

$$f(x, y) = f_l(x, y) + f_o(x, y) + f_e(x, y) \quad (10)$$

where $f_l(x, y)$ - a straight lines component of the image, $f_o(x, y)$ - circles component, and $f_e(x, y)$ - noise (Tab. 1).

Tab. 1. Edge image and its representation in the RT domain for individual components

	Spatial domain	Radon domain
$f(x, y)$		
$f_l(x, y)$		
$f_o(x, y)$		
$f_e(x, y)$		

The proposed algorithm consists of two independent stages:

- lines detection in the image,

- circle detection (position for circle axis of symmetry).

As it was mentioned earlier, straight lines detection in the image $f(x,y)$ is limited to the search finding local maxim (peaks) in the image transform. To limit the information contained in the RT coefficients original image is transformed with the use of Sobel filter. Radon transform is applied to the resulting image containing edges information. In the resulting array of RT coefficients, depending on the class of the analyzed image, search of 8 up to 10 local maxims is performed $\max_{\text{local}} \max_{\theta} (R_{\theta}(x'))_n$ for $n \in \{1, \dots, 10\}$. Using located angle θ and x' values position of individual straight lines can be calculated, depending on the position of individual marks needed to proceed with a alignment task the device.

Knowing already, the characteristics of RT parameters for $f_i(x,y)$ defined by calculated straight lines parameters occurring in the given image, it is possible to calculate the for $f_o(x,y) + f_e(x,y)$. Mentioned decomposition of the edge images, the best is to make in the spatial domain, because when transforming the discrete image both ways (including its inverse transformation), some simplifications can take place (rounding) what may lead to a number of imprecision.

The proposed method creates a synthetic image representing straight lines $f_i(x,y)$ - replacing (overwriting) information from the edge image. Resulting image is converted using the Radon transformation. The resulting RT coefficients represent concentric circles and noise only.

In order to eliminate component $f_e(x,y)$ we propose to use the classifier based on the parameters of the circle. In the RT domain given circle is basically defined by two curves, parallel to each other. Distance in Euclidean space between them for any θ is equal to diameter of the circle. While the curve of arithmetic average value in the spatial domain is a circle center. It should be added that any two values of the curve are enough $F(\theta)$ to designate a point in spatial domain.

Based on the above assumptions, for a classifier purpose, it has to be determined:

$$R_{\theta}(x') = RT(f(x,y) - f_i(x,y)) = RT(f_o(x,y) + f_e(x,y)) \quad (11)$$

The resulting image we transform using Sobel filter, and the result of this operation we interpret as a graph of several curves of $R_{\theta}(x') \rightarrow F_k(\theta)$, where k is the index of a point in spatial domain.

Point to find (center of the circle) must meet the following criteria

- for each θ couple $F_k(\theta)$ and $F_{k+1}(\theta)$ distance in Euclidean space
- for any θ couple $F_o(\theta_n)$ and $F_o(\theta_{n+m})$

$$(x_o, y_o) = \max \{ iRT(F_o(\theta_n), F_o(\theta_{n+m})) \} \quad (12)$$

where $iRT(\cdot)$ is a inverse Radon transform.

Given point is a center of the circle to find for a diameter d (see Fig. 7).

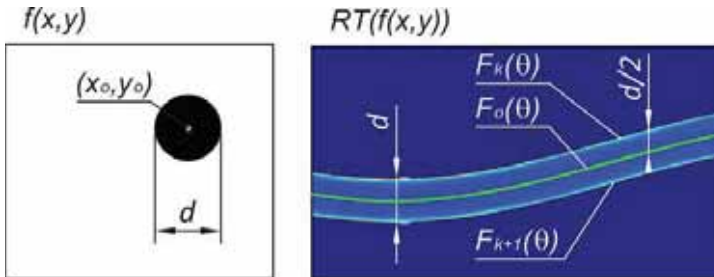


Fig. 7. Circle representation in the RT domain

3 Experimental results

The registration method described above and its implementation, like shown on Fig. 3, was used in the frame of exposure unit, for positioning the film in the outer layer mode. Marks placed on the films and panel in regard to propose shown in Fig. 6. Following results are presented below:

- Results of alignment for the outer layers including the images obtained from cameras used to make final verification,
- Assessment of marks position deviations for the films and panel in relation to the calculated optimal value,
- Example of verification for the films and panel alignment based on images from the measuring machine OPTEK Video Optical Coordinate Measuring Machine.

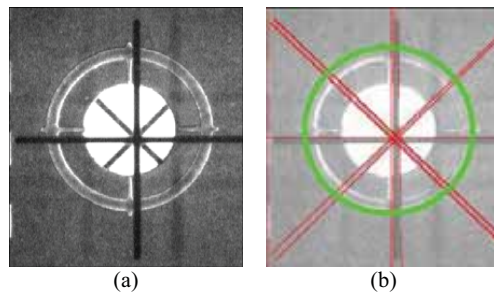


Fig. 8. Image from the camera Q1; (a) Source image from the camera, (b) results of the image processing

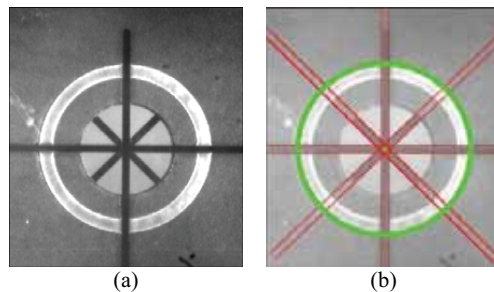


Fig. 9. Image from the camera Q2; (a) Source image from the camera, (b) results of the image processing

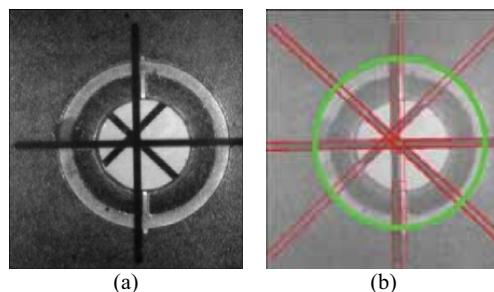


Fig. 10. Image from the camera Q3; (a) Source image from the camera, (b) results of the image processing

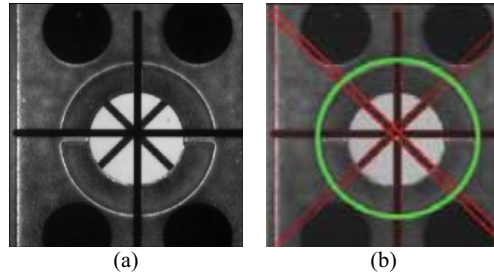


Fig. 11. Image from the camera Q4; (a) Source image from the camera, (b) results of the image processing

For the given alignment and definition of targets, on the Fig. 8, 9, 10, 11, images from cameras placed in quadrants 1, 2, 3, 4, marked as Q_1, Q_2, Q_3, Q_4 , are shown. Resulting position of films and panel marks reached during alignment process is presented. At this stage, the plate is ready for exposure. The image on the left is processed and the right one shows the result of image processing together with information describing the calculated coordinates of the marks. Deviation values in microns measured for all film marks in relation to the holes in the panel are shown in Fig. 12. All values obtained for the analyzed marks are presented in table Fig. 12, together with calculated values of dX, dY, dPD limited by predefined tolerances.

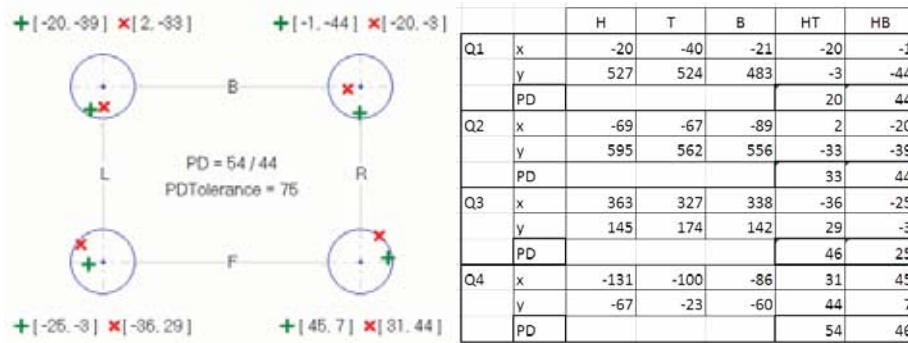


Fig. 12. The result of films and panel alignment (a). Coordinates of marks and deviation values (b) measured at the verification stage before exposure for the outer layer job

Obtained values, like those shown on Fig. 12, are compared with calculated optimum. For each mark the PD value obtained in the alignment process is compared with calculated optimal PD and the maximum difference is limited by the value of tolerance. Optimal position for both films and marks from our experiment are shown on Fig. 13 and 14.

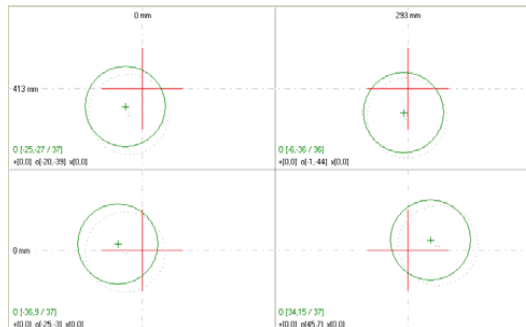


Fig. 13. Calculated optimal position of the bottom film used for verifying alignment of the outer layer

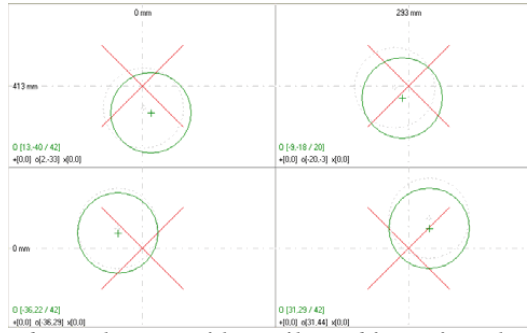


Fig. 14. Calculated optimal position of the top film used for verifying alignment of the outer layer

As shown in Fig. 13 and Fig. 14, the corresponding optimal values calculated for the *PD* are respectively $37 \mu\text{m}$ for the bottom film and $42 \mu\text{m}$ for the top. Both values, when compared to the deviations obtained after alignment are respectively $44 \mu\text{m}$ and $54 \mu\text{m}$, what gives $7 \mu\text{m}$ difference for the bottom film and $12 \mu\text{m}$ for the top. In this case, according to the algorithm from Fig. 6, depending on defined value of tolerance the board will be exposed for the tolerances *PD* greater than $12 \mu\text{m}$, and for the smaller ones alignment will be repeated. To move the films to the optimal position, which will make the difference between the values, obtained in the alignment and calculated, to equal zero, both films position adjustments must be made with the parameters:

- Bottom film: $(dx = 11, dy = -15, d\alpha = 1.211e^{-5})$,
- Top film: $(dx = 11, dy = -15, d\alpha = 1.211e^{-5})$.

Verification of the alignment system operation can be done by an external optical measuring device (OPTEK Video Optical Coordinate Measuring Machine). Images obtained from such system used for the verification are shown on Fig. 15.

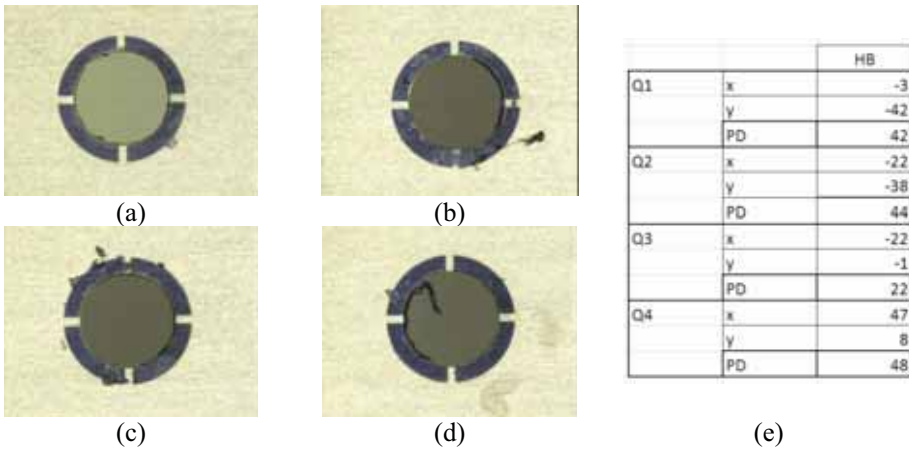


Fig.15. Images used for alignment external verification with exposed and developed targets (a),(b),(c),(d), for bottom film obtained from measuring machine (OPTEK) and table (e) of values for quadrants

The verification of the alignment process (Fig. 14) is only possible after exposure and panel development. Of course, such action is necessary only in order to confirm behavior of the alignment system, verify internal calibration and validate results. The maximum deviation of the measured values and the resulting positioning was less than $3 \mu\text{m}$.

4 Conclusions

The presented system can be used as a tool for very precise films alignment in the exposure unit, with user-defined parameters. Cameras and obtained images allow to measure special targets' positions. Using position of targets measured on the base of image processing, current process deviations can be calculated and optimal film position as well. Alignment controller will use all those values to calculate displacement for the films, and using controller will move them into a location as close as possible to the optimal. Described process will minimize deviation for each of the films by appropriate corrections, evaluated and introduced independently for every film. Control for the alignment system is complex and requires taking into account many factors that may limit its accuracy, actually not mentioned in this paper. As a result, in addition to the basic alignment function, we get coordinates of film and panel marks that can be used to optimize, in a broader sense, process of manufacturing multilayer circuit boards.

References

- [1] Coombs, C. F., Jr., *Printed Circuit Handbook 6th Edition*, McGraw-Hill, 2007.
- [2] Gur, E., Weizman, Y., Zalevsky, Z., *Radon transform based image enhancement for microelectronic chips inspection*. IEEE Transactions on Device and Materials Reliability, 2010.
- [3] Holden, H., *Calculate Your Fabrication Capability Coefficient*, Happy Thoughts, CircuiTree, Feb 15, BNP, pp. 23.5, 2006.
- [4] Leavers, V. F., Boyce, J. F., *The radon transform and its application to shape parametrization in machine vision*. Image Vision Comput, 5:161--166, May 1987.
- [5] Marchewka, A., Zdrojewski, J., *Film Alignment Before Solder Mask Exposure* In: Choras R (ed.): Image Processing and Communications Challenges 3. Springer (accepted for printing), Heidelberg 2011.
- [6] Ohlig, B., *Registration and Knowledge Through and Across Your Panel*, CircuiTree, April 1, 2002.
- [7] Radon, J., *On the determination of functions from their integrals along certain manifolds*, in: The radon transform and some of its applications, annexe a. Wiley, New York, 1983, (translation of Radon's 1917 paper by R. Lohner), 1917.
- [8] Toft, P.: Detection of lines with wiggles using the radon transform, 1996.
- [9] Wocianiec, R., Zdrojewski, J., *Film Position Optimization Before Exposure*, Image Processing & Communication An International Journal, 5(2)35-46, 2010.



NON-CONVENTIONAL MILLING USING INDUSTRIAL ROBOT

Tadeusz Mikołajczyk, Robert Polasik

University of Technology and Life Sciences in Bydgoszcz
Al. Prof. Kaliskiego 7, 85-796 Bydgoszcz, Poland
tel.: +48 53 3408743
e-mail: tami@utp.edu.pl
e-mail: robpol@utp.edu.pl

Abstract

The system for 3D sculpture surface cutting using robot, based on a 2D picture was described in this paper. Picture pixels analysing system, using procedures of 3D tool path-hybrid; radial and X-Z Cartesian coordinates system, milling was presented. The original ROBOART software, designed for IRb60 robot milling, using special milling tool connected with robot wrist was showed and analyzed.

Keywords: picture analyse, milling, robot machining, non-conventional milling

1. Introduction

The kinematic possibilities of robots [1,2,6] and applied software [11] make possible their use in many different jobs. Robots for surface machining are used in cutting [2,3,4,6,10] and grinding [2,6,8,11] processes. These solutions are cheaper than conventional numeric control machine systems. Most surface processing with robots are programmed using CAD geometry model [6,10,11]. IRBCAM supports external axes, which can extend the workspace. Typical accuracy that can be achieved with an ABB IRB-type robot is 0.3 mm, with a repeatability of 0.1 mm and a workspace volume with radius up to 3.9 m. New idea of robot machining can be used for unknown surface geometry machining [6,8,9] and using robots for turning [6,10] or rapid prototyping [5,6].

Some CAM applications (ARTCAM [11], BOBCAD-CAM ART [12], BMP2CNC2 [13]) are useful to make a 3D CNC machining tool paths, based on a 2D picture.

OPTIROB
2011

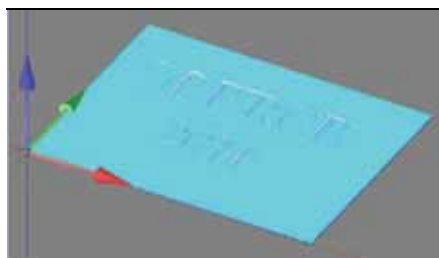


Fig. 1. Example of picture

Fig. 2. Picture from fig. 1 interpreted using BMP2CNC2

Picture's shadow or grayscale is quantified to: adjust Z-axis depth, different tool overlaps, depths and tool radius. Final sizes of X-Y output can be scaled and stored into CNC files that could run with most computer numerical control routers and mills. Example of virtual model 2D image interpretation (fig. 1) is showed on Fig. 2 (made, using BMP2CNC2 DEMO - 12600 G-Code lines, simulate milling time 4 h 40 min).

The new idea of 3D robot machining model, using 2D picture, elaborated in Production Engineering Department, University of Technology and Life Sciences (Bydgoszcz - Poland) is described in this article. Principles of idea and special 3D milling tool path software for IRb60 industrial manipulator are presented and discussed below.

2. IRb 60 robot control system

In the Department's of Production Engineering technological laboratory works on the use of robots for manufacturing have been conducted for many years [3-10]. For these jobs the IRb60 industrial robot with a modified control system was used. Robot was controlled using computer. In this system the manual control panel was combined with the computer via a special interface with 16 relays, controlled by the LPT [7] (Fig. 3).

Direct use LPT interface due to the number of channels did not provide the control capabilities of all robot's five axis, gripper and speed settings. To exhaust all robot's controll possibilities for increase the number of supported transmitters multiplexer was used. But this limited the possibility of use only one sequence of robot's movements at the selected speed from the palette of available values. This is a serious limitation of the developed system control. At the same time, due to the use of mechanical relays, control ability is limited by steps providing the possibility to obtain high-precision displacement and variable speed control.

Control system for IRb60 allows controlling movements of the robot head in one plane in the X-Z Cartesian coordinates directions x, z (Fig. 4). This possibility comes from the construction of control system ensuring the submission of rotation in two axes to obtain horizontal and vertical movements of the wrist. Lateral movement is performed in a radial coordinate system around the robot rotation axis (Fig.4).

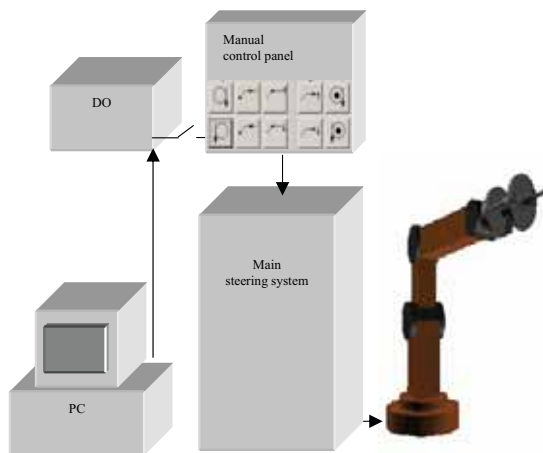


Fig. 3. IRb60 control system [7]

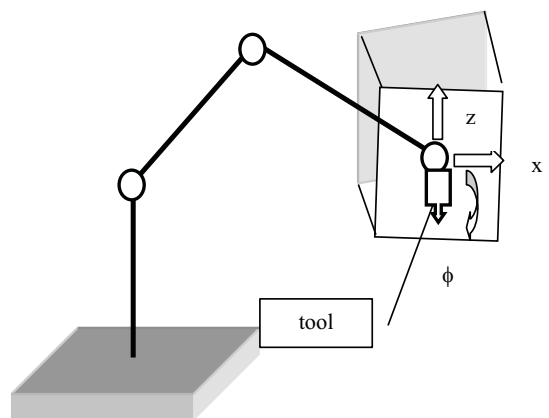


Fig. 4. IRb60 coordination of wrist move

3. Machining system solution

For to the IRb60 robot, according with kinematics constraints and the implemented control system, the concept of pixel image analysis and robot control system for surface machining were developed.

3.1. Pictures analysis

The essence of the applied control solutions relief treatment is use of image's scans due to the brightness level of pixels and the proper interpretation of these values on the axis z displacement scale. This enables to a 3D visualization of the analyzed image (Fig. 5). Modernized process was used for surface machining using robot. To avoid unnecessary operations in the radial transformation for the Cartesian system a hybrid Cartesian-radial robot system of image analysis was made (Fig. 6). This simplified the procedure for machining tool tracks correction in accordance with the local gray-level image by the trajectory consistent with the radial robot system.

Developing a machining procedure procured in three steps. In the first step analysis of the image, selection the area of picture for robot milling was made (Fig. 5). The second one determined the trajectory of tool movement in the horizontal plane in accordance with the selected machining area (Fig. 6). This meant the creation of grid tool movements with successively increasing arc radius of the robot head rotation. This data was saved in a G-Code. In the third stage after switching to the machining process the movement of the robot wrist was followed with tool in accordance with the established trajectory. The $x_i - y_i$ position in radial system was calculated (Fig. 7, Fig.8), which illustrates the visualization of the trajectory of the tool tip. The tool's "vertical" movements depend on the pixels brightness and the scale of the interpretation, adopted by gray shades. In the case of graphic black-and-white image obtained possessed two levels in height.

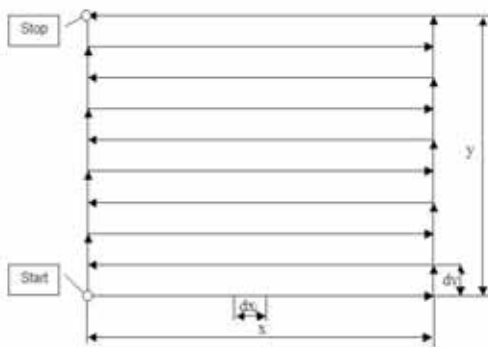


Fig. 5. Area of picture analyse

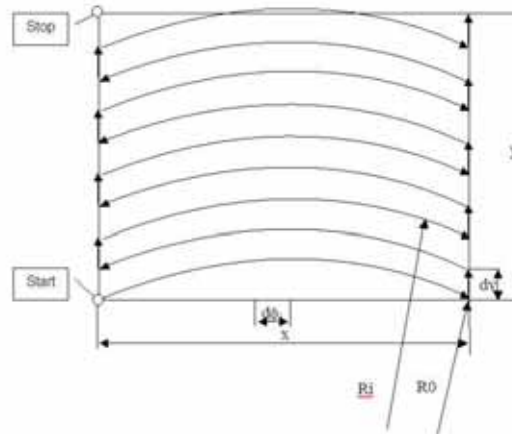


Fig. 6. Trajectory of picture pixels analyse

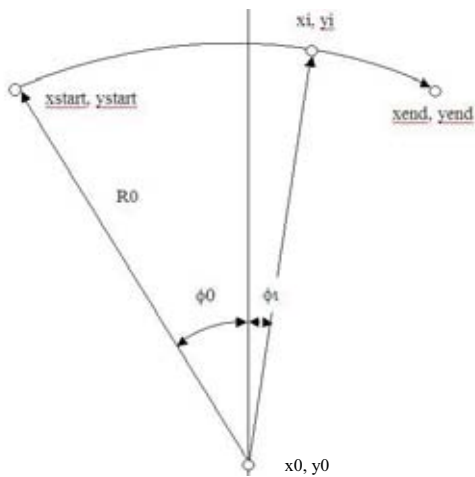


Fig. 7. Coordination of radial system

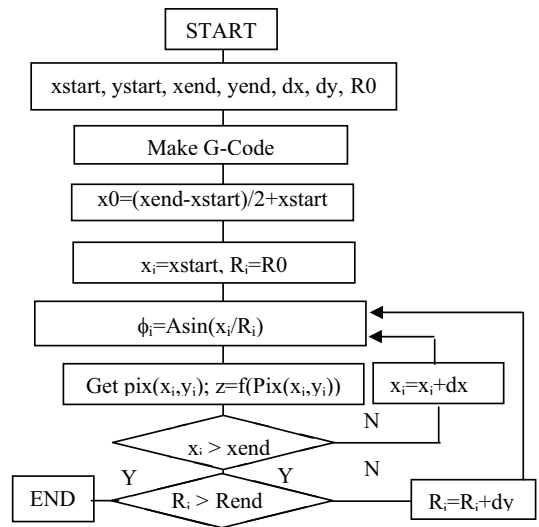


Fig. 8. Algorithm of radial system calculation

3.2. Machining control software

The ROBOART control software (fig. 9) was developed in VB6 environment, according to the approach presented.



Fig. 9. Main form of ROBOART software

The developed program includes a manual control panel for robot's movements. It can be used to bring the tool in machining zone. In addition, the program includes:

- a) USB camera panel,
- b) image analysis panel,
- c) visualization processing panel,
- d) trajectory code tool panel.

Selection of an area of image analysis (indicating the area of processing) is performed by two corner points of the image (corners: lower left and upper right). After entering the distance between the lines of the trajectory G-Code is generated (G-Code button) according to which stage of processing is done with on-line analysis of image pixels, by starting with NC run button. The results of this analysis are transferred to the robot. The trajectory of the robot commands are added to the vertical displacement imaging according to the generated file G-Code (fig. 9). Source images for the processing of the robot may be placed in a file or simultaneously obtained by using a USB camera.

4. Conclusions

Presented in the paper CAM system is a novel application of the working robot. By using the robot kinematics in accordance with the procedure significantly reduced, in compare with number of the BMP2CNC2 code orders. Because of direct control of the IRb60 robot via a PC control code has been reduced to a minimum. The G-Code analysis system is used to control the acquisition of information about the state of pixels in the image and also on-line used to control vertical machining tool movements.

The developed system is in a trial phase. An additional advantage of the system is able to directly obtain an image from a system connected by USB camera. It's important end expected to carry out tests according to the time-consuming processing of automatically generated programs.

5. Acknowledgements

We would like to especially thanks the students of Division of Production Engineering, the Faculty of Mechanical Engineering from University of Technology and Life Sciences (POLAND, Bydgoszcz). They participated in the old generation of IRb60 robot computer system control works and developments. This created the possibility to perform very progressive jobs [3-10].

References

- [1] Chen, Y. H., Hu, Y. N., *Implementation of a robot system for sculptured surface cutting. Part 1. Rough machining*. International Journal Advanced Manufacturing Technology, v. 15, pp. 624-629, 1999.
- [2] Hu, Y. N., Chen, Y. H., *Implementation of a robot system for sculptured surface cutting. Part 2. Finish machining*. International Journal Advanced Manufacturing Technology, v. 15, pp. 630-639, 1999.
- [3] Latoś, H., Mikołajczyk, T.: *Surface shaping with industrial robot*. 1st International Conference "Optimization of the Robots and Manipulators" OPTIROB-2006, Predeal, Romania, University "POLITEHNICA" of Bucharest, Faculty IMST, Department MSP, pp. 265-269, Romania, 2006.
- [4] Latoś, H., Mikołajczyk, T., *Virtual aid design of geometric and kinematics flexible tools*. XII Workshop on Supervising and Diagnostics of Machining Systems. Virtual Manufacturing, pp. 145-152, Karpacz, Poland, 2001.

- [5] Lewandowski, J., Mikołajczyk, T., *Rapid prototyping using robot*, 10th Int. Conf. Automation/Robotics in Theory and Practice, ROBTEP'2010, pp. 201-206, Slovakia, Bardejov, July 2010.
- [6] Mikołajczyk, T., *Manufacturing Using Robot*, Proceedings of 2010 Int. Conf. on Mech. Eng. Rob. and Aero. ICMERA'2010, pp. 26-35, IEEE. (printed Chengdu, China), Bucharest, Romania 2010.
- [7] Mikołajczyk, T., *Modernisation of IRb60 industrial robot steering system*. The 2nd edition of the international conference Optimization of the Robots and Manipulators, OPTIROB'2007, University "POLITEHNICA" of Bucharest, Faculty IMST, Department MSP, pp.149-152, Predeal, Romania 2007.
- [8] Mikołajczyk, T., *The robot machining system with surface shape active control*. The 2nd edition of the international conference Optimization of the Robots and Manipulators, OPTIROB'2007, University "POLITEHNICA" of Bucharest, Faculty IMST, Department MSP, pp. 205-209, Predeal, Romania 2007.
- [9] Mikołajczyk, T., *Robot application to surface finishing*, Journal of Polish CIMAC, Vol. 5, Nr 3, pp. 107-112, 2010.
- [10] Mikołajczyk, T., *Robot Turner*, 5th int. conf. Optimiz. of the Robots and Manip., OPTIROB'2010, Calimenesti, Romania, Univ. "POLITEHNICA" of Bucharest pp. 312-316, Romania, 2010.
- [11] www.artcam.com (access date: 27.02.2010).
- [12] www.bobcad.com/products/software/v24/art (access date: 27.02.2010).
- [13] www.8bitsoft.com/Windows/Graphic-Apps/CAD/bmp2cnc/ (access date: 27.02.2010).



THE INFLUENCE OF THE BUTT WELD ON FATIGUE LIFE

Stanisław MROZIŃSKI¹, Jarosław PEPLIŃSKI²

^{1,2} *University of Technology and Life Sciences in Bydgoszcz, Faculty of Mechanical Engineering, Al. Prof. S. Kaliskiego 7, 85-789 Bydgoszcz,
tel.: 48 52 340-82-64, fax: 48 52 340-82-71, e-mail: mrozinski.stanislaw@utp.edu.pl*

Abstract

In the paper there were presented tests results which were aimed at determination of the influence of the butt welds on fatigue life. Basing on the comparative analysis of the fatigue tests results of welded joints and specimens without butt welds it was found that fatigue life of the welded joint undergoing the mechanical working is comparable with the fatigue life of the homogeneous material. The Locati method used during the tests allows for the approximate determination of the fatigue limit.

Keywords: *welded joints, fatigue life of construction elements*

1. Introduction

The idea of construction element is inseparably associated with existence of various types of notches formed for designing reasons or occurring as a result of various technological operations including welding process. Because of that, joints are natural locations of fatigue cracks initiation which, when developing, may lead to serious failures or catastrophes [1].

Research work presented in this paper is a part of a research program carried out in the framework of doctoral dissertation. Its main aim is the fatigue life improvement of welded elements. In this work there were presented preliminary tests results, which aim to determine the influence of butt weld on static strength and fatigue life of welded joints.

2. Description of tests

Specimens used in the tests were made of 355J2+M steel according to standards [2] and [3]. They were cut out from two 180E channel irons joined with butt weld. The location on channel iron from where the specimens were cut out is shown in Fig. 1.

After specimens have been cut out they were subjected to mechanical treatment (milling and grinding). In order to define the influence of butt weld on static strength and fatigue life, specimens made of homogeneous material were also prepared (Fig. 1 – specimens without welds). Specimens without welds were given the same mechanical treatment as the samples with welds. Before fatigue and static tests the specimens with welds underwent the non-destructive tests.

Static tests were performed according to the standard [2]. They were performed on Instron 8501 strength machine. Specimens strains during static tests were measured with the use of extensometer of gauge length – 50 mm.

Because few specimens were accepted in the tests (3 specimens) and because of practical aim of the tests (quantitative valuation of the welds influence on fatigue life) they were performed with the use of preliminary Locati method [4, 5, 6].

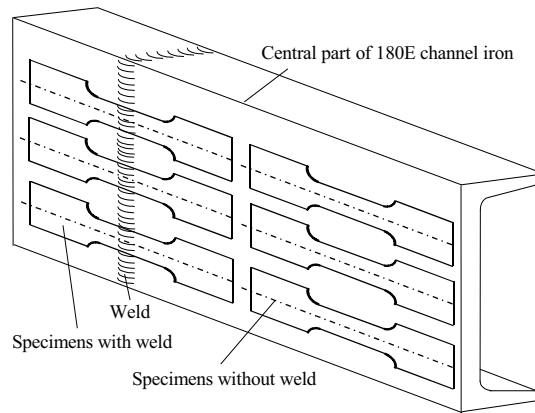


Fig 1. The location of specimens on channel iron

Locati method can be used when approximate data describing fatigue properties of given group of elements are already known, for example shafts, cog wheels, in the form of fatigue diagram equation described with the equation:

$$\log \sigma_a = a \cdot \log N + b \quad (1)$$

In Locati method a specimen is under gradually increasing loading (Fig. 2a).

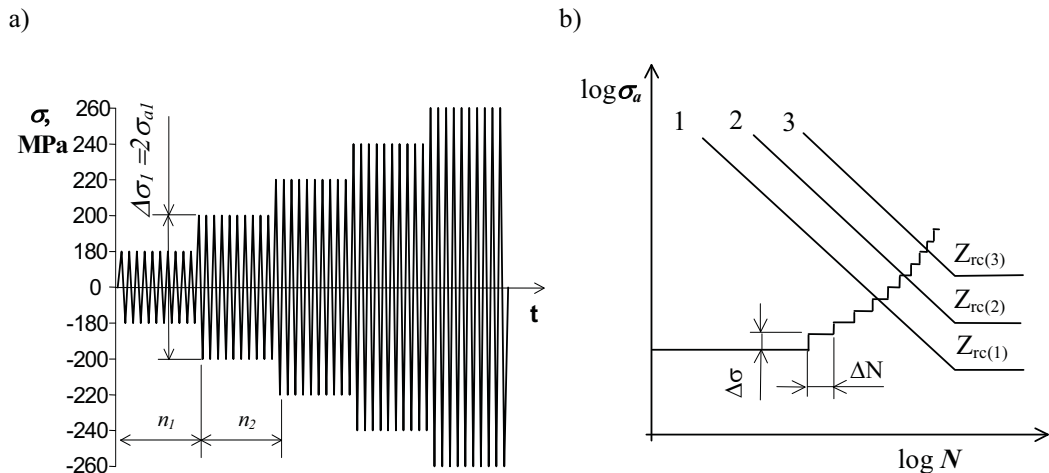


Fig 2. Model to define fatigue limit with the use of Locati method: a) loading program, b) interpretation of results

On each step the same number of loading cycles n_i is performed (in this test $n_i = 10^5$ cycles). The stress increase $\Delta\sigma$ depends on test conditions and volume of loading (in this test $\Delta\sigma = 20$ MPa). The stress level on the first step (σ_{a1}) should be lower than determined fatigue limit $Z_{rc(2)}$ (in this test $\sigma_{a1} = 180$ MPa). Final loading, however, for which the failure of the element takes place,

should be higher than upper fatigue limit $Z_{rc(3)}$. Loading frequency accepted during the test was equal 5 Hz. In fatigue limit calculations with the help of Locati method the Palmgren-Miner fatigue damage cumulation hypothesis is used [7, 8]. According to this hypothesis fatigue failure appears when:

$$\sum \frac{n_i}{N_i} = 1 \quad (2)$$

where:

n_i – number of loading cycles on stress level σ_{ai} ,

N_i – number of loading cycles until fatigue failure on stress level σ_{ai} .

In Fig. 2b there was presented graphical interpretation of Locati method. Fatigue curves 1, 2 i 3 (Fig. 2b) limit the area of dispersion of fatigue tests results from the bottom and top. This dispersion is most often unknown, so the curves, in such a case, will have approximated courses. The damage cumulations $\sum n_i/N_i$ are calculated after tests with the use of individual fatigue curves and performed loading programs. Mostly, none of the sums $\sum n_i/N_i$ equals 1,0. So for final determination of fatigue limit an auxiliary curve is produced for the interpolated determination of fatigue limit. Detailed description of Locati method can be found among others in the work [4].

3. Test results

3.1. Static tensile tests

The results sample of static tests are shown in Fig. 3 (curves of static tensile).

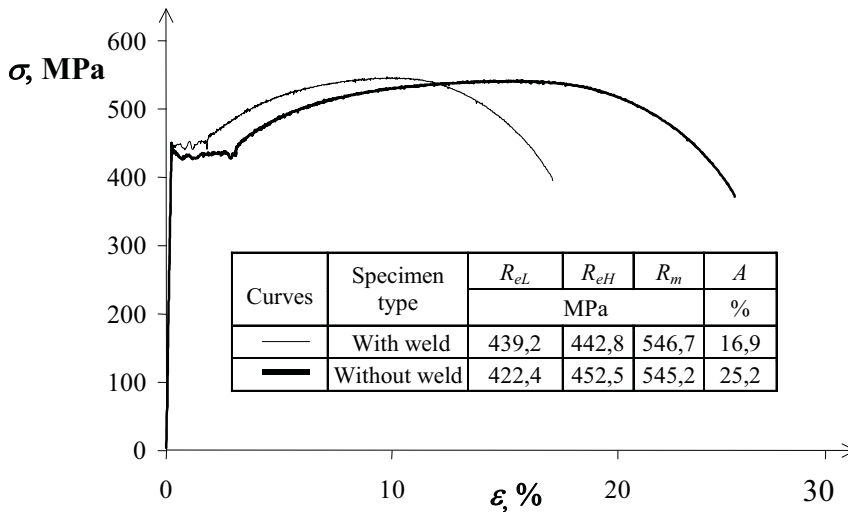


Fig. 3. The results of static tensile tests

As it was expected, during static tests no significant influence of butt weld on strength was observed (Fig. 3). On the basis of comparative analysis of strength parameters it can be stated that influence of weld is visible only as decreasing of the total elongation of the specimen until failure (A). Specimens with welds are characterised by smaller elongation (about 32%). In the case of the other parameters (R_m , R_{eH} , R_{eL}) weld had no significant impact on the results.

The cracking of all the examined specimens took place within the gauge length of

extensometer. As it was expected the cracking of the specimen with weld occurred always outside the welded area (Fig. 3). Detailed examination of the cracks did not show any defects or interferences. The shapes of damages of examined specimens are shown in Fig. 4 and 5.



Fig. 4. Shape of damage of specimen without welds



Fig. 5. Shape of damage of specimen with weld

3.2. Fatigue tests

Fatigue cracks of the specimens without welds occurred in the measuring area or in the place where measuring area turns into grapppling area. Fatigue cracks of the specimens with welds occurred in the area of thermal influence or in the place where measuring area turns into grapppling area. The location of cracks in specimens with welds (outside the welded area) is the proof of very high quality of welds. The shapes of cracks in both types of specimens are shown in Fig. 6.

Basing on the comparative analysis of the cracks which occurred in specimens with and without welds it can be stated that welds had no influence on the shape of damages. The above statement was proved by the results of comparative analysis of cyclic properties and fatigue life of the two types of specimens.

a)



b)



Fig 6. Shape of cracks in specimens with welds in the measuring part of the specimen

During analysis of the fatigue tests results, there were used momentary force and strain values of the specimen recorded for chosen loading cycles on succeeding levels of loading program. (Fig. 2a). In Fig. 7 there are shown an examples of one hysteresis loop which corresponds with the first loading cycle for each step of loading program.

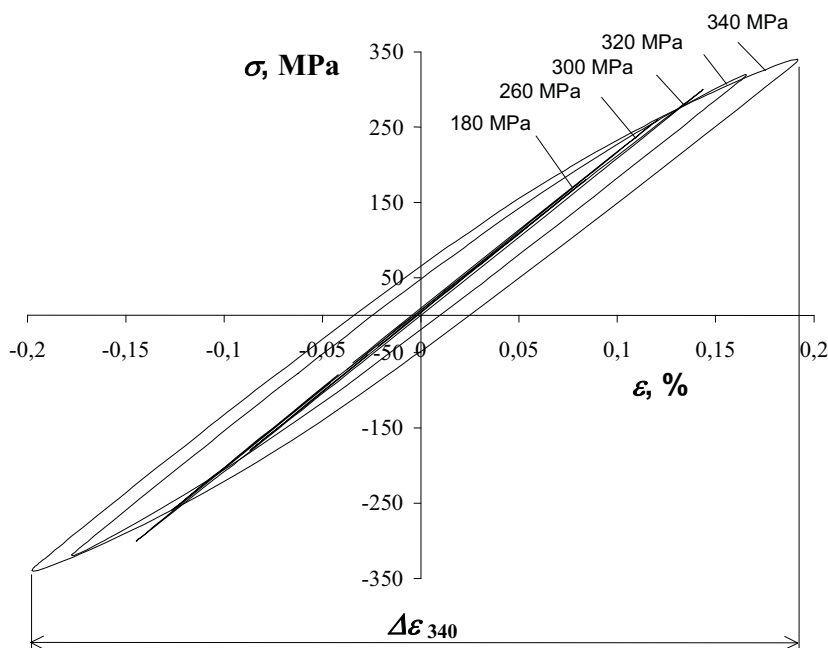


Fig. 7. Hysteresis loops recorded during tests (specimens without welds)

Basing on the analysis of the presented diagrams it can be stated that for the last three levels of stress ($\sigma_a=300, 320$ and 340 MPa) in the result of oscillatory loading there occurs stress - strain loop, which proves the presence of plastic strains on these stress levels. The above was observed both in samples with and without welds. On the basis of recorded loops it can be stated that although the level of stress was controlled, ($\sigma_a=\text{const}$) strain symmetry occurs on respective steps of loading program. Average strain values close to zero can be the proof of this. What is more, in spite of the stress controlling, no cyclic creeping of the material, which is often observed in such conditions, was observed.

In this paper there was carried out the comparative analysis of cyclic properties of the specimens with and without welds. During analysis the parameter of hysteresis loop (range of strain change $\Delta\varepsilon$) was used. Interpretation of this parameter was shown in Fig. 8 on the example of loops obtained for two stress levels ($\sigma_a=320$ and 340 MPa). In Fig. 8 there were shown changes in range of strain $\Delta\varepsilon$ in the function of the loading cycles number on succeeding stress levels obtained for both types of specimens.

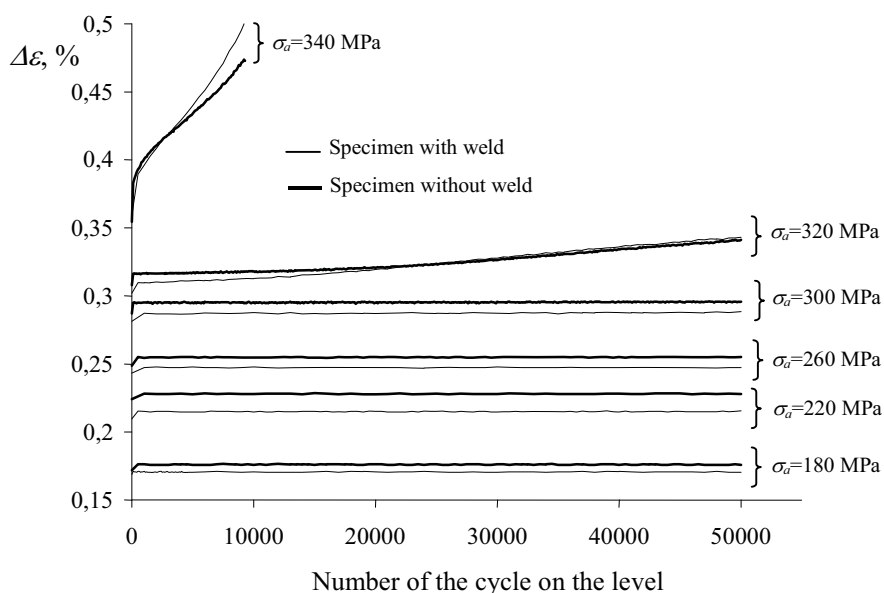


Fig. 8. Range of strain change $\Delta\varepsilon$ of the specimen in relation to the loading cycles number and stress level

Basing on the location of curves of the range of strain changes $\Delta\varepsilon$ it can be found that specimens with weld is characterised by smaller range of strain changes than the specimen without weld. However, those differences are very small and practically disappear on the highest performed levels of stress amplitude ($\sigma_a=320, 340$ MPa). On these levels significant increase of strain range is also observed.

Narrower strain range $\Delta\varepsilon$ on the individual loading levels of the specimens with weld can be explained by its diversified material properties in the area of measuring length (about 30 mm). The welding material (about 10 mm) is characterised by significantly higher strength parameters than strength parameters of joined elements. The above observation was verified in many works, among others, in the work [1]. Diversification of cyclic properties of the specimens with and without welds is illustrated by mutual location of diagrams in $\varepsilon - \sigma$ coordinates system (Fig. 9). These diagrams were obtained by joining coordinates describing the vertices of hysteresis loop on the succeeding levels of loading (Fig. 7).

Quantitative similarity of specimens strains which were recorded on different levels of loading was confirmed by fatigue life results. The specimens with and without welds cracked on similar stress levels. In Fig. 9 there were confronted results of total life N_c (Table in Fig. 9b) obtained for the specimens with and without welds.

The results of fatigue life obtained under gradually increasing loading were used for the fatigue limit calculations. Calculations were performed according to the description presented in point 2. In calculations, there was used the equation (1) of fatigue diagram obtained from the fatigue tests of the specimens made of 18G2A steel. During calculations of fatigue limit, the optimization procedure was accepted, which allows to find a parameter b (for which cumulative sum of damages in gradually increasing loading described by relation (2) is equal 1,0) when constant factor of fatigue curve a is given and base number of cycles N_g is assumed.

In the tests as a base cycles number of fatigue $N_g=10^7$ was accepted. Obtained results of fatigue limit calculations for specimens with and without weld are shown in Table 1.

Basing on the presented results it can be stated that both kinds of the specimen have similar fatigue limit Z_{rc} . It is equal accordingly: $Z_{rc}=212,4$ Mpa - for the specimen without weld and $Z_{rc}=218,6$ MPa- for the specimen with weld.

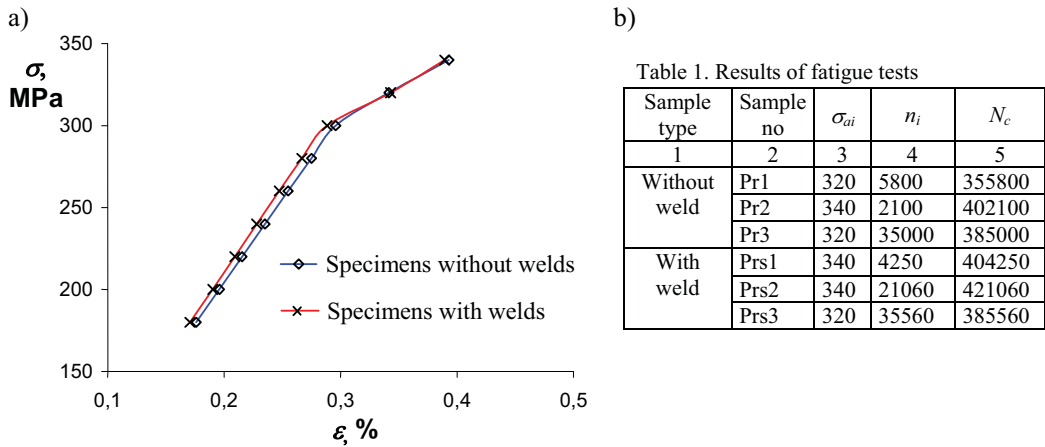


Fig. 9. The results of fatigue tests: a) loading program, b) results of fatigue life

The fatigue limit can be approximately estimated when temporary tensile strength of the material R_m is known. On the basis of analysis of many previous tests results it was found that fatigue limit Z_{rc} for standardized or thermally improved carbon steel and alloy steel is equal about $0,35R_m$ [9]. Basing on the results of static tests, which are shown in point 3.1, fatigue limit of specimens with and without welds was determined. Obtained calculations results are presented in Table 2 (column 5).

Table 2. Fatigue limits from tests and calculations

Type of specimen	Specimen marking	$Z_{rc} (Locati)$ MPa	R_m MPa	$Z_{rc}=0,35R_m$ MPa
1	2	3	4	5
Without weld	Sample PR1	205,3	546,7	191,3
	Sample PR2	218,1		
	Sample PR3	213,9		
	MEAN	212,4		
With weld	Sample PRS1	217,2	545,2	190,8
	Sample PRS2	224,5		
	Sample PRS3	214,1		
	MEAN	218,6		

Basing on the obtained results it can be stated that the fatigue limit determined with the use of static tensile test data is lower than fatigue limit defined with the use of Locati method.

4. Summary

Basing on the comparative analysis of fatigue tests results (shape of cracks and fatigue life) it can be stated that welds present in specimens have no significant influence on them.

The results obtained in the paper confirm the literature data which state that fatigue life of

welded joint when exposed to mechanical treatment is comparable with the fatigue life in specimens made of original material (without welds).

Accelerated methods of calculating the fatigue life (Locati method) and methods based on the static tests results allow to estimate roughly the fatigue limit.

References

- [1] Szala J., Boroński D., 2008. Ocena stanu zmęczenia materiału w diagnostyce maszyn i urządzeń, ITE-PIB Bydgoszcz-Radom.
- [2] PN-EN 10002-1:2004. Metale. Próba rozciągania. Metoda badania w temperaturze otoczenia.
- [3] PN-76/H-04326 Badania metali na zmęczenie. Próba osiowego rozciągania-ściskania przy stałym cyklu obciążeń zewnętrznych.
- [4] Buch A., 1964. Zagadnienia wytrzymałości zmęczeniowej, PWN, Warszawa 1964.
- [5] Badami M., Marino F., 2006. Fatigue tests of un – HIP'ed γ -TiAl engine valves for motorcycles, International Journal of Fatigue 28, 722-732.
- [6] La Rosa G., Risitano A., 2000. Thermographic methodology for rapid determination of fatigue limit of materials and mechanical components, International Journal of Fatigue 22, 65-73.
- [7] Palmgren A., 1924. Die Lebensdauer von Kugellagem. Verfahrenstechnik Berlin 68, 339-341.
- [8] Miner M.A., 1945. Cumulative Damage in Fatigue. Transactions of the American Society of Mechanicals Engineers, Journal of Applied Mechanics 67, 159-164.
- [9] Kocańda S., Szala J., 1991. Podstawy obliczeń zmęczeniowych, PWN, Warszawa.

The paper was elaborated on the base of the research studies BS-25/2009 under the title "Experimental tests methods for mechanical properties of materials and structures for designing and diagnosing technical objects"



SOFTENING OF MARTENSITIC CAST STEEL

Stanisław MROZIŃSKI¹, Radosław SKOCKI²

^{1,2} *University of Technology and Life Sciences in Bydgoszcz, Faculty of Mechanical Engineering, Al. Prof. S. Kaliskiego 7, 85-789 Bydgoszcz,
tel.: 48 52 340-82-64, fax: 48 52 340-82-71, e-mail: mrozinski.stanislaw@utp.edu.pl*

Abstract

In this paper there were presented test results of low cycle fatigue (LCF) behavior of martensitic cast steel under constant-amplitude loadings. Analysis of stabilization course was carried out by using two parameters of hysteresis loop. It was found that among physical quantities used in description of the fatigue process there was no one which would be insensitive to the changes of cyclic properties. Parameter, which was less sensitive to the changes of cyclic properties was plastic strain.

Keywords: cyclic properties, softening, fatigue life, martensitic cast steel

1. Introduction

The range of low cycle fatigue (LCF) in metals in comparison to the range of high cycle fatigue (HCF) basically differs in value of observed plastic strains during cyclic loadings. Cyclic plastic strains generate complex series of phenomena in a material which depend on many factors [1,2,6, 7,9]. Generally they are called fatigue changes. Various physical quantities, which are calculated and measured during cyclic loading, can be accepted for their description. The most important ones include such hysteresis loop parameters as ε_{ac} , ε_{ap} , ε_{ae} , σ_a , (Fig. 1)[8].

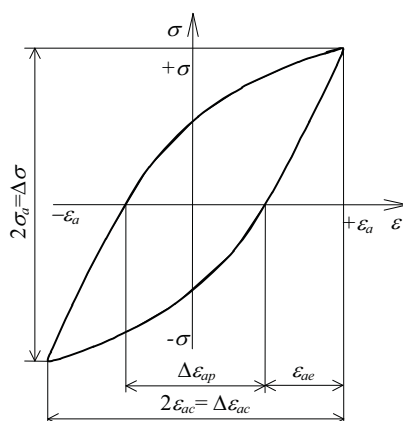


Fig. 1. Hysteresis loop with its basic parameters

Some of these parameters can be treated as criterial quantities which at present are employed in description of the fatigue process (strain, stress description) [3,4]. These descriptions are phenomenological and they are not directly connected with the real metal structure and physical character of occurring changes [5]. Observed relationships in various periods of fatigue life among hysteresis loop parameters and the number of loading cycles N are generally called cyclic properties and their values may change. When the cyclic properties changes, then this situation is called cyclic hardening or softening or when it is constant it is called cyclic stabilization. The research problem is both analytical description of the course of changes of cyclic properties during irregular or constant amplitude loadings and possibility to predict this course.

The main aim of this paper is the determination of the influence of strain level on the course of cyclic properties. The additional aim is an analytical description of changes of cyclic properties and also sensitivity of specific parameters of hysteresis loop to the changes of cyclic properties.

2. Description of tests

Specimens for the tests were made of GX12CrMoVNB9-1 martensitic cast steel. The shape and dimensions of the specimens were in agreement with the standard [8] (Fig. 2.).

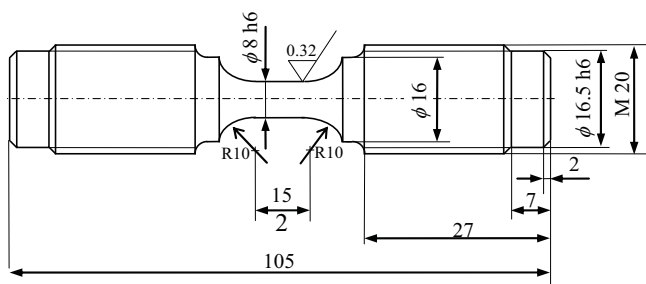


Fig. 2. Shape and dimensions of specimens used in tests

Fatigue tests were preceded by carrying out static tensile tests. The specimens used in the tests are shown in fig. 2. The specimens underwent increasing loading with the rate of machine piston displacement speed of 0.05 mm/s. Specimen's elongation was measured by a 12.5 mm gauge length axial extensometer with measuring range of 3.75 mm. The static tensile tests were carried out under temperature of 20°C. During these tests momentary loading forces and elongation of the specimen were recorded. After analyzing static tensile tests five levels of total strain ε_{ac} were accepted in low cycle tests according to table. 1.

Table 1. Parameters of loading programs

Course of loading	Parameters
	$\varepsilon_{ac1}=0.25\%$
	$\varepsilon_{ac2}=0.30\%$
	$\varepsilon_{ac3}=0.35\%$
	$\varepsilon_{ac4}=0.50\%$
	$\varepsilon_{ac5}=0.60\%$
	$f=0.2 \text{ Hz}$

LCF tests were conducted under controlled total strain $\varepsilon_{ac}=\text{const}$. The same procedure of measuring strain was employed for static tensile test. Test temperature of 20 °C and frequency of 0.2 Hz were employed. Accepted sampling frequency of force signal and strain signal allowed to describe loading cycles with set of 200 points. As the end criterion of the fatigue test, the

deformation of hysteresis loop (during semi cycle of compression) is accepted. During the tests momentary values of loading force and strain for selected loading cycles were recorded.

3. Test results

3.1. Static tensile tests

Static tensile tests results are shown in Fig. 3a – in stress σ - strain ε coordinate system. Stresses in the specimen under tensile loading were calculated as the ratio of momentary value of loading force per cross-sectional area before the specimen loading.

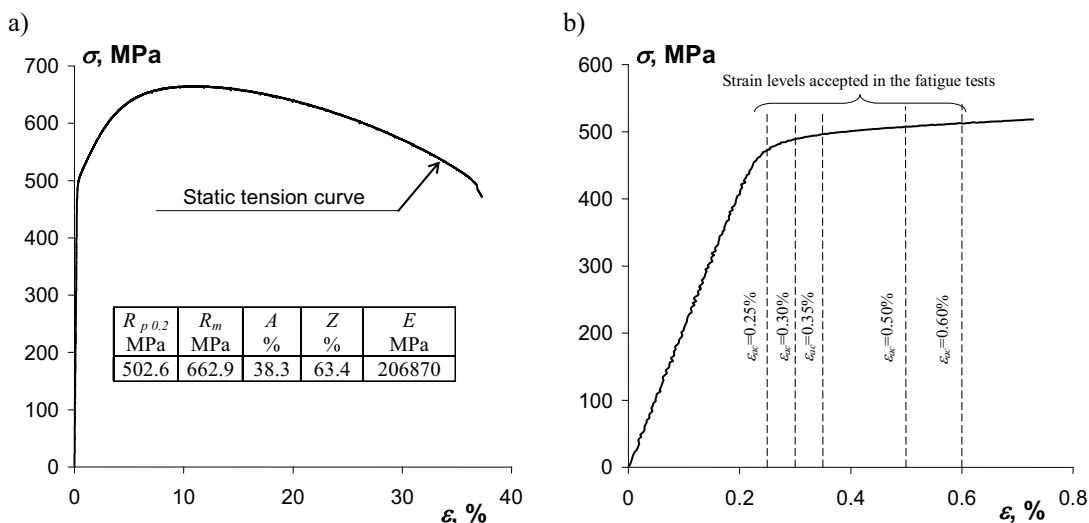


Fig. 3. Stress-strain curve: a) full plots, b) levels of total strain employed in LCF

Stress-strain curve was minutely investigated to determine basic strength parameters. The most important results are collected in table in Fig. 3a. Figure 3b illustrates a part of stress-strain curve which is bonded only to strain of 0.8%. Strain levels accepted in the fatigue tests were placed on this graph.

3.2. Fatigue tests

Analysis of cyclic properties of cast steel specimens was carried out with the use of hysteresis loop parameters (ε_{ap} and σ_a) which influence directly the test results (according to [8]). Momentary stress values σ in the specimen were calculated by dividing momentary value of loading force by cross-sectional area before the specimen was loaded.

During LCF changes of the basic hysteresis loop parameters were observed in the function of the number of cycles. The above is the proof of the changes of cyclic properties of tested material. In the result of the changes, the shape of hysteresis loop registered during various periods of fatigue life also changes. In order to illustrate this problem in Fig. 4 there were presented exemplary hysteresis loops which were obtained only for two levels of strain - the lowest

$\varepsilon_{ac}=0.25\%$ and the highest $\varepsilon_{ac}=0.60\%$ in various periods of the fatigue life. The numbers of cycles corresponding to the presented loops are placed on the diagram.

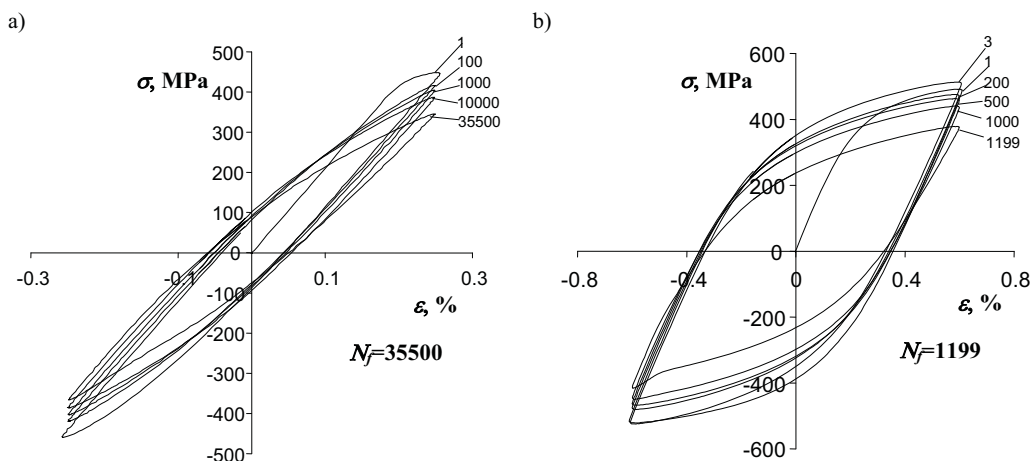


Fig. 4. Hysteresis loops obtained for two levels of total strain and during various periods of fatigue life:
a) $\varepsilon_{ac}=0.25\%$, b) $\varepsilon_{ac}=0.60\%$

Basing on the presented hysteresis loops it can be stated that on both levels of strain changes of the loops are noticeable with increasing of the number of cycles. Stress amplitude decreases and plastic strain amplitude increases with increasing of the number of cycles. In Fig. 5. there are presented the courses of stress amplitude σ_a and plastic strain amplitude ε_{ap} in the function of the number of loading cycles obtained for all implemented levels of total strain ε_{ac} .

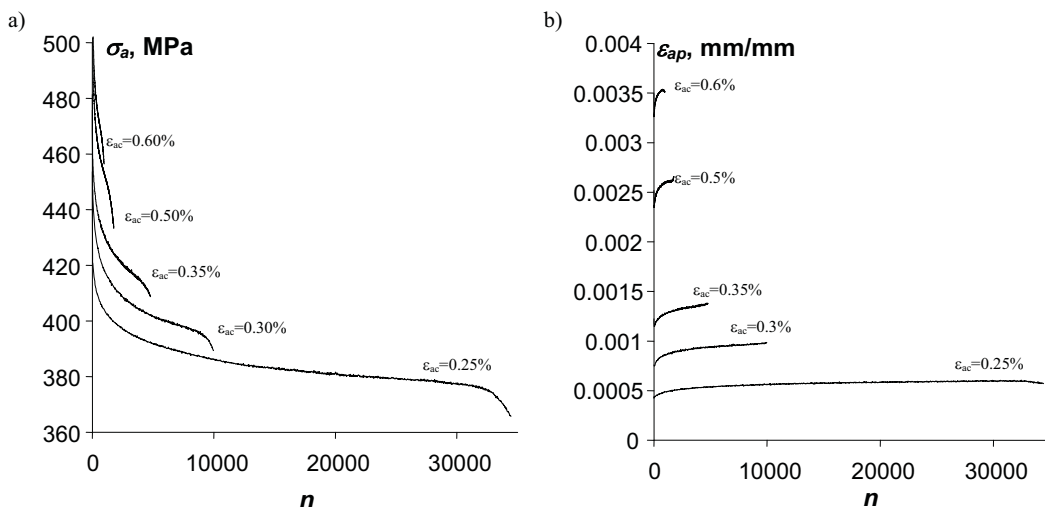


Fig. 5. Changes of hysteresis loop parameters for five levels of strain: a) $\sigma_a=f(n)$, b) $\varepsilon_{ap}=f(n)$

Basing on the obtained results it can be stated that momentary values of the loop parameters (σ_a and ε_{ap}) depend on fatigue damage degree (the number of cycles) and total strain level ε_{ac} . In order to illustrate course of changes of cyclic properties and to discuss characteristic stages accompanying the fatigue process in Fig. 6 there were shown example diagrams of changes of loop parameters (σ_a and ε_{ap}) for the highest level of total strain ($\varepsilon_{ac}=0.60\%$).

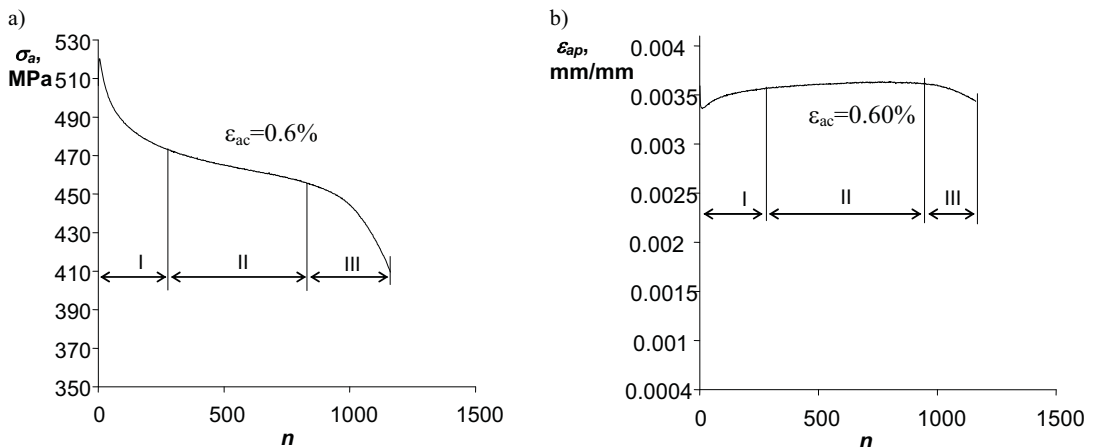


Fig. 6. Changes of hysteresis loop parameters for total strain level of $\varepsilon_{ac}=0.6\%$: a) $\sigma_a=f(n)$, b) $\varepsilon_{ap}=f(n)$

Basing on the analysis of diagrams (Fig. 5-6) it can be stated that independently on the level of total strain in the course of changes of the hysteresis loop parameters, three distinctive stages can be drawn:

- Stage I – cast steel clearly softens. Characteristic feature of this stage is high speed of softening which decreases with increase of the number of cycles. Length of this stage depends on the level of strain and equals from 5 % of all cycles N_f until failure on the level of $\varepsilon_{ac}=0.25\%$ to about 25% of all cycles on the level of $\varepsilon_{ac}=0.60\%$.
- Stage II – hysteresis loop parameters change insignificantly. Softening speed is constant. Length of this stage covers about 50% of all cycles until failure on the level of $\varepsilon_{ac}=0.60\%$ and about 90% of all cycles on the level of $\varepsilon_{ac}=0.25\%$
- Stage III – cast steel undergoes further significant softening, the speed of which increases. Crack initiation takes place here and eventually leads to fatigue failure. The length of this stage depends also on total strain level with the range from a few percent (for $\varepsilon_{ac}=0.60\%$) to 15% (for $\varepsilon_{ac}=0.25\%$) of all cycles until failure.

The characteristic stages of changes of cyclic properties of the martensitic cast steel can be observed both on the diagrams which depict changes of stress amplitude $\sigma_a=f(n)$ and diagrams of plastic strain changes $\varepsilon_{ap}=f(n)$. Independently on the total strain level, the stage II is always the longest stage.

An attempt was made of analytical description of changes of the hysteresis loop parameters for the stage II in the function of the number of loading cycles. Description was made in semi logarithmic coordinate system with the use of the following equations:

$$\sigma_a = a \cdot \log N + b \quad \text{- for stress } \sigma_a \quad (1)$$

$$\varepsilon_{ap} = a \cdot \log N + b \quad \text{- for strain } \varepsilon_{ap} \quad (2)$$

In Fig. 7 there are shown diagrams of the stress and the strain in the semilogarithmic coordinate system (semi-log plots $\log N - \sigma_a$ in Fig. 7a and $\log N - \varepsilon_{ap}$ in Fig. 7b) in the function of the number of cycles. The tables of slope values are also presented here.

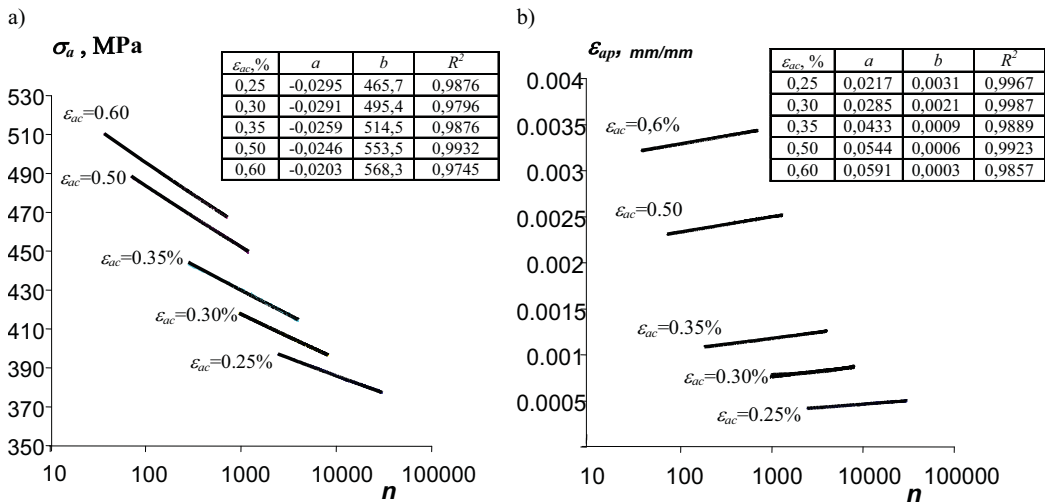


Fig. 7. Changes of hysteresis loop parameters during II stage of fatigue life: a) $\sigma_a = f(n)$, b) $\varepsilon_{ap} = f(n)$

Basing on the presented diagrams it can be stated that during stage II of fatigue process, changes of cyclic parameters can be approximated by power function. Confirmation of this fact are high values of coefficient of determination R^2 . Moreover it can be stated that both parameters (ε_{ap} and σ_a) were constantly changing without visible stabilization period. Magnitude of changes of the hysteresis loop parameters depends on the total strain level. For the σ_a stress the most significant changes take place for the lowest total strain levels whereas for the plastic strain ε_{ap} the most significant changes are visible for the highest total strain levels. Changes of slope values in the function of total strain level ε_{ac} are shown in Fig. 8.

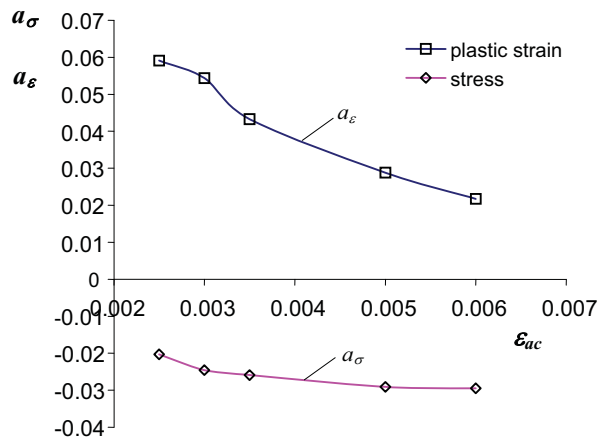


Fig. 8. Slopes of the regression line describing hysteresis loop parameters according to the level of total strain

The comparative analysis of the slopes values allows for a statement that among assumed hysteresis loop parameters changes in the function of the number of loading cycles are lower in the case of the stress amplitude σ_a for all accepted strain levels. Obtained results have very essential practical meaning. This is so because they confirm validity of conducting LCF tests under both controlled total strain ($\varepsilon_{ac}=\text{const}$) and stress ($\sigma_a=\text{const}$).

4. Conclusions

1. Martensitic cast steel is a material, which significantly softens during LCF tests. Process of softening is visible on all strain levels.
2. Course of the softening process can be divided into three characteristic stages with different speed of softening. Independently on the total strain level there always occurs the stage where the softening speed is constant. In this stage changes of the hysteresis loop parameters (σ_a and ε_{ap}) can be described by a power function.
3. Among hysteresis loop parameters, the one which is less sensitive to changes of cyclic properties of cast steel is the stress amplitude.
4. Lack of cyclic stabilization of the cast steel in the strain and stress approach demonstrates the need to search for other hysteresis loop parameters which would be insensitive to the changes of the cyclic properties. For example such a parameter is plastic strain energy described by the area of hysteresis loop. This parameter takes into account mutual interactions between stress and strain, therefore energy description is being accepted as more relevant than stress and strain description.
5. Conducted tests of the cast steel softening included only constant-amplitude loadings. In order to generalize formulated conclusions it is necessary to verify observations under irregular loadings.

References

- [1] Chakraborti, P.C.; Mitra, M.K., 2005. Room temperature low cycle fatigue behaviour of two high strength lamellar duplex ferrite–martensite (DFM) steels. *International Journal of Fatigue* Volume: 27, Issue: 5, 511-518
- [2] Collins J.A., 1993. *Failure of Materials in Mechanical Design, Analysis, Prediction, Prevention*. John Wiley & Sons, New York.
- [3] Kocańda S., Kocańda A., 1989. *Niskocyklowa wytrzymałość zmęczeniowa metali*. PWN Warszawa.
- [4] Manson S.S., Halford G.R., 1986. Re-Examination of Cumulative Fatigue Damage Analysis – an Engineering Perspective. *Engineering Fracture Mechanics* 25(5/6), 539-571.
- [5] Mroziński S., 2008. Stabilizacja własności cyklicznych metali i jej wpływ na trwałość zmęczeniową. *Wydawnictwo Uczelniane Uniwersytetu Technologiczno-Przyrodniczego w Bydgoszczy*, Rozprawy Nr 128.
- [6] Mughrabi, Hael; Höppel, Heinz Werner, 2010. Cyclic deformation and fatigue properties of very fine-grained metals and alloys. *International Journal of Fatigue* Volume: 32, Issue: 9, 1413-1427
- [7] Plumtree, A.; Abdel-Raouf, H.A., 2001. Cyclic stress–strain response and substructure. *International Journal of Fatigue* Volume: 23, Issue: 9, 799-805
- [8] PN-84/H-04334 *Badania niskocyklowego zmęczenia metali*.
- [9] Xianjie Yang, 2005. Low cycle fatigue and cyclic stress ratcheting failure behavior of carbon steel 45 under uniaxial cyclic loading. *International Journal of Fatigue* Volume: 27, Issue: 9, 1124-1132

The paper was elaborated on the base of the research studies BS-25/2009 under the title “Experimental tests methods for mechanical properties of materials and structures for designing and diagnosing technical objects”



ELECTRODE VIBRATIONS SYNCHRONIZATION IN ELECTROCHEMICAL MACHINING

Tomasz Paczkowski

University of Technology and Life Sciences in Bydgoszcz
Faculty of Mechanical Engineering
al. Prof. S. Kaliskiego 7, 85-789 Bydgoszcz, Poland
tel.: +48 52 340-87-47, fax: +48 52 340-82-45
tel. 52 340-87-47
e-mail: tompacz@utp.edu.pl

Abstract

The article deals with a theoretical analysis of electrochemical machining using a tool electrode with curvilinear profile, vibrating into two directions.

Physical phenomena occurring within the interelectrode gap have been described by a partial differential equations resulting from the balance of mass, momentum and energy of the electrolyte flowing through the gap.

Equations formulated in the paper which describe the work-piece surface shape evolution and the electrolyte flow (mixture of fluid and gas) through the gap, were simplified by means of assumptions concerning the flow, distribution of the volume fracture, and the gap thickness. Then, they were solved, in part analytically, and in part numerically. Calculations were performed for the assumed machining parameters, with presentation of the calculation results in the sections across and along the interelectrode gap.

In the charts, the electrolyte longitudinal and transverse flow rate distributions, pressure, temperature distributions and distributions of chosen physical quantities of the electrochemical machining are demonstrated for the considered case of electrode vibrations synchronization.

Keywords: ECM machining, computer simulation, oscillating electrode

1. Introduction

Current pace of development and market demands motivate people to introduce innovations and improve already existing products. This, in turn, results in creation of specialist modules and independent modelers for the design of objects based on free curvilinear surfaces modeling, e.g. of NURBUS type. Representation of NURBUS is the most universal representation form for curvilinear surfaces and surfaces for all applications in the field of CAD-CAM or computer graphic [4]. Mathematical description of these surfaces is quite complicated due to their being curvilinear which makes it difficult to model the processes occurring during ECM.

Apart from the electrode geometry determination, the choice of the electrolyte composition and the machining parameters is of great importance for the design of a technological machining process with the use of a curvilinear tool electrode.

During the constant process, the electrode usually performs translation in the direction of the machined surface. The electrolyte is supplied with relatively high velocity to the interelectrode gap causing that dissolution products are carried away from the interelectrode space.

Hydrodynamic parameters of the flow and properties of the medium determine the processes of mass, momentum and energy exchange within the interelectrode gap. Properly chosen, they prevent from formation of cavitation zones, critical flow, circulation, excessive rise of the electrolyte temperature and volume fracture [1,2]. The listed above processes are closely related to each other and they largely affect the shape and applicability of the machined surface [6,10,11].

Due to the machining accuracy the process should be performed with possibly small thickness of the interelectrode gap. With the use of constant current, decreasing the gap thickness is connected with the increase of volume fracture in the electrolyte and its temperature. Use of gaps smaller than 0,1mm is limited by possibilities of dissolution product removal from the machining area [9]. Introduction of the electrode tool vibrations results in changes of the interelectrode gap thickness during the process of machining which, with a minimal gap, allows for improvement of the machining accuracy. Whereas, with a maximum gap, there are created good conditions for the electrolyte exchange. The electrode vibrations induced into two directions improve the machining accuracy in all the directions normal for curvilinear surfaces. The electrode vibrations synchronization additionally influences the process conditions.

For the purpose of appropriate choice of the process parameters and determination of the electrode geometry, mathematical modeling of phenomena occurring within the interelectrode gap is indispensable.

2. Mathematical modeling of the process

The purpose of modeling is a mathematical description of ECM process, which allows us to determine:

- the connection of the shape of the tool electrode (TE) and work piece (WP),
- the conditions in the inter-electrode gap (IEG),
- basic characteristics of the ECM process for vibrating electrodes.

For the considered curvilinear surfaces of the electrodes a superposition method of the obtained equations describing the two-dimensional electrolyte and hydrogen flow was used. The flow was considered in the local xy -system determined by the vector normal to the work electrode surface. The calculations were made for the consecutive xy surfaces defined along the Z -axis (Fig. 1). The coordinate systems were connected to the anode.

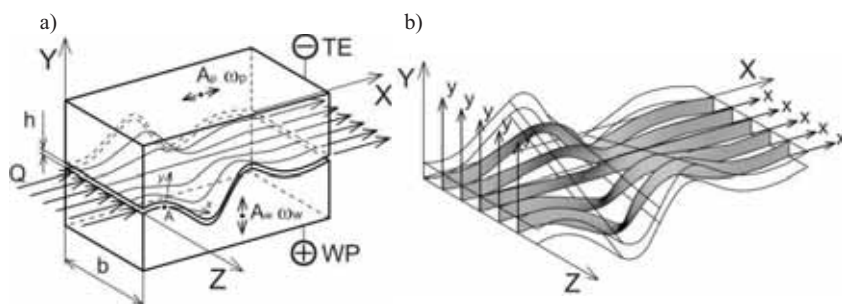


Fig. 1. Area flow of electrolyte in interelectrode gap: a) the shape of the electrodes, b) local coordinate system xy

The system of equations describing two-dimensional flow of the electrolyte and hydrogen through the interelectrode gap results from the principles of mass and momentum preservation [3].

Having introduced the following denotations:

- electrolyte flow is stable, two dimensional, homogenous,
- pressures $p_e = p_H = p$,
- volume fracture $\beta = \beta(x)$,
- the gap thickness is small compared to the interelectrode gap length ($h \ll L$),
- IEG power supplying with a constant volume flow of $Q = \text{const}$ electrolyte.

The equation system of the compound motion in the local orthogonal system of coordinates x, y connected with the anode (Fig. 1) is as follows:

$$\frac{\partial(\rho_e v_x)}{\partial x} + \frac{\partial(\rho_e v_y)}{\partial y} = 0 \quad (1)$$

$$\frac{\partial(\rho_H v_x)}{\partial x} + \frac{\partial(\rho_H v_y)}{\partial y} = j \eta_H k_H h^{-1} \quad (2)$$

$$\rho_e \left(\frac{\partial v_x}{\partial t} + v_x \frac{\partial v_x}{\partial x} + v_y \frac{\partial v_x}{\partial y} \right) = - \frac{\partial p}{\partial x} + \mu_e \left(\frac{\partial^2 v_x}{\partial y^2} \right) \quad (3)$$

$$v_x \frac{\partial T}{\partial x} + v_y \frac{\partial T}{\partial y} = \frac{\partial}{\partial x} \left((a + a_T) \frac{\partial T}{\partial x} \right) + \frac{j^2}{\rho_e c_p \kappa} \quad (4)$$

- where:
- η_H – current efficiency of gas emission,
 - h – the inter-electrode gap height,
 - k_H – hydrogen electrochemical equivalent,
 - μ_e – the electrolyte dynamic viscosity,
 - a, a_T – thermal diffusivity coefficient in laminar and turbulent motion [7,8],
 - ρ_e, ρ_H – density of the electrolyte, hydrogen,
 - c_p – specific heat of the electrolyte,
 - κ – electrolyte conductivity.

Equations (1-4) should satisfy the following boundary conditions for:

- flow rate

$$v_x, v_y = 0 \quad \text{for} \quad y = 0,$$

$$v_x = A_p \omega_p \cos \omega_p t \quad v_y = \frac{\partial h}{\partial t} \quad \text{for} \quad y = h,$$
- pressure

$$p = p_z \quad \text{for} \quad x = x_z,$$
- temperature:
 - on the walls: $T = T_s \quad \text{for} \quad x \geq x_w \quad i \quad y = 0 \quad \text{and} \quad y = h$
 - on the inlet $T = T_w$
 where: x_z – coordinate of the interelectrode gap end,
 T_s – temperature of electrodes, T_w – temperature on the inlet.

2.1. Motion equation integrals

Having introduced dimensionless quantities defined by formulas:

$$\tilde{x} = \frac{x}{L_o}, \quad \tilde{y} = \frac{y}{h_o},$$

$$\tilde{v}_x = \frac{v_x}{v_o}, \quad \tilde{v}_y = \frac{v_y R_o}{v_o h_o}, \quad \tilde{p} = \frac{p h_o}{\mu_e v_o L_o}$$

motion equations, describing flow of the electrolyte and oxygen compound, can be presented in the form:

$$\lambda \left(\bar{v}_x \frac{\partial \bar{v}_x}{\partial \bar{x}} + \bar{v}_y \frac{\partial \bar{v}_x}{\partial \bar{y}} \right) = - \frac{\partial \bar{p}}{\partial \bar{x}} + \frac{\partial^2 \bar{v}_x}{\partial \bar{y}^2} \quad (5)$$

$$\frac{\partial \bar{p}}{\partial \bar{y}} = 0 \quad (6)$$

Quantities denoted by index ‘zero’, are mean quantities within the considered flow area, $\lambda = Re \frac{h_0}{L_0}$ - Reynold’s modified number.

In motion equation (5) Reynold’s modified number is the system small parameter. Thus, its solution can be found in the form of a power series in relation to λ in the form:

$$v_x = \sum_{i=0}^{\infty} \lambda^i v_x^i, \quad v_y = \sum_{i=0}^{\infty} \lambda^i v_y^i, \quad p = \sum_{i=0}^{\infty} \lambda^i p^i \quad (7)$$

Substituting series (7) into equation motion (5), and the flow continuity equations (1), ordering and grouping expressions in relation to the same powers λ , for linear approximation in a dimensional form, the following sequence of equations can be obtained:

$$\frac{\partial(\rho_e v_x^0)}{\partial x} + \frac{\partial(\rho_e v_y^0)}{\partial y} = 0 \quad (8)$$

$$\frac{\partial(\rho_H v_x^0)}{\partial x} + \frac{\partial(\rho_H v_y^0)}{\partial y} = j \eta_H k_H h^{-1} \quad (9)$$

$$0 = - \frac{\partial p^0}{\partial x} + \mu_e \frac{\partial^2 v_x^0}{\partial y^2} \quad (10)$$

$$\frac{\partial(\rho_e v_x^I)}{\partial x} + \frac{\partial(\rho_e v_y^I)}{\partial y} = 0 \quad (11)$$

$$\rho_e \left(v_x^0 \frac{\partial v_x^0}{\partial x} + v_y^0 \frac{\partial v_x^0}{\partial y} \right) = - \frac{\partial p^I}{\partial x} + \mu_e \frac{\partial^2 v_x^I}{\partial y^2} \quad (12)$$

Boundary conditions are now in the form:

$$\begin{aligned} v_x^0 &= 0, \quad v_y^0 = 0, \\ v_x^I &= 0, \quad v_y^I = 0, \quad \text{for } y = 0 \end{aligned} \quad (13)$$

$$v_x^0 = A_p \omega_p \cos \omega_p t, \quad v_y^0 = \frac{\partial h}{\partial t},$$

$$v_x^I = 0, \quad v_y^I = 0, \quad \text{for } y = h$$

$$p^0 = p_z \quad p^I = 0 \quad \text{for } x = x_z \quad (14)$$

Having solved the obtained sequences of equations (8 ÷ 12), and using boundary conditions (19) and (20), we obtain the field of velocity and pressure, respectively:

$$v_x = \frac{6Q}{h^3} (hy - y^2) - \frac{13}{70} \frac{\rho_e}{\mu_e} \frac{QV}{h^2} (hy - y^2) + \frac{1}{10} \frac{\rho_e}{\mu_e} \frac{QV}{h^5} (21hy^5 - 12y^6 - 10h^2y^4 + h^5y) \quad (15)$$

$$\begin{aligned} v_y &= \frac{V}{h^3} (3hy^2 - 2y^3) - \frac{1}{\rho_e} \frac{\partial}{\partial x} \frac{\rho_e^2}{\mu_e} \left[\frac{13}{420} (2y^3 - hy^2) - \frac{1}{2100} (420h^2y^5 - 735hy^6 + 360y^7 - \right. \\ &\quad \left. 110h^5y^2) \right] \end{aligned} \quad (16)$$

$$p = \frac{12\mu Q}{h^3}(x - x_z) + \frac{13}{35} \frac{\rho_s Q V}{h^2}(x - x_z) \quad (17)$$

In order to account for a turbulent flow through the interelectrode gap, in an orthogonal coordinate system, dependencies describing distributions of the rate, have been accepted:

$$v_x = v_{xmax} \left[1 - \left| \frac{h-2y}{h} \right| \right]^{\frac{1}{n}} \quad (18)$$

$$v_y = V \left(\frac{2y}{h} \right)^{\frac{n+1}{n}} \quad (19)$$

where: $v_{xmax} = \frac{n+1}{n} \frac{Q}{bh}$ maximum longitudinal flow rate in the cracks cross-section when the Q volume flow is represented by $\left[\frac{m^3}{s} \right]$

Values of Reynold's number Re , for which there occurs transition from laminar into turbulent flow ($Re_{kr} = 2500$) [3], can be determined from the formula:

$$Re = \frac{v_{sr} 4r_h}{\nu}, r_h = \frac{bh}{2(b+h)}, v_{sr} = \frac{Q}{hb}, \nu = \nu_s (1 + 2.5\beta) \beta \ll 1.$$

Distribution of volume fracture β is determined from the balance of hydrogen mass, produced on the cathode:

$$\frac{\partial}{\partial x} \left(\frac{p}{T} \beta \right) = \frac{\eta_H k_H R}{\mu_H Q} j \quad (20)$$

where:

- $\rho_{Ho} = \frac{\mu_H p}{RT}$ – hydrogen density,
- R – gas constant,
- μ_H – dynamic hydrogen viscosity.

2.2. Equation of the shape evolution

Equation of the surface electrochemical dissolution in the direction of Y axis of the XYZ -system related to the anode for the considered case, is defined by dependence [5]:

$$\frac{\partial Y_A}{\partial t} = k_v \kappa_0 \Phi_{TG}^{-1} \frac{U - E}{h} \sqrt{1 + \left(\frac{\partial Y_A}{\partial X} \right)^2 + \left(\frac{\partial Y_A}{\partial Z} \right)^2} \quad (29)$$

$$\Phi_{TG} = \frac{1}{h} \left[\int_0^h \frac{dy}{(1 + \alpha_T (T - T_0))(1 - \beta)^{\frac{1}{2}}} \right] \quad (30)$$

where:

- k_v – electrochemical machinability coefficient,
- α_T – temperature coefficient of electrical conductivity,
- κ_0 – the medium conductivity.

2. Numerical model

Determination of the machined surface shape evolution Has been described by equation (29) defining the real change of the machined surface shape.

The machined surface initial shape and the tool electrode were defined in 3D CAD program as free surfaces of NURBUS type.

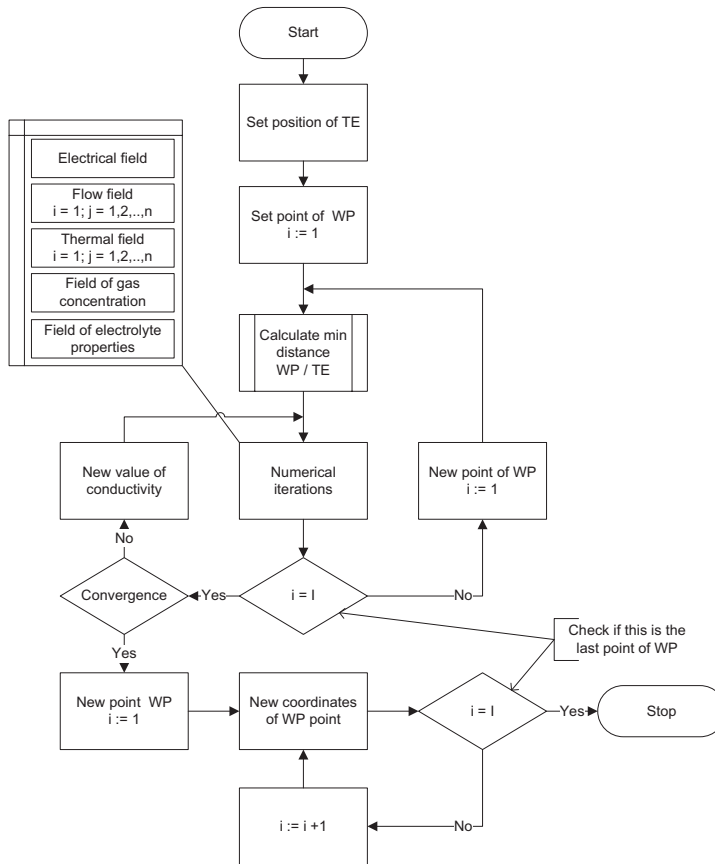
For numerical calculations, discretion of MS and TE was made through the surface approximation by curves. In this way, a set of curve pairs TE_k , MS_k was obtained which next were described by points, in a global coordinate system, with assigned accuracy (Fig. 2).

$$x_i = \sum_{i=1}^i \Delta x_i \quad (31)$$

where: $i = 0, 1, 2 \dots I$

After having performed discretion of TE and WP surfaces, the work piece shape evolution equation was solved with the use of successive approximation method, applying the method of time steps according to the algorithm (Fig. 2a).

a)



b)

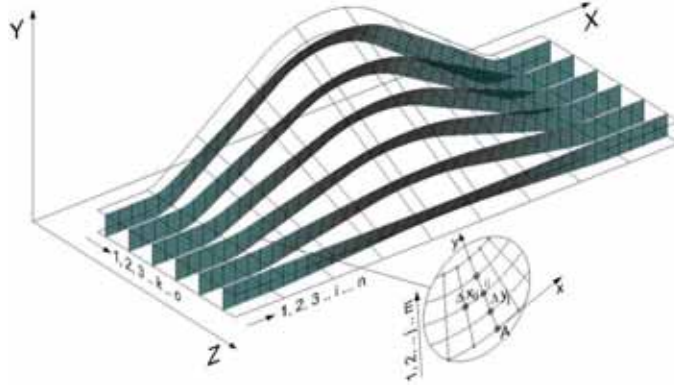


Fig. 2. ECM numerical model: a) algorithm for solving equations describing the process (i - current and last points of WP describing curve), b) IEG digitization

Time t has been presented by means of a set of points:

$$t_k = t_0 + k \Delta t \quad (32)$$

where: $k = 0, 1, 2, \dots, K$

The sequence of calculations is carried out here with the gap thickness distribution, “frozen” for a given time step.

In case of shape surfaces calculating the minimal WP and TE distances is a complex process. It's caused by the fact that analysis of a given WP point should be conducted accordingly with the TE points that are in the vicinity with the considered point, in all possible directions of 3D plane. To optimize the calculations a matrix of all points laying on TE over the considered WP point is created (Fig. 3). A sequence of these actions is shown on a diagram (Fig. 3).

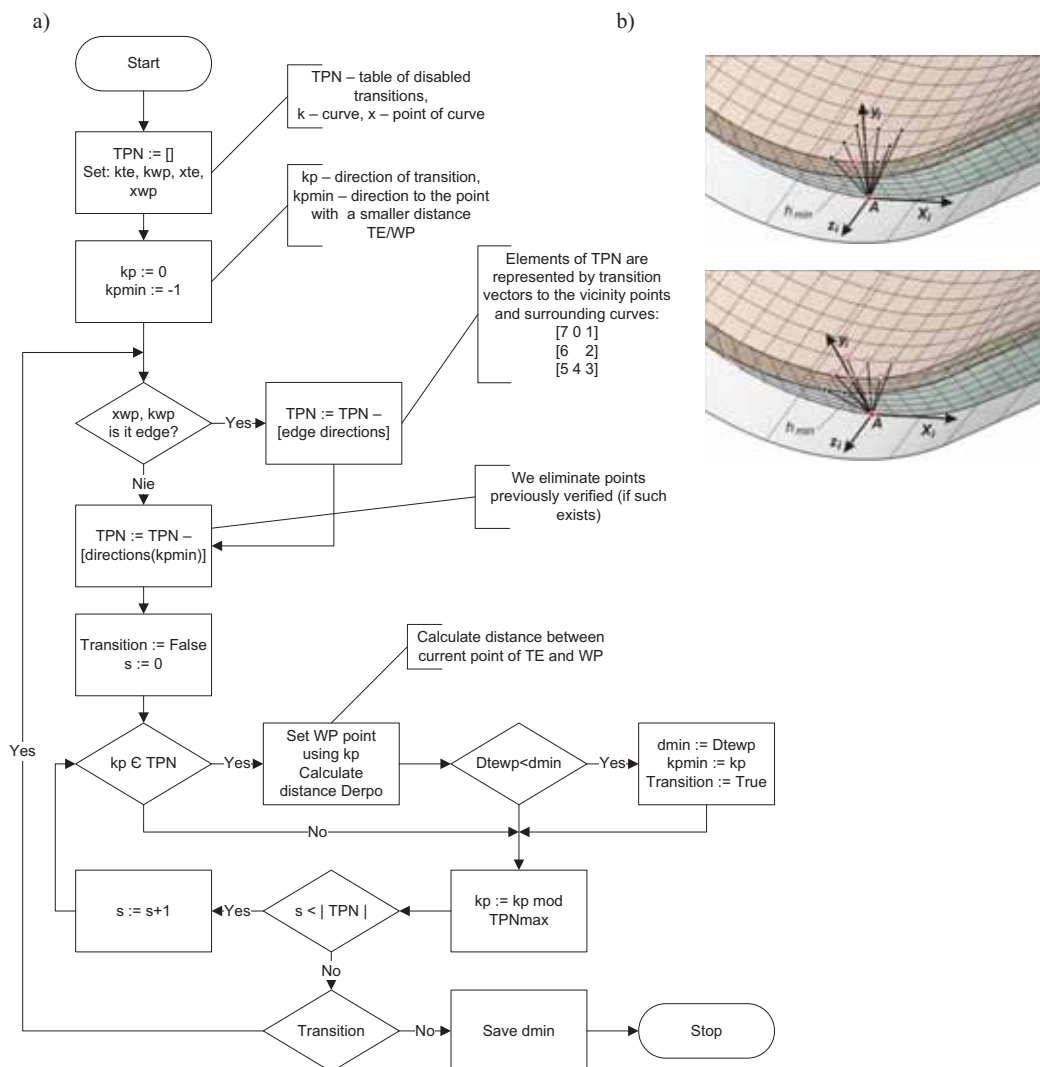


Fig. 3. Designing a minimal distance of the electrodes: a) h_{min} designing algorithm, b) momentary point matrixes

Symbols for Fig. 3:

- kp – variable representing transition direction to the neighborhood point,
- Dtewp – distance between points defined by transition kp for TE and WP points,
- Transition – variable to carry on information “point with a smaller distance discovered”,
- TPNmax – constant value representing number of neighborhood points equal 9,
- s – work variable used to index table elements
- TPN – power of TPN represents number of points to verify if is closer.

Figure 3 demonstrates a scheme of time steps for composition of the tool electrode two vibrating motions:

- longitudinal vibrations (main Y-axis direction) – with vibration frequency f_v and vibration amplitude A_v , performed in the direction of the main move,

- transverse vibrations (X -axis direction) – with vibration frequency f_p and vibration amplitude A_p , performed along X axis within the plane, perpendicular to the main motion direction.

Vibration frequency of $f_w = 4f_p$ was assumed, no phase shift for $\phi_w = 0$ amplitudes.

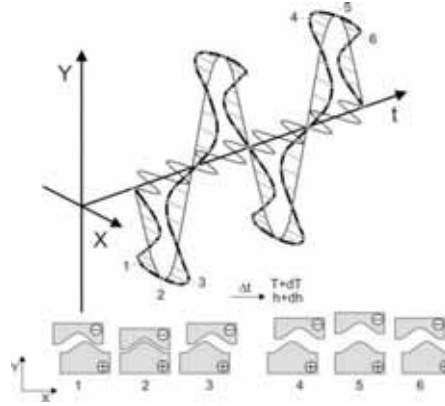


Fig. 4. Scheme of time step

Such a shift of vibration amplitudes in relation to each other provides a symmetrical, resultant motion of TE in relation to the main vibrations with extreme deflections. This case is very advantageous in terms of ECM machining accuracy. In Fig. 5 exemplary vibrations for different synchronizations are shown. It can be noted here that in extreme positions the resultant motion of the tool electrode results in different deflection of the tool electrode motion path in relation to the main vibrations. It has a direct influence on the conditions in SM and in result on the processing precision.

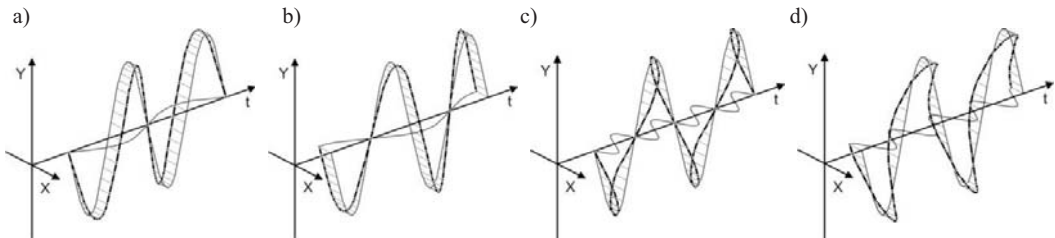


Fig. 5. Longitudinal and transverse vibrations compound : a) $\frac{1}{2}f_p = f_w$, $\phi_w = 0$, b) $\frac{1}{2}f_p = f_w$, $\phi_w = \pi/2$, c) $2f_p = f_w$, $\phi_w = 0$, d) $2f_p = f_w$, $\phi_w = \pi/2$

3. CONCLUSIONS

The calculations have been performed for shaping electrodes with geometric features presented in Fig. 5. Also, there have been shown sections along and across the interelectrode gap, for which calculation results are depicted in charts. This is a curvilinear surface, curved also in the direction of z axis. Viewing the issue as being flat involves seeking planes for performing calculations, defined as planes normal to the anode surface though, at the same time, limited by the electrode surfaces. The assumption is that the feed system provides a constant flow rate in IEG. Calculations had been performed until a quasi-stationary state was reached, i.e. the state for which thickness of MP and physical conditions between the electrodes changes occur periodically.

Machining parameters of more importance have been presented in calculations:

- initial gap - 0.2 mm,

- velocity of sliding motion of TE - 0.0125 mm/s,
- interelectrode voltage - 15 V,
- parameters of longitudinal vibrations $A_w=0.1$ mm, $f_w=25$ 1/s,
- parameters of transverse vibrations $A_p=0.05$, $f_p=100$ 1/s.

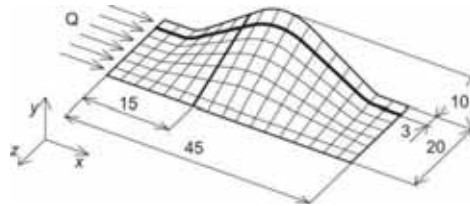


Fig. 6. The geometrical features of electrodes

Distributions of T temperature for a chosen section are presented in Fig. 7 as well as velocities V_x (Fig. 7b) along the gap thickness. Initial course of these distributions results from the laminar electrolyte flow next from the turbulent electrolyte flow.

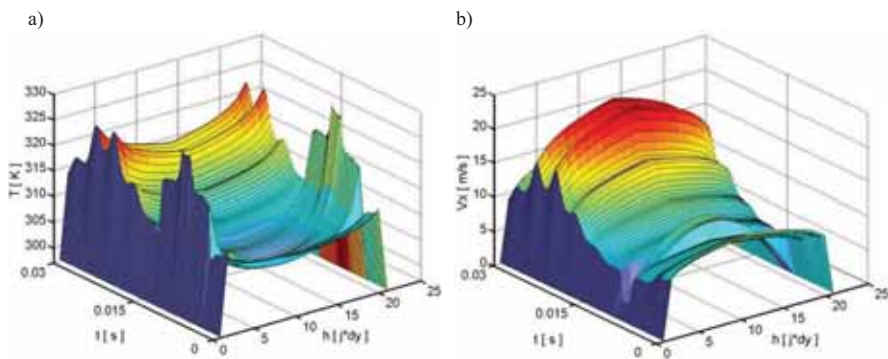


Fig. 7. Distribution along thickness: a) temperature, b) velocity of flow electrolyte

In charts (Fig. 8) there are presented distributions of p pressure, mean flow rate of the electrolyte v_{mean} , current density j and gap thickness IE h along the interelectrode gap. The periodic changes for distribution along thickness IEG for temperature and velocity of flow electrolyte are shown in Fig. 8.

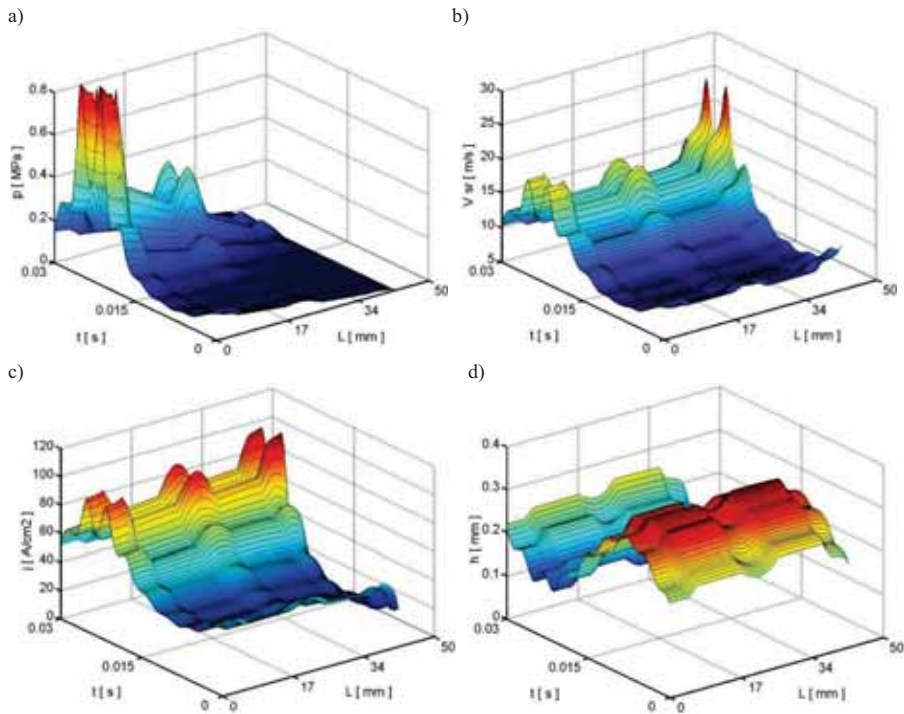


Fig. 8. Distribution along SM: a) pressure p , b) velocity of flow electrolyte V_{sr} , c) current density j d) crack height IEG h

In addition, an analysis of the average current density for a portion of the longitudinal vibration period was performed, where the processing takes place most intensively (Fig. 9). The analysis was performed for the symmetric vibration system: 1 - $\frac{1}{2} f_p = f_w$, $\phi_w = 0$, 2 - $f_p = f_w$, $\phi_w = \pi/2$, 3 - $2f_p = f_w$, $\phi_w = 0$, 4 - $4f_p = f_w$, $\phi_w = 0$.

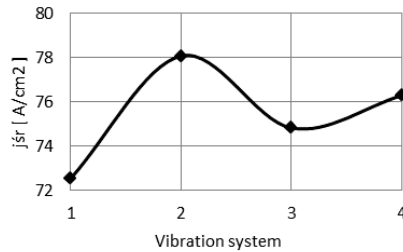


Fig. 9. Average current density for selected systems synchronize oscillations

The received calculation results confirm the expected quality change courses of chosen parameters:

- method of synchronize the vibrations affect the average values of current density,
- induction of the tool electrode vibrations case the profile deformation of the electrolyte flow rate along thickness IEG which additionally influences the electrolyte temperature change near the vibrating wall (Fig. 7),
- deformation of the electrolyte flow rate profile along IEG thickness grows along with the electrode vibration frequency increase. Thus, there are certain boundary values of vibration

frequencies and amplitudes for which there will occur the phenomenon of the electrolyte reversal in IEG,

- the electrolyte turbulent flow in the gap results in flattening the profile of the electrolyte flow rate which has a direct influence on temperature distribution along the interelectrode gap,
- local thicknesses of the inter-electrode gap (Fig. 8d) undergo changes. This has an impact on the variability of electrochemical dissolution velocity and inclination angle of the tool electrode profile in relation to the machining direction and electrode vibrations synchronization (Fig. 5) non-uniform distribution of the interelectrode gap thickness largely affects the distribution of pressure and the electrolyte flow rate (Fig. 7a-b),
- the mathematic model indicates that the gas phase concentration and the electrolyte temperature has an influence on variability of physical conditions along the flow (Fig. 7 c-d). These factors affect the change of such physical quantities as: the electrolyte viscosity, density, conductivity, and in consequence the electrochemical dissolution and machining accuracy.

In case when electrode vibrations are used it seems to be necessary to create mathematical models of ECM for the purpose of an optimal choice of the process parameters. Apart from the choice of amplitudes and vibration frequencies, their mutual synchronization is of special importance. Further simulation and experimental tests will allow for quantitative verification of the accepted mathematical model.

References

- [1] Dąbrowski, L., Paczkowski, T., *Computer simulation of two-dimensional electrolyte flow in electrochemical machining*, Russian Journal of Electrochemistry, vol. 41, No. 1, 2005, pp. 91-98.
- [2] Dąbrowski, L., *Podstawy komputerowej symulacji kształtowania elektrochemicznego*, Prace Naukowe, Mechanika z. 154, Wydaw. Politechniki Warszawskiej, Warszawa, 1992.
- [3] Gryboś, R., *Podstawy mechaniki płynów*, PWN Warszawa 1998.
- [4] Kiciak, P., *Podstawy modelowania krzywych i powierzchni*, Zastosowania w grafice komputerowej, Wyd. 1. WNT, Warszawa 2000.
- [5] Kozak, J., *Kształtowanie powierzchni obróbką elektrochemiczną bezstykową (ECM)*, Prace Naukowe PW, Mechanika nr 41, Wydawnictwo Politechniki Warszawskiej, Warszawa. 1976.
- [6] Kozak, J., *Mathematical models for computer simulation of electrochemical machining process*, Journal of Materials Processing Technology, Vol. 76, 1976.
- [7] Kozak, J., *Komputerowe wspomaganie technologii drążenia elektrochemicznego*, SNOE nr 5, Warszawa 1999.
- [8] Kozak, J., *Computer simulation system for electrochemical shaping*, J. Mater. Process. Technol. 109, 354–359, 2001.
- [9] Łubkowski, K., *Stany krytyczne w obróbce elektrochemicznej*, Prace naukowe, Mechanika, z.163, Oficyna Wydawnicza PW, Warszawa, 1996.
- [10] Paczkowski, T., Sawicki J., *Analysis of influence of physical conditions inside interelectrode gap on work piece shape evolution*, Engineering Mechanics, vol. 13, 2006, No. 2, p. 93-100.
- [11] Paczkowski T., Sawicki, J., *Electrochemical machining of curvilinear surfaces*, (MST410/07), Journal of Machining Science and Technology, 2008 USA.



BOUNDARY CONDITIONS ANALYSIS OF ECM MACHINING FOR CURVILINEAR SURFACES

Tomasz Paczkowski¹⁾, Jarosław Zdrojewski²⁾

University of Technology and Life Sciences in Bydgoszcz

¹⁾Faculty of Mechanical Engineering

²⁾Faculty of Telecommunications and Electrical Engineering

al. Prof. S. Kaliskiego 7, 85-789 Bydgoszcz, Poland

tel.: +48 52 340-87-47, fax: +48 52 340-82-45

tel. 52 340-87-47

e-mail: tompacz@utp.edu.pl

e-mail: jaz@utp.edu.pl

Abstract

Electrochemical machining of curvilinear surfaces is one of the most basic and widely spread among electrochemical technology procedures for machine and tool parts. Constant parameters for preset machining time are hard to determine in this technology. This article presents a method of boundary conditions analysis based on computer simulation of the process. Resulting from calculation controlling code for ECM processing for which machining parameters changing over time are determined in a computer simulation of the process. An example of carrying out calculations leading to determining process controlling code for preset electrode surfaces is also presented.

Keywords: computer simulation, electrochemical machining, boundary conditions analysis

1. Introduction

Among very important issues stimulating further development of technology we can distinguish: learning and increasing its ability to achieve the desired geometry of the machined surfaces, minimizing the distribution of workpiece shape deviations, and increasing the rate of machining performance indicators repeatability. Issues of the surface machining using ECM process are directly linked to its researches field.

Machined surface development issues include [3]:

- shape change in time analysis,
- determining the final shape and its variation when changing machining conditions,
- determining the geometry of the tool electrode to obtain the desired machined shape,
- process conditions optimization with respect to minimization of machined shape deviations,
- searching for new ways to increase machining accuracy.

Conventional methods of machining have reached the current stage of development thanks to

the introduction of: numerical control, optimization of the process structure and machining parameters, control by using microcontrollers or computers. Multidimensional, dynamic process of ECM requires a computer based design system and sophisticated control of machining. The condition for the development of modern ECM technology, is a good understanding of the nature of physical phenomena that occur during machining and the process of electrochemical dissolution inherent limitations. Precise quantification of these constraints will enable selection of optimal value of parameters at any given time of machining. This will ensure both high quality and economic rates, and at the same time will not lead ECM process to the so-called critical state, in which the machining is interrupted and electrodes are damaged [5].

2. Modeling of the electrochemical process shaping

Modeling ECM machining means designation the changes of the inter-electrode gap (IEG) width, evolution of the machined surface shape in time and distribution of the physical-chemical conditions occurring in the machining area, like: static pressure distribution, the electrolyte flow speed, temperature and volume concentration of the gas phase. Determination of these distributions for each time step during the simulation process allows the adaptive control of the process. This is particularly important when machining curvilinear surfaces.

2.1. Mathematic and numeric modeling

A two-dimensional, two-phase vesicular electrolyte flow in IEG is assumed. At the same time, triggering a complex tool electrode (TE) vibrating movement in mutually perpendicular directions, that is TE progressive and electrolyte flow. Detailed assumptions and mathematical model of electrochemical machining with vibrating TE for curvilinear shaped surfaces is presented in works [1,8,9].

Determination of the machined surface (anode) shape evolution in time is described by equation of evolution [2,3,8,9] showing the real shape change of the machined surface.

The initial shape of the machined surface and the TE was defined in the modeler 3D as free surfaces of the type NURBS. For numerical calculations digitization work piece (WP) and TE was performed by an approximation of the surface with curves. Detailed algorithms developed for the numerical model were presented in the works [9,10].






2.2. Boundary conditions analysis

Both theoretical and empirical studies have proved that in case of complex curvilinear surfaces for which the electrolyte flow route differs for different inter-electrode gap intersections it is very hard to select constant machining parameters for a preset process time. This is a reason why boundary conditions analysis (BCA) was developed. Assumed values considered machining parameters, for which ability to reach boundary values (critical state) will be examined, where in practice, interruption of the process will take a place. Table 1 shows the examined process parameters, considered for boundary conditions occurrence and ways to modify them.

Then interconnections between considered parameters and ways to modify them were developed. Considered parameters with possible system reactions were associated in a way to have a control on the strength of their impact. Fig.1 shows a diagram of boundary conditions analysis.

In the case of critical states CS of controlled parameters CP machining simulation will back in time to pre-determined in time control points t_k , where an appropriate modification of parameters will take a place. It should be emphasized that the modified machining parameters are reset to the output parameters value P_w in the case of no occurrence of boundary conditions within a specified simulation time.

Tab. 1. Examined ECM process parameters

Examined parameter	Modification way for ECM parameter
	Reduce feed rate V_f Temporary stop of TE Retract TE
	Reduce feed rate V_f Temporary stop of TE Retract TE
	Reducing the frequency ω_w Reducing the frequency ω_p
	Reduce feed rate V_f Temporary stop of TE Retract TE
	Reduce feed rate V_f Temporary stop of TE Retract TE

The consequence of such analysis are time-varying machining parameters. This forces the need to generate control code to run machining process.

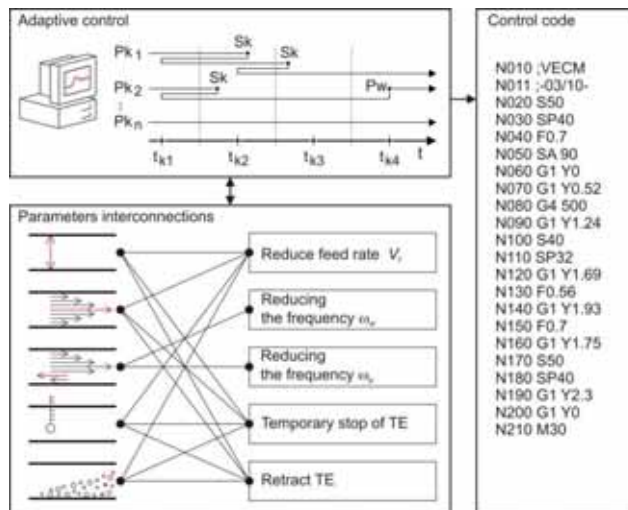


Fig. 1. Boundary conditions analysis diagram

A fragment of such a control code is shown on Fig.1. In the code for the given location of the TE in the direction of Z axis, new machining parameters are defined based on the BCA analysis. For example:

- | | |
|------------|--|
| N020 S50 | - longitudinal vibrations, |
| N030 SP40 | - transverse vibrations, |
| N040 F0.7 | - feed rate mm/min, |
| N050 SA 90 | - oscillation phase shift by 90 degrees, |

N060 G1 Y0	- move to the starting point,
N070 G1 Y0.52	- machining endpoint,
N080 G4 500	- Temporary stop 500 ms,
N090 G1 Y1.24	- parameters update,
N100 S40	- longitudinal vibrations,
N110 SP32	- transverse vibrations,
N120 G1 Y1.69	- parameters update,
N130 F0.56	- feed rate mm/min
N140 G1 Y1.93	- parameters update
N150 F0.7	- initial - feed rate mm/min
N160 G1 Y1.75	- parameters update

3. Machining simulation program

This assumption allowed new algorithms to be developed for numeric models, in order to accomplish boundary conditions analysis (Fig. 2) Consequently, this allowed to expand the ECM simulation program with another module.

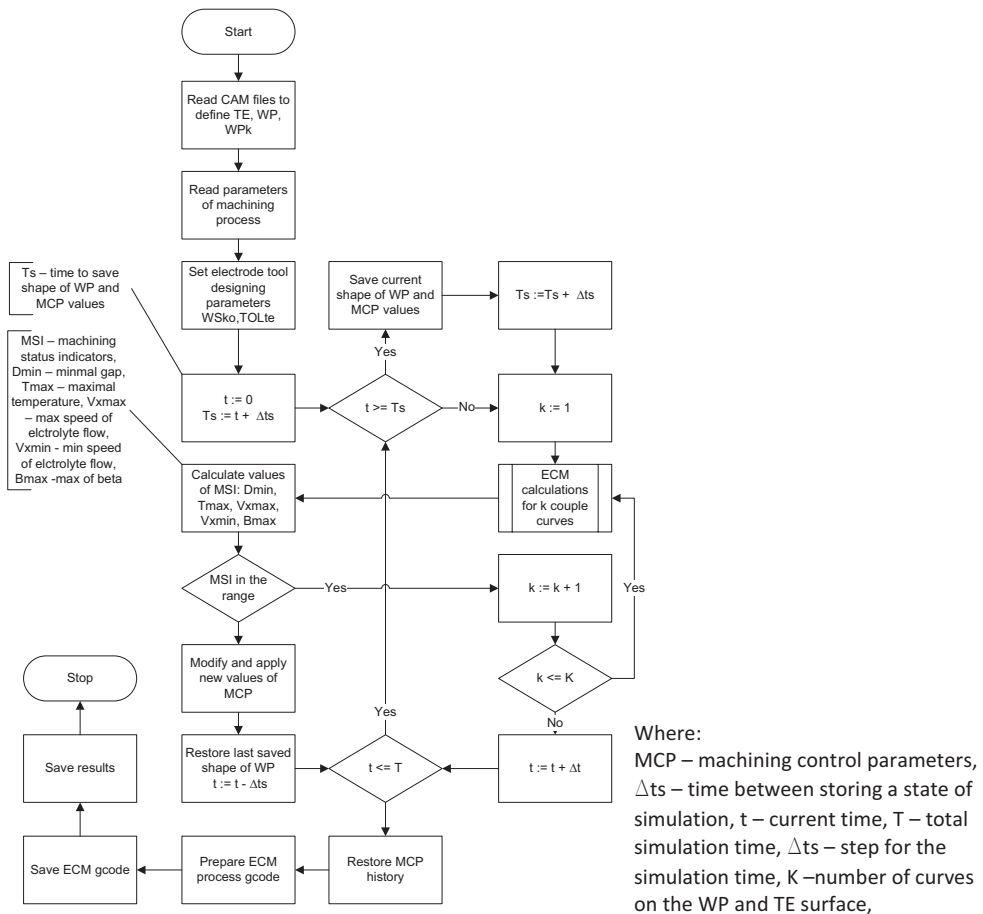


Fig. 2. Boundary conditions analysis flowchart

Fig. 3 shows a modified machining simulation program. In the first tab of this program initial process parameters are entered. They are at the same time reference parameters for boundary

conditions analysis. In a new program module a choice of mutual interrelationships between parameters and system reaction can be made, with a given level of interaction.

a)

b)

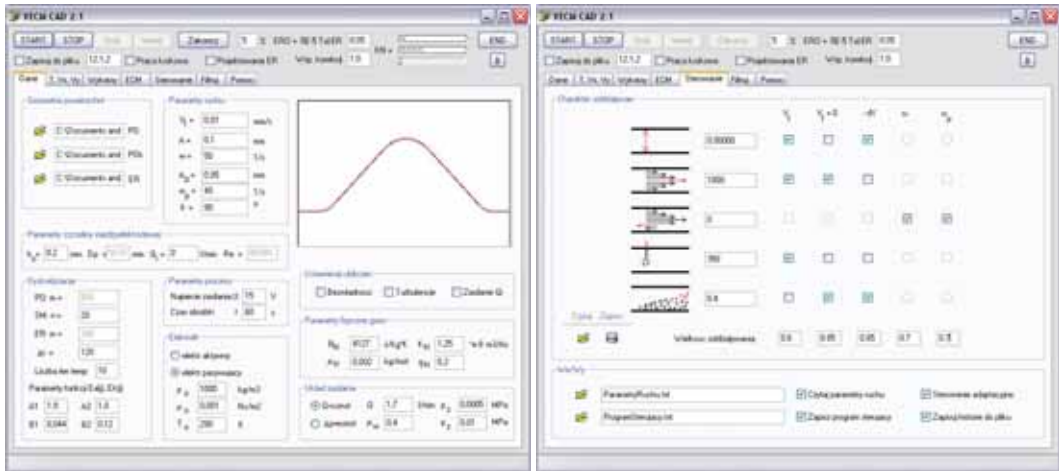


Fig. 3. Machining simulation program: a) initial machining parameters, b) boundary conditions analysis module

Additionally, the module enables loading and saving selected settings, modification of initial parameters for any machining moment (for example in the final part of the process, as optimal parameters for finishing machining), generating a code controlling hallowing.

Fig. 4 shows a process control diagram with regard to ECM machining simulation input parameters.

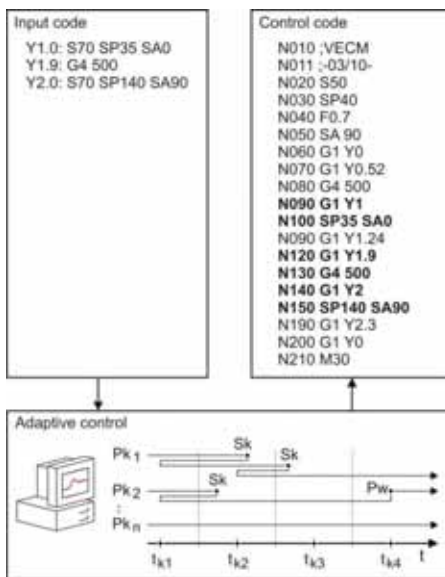


Fig. 4. Process control diagram with regard input parameters

In the body of control code (Fig. 4) input parameters are marked using bold capital letters.

6. Summary

In this work we presented a method boundary conditions analysis of ECM machining for complex electrode surfaces, as a result of which control code changing machining parameters in time was acquired.

Presented methods of modeling and controlling ECM process made possible an increase of machining stability and accuracy, especially for electrodes with complex shapes. Electrochemical drilling is a very complex process, therefore computer modeling of ECM machining process allows machining parameters to be chosen properly, and thus saving time and expenses.

It should be noted that the presented solution was obtained by analytical and numerical integration of complex systems of partial differential equations. This allowed to design complex numerical algorithms to simulate and analyze simultaneously an ECM machining for curvilinear surfaces when modifying machining parameters. IEG distribution, temperature, concentration of the gas phase and a flow rate of electrolyte, is analyzed for boundary conditions occurrence.

References

- [1] Dąbrowski, L., Paczkowski, T., *Computer simulation of two-dimensional electrolyte flow in electrochemical machining*, Russian Journal of Electrochemistry, vol. 41, No. 1, 2005, pp. 91-98.
- [2] Dąbrowski, L., *Podstawy komputerowej symulacji kształtowania elektrochemicznego*, Prace Naukowe, Mechanika z. 154, Wydaw. Politechniki Warszawskiej, Warszawa, 1992.
- [3] Kozak, J., *Kształtowanie powierzchni obróbką elektrochemiczną bezstykową (ECM)*, Prace Naukowe PW, Mechanika nr 41, Wydawnictwo Politechniki Warszawskiej, Warszawa, 1976.
- [4] Kozak, J., *Mathematical models for computer simulation of electrochemical machining Process*, Journal of Materials Processing Technology, Vol. 76, 1976.
- [5] Łubkowski, K., *Stany krytyczne w obróbce elektrochemicznej*, Prace Naukowe, Mechanika, z.163, Oficyna Wydawnicza PW, Warszawa, 1996.
- [6] Paczkowski, T., Sawicki, J., *Analysis of influence of physical conditions inside interelectrode gap on work piece shape evolution*, Engineering Mechanics, vol. 13, 2006, No. 2, p. 93-100.
- [7] Paczkowski, T., Sawicki, J., *Electrochemical machining of curvilinear surfaces (MST410/07)*, Journal of Machining Science and Technology, 2008 USA.
- [8] Paczkowski, T., *Wpływ sił bezwładności na profile prędkości w laminarnym płaskim przepływie elektrolitu podczas obróbki elektrochemicznej kształtowych powierzchni krzywoliniowych*, Sesja Naukowa Mechanika Stosowana 2008, Book of Abstracts, Bydgoszcz, 2008, s. 77-78.
- [9] Paczkowski, T., *Modelowanie obróbki ECM powierzchni o zarysie krzywoliniowym*, Inżynieria Maszyn, zeszyt 2-3, 2009.
- [10] Paczkowski, T., Zdrojewski, J., *Electrode tool designing in the ECM machining for curvilinear surfaces*, Journal of Machine Engineering, Vol. 10, No 1, 2010, s. 58-69.



ANALYSIS OF ACCELERATED METHODS FOR DETERMINATION OF FATIGUE CURVES

Łukasz Pejkowski, Dariusz Skibicki

University of Technology and Life Sciences

al. Prof. S. Kaliskiego 7, 85-789 Bydgoszcz

tel.: +48 52 3408202, +48 52 3408247

e-mail: lukasz.pejkowski@utp.edu.pl, dariusz.skibicki@utp.edu.pl

Abstract

Specification of a full fatigue characteristic for a material and its structure elements takes a very long time and generates significant costs. There are many methods for accelerated obtainment of fatigue characteristics. In this work, a comparative analysis of selected methods of fatigue life specification for 12 kinds of materials has been made, on the basis of literature study. In the conclusions, distinctive features of results obtained by using these methods have been pointed out.

Keywords: *fatigue of materials, fatigue curves, accelerated methods*

1. Introduction

A material fatigue behavior for a high cycle range is usually described by a fatigue curve combining the number of cycles and stresses, that is, Wohler's diagram. The curve, also called S-N curve, is obtained by bringing a certain number of samples to destruction in result of sinusoidal action of load with different values. Standard [1] recommends that the number of samples examined at a given level of stress cannot be smaller than 3 and the number of levels should not be smaller than 5. The norm also says that the frequency of load changes should be contained in interval from 5 to 100Hz.

Such a way of Wöhler diagram obtainment is time consuming and generates high costs. For this reason, different methods for accelerated determination of fatigue curves have been developed and described in literature.

The purpose of this paper is a comparative analysis of these methods.

2. Description of selected methods for accelerated determination of fatigue curves

Below, there have been described selected methods for accelerated determination of Wöhler diagrams for the high cycle range.

The first of the discussed methods was discussed in work [2]. It assumes the Wöhler curve model as a straight line in a binary logarithmic scale whose beginning is in the point corresponding to monotonic tensile strength, denoted by the authors as S_u , with the number of N cycles equal to 1. For metals, the line end goes through the point corresponding to fatigue limit S_f with the number of N cycles equal to 1 which amounts from 10^6 or 10^7 to $5 \cdot 10^8$. This number depends on the material type, its microstructure and its machining method. For so defined beginning and end of the curve, it can be described by Basquin equation in the form:

$$S_a \text{ lub } S_{Nf} = A(N)^b, \quad (1)$$

where S_a is fatigue amplitude of the cycle whose stress ratio R assumes random values, S_{Nf} is fatigue life, that is, stress amplitude for an oscillatory a cycle, such one for which $R = -1$, A is a coefficient whose value can be equal to S_u , real tensile strength σ_f or can be determined by means of real data regression. The curve slope is denoted by b letter.

For the purpose of further acceleration of S-N diagram obtainment process, the studied model assumes that the fatigue limit S_f for polished samples made of steel, can be estimated in the following way:

$$S_f \approx 0,5S_u \quad \text{jeżeli } S_u \leq 1400 \text{ MPa}, \quad (2)$$

$$S_f \approx 700 \text{ MPa} \quad \text{jeżeli } S_u \geq 1400 \text{ MPa}. \quad (3)$$

For aluminum alloys S_f can be determined using dependence:

$$S_f \approx 0,35S_u \quad (4)$$

Next, coefficient b is calculated from the formula:

$$b = \frac{1}{6} \log \left(\frac{S_f}{S_u} \right), \quad (5)$$

This method can be additionally modified with assessment of monotonic tensile strength S_u , on the basis of hardness according to Brinell scale [3], [2]. Steel with low and medium strength is estimated using the following formula:

$$S_u \approx 3,45HB. \quad (6)$$

Tensile strength for cast iron can be determined in a similar way:

$$S_u \approx 1,58HB - 86. \quad (7)$$

The other analyzed method has been presented in work [3]. It assumes that high cycle fatigue covers interval from 10^3 to 10^6 cycles. According to this method, Wöhler diagram for a high cycle area is created by connecting with a straight line a point corresponding to fatigue life S_{1000} for 10^3 cycles with point S_e being the fatigue limit for 10^6 , $5 \cdot 10^7$ or $5 \cdot 10^8$. The value of fatigue strength can be estimated on the basis of formulas in table 1.

Tab. 1. Formulas for determination of fatigue life S_{1000}

Type of material	Type of load	S_{1000}
All types	Bendindg	$0,9 \cdot S_u$
All types	Axial	$0,75 \cdot S_u$
Steels	Torsion	$0,72 \cdot S_u$
Non iron	Torsion	$0,63 \cdot S_u$
Želiwo	Torsion	$1,17 \cdot S_u$

The authors also recommend to take into consideration reliability level $S_{1000,R}$ while determining S_{1000} :

$$S_{1000,R} = S_{1000} \cdot C_R, \quad (8)$$

The values of C_R coefficient have been presented in table 2.

Tab. 2. Values of C_R coefficient

Reliability level	C_R
0,5	1
0,9	0,897
0,95	0,868
0,99	0,814
0,999	0,753
0,9999	0,702
0,99999	0,659
0,999999	0,62

The value of fatigue limit S_e is determined according to a scheme expressed by the following formula:

$$S_e = S_{be} \cdot C_L \cdot C_S \cdot C_D \cdot C_R, \quad (9)$$

First of all, fatigue limit for bending S_{be} is calculated according to formulas which have been presented in table 3.

The next step is to determine amplitudes of stress S_f , on the basis of the number of cycles, using formula:

$$\frac{\log(10^3) - \log(10^6)}{\log(S_{1000}) - \log(S_e)} = \frac{\log(10^3) - \log(N)}{\log(S_{1000}) - \log(S_f)}, \quad (10)$$

Calculation of S_f from the formula is relatively complicated and inconvenient. However, it can be transformed into Basquin equation, determining b exponent and B coefficient on the basis of formulas:

$$b = -\frac{1}{3} \log\left(\frac{S_{1000}}{S_e}\right), \quad (11)$$

$$B = \frac{S_{1000}^2}{S_e}, \quad (12)$$

Tab. 3. Formulas for determination of fatigue limit S_{be} for bending

Type and microstructure of material	S_{be}	Cycles	Comments
Steel - ferrite	$0,58 \cdot S_u$	10^6	-
Steel – ferrite + pearlite	$0,38 \cdot S_u$	10^6	-
Stal – pearlite	$0,38 \cdot S_u$	10^6	-
Stal – untempered martenzite	$0,26 \cdot S_u$	10^6	-
Stal – highly tempered martenzite	$0,55 \cdot S_u$	10^6	-
Stal – highly tempered martenzite + tempered bainite	$0,5 \cdot S_u$	10^6	-
Stal – tempered bainite	$0,5 \cdot S_u$	10^6	-
Stal – austenite	$0,37 \cdot S_u$	10^6	-
Wrought Steels	$0,5 \cdot S_u$	10^6	$S_u < 1400 \text{ MPa}$
Wrought Steels	700 MPa	10^6	$S_u \geq 1400 \text{ MPa}$
Cast iron	$0,4 \cdot S_u$	$5 \cdot 10^7$	-
Aluminum alloys	$0,4 \cdot S_u$	$5 \cdot 10^8$	$S_u < 336 \text{ MPa}$
Aluminum alloys	130 MPa	$5 \cdot 10^8$	$S_u \geq 336 \text{ MPa}$
Sand cast aluminum	55 MPa	$5 \cdot 10^8$	-

Next, values of coefficients are determined: C_L – type of load coefficient (tab. 4) C_S – coefficient of the surface finish (fig.1 and 2) C_D - coefficient of size (fig. 3). C_R is determined in the same way as for $S_{1000,R}$.

Tab. 4. Values of coefficient C_L

Type of load	C_L	Uwagi
Pure axial	0,9	
Axial (with slight bending)	0,7	
Bending	1	
Torsional	0,58	Steels
Torsional	0,8	Żeliwa

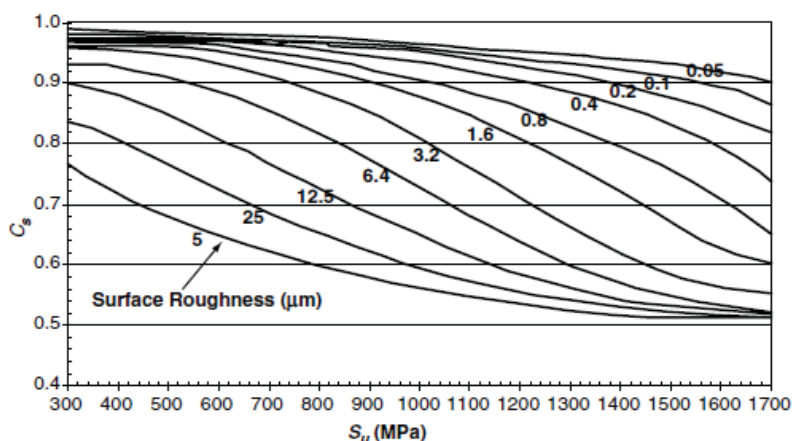


Fig. 1 – Chart for determination of C_s for known surface roughness (source – [3])

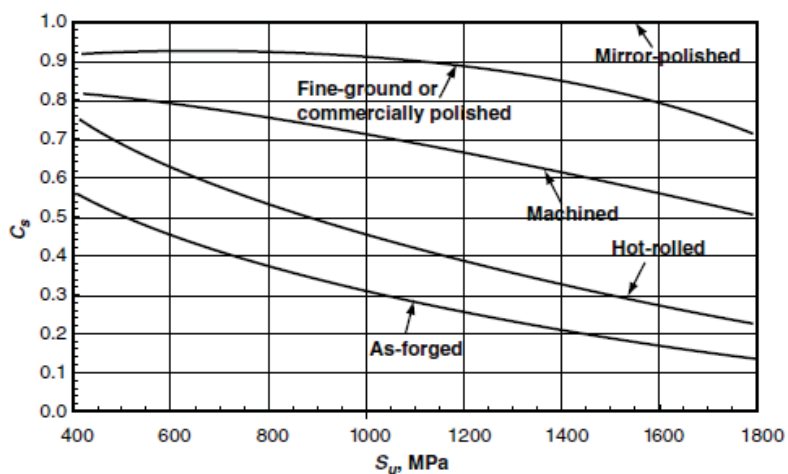


Fig. 2 – Chart for determination of C_s according to the machining type (source - [3])

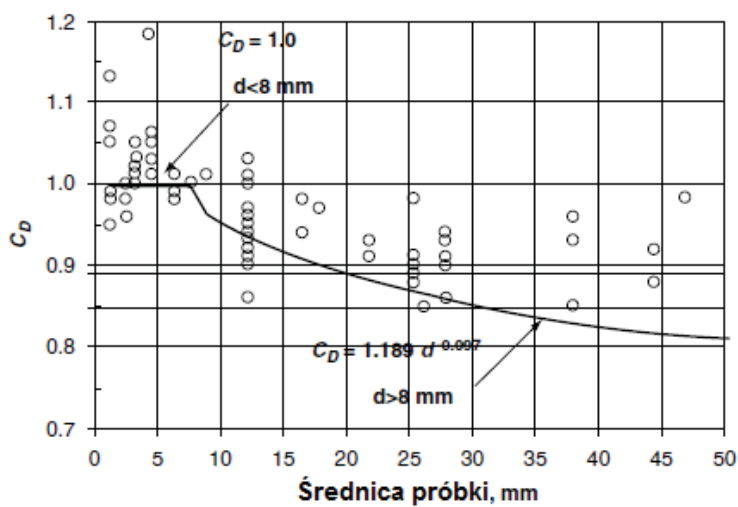


Fig. 3 – Chart for determination of C_D (source – [3])

For so calculated quantities Basquin equation assumes the following form:

$$S_f = B(N)^b, \quad (13)$$

The third analyzed method for accelerated determination of Wöhler curve is an approach described by FITNET procedures and work [4]. Fatigue diagram model described by FITNET procedures involves defining the angle of a straight line inclination and defining its end which is situated in the point corresponding to fatigue limit, denoted as Z_G .

The angle of a straight line inclination symbolized by coefficient m is determined from dependence presented in table 5.

Tab. 5. Values of m coefficient

Value of m coefficient	Type of specimen
$16 \div 20$	Surface hardened elements
$8 \div 12$	Fine Ground and polished elements
$4 \div 10$	Notched elements
$3 \div 4$	Welded elements

The value of fatigue limit is determined by multiplying tensile strength, denoted in FITNET procedures as R_m , through a proper coefficient selected from table 6.

Tab. 6. Coefficient for determination Z_G

Type of material	Values of Z_G for normal stresses	Values of Z_G for tangent stresses
Surface hardened steel	$0,4 \cdot R_m$	$0,577 \cdot R_m$
Stainless steel	$0,4 \cdot R_m$	$0,577 \cdot R_m$
Forged steel	$0,4 \cdot R_m$	$0,577 \cdot R_m$
Cast steel	$0,34 \cdot R_m$	$0,577 \cdot R_m$
Steels different from the above listed	$0,45 \cdot R_m$	$0,577 \cdot R_m$
Spheroidal cast iron	$0,34 \cdot R_m$	$0,65 \cdot R_m$
Ductile cast iron	$0,3 \cdot R_m$	$0,75 \cdot R_m$
Gray cast iron	$0,3 \cdot R_m$	$0,85 \cdot R_m$
Plastically worked aluminum alloys	$0,3 \cdot R_m$	$0,577 \cdot R_m$
Cast aluminum alloys	$0,3 \cdot R_m$	$0,75 \cdot R_m$

According to FITNET procedure, value N_G is 10^7 for steel and 10^8 for aluminum alloys. Coefficient of inclination of a straight line being a model of the fatigue curve is defined by formula:

$$ctg(\alpha) = m = \frac{\log \frac{N_G}{N}}{\log \frac{\sigma_a}{Z_G}}, \quad (12)$$

where σ_a denotes permissible stress amplitude (fatigue life). Also, in case of this method, the above formulas can be transformed into the form of Basquin equation. Quantities b and B are determined in the following way:

$$b = -\frac{1}{m}, \quad (13)$$

$$B = Z_g N_g^{\frac{1}{m}}, \quad (14)$$

$$\sigma_a = B(N)^b. \quad (15)$$

For comparison, formulas and schematic diagrams, representing the above mentioned methods, were presented in figure 4.

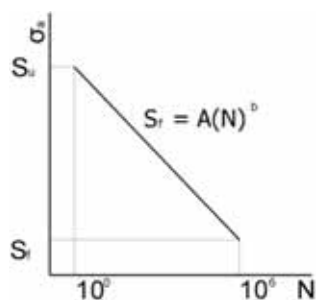


Fig. 4a. Scheme representing method $S-N_{Su}$

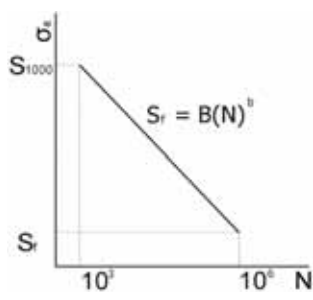


Fig. 4b. Scheme representing method $FTaA$

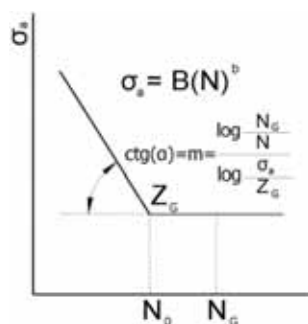


Fig. 4c. Scheme representing method $FITNET$

3. Verification of selected methods

Below, there have been presented results of verification of accelerated methods for determination of fatigue characteristics for a high cycle range. Abbreviations included in the legend denote: „ $S-N_{Su}$ ” – method for determination of fatigue diagram, the basis of tensile strength described in [2]; „ $S-N_{HB}$ ” – method for estimation of tensile strength on the basis of Brinell hardness, described in work [2]; „ $FITNET$ ” – methods described in $FITNET$ procedures; „ $FTaA$ ” – method described in work [3]. These abbreviations are also used in the text for verification of the methods. Verification is carried out on the basis of the authors' own research.

Fig. 2 shows the result of verification for steel 10HNAP. For this material, characteristic most similar to the one obtained from experimental test is provided by “ $FITNET$ ” method. However, it should be noted that the diagram obtained from this method runs above the real diagram throughout its whole length which means overestimation of fatigue life. The method which is based on tensile strength „ $S-N_{Su}$ ”, yields a diagram which varies considerably from the real one in terms of direction coefficient, thereby, a part of the diagram runs below and a part above it.

„*FTaA*” method also yields a diagram which runs below the real one. However, attention is focused on the fact that they are parallel.

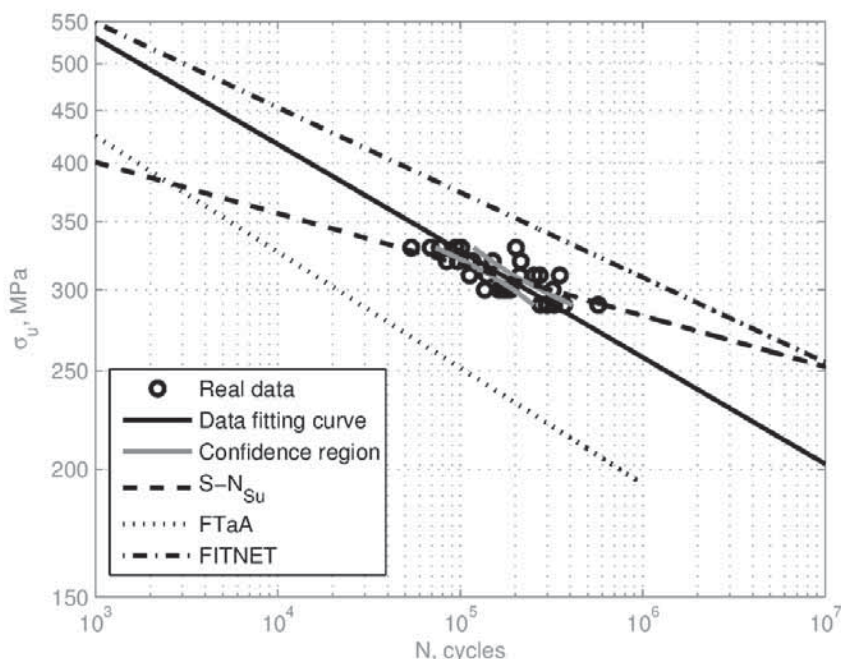


Fig. 5. Results of verification of method for accelerated determination of Wöhler diagram for steel 10HNAP

The next, presentation of diagrams (fig. 6) demonstrates the results for steel 30rNiMo8. In this case, a diagram, most similar to the real one, is provided by „*S-N_{Su}*” method. However, again the lines differ from each other in terms of direction. The diagram obtained with the use of “*FITNET*” method is situated significantly higher than the real one which means reassessment of fatigue life. The diagram obtained by „*FTaA*” method runs significantly lower than the real one and departs from it in respect of direction coefficient.

The next verified material is steel 40 CrMo4 (fig. 7). Also, for this steel, the diagram according to method „*S-N_{Su}*” is the most similar to the real one. However, it runs slightly above it throughout its whole length. .

Again, the diagram according to “*FITNET*” procedure is situated higher than the real one though is similar to it in terms of direction coefficient. “*FTaA*” method yields a diagram which runs significantly lower than the real one, and departs from it in terms of direction coefficient.

For BHW 25 steel (fig. 8), fatigue life characteristic from “*FITNET*” method is also situated higher than the real one throughout its whole length, and the two remaining ones, below. For this material, both the diagram from “*FITNET*” and from “*S-N_{Su}*” method differ from the real one in terms of direction coefficient. Diagram from “*FTaA*” method again differs significantly from the real one, both in terms of its position and direction.

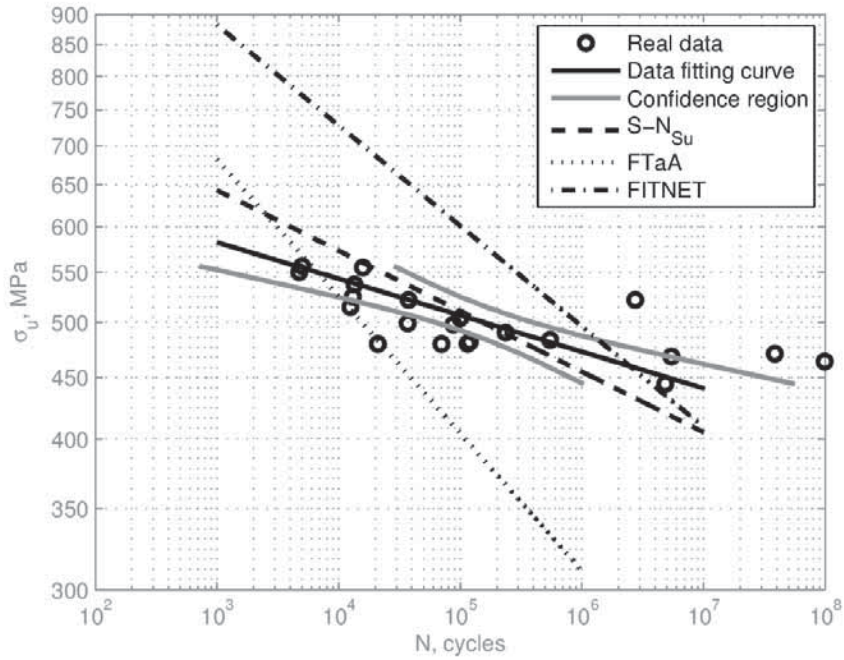


Fig. 6. Results of verification of method for accelerated determination of Wöhler diagram for steel 30CrNiMo8

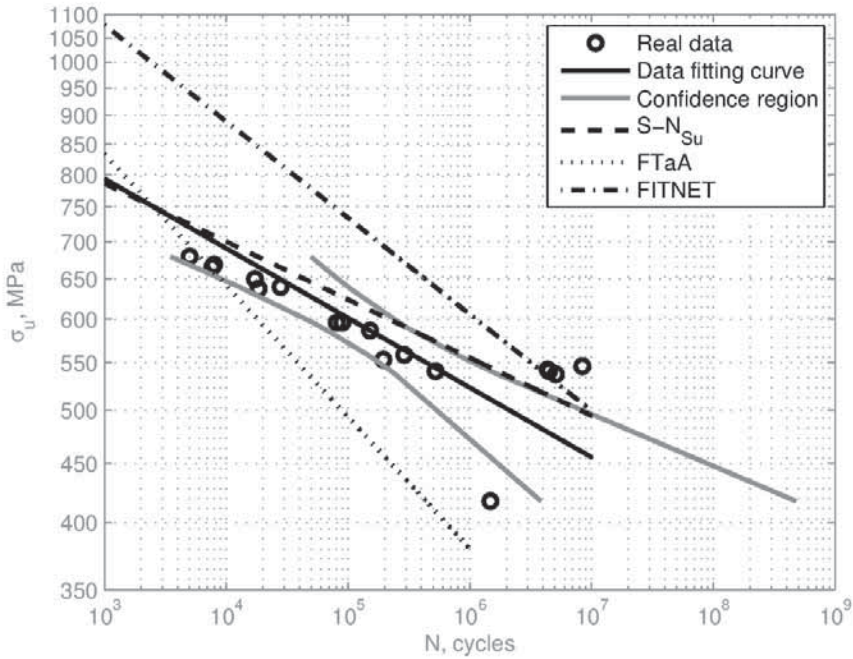


Fig. 7. Results of verification of method for accelerated determination of Wöhler diagram for steel 40 CrMo 4

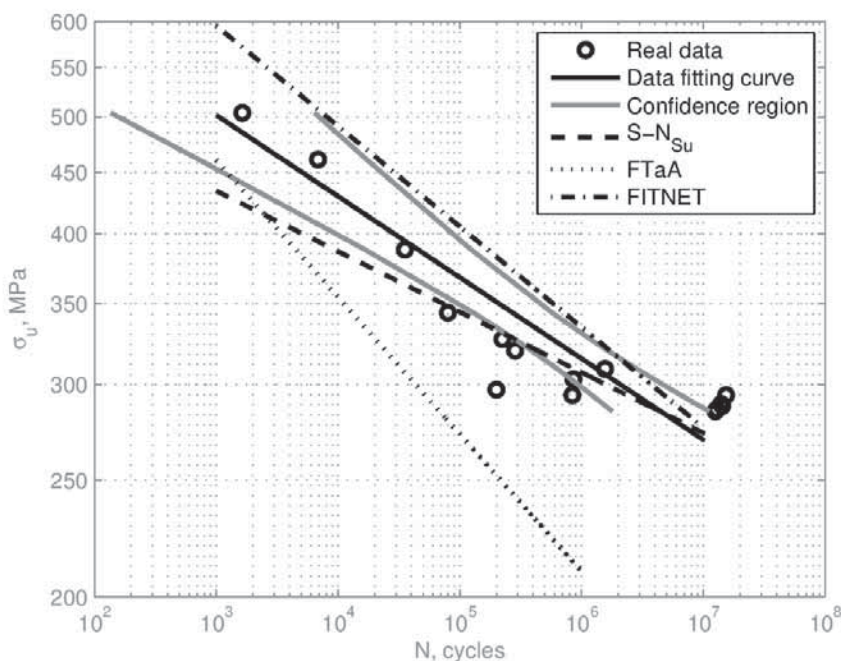


Fig. 8. Results of verification of method for accelerated determination of Wöhler diagram for steel BHW 25

The tendency for reassessment of “FITNET” procedure fatigue life is observed for steel Ck45 (fig. 9). Fatigue characteristic obtained using it is situated significantly higher than the real one. It is also different from it in terms of direction coefficient. For this material, the most similar in terms of direction and fatigue value appeared to be the characteristic obtained on the basis of “ $S-N_{Su}$ ” method. The diagram obtained on the basis of Brinell toughness is also parallel to the real one but it runs significantly higher than it. Characteristic obtained on the basis of “FTaA” method departs from the real one in terms of direction and fatigue life value.

The following material for which methods for accelerated determination of Wöhler diagram have been verified is steel HSB 55 (fig. 10). For this material, the fatigue curve obtained from “FITNET” procedure is the most convergent with the real one in terms of the fatigue life value. However, again, for this material both these diagrams differ in terms of direction coefficient, thereby, the diagram from “FITNET” method lies in a hazardous area throughout up to $5 \cdot 10^4$ of fatigue life. Characteristic developed on the basis of “ $S-N_{Su}$ ” method lies significantly lower than the real one, however, is consistent with it in terms of direction coefficient. “FTaA” method yields Wholer diagram which is most different from the real one.

Fig. 11 presents calculation results for another material, steel SPV 50. Like previously, the diagram from “FITNET” method is different from the real one in terms of direction coefficient, thereby, it lies in the area of hazard through up to $2 \cdot 10^5$ cycles. Methods „ $S-N_{Su}$ ” and „ $S-N_{HB}$ ” yield diagrams consistent with the real one, though, more inclined. The diagram according to “FTaA” approach differs most from the real one, in this case as well.

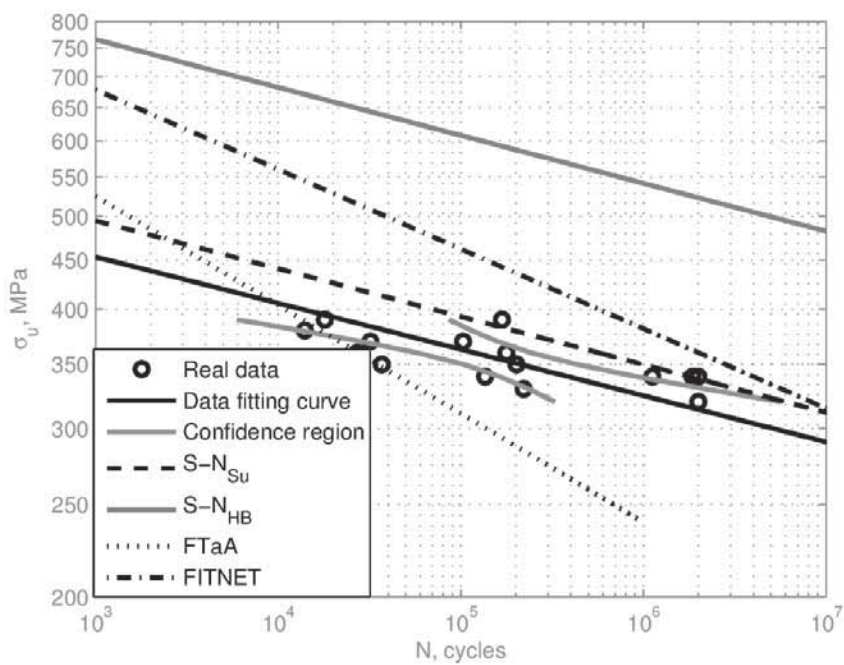


Fig. 9. Results of verification of method for accelerated determination of Wöhler diagram for steel Ck45

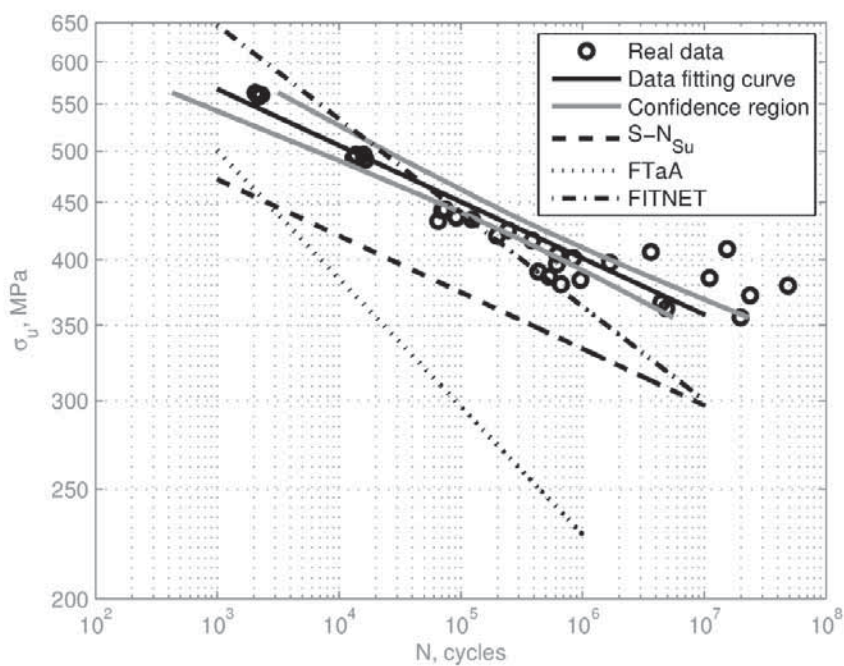


Fig. 10. Results of verification of method for accelerated determination of Wöhler diagram for steel HSB55

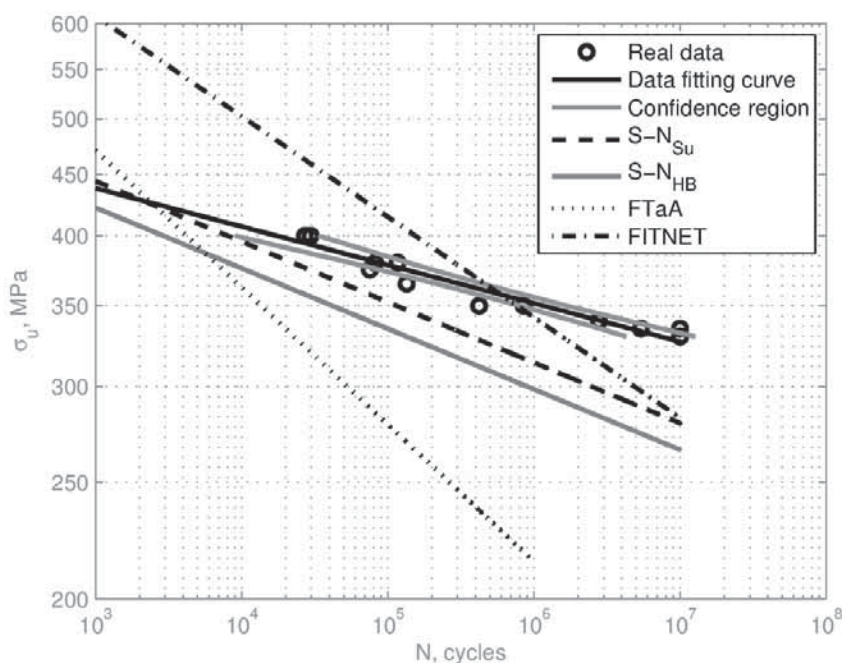


Fig. 11. Results of verification of method for accelerated determination of Wöhler diagram for steel SPV 50

The diagram created for steel St52 on the basis of “*FITNET*” procedure is very similar to the real data diagram in terms of direction coefficient, however, also for this material it is reassessed (fig. 12.). “*S-N_{Su}*” approach provides a diagram which is more consistent with the real one in terms of fatigue life but different from it in terms of direction coefficient. “*FTaA*” method yields a diagram mostly consistent with the real one but lying significantly lower than values obtained from tests.

Comparison of methods was also made for steel St37 (fig. 13). Besides, Wöhler diagram obtained from “*FITNET*” procedure is consistent with the real one in respect of direction coefficient, though it lies above it, in the area of hazard. The method using tensile strength “*S-N_{Su}*” provides a diagram situated similarly to the real one in terms of stress amplitude values, however, different from it in respect of direction. The diagram direction is more similar for “*FTaA*” method, though it lies below the real one.

In figure 14 there are diagrams obtained for steel StE 460. Again, the diagram created according to “*FITNET*” procedure lies above the material fatigue characteristic and it is most similar in terms of direction coefficient. Like for the previous material, the diagram created on the basis of tensile strength, “*S-N_{Su}*”, departs from the real one in respect of slope. This time almost throughout its length it lies above it. “*FTaA*” method provides a diagram situated closer to the real one differing, though, in terms of direction coefficient.

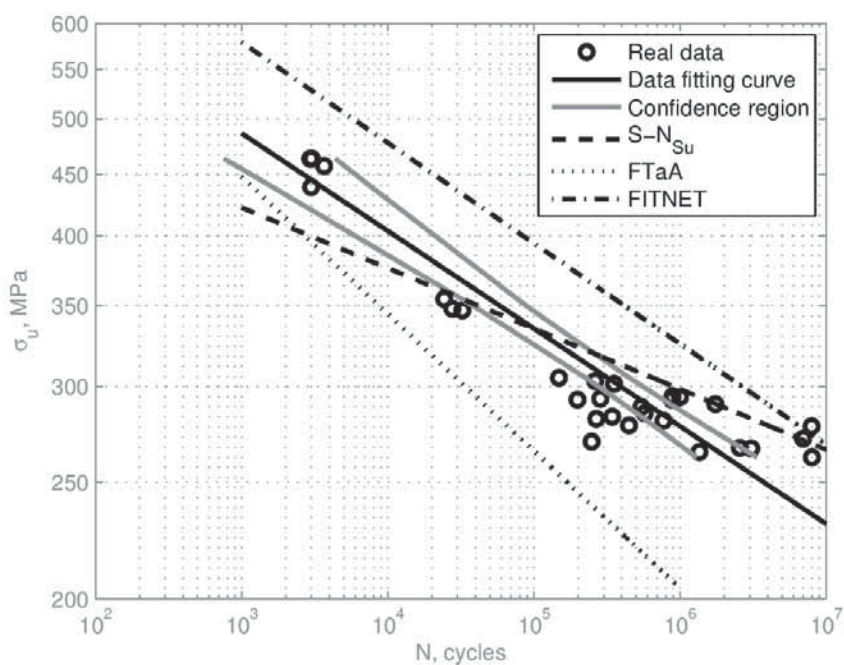


Fig. 12. Results of verification of method for accelerated determination of Wöhler diagram for steel St52

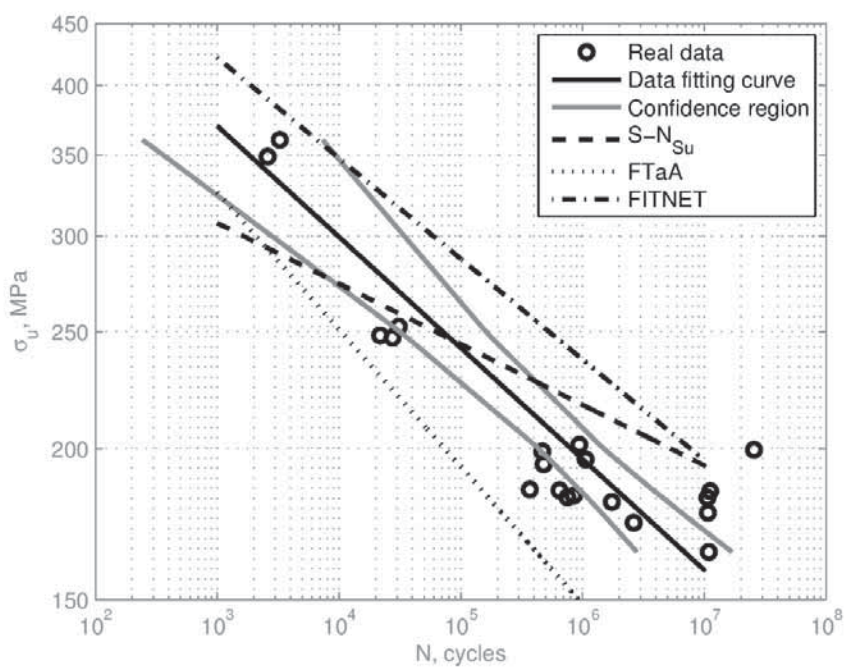


Fig. 13. Results of verification of method for accelerated determination of Wöhler diagram for steel St37

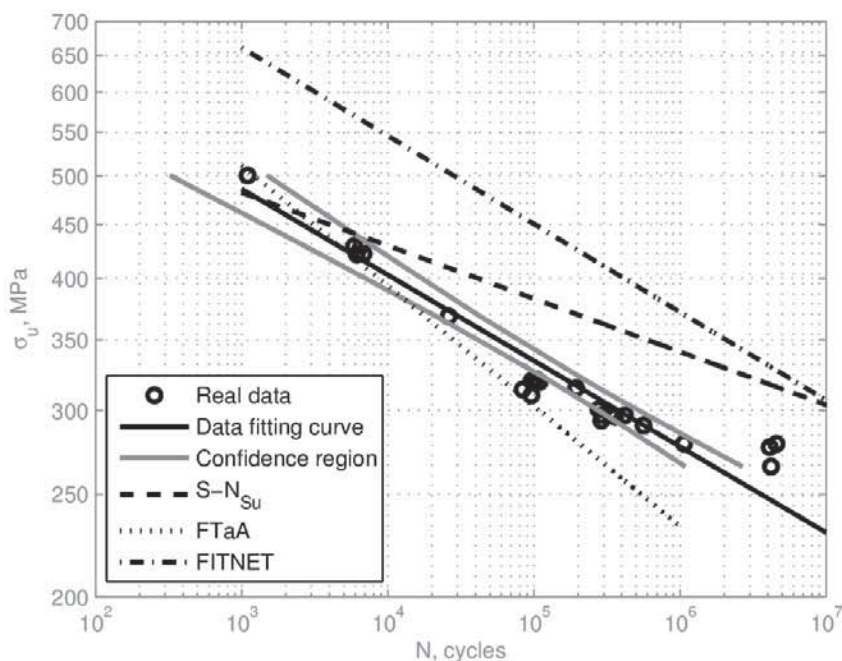


Fig. 14. Results of verification of method for accelerated determination of Wöhler diagram for steel StE 460

The next presentation of Wöhler diagrams (fig. 15) was made for steel StE 690. „ $S-N_{Su}$ ” method yields a diagram lying closest to the real one and similar in terms of direction. Method from “FITNET” procedure again provides a diagram situated in the area of hazard. For StE 690 steel also departs from the real one in respect of direction coefficient. The diagram obtained from “FTaA” method lies below the real one, also for this material and differs from it in terms of direction.

The last material for which accelerated methods for Wöhler diagram determination have been compared is steel X5CrNi18 (fig.16). For this material the diagram obtained from “FITNET” procedure departs from the real one, thereby, up to 10 cycles lie above it, running below the real line. Also in this case, „ $S-N_{Su}$ ” method appears to be an approach providing a diagram most similar to fatigue characteristic in terms of both direction and fatigue life. The diagram obtained on the basis of “FTaA” method is most divergent from the real one.

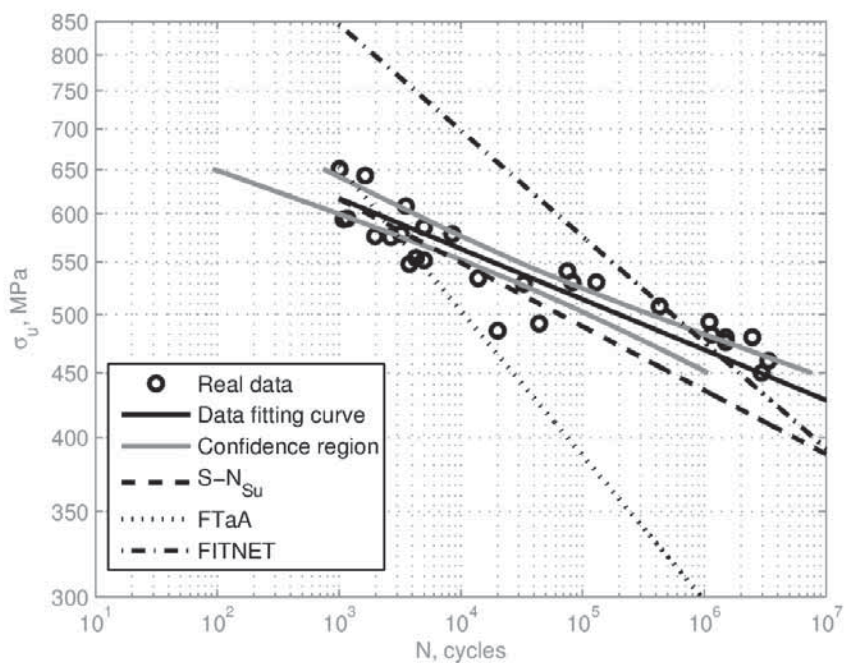


Fig. 15. Results of verification of method for accelerated determination of Wöhler diagram for steel StE 690

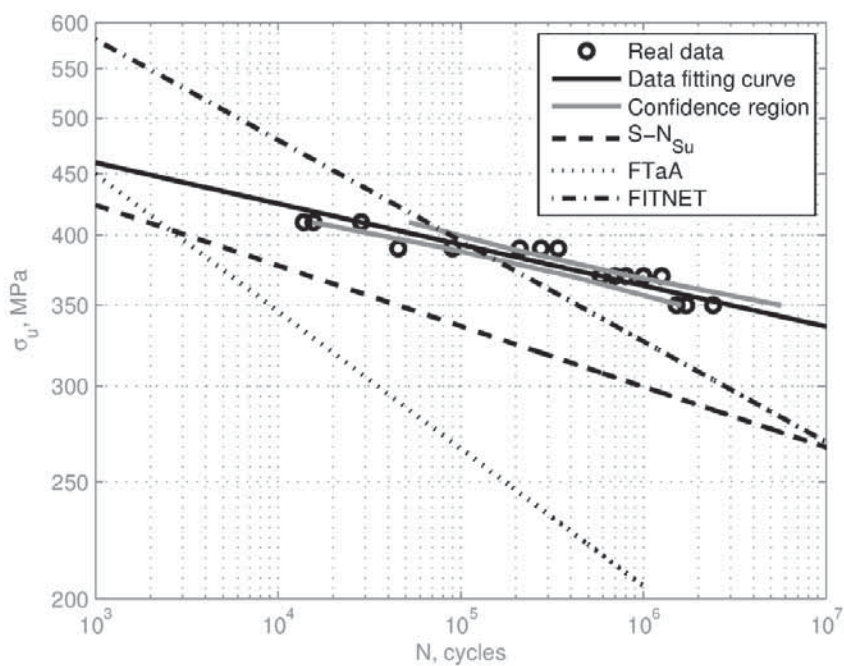


Fig. 16. Results of verification of method for accelerated determination of Wöhler diagram for steel X5CrNi18

4. Conclusions

Summing up, it can be said that Wöhler diagram which is most similar to the real one is obtained from methods “ $S-N_{Su}$ ” and “ $S-N_{HB}$ ” However, they usually differ in terms of direction coefficient. Most often it is situated, partly or entirely, below the real characteristic, that is, in the area of no hazard. The method described in “*FITNET*” procedure most frequently provides a diagram lying above the real one, that is, in the area hazardous due to reassessment of fatigue life. They also differ with direction coefficients. “*FTaA*” method using the diagram initial point as fatigue life for a thousand of cycles provides a diagram which is the least similar to the real one. Usually, they differ significantly in respect of direction coefficient, and the estimated diagram most frequently lies below the experimental one.

References

- [1] PN-76/H-04325
- [2] Stephens R. I., Fatemi A., Stephens R. R., Fuchs H. O., Metal fatigue in engineering, Wiley-IEEE, 2001.
- [3] Lee Y., Pan J., Hathaway R. B., Barkey M. E., Fatigue Testing and Analysis (Theory and Practice), Butterworth-Heinemann, 2005.
- [4] Kocańda S., Szala J., Podstawy obliczeń zmęczeniowych, PWN, Warszawa 1985.



ANSYS POLYFLOW SOFTWARE USE TO OPTIMIZE THE SHEET THICKNESS DISTRIBUTION IN THERMOFORMING PROCESS

Karol Pepliński, Arkadiusz Mozer

University of Technology and Life Sciences in Bydgoszcz
ul. Prof. S. Kaliskiego 7, 85-789 Bydgoszcz, Poland
tel.: +48 52 3408224, fax: +48 52 3408222
e-mail: karolpep@utp.edu.pl

Abstract

Thermoforming is a manufacturing process widely used to produce thin thermoplastic parts from small blister packs to display AAA size batteries to large skylights and aircraft interior panels. In this paper was presented numerical simulation of the inflation phase of a thermoforming process under which a thin polymer sheet is deformed into a mould under the action of applied pressure. Two cases of blowing sheet were considered. In the first, preapproved on the basis of a constant sheet temperature ($T = 150^{\circ}\text{C}$) examined the distribution of the container wall thickness. There has been excessive thinning (about 0,2mm) in the cup corners after forming. Also simulation it was made for other constant temperature (160, 170, 180, 190 and 200°C). On this basis, was made optimization of the sheet profile temperature (in range $150\pm 200^{\circ}\text{C}$) to remove excessive thinning. Noted was a significant effect of the initial sheet temperature distribution on the final wall thickness distribution in the considered container. The Ansys Polyflow procedure of optimizing the sheet temperature distribution allowed eliminating excessive thinning in the considered cup walls corners.

Keywords: thermoforming, Ansys Polyflow simulation, non-isothermal conditions, optimization sheet temperature

1. Introduction

Thermoforming is a manufacturing process widely used to produce thin wall thermoplastic products. The temperature of a previously extruded thermoplastic sheet is raised far above the glass transition temperature and next deforms the material to the desired shape using a differential pressure and a male or female mould [3,11]. This process is used mostly for various packaging industries, such as food, because of various advantages like, ease of production, low cost, high speed and high performance [1,7]. The major raw materials used for thermoforming are high impact polystyrene ABS, PVC, polypropylene, HDPE, Polycarbonate etc. The choice of each material depends upon the end-use requirements and cost. The most common materials used for disposable wares are high impact polystyrene, PVC and polypropylene (considered in work) [2,8].

Nowadays the thermoplastic forming industry is mostly based on trial and error methods to design and develop new products. These procedures, however, result relatively time and money expensive [6,10]. Helpful solution is to use CAE software Ansys Polyflow. This software makes it possible to determine the behavior of the plastics during the process, identify areas where there may be the biggest product wall thinning, which reduce the mechanical properties of the product.

At the end of a thermoforming process, we can observe non-uniformities in the thickness distribution in some areas, the sheet can be too thick, while in other areas, it is too thin. Instead of

increasing the initial thickness of the sheet in order to obtain a minimum thickness everywhere, it is possible to play with initial temperature distribution. Sheet temperature is one of the most critical elements of the thermoforming process. It is sheet temperature that dictates the process, the end result being not just a better product, but also decreased cycle time, less scrap and reduced energy and labor costs. We can increase the heat on a part of the initial sheet that eventually leads to an area with an excess of matter. This makes it possible to improve the thickness distribution in the final sheet product without increasing the mass of the sheet. Software Ansys Polyflow own ability to optimization initial temperature of the sheet.

The purpose of this paper is determined the impact temperature distribution along the sheet on the final cup thickness is taken into account. Simulations are carried out using Ansys-Polyflow 12.1 software [13].

In an earlier some author study [9] considered only a one constant temperature distribution sheet, and then optimized structure of sheet temperature distribution. Whereas, not studied the influence of different range of constant initial sheet temperatures on the final product thickness distribution of what this has been presented below.

2. Modeling and numerical algorithm

From a geometrical point of view, the thermoforming process involves a fluid region – the sheet, the thickness of which is two to three orders of magnitude lower than the other dimensions [13]. This specific geometric aspect ratio enables the use a membrane approach. This issue allows the study of complex situations at a moderate computational cost. The fluid sheet will be geometrically described by means of a membrane representing its mid-surface. Let h and v denote the sheet thickness and the mean velocity vector in the mid-surface of the membrane respectively. During sheet inflation, the sheet motion will be governed by the equations of mass and momentum conservation combined to a constitutive relationship. In the membrane approach, the thickness h is considered as an unknown and obeys the following continuity equation [5,13]:

$$\frac{Dh}{Dt} + h \nabla \cdot v = 0. \quad (1)$$

In equation (1) expression D/Dt mean denotes the material derivative with respect to time t .

The momentum equation is a balance of several forces: contact forces at the mold surface, inflation pressure, fluid stresses, inertia. By simultaneously considering the moderate dimensions of the part presently investigated and the short time scales involved, gravity effects are negligible. The momentum equation is weighted by the thickness h and is given by [5,13]:

$$\nabla \cdot N + f_p = \rho h \frac{Dv}{Dt}. \quad (2)$$

In equation (2), ρ is the fluid density, f_p is a surface force which stands for the inflation pressure, while N is the tensor of contact forces per unit length. N is obtained by weighting in h the extra-stress tensor T built by using the assumption of stress free inner and outer surfaces of the membrane. For a Newtonian fluid, the extra-stress tensor T is given by [4,5]:

$$T = 2\eta D. \quad (3)$$

In equation (3) η is the fluid viscosity and D is the rate of deformation tensor.

The treatment of the sheet – cavity contact is an important ingredient in the simulation. In absence of contact, the location x of a fluid particle is controlled by kinematic equation [4]:

$$\frac{\partial x}{\partial t} = v. \quad (4)$$

When a fluid particle enters into contact with the mould, its relative motion with respect to the mould wall vanishes, and equation (4) is replaced by a velocity condition. This new condition is introduced by means of a penalty formulation [4,13]:

$$f = k(v - w). \quad (5)$$

In equation (1) k is the penalty coefficient and w is the mould velocity.

During sheet inflation, w vanishes. Wall slipping at contact may also be taken into account [4,5].

The finite element method is used for solving the flow governing equations (1) and (2) with the kinematic equation (4). In the case displayed in Fig. 2, the mesh covering the sheet domain contains 40856 triangular surface elements. The time integration of equations (1), (2) and (4) is performed by means of a time-marching scheme.

3. Process description

The object considered in the Polyflow simulation is axially symmetric cub, whose shape and dimensions are illustrated below. Fig.2 illustrated the initial configuration of sheet and mold cavity

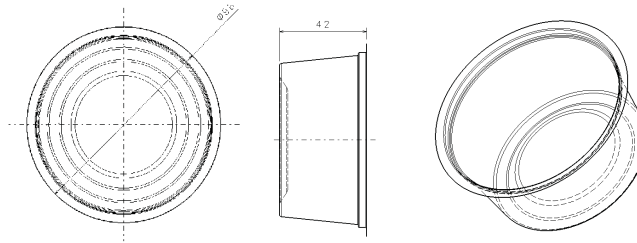


Fig. 1. Considered model [9]

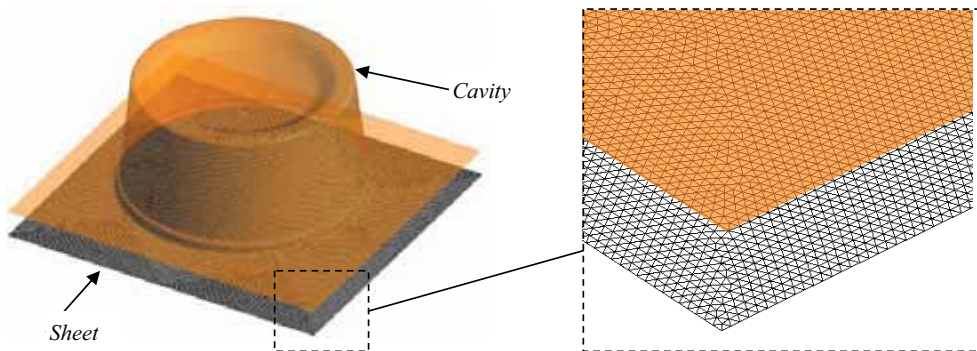


Fig. 2. Initial configuration of polymer sheet and mold cavity with sheet MES grid configuration

position adopted for the simulation run. Sheet and mold are located $s = 10$ mm to each other. Sheet dimensions are 120×120 mm and initial thickness is $g = 1$ mm. The material for the sheet is the PP, which have a temperature of $T = 150$ °C, viscosity $\mu = 8630$ Pa•s and density $\rho = 0.9$ g/cm³ and was used in thermoforming process in rang of temperature $(150 \div 200)$ °C [12]. The run of the

whole process starts with the closure of the mold. The mold is moving with a velocity $v = 50$ mm/s. Then blowing pressure is accompanied with a value of $p = 0.5$ MPa and running until the cup is blown. Total time blowing process simulation is 1 second. Seventh cases of blowing sheet were considered, six with uniform temperature across the sheet (150, 160, 170, 180, 190 and 200°C) and one with optimized temperature profile in range (150÷200)°C. An established criterion for a minimum wall thickness in the final product was 0,3 mm.

4. Simulation results and their analyses

Realized simulations generated series of results, which the selected part is presented below. Fig. 3 shows a comparison the distribution of thickness cup obtained from the sheet with constant and varied temperature distribution, along a given line of measurement. An established optimized criterion for a minimum wall thickness (0,3 mm) in the final product was achieved only for case 7, in which the temperature of sheet was optimized. Presented 1-6 simulations showed significant differences in the value of the cup wall thickness distribution compared to the case 7. Visible improvements of the wall and corner thickness distribution were observed in case 7. Graphical

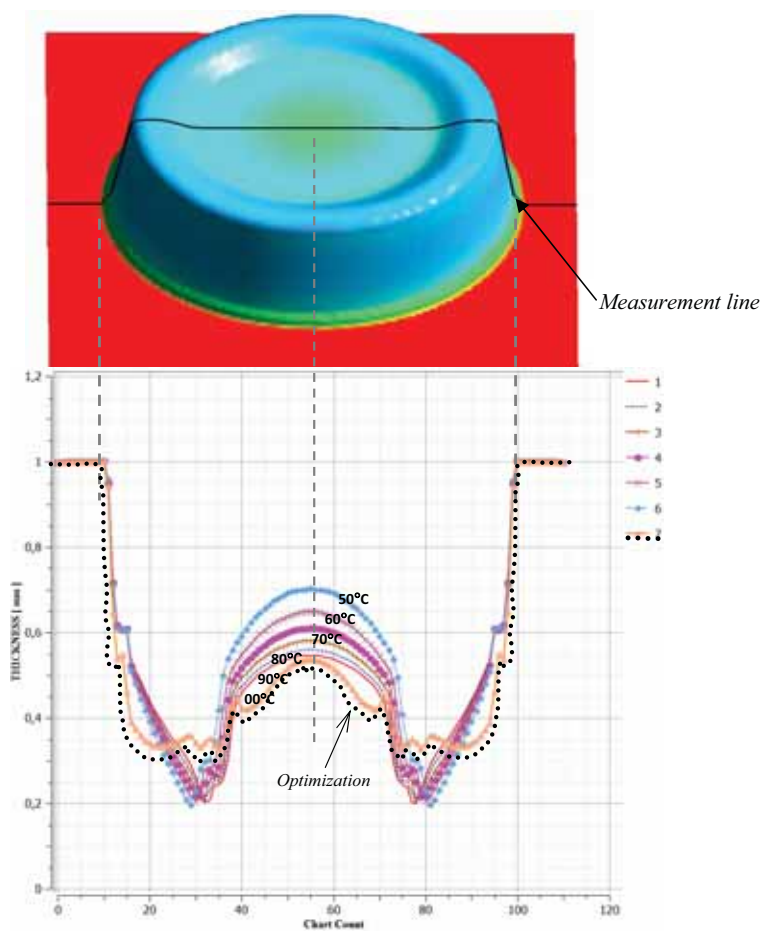


Fig. 3. Comparison part thickness distribution along the measurement line: 1 – sheet with temperature $T = 150^{\circ}\text{C}$, 2 – sheet with temperature $T = 160^{\circ}\text{C}$, 3 – sheet with temperature $T = 170^{\circ}\text{C}$, 4 – sheet with temperature $T = 180^{\circ}\text{C}$, 5 – sheet with temperature $T = 190^{\circ}\text{C}$, 6 – sheet with temperature $T = 200^{\circ}\text{C}$, 7 – sheet with optimized temperature $T = (150\div 200)^{\circ}\text{C}$

display before and after blowing container for two cases is shown in Fig. 4 and Fig. 5.

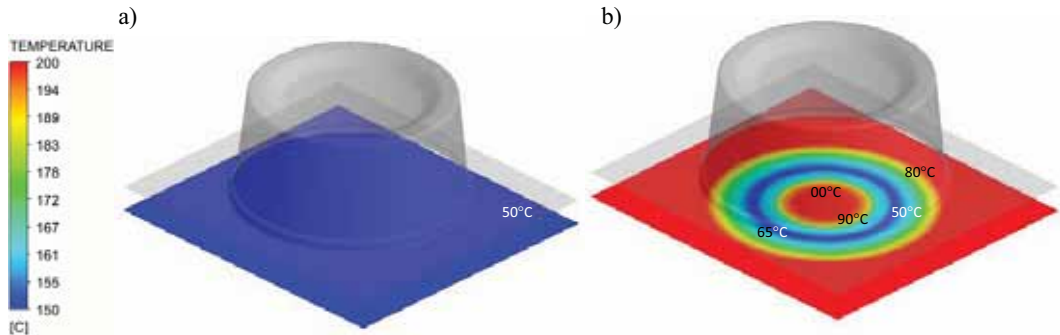


Fig.4. Schedule sheet temperature: a) constant $T = 150^{\circ}\text{C}$, b) optimized temperature profile $T = (150\div 200)^{\circ}\text{C}$

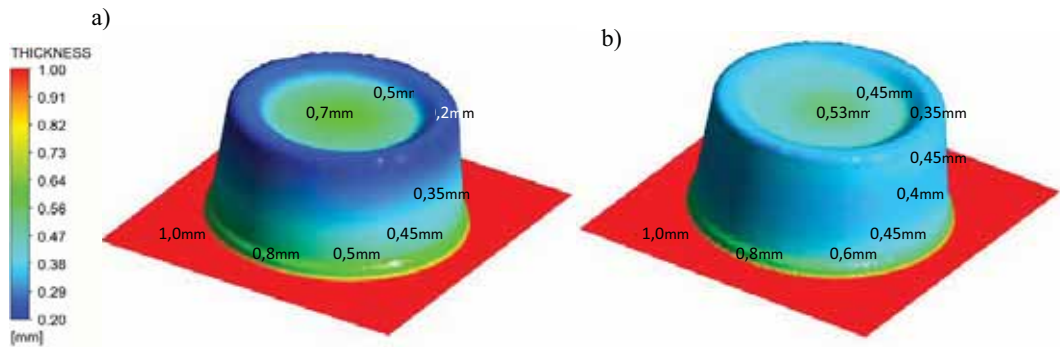


Fig.5. Final part thickness distribution for: a) constant temperature $T = 150^{\circ}\text{C}$, b) optimized temperature profile

5. Final consideration and summary

Assumption of equal heated sheet, caused the largest thinning container, and the most exposed to loss of continuity of the material were the corner of the packing (Fig. 4a, 5a). Completed subsequent simulations for different ranges of constant temperatures indicate a gradual bottom packaging thinning with increasing initial temperature of the sheet.

However a significant influence of the sheet temperature on the corner thickness isn't noticed. However, next three carried out optimized simulations with modified and diversified field temperatures while heating the sheet, considerably reduce differences in wall thickness distribution.

They achieved good results for the variant described on fig. 4b, 5b, for which achieved better wall thickness distribution with smaller thickness differences. The best results were achieved in corners where the value of the thickness is averaging 0.35 mm (and was below 0.2 mm). On the circumference of the package was improved wall thickness distribution in average range 0.4÷0.6 mm (was 0.25÷0.5mm). It provides the greater structural stiffness for the package while using.

Software Ansys Polyflow, enables to carry numerical experiment in the range of phenomena modeling during the thermoforming process. By steering specific sections of the immersion heaters it is possible to get the more profitable wall thickness distribution of formed elements. Especially in the case of complex geometry we have new opportunities of applying the technology

of the vacuum forming. Numerical analyses are reducing the financial outlays and are shortening the time of starting production of new thin-walled thermoforming products.

Applying the Ansys Polyflow program can support technical production steps like optimizing the process in the range of wall thickness distribution what in the end the field of the tolerance is narrower and increasing product quality.

References

- [1] Berdyshev, B., Hosseini, H., Modeling of deformation processes in vacuum thermoforming of a pre-stretched sheet, *Polymer-Plastics Technology and Engineering*, 45, pp. 1357–1362, 2006.
- [2] Bourgin, P., Cormeau, I., *A first step towards the modeling of the thermoforming of plastic sheets*, *Journal of materials processing technology*, 54, pp. 1–11. 1995.
- [3] Carlone, P., James, L., *Finite element analysis of the thermoforming manufacturing process using the hyperelastic Mooney-Rivlin model*, Springer-Verlag Berlin Heidelberg, pp. 794–803, 2006.
- [4] Debbaut, B., *Prediction of extensions in 3-D blow moulding simulation*, *Journal of Reinforced Plastics and Composites*, 16, pp. 1255–1262, 1997.
- [5] Debbaut, B., Homerin, O., *A comparison between experiments and predictions for the blow molding of an industrial part*, *Polymer Engineering and Science*, 39, pp. 1812–1822, 1999.
- [6] Dong, Y., Lin, R. J., *Finite element simulation on thermoforming acrylic sheets using dynamic explicit method*, *Polymers & Polymer Composites*, 14, pp. 307–328, 2005.
- [7] Klein, P., *Fundamentals of Plastics Thermoforming*, Morgan & Claypool Publishers, Ohio University, 2009.
- [8] Piecyk, L., *Termoformowanie wyrobów wielkogabarytowych*, *Laboratorium*, 7, pp. 27–31, 2006.
- [9] Sykutera D., Pepliński K.: *Zastosowanie oprogramowania Ansys-Polyflow do wspomagania wytwarzania opakowań formowanych próżniowo*. *Inżynieria i Aparatura Chemiczna* 1/2011.
- [10] Warby, M. K., Whiteman, J. R., *Finite element simulation of thermoforming processes for polymer sheets*, *Mathematics and Computers in Simulation*, 61, pp. 209–218, 2003.
- [11] Wiesche, S., *Industrial thermoforming simulation of automotive fuel tanks*, *Applied Thermal Engineering*, 24, pp. 2391–2409, 2004.
- [12] Żenkiewicz, M., Szach, A., *Wybrane problemy termoformowania materiałów polimerowych*, *Polimery*, 55, pp. 337–350, 2010.
- [13] Ansys Polyflow User's Guide, Ansys Inc., 2010.



DESIGN OF EXTRUSION DIE FOR PLASTIC PROFILE USING ANSYS POLYFLOW SOFTWARE

Karol Pepliński, Arkadiusz Mozer

University of Technology and Life Sciences in Bydgoszcz
ul. Prof. S. Kaliskiego 7, 85-789 Bydgoszcz, Poland
tel.: +48 52 3408224, fax: +48 52 3408222
e-mail: karolpep@utp.edu.pl

Abstract

Extrusion is one of the most widely used processes for polymer processing. Example: extrusion is a technique for producing film, pipe, sheet, profiles, cable and coatings in coextrusion process. The main tool used in this process for the manufacturing final shape product is die. The task of this article is to design the last part of extrusion die (die land) for plastic profile, using numerical simulation. In this paper was presented methodology of numerical simulation for the die design. A commercial computer fluid dynamics program Ansys Polyflow was used to design the die passage. The objective of the simulation is to determine the die passage that results in a balanced mass flow exiting the die that closely matches the target profile. The die land shape modification with using optimization algorithm is very helpful to obtain geometry and dimension of extrudate desired profile.

Keywords: profile extrusion, die design, die land, inverse die design, simulation Ansys Polyflow,

1. Introduction

Extrusion is one of the main processing methods for production of thermoplastic parts. It is used to manufacture pipes, films, fibers, cables, wires, and various continuous profiles [8]. In each type of extrusion, the polymer is forced through a die to create the desired shape [11]. Extrusion dies vary in shape and complexity to meet the demands of the product being manufactured. There are five basic shapes of products made with extrusion dies: 1) sheet dies; 2) flat-film and blown-film dies; 3) pipe and tubing dies; 4) profile extrusion and 5) co-extrusion dies. Furthermore, each product type has unique hardware downstream of the die to shape and cool the extruded melt [9].

In extrusion die design there are two main issues to be solved: how to make the flow distribution more uniform and how to anticipate post-extrusion effects. Trial and error procedures have been the common base to design these tools. The main objective to achieve when designing a new die is to reach the best possible production rate at the highest quality product level with dimensional accuracy, aesthetics and mechanical performance [2,4,6].

Predicting the required die profile to achieve the desired product dimensions is a very complex task and requires detailed knowledge of material characteristics and flow and heat transfer phenomena, and extensive experience with extrusion processing [9]. Design of the dies for extrusion of products having complicated cross sectional shapes is still an art rather than a science. Die design for a new product is developed on the basis of previous experience and experimentation. In many case costly experiments and in-plant trials can be replaced by numerical simulation [1,6]. Several commercial polymer flow simulation programs are used for profile die

design today. For example: Ansys Polyflow, Flow 2000, Dieflow, HyperXtrude [10]. Numerical simulation has the potential to uncover important interior details of the extrusion process, such as velocity, shear stress, pressure, and temperature fields in the region of interest, which is not possible to do experimentally [9,12]. Typically, designers know the requested shape of the final profile but do not know the corresponding die shape. The required die shape can be determined by method inverse die design. For example Ansys Polyflow program implements an “inverse extrusion” solution algorithm, which computes the shape of the die exit (die land profile) required to achieve the target profile dimensions at the exit of the free surface domain. The program solves for the shape of the die land that will achieve the target profile after die swell occurs [5,9,11]. In the design stage it is important that die land length profile should be average 10 times longer than the thickness of thick extrudate portion place to relax the viscoelastics stresses in the melt before leaving the die and forms the shape of the extrudate leaving the die. The die land profile has the required shape to compensate for extrudate deformation after the die (die swell and drawdown) and yield the desired shape downstream [9].

2. Ansys Polyflow CFD software capabilities

Ansys Polyflow is a finite element computational fluid dynamics (CFD) program designed primarily for simulating applications where viscous and viscoelastic flows play an important role. The flows can be isothermal or non-isothermal, two- or three-dimensional, steady-state or time-dependent. Ansys Polyflow is used primarily to solve flow problems in polymer and rubber processing, food rheology, glass-work furnaces, and many other rheological applications. This program can perform a number of complex calculations such as multi-domain simulations, coextrusion of several fluids, three-dimensional extrusion and time-dependent calculation of free surfaces [14].

Ansys Polyflow consist of few interdependent modules used to prepare analyze geometry, define data, calculations and presents results. Typical flowchart for numerical simulation was presented on figure 1.

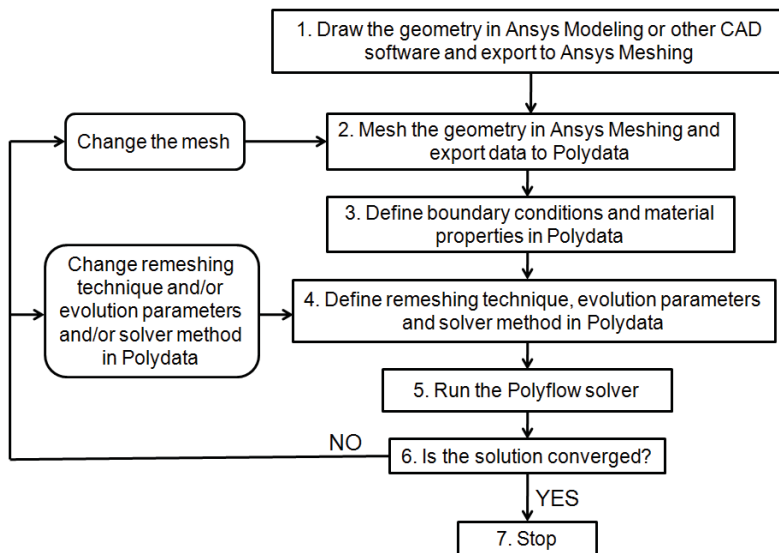


Fig. 1. Flowchart for numerical simulation using Ansys Polyflow [14]

3. Modeling and numerical algorithm of die design

This problem deals with the flow of a Newtonian fluid through a three-dimensional die. The design process begins with a target product shape. In this work, the product is a hollow chamber profile (Fig. 2a) – 40 mm x 50 mm rectangular cross section with inside 5 mm rib. Due to the symmetry of the die, only one-half of the passage is modeled as shown in Fig. 2b. In our case we considered only a die land profile, which is one of the most important tooling place in extrusion process, because it must cope with the phenomena occurring in the course of flowing plastics – to compensate for extrudate deformation after the die and yield desired shape downstream [9]. The domain for the problem is divided into four sub-domains (as shown in Fig. 2b: Sd.1, Sd.2, Sd.3, Sd.4) so that specific remeshing algorithms can be applied in each sub-domain to accurately predict the die profile. Subdomain 1, 2 and 3 represent the die where the fluid is confined, while subdomain 4 represent the extrudate that is in contact with the air.

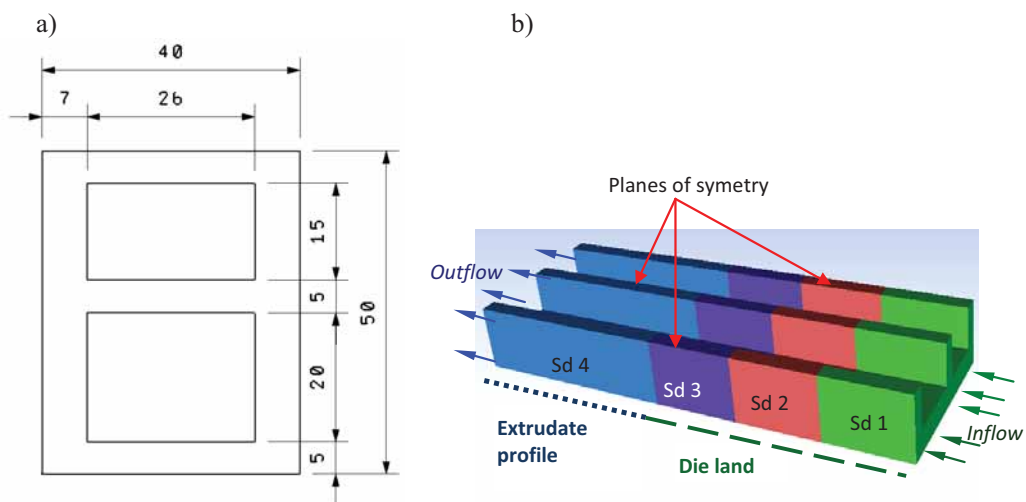


Fig. 2. Considered model: a) dimensions of the profile, b) initial configuration implemented to the simulations

The objective of the simulation is to determine the die passage that results in a balanced mass flow exiting the die and an extrudate shape downstream of the die that closely matches the target profile. The shape of the die exit is determined by solving an inverse flow problem where the target profile is given as the downstream shape of the extrudate. The program computes the die exit shape that results in the target profile downstream of the die after melt velocities equalize in the free-surface region.

A HDPE is used as extrusion material in numerical simulations and the Bird-Carreau viscosity model is used to characterize the shear rate dependence of viscosity [14]:

$$\eta = \eta_{\infty} + (\eta_0 - \eta_{\infty}) \cdot \left(1 + \left(\lambda \cdot \dot{\gamma} \right)^2 \right)^{\frac{n-1}{2}}, \quad (1)$$

where:

η – viscosity,

η_0 – zero share rate viscosity,

η_{∞} – infinite shear rate viscosity,

λ – time scale,

n – power-law index.

In this study it was assumed that temperature distribution of polymer is uniform and equal 180°C and for this temperature related parameters for Bird-Carreau viscosity model equals: $\eta_0 = 5630 \text{ Pa}\cdot\text{s}$, $\lambda = 0,32$, $n = 0,64$. The polymer melt flow is assumed to be incompressible [7,13,14]:

$$\nabla \cdot \mathbf{v} = 0. \quad (2)$$

Gravitational and inertial forces are neglected. The momentum equation yields a balance between viscous and pressure forces [13]:

$$\nabla \cdot \mathbf{p} = \nabla \cdot \boldsymbol{\tau}_{ij}. \quad (3)$$

In this study it is also assumed that viscoelastic effects were neglected. Fully developed velocity profile is assumed at the inlet $Q = 10000 \text{ mm}^3/\text{s}$, and no-slip boundary condition is applied at the die wall.

4. CFD simulation results and their analyses

CFD simulation was carried out to obtain target final hollow profile design under assumptions and parameters. In the first stage of simulation authors obtain the profile result without compensation Barus and other flow effects, what was shown in Fig. 3. Wrong shape of final product (inter alia) is caused by different local pressure and share rate during flow for the die passage. Other difficult during extrusion in this profile shape is different wall thickness (5 and 7 mm). Different local thickness caused faster flow polymer particles in thickness section ($v = 21,25 \text{ mm/s}$), what is showed in figure 3. Based on the results obtained from the first simulation, in next step with Polyflow implements an “inverse extrusion” solution algorithm, realized automatic calculation to obtain final desired shape. Program change the die land geometry (60 mm length) to find target final shape of our extrudate hollow profile in ten iterations. These results are visible in figure 4, 5 and 6. In each place of extrusion land observer can see how the polymer flow and see if they have example areas with a slow movement of polymer material, which can cause its local degradation. Final result of realized simulation was achieved.

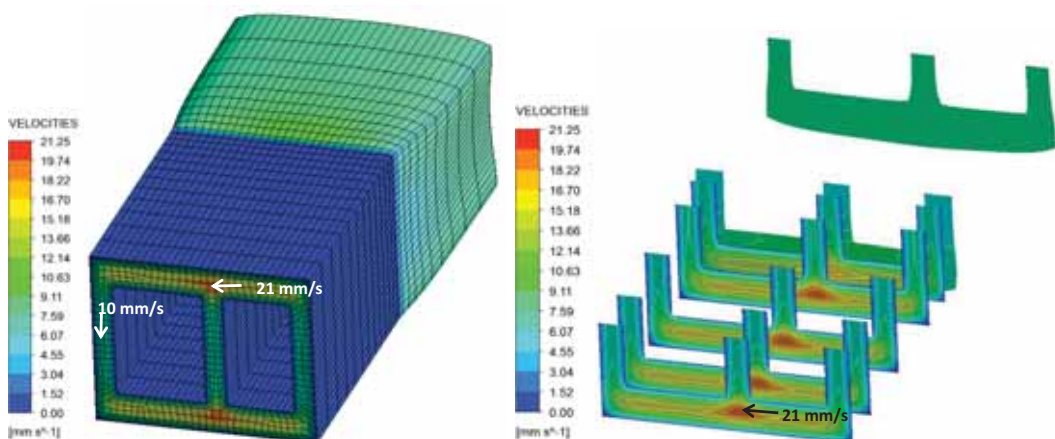


Fig. 3. Velocity distribution for the die without optimized die land

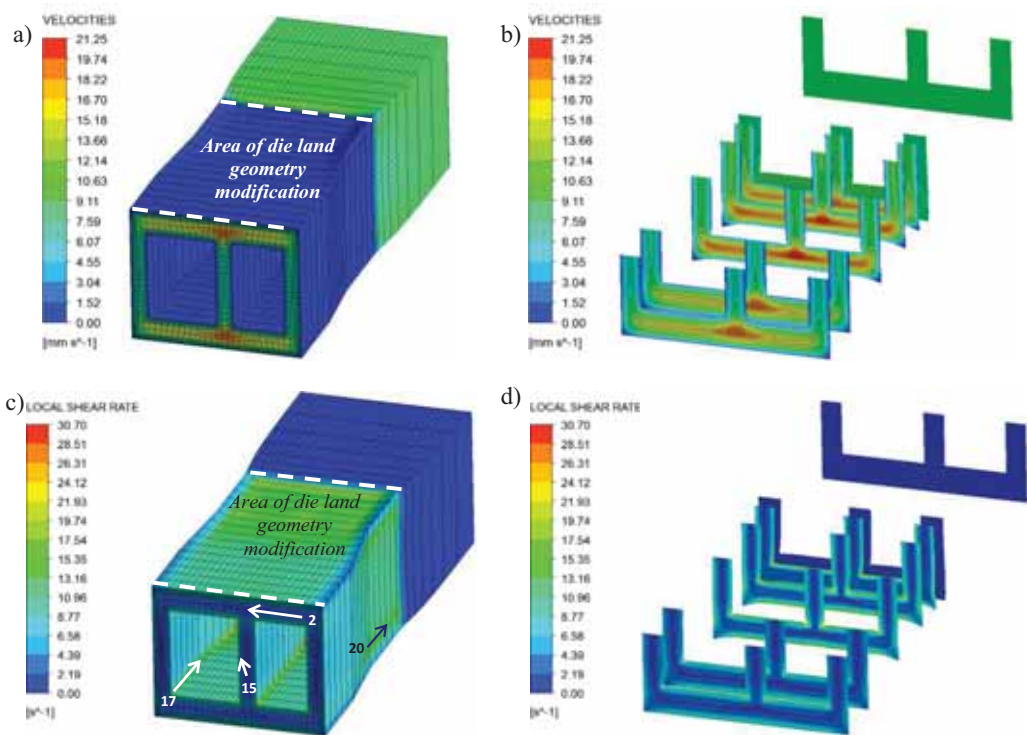


Fig. 4. Velocity (a, b) and local share rate (c, d) distribution fort the die with optimized die land

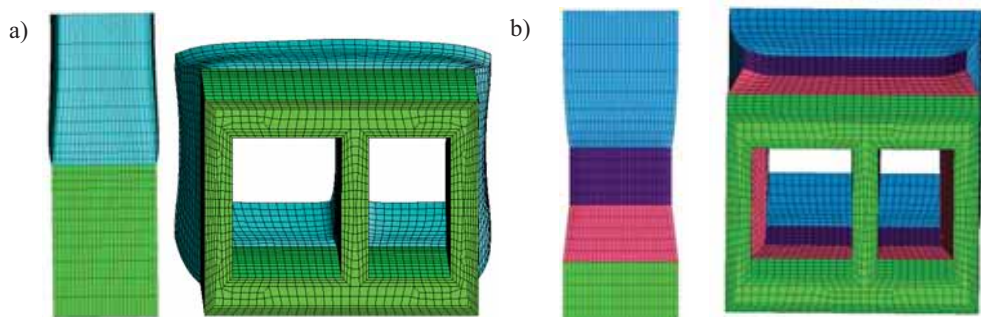


Fig. 5. View of extrudate shape profile with: a) non-optimized shape of die land, b) optimized shape of die land

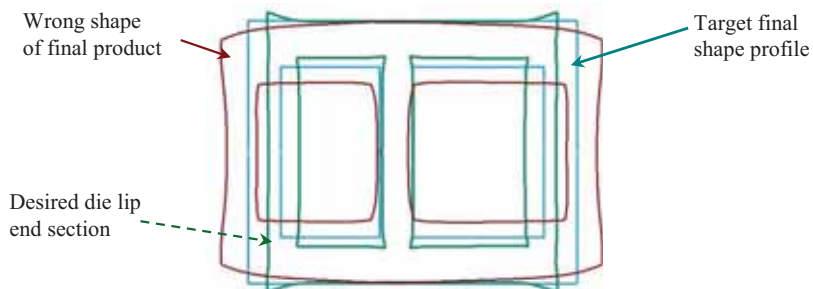


Fig. 6. A cross section in die lip section, compared with outlet section obtain from non-optimized shape of die land and optimized shape of die land

5. Final consideration and summary

Design of extrusion dies for plastic profile is a complex task because the extrudate final profile dimension depends not only on the die shape design, but also on the plastics properties and technological extrusion process parameters. Overall design of extrusion process should include each plate of extrusion dies: mounting, adapter, transition, preland and die land plate. It is important to know that two last plates have the most significant role in extrusion stage. In our study we only show the capabilities of geometry prediction in the last die land plate for the made an assumption. The powerful of Polyflow software is in predict of the preland and die land geometry for the individual complex geometry. Each simulation process is more shorter and more costly than trial end error iterations.

Engineering Polyflow simulation can provide crucial help to manufacturing extrusion tooling that must resolve critical issues related to reality of industry: cost and time savings in developing extrusion dies.

References

- [1] Biba, N., Stebunov, S., *3D FEM Simulation system for optimization of profile extrusion*, Quantor Form, 2004.
- [2] Carneiro, O. S., Nobrega, J. M., Pinho, F. T., *Computer aided rheological design of extrusion dies for profiles*, Journal of materials processing technology, 114, pp. 75–86, 2001.
- [3] Carneiro, O. S., Nobrega, J. M., Pinho, F. T., *Flow balancing in extrusion dies for thermoplastic profiles*, International Polymer Processing, 3, pp. 1-11, 2004.
- [4] Carneiro, O. S., Nobrega, J. M., *Recent developments in automatic die design for profile extrusion*, Plastics Rubber and Composites, 33, pp. 400-408, 2004.
- [5] Graham, A. L., Tran-Cong T., *An inverse problem by boundary element method*, Polymer Engineering and Science, 1996.
- [6] Gonçalves, L., Neves, T., *DieTech - A Virtual Reality Environment For Extrusion Dies*, University of Minho.
- [7] Kevin, R. J., Ellwood, T. C., Wilkes, O. J., *Three – dimensional streamlined finite elements: design of extrusion dies*, International journal for numerical methods in fluids, 14, pp. 13-24, 1992.
- [8] Kim, J., Youn, J. R., *Three dimensional flow analysis within a profile extrusion die by using control volume finite-element method*, Korea - Australia Rheology Journal, 13, pp.97-106, 2001.
- [9] Kostic, M. M., Reifschneider, L. G., *Design of Extrusion Dies*, Encyclopedia of Chemical Processing, pp. 633-649, 2006.
- [10] Kostic, M. M., Reifschneider, L. G., *Computational design of a U-profile die and calibrator*, ANTEC, pp. 246 - 250, 2004.
- [11] Metwally, H., *A Methodology for Superior Die Design - Combining the Best of Art and Science*, Fluent INC.
- [12] Sienz, J., Goublomme, A., Luege, M., *Sensitivity analysis for the design of profile extrusion dies*, Computers and Structures, 88, pp. 610-624, 2010.
- [13] Yilmaz, O., Hirkkopru K., *A method to obtain balanced flow in profile extrusion dies*, ANTEC, pp. 1566-1571, 2009.
- [14] ANSYS POLYFLOW User's Guide, Ansys Inc., 2010.



SELECT TECHNICAL ASPECT OF ENERGY USING AND MANAGEMENT IN INJECTION MOLDING PROCESS

Karol Pepliński

University of Technology and Life Sciences in Bydgoszcz
ul. Prof. S. Kaliskiego 7, 85-789 Bydgoszcz, Poland
tel.: +48 52 3408224, fax: +48 52 3408222
e-mail: karolpep@utp.edu.pl

Abstract

Technical aspect of energy using and management in Poland industry of injection molding plant are not well known. Energy management is assignment of increasing importance to plastics processors. However there is no well-known structure for measurement, estimation and prediction. Many technical workers sometimes are trying to measure something, but don't know techniques how to do it in a good way. Next then get the bad answers. This paper describes and illustrates some basic techniques and aspect of measurement, estimation and prediction. This engineering element can be used for most plastics processing companies. More importantly, the paper looks at how this information can be used to get better both operations and performance in injection molding industry and per analog in other plastics industry.

Keywords: *energy using, management, plastics processing, injection molding*

1. Introduction

The idea of aspect in energy using and management is relatively new to the injection plastics industry but is now being strongly driven by the recent rises in world energy costs and the rising unreliability of supplies for the near future. Twelve years ago a topic of energy using and management was a marginal activity in Europe. It was not easy attract the interest of plastics industry in energy management. During the time this thinking was changing and today this area is a real business issue. Very often this area is not visible yet in Poland industry, but this thinking are slowly changing. The reason of this situation is small amount of specialized institution in energy management of plastics industry [3, 9]. Energy costs represent the third largest variable cost (after materials and direct labour) and in some companies is even the second largest variable cost. No information on energy consumption by individual plant (site) in the plastics processing technologies, not to take steps to reduce energy consumption in each technical process can be fatal to the company [1, 4, 5].

Aim of this work is describes and illustrates some basic techniques and aspect of measurement, estimation and prediction that can be used for most plastics processing companies (internal benchmarking) [3]. Also looks how this information can provide real benefits in realized plastics process. The basic structure of energy using and management system in plastics processing is shown in Fig. 1. Example graph about typical average energy consumption in plastics plant is show in Fig. 2. The main energy usage and cost is in processing machinery and services (92%). Lighting, heating, and offices are minor energy costs (8%) [7].

We will first look at concept base and process load in internal benchmarking [3] for the site with hypothetical example for injection molding and next present some area of technical improvement affecting minimize energy using in injection molding process and show results.

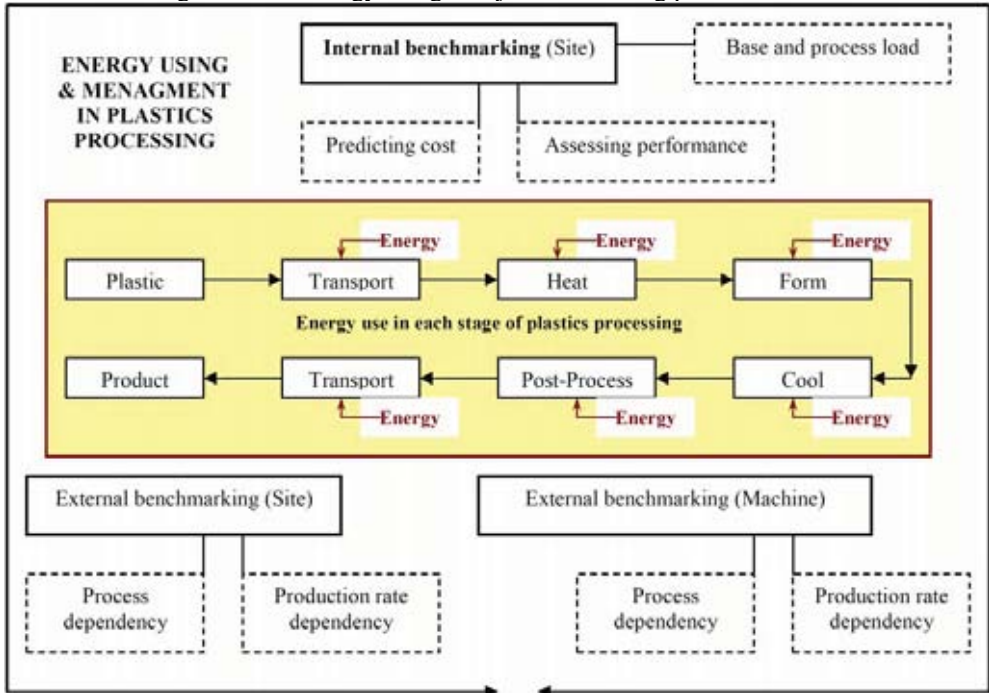


Fig. 1. System of energy using and management in plastics processing

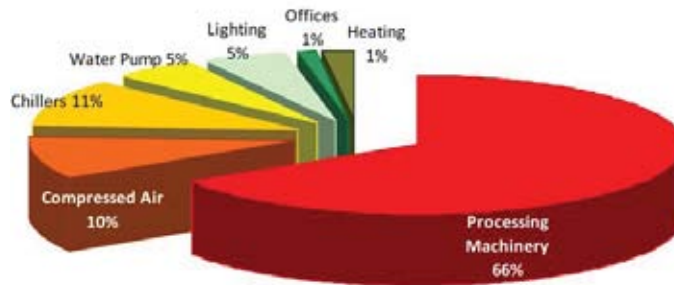


Fig. 2. Average energy use in plastics plant [7]

2. Base and process load in internal site benchmarking

The base load inform about energy consumption when plastic machine is stopped but all service media are available. Most factories will have a base load, which will be present even when there is no production. This may be background heating, water pump, light, compressed air and equipment that have been left on standby. Process load inform about using energy during running processing and has different value for plastics techniques ex. injection molding, extrusion [10].

In injection molding processing site, also in other plastics manufacturing method, it is possible to determine the base and process/variable loads for the site. This is possible when simple energy

usage and production volume data are available. On the start it will be illustrate the method using a sample injection molding factory (hypothetical) and next information that can be obtain from this data. There are two basic steps to get base and process load [3]:

- write or record factory output (in kg) for a number of weeks or months and write at this same time the energy usage (in kWh). Some hypothetical data for injection molding factory shown in [Tab. 1](#).
- next plot the energy usage (in kWh) versus production level (in kg) in a Excel chart. A graph with this data is shown in [Fig. 3](#). Point graph are with trend line (linear) and the best fit. Visible intersection of the line 'kWh' axis indicates the base load of factory. Base load is like something no effective production but all service media and injection molding plant are available. The slope of the best fit line is the process load. Observer manager can see the average energy consumption for each kilogram of processing plastics. In our case the equation of the best fit liner is:

$$kWh = 1,6 \cdot Production\ volume + 143297. \quad (1)$$

The R^2 value about 0,95 indicates that the data set is relatively consistent with the function line. Reading of this line can show that the base load is a constant energy cost for 143297 kWh and process load is 1,6 kWh/kg of polymer processed. Next observer can obtain the middle cost of base load assuming 0,40 PLN/kWh, which is 57318 PLN/month or 687825 PLN for a year. In literature data can see that base load is about 20% even to 50% of factory energy consumption [1].

Tab. 1. Energy usage and production volume date during 1 year (sample hypothetical data)

Num.	Month	Energy usage, kWh	Production volume, kg
1	January 2009	425000	181000
2	February 2009	460000	198000
3	March 2009	505000	249000
4	April 2009	440000	205000
5	May 2009	492000	210000
6	June 2009	518000	225000
7	July 2009	535000	220000
8	August 2009	460000	205000
9	September 2009	680000	350000
10	October 2009	720000	340000
11	November 2009	680000	330000
12	December 2009	400000	150000

Reduction of the base load can be generally made and achieved without influence on production part rate. It is very important to making some technical aspect that influence on reduction energy using. The process load inform us (for our hypothetical sample factory, [Fig. 1](#)) that for each polymer kilogram whole plant using 1,6 kWh and how management and efficiency is in this place.

Reducing the line slope is in more case difficult to achieve [3]. However knowledge of this information is very important to start doing technical service improvement and note the information about base/variable load.

In other hand equation (1) can be name Performance Characteristic Line (PCL) [1], because this line provides an operational signature of the plant that is closely related to the way the plant management runs the plant.

Base load and process load for different plastics processing technique have different value. Example extrusion typically has a lower process load (flatter slope of the PCL) than injection molding. In turn extrusion blow molding has a relatively low base load but a higher process load than extrusion or injection. Note is also that extrusion plus thermoforming generally has a process load in the range of injection molding [10].

Typical example of site energy day usage over the time can be note in each hour. This is very important for understanding how plastic machine work and for get invaluable information on how to reduce the energy cost (Fig. 4). This information should be analyzed to critical asses where and when energy is being used. In unproductive injection molding time, longer then (30-50) minutes, sometimes less energy will be consumed if machine turn off and next turn on [2].

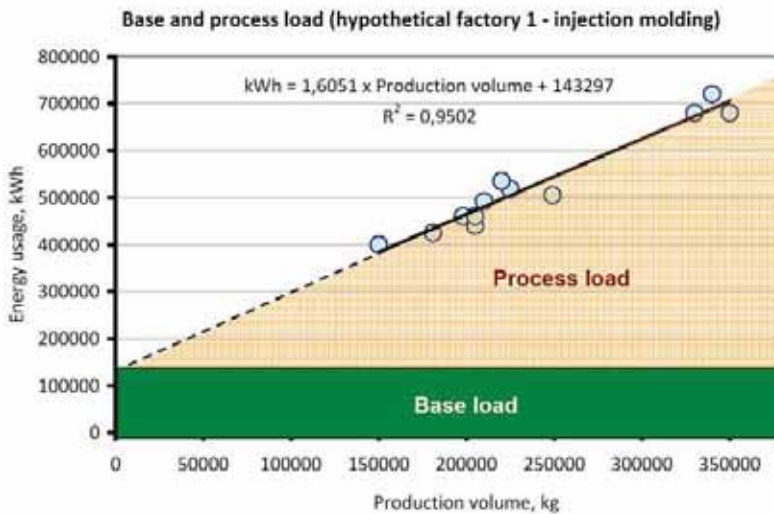


Fig. 3. Base and process load for hypothetical injection molding plant/machine

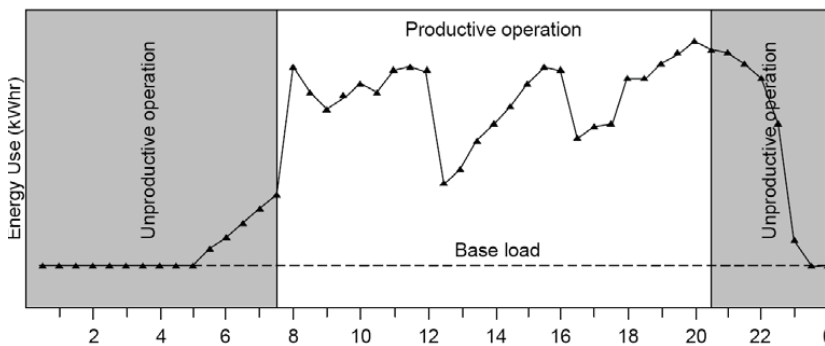


Fig. 4. Typical example site energy usage over time [2]

3. Technical improvements affecting minimize energy using in injection molding

It is commonly known that often with most machines, the initial cost of an injection molding machine will be less than the cost of energy used during its lifetime [4]. The energy cost can be even more for machines that are not energy efficient. Though it may cost more initially, energy efficiency is more economic in the long term. Also other aspects are important not only machine. Smaller energy using can be achieved for other basic technical service equipment and elements

which include: motors, compressed air, cooling fluid and construction of injection mould etc. In Fig. 5 presented the area where technical improvement can be made to achieve lower energy consumption. There are four basic areas: processing, utilities, materials, administration offices [2].

Motors are the largest energy user in injection molding processing. Turning motors off when they are not using (and it is possible) is one of the most effective methods of reducing energy usage. It should be know that maximum efficiency of motor is when they have right size. Variable speed drives (VSDs) allow motors to be slowed down to match the demand and offer energy savings and improved process control. VSDs are one of the most important tools available to plastics processors to reduce energy usage and costs. Motor management of their technical aspect is a necessity for modern plastics processing. This allows plastic sites to make the repair/replace decision before the motor fails [5].

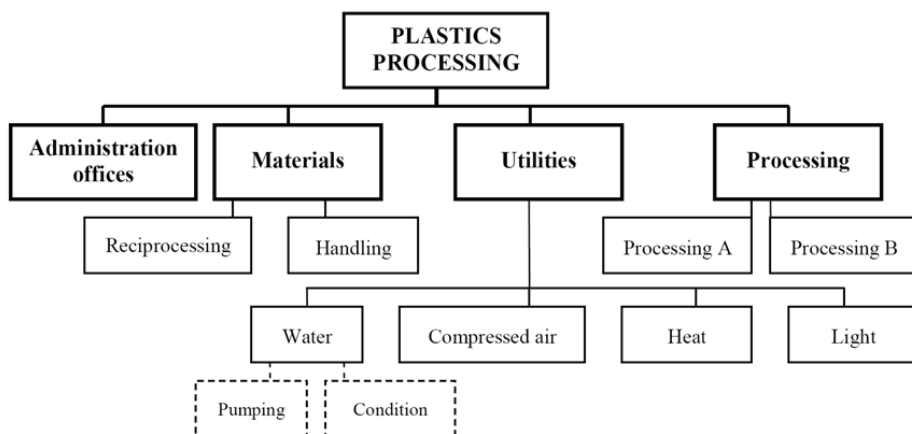


Fig. 5. Opportunities for energy savings through technical investment [2]

Often in injection molding plants other second basic using medium is compressed air. Producing of this medium is not cheap. The biggest problem in compressed air installation is leakages. Even this smallest installation leakages uses between 20 to 40% of producing air medium. Only little hared leakage can use 1000 kWh/year. It is important economical aspects. Sum of this leakages give a big amount of the energy which is not free. Moreover in injection molding plant compressed air usage should be reduced by using other means of power where possible. For air supply power tools the delivered power costs 7-8 times that of direct electric drives. Besides this compressed producer should only generate required demand pressure for machine sites [8].

Thermal efficiency of injection molding system can also be improved by barrel and pipe line insulation. Product cooling time is generally more than 50% of the cycle time. Efficient cooling can greatly reduce cycle times and energy usage - a double benefit. Conformal cooling is very important technical aspect to short cycle time and using energy [2].

Each technical improvement which influence on less energy consumption can give different benefits but it is always a payback. Overall aspect of equipment and process improvements always give lower energy consumption: lower base and process load. Typical example of this can show on graph comparison (Fig. 6) with energy consumption.

This simple data presentation and equation can also be used to assess the performance of the factory on a monthly basis. The equation of the line of best fit for the data of Fig. 6 is:

$$kWh = 1,5702 \cdot production\ volume + 110000. \quad (2)$$

This equation can be then be used to assess the energy usage for a given production volume in a month, e.g. If the production volume is 100 000 kg, then the predicted energy usage will be:

$$kWh = 1,5702 \cdot 100000 + 110000. \quad (3)$$

Therefore the predicted energy use is 267020 kWh and predicted energy cost is 106808 PLN for the month. For pervious state of technical state machine and equipment the cost will be achieve the value of 136483 PLN. Benefits are visible. Year cost saving is about 356100 PLN. The equation (2) can be used to assess performance and generate production responsibility. This include: determine the volume of material processed in a week/month/year and calculate the energy usage in the future, compare the predicted energy usage to the actual energy usage and if energy usage is higher than predicted energy usage then find what the machine/site/factory did wrong. Also it can be visible when plastics factory using less energy then predicted value.

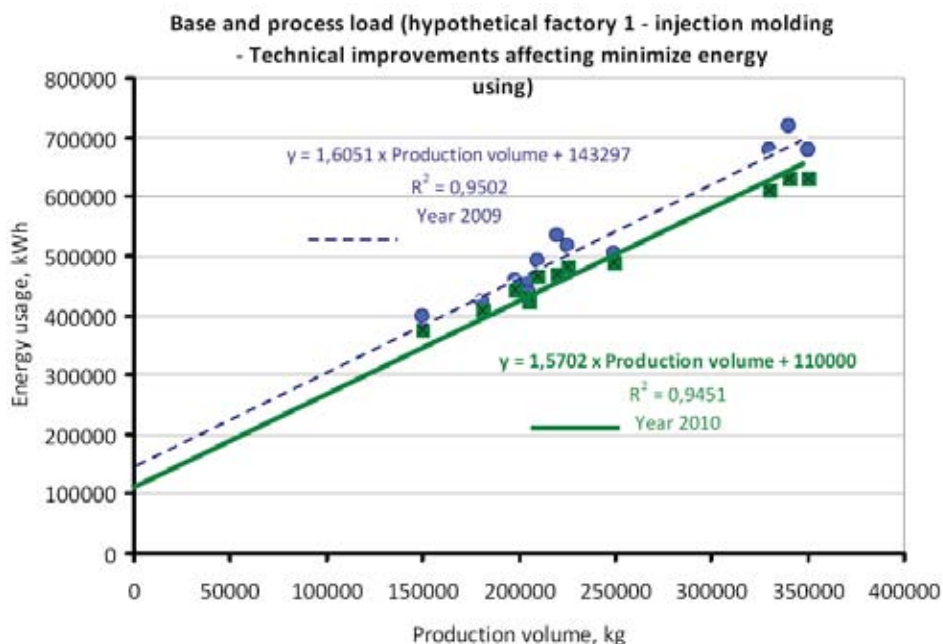


Fig. 6. Comparing base and process load after overall technical improvement with some new injection molding plant and equipment

4. Final consideration

Presented concept on energy using and management for injection molding machines and plant can be using for other plastics machines like extrusion blow molding or thermoforming. Making simple periodic measurements of energy consumption can be extremely helpful to evaluate the plastics processing system performance, as well as planning and cost comparison of energy consumption during processing in the near future (for example: 1month, 1 year). Also, the objective of this paper has been to provide an easily understood structure that will generate real improvement rather than paper and statistics.

Possession of knowledge about technical aspect of energy using and management in injection molding process is really at the sensitivity of energy efficiency, without good management, neither energy efficiency nor any other change in operating practices will be valuable. Energy efficient

injection molding is simply good quality molding practice. It is low-cost and reduces all costs – not just energy costs.

References

- [1] Archila S., Goltzarian S.: *Energy Reduction and Sustainability through Total Energy Management* (TEM), Husky 2009, www.husky.ca.
- [2] Kent R.: *Energy efficiency in plastics Processing. Practical worksheets for industry*, Tangram Technology Ltd. 2007, www.tangram.co.uk.
- [3] Kent R.: Energy management in plastics processing — framework for measurement, assessment and prediction, *Plastics, Rubber and Composites* 2008 vol. 37 no 2/3/4.
- [4] Kanungo A., SwanAll E.: *Electric Injection Molding Machines:How Much Energy Can You Save?* Proceedings from the Thirtieth Industrial Energy Technology Conference, New Orleans, LA, May 6-9, 2008.
- [5] *Guide to energy efficiency opportunities in the Canadian plastics processing industry*, Canada 2007, www.cpia.ca.
- [6] *Accounting for energy efficiency*, Tangram Technology Ltd. 2007, www.tangram.co.uk.
- [7] Kent R.: *Introduction to energy management for plastics processors*. Plastic Technology 2009, www.ptonline.com.
- [8] *Energy management in plastics processing – top tips*, Tangram Technology Ltd. 2007, www.tangram.co.uk
- [9] Jones F. R.: *Strategic Management for the Plastics Industry*, 2003 by CRC Press LLC.
- [10] Kent R.: *Know Your Plant's 'Energy Fingerprint'*, Plastic Technology 2009, www.ptonline.com.



RANGES OF APPLICATION OF SORTING MANIPULATORS

Tomasz Piątkowski, Janusz Szempruch

*University of Technology and Life Sciences
ul. Prof. S. Kaliskiego 7, 85-789 Bydgoszcz, Poland
tel.: +48 52 3408145
e-mail: topiat@utp.edu.pl*

Abstract

In the paper the applications ranges of sorting manipulators of unit loads (cubiform objects – e.g. postal packages) transported on conveyors in the continuous manner are presented. The exploitation properties of manipulators have been assigned on the basis of numeric optimization of the sorting process. Theoretical models (indispensable for optimization) include the development of physical phenomena occurring while interaction between the object and manipulator actuators. The reaction forces of impact character appearing between the object and the working element of manipulator are defined by means of modified non-linear Kelvin model. The frictional proprieties of the object are modelled by the non-linear friction coefficient using B-spline curve of third degree. The kinematic structures of the manipulators (taken into consideration during research) are representative technical solutions of currently applied methods of impulse exertion directing the objects on the new transports lines in the logistic centres.

Keywords: *sorting process, unit load, nonprehensile manipulator, conveyor, optimization*

1. Introduction

The problem of sorting of unit loads exists in transport nodes which characterize big concentration of goods. Sorting process accompanies the tasks of completion and de-completion of the loads' deliveries in the logistic distributional centres, e.g.: at central post offices, warehouses, airports [1]. Division of the loads into suitable directions (according to destination) is performed by means of nonprehensile manipulators, built in conveying transportation system. These manipulators have no gripping devices, and act on the objects through a push, or through a sequence of pushes or strikes.

The contemporary technical solutions of sorting manipulators are equipped with executive elements which cause: scraping the loads from the conveyor (presented in Fig. 1b, c), moving the objects by directionally-oriented field of friction forces (Fig. 1d), or extorting the gravitational objects' motion to the new line of further transportation (Fig. 1a).

Sorting systems are spatially complex, compound and expensive investment undertakings. The optimum technical solution of executive systems of manipulators should be determined depending on assumed intensity flow of handled objects and their physical properties.

In order to carry out the reasonable selection of sorting manipulators, it is needed an access to an objective data characterizing basic usable features – e.g. used by potential investors or designers of transport centres. One of the more important sources of the data collection is the results analysis of numeric optimization of the sorting process – that is the subject of presented

work. The theoretical models have been developed on the basis of selected devices which cover an area of manipulators currently used in the logistic centres and offered by manufacturers.

a)



b)



c)



d)



Fig. 1. Examples of executive systems of sorting manipulators: a) tilt tray [2], b) divert shoes [3], c) active rotary fence [4], d) torsional disks [5]

2. Kinetic structures of nonprehensile manipulators

Simple in its form nonprehensile manipulator the ability to manipulate the object obtains as a result of bond with the transportation functions of conveyors – these manipulators usually cooperate with conveyors (e.g. belt or link-belt). Due to the difference in the use of transportation functions of conveyors the manipulators can be divided into two groups: stationary (Fig. 2a) and stream manipulators (Fig. 2b). Stationary manipulators (Fig. 3) are combined with the supporting structure of the conveyor and stand still with respect to them ($v_R = 0$). Executive elements of such manipulators perform their working motions above the surface of the conveyor and have mostly the form of an active rotary fence (the figs. 3a), also an active fence with translational motion (Fig. 3b), or a system of torsional discs Fig. 3c).

In the stream manipulators (Fig. 4), the role of executive elements is played by segments of the link-belt conveyor. These segments are equipped in additional features which can be in the form of: tilt trays (Fig. 4a), the trays with bearing surfaces covered transverse conveyor belts (Fig. 4b), divert shoes sliding along the slats (Fig. 4c). Working elements of the manipulator (which are also segments of the conveyor) wander in the conveyor with the velocity of loads' stream ($v_R = v$).

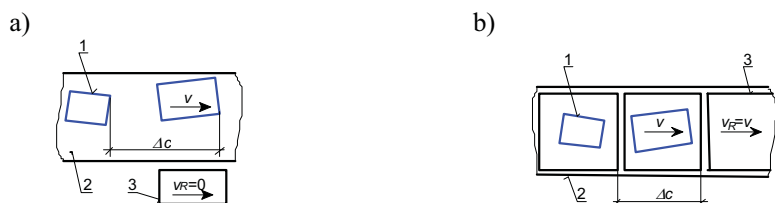


Fig. 2. Nonprehensile manipulators: a) stationary, b) stream; 1 – handled object, 2 – conveyor, 3 – working element of manipulator, v – velocity of load stream, v_R – velocity of manipulator, Δc – distance between heads of loads

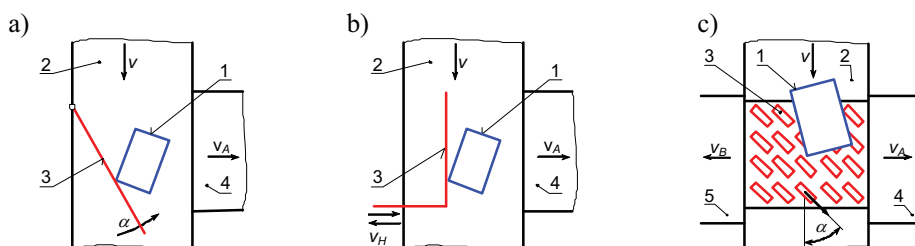


Fig. 3. Examples of kinematic structures of stationary nonprehensile manipulators: a) manipulator with an active rotary fence, b) manipulator with an active fence with translational motion, c) manipulator with torsional disks; 1 – unit load, 2 – main conveyor, 3 – working element, 4 and 5 – delivery lines, v – velocity of transportation of main conveyor, v_A i v_B – velocity of transportation of new transport lines

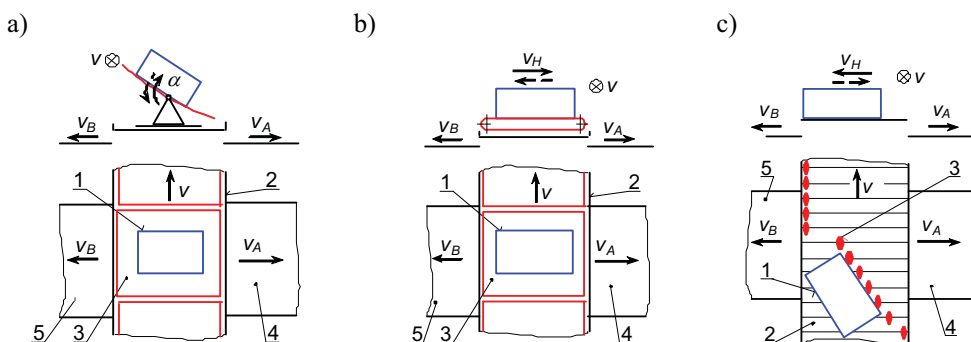


Fig. 4. Examples of kinematic structures of stream nonprehensile manipulators: a) tilt tray, b) belt tray, c) divert shoes; 1 – unit load, 2 – main conveyor, 3 – working element, 4 i 5 – delivery lines, v – velocity of transportation of main conveyor, v_H – velocity of working element, v_A i v_B – velocity of transportation of delivery conveyor

3. Basic assumptions of sorting process models

The indications and indispensable recommendations necessary for design new solutions of manipulators and to define an application ranges of existing sorting devices are obtained from the analysis of the results of numeric optimization [9], [10], [11], [12], [14]). In the study there were used the theoretical models of the sorting process, which include the development of physical phenomena occurring while interaction between the object and manipulators actuators (oblique impact, the dry friction). The reaction forces of impact character appearing between the object and the working element of manipulator are defined by means of modified non-linear Kelvin model [8]. The frictional proprieties of the object are modeled by the non-linear friction coefficient using B-spline curve of third degree [13]. The sorting process is treated as a sequence of discrete stages of the movement, which occur one after the other until it reaches its location in the

destination place. The stages, into which one can divide the considered continuous process, are distinct kinematic-dynamic states of the load, significantly different from one another, resulting from current interactions of the object and depending on its location relative to the sorting device.

The physical proprieties of the manipulated objects, indispensable from the point of view of the assumed models, are determined during experimental tests. The friction proprieties of the objects are investigated with the use of method of backward friction force fields [13], while the elastic-damping properties are examined by means of free fall method consisting in dropping the object down from a height on a rigid ground or an elastic beam [8]. Moreover, these tests give the possibility of experimental verification to confirm the correctness of the assumptions accepted in modelling the phenomena of dry friction and inelastic impact of bodies.

4. General recommendations of applying various groups of nonprehensile sorting manipulators

The data presented in Fig. 5÷Fig. 10 constitute synthesis of the basic structural-exploational properties of manipulators specialized in sorting stream of unit loads, developed on the basis of the numeric optimization results [9], [10], [11], [12], [14].

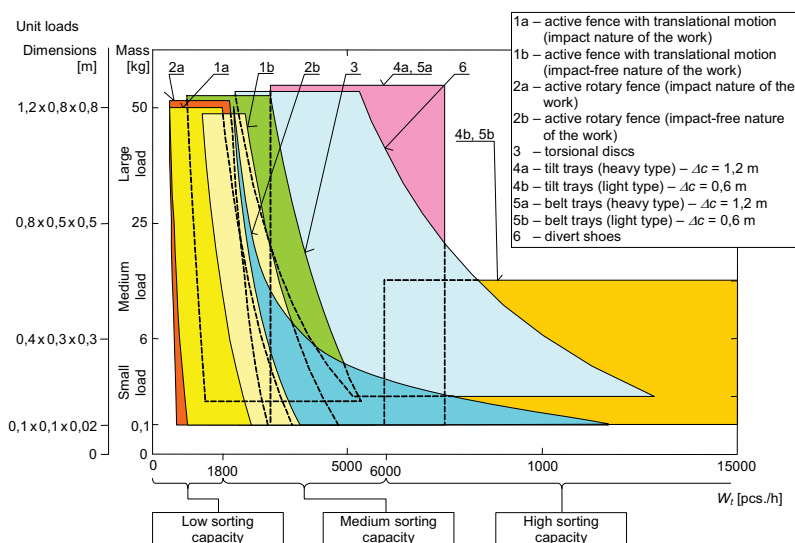


Fig. 5. Space of constructional solutions of sorting manipulators

There were studied the potential utilitarian properties of selected kinematic structures of manipulators relating to sorting the cuboidal objects (in rectangle shape in the conveyor plane) of length $A \in \langle 0,1; 1,2 \rangle$ m and width $B \in \langle 0,1; 0,8 \rangle$ m at the transportation velocity of unit load stream $v \in \langle 0,2; 2,5 \rangle$ m/s and the conveyor width $s = 0,7$ m. The most inconvenient variants of the load stream location to obtain the successful course of the sorting process were considered. These variants result from association of the extreme values of the objects' parameters: their geometrical dimensions, density distribution, frictional properties, and initial position on the main conveyor. An accepted admissible dynamic reactions which can be exerted on the sorted objects are equivalent to the overload risen during the object impact at free fall on the undeformable ground from the height $H_{dop} = 0,3$ m.

The values of exploational properties of manipulators (presented in the charts) are marked through shaded areas. Each manipulator has attributed area of different colour whose meaning was explained in the legend of Fig. 5. The interpretation of marks (occurring on all drawings) is

common. Simultaneous mapping of the properties of several manipulators in one drawing leads sometimes to mutual covering of areas attributed to the manipulators. In order to enable their full identification, each area at least partly is drawn in the foreground, and the hidden edges are mapped by a dotted line. For a few areas there have been difficulties in their presentation in the foreground – even partial one. An improvement of visibility of these areas was obtained by their insignificant „extraction” beyond the declared maximum value of the dimensions of objects – from this reason some areas goes beyond dimensions 1,2 x 0,8 x 0,8 m.

The division of the capacity of sorting manipulators into ranges (low, middle and high – Fig. 5) is based on definitions used in the work [6], and division relating to the loads' sizes (small, middle and large) – in the work [7]. The divisions mark out the ranges associating the manipulator groups with the sorting process properties – they attribute the suitable technical solution in the reference to exploational expectations.

The markings of manipulators with active fences take into account two types of work nature: impact (1a, 2a) or impact-free (1b, 2b). Accepted types, result from the organization of the stream of loads on the conveyor. Initial position of load decides, if while sorting the object will impact against the fence or only slides (without impact) along this fence.

The sorting capacity of the tray manipulators is closely related to the size of applied trays – not to the sizes of objects resting on their bearing surfaces. The largest foreseen object for sorting should fall inside the tray in whole. Due to this reason, the areas concerning tray sorting devices have shapes of rectangles (Fig. 5).

The division of tray manipulators into two types: heavy (4a, 5a) and light (4b, 5b) is dictated the economic consideration: light trays are designed for objects of small dimensions, and heavy – for large objects [7].

The data relating to belt tray devices (5a, 5b) characterizes the close affinity to tilt tray manipulators (4a, 4b) in the range of the achieved capacity of sorting in the function of the objects' dimensions (Fig. 5) and the velocity of main conveyor (Fig. 7 and Fig. 8). Difference between these solutions concerns the level of dynamic interactions exerted on objects (Fig. 6) and the frictional properties of objects provided for sorting. The objects (in the case of belt trays) are exposed to the dynamic overload whose value results from friction coupling between object and the active bearing surface of manipulator – similarly, like in case of manipulator with torsional discs (3). An acceleration which is exerted by tilt tray on the object, can be larger - it can reach approx. 1,5g (g – gravity acceleration) [9]. Manipulators with tilt trays are not designed for objects' sorting of too large friction properties. Belt tray manipulators do not possess such limitation – the conveyors covering trays are made of materials of high friction coefficient – considerably higher than in case of surface of tilt trays.

The edges limiting the areas from the left side (presented in Fig. 5) relate to sorting capacity obtained at minimum dynamic overload exerted on loads (Fig. 6) and at the low velocity of conveyor transportation (Fig. 7 and Fig. 8). The movement in the range of area in the direction of the right edge causes obtainment of higher sorting capacity, an increase of dynamic overloads exerted on the load and conveyor velocity increase. This rule obviously does not apply to the tray manipulators (4a, 4b, 5a, 5b).

The values of dynamic interaction exerted on the object by manipulators (presented in Fig. 6) are expressed through the impact velocity, height H of the load free fall on undeformable ground, and acceleration a_N . The values of each quantities have been so calculated to reconstruct relationships occurring between these quantities during the load impact (in [8], according to Table 1 – tested load with placed inside seismic sensor is surrounded by a sponge of thickness 0,03 m) at the free fall on undeformable ground from the height H . The conversion of the impact velocity into adequate acceleration w_n transmitted to load, do not take into account actuators flexibility of manipulators. An influence of this flexibility on mitigation of dynamic interaction exerted on the objects is presented in [10].

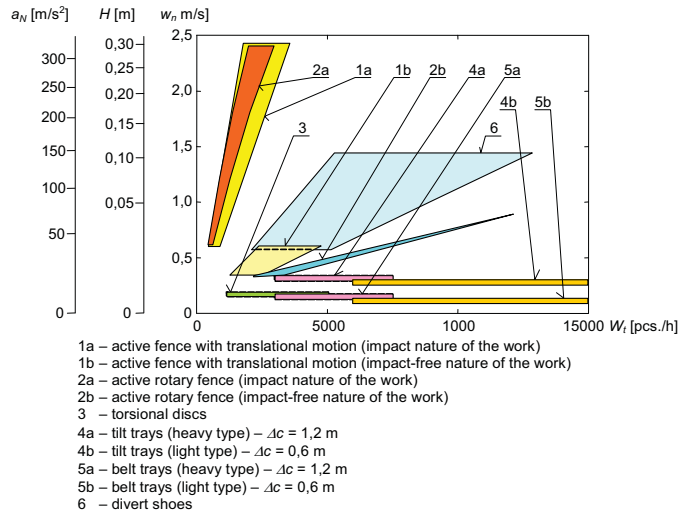


Fig. 6. Space of dynamic overloads exerted on objects by manipulators: a_N – acceleration exerted on object, H – height of free fall of the object on undeformable ground, w_n – relative impact velocity of the object against working element in normal direction

An increment of the sorting capacity has the small influence on the value variation of the objects' overload in case of tilt manipulators (4a, 4b, 5a, 5b) and with torsional discs (3) (Fig. 6) – in contrast to manipulators with an active fences (1a, 1b, 2a, 2b) and with divert shoes (6). The edges of the left side of the areas (Fig. 6 and Fig. 7) designate the capacity of sorting loads with the maximum dimensions, and right edges – loads of minimum dimensions.

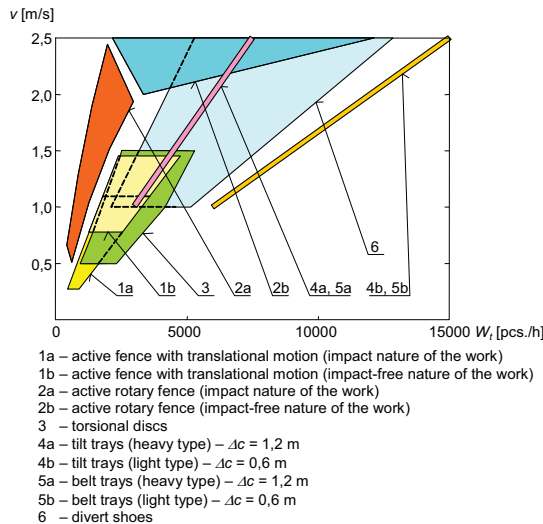


Fig. 7. Ranges of transportation velocity of main conveyor during sorting

The chart in Fig. 8 is worked out on the basis of information contained in Fig. 7, using one of the coordinate data – preferred velocity of loads' stream. Recommendation of the objects' sorting at the range of low velocity of the main conveyor refers to the manipulators with an active fences with translational motion (1a, 1b) and manipulators with torsional discs (3). Higher velocity of

transportation of load stream is appropriate for the work of manipulators: with trays (4a, 4b, 5a, 5b), with an active rotary fence (2a, 2b) and with divert shoes (6).

One of the basic features characterising the loads stream, subjected to automatic sorting process is the distance Δc between the heads of transported loads. This distance should be so chosen to obtain continuous and collision-free supply the workspace of manipulator. Dependencies occurring between sorting capacity of manipulators and recommended distance between the heads of loads transported on the main conveyor are shown in Fig. 9. The upper edges of the areas (presented in the figures) relate to the objects of the maximum external dimensions, lower – to the minimum dimensions of objects. The required distance Δc becomes smaller and smaller along with an increase of sorting capacity (excluding tray manipulators – (4a) (4b) (5a) (5b)). Obtained effect is a natural consequence of the relationship between the dimensions of load and the sorting capacity: the smaller the load, the less possible distance Δc and higher capacity of sorting (Fig. 5). The requirement of the largest distance application ($\Delta c \cong 5,5$ m) is assigned to the manipulators with an active rotary fences (2a) and (2b), and the smallest distance ($\Delta c \cong 0,6$ m) – to the manipulators with trays (4b) and (5b).

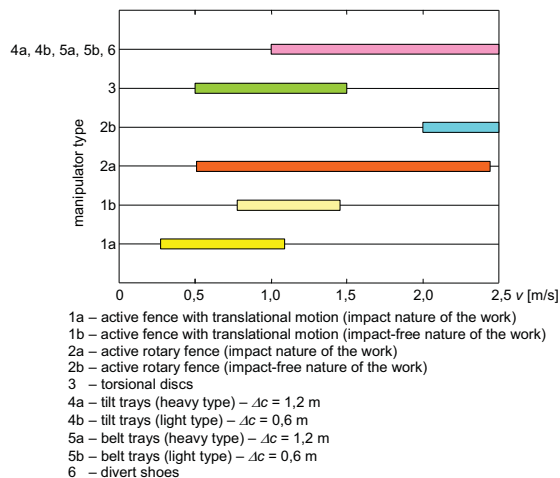


Fig. 8. Velocity of conveyors co-operating with sorting manipulators (worked out on the basis of Fig. 7)

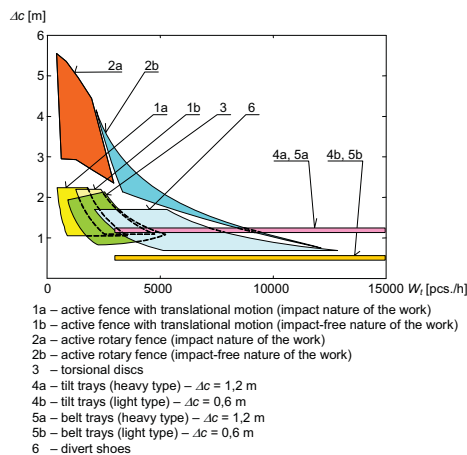


Fig. 9. Distance between heads of loads transported in the main conveyor, ensuring uninterrupted and collision-free supply of the manipulators

Shaded areas shown in Fig. 10 present the minimum lengths of the working space occupied by the manipulators. These lengths also determine the length of the minimum distance between destination chutes – have an influence on the number of division lines attributed to the unit length of an automatic sorting line. The longest workspace can be attributed to the manipulators with tilt trays (4a) and (4b), and the shortest – to manipulators with torsional discs (3). Manipulator with an active rotary fence (2b) can be simultaneously qualified to sorting devices with the shortest required working space (in case of loads sorting of minimum dimensions, and transported at high velocity of main conveyor) and to devices with large length of this space (in case of loads sorting of maximum size). The length of the workspace of manipulator with divert shoes (6) does not depend on the sorting capacity.

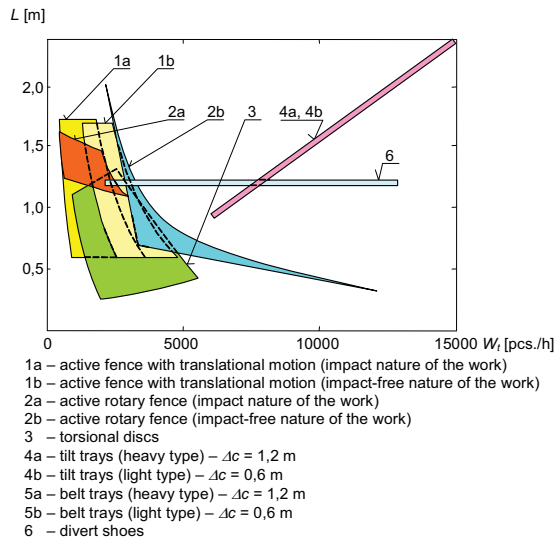


Fig. 10. Ranges of minimum length of working manipulators' spaces

5. Summary

The analyses of research results of the sorting process of unit loads transported on conveyors indicate that:

- Highly efficient sorting devices belong to the class of nonprehensile manipulators. Basic methods of impulse generation that leads the objects to the new transport lines are achieved through: pushing of the object by working elements of manipulator, effect of the directionally-oriented fields of friction forces, and an influence of gravity force on the object causing its sliding down from the conveyor.
- Presented results of investigations fulfill cognitive function – they can be used, as guidelines on the stage of formulating the constructional assumptions of new technical solutions of sorting manipulators, and for optimum control already existing manipulators.
- The main constraints to obtain higher sorting capacity are: the dynamic effects exerted on the loads, considerable velocity achievement by loads leaving the main conveyor, the increase of the length of the working space occupied by the manipulator causing reduction of the amount of new transport lines that fall on unit length of the main conveyor. An activity of these constraints depends on the kinematic structure of each group of manipulators.

References

- [1] *Postal Technology International*, UK & International Press, Dorking, 2007.
- [2] *Tilt Tray Sorter DDS*, Commercial folder published by Mannesmann Dematic AG, Offenbach, Niemcy, www.dematic.com (accessed: 2010-10-27).
- [3] *DRS Demag Rapid Sorter*, Commercial folder published by Mannesmann Dematic AG, Offenbach, Niemcy, www.dematic.com (accessed: 2010-10-27).
- [4] *Autosort 4 – Flat Face Arm Sorter*, Commercial folder published by Automotion Inc., Oak Lawn, IL, USA, www.automotionconveyors.com/Cut%20Sheet%20PDFs/SC4%20Flat%20Face.pdf (accessed: 2010-07-24).
- [5] *ProSort SC1*, Commercial folder published by Hytrol Conveyor Company Inc., Jonesboro, AR, USA, www.hytrol.com/mediacenter/catalog_sheets/ca_prosortsc.pdf (accessed: 2010-07-28).
- [6] *Sortation Systems*, Commercial folder published by Diamond Phoenix Corporation (USA), www.diamondphoenix.com/page.php?page=sortSys (accessed: 2010-09-04).
- [7] *Sandvik Sorting Systems. Range of Products*, Commercial folder published by Sandvik Materials Technology, Sandviken, Sveden, www.sorting.com (accessed: 2007-09-04).
- [8] Piątkowski T., Sempruch J., *Model of inelastic impact of unit loads*, Packaging Technology and Science, John Wiley & Sons, 22/1, 2009, 39-51.
- [9] Piątkowski T., *Modelling and analysis of dynamic properties of tilt tray manipulator*, Editors: Cretu S.-M., Dumitru N., New trends in mechanisms, Academica-Greifswald, Germany, 2008, 157-176.
- [10] Piątkowski T., *Active fence with flexible link. Journal of Theoretical and Applied Mechanics*, 1, 48, 2010, 87-109.
- [11] Piątkowski T., *Analiza i modelowanie procesu sortowania strumienia małogabarytowych ładunków jednostkowych*, Monograph 139, University of Technology and Life Sciences UTP in Bydgoszcz, 2010.
- [12] Piątkowski T., *Model and analysis of the process of unit-load stream sorting by manipulator with torsional disks*, Journal of Theoretical and Applied Mechanics, 4, 47, 2009, 871-896.
- [13] Piątkowski T., *Analysis of translational positioning of unit loads by directionally-oriented friction force fields*, Mechanism and Machine Theory, Elsevier, 46, 2011, 201–217.
- [14] Piątkowski T., *Dynamic identification of sorting process of unit loads stream performed by means of active fence with translational motion*, Logistyka 6/2008, 281-286.



ANALYSIS OF THE HETEROGENEOUS WELD JOINTS IN ASPECT OF FRACTURE MECHANICS

Eugeniusz Ranatowski

University of Technology and Life Sciences, Faculty of Mechanical Engineering,

Al. Prof. S. Kaliskiego 7, Pl - 85-789 Bydgoszcz, Poland

e-mai: ranatow@utp.edu.pl

Abstract

This paper will discuss the issues relating to the effect of constraint on the fracture safe design. At first the attention is focused on the relation between the microstructure and selected mechanical properties. This aspect is illustrated with presenting a brief consideration of the constraint effect in relation: microstructure - mechanical properties in microscopic scale. The same problem is account in macroscopic scale of the heterogeneous weld joints. After formulating a simplified model of mismatched weld joints a concise review of stress was made at interfaces between zones (W) and (B). Conclusions from above analysis form a constraint parameters $K_R^{un/ov}$ which were used to an assessment of the fracture parameters as ratio of driving forces $\delta_R^{un/ov}$ by modified of the classical solution presented by Engineering Treatment Model (E-T-M).

Key words: *material microstructure, constraint effect, fracture parameters*

1. Introduction

The weld joints are often highly heterogeneous. It is known that a fracture of welded structures is generally caused by various defects in welded joints, while macro - mechanical heterogeneity is one their primary features. The heterogeneous nature of the weld joints are characterised by macroscopic dissimilarity in mechanical properties. This dissimilarity is caused by different mechanical and chemical properties of the weld and base materials as well as by the thermal and strain cycles during welding and may occur through the fusion line and heat affected zone (HAZ) of welds. The most reliable and practically feasible design concept is designing against fracture initiation from crack like defects in weldments. This design concept suggests that the fracture toughness of all parts of the welded joints must be went over and the lowest toughness region should be recognised. A weld joint includes the weld metal, HAZ and the base metal parts having different properties. Welding is probably the most popular manufacturing process for joining metals used in structural applications. In this situation we will focus our attention on a model in which the weld metal or part of the heat affected zone (HAZ) is imitated by layer (W) - Fig. 1c and d. Strength mismatching occurs as an overmatching - Fig. 1a or as an undermatching - Fig. 1c. The essential physical phenomena affecting the mechanical properties of this model occur at the interfaces of zones (B) and (W) - Fig. 1c and d. The presence of the interfaces in these models naturally gives rise to mechanical constraint on the weld joints. A fracture safe design also can be

influenced by constraint. The analysis of failure in a structural component depends on two inputs, the fracture behaviour and deformation behaviour - both depend on constraint. Current work has concentrated more on looking at constraint effects on the fracture behaviour.

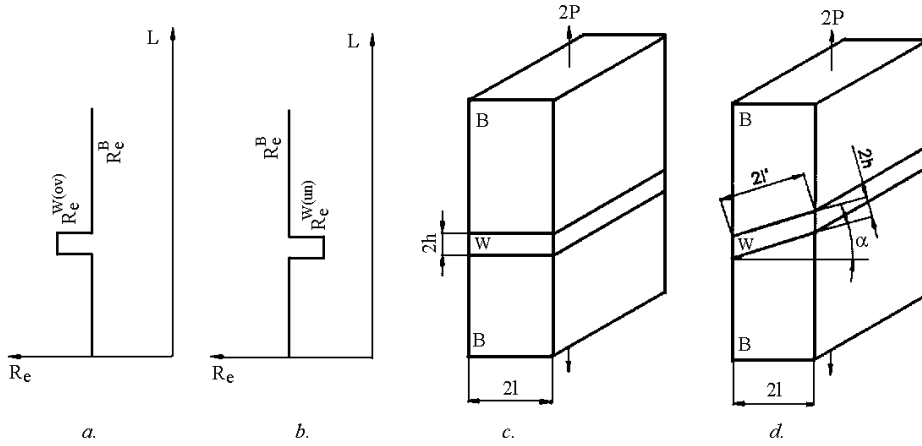


Fig.1. Characteristic of the models of the mismatched weld joints: (a) change of the yield point $R_e^{W(ov)}$ in the overmatched weld joint; (b) change of the yield point $R_e^{W(um)}$ in the undermatched weld joint; (c, d) geometrical configuration - layer W as perpendicular or incline to external load $2P$.

2. Influence of the constraint effect on the material microstructure

The normal way to calculate the strength of a multiphase alloy is to use a rule of mixtures, i.e. to estimate a mean value from the weighted average of each component:

$$\sigma = V_\alpha \sigma_\alpha + V_b \sigma_B + V_p \sigma_p + V_M \sigma_M + V_\gamma \sigma_B + \dots, \quad (1)$$

where:

σ_i - the property assigned to phase i ,

V_i - volume fraction of phase i .

Above approximation may not be valid in circumstances where the phases have very different mechanical properties. This take place because of constraint effect between different components of microstructure. For example on Fig. 2 is presented plots of normalised strength of bainite as the function of fraction of bainite in martensitic matrix and change of proof stress of bainite and martensite in mixed microstructure which has been tempered.

Then the strength of constrained bainite is established as follows [1]:

$$\sigma_b \cong \sigma_{bo} [0,65 \exp(-3,3V_b) + 0,98] \leq \sigma_M, \quad (2)$$

where:

σ_b - strength of constrained the bainite,

σ_{bo} - strength of unconstrained the bainite,

- V_b - volume fraction of bainite,
 σ_M - strength of the martensite.

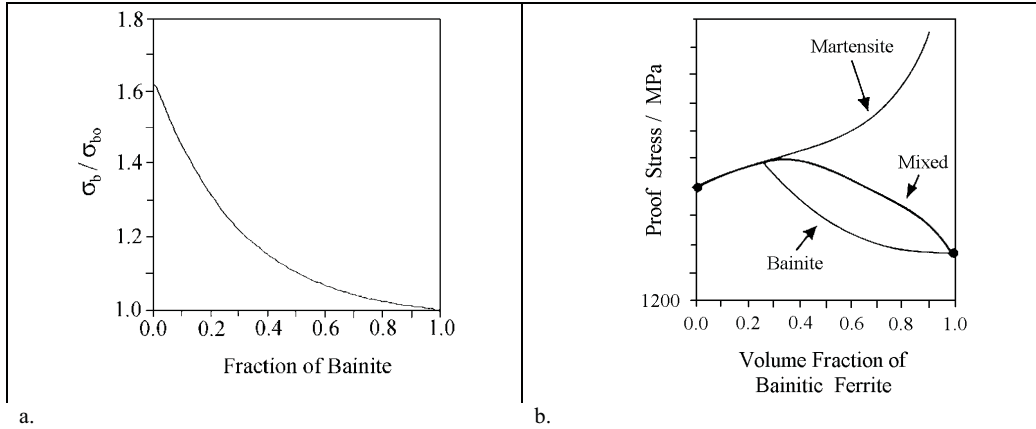


Fig. 2. Characteristic of the strength of constrained bainite in martensite matrix [1]:

(a) the normalised strength of bainite as the fraction of bainite in martensitic matrix; (b) the strength contributions of bainite and martensite in the mixed microstructure which has been tempered.

When the volume fraction V_b of bainite is small, its strength nearly matches that of martensite - Fig. 2. In accordance with above established rules the constraint effect are important in determining the mechanical behaviour of weld and HAZ microstructures in many respects. For example, it was indicated that hard-phase islands present in HAZ microstructures are most detrimental when they are severely constrained by the surrounding microstructure. It was also noted that microstructural inhomogeneities such as hard pearlite island, can lead to a significant variations in measured fracture toughness values of the same material.

3. Influence of constraint effect on the fracture of heterogeneous weld joints - macroscopic scale

Determination of change in the state of stress occurring at the interface of zones (B) and (W) is than of primary importance for a correct interpretation and estimation of a new mechanical properties. The stress analysis in this area is made previously in [2]. A very useful form of the stress state we can received by change the parameters: $\gamma \rightarrow q$. The parameter γ represent the internal normalised tangential stress at interfaces and the parameter q is represent the external normalised tangential stress caused by force $2Q$. With use the relation between γ and q as:

$$\gamma + 1 = 2q \rightarrow \gamma = 2q - 1, \quad (3a, b)$$

we can transform the stress state which was established previously [2] on the form very useful in practice as follows:

- undermatching case:

$$\sigma_{xx(rel)}^{un} = \frac{\sigma_{xx}^{un}}{k} = \frac{1}{2(1-q)} \left[\left(\frac{\pi}{2} + 2(1-2q)\sqrt{q(1-q)} - \arcsin(2q-1) \right) \right] + (1-q)\frac{\xi}{\kappa} - \quad (4)$$

$$-2\sqrt{1-\left(q+(1-q)\frac{\eta}{\kappa}\right)^2},$$

$$\sigma_{yy(rel)}^{un} = \frac{\sigma_{yy}^{un}}{k} = \frac{1}{2(1-q)} \left[\frac{\pi}{2} + 2(1-2q)\sqrt{q(1-q)} - \arcsin(2q-1) \right] + (1-q)\frac{\xi}{\kappa}, \quad (5)$$

$$\sigma_{xy(rel)}^{un} = \frac{\sigma_{xy}^{un}}{k} = q + (1-q)\frac{\eta}{\kappa}, \quad (6)$$

$$q = \frac{\tau_Q}{k}, \quad k = \frac{R_e^{W(un)}}{\sqrt{3}}, \quad R_e^{W(un)} \leq R_e^B, \quad \tau_Q = \frac{Q}{A}$$

- overmatching case

$$\sigma_{xx(rel)}^{ov} = \frac{\sigma_{xx}^{ov}}{k} = - \left[\frac{1}{2(1-q)} \left[\left(\frac{\pi}{2} + 2(1-2q)\sqrt{q(1-q)} - \arcsin(2q-1) \right) \right] + (1-q)\frac{\xi}{\kappa} - \right. \\ \left. - 2\sqrt{1-\left(q+(1-q)\frac{\eta}{\kappa}\right)^2} \right], \quad (7)$$

$$\sigma_{yy(rel)}^{ov} = \frac{\sigma_{yy}^{ov}}{k} = \frac{1}{2(1-q)} \left[-\frac{\pi}{2} - 2(1-2q)\sqrt{q(1-q)} + \arcsin(2q-1) \right] + (1-q)\frac{\xi}{\kappa}, \quad (8)$$

$$\sigma_{xy(rel)}^{ov} = \frac{\sigma_{xy}^{ov}}{k} = q + (1-q)\frac{\eta}{\kappa}, \quad (9)$$

$$q = \frac{\tau_Q}{k}, \quad k = \frac{R_e^{W(ov)}}{\sqrt{3}}, \quad R_e^{W(ov)} > R_e^B, \quad \tau_Q = \frac{Q}{A}, \quad \kappa = \frac{2h}{2t}; \quad \eta = \frac{2y}{2t}; \quad \xi = \frac{2x}{2t}; \quad \kappa \geq \eta.$$

In practice, by used to consideration the external force 2P and inclined layer we can determining the value of external tangential stress acting at interface as follows:

$$\tau_Q = \frac{\sigma_l}{2} \sin 2\alpha, \quad (10)$$

where:

$$\sigma_l = 2P / A$$

- 2P - tensile force, Fig.1,
- A = 2 t · L - cross - section perpendicular to 2P,
- α - angle, Fig. 1.

Then it is possible to assess the value of q as:

$$q = \frac{\sigma_l}{2k} \sin 2\alpha, \quad (11)$$

The stress analysis to enables establish the quantitatively assessment of constraint effect by introduce the constraint factor for the under- and overmatched weld joints in accordance to references [3], as follows:

$$K_W^{un} = \frac{2}{\sqrt{3}} \left(\frac{l}{4(l-q)} \left[\frac{\pi}{2} + 2(l-2q)\sqrt{q(l-q)} - \arcsin(2q-l) \right] + (l-q)\frac{l}{4\kappa} \right), \quad (12)$$

$$K_W^{ov} = \frac{2}{\sqrt{3}} \left(\frac{l}{4(l-q)} \left[-\frac{\pi}{2} - 2(l-2q)\sqrt{q(l-q)} + \arcsin(2q-l) \right] + (l-q)\frac{l}{4\kappa} \right), \quad (13)$$

Fig. 3a, b presents the dependence of the constraint factors $K_W^{un/ov}$ on the parameters κ and q . Because of that the model is based on the assumption that the materials of zones B and W are ideal plasticity than the new value of yield point of the layer is equal:

- undermatching case ($R_e^W < R_e^B$):

$$R_e^{W(un)} = K_W^{un} \cdot R_e^W, \quad (14)$$

- overmatching case ($R_e^W > R_e^B$):

$$R_e^{W(ov)} = K_W^{ov} \cdot R_e^W, \quad (15)$$

The change in state of stress also leads to conversion in crack resistance in these zones, the procedure of destruction and kind of fracture. For example consider the above - mentioned problem when the crack is located in the middle part of the layer parallel to the interfaces and in the homogeneous material in which the constraint effect is not effecting.

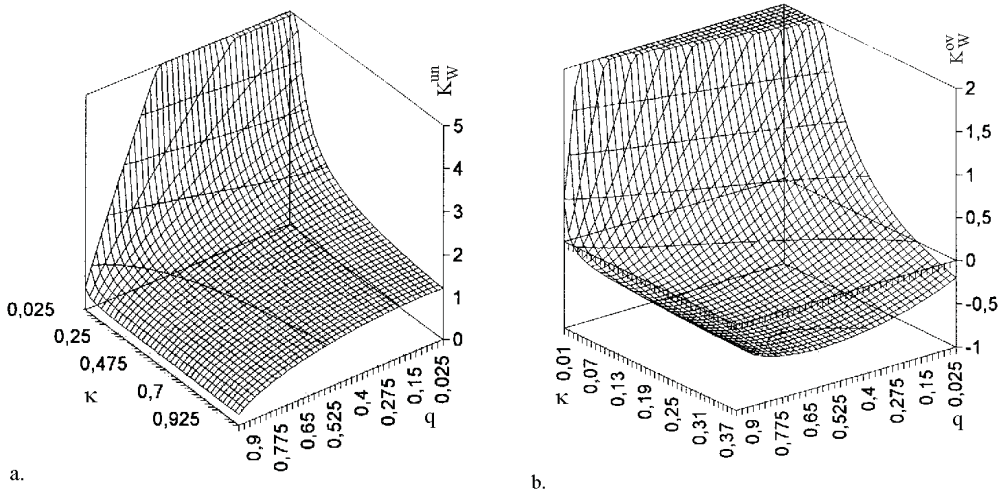


Fig. 3. Diagrams of K_W^{un} , K_W^{ov} for: (a) undermatched; (b) overmatched models of weld joints.

One of the most important procedures is the recently introduced Engineering Treatment Model (ETM) relates CTOD to the applied load or strain for work hardening materials [3, 4]. In according to the previously determined equations by Schwalbe for assessing the ratio of the driving forces in mismatching model - Fig. 1 and after taking the constraint factor $K_W^{un/ov}$. It will be able to determine the normalised parameter $\delta_R = \delta_W / \delta_B$ as follows:

- undermatching case at matching ratio $K_S = R_e^B / R_e^{W(un)} > 1$:

$$\sigma_1 < R_e^{W(un)} < R_e^B$$

lower limit:

$$\delta_R = K_S, \quad (16)$$

upper limit:

$$\delta_R = \frac{3}{2} \frac{I}{\frac{I}{K_S} + \frac{I}{2K_S^3}}, \quad (17)$$

$$R_e^B > \sigma_1 \geq R_e^{W(un)}$$

$$\delta_R = \left(\frac{K_W^{un}}{K_S} \right)^{\left(I - \frac{I}{n_W} \right)}, \quad (18)$$

$$\sigma_1 \geq R_e^B \geq R_e^{W(un)}$$

$$\delta_R = \left(\frac{K_W^{un}}{K_S} \right)^{\left(\frac{I}{n_W} - \frac{I}{n_B} \right)} \left(\frac{I}{K_S} \right)^{\left(I - \frac{I}{n_W} \right)}, \quad (19)$$

- overmatching case at matching ratio: $K_S = R_e^B / R_e^{W(un)} < 1$:

$$\sigma_1 < R_e^B < R_e^{W(ov)}$$

lower limit:
$$\delta_R = K_S, \quad (20)$$

upper limit
$$\delta_R = \frac{K_S(2 + K_S^2)}{3}, \quad (21)$$

$$R_e^{W(ov)} > \sigma_1 \geq R_e^B \quad \delta_R = \left(\frac{K_W^{ov}}{K_S} \right) \left(1 - \frac{1}{n_B} \right), \quad (22)$$

$$\sigma_1 \geq R_e^{W(ov)} \geq R_e^B \quad \delta_R = \left(\frac{K_W^{ov}}{K_S} \right) \left(\frac{1}{n_W} - \frac{1}{n_B} \right) \left(\frac{1}{K_S} \right) \left(1 - \frac{1}{n_W} \right), \quad (23)$$

The results of this study of mismatched weld joints reveals high dependence of the fracture parameter δ_R according to equations (16)÷(23) on the such parameters as $K_W^{un/ov}$, K_S and n_W, n_B .

Conclusions

Constraints are of important in determining the mechanical of weld structures in many respects - microscopical and macroscopical scale. There are presenting a brief consideration of the constraint effect in relation microstructure - mechanical properties and the same problem was account in the macroscopic scale of the heterogeneous weld joints. After characteristic of the stress state there was made an analytical assessment of the fracture resistance of an undermatched and overmatched weld joints and reveals dependence of driving forces ratio δ_R according to equations (16)÷(23) on the such parameters as constraint factors $K_W^{un/ov}$, matching K_S and strain hardening exponents n_W, n_B .

The thus determined parameter δ_R gives the basic information about how in simple way to choose the critical parameter CTOD in mismatched weld joints for having strength equal to base metal.

References

- [1] Bhadeshia H.K.D.H., *Mathematical Modelling of Weld Phenomena 3*, Cambridge, UK, pp. 249 ÷ 284, (1997).
- [2] Ranatowski E., *Influence of the constraint effect on fracture resistance of mismatched weld joints*, Mechanism and Mechanics of Damage and Failure, ECF-11, United Kingdom, EMAS, Vol.3, pp. 2061 ÷ 2066, ISBN 0947817 - 93X, (1996).
- [3] Ranatowski E., *Some remarks on stress state at interface of the mismatched weld joints*, Mis - Matching of Interfaces and Welds. Editors: K.-H. Schwalbe, M. Koçak, GKSS Research Center Publication, Geesthacht, FRG, ISBN 3-00-001951-0, pp. 185 - 196, Germany, (1997).
- [4] Schwalbe K.-H., *Effect of weld metal mis-match on toughness requirements: some simple analytical considerations using the Engineering Treatment Model (ETM)*, International Journal of Fracture, pp. 257 ÷ 277, Nr 56, (2005).



THE ASPECTS OF DIMENSIONING OF THE CONSTRUCTIONS WITH USE OF THE FRACTURE MECHANICS

Eugeniusz Ranatowski

University of Technology and Life Sciences, Faculty of Mechanical Engineering,

Al. Prof. S. Kaliskiego 7, Pl - 85-789 Bydgoszcz, Poland

e-mail: ranatow@utp.edu.pl

Abstract

In the first part of this work the classic strength effort hypothesis and their usefulness to dimensioning of the materials and constructions were characterised. There was given their small usefulness when the defects such as cracks are presented. In this situation very useful to dimensioning of the materials and constructions may be the fracture mechanics with their parameters and criterions. The further part of this work was devoted to characterising of the basic parameters and criterions of the fracture mechanics. Such parameters as stress intensity factor K_n , strain energy release rate G , crack tip opening displacement δ (CTOD) and integral Rice – Čerepanov J and their criterions are presented. Last part is devoted to practical aspect of use of above parameters and criterions to dimensioning of the constructions.

Key words: *rules of dimensioning, fracture mechanics, parameters and criterions, analytical examples*

1. Introduction

The problem of optimal design of the welded structures is very complex and various attempts have been made to obtain effective methods which might be used in engineering, with requires appropriated dimensioning of the materials and constructions. The application of the classical strength effort hypothesis is inconsiderable when defects, such as cracks, occur. The classical effort hypothesis, such as Huber – Mises equivalent of stress and their modifications, does not assess the effort of the construction as no real conditions of material effort are considered. For example [1], [2]:

- the “scale effect” and the geometric feature of the constructions has not taken into consideration,
- the state of the microstructure of the materials, their heterogeneity, internal discontinuity and other defects which are formed under manufacturing process and exploitation leaves out of account,
- a question of the run of the material damage does not consider,
- the constitutive physical rules are created by use of the continuum model of material.

Various approximate methods of calculation are often used in designing, e.g. reducing internal forces, yet the best approach is based on fracture mechanics and their parameters and criterions. The application of fracture mechanics parameters to materials and constructions dimensioning is in a great step towards effort process modelling compliant with the modelling rules, which justifies

the aim of the mechanics and its applicability to welded structure designing and dimensioning [2].

2. Characteristic of the fracture mechanics parameters and criterions

Stress intensity factor K_n

The stress intensity factor is a parameter which determines the level of the stress or of the strain, energy density, elastic singularities near the tip of an ideal crack in a stressed linear elastic solid. The asymptotic stress and displacement components may be expressed as follows [1],[2]:

$$\sigma_{ij}(r,\theta) = \frac{I}{\sqrt{2\pi r}} \left[K_I f_{ij}^I(\theta) + K_{II} f_{ij}^{II}(\theta) + K_{III} f_{ij}^{III}(\theta) \right], \quad (1)$$

$$u_i(r,\theta) = \frac{I}{2\mu} \sqrt{\frac{r}{2\pi}} \left[K_I g_{ij}^I(\theta) + K_{II} g_{ij}^{II}(\theta) + K_{III} g_{ij}^{III}(\theta) \right], \quad (2)$$

where:

- r - distance from the crack tip,
- θ - angle, second polar coordinate,
- $f_i^n(\theta), g_i^n(\theta)$ - are dimensionless functions of the angle θ ,
- K_n - stress intensity factor ($n = I, II, III$ distinguish the models: I –opening mode, II–sliding mode, III–tearing or antiplane mode),
- i, j - the index refer to either the cartesian coordinates (x, y, z) or the cylindrical co-ordinates (r, θ, z).

Compliant with above, the stress intensity factor K_n is a fundamental quantity that governs the level of stress field in the vicinity of the crack tip or of the strain. Furthermore, it affects the strain energy density, elastic singularities near the tip of an ideal crack in a stressed linear elastic solid at $r = 0$ ($r \rightarrow 0, \sigma_{ij} \rightarrow \infty$) – Fig. 1a. In reality some inelasticity in the neighbourhood of the crack tip is always present in the form of plasticity Irwin presents a simplified model for determination of the plastic zone attending the crack tip under small-scale yielding. The observation led Irvin to suggest that the effect of plasticity makes the plate behave as if it had a crack longer than the actual crack size, Fig.1b: $a_{eff} = a + r_p$.

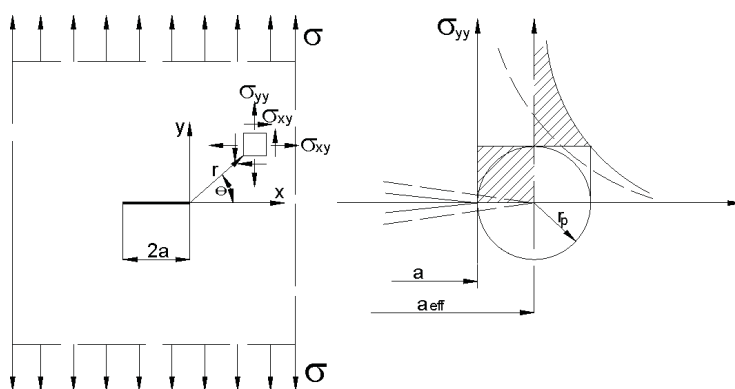


Fig.1. Model of the plate with the crack $2a$ and the state of stress at the crack tip:
a. in elastic state of material with ideal crack under tension,
b. with extended crack length by plastic deformation a_{eff} – fictitious crack length.

A study of the local stress fields for the three models (I, II, III) of loading showed their general applicability and can be generally given by the values of three stress intensity factors [4]:

$$K_I = \lim_{x \rightarrow a} \sqrt{2\pi(x-a)} \sigma_{yy}(x,0,0) = \lim_{x \rightarrow a} \sqrt{2\pi r} \sigma_{yy}(x,0,0), \quad (3)$$

$$K_{II} = \lim_{x \rightarrow a} \sqrt{2\pi(x-a)} \sigma_{xy}(x,0,0) = \lim_{x \rightarrow a} \sqrt{2\pi r} \sigma_{xy}(x,0,0), \quad (4)$$

$$K_{III} = \lim_{x \rightarrow a} \sqrt{2\pi(x-a)} \sigma_{yz}(x,0,0) = \lim_{x \rightarrow a} \sqrt{2\pi r} \sigma_{yz}(x,0,0), \quad (5)$$

For structural elements different then infinity plate and unit thickness with crack $2a$ the stress intensity factor is a function of the loading of the body, including applied loads and displacements, of the crack size, of the geometry of the body and of the crack. For example, at the plate with finite dimension $2H \times W$ and thickness B with the crack $2a$ is affected by the action from tension stress σ then the stress intensity factor is eq. [2, 3]:

$$K_I = \sigma \sqrt{\pi a} F_I(\alpha, B), \quad (6)$$

where: $\alpha = 2a/W$, $B = 2H/W$.

The diagram of the function $F_I(\alpha, B)$ is presented in Fig. 2.

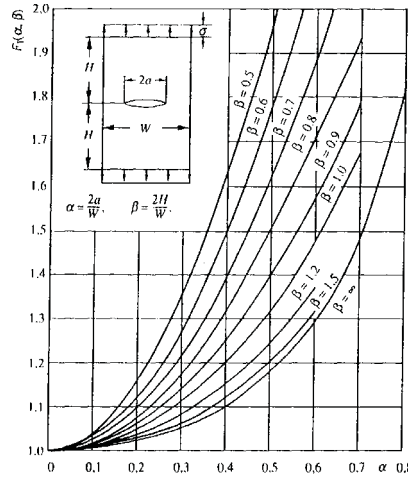


Fig.2. Diagram of the function $F_I(\alpha, B)$ [5].

The above solutions are obtained by making the assumption that the radius of curvature at the crack tip $\rho_c \rightarrow 0$. When $\rho_c \neq 0$, K_I can be assessed as follows:

- plane strain
$$K_I = \sqrt{2\pi} (1-\nu) \mu \sqrt{\rho e}, \quad (7)$$

- plane stress

$$K_I = \sqrt{4\pi} \mu \sqrt{\rho e}, \quad (8)$$

where:

- ν - Poisson ratio,
- μ - Shear modulus.

In dynamic problems the stress intensity factor is the functions of time $K_n(t)$ for models $n = I, II, III$.

Strain energy release rate G

The parameter G is related to the stress intensity factors as follows:

- in plane stress

$$G_I = \frac{K_I^2}{E}, \quad (9)$$

$$G_{II} = \frac{K_{II}^2}{E}, \quad (10)$$

$$G_{III} = (1 + \nu) \frac{K_{III}^2}{E} = \frac{K_{III}^2}{2\mu}, \quad (11)$$

- in plane strain

$$G_I = (1 + \nu^2) \frac{K_I^2}{E}, \quad (12)$$

$$G_{II} = (1 + \nu^2) \frac{K_{II}^2}{E}, \quad (13)$$

$$G_{III} = (1 + \nu^2) \frac{K_{III}^2}{E} = \frac{K_{III}^2}{2\mu}, \quad (14)$$

At the composed state of loading ($n = I, II, III$) the total value of G as:

$$G = G_I + G_{II} + G_{III}, \quad (15)$$

After inserting the equations (9)÷(11) and (12)÷(14) into (15) we received:

$$G = \frac{(K_I^2 + K_{II}^2)}{E} + \frac{K_{III}^2}{2\mu}, \quad (16)$$

$$G = \frac{(K_I^2 + K_{II}^2)(1 - \nu^2)}{E} + \frac{K_{III}^2}{2\mu}, \quad (17)$$

G is also related to the variation of the compliance C of the element with as follows:

$$G = \frac{1}{2} F^2 \frac{\partial C}{\partial A}, \quad (18)$$

where:

- C - compliance ($u = CF \rightarrow C = uF^{-1}$) $N^{-1}m$,
F - force, N.

Crack tip opening displacement CTOD - δ

According to [4] the opening of the effective crack at the tip of the crack is given by:

$$\delta = \frac{8\sigma_y a}{\pi E} \ln \left(\sec \frac{\pi \sigma}{2\sigma_y} \right), \quad (19)$$

By expanding equation (19) in Maclaurin series and retaining only the first term for small value of σ / σ_y we get:

$$\delta = \frac{K_I^2}{E\sigma_y}, \quad (20)$$

If we base on the Irwing's solution the distance δ of the faces of the fictitious crack at the tip of the initial crack at the tip of the initial crack of length a is given by:

$$\delta = \frac{4}{\pi E} \frac{K_I^2}{\sigma_y}, \quad (21)$$

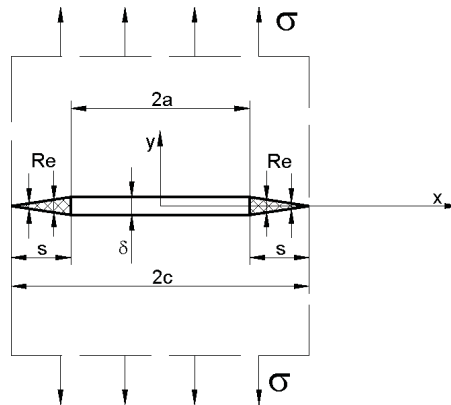


Fig. 3. Dougdale model for the mode I crack of length $2a$ situated in very thin and an infinite plate subjected to uniaxial uniform stress σ at infinity perpendicular to the crack plane.

By comparing eq. (20) and (21) we can deduce that the Irwin model over-estimates δ as compared to the Dougdale model by 27 per cent.

The eq. (20), (21) combined with eq. (9) yield, respectively:

$$G = \sigma_y \delta, \quad (22)$$

$$G = \frac{\pi}{4} \sigma_y \delta, \quad (23)$$

Experimental investigations to indicate that above relations are appropriate when $\sigma \leq \sigma_y$.

Rice – Čerepanov J integral

The mathematical formulation of the conservation laws applicable in elasto-statics in the form of path independent integrals of some functionals of the elastic field over the bounding surface of a closed region lastly was proposed by J.R.Rice and independently Čerepanow [4]. The J-integral applied to notch problems was introduced by them.

The increment of the difference between the stored elastic energy W_e and work of the external loads U per unit increment of an ideal crack surface area A in nonlinear elasticity enable to establish the J as [1, 4]:

$$J = -\frac{\Delta P}{\Delta A}, \quad (24)$$

or

$$J = -\frac{\partial P}{\partial a}, \quad (25)$$

where: P – potential energy.

In elasticity the strain energy release rate J is equal to the Rice–Čerepanov J integral defined as:

$$J = \int_F \left(W dy - \sigma_{ij} n_j \frac{\partial u_i}{\partial x} ds \right), \quad (26)$$

where:

- W - the strain energy density,
- Γ - the contour around the tip joining one point on a face of the crack to another point on the opposite face, Fig.4,
- ds - is a differential element of the contour,
- u_i - is a displacement vector,
- n - the unit outward normal to Γ ,
- $\sigma_{ij}n_j$ - the normal component of the stress tensor to the contour Γ at ds , called as a traction vector,
- σ_{ij} - stress tensor.
- $\sigma_{ij} n_j \frac{\partial u_i}{\partial x} ds$ - the unit energy density release from stress field σ_{ij}
- x, y - is a cartesian coordinate system.

In linear elasticity $J = G$. Furthermore, the J integral is independent of the contour in elasticity. This property is also extended in plasticity in monotonic radial loading. Under the same conditions the strain energy release rate can be assumed to be equal to the J integral, as in elasticity.

The J integral characterises the crack tip singularities of stress, strain and strain energy density in non-linear elasticity and in plasticity.

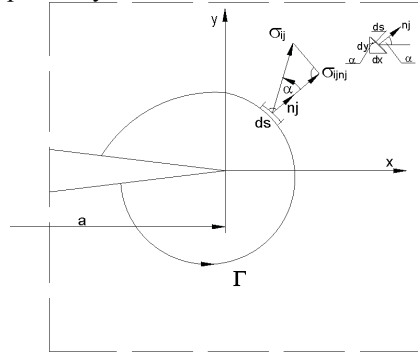


Fig. 4. A two-dimensional cracked body with a path Γ starting from lower and ending to the upper face of a notch with traction vector.

In the framework of deformation plasticity, it can be shown that J control the stress and strain near-tip fields as K does in linear elasticity. The proof was given by Hutchinson, Rice and Rosengreen [1, 3] and are designated as (HRR) fields. Let (r, φ) be polar coordinates with origin in the crack tip. Then for $r \rightarrow 0$ the stress and deformation as a function of J integral we assess as:

$$\sigma_{ij} = \sigma \left[\frac{J}{I_n \sigma_o \varepsilon_o A r} \right]^{\frac{1}{n+1}} \cdot \tilde{\sigma}_{ij}(\varphi, n), \quad (27)$$

$$\varepsilon_{ij} = \varepsilon \left[\frac{J}{I_n \sigma_o \varepsilon_o A r} \right]^{\frac{1}{n+1}} \cdot \tilde{\varepsilon}_{ij}(\varphi, n), \quad (28)$$

where:

- A, n, ε_o , σ_o - are the constants of the Ramberg–Osgood law [2],
- I_n - is the dimensionless factor depends on the hardening exponent n and on the crack mode (I, II, III) and is tabulated, e.g. in [4],
- $\tilde{\sigma}_{ij}(\varphi, n)$ - are the dimensionless function determined in [1, 3].
- $\tilde{\varepsilon}_{ij}(\varphi, n)$

Near the crack tip, the strain energy density, which varies as r^{-1} , is proportional to J.

Fracture criterions

In agreement with [2, 4] the basic fracture criterions can be established as follows:

$$K_n = K_{nC}, \quad (29)$$

$$G_n = G_{nC}, \quad (30)$$

$$\delta = \delta_C, \quad (31)$$

$$J_n = J_{nC}, \quad (32)$$

where: $n = \text{I, II, III modes}$.

The left side-hand of criterions (31)-(32) are characterised previously as above. The right-hand side of this equation are characterised the fracture toughness which described a material resistance to crack extension. The criterions (33) and (34) are mainly used for brittle fracture in the range of linear elastic fracture mechanics. The residual criterions (35), (36) are used in elasto-plasticity.

For example at I mode condition the criterions be express as follow:

$$K_I = K_{IC}, \quad (33)$$

$$G_I = G_{IC}, \quad (34)$$

$$\delta = \delta_C, \quad (35)$$

$$J_I = J_{IC}, \quad (36)$$

The fracture resistance at unstable crack propagation prior to 0,2 mm of crack growth or to a pop-in [2, 4].

Under plane strain condition the critical value of J , J_{IC} is related to the plane strain fracture toughness K_{IC} by equation:

$$J_I = \frac{1-\nu^2}{E} K_{IC}^2, \quad (37)$$

3. Conclusion

Fracture mechanics design methodology is based on more realistic parameters and criterions than the classic continuous mechanics. With the above procedures there were determined the maximum allowable loads applied for a specified crack size, or the maximum permissible crack size for specified load applied. Some further effort is needed on the effects of constraint on deformation behaviour during the fracture process, specially in weldments.

References

- [1] Neimitz A., *Ocena wytrzymałości elementów konstrukcyjnych zawierających pęknięcia (podstawowe elementy procedur SINTAP)*, Politechnika Świętokrzyska, Kielce, 2004.
- [2] Ranatowski E., *Obliczeniowa mechanika spawania, (Computational welding mechanics)*, Wydawnictwo Uczelniane, UTP, Bydgoszcz, 2009.
- [3] Ranatowski E., *Characteristic of the constraint effect at interface of the thin layer in mismatched welded joints*, B. Michel, K.-D. Lang (Eds), ISBN 978-3-932434-77-8, pp.480-492, Dresden, 2010.
- [4] Schwalbe K.H., *Effect of the weld metal mismatch on toughness requirements*, International Journal of Fracture, No 1, 2004.



RELATION BETWEEN STRESS STATE AND FRACTURE RESISTANCE IN MISMATCHED WELD JOINTS.

Eugeniusz Ranatowski

University of Technology and Life Sciences, Faculty of Mechanical Engineering,

Al. Prof. S. Kaliskiego 7, Pl - 85-789 Bydgoszcz, Poland

e-mai: ranatow@utp.edu.pl

Abstract

After formulating a simplified model of under- and overmatched welded joints an analysis was made of stress at interface for the cases of perpendicular and non - perpendicular orientation of the zones (soft layer and hard layer) relative to the load action direction under tension. Conclusions from the theoretical analysis form a basis to an assessment of effort and fracture of the mismatched welded joints. Conditions for producing brittle and ductile fracture in mismatched welded joints in relation to geometrical conditions of the layer (W), expressed by κ , and the mechanical properties of the layer materials, R_e^W , R_0 and equivalent stresses σ_H , σ_v are established in further experiments.

Key words: stress state, fracture resistance, mismatched weld joints

1. Introduction

Considerable local diversification of the material structure and consequently, of the mechanical properties may occur in the weld or in the heat affected zone (HAZ). This dissimilarity is caused by different mechanical and chemical features of the weld and base materials as well as by the thermal and strain cycles during welding and may occur through the fusion line and HAZ of welds. The effect of strength mis-match in steel weldments has received much attention over the last years and a main reason for this interest is the increased use of steel with higher strength and the difficulties in specified weld metal toughness. The mechanical properties and effects of strength mis-match depends on the presumption, and many misunderstandings have occurred because the purpose with the examinations and the selection of boundary conditions have not been clearly specified. Considering the above - mentioned problem of heterogeneous weld joints we will focus our attention on a simplified model with thin layer-soft or hard- which are presented on Fig. 1. Considering the above - mentioned problem of a mis-match welded joint, it is essential that a model which shows the real conditions of the joint is presented. It should be assumed that the respective model presents the physical reality precisely enough to ensure the physical or technical sense of the models analysis. Thus, the physical model is a simplification of the real welding system and only matches the system in respect of its essential features.

The essential physical phenomena affecting the mechanical properties of these models occur at the interface of zones (B) and (W). Determination of change in the state of stress occurring in this area is of primary importance for correct interpretation and estimation of mechanical properties and

fracture resistance of these models. The main difficulty adequately estimating the state of stress is that the material of an undermatched weld joint undergoes heterogeneous deformations which result in non-uniform stress pattern. It is possible for discontinuities of stress to arise, but these should not disturb the equilibrium state.

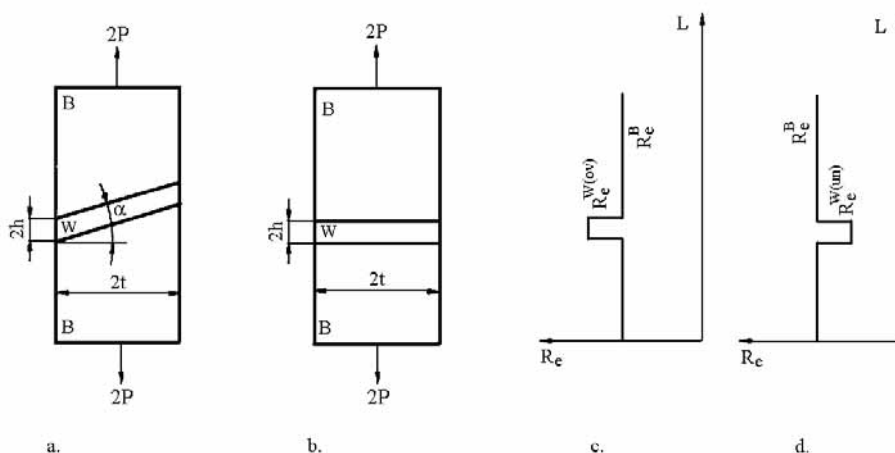


Fig. 1. Characteristic of the models of the mismatched weld joints:
a. geometrical configuration - layer W is incline to external load,
b. geometrical configuration - layer W is perpendicular to external load,
c. change of the yield point R_e in the overmatched weld joint,
d. change of the yield point R_e in the undermatched weld joint.

2. Characterisation of the state of stress at interface of zones (B) and (W)

Components of the state stress in mis-matched weld joints under static tension are determined by the equilibrium equations and the equation of the plasticity condition which fulfilling the boundary condition of the interfaces of zones B and W (Fig.1). A suitable analytic models are presented in Figs.2 and 3.

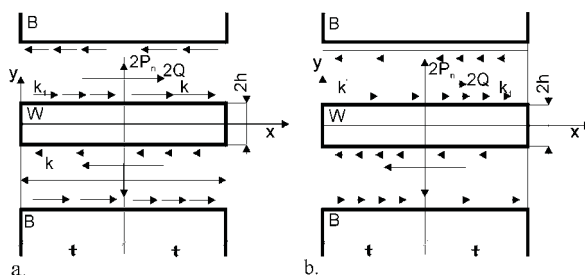


Fig. 2. Characteristic of analytic models of mismatched weld joints with inclined layer to force $2P$:
a. undermatching case, b. overmatching case.

The components σ_{xx} , σ_{yy} and σ_{xy} for the undermatched and overmatched weld joints with inclined layer W to be determined as follows [1]:

- undermatched weld joints (Fig.1a, d and 2a):

$$\sigma_{x(rel)}^{un} = \frac{\sigma_{xx}^{un}}{k} = \frac{1}{1-\gamma} \left(\frac{\pi}{2} - \gamma \sqrt{1-\gamma^2} - \arcsin \gamma \right) + \frac{1-\gamma}{2} \frac{\xi}{\kappa} - 2 \sqrt{1 - \left(\frac{1+\gamma}{2} + \frac{1-\gamma}{2} \frac{\eta}{\kappa} \right)^2}, \quad (1)$$

$$\sigma_{y(rel)}^{un} = \frac{\sigma_y^{un}}{k} = \frac{1}{1-\gamma} \left(\frac{\pi}{2} - \gamma \sqrt{1-\gamma^2} - \arcsin \gamma \right) + \frac{1-\gamma}{2} \frac{\xi}{\kappa}, \quad (2)$$

$$\sigma_{xy(rel)}^{un} = \frac{\sigma_{xy}^{un}}{k} = \frac{1+\gamma}{2} + \frac{1-\gamma}{2} \frac{\eta}{\kappa}, \quad (3)$$

$$\gamma = \frac{k_1}{k}, \quad |\gamma| \leq 1, \quad k = \frac{R_e^{W(un)}}{\sqrt{3}}, \quad -k \leq k_1 \leq k, \quad R_e^{W(un)} \leq R_e^B.$$

- overmatched weld joints (Figs 1a, c and 2b):

$$\sigma_{xx(rel)}^{ov} = \frac{\sigma_{xx}^{ov}}{k} = - \left[\frac{1}{1-\gamma} \left(-\frac{\pi}{2} + \gamma \sqrt{1-\gamma^2} + \arcsin \gamma \right) + \frac{1-\gamma}{2} \frac{\xi}{\kappa} + 2 \sqrt{1 - \left(\frac{1+\gamma}{2} + \frac{1-\gamma}{2} \frac{\eta}{\kappa} \right)^2} \right], \quad (4)$$

$$\sigma_{yy(rel)}^{ov} = \frac{\sigma_{yy}^{ov}}{k} = \frac{1}{1-\gamma} \left(-\frac{\pi}{2} + \gamma \sqrt{1-\gamma^2} + \arcsin \gamma \right) + \frac{1-\gamma}{2} \frac{\xi}{\kappa}, \quad (5)$$

$$\sigma_{xy(rel)}^{ov} = \frac{\sigma_{xy}^{ov}}{k} = \frac{1+\gamma}{2} + \frac{1-\gamma}{2} \frac{\eta}{\kappa}, \quad (6)$$

$$\gamma = k_1 / k, \quad |\gamma| \leq 1, \quad k = R_e^{W(ov)} / \sqrt{3}, \quad R_e^{W(ov)} \geq R_e^B,$$

$$\kappa = \frac{2h}{2t}, \quad \eta = \frac{2y}{2t}, \quad \xi = \frac{2x}{2t}, \quad \kappa \geq \eta.$$

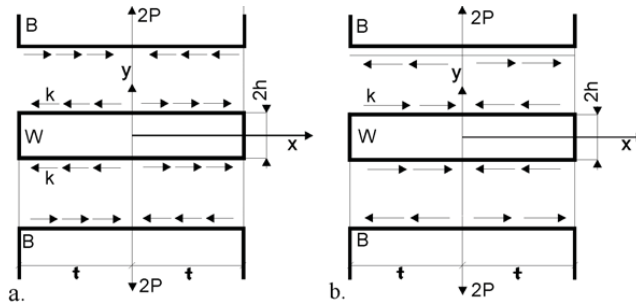


Fig. 3. Characteristic of analytic models of mismatched weld joints with perpendicular layer to force 2P.
a. undermatching case, b. overmatching case.

If the layer is perpendicular to the tension force $2P$ the parameter γ is eq. (- 1) and equation (1)÷(3), (4)÷(6) are transformed in the following shape:

- undermatched case (Fig. 1b, d and 3a):

$$\sigma_{xx(rel)}^{un} = \frac{\sigma_{xx}^{un}}{k} = \frac{1}{2}\pi + \frac{\xi}{\kappa} - 2\sqrt{1 - \frac{\eta^2}{\kappa^2}}, \quad (7)$$

$$\sigma_{yy(rel)}^{un} = \frac{\sigma_{yy}^{un}}{k} = \frac{\pi}{2} + \frac{\xi}{\kappa}, \quad (8)$$

$$\sigma_{xy(rel)}^{un} = \frac{\sigma_{xy}^{un}}{k} = \frac{\eta}{\kappa}, \quad (9)$$

- overmatched case (Figs 1b, c and 3a):

$$\sigma_{xx(rel)}^{ov} = \frac{\sigma_{xx}^{ov}}{k} = \frac{\pi}{2} - \frac{\xi}{\kappa} + 2\sqrt{1 - \frac{\eta^2}{\kappa^2}}, \quad (10)$$

$$\sigma_{yy(rel)}^{ov} = \frac{\sigma_{yy}^{ov}}{k} = -\frac{\pi}{2} + \frac{\xi}{\kappa}, \quad (11)$$

$$\sigma_{xy(rel)}^{ov} = \frac{\sigma_{xy}^{ov}}{k} = \frac{\eta}{\kappa}, \quad (12)$$

These above equations (7)÷(9) assumes the form previously determined by Prandtl for undermatched case. It were reveals a non-linear stress state of σ_{xx} , σ_{yy} in inclined soft and hard layers and some analytical examples are presented in Figs 4 and 5.

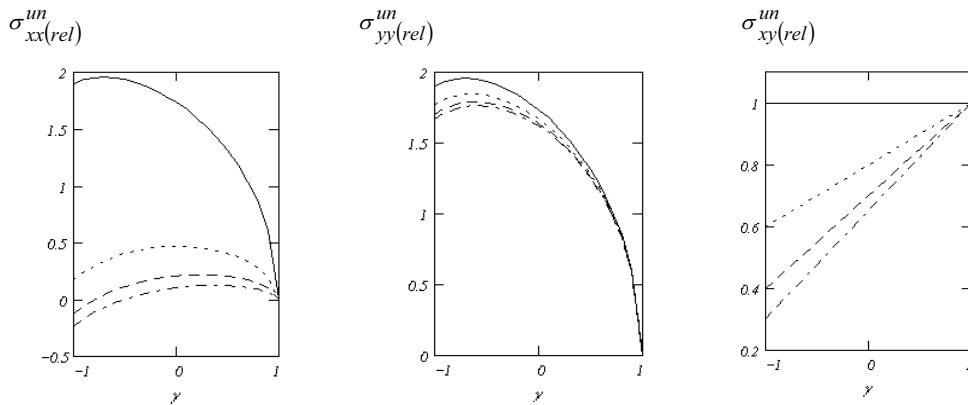


Fig. 4. Characteristic of stresses, $\sigma_{xx(rel)}^{un}$, $\sigma_{yy(rel)}^{un}$, $\sigma_{xy(rel)}^{un}$
at $\kappa = 0,3; 0,5; 0,75; 0,99$ and $\eta = 0,3; \xi = 0,1$.

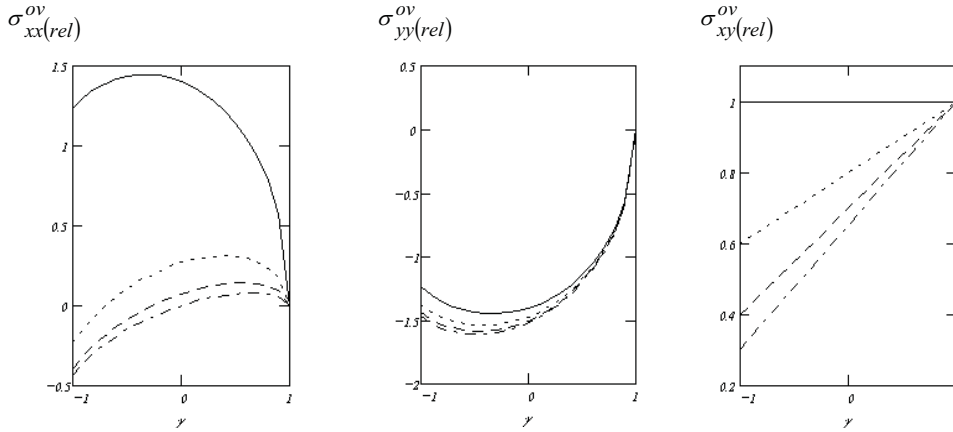


Fig. 5. Characteristic of stresses $\sigma_{xx}^{ov}(rel)$, $\sigma_{yy}^{ov}(rel)$, $\sigma_{xy}^{ov}(rel)$
at $\kappa = 0,3; 0,5; 0,75; 0,99$ and $\eta=0,3; \xi=0,1$.

3. Influence of the state of stress on the mechanical properties and fracture resistance of mismatched weld joint models

From the practical point of view, the effect of the change in the state of stress on the mechanical properties of the welded joint model at static tension is very interesting. It can be expressed by the average values of stresses that can be transferred by a joint with a soft or hard layer as [2]:

$$\sigma_{ever}^{un} = \frac{2R_e^{W(un)}}{\sqrt{3}} \left\{ \frac{1}{4(1-q)} \left[\frac{\pi}{2} + 2(1-2q)\sqrt{q(1-q)} - \arcsin(2q-1) \right] + (1-q)\frac{1}{4\kappa} \right\}, \quad (13a)$$

$$\sigma_{ever}^{ov} = \frac{2R_e^{W(ov)}}{\sqrt{3}} \left\{ \frac{1}{4(1-q)} \left[-\frac{\pi}{2} - 2(1-2q)\sqrt{q(1-q)} + \arcsin(2q-1) \right] + (1-q)\frac{1}{4\kappa} \right\}, \quad (13b)$$

where:

- $R_{ever}^{W(un)}$, $R_{ever}^{W(ov)}$ - the tensile yield point of the layer (W) for under- and overmatched case,
- q - the factor which allows for the effect of interface normalised tangential stresses $0 \leq q < 1$.

By converting the above equation and introducing the following ratio:

$$K_W^{un} = \frac{2}{\sqrt{3}} \left(\frac{1}{4(1-q)} \left[\frac{\pi}{2} + 2(1-2q)\sqrt{q(1-q)} - \arcsin(2q-1) \right] + (1-q)\frac{1}{4\kappa} \right), \quad (14a)$$

$$K_W^{ov} = \frac{2}{\sqrt{3}} \left(\frac{1}{4(1-q)} \left[-\frac{\pi}{2} - 2(1-2q)\sqrt{q(1-q)} + \arcsin(2q-1) \right] + (1-q)\frac{1}{4\kappa} \right), \quad (14b)$$

we can evaluate the effect of the change of mechanical properties of the soft or hard (zone) (W) as a result of the change in the state of stress as a constraint factors K_W^{un} , K_W^{ov} . The above data indicate that the greater value of K_W , the smaller the value of κ and q but different for under- and overmatched case. If $q = 0$ ($2Q=0$, $\alpha=0$), equation (13a) assumes the form previously determined by Kačanov for undermatched case:

$$\sigma_{ever}^{un} = \frac{2}{\sqrt{3}} R_e^{W(un)} \left(\frac{\pi}{4} + \frac{1}{4\kappa} \right), \quad (15)$$

For overmatched case equation (13b) takes the following form:

$$\sigma_{ever}^{ov} = \frac{2}{\sqrt{3}} R_e^{W(ov)} \left(-\frac{\pi}{4} + \frac{1}{4\kappa} \right), \quad (16)$$

The theoretical values of K_W^{un} indicate that the mechanical properties of the so-called soft layer can be considerably improved due to the change in stresses of that area. Apart from the geometrical conditions, the upper limit of the strength is determined by the mechanical properties of the zones (B) and (W).

If the mechanical properties of the material in the zone (B), determined as R_m^B (tensile strength) and R_e^B (tensile yield strength), correspond in principle with the mechanical properties of the material in its initial state before welding, and it is assumed that $\sigma_{ever} = R_m^B$, then the relative thickness of the layer (W) which has no negative effect on the whole strength of the welded joint can be calculated from the following equation ($K_s = R_e^B / R_e^{W(un)}$, $\gamma^B = R_m^B / R_e^B$):

$$\kappa_{cr} = \frac{1-q}{2\sqrt{3(1-q)K_s \cdot \gamma^B - \left[\pi/2 + 2(1-2q)\sqrt{q(1-q)} - \arcsin(2q-1) \right]}}, \quad (17)$$

Conditions which cause brittle fracture can be determined based on the conception of Pełczyński [3] as:

- undermatching case

$$\frac{\sigma_{ever}^{un}}{R_0^{un}} = \frac{\sigma_H^{un}}{\sigma_v^{un}}, \quad (18a)$$

- overmatching case

$$\frac{\sigma_{ever}^{ov}}{R_0^{ov}} = \frac{\sigma_H^{ov}}{\sigma_v^{ov}}, \quad (18b)$$

where:

- R_0 - cohesive strength,
- σ_H, σ_v - the equivalent stress according to Huber-Mises and Saint-Venant, respectively.

The equivalent stresses σ_H^{un} , σ_H^{ov} can be calculated from:

- undermatching case

$$\sigma_H^{un} = \sqrt{(\sigma_{xx}^{un} - \sigma_{yy}^{un})^2 + \sigma_x^{un} \sigma_y^{un} + 3\sigma_{xy}^{un^2}}, \quad (19a)$$

- overmatching case

$$, \sigma_H^{ov} = \sqrt{(\sigma_{xx}^{ov} - \sigma_{yy}^{ov})^2 + \sigma_x^{ov} \sigma_y^{ov} + 3\sigma_{xy}^{ov^2}}, \quad (19b)$$

Instead of σ_v^{un} , σ_v^{ov} we can write:

- undermatching case

$$\sigma_v^{un} = \frac{(\sigma_{xx}^{un} + \sigma_{yy}^{un})(1 - \nu)}{2} + \frac{1 + \nu}{2} \sqrt{(\sigma_{xx}^{un} + \sigma_{yy}^{un})^2 + 4\sigma_{xy}^{un^2}}, \quad (20a)$$

- overmatching case

$$\sigma_v^{ov} = \frac{(\sigma_{xx}^{ov} + \sigma_{yy}^{ov})(1 - \nu)}{2} + \frac{1 + \nu}{2} \sqrt{(\sigma_{xx}^{ov} + \sigma_{yy}^{ov})^2 + 4\sigma_{xy}^{ov^2}}, \quad (20b)$$

Therefore, with regard to equation (15), (16) and (18a), (18b) we can evaluate the geometrical conditions of the layer (W) expressed by the parameter κ which can be calculated from:

- undermatching case

$$\kappa = \frac{R_e^{W(un)} \sigma_v^{un}}{2\sqrt{3}\sigma_H^{un} R_0^{un} - \pi R_e^{W(un)} \sigma_v^{un}}, \quad (21a)$$

- overmatching case

$$\kappa = \frac{R_e^{W(ov)} \sigma_v^{ov}}{2\sqrt{3}\sigma_H^{ov} R_0^{ov} + \pi R_e^{W(ov)} \sigma_v^{ov}}, \quad (21b)$$

The solution of the above equation gives a value for parameter κ after which brittle fracture may occur. Mismatched weld joints fail in ductile mode in soft or hard layer when:

- undermatching case

$$\frac{\sigma_{ever}^{un}}{R_0^{un}} < \frac{\sigma_H^{un}}{\sigma_v^{un}}, \quad (22a)$$

- overmatching case

$$\frac{\sigma_{ever}^{ov}}{R_0^{ov}} < \frac{\sigma_H^{ov}}{\sigma_v^{ov}}, \quad (22b)$$

We can now evaluate the geometrical conditions of the layer (W) expressed by parameter κ when the mismatched weld joints fail in the ductile mode:

- undermatching case

$$\kappa > \frac{R_e^{W(un)}(1-q)\sigma_v^{un}}{2\sqrt{3}\sigma_H^{un}R_0^{un} - R_e^{W(un)}\sigma_v^{un}\left[\pi/2 + 2(1-2q)\sqrt{q(1-q)} - \arcsin(2q-1)\right]}, \quad (23a)$$

- overmatching case

$$\kappa > \frac{R_e^{W(ov)}(1-q)\sigma_v^{ov}}{2\sqrt{3}\sigma_H^{ov}R_0^{ov} - R_e^{W(ov)}\sigma_v^{ov}\left[-\pi/2 - 2(1-2q)\sqrt{q(1-q)} + \arcsin(2q-1)\right]}, \quad (23b)$$

Regarding the requirements of, e.g., standards concerning the estimation of K_{IC} , it should be noted that in the zone (W) favourable conditions for passing $K_C \rightarrow K_{IC}$ occur when the value of $K_W^{un/ov}$ is increased. K_C and K_{IC} are the critical values of stress intensity factors adequate for plane stress and strain [3].

Conclusions

The following revealed features of undermatched and overmatched weld joints models were established:

- state of stress is mismatched weld joint models under static tension,
- constraint factor $K_W^{un/ov}$ which described change of mechanical properties of the soft or hard zones (W) as a result on the conversion in the state of stress,
- relative thickness $\kappa_{cr} = f(K_s, \gamma^B, q)$ of the layer (W) for undermatched weld joint model which has no negative effect on the strength at static tension,
- conditions for producing brittle and ductile fracture in mismatched weld joint models in relation to geometrical conditions of the layer (W), expressed by κ , and the mechanical properties of the layer materials, $R_e^{W(un)/(ov)}$, $R_0^{un/ov}$ and equivalent stresses $\sigma_H^{un/ov}$, $\sigma_v^{un/ov}$ are established.

References

- [1] Ranatowski E., *Characteristic of the constraint effect at interface of the thin layer in mismatched welded joints*, B. Michel. K-D. Lang (Eds.), Smart Systems Integration and Reliability, Goldenbogen Verlag, ISBN 978-3-932434-77-8, pp. 480-492, Dresden, 2010.
- [2] Ranatowski E., *Influence of the constraint effect on fracture resistance of mismatched weld joints*, Mechanism and Mechanics of Damage and Failure. ECF-11. EMAS, Vol.3. pp. 2061÷2066. ISBN 0947817 - 93X, United Kingdom, (1996).
- [3] Ranatowski E., *Some remarks on stress state at interface of the mismatched weld joints*, Mismatching of Interfaces and Welds, Editors: K.-H. Schwalbe, M. Koçak, GKSS Research Center Publication, Geesthacht, FRG, ISBN 3-00-001951-0, pp. 185÷196, Germany, (1997).



ANALYSIS OF INFLUENCE OF ELECTROLYTE FLOW VOLUME RATE IN INTERELECTRODE GAP ON PHYSICAL AND GEOMETRIC PARAMETERS OF ELECTRO-CHEMICAL MACHINING

Jerzy Sawicki

*University of Technology & Agriculture, Faculty of Mechanical Engineering,
ul. Prof. S. Kaliskiego 7, 85-791 Bydgoszcz, Poland,*

Tel. +48523408277,

e-mail: Jerzy.Sawicki@utp.edu.pl

Abstract

In the paper has been presented an analysis of the influence of the electrolyte flow volume stream on the geometry of the work-piece and physical parameters of ECM electrochemical machining. Equations resulting from the principles of momentum, mass and energy conservation describing the physical phenomena which occur during electrochemical machining have been formulated and solved.

Keywords: *electrochemical machining, electrolyte flow, mathematical model*

1. Introduction

Electrochemical machining with the use of a tool-electrode is today one of the basic operations of electrochemical machining technology for machine elements and other mechanical devices [1], [2].

In the constant process the tool-electrode (TE) performs most often a translation motion towards the machined surface. Electrolyte is supplied to the inter electrode gap with high velocity causing carrying away erosion products from the interelectrode gap (IEG). These are mainly particles of hydrogen and ions of the digested metal. Thus, in such conditions we obtain multi-phase, in general, three dimensional flow [3].

Hydrodynamic parameters of the flow and the medium properties determine the processes of mass, momentum and energy exchange within the inter electrode gap. Properly matched they prevent from occurrence of cavitation, critical flow and void fracture [4].

The above mentioned processes have significant influence on the electrochemical machining velocity and application properties of the machined surface [5].

Modelling of ECM involves: determination of the inter electrode gap thickness changes, the machined surface shape evolution in time, and distribution of physics-chemical conditions in the machining area, such as: static pressure distribution, electrolyte flow velocity, temperature and void fracture.

Many authors have dealt with the mathematical description of ECM machining, including:

Tipon [8], Fitzgerald, McGeough and Marsh[9], Alkire[10], Davydov, Kozak[11], Sautebin[12], Jain and Pandey[13], Prentice, Tobias,[14], Bialecki[15], Hume [16], Zouh [17], Prentice and Tobias [18] and Dukovic [19] and others.

The purpose of this work is to analyze the influence of the electrolyte flow volume stream inside the interelectrode gap on the machined surface physical parameters and its geometry.

2. Mathematical model of ECM process

Fig. 1 shows the area of electrolyte flow inside the interelectrode gap (IEG), between curvilinear, axially symmetrical surfaces.

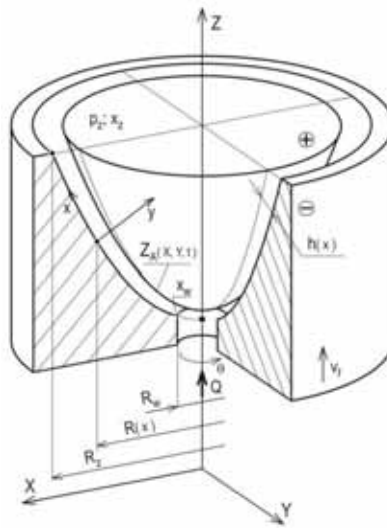


Fig.1. Area flow of electrolyte in interelectrode gap IEG

A general differential equation describing shape evolution of the surface machined by anode dissolution according to ECM dissolution theory, has the form [4,5,6,7]:

$$\frac{\partial F}{\partial t} + k_v \vec{j}_A \text{grad} F = 0 \quad (1)$$

with initial condition $F(X, Y, 0) = F_0$

where:

$\vec{j}_A = \vec{j}(X_A, Y_A, t)$ - distribution of current density on the machined surface,

k_v - coefficient of electrochemical machinability

$F_0(A, 0) = 0$ - an equation describing the initial workpiece (WP),

$F(A, t) = 0$ - an equation describing the anode surface in time t .

Current density results from Ohm's law [4,5,6,7]:

$$\vec{j} = -\kappa \text{grad} u|_A \quad (2)$$

where: u - potential of the electrical field between the electrodes,
 κ - conductivity.

In rectangular axis X, Y, Z connected with the immovable anode, the anode surface equation has the form:

$$Z = Z_a(X, Y, t) \quad (3)$$

Introducing equation(3) into dependence (1), one obtains:

$$\frac{\partial Z_a}{\partial t} = k_v j_A \sqrt{1 + \left(\frac{\partial Z_a}{\partial X}\right)^2 + \left(\frac{\partial Z_a}{\partial Y}\right)^2} \quad (4)$$

where: k_v - coefficient of electrochemical machinability
for $t=0$ $Z_a = Z_0(X, Y)$.

Assuming linear distribution of the electrical field potential along IEG the current density in the anode, in a locally orthogonal coordinate system x, y (Fig.1) is expressed in the following way [6,7,20,21].

$$j_A = \kappa_0 \Phi_{TG}^{-1} \frac{U - E}{h} \quad (5)$$

Function Φ_{TG} describes the influence of conductivity changes within the interelectrode gap (IEG) and is determined in the following way:

$$\Phi_{TG} = \frac{1}{h} \left[\int_0^h \frac{dy}{(1 + \alpha(T - T_0))(1 - \beta)^{3/2}} \right] \quad (6)$$

In order to close equation system (4),(5) and (6) it is necessary to determine temperature rises $\Delta T = T - T_0$ and the distribution of void fracture β . This requires definition of pressure, speed and temperature distributions within the curvilinear interelectrode gap.

Mathematical modeling of the electrolyte flow through the interelectrode gap has been performed in a curvilinear, locally orthogonal coordinate system connected with immobile surface [4].

Having accepted for consideration a model of two phase, anti-slide flow, the mixture movement equations resulting from laws of mass, momentum and energy preservation in curvilinear locally rectangular axis, are in the form [20]:

$$\frac{1}{R} \frac{\partial (\rho_e R v_x)}{\partial x} + \frac{\partial (\rho_e v_y)}{\partial y} = 0 \quad (7)$$

$$\frac{1}{R} \frac{\partial (\rho_H R v_x)}{\partial x} + \frac{\partial (\rho_H v_y)}{\partial y} = j \eta_H k_H h^{-1} \quad (8)$$

$$0 = -\frac{\partial p_e}{\partial x} + \mu_e \frac{\partial^2 v_x}{\partial y^2} \quad (9)$$

$$0 = -\frac{\partial p_e}{\partial y} \quad (10)$$

$$\rho_e = \rho_{e0}(1 - \beta), \quad \rho_H = \rho_{H0}\beta \quad (11)$$

where: v_x, v_y - components of velocity vector,

- p_e - electrolyte pressure,
 ρ_{eo} - electrolyte density,
 ρ_{Ho} - hydrogen density,
 μ_e - dynamic coefficient of electrolyte viscosity,
 μ_H - dynamic coefficient of hydrogen viscosity,
 β - void fraction,
 j, η_H, k_H - are, respectively, current density, current efficiency of hydrogen emission, hydrogen electrochemical equivalent,
 R - tool electrode surface radius.

Energy equation for the considered flow, taking into consideration Joule's heat, emitted during the current flow, forced heat convection caused by the electrolyte flow, heat exchange by electrodes and negligence of the dispersed energy, has now the form [22]:

$$v_x \frac{\partial T}{\partial x} + v_y \frac{\partial T}{\partial y} = \frac{1}{R} \frac{\partial}{\partial x} \left(a R \frac{\partial T}{\partial x} \right) + \frac{\partial}{\partial y} \left(a \frac{\partial T}{\partial y} \right) + \frac{j^2}{\rho_e c_p \kappa} \quad (12)$$

where: a - coefficient of electrolyte thermal diffusivity,
 κ - electrolyte conductivity,
 T - electrolyte temperature,
 c_p - specific heat with constant pressure,

Formulated equation system (7)-(12) is the principal system of equations for the analysis of an axially-symmetrical flow of the electrolyte and hydrogen mixture flow through the interelectrode gap.

The solution of equation system (7)-(12) will enable to define distributions of velocities, pressures and temperature in the interelectrode gap. The obtained formulas defining the temperature distribution in the gap will be utilized for determination of the workpiece (WP) shape evolution (anode) on the basis of equation (4).

Solutions of equations (7)-(12) should satisfy boundary conditions with regard to :

- pressure and velocity components:

$$\begin{aligned}
 v_x = v_y = 0 \quad dla \quad y = 0, \\
 v_x = v_y = 0 \quad dla \quad y = h, \\
 p = p_z \quad dla \quad x = x_z
 \end{aligned} \quad (13)$$

- for temperature:

$$\begin{aligned}
 &\text{- on the walls: } T = T_s \quad dla \quad x \geq x_w \quad i \quad y = 0 \quad \text{oraz } y = h \\
 &\text{- on the inlet: } T = T_w
 \end{aligned} \quad (14)$$

where: p_z – pressure on the interelectrode gap outlet,
 x_z – coordinate of the interelectrode end
 x_w - coordinate of the interelectrode beginning
 T_s - temperature of electrodes, T_w – temperature on the inlet,

When integrating motion equations (7) – (10), one can obtain formulas defining velocities and pressures within the interelectrode gap.

$$v_x = \frac{3Q}{\pi R h^3} (hy - y^2) \quad (15)$$

$$p(x) = -\frac{6\eta_H Q}{\pi h^3} (A_x - A_z) + p_a, \quad A_x = \int \frac{dx}{R}, \quad A_z = A(x_z) \quad (16)$$

Dependencies (15)-(18) describe velocity and pressure distributions in the mixture laminar flow through the gap, with a random profile of surfaces limiting the flow. The assumption of specific geometry of the axially-symmetrical surface leads to accurate definition of velocity and pressure distributions.

Distribution of void fracture β was determined from the mass balance of hydrogen, given off on the cathode.

When integrating equation (8) across the gap

$$\frac{1}{R} \frac{\partial}{\partial x} \left(\rho_H R \int_0^h v_x dy \right) + \rho_H v_x \Big|_0^h = j \eta_H k_H \quad (17)$$

and, next, accepting the assumption that $\beta = \beta(x)$ one can obtain, after transformations:

$$\frac{\partial}{\partial x} \left(\frac{P}{T} \beta \right) = \frac{2\pi \eta_H k_H}{\mu_H Q} j R \quad (18)$$

whereas: β - void fracture, $\rho_{H_2} = \frac{P_{H_2}}{R_H T}$ - hydrogen density, η_H - current efficiency of gas emission, k_H - hydrogen electrochemical equivalent, R_H - hydrogen gas constant, μ_H - hydrogen molar mass.

Solution to equation of the machined surface shape evolution (4) was based on the method of successive approximations in combination with the time step method [6,7,20,21,22].

3. Numerical model of ECM process

This problem is accounted for according to a successive approximation method for all used numerical schemes using at the same time the time steps method [6,7,20,21].

Energy equation (12) has been solved numerically with the use of finite difference method replacing the temperature derivatives with algebraic expressions.

Simplified algorithm of a mathematical model solution is presented in Fig. 2.

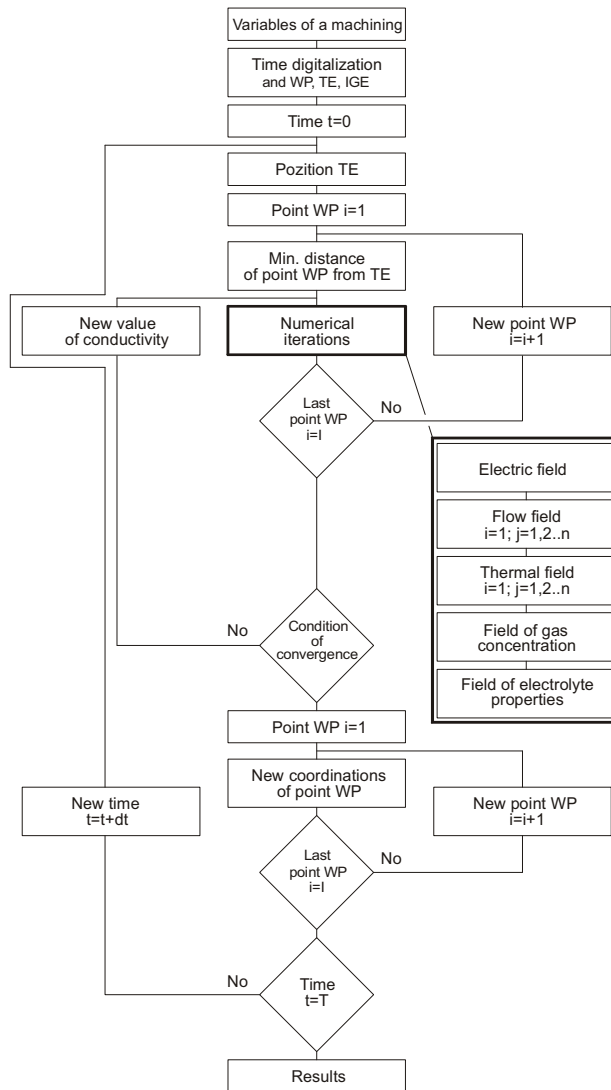


Fig.2. ECM computer simulation algorithm

4. Exemplary calculations

Calculations were performed for shaping rotary electrodes with spherical surface profiles. The supply system ensures the electrolyte fixed flow rate in the interelectrode gap. Passivating electrolyte was accepted for calculations. Calculations had been performed until a quasi – stationary state was reached.

For calculations the following, machining parameters were accepted:

initial gap	$h_o = 0.2 \text{ mm}$
speed of move forward of TE	$V_f = 0.01 \text{ mm/s}$
interelectrode voltage	$U = 15 \text{ V}$
volume rate	$Q = 3, 4, 5 \text{ dm}^3/\text{min}$
pressure	$p_z = 0,1 \text{ MPa}$

The obtained results have been illustrated in charts (Fig.3-8) which demonstrate distributions of: interelectrode gap height h , current density j , temperature T , void fraction β , velocity V_m , and pressure p along the interelectrode gap (IEG).

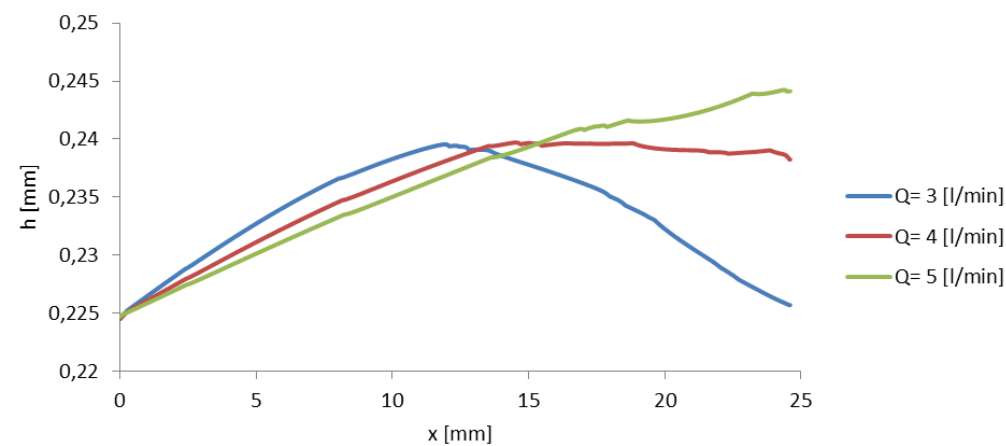


Fig. 3. Distribution of gap height h along IEG

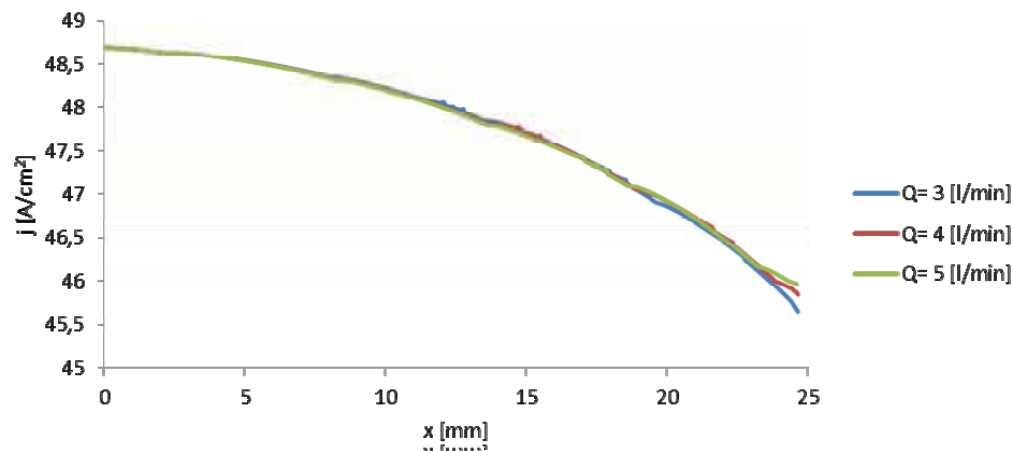


Fig. 4. Distribution of current density j along IEG

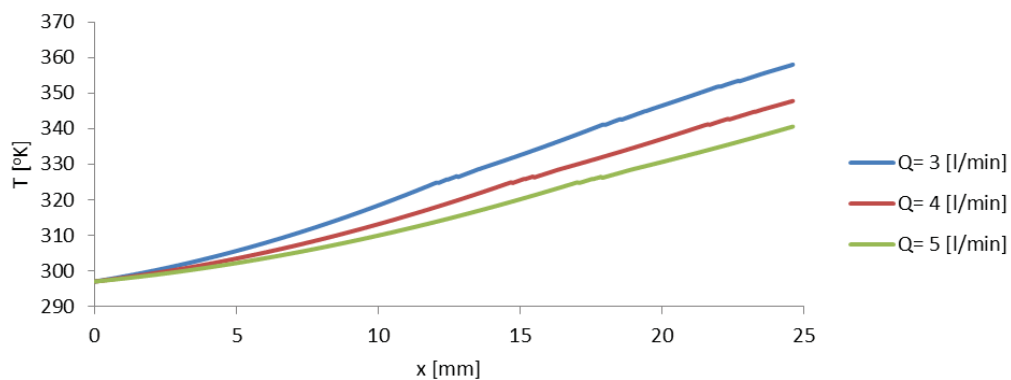


Fig. 5. Distribution of average temperature T along IEG

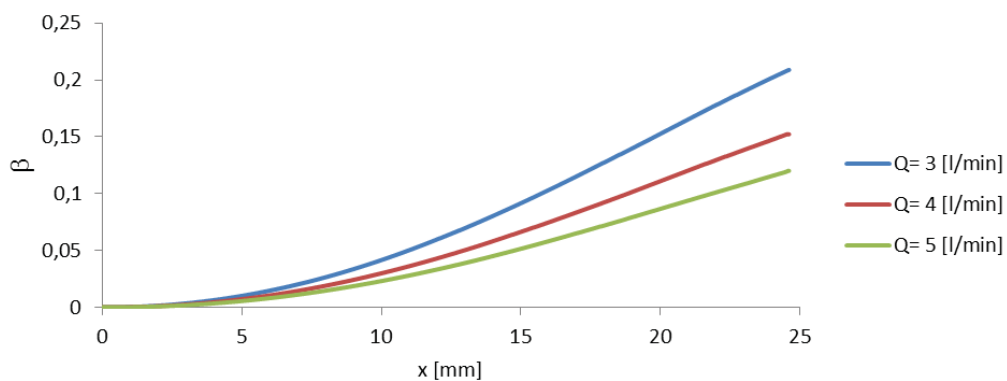


Fig. 6. Distribution of void fraction β along IEG

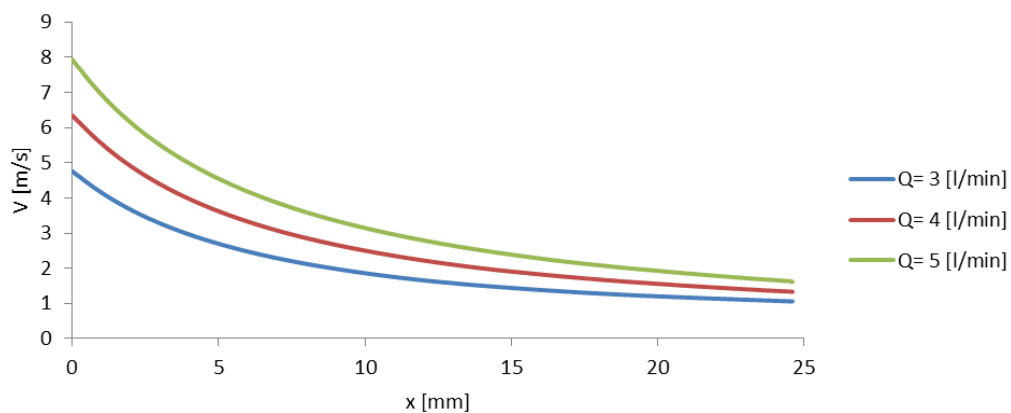


Fig. 7. Distribution of average velocity V along IEG

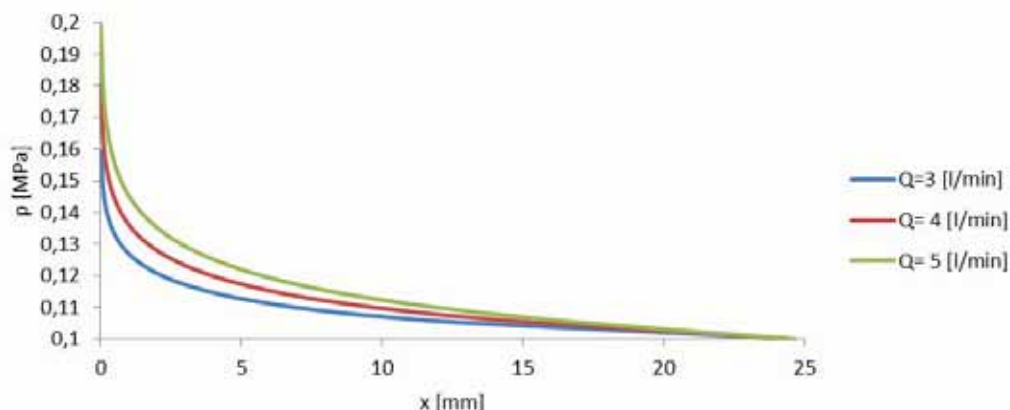


Fig. 8. Distribution of pressure p along IEG

5. Conclusions

The above presented charts allow for formulation of the following conclusions:

- Changes of the inter-electrode gap are caused by dynamically changing physical conditions inside the gap (variable viscosity, density, electrolyte conductivity and also significantly changing velocity of the flow and pressure) Increase in the volume stream has a considerable influence on the interelectrode gap thickness.
- Distribution of the volume fracture (of hydrogen) along the interelectrode gap increases nonlinearly. Value of β on the gap outlet decreases along with an increase in the volume stream and is significantly smaller than the boundary value, above which there occurs a transition from a bubble into the so called corks flow. According to Gryfith and Snyder the critical value is $\beta_{gr}=0.5$,
- Distributions of mean velocity, pressure and temperature along the inter-electrode gap definitely depend on the volume stream value. They result from the gap cross-section field change and rapidly changing physical parameters of the flow caused by electrochemical dissolution. The maximum velocity inside the gap, right behind the inlet, does not exceed the speed of sound in a two-phase medium. The minimal value of pressure in the area of inter-electrode gap (beyond the gap inlet) is considerably higher than pressure of saturated vapor. The temperature distribution indicates a distinct increase in temperature on the inter-electrode gap outlet. It is caused by an increase of the volume fracture at the end of the gap and rapid drop of pressure along the gap.
- Distribution of current density along the inter-electrode gap depends on its local thickness. Increase in the stream volume slightly raises the current density values, especially on the gap outlet.

References

- [1] Wilson, J.F., *Practice and Theory of Electrochemical Machining*, New York, Wiley, 1971.
- [2] McGeough, J.A., *Principles of Electrochemical Machining*, London: Chapman & Hall, 1974.
- [3] Ruszaj, A., *Niekonwencjonalne metody wytwarzania elementów maszyn i narzędzi*, IOS Kraków 1999.

- [4] Kozak, J., *Kształtowanie powierzchni obróbką elektrochemiczną bezstykową*, (ECM). Pr. Naukowe PW, Mechanika nr 41, Wydawnictwo Politechniki Warszawskiej, Warszawa. 1976.
- [5] Kozak, J., *Mathematical Models for Computer Simulation of Electrochemical Machining Process*, Journal of Materials Processing Technology, Vol. 76, 1976.
- [6] Dąbrowski, L., *Podstawy komputerowej symulacji kształtowania elektrochemicznego*, Prace Naukowe, Mechanika, z. 154, Wydaw. Politechniki Warszawskiej, Warszawa, 1992.
- [7] Łubkowski, K., *Stany krytyczne w obróbce elektrochemicznej*, Prace naukowe, Mechanika, z.163, Oficyna Wydawnicza PW, Warszawa, 1996.
- [8] Tipton, H., *Calculation of tool shape for ECM in fundament of Electrochemical Machining*, (Edited by C.I. Faust), Electrochemical Society Softbound Symposium Series, Princeton. 1971.
- [9] Fitz-Gerald, J. M., McGeough, J. A., Marsh, L. McL., *Mathematical theory of electrochemical machining*, 2. Anodic shaping. J. Inst. Maths Appl. 5, 1969.
- [10] Alkire, R., c.. Bergh, T., Sani, R. L., *Predicting electrode shape change with use of finite element methods*, J. Electrochem. Soc. 125. 1978.
- [11] Davydov, A.D., Kozak, J., *Wysokoskorostnyje elektrokhimicheskoje formo obrazowanie*, Nauka, Moskwa, 1990.
- [12] Sautebin, R., Froidevaux, H., Landolt, D., *Theoretical and experimental modeling of surface leveling in ECM under primary current distribution conditions*, J. Electrochem. Soc. 127(5), 1980.
- [13] Jain, V. K., Pandey, P. C., *Tooling design for ECM-A finite element approach*, Trans.ASME. J. Engng Industry 103, 1981.
- [14] Prentice, G. A., Tobias, C. W., *A survey of numerical methods and solution for current distribution problems*, J. Electrochem. Soc. 119(1), 1982b.
- [15] Bialecki, R., Nahlik, R., Lapkowski, M., *Applying the boundary element method to electrochemical calculations of primary current distribution*, Electrochim. Acta 19(7). 1984.
- [16] Hume III, E. C., Deen W. M., Brown, R. A., *Comparison of boundary and finite element methods for moving-boundary problems governed by a potential*, Int. J. Numer. Methods Engng 21, 1985.
- [17] Zhou, Y., *Finite element analysis of electrochemical machining problems validity of electroneutrality assumption and flow in solution crystal growth system*, Ph.D. thesis. Department of Chemical Engineering and Materials Science, University of Minnesota, Minneapolis. MN. 1995.
- [18] Prentice, G. A., Tobias, C. W., *Simulation of changing electrode profiles*, J. Electrochem. Soc. 119(1), 1982.
- [19] Dukovic, J. O., *Computation of current distribution in electrodeposition*, A Review, IBM J. Res. Develop. 34, 1990.
- [20] Sawicki, J., Paczkowski, T., *Obróbka elektrochemiczna krzywoliniowych powierzchni obrotowych*, Zeszyty Naukowe ATR nr 234 Mechanika 54, Bydgoszcz, 2004 r.
- [21] Paczkowski, T., Sawicki, J., *Electrochemical machining of curvilinear surfaces*, Journal of Machining Science and Technology, 2008 USA.
- [22] Sawicki, J., *ECM machining of curvilinear rotary surfaces by a shaping tool electrodeperforming composite motion*, Advances in Manufacturing Science and Technology, Vol. 34, No 2, 2010.



APPLICATION OF MINI SPECIMENS TO HIGH-CYCLE FATIGUE TESTS

Janusz Sempruch, Tomasz Tomaszewski

*University of Technology and Life Sciences in Bydgoszcz
ul. Kaliskiego 7, 85-796 Bydgoszcz, Poland
tel.: +48 52 3408202, fax: +48 52 3408245
e-mail: tomaszewski@utp.edu.pl*

Abstract

Determining complete material fatigue characteristics (S-N curve) is time-consuming and very expensive. Searching for faster procedures of determining the S-N curve, one can use approximate methods which are burdened with qualitative and quantitative error. Such characteristics differ from the real experimental studies results. Yet another method involves the use of mini specimens; the specimens the dimensions of which are lower than the normative sample. It allows for performing tests using much cheaper test stands. In the specimens researched there is a size effect which is broadly discussed in the available literature. The present work offers a review of the current theoretical knowledge on the size effect. There was analysed the geometry of mini specimens applied in experimental studies. Selected works with the use of mini specimens have been reviewed. Areas have been defined in which the mini specimen application is justifiable.

Keywords: size effect, mini specimen, S-N curve, fatigue

1. Fatigue tests in the high number of cycles range

An indispensable part of calculations of design elements exposed to fatigue loads is the knowledge of basic material characteristics, namely the Wöhler characteristics, also referred to in literature as the S-N curve (Fig. 1). In the range of high number of cycles it shows two characteristic areas; limited fatigue life (the area under the section defined with slope m , but above Z_G) and unlimited fatigue life (the area below Z_G).

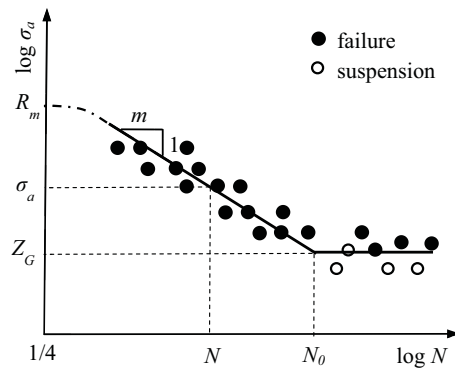


Fig. 1. S-N curve plotted on $\log \sigma_a - \log N$ coordinates

The diagram presented (Fig. 1) shows approximate numbers of specimens necessary to determine the S-N curve. The tests are performed in the area of high-cycle fatigue life in the range 5×10^3 cycles to 2×10^6 to 10×10^6 cycles (N_0). The tests are therefore very time-consuming. To perform such tests, typical servo-hydraulic material-testing machines are used (Fig. 2). The cost of these machines, plus additional indispensable equipment (e.g. extensometer) is, in the case of normative specimens, very high (a few hundred thousand Euro), which makes us encounter material testing machines only in a few laboratories, which, in turn, implies the situation that the real fatigue tests to determine the real Wöhler characteristics, are performed quite rarely. Even if executed, they are considered very expensive due to their time-consuming nature and the high cost of equipment.



Fig. 2. INSTRON servo-hydraulic material-testing machines, laboratory of University of Technology and Life Science

With that in mind, literature offers proposals of approximate definition of the quantities determining the S-N curve. Importantly, the methods are always burdened with a considerable quantitative and qualitative error. They are not, therefore, and cannot be in the future a replacement for real experimental tests.

One of the ways to find a compromise between the identified, due to the accuracy, justification of performing experimental tests and the tests costs is the use of specimens small in size (mini specimens). In the mini specimens tests one can use the test stands of a very simplified structure, due to the range of forces applied. A direct use of the mini-specimen test results calls for determining the size effect on the results and defining, due to normative definition missing, what the mini specimen is.

2. Literature approach to the size effect

Most works [6, 7, 9] assume that fatigue strength decreases with an increase in the dimensions of the element. A graphic representation of that effect is given in Fig. 3. The size effect is explained based on the probabilistic models referring back to the probability of destroying the weakest link in the material structure in the cross-section analysed. With the material volume getting bigger and bigger, there increases the probability of the occurrence of material defects which are caused by the centre of fatigue cracking. This physical model of the size effect, however, is not reflected in the recommended relationships to be applied. It is assumed that the size effect is characterised by the co-efficient [6]:

$$K_d = \frac{Z_d}{Z}, \quad (1)$$

where:

- Z_d – fatigue strength of specimen of any diameter,
- Z – fatigue strength of specimen of the same material, diameter $7 \div 10$ mm.

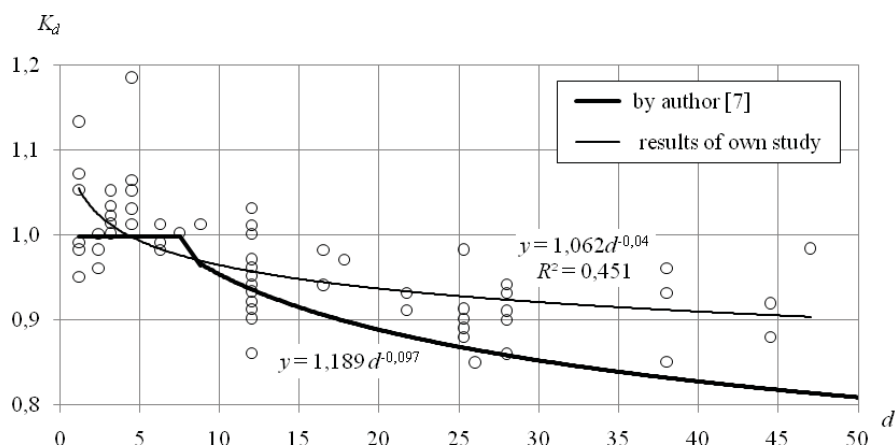


Fig. 3. Quantitative description of the size effect (K_d) [7]

Work [9] makes values K_d depend on the material the element has been made of:

- a) for grey cast iron:

$$K_d = \begin{cases} 1.207 & \text{for } d \leq 7.5, \\ 1.207 \left(\frac{d}{7.5} \right)^{-0.1922} & \text{for } d > 7.5, \end{cases} \quad (2)$$

where:

- d – specimen diameter [mm].

- b) for stainless steel within the dimensions given in material standards:

$$K_d = 1, \quad (3)$$

- c) other types of steel and cast iron materials:

$$K_d = \begin{cases} 1 & \text{for } d \leq d_{min}, \\ \frac{1 - 0,7686 a_d \lg\left(\frac{d}{7,5}\right)}{1 - 0,7686 a_d \lg\left(\frac{d_{min}}{7,5}\right)} & \text{for } d_{min} < d \leq d_{max}, \\ \frac{1 - 0,7686 a_d \lg\left(\frac{d_{max}}{7,5}\right)}{1 - 0,7686 a_d \lg\left(\frac{d_{min}}{7,5}\right)} & \text{for } d \geq d_{max}, \end{cases} \quad (4)$$

where:

- d_{min} – diameter complied with table in work [9],
- d_{max} – maximum diameter adopted in experiment,
- a_d – co-efficient complied with table in work [9].

- d) for wrought aluminium alloys (although R_m , depend on the diameter or thickness of the component):

$$K_d = 1, \quad (5)$$

- e) for cast aluminium alloys:

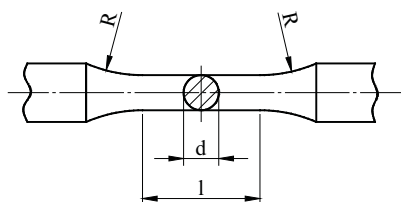
$$K_d = \begin{cases} 1 & \text{for } d < 12, \\ 1,1 \left(\frac{d}{7,5}\right)^{-0,2} & \text{for } 12 < d \leq 150, \\ 0,6 & \text{for } d \geq 150, \end{cases} \quad (6)$$

The co-efficient of the size effect is mostly introduced in the elements exposed to bending and torsion. At those states of load the susceptibility to the size effect is clearly connected with the gradient of stress (strain). In the specimens with axial load the gradient of macroscopic stresses does not exist and so in some works, e.g. [6] it is assumed that there is no need to apply the co-efficient. Direct fatigue tests, however, demonstrated a little impact of the size effect for components with axial load and its application is recommended, which is reported by e.g. work [7].

The analysis of the range of diameter from 8 to 40 mm is covered by work [2] which presents the size effect based on the fractal theory referring back to the material structure. The fractal theory concerns the description of plants of irregular structure magnified to any extent. The ultimate tensile strength and fatigue life were decreasing with an increase in the specimen size. The decrease is relatively bigger for materials showing structure heterogeneity. Increasing the volume of the design element there increases the probability of damaging the element due to greater probability of finding critical micro-fractures causing the development of the fracture.

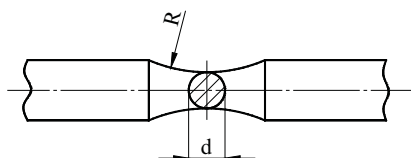
3. Mini specimen geometry

The results of experimental studies reported in other works [3, 4, 5] were recorded for reference specimens (normative) the shape of which complied with standard PN-74/H-04327 [10] (Figs 4, 5).



d [mm]	l [mm]	R_{min} [mm]
6	24	24
7,5	30	32
10	40	45
12	48	48

Fig. 4. Geometry round specimens of a fixed cross-section [10]



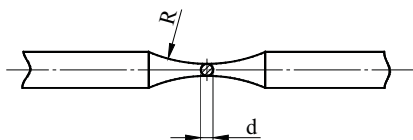
d [mm]	R_{min} [mm]
6	24
7,5	32
10	45
12	48

Fig. 5. Geometry round specimens of variable cross-section [10]

Works [3, 4, 5] were drawing directly on the specimens made according to norm ASTM E-466 [1] for which measurements were defined for round specimens of a fixed cross-section ($d = 5.08 \text{ mm} \div 25.4 \text{ mm}$, $R_{min} = 8 \times l$, $l = 2 \div 3 \times d$) and round specimens of variable cross-section ($d = 5.08 \text{ mm} \div 25.4 \text{ mm}$, $R_{min} = 8 \times d$).

Mini specimens in literature are various in shape. There dominates the shape similar to the normative specimen (Fig. 6a), namely a round specimen of varied cross-section in the shape of the hour-glass. This type of geometry shows a good buckling strength, which is an essential aspect in the miniaturization of specimens with axial load, however, it is also useful to tests with a variable bending and turning moment.

a)



d [mm]	R_{min} [mm]	By work
1	36	[4]
2	80	
1,25	10	[5]
3	31	[3]

b)



d [mm]	By work
0,1, 0,2, 0,6	[8]

Fig. 6. Mini specimen geometry round specimens of variable cross-section, complied with work: a) [3, 4, 5], b) [8]

Besides, one can encounter specimens the shape of which is presented in Fig. 7 (the shape conditioned by the initial material for tests) and the samples presented in Fig. 6b (the specimens shape conditioned by the load method, in that case the tensile specimen).

4. Experimental studies referring to the use of mini specimens in tests

Work [5] presents the impact of the size effect on the fatigue life of the irradiated specimens and weldments (TIG) made from Japanese steel of a reduced ferritic-martensitic activity JLF-1

(Fe-9Cr-2W-V-Ta). Steel JLF-1 is used in the structure of shields of nuclear reactors using the fusion reactors D-T. There were applied two kinds of the specimen sizes; the shape complied with the norm ASTM E-606 and the sample diameters equalled 6 mm (normative specimen) and 1.25 mm (mini specimen) (Fig. 7). The samples were exposed to fatigue tests monitoring strain. In both cases (base material and weld material), the mini specimen showed a greater fatigue life that the normative specimen; the original results are provided in Fig. 8 following work [5].

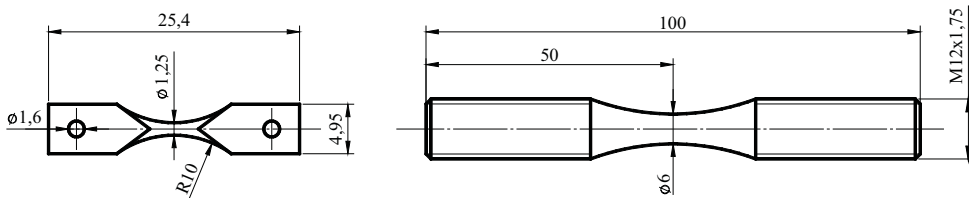


Fig. 7. Specimen geometry used in work [5]

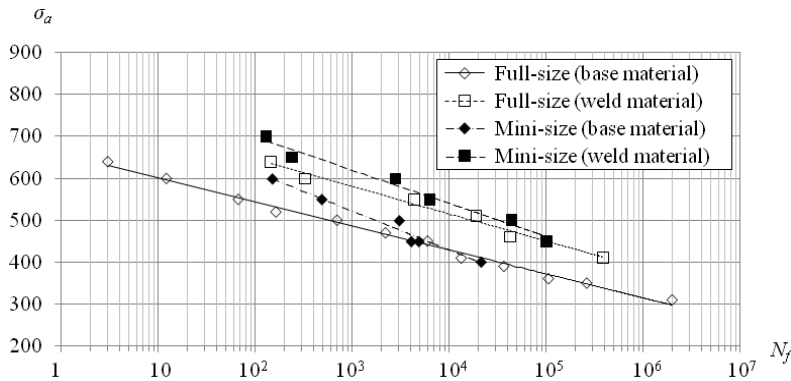


Fig. 8. Relation between stress amplitude and number of cycles [5]

The springboard for the authors of work [8] was the thought that machinery design more and more often focuses on miniaturization. With that in mind, it is indispensable to perform fatigue tests for the plants of real (small) dimensions. Work [8] presents the impact of the effect of scale on fatigue life of materials used in micro-machines (space satellites, medical care). As claimed by the authors of the work, the specimens are made from pure iron and pure aluminium (original names taken after work [8]) 0.2 mm, 0.3 mm and 0.6 mm in diameter. The electrolytic polishing apparatus was used. The test stand has been built from the electrodynamic actuator generating low stress amplitudes. The specimens were with axial loads. The pure aluminium specimens were independent of the diameter. For the same values of the stress amplitude the fatigue life was comparable, while the samples of a smaller diameter made from pure iron showed lower fatigue life.

Work [4] presents the impact of the size effect in the rotationally-bended specimens in the environment of high humidity (60%, 70%, 80%, 90%) and water at the temperature of 25°C. The tests will allow for the selection of materials of e.g. small parts of machines used in the robot driver shafts. The samples were made from steel SS400 and S45C, 8 mm (normative specimen), 2 mm and 1 mm in diameter (mini specimen), respectively. The surfaces of the specimens were polished with abrasive paper grade 1200 (emery paper). It was shown that in the environment of a high humidity the fatigue strength increases with a decrease in the specimen diameter (Fig. 9). In the case of smaller specimen diameters, the water molecules adhere to the surface more easily

forming a layer. Water drops cause a faster initiation of corrosion and cracks than the water layer on the specimen surface.

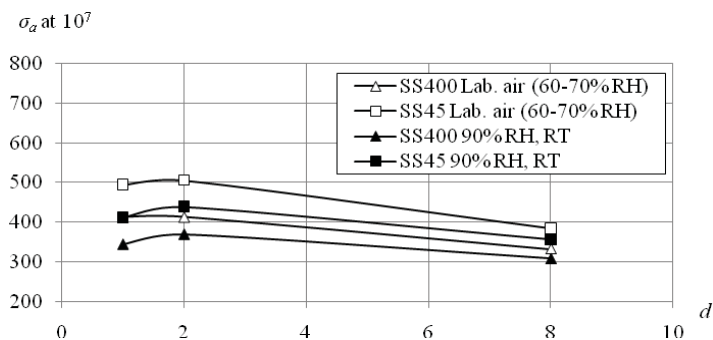


Fig. 9. Relation between fatigue strength at 10^7 cycles and specimen diameter [4]

Research work [3] is of different nature; it presents the application of ultrasonic to research the fatigue life of high-strength steel. The main advantage of the use of ultrasonic is very high working frequency reaching 20 kHz, thanks to which reaching the number of cycles of 10^9 is possible within the time shorter than for the typical frequencies reaching 100 Hz. The tests were performed for the samples 8 mm, 7 mm, 3 mm (mini specimen) in diameter made from steel 40HMA (42CrMo4). The reference specimen was a normalised specimen 6 mm in diameter tested in the servo-hydraulic fatigue machine. The surface of the specimen was given its finish with the abrasive powder $1\mu\text{m}$.

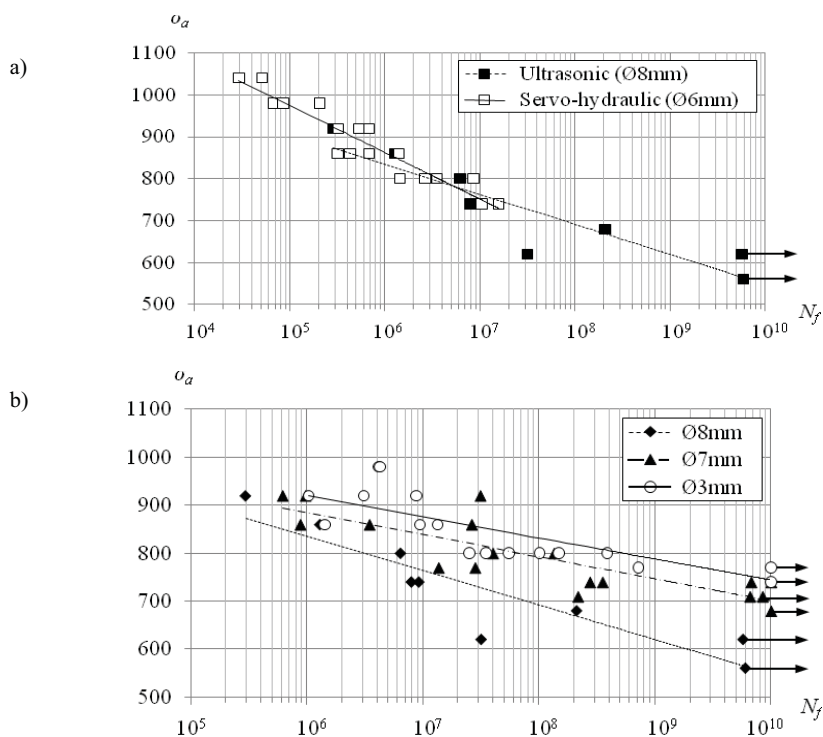


Fig. 10. Relation between stress amplitude and number of cycles:
a) ultrasonic loads and servo-hydraulic loads, b) specimen of different diameters [3]

In the ultrasonic fatigue tests the samples were cooled with the air to decrease the temperature increase. The tests were interrupted to maintain the specimen temperature on the surface not exceeding 30°C. The fatigue life obtained with the method using ultrasonic is similar to the fatigue life obtained on servo-hydraulic fatigue machine (Fig. 10a). There was observed an impact of the size effect. For the samples of lower diameter there were reported higher fatigue life values than the normalized specimens (Fig. 10b).

5. Conclusions

There is some state of knowledge on the size effect, including the model commonly considered the applicable one; it assumes that the size effect does not get identified in the range of samples the dimensions of which are below $7 \div 12$ mm (depending on the source). Such state of knowledge is reflected in the recommended calculation models and their related dependences. The sample data come from literature where for the diameters from 1 mm to $7.5 \div 12$ mm, depending on the material, the co-efficient of the size effect is defined at level 1. The application of the formula depending on the material of the element shows that the size effect depends on the material structure. In the case of materials of heterogeneous structure there is a greater sensitivity to the change of dimensions.

Work [7] provides interesting experimental results of the quantitative effect of the cross-section value, which shows clearly the justifiability of the statement of no size effect in a very narrow range. In general, the effect is also found in the range of the smallest diameters ($1 \div 5$ mm).

The impact of the size effect in the range of the smallest diameters is shown in the experimental studies referred to in item 5. It was experimentally proven that fatigue strength and life of mini specimens ($1 \div 3$ mm) are greater than the normative specimens (6 mm). Those works comply with the relationships presented following work [7] in Fig. 3. The present tests were performed when exposed to bending and tensile loads.

The work has formulated a hypothesis on the justifiability of searching for the test methodology and using mini specimens as a way to lower the costs of tests. With the review of the state of knowledge provided here, assuming the above reasoning as the major one, one shall note that the application of mini specimens is also justifiable due to:

- widening the scope of the possibilities of identifying the material characteristics when sampling a normative specimen is impossible (e.g. elements embossed from aluminium),
- using low values of displacements in the tests, which is favourable to the use of high frequencies and, as a result, shortens the test time,
- using low values of specimen of strain in the tests (on purpose due to selected material groups).

References

- [1] ASTM E-466, *Standard Practice for Conducting Force Controlled Constant Amplitude Axial Fatigue Tests of Metallic Materials*.
- [2] Carpinteri, A., Spagnoli, A., Vantadori, S., *Size effect in S-N curves: A fractal approach to finite-life fatigue strength*, Italy, 2009.
- [3] Furuya, Y., *Specimen size effects on gigacycle fatigue properties of high-strength steel under ultrasonic fatigue testing*, Japan, 2008.
- [4] Haftirman, *The size effect on fatigue strength of structural steel materials in high – humidity environment*, Malaysia, 2009.
- [5] Hirose, T., Sakasegawa, H., Kohyama, A., Katoh, Y., Tanigawa, H., *Effect of specimen size on fatigue properties of reduced activation ferritic/martensitic steels*, Japan, 2000.

- [6] Kocańda, S., Szala, J., *Podstawy obliczeń zmęczeniowych*, Poland, 1997.
- [7] Lee, Y., Pan, J., Hathaway, R. B., Barkey, M. E., *Fatigue Testing and Analysis. Theory and Practice*, United States of America, 2005.
- [8] Nakai, Y., Hashimoto, A., Imanishi, T., Hiwa, C., *Size effect on fatigue strength of metallic micro-materials*, Japan, 1999.
- [9] Neimitz, A., Dzioba, I., Graba, M., Okrajni, J., *Ocena wytrzymałości, trwałości i bezpieczeństwa pracy elementów konstrukcyjnych zawierających defekty*, Poland, 2008.
- [10] PN-74/H-04327, *Badanie metali na zmęczenie. Próba osiowego rozciągania – ściskania przy stałym cyklu obciążeń zewnętrznych*.



MODYFICATION OF SELECTED METHODS OF RAPID DETERMINATION OF FATIGUE CHARAKTERISTICS IN THE RANGE OF LIMITED FATIGUE LIFE

Przemysław Strzelecki*, Janusz Sempruch**

*University of Technology and Life Sciences
Faculty of Mechanical Engineering
ul. Prof. S. Kaliskiego 7, 85-789 Bydgoszcz
tel.: 693 897 581*
email: p.strzelecki@utp.edu.pl*
email: janusz.sempruch@utp.edu.pl***

Abstract

In a number of design situations acquiring complete experimental data on fatigue properties used in material design solutions is impossible. It is justifiable then to use one of the common approximate (analytical) methods, preferably a method of verified accuracy. The problem of accuracy of analytical methods was earlier addressed in a publication [12]. The fatigue life assessment errors shown there for the range of limited fatigue life must be considered unacceptably high. This paper quotes selected, known from literature, applicable proposals and own modifications suggested by the Authors. The modifications were verified based on experimental data from a number of papers. A significant decrease in the fatigue life assessment error was reported.

Keywords: *high-cycle fatigue strength, fatigue plots, analytical methods of estimating Wöhler characteristics*

1. Wöhler characteristics and their importance

In design calculations it is necessary to know fatigue properties of the construction materials applied. As for the construction elements exposed to fatigue loads, the properties (for the calculations in the range of a high cycle number) are determined based on the S-N curve. The curve is applied, in practise, in the area of unlimited fatigue life and limited fatigue life. Performing design calculations in the first of the areas has a much more profound tradition and it has been applied by designers for a few dozen years already. The methods and relationships used in that way have been well verified and recognised. Design element dimensioning due to the limited life has been used only for the recent years and the state of knowledge and the accumulated sources of numerical quantities describing that area are definitely less satisfying. With that in mind, the attention of the Authors of this paper focuses on the second area.

In the range of limited fatigue life the Wöhler curve is also described with equation (1), for the determination of quantities, see Table 1. Considering the knowledge of the value of fatigue limit Z_G and the related limit number of cycles N_0 , one can write the equation (2) or such notation to determine the value of slope m describing the curve in the range we are interested in. The scope of experimental studies necessary to determine value m applying experimental methods is given symbolically in Fig. 1a. The result of value m is accurate, however, unfortunately, due to a high

number of samples which would need to be brought to fatigue damage, it is time-consuming. For example norm [9] recommends performing tests at a minimum of 5 load levels and at least 3 samples for each, which gives us at least 15 samples to be damaged. Besides the result is conservative in a sense of being related to the conditions of the test.

$$\sigma_a^m N = const., \tag{1}$$

$$\sigma_a^m N = Z_G^m N_0, \tag{2}$$

$$m = \frac{\log(\frac{N_0}{N})}{\log(\frac{\sigma_a}{Z_G})}, \tag{3}$$

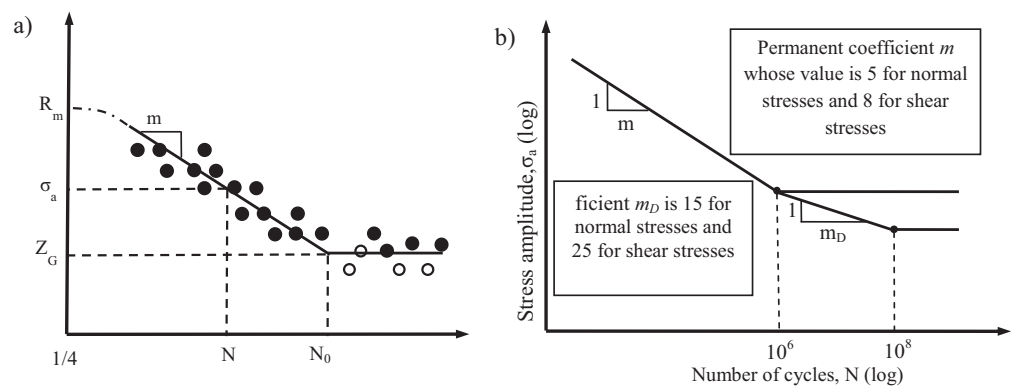


Fig. 1. Method of plotting the S-N curve according to a) experimental and b) analytic approach according to the FITNET method

Tab. 1. Breakdown of sample relationships from calculation methods in the high-cycle fatigue area

Method characteristics		Determined quantities	Model applied	Required input quantities
High-cycle range calculations	Real fatigue factor	δ – real fatigue factor in the range of limited fatigue life	$\delta = \frac{Z_N}{\sigma_{na}}$ $Z_N = Z_G \sqrt[m]{\frac{N}{N_0}}$	$Z_G, \sigma_a, \sigma_m, \varepsilon, \beta, N, N_0, m$
Hypotheses of totalling of fatigue damage in the aspect of stress	Palmgren-Miner hypothesis	D_n – admissible sum of accumulated damage	$D_{PM} = \sum_{i=1}^q \frac{n_i}{N_i}$ $N_i = \left(\frac{Z_G}{\sigma_a}\right)^m N_0$	$\sigma_{ab}, n_i, N_0, Z_G, m$
Legend: Z_G – fatigue limit, σ_a – stress amplitude, σ_m – mean stress, ε – object size coefficient, β – notch effect coefficient, N – executed number of cycles, N_0 – limit number of cycles, N_i – executed number of cycles at a given load level, m – exponent.				

The importance of knowing exponent m , shown with selected examples, is given in Table 1. Table 1 presents sample notations connected with performing calculations of the values of the real fatigue factor and the values of fatigue damage determined according to the hypothesis by Palmgren - Miner. More details on the importance of that quantity in fatigue calculations are provided by the authors of monographs, e.g. [4].

2. Selected methods of acquiring fatigue characteristics and developing the paper hypothesis

Acquiring data on the fatigue characteristics (mostly equation exponent) can be made experimentally (treating the method as accurate) or with the analytic method, treating the method to be approximate.

The experimental method is described in detail in a number of norms, e.g. [9]. Sample analytic methods, namely the FITNET method and the method from the publication [5], were described in article [13]. The methods were selected for verification since they refer to fatigue life in the range of limited fatigue life. Those are the methods which have been proposed relatively recently, to address practical applications by experts. Besides determining the fatigue curve, according to the authors of those methods, can be supported by performing a simple experiment which involves a static test of determining material tensile strength. The verification of the accuracy of calculations of those methods is addressed in paper [12], which demonstrates considerable errors in the fatigue life assessment. For selected conditions the errors range from 14% to 573 %.

The authors of this paper have formulated a working hypothesis of the justifiability of a modified, analytically-experimental, approach which would involve the use of common analytical methods and a partial support from a simple fatigue experiment, own or provided in literature. Applying common methods of rapid determining of fatigue characteristics, offered in literature, accompanied by experimental support, it is possible to obtain satisfactory approximation accuracy result of the estimation for accurate characteristics. The aim of the paper is to verify, in a selected field, the above hypothesis.

3. Analytic-experimental method – own proposal

The own proposal has been based on the notations of FITNET procedure. Since, as demonstrated, determining characteristics according to FITNET methodology in the range of limited fatigue life is insufficiently accurate, the procedure of plotting the S-N curve in that range has been modified. The modification involves the variation of coefficient m in a wider range than in the

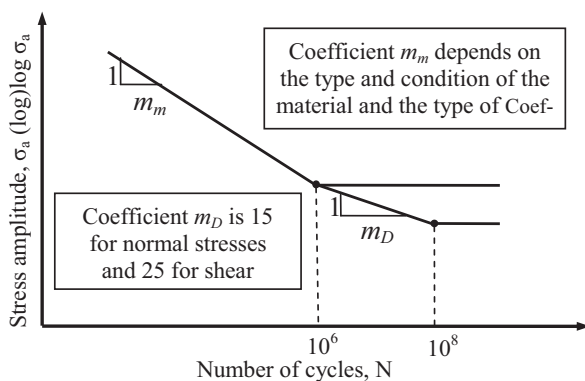


Fig. 2. Proposed modified curve

original methodology. Coefficient m depended on the type of material and the type of load. The numerical values of the slope used to implement that idea will be proposed based on the literature data and experiments. Fig. 2 presents, in a form of a diagram, the way the S-N curve is plotted according to the modified FITNET method. Plotting the curve in the range of unlimited fatigue life is made following the original method.

4. Verification of the hypothesis

4.1. Conditions of verification

Setting-up of the values of exponent m_m (symbols, see Fig. 2) for the reporting verification range in this paper is given in Table 2. The data are taken from papers [2,4,5,8] in which the ranges of variation of coefficient m are quoted.

Tab. 2. Values of the slope m_m

Type material	State	Data source	Value of coefficient m_m	
			Normal stress	Shear stress
Steel	Smooth specimen	[2],[4],[8]	12	12
Steel	Element with notch	[4],[5]	7	7
Steel	Heat treatment	[4]	18	18
Iron	Smooth specimen	Own proposal	11	
Aluminium alloy	Smooth specimen	Own proposal	8	8

At attempt at generalising the notation of value m involves formulating a general equation describing the dependence of slope m on the value of the ratio of the yield limit (R_e) to tensile strength (R_m). The notation has been presented as equations (4) and (5). To differentiate from the values in Table 2, symbol m_e has been introduced. In those equations there was assumed limiting the range of limited fatigue life in advance, by value $0.9 R_e$.

$$m_e = \frac{\log\left(\frac{10^6}{N_{Re}}\right)}{\log\left(\frac{0.9R_e}{Z_G}\right)}, \quad (4)$$

$$N_{Re} = 400 \left(\frac{R_e}{R_m}\right)^{-10}, \quad (5)$$

Fig. 3a presents the regression curve described with equation (5). The curve was plotted based on the experimental data reported in literature (quoted in Table 3). For the curve plotted in that way the coefficient of correlation is 0.831, while the graphic interpretation of the formula (4) is presented in Fig. 3b.

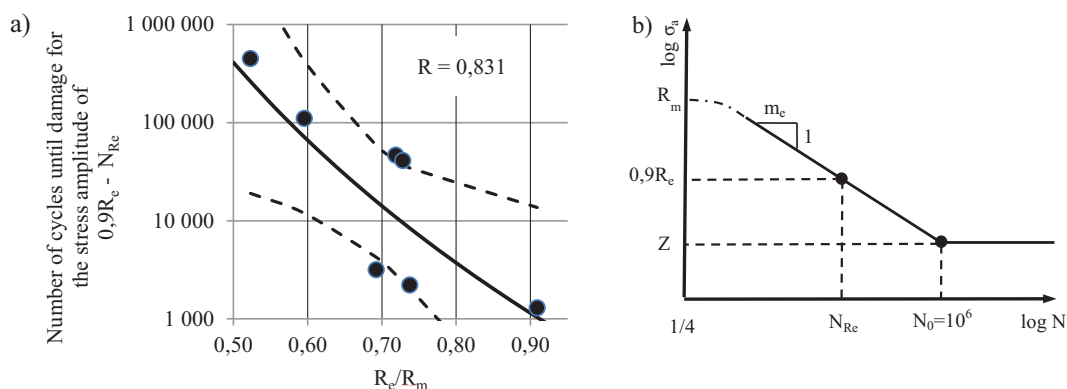


Fig. 2. a) Relationship between the number of cycles until damage and the ratio of R_e/R_m b) graphic representation of symbols from formula 4

4.2. Results of the verification

The verification of the proposed analytical-experimental approach was made based on the calculations for the stress amplitude corresponding to the level of 10^5 cycles on the experimental curve. A comparison was made between the fatigue life determined from the experimental curve (namely 10^5 cycles) with the fatigue life determined for the same stress amplitude from the estimated curve. The results of that comparison are shown in Table 4. The results of the fatigue life assessment error range from 12% to 286%. A graphic representation of selected results of curve calculations estimated according to the original FITNET method and the modified method are given in Figs. 4a, 4b and 4c.

Tab. 3. Comparison of the recorded fatigue life according to the proposal conditioning 0.9 value of the yield limit with the number of cycles until damage and the experimental data.

Material	Value of slope m according to the experiment		R_e/R_m	Number of cycles for crossing of 0.9 of the yield limit with the experimental curve	Calculated number of cycles N_{Re}	Determined value of slope m
S355J0	12.3	[12]	0.74	2.21×10^3	8.41×10^3	12.3
C40	12.8	[1]	0.60	1.10×10^5	7.11×10^4	15.1
C45	11.1	[6]	0.52	4.46×10^5	2.61×10^5	29.8
34CrMo4	8.4	[1]	0.72	4.63×10^4	1.09×10^4	12.5
42CrMo4	23.2	[1]	0.73	4.09×10^4	9.54×10^3	12.4
42CrMoS4	14	[10]	0.91	1.30×10^3	1.03×10^3	11.5
D38MSV5S	17.7	[4]	0.69	3.16×10^3	1.58×10^4	12.7

An attempt at generalising the notation of value m was verified for the materials specified in column 1 Table 3. The table makes it possible to compare exponent m taken directly from the experiment (column 2) with the value estimated based on Fig. 3a (the last column).

Tab. 4. Comparison of the recorded fatigue life according to the modified FITNET method (constant m for a group of materials) and the experimental data

Material	Value of slope m according to the experiment		Value of slope m	Number of cycles until damage	Difference between the experimentally determined number of cycles and the number of cycles recorded	Fatigue life assessment error [%]
Normal stresses						
S235JR	11.5	[9]	12	9.4×10^3	9.1×10^4	91
S355J0	12.3	[13]	12	3.9×10^5	-2.9×10^5	-286
E355	18.8	[3]	12	3.1×10^5	-2.1×10^5	-214
C40	12.8	[2]	12	1.12×10^5	-1.2×10^4	-12
C45	11.1	[7]	12	1.16×10^5	-1.6×10^4	-16
15Cr2	20	[9]	18	3.6×10^3	9.6×10^4	96
14CrMoV69	16.1	[2]	18	4.1×10^2	9.96×10^4	99,6
30CrNiMo8	11.7	[12]	18	1.3×10^5	-3×10^4	-30
34CrMo4	8.4	[2]	12	3.8×10^4	6.2×10^4	62
42CrMo4	23.2	[2]	12	1.7×10^4	8.3×10^4	82
42CrMoS4	14	[11]	18	3.2×10^4	9.4×10^4	94
SAE 8630	11.8	[2]	18	2.4×10^5	-1.4×10^5	-139
D38MSV5S	19.5	[5]	12	2.1×10^5	-1.1×10^5	-110
Shear stresses						
C45	10,1	[6]	12	1.4×10^5	-4×10^4	-40
30CrNiMo8	19,3	[12]	18	4×10^3	9.6×10^4	96
D38MSV5S	10,9	[4]	12	2.1×10^4	7.9×10^4	79

Tab. 5. Comparison of the fatigue life recorded according to the modified FITNET method (m dependent on the ratio R_e to R_m) and the experimental data

Material	Value of slope m according to the experiment		Determined value of slope m	Number of cycles until damage	Difference between the experimentally determined number of cycles and the number of cycles recorded	Fatigue life assessment error [%]
S355J0	12.3	[12]	12.3	3.77×10^5	-2.77×10^5	-277
C40	12.8	[1]	15.1	6.35×10^4	3.65×10^4	36.5
C45	11.1	[6]	29.8	4.77×10^3	9.52×10^4	95.2
34CrMo4	8.4	[1]	12.5	3.39×10^4	6.61×10^4	66.1
42CrMo4	23.2	[1]	12.4	1.54×10^4	8.46×10^4	84.6
42CrMoS4	14	[10]	11.5	1.55×10^4	8.45×10^4	84.5
D38MSV5S	17.7	[4]	12.7	1.91×10^5	-9.06×10^4	-90.6

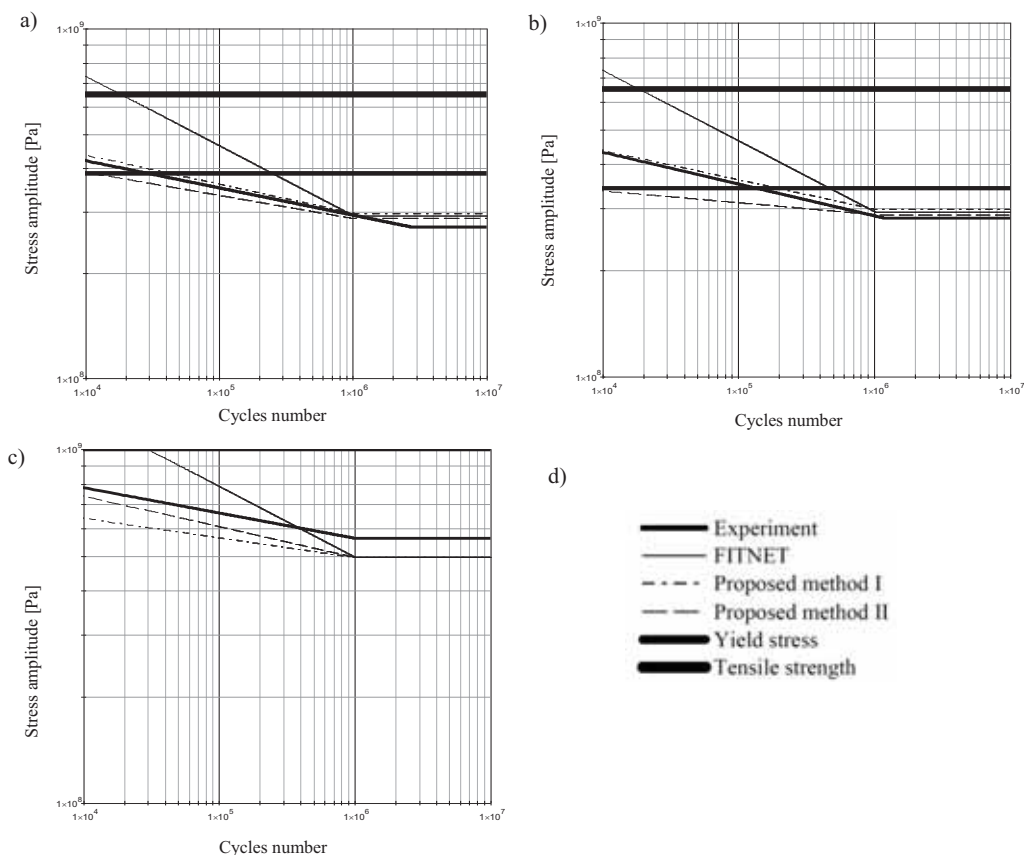


Fig. 3. Diagrams presenting a comparison of methods of evaluating the high-cycle fatigue life for: a) steel C40 in normalized state, b) steel C45 in normalized state, c) steel 42CrMoS4 in thermally improved state, and d) legend

6. Summary and conclusions

Based on the above verification results the following conclusions can be formulated:

- Using only analytical methods can lead to considerable fatigue life assessment errors (as much as 573%).
- The application of experimental methods results in considerable financial inputs and leads to the results conservative in use.
- As pointed in this paper, it is possible to combine the existing knowledge on analytical methods with purposeful support with data from similar experiments; such approach has been referred to as the analytical-experimental approach or it can be referred to in short as the hybrid approach.
- An essential quality of the hybrid approach is the dependence of exponent m from the type and state of the construction element material the approximate value of which can be determined based on the literature data or experimental data of similar materials.
- Two analytical methods have been recognised as are worth considering for engineering applications; the method with a proposed value of exponent m for a specific group of materials and the method with the slope exponent dependent on the ratio of R_e to R_m .
- The application of the hybrid approach leads to decreasing the fatigue life assessment error from 573% (as shown in paper [12]) to 286%, as demonstrated in Tables 4 and 5 (for the assumed area of analysis).

Interestingly, the presented breakdown of data, the analysis and its conclusions concern a limited group of materials. The verification points to specific tendencies and finds it justifiable to present it for a wider group of materials.

References

- [1] Boyer H.E., *Atlas of fatigue curves*, American Society for Metals, 2003.
- [2] Dyląg Z., Orłoś Z., *Wytrzymałość zmęczeniowa Materiałów*, WNT, Warszawa, 1962.
- [3] Kocańda D., *Badania krótkich pęknięć zmęczeniowych, Metody doświadczalne w zmęczeniu materiałów i konstrukcji* Badania podstawowe, Zbiór monografii pod redakcją Szali J., ATR Bydgoszcz, 2000.
- [4] Kocańda S., Szala J., *Podstawy obliczeń zmęczeniowych*, PWN, Warszawa, 1997.
- [5] Lee Yung-Li, Pan Jwo, Hathaway R. B., Barkey M. E., *Fatigue testing and analysis*, University of Alabama, Elsevier 2005.
- [6] Marines-García I., Galván-Montiel D., Bathias C., *Fatigue Life Assessment Of High-Strength Low Alloy Steel At High frequency*, The Arabian Journal for Science and Engineering, Volume 33, Number 1B, 2007.
- [7] Neimitz A., Dzioba I., Graba M., Okrajni J., *Ocena wytrzymałości, trwałości i bezpieczeństwa pracy elementów konstrukcyjnych zawierających defekty*, Politechnika Świętokrzyska, Kielce 2008.
- [8] Niezgodziński M.E., Niezgodziński T., *Obliczenia zmęczeniowe elementów maszyn*, PWN Warszawa 1973.
- [9] PN-H-04325:1976, *Pojęcia podstawowe i ogólne wytyczne przygotowania próbek oraz przeprowadzania prób*.
- [10] Pyttel B., Schwerdt D., Berger Ch., *Fatigue strength and failure mechanisms in the VHCF-region for quenched and tempered steel 42CrMoS4 and consequences to fatigue design*, Procedia Engineering 2, 2010.
- [11] Romanowicz P., *Analiza zmęczeniowa wybranych elementów maszyn pracujących w warunkach kontaktu tocznego*, Praca doktorska, Kraków 2009.
- [12] Sempruch J., Strzelecki P., *The error of fatigue life determined according to the FITNET method*, 17th International Conference ENGINEERING MECHANICS 2011, Svratka, 2011.
- [13] Strzelecki P., Sempruch J., *Verification of selected methods for rapid determination of Wöhler curve considering high-cycle fatigue*, Journal of POLISH CIMAC Selected problems of designing and operating technical systems, Vol. 5 No 3, 2010; ss. 177.
- [14] Szala G., Ligaj B., *Badania doświadczalne wpływu współczynnika asymetrii cyklu obciążenia na trwałość zmęczeniową stali S355J0*, Materiały XXIII Sympozjum Zmęczenie i Mechanika Pęknięcia, UTP 2010.
- [15] Xue H.Q., Bayraktar E., Marines-Garcia I., Bathias C., *Torsional fatigue behaviour in gigacycle regime and damage mechanism of the perlite steel*, Journal of Achievements in Materials and Manufacturing Engineering, Volume 31 issue 2, 2008.



FACTORS DETERMINING HOISTING SHAFT ROPE DURABILITY

Michał Styp-Rekowski¹⁾, Eugeniusz Mańka²

¹⁾University of Technology and Life Sciences
Prof. S. Kaliski Av. 7, 85-789 Bydgoszcz, Poland
tel.: +48 52 3408623, e-mail: msr@utp.edu.pl

²⁾Research and Supervisory Centre of Underground Mining Co.Ltd.
Łędzińska str. 8, 43-143, Łędziny, Poland

Abstract

The paper deals with factors determining the run and intensity of the wear-out process of mining hoist mechanisms. On the basis of the carried out experimental tests of a balance rope being a part of such a mechanism it was proven that conditions of the rope operation have a great influence on the kind and effects of its wear-out process. It was found that the basic cause of the rope strength features degradation is electrochemical corrosion and particularly – a chemical variant of this process. Of course, tribological wear is observed too.

Keywords: rope, hoisting shaft, durability, operation environment

1. Introduction

The wear process each of machine elements result in degradation of strength features of the material from which are made these elements or machines, generally referred to as technical objects. Exceeding permissible values of features which are significant in terms of the object operation (diagnostic symptoms) causes its transition from the fitness for use to unfitness for use state [2]. In case the fault is of permanent character the object life is affected, as well. Such a sequence of events and their results mean that the main goal of each technical object user is to reach the features boundary values over possibly the longest time, which means obtainment of its possibly longest life. The destruction process occurs in result of the technical object being influenced during its operation by different forcing factors such as: excitation forces, heat and chemical processes. In many cases, the listed above factors act simultaneously contributing to the wear-out process. Such a situation occurs when the object is used in a chemically active environment, for instance machines operating in mines. Tests proving rightness of this thesis were carried out with the use of a shaft hoist

In presented paper, tests of balance ropes of a mining hoist, shown in Fig. 1, have been discussed. The main practical aim of conducted research was to confirm the rightness of the decision concerning an exchange of a used rope for a new one, whereas the cognitive goal was to determine the causes of its accelerated wear-out. Achievement of both goals will be of great practical importance as the tests results will make up a database useful for making similar decisions in the future; besides, they may provide information for users how such mechanisms should be operated.

2. Object of investigations and its operation conditions

The durability of balance ropes operating in mining hoists depends mainly on synergy of such constructional factors as: material of wires and the rope core and characteristics of the used lubrication substances. Also, important are lubricants of the core and the wires used during the rope production process, the rope length of lay, its relief and untightness [1]. In case of mechanisms of ropes used in mining, especially underground, whose scheme is presented in Fig.1, a significant factor affecting their life is the environment in which they operate. For ropes operating in a strongly corrosive environment, this is the wire coating that is of primary importance, including: thickness, uniformity, and adhesion of the anti-corrosion coating to the wires throughout their length.

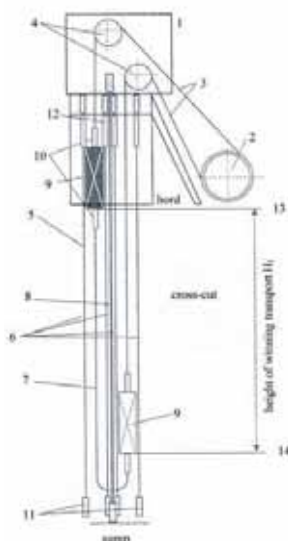


Fig. 1. Structural scheme of a shaft hoist: 1 – hoist tower, 2 – hoist wheels, 3 – lifting ropes, 4 – steering wheels, 5 – shaft, 6 – guide ropes, 7 – balance rope, 8 – fender rope, 9 – hoisting vessels, 10 – suspension gears, 11 – guide ropes weights, 12 – emergency breaks device, 13 – upper loading level, 14 – lower loading level

Confirmation of the influence of the work environment on the wear process intensity needs the tests of a mining hoist balance rope. Its basic, catalogue parameters are as follows:

- type (the rope marking): 45,0-33x7+A0-Z/z-n-N-G-1180-ZN-80/019-5021-170,
- the rope structure: 6x7x2,30+11x7x2,30+16x7x2,30,
- bearing cross-section: 959,80mm²,
- nominal mass of 1 meter: 8,9kg.

The tested rope was characterized by the below strength features:

- tensile force the whole rope: 1009,00 kN,
- tensile force wires according to the manufacturer: 1286,23 kN,
- tensile force wires according to the user: 1273,47 kN,
- safety coefficient for start of operating: 13,23.

Conditions in which the tested rope operated is defined also by the below, selected operation values:

- the rope maximum static loading: 76,256 kN,
- the rope length from the upper location of the vessel to the return: 870 m,
- kind of grease used for maintenance: Nyrosten N113.

In the presented case, the rope was operated in a medium – wet, downcast shaft, used both, for transporting materials and people. The torsion transmission drive was provided by a double rope lift machine situated on the hoist horst. In order to balance the static moment on the machine shaft, two round balance ropes were applied ϕ 45 mm. The hoist depth was 850m. whereas the rope maximum length, from the rope wheel axles to the head of the cabin on the coal pit, was 883 m. After about 32 months of operation with an average work intensity, about 200 extractions per 24 hours, the rope executed approximately 64000 cycles and due to the safety factor decrease by approximately 29,5%, it was exchanged.

It should be mentioned here that the mean operation time of previously used ropes was 42 months, which was about 30% longer than the operation time of the research rope.

3. The experimental rope investigations

The standard procedure concerning research of ropes consists of three kinds of tests: organoleptic, magnetic and fatigue ones, and this is the order in which they will be discussed in this paper.

Fatigue tests results are of special practical value, as being of destructive character – they can be carried out only on a rope which had been removed. On the basis of their results it is possible to define explicitly and undoubtedly the degree of its destruction and its strength features decline which is a criterion important for making decisions on further destination of the hoist critical element. The above listed factors make the fatigue tests the most informative [5, 9].

3.1. Organoleptic tests

As the result of a carried out inspection, there was found a deep corrosion of the external layer wires spreading onto the inner layer wires, especially on the return sections – when the hoist cabins were at the level of 850m. below the vessels. Traces of the corrosion related wear-out process are shown in Fig. 2, where a fragment of a partly unlaid rope has been presented.



Fig. 2. Some fragment of the rope before the tests with visible corrosion

After being dismantled, the rope was found to have local losses and losses in soldering, though on not more than three wires of the external and internal layers, at the length equal to the rope seven diameters (~270mm.). Material losses in the wires due to friction and dents at the place of the layers contact, were not found.

After being cleaned, the broken wire of the external layer had a diameter about 2,0 mm. which means a decrease in the wire diameter by 13% compared to new wires and respectively, 24,4% decrease in their cross-sections. However, a visual examination revealed that the discovered loss was not caused by a friction wear-out but rather by corrosion whose effects were partly removed by cleaning.

3.2. Magnetic tests

Magnetic tests are not of destructive character and therefore are especially advised in cases when it is necessary to make a decision on the rope mechanism further operation. Places of the rope biggest weakening and their intensity can be indicated with high precision (of course accounting for the object size) [3,7,8].

A fragment of the test result records has been presented in Fig.3. The record concerns the rope sections in the places of its returns (from 10 to 30 meters) under both cabins.

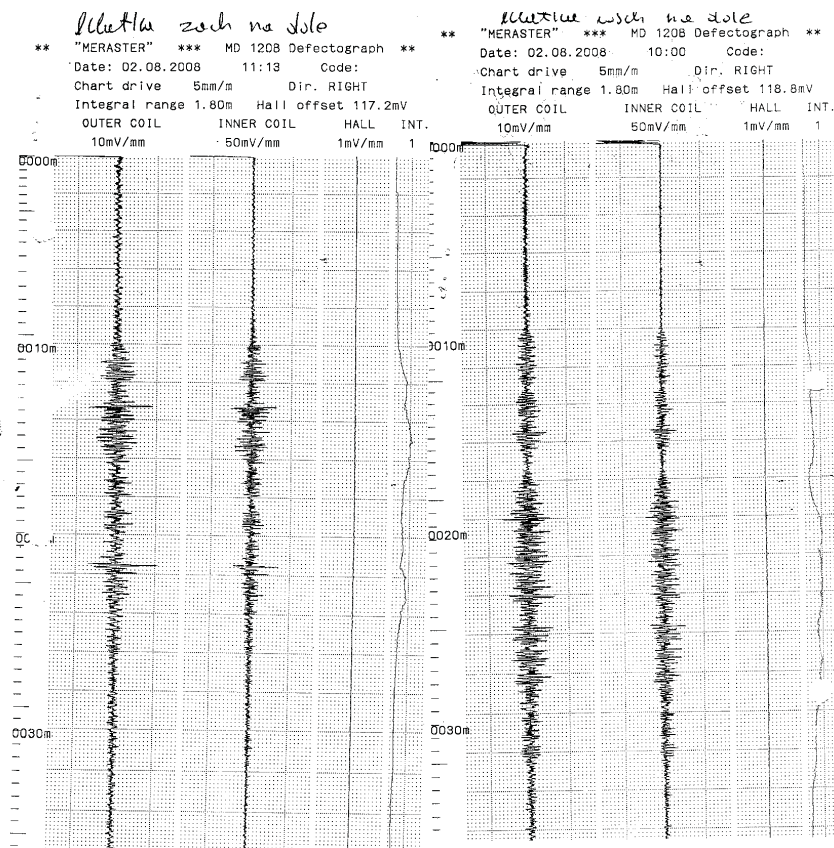


Fig. 3. Records of results of ropes magnetic tests in the place of the rope biggest weakening (the test parameters in the head of the record)

On the ground of the calculations using the indications of the internal coil integrator [3,10] it was found that losses of the metallic section (sum of cross-sections of particular wires) range from 15,1 to 29,5%, compared to a new rope. The rope changes (losses in the cross-section), found on the basis of magnetic tests, confirm the earlier observations – made during organoleptic tests.

3.3. Fatigue tests of the examined rope wires

The wires were tested in Non-destructive Research Laboratory of Research and Supervisory Centre of Underground Mining in Mysłowice. Break tests were performed on fatigue machines of the type FM - 1000 manufactured by Rauenstein Company and the type 10/Z1032 by Amsler. The

range and methodology of the breaking, bending and torsion tests were carried out according to the binding norms, including [6].

Wires of an untangled, two meter long section of the rope, coming from the return under the eastern case, were tested. The tests covered 100% of the wires which had been straightened, cleaned from the lubrication and partially, mechanically- from corrosion products – Fig.4.



Fig.4. Prepared for tests segments of wires of the rope layers: a) external, b) central, c) internal and d) core

Tensile Tests

Describe below tests, like the following ones (bend, and torsion ones) were conducted on samples which came from different layers of the rope: external, central and internal.

The tensile tests carried out in particular layers of the rope revealed that only 16 wires of the external layer did not meet the requirements of the standard on the minimal tensile force. The total tensile force for the old (used) rope, obtained during tests, was 1 220 490N, whereas this force for the new line was 1 286 230 N. Thus, the difference in values (loss) accounts for 5,11% of the initial value.

The total tensile force, according to the manufacturer's certificate, is a value calculated from the formula:

$$P_{zr} = \frac{\sum_{i=1}^{i=99} P_{zri}}{99} \cdot n_d , \quad (1)$$

where:

- P_{zr} – the rope tensile total force, N,
- P_{zri} – tensile force of individual wire, N,
- n – number of wires in the tested rope

The average value, determined from a 99 element sample is consistent with requirements of the standard for ropes of II class [6].

Bend Tests

In a two direction bend test, the minimal number of bends for all wires is 12. The conducted tests showed that not all of the represented layers fulfilled the fatigue criterion, whereas changes which occurred in particular layers were of diversified character:

- from 112 wires of the external layer, 26 (23,2%) did not meet the required criterion,
- from 77 wires of the central layer, 21 wires (27,3%) did not withstand the required number of bends, for the internal layer – only 5 (11,9%) in 42, did not meet this criterion.

Overall, 52 wires out of 231 wires making up the whole line did not meet the standard requirements, which accounts for 22,5% of all wires.

Torsion Tests

The required number of torsions for a standard torsion test, for wires of all the layers, is 16. Like for the bend tests, the number of wires which did not meet this criterion was different for each layer. The results of these tests were as follows:

- in the external layer none of the 112 wires completed the required number of torsions,
- from 77 wires of the central layer , 67(87,0%) met the criterion,
- in the internal layer 10 wires, out of 42 (23,8%), did not meet this criterion.

Totally, 189 out of 189 wires of the tested rope did not meet this criterion, which accounts for 81,8% of all the wires.

4. Analysis of tests results and their interpretation

Results of the tests described in the previous section are taken down in Table 1. They show the picture of strength features changes for wires making up a tested rope, and indirectly of the whole rope. Weakening of the whole rope strength features is mainly caused by the conditions in which the rope operates [4,10]. The places of the rope biggest weakening occur in its return points – when cabins are in the lowest or highest positions – see Fig. 1. In these places, during stops (loading or unloading) the rope stands still and is affected by environmental factors such as humidity getting through the hoist walls and gases contained in the resource. Chemical aggressiveness of gases which make up one of the rope environment elements, depends on the kind of shaft , whether it is a downcast or upcast shaft, and it is higher for the latter one. In these places ropes are exposed to mechanical damage by pieces of coal. The factors listed above, cause that the wear-out process occurs faster in such places than in others.

Table 1. Statement of strength tests results for the rope wires

Rope tested fragment	Total number of wires	Bend test		Torsion test	
		number of wires which do not meet the criterion	percentage of changes(losses) %	number of wires which do not meet the criterion	percentage of changes(losses) %
External layer	112	26	23,2	112	100,0
Central layer	77	21	27,3	67	87,0
Internal layer	42	5	11,9	10	23,8
The whole rope	231	52	22,5	189	81,8

Corrosivity of operating environment for mining mechanisms can be well reflected not only by rope but also by traces of corrosion on the hoist structure – see Fig.5. Thus, it can be said with high probability that one of the causes of the rope weakening is the influence of the environment factors. This can be proved by the fact that the external layer of the rope was more damaged that

the other ones which results from its being more exposed to the environment components which appear in the form of moisture and gases.



Fig.5. Fragment of the shaft bearing structure with visible traces of corrosion

Analyzing forms and effects of the environment factors, it can be said that the products of corrosion observed on the surface of the rope and its particular wires are the effect of mainly electrochemical corrosion. Accounting for the operation conditions of the rope mechanisms it can also be stated that corrosion products occurred in result of formation of many oxygen micro-cells which appeared in places where water particles settled on the rope.

The fact that in the environment of mining machines operation (especially upcast shafts) there also occurred numerous elements which when mixed with air and moisture, created a reactive medium and generated chemical corrosion which undoubtedly intensified the corrosion process. In order to be able to estimate the share of particular kinds of corrosion in the rope destruction process it would be advisable to make a detailed chemical analyses, though their results would be of minor importance for the considered issue.

The influence of excitation forces, in case of balance ropes, is less significant in terms of their wear [4]. As observed earlier, the task of balance ropes is to balance the static moment coming from bearing ropes weight. The value of this weight, dependent on the rope length and unit weight, is rather small, compared to the loading (about a few percent), therefore, this factor contributes to the line weakening only insignificantly.

5. Closure

The carried out tests allowed to formulate a series of conclusions concerning the wear-out process of balance ropes used in a mining hoist mechanisms and discover the consequences of this process, the most important ones being:

- the wear process of the tested balance lines is of corrosive character, with the biggest share of electrochemical corrosion,
- forces acting on the ropes do not have a significant influence on the wear-out process intensity.

The observations made during the tests, concerning the wear-out process effects, are also results of the research, they include:

- corrosion traces are unevenly distributed along the rope: there are more on the external layer wires than on the internal and central ones,

- the rope biggest weakening was located in its reversal points – in these points destructive factors affect the rope most heavily.

Thus, the main goal of the research has been achieved, that is, it has been proved that the decision on the rope removal from operation was right as it lost its operational features to a degree which justified such a choice.

Another important effect of the carried out research on the rope methodology is a possibility of verification and comparison of results of different kinds of tests: organoleptic, magnetic and fatigue ones. The results of such actions can be used for informativeness improvement of noninvasive rope tests which, in turn, can improve safety of the mining rope mechanisms operation, even for an increased resurse [2].

References

- [1] Hankus J., *Budowa i właściwości mechaniczne lin stalowych*, Główny Instytut Górnictwa, Katowice 1990.
- [2] Hansel J., *Metodyka poprawy niezawodności i bezpieczeństwa systemów maszynowych transportu pionowego*, Materiały XXXV Zimowej Szkoły Niezawodności, Szczyrk 2007.
- [3] Kawecki Z., Stachurski J., *Defektoskopia magnetyczna lin stalowych*, Wydawnictwo „Śląsk”, Katowice, 1969.
- [4] Mańka E., Skrok T., Styp-Rekowski M., *Eksploatacyjne czynniki determinujące proces zużywania lin górniczych wyciągów szybowych*, Materiały XVI Międzynarodowej Konferencji TEMAG 2008, Katowice – Ustroń 2008, s. 227-237.
- [5] Mańka E., Styp-Rekowski M., *Analiza informatywności badań lin w aspekcie możliwości jej zwiększenia*, Materiały V Międzynarodowej Konferencji „Bezpieczeństwo pracy urządzeń transportowych w górnictwie”. Gliwice–Ustroń 2009, materiały na CD.
- [6] Norma PN-90/M-80255. *Liny stalowe. Wytyczne oceny zużycia i wymiany*.
- [7] Norma PN-92/G-46603: *Liny stalowe okrągłe. Oznaczenie stopnia zużycia metoda magnetyczną*.
- [8] Norma PN-92/G-46604: *Liny kopalniane płaskie, stalowo-gumowe. Oznaczenie stopnia osłabienia metoda magnetyczną*.
- [9] Polański Z., *Metody optymalizacji w technologii maszyn*, PWN, Warszawa 1977.
- [10] Tytko A., *Eksploatacja lin stalowych*, Wydawnictwo „Śląsk”, Katowice 2003.



COMPARATIVE ANALYSIS OF CYCLIC PROPERTIES OF METALS OBTAINED IN CONDITIONS OF STRESS AND STRAIN RANGE DIVERSIFICATION CONTROL ON THE EXAMPLE OF C45 STEEL

Grzegorz Szala

University of Technology and Life Sciences in Bydgoszcz
ul. Prof. Kaliskiego 7 85-789 Bydgoszcz, Poland
tel.: +48 52 340 82 95, fax: +48 52 340 82 71
e-mail: gszala@utp.edu.pl

Abstract

Cyclic properties of metals are obtained in conditions of sinusoidal loading at stress constant temperature or at constant amplitude of total strain. In the first case fatigue is characterized by the S-N Wohler curve applied in calculations in the range of high cycle fatigue. In the second case fatigue is characterized by the Mason-Coffin curve ($\epsilon_{ac} - 2N_f$) applied in low cycle fatigue calculations. Characteristic that enables transformation of the curve into the one and suitable reverse transformation is the Ramberg-Osgood ($\epsilon - \sigma$) cyclic strain curve. In the paper there was confirmed that there are differences between ($\sigma - N$) and ($\epsilon_{ac} - 2N_f$) curves determined in stress and strain control conditions. The fact may have an essential influence on results of fatigue calculations in amplitude variable loading conditions (i.e. random loading or programmed) that values belong to both ranges LCF and HCF of fatigue.

Keywords: fatigue of materials, fatigue life curves, cyclic properties of materials

1. Introduction

Elements of machines and designs in operating conditions are subjected to variable loading and in general case to randomly variable loading. If the source of loading are i.e. vibrations of a system with defined distribution of masses it causes loading from mass forces (soft loading) and consequently to this loading cyclic properties are determined in tests where variable stress is a parameter. If the source of loading is variable distribution i.e. as a result of misalignment of shaft gudgeons in a clutch (hard loading) then cyclic properties are determined in tests where variable strain is the parameter [1].

The above statement has an essential value in the case of tests and calculations in ranges of high cycle loading and low cycle loading. In the first case calculations are based on the S-N curve, while in the second case calculations are based on the Mason-Coffin curve. In operating conditions randomly variable loading appears and it is possible the high values are in the range of LCF and small values in the range of HCF. So there is doubt if the change of calculation conditions in LCF and HCF connected with acceptance of the Mason-Coffin curve for calculations in the first case, and the S-N curve in the second one does not lead to significant mistakes. No doubt there is a significant lack of consistency.

The answer on the above question results from the analysis of fatigue characteristics in the shape of $\sigma - N$ and $\epsilon_{ac} - 2N_f$ curves and (Ramberg - Osgood) cyclic strain curves $\epsilon - \sigma$, obtained in conditions of stress and strain "control".

The aim of the paper is comparative analysis of cyclic properties of metals obtained in conditions of control of stress ($\sigma - N$ curves) and strain ($\epsilon_{ac} - 2N_f$ curves) range changes for C45 steel.

Scope of the paper covers description of:

- tests in the conditions of static loading,
- tests in conditions of cyclic loading,
- comparative analysis of fatigue characteristics obtained in conditions of controlled stress with fatigue characteristics obtained in controlled strain conditions.

The paper is concluded with reference to fatigue life calculation methods in operating loading conditions that values lie in the range of HCF and LCF.

Tests are performed for the following assumptions:

- C45 steel is a material assumed for tests
- cyclic properties of C45 steel are estimated in sinusoidal stress conditions and total strain with constant amplitude and asymmetry coefficient of cycles $R=-1,0$.

2. Experimental tests

2.1. Test object

For tests there are assumed specimens with a shape shown in fig. 1, made with the accordance to the standard: PN – 74/ H-04327.

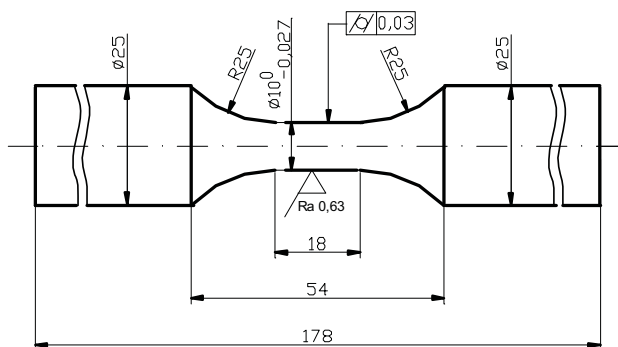


Fig. 1 Specimen for tests with the accordance to PN – 74/ H-04327.

Specimens were made of C45 toughened steel. Chemical composition of C45 steel with accordance to the standard PN-EN 10083-1+A1:1999 and PN-EN 10083-2+A1:1999 and with accordance to own tests are presented in the table 1.

Table 1. Chemical composition of C45 steel

	Contents in %								
	C	Mn	S	P	Si	Cr	Mo	Ni	Cr+Mo+Ni
						Max			
According to PN-EN	0,42÷0,5	0,5 ÷ 0,8	0,045	0,045	0,4	0,4	0,1	0,4	0,63
According to own test	0,476	0,593	0,027	0,015	0,201	0,16	0,047	0,116	0,323

Tests in conditions of static and cyclic loading were performed on the INSTRON 8501 fatigue machine with a control – measurement unit additionally equipped with extensometers, data acquisition system ESAM TRAVELLER 1 and a PC computer.

2.2. Test results in static loading conditions

The curve obtained with accordance to the standard PN-EN 10002-1+AC1 in the range of tension and compression is placed in fig. 2, whereas mechanical properties are presented in the table 2.

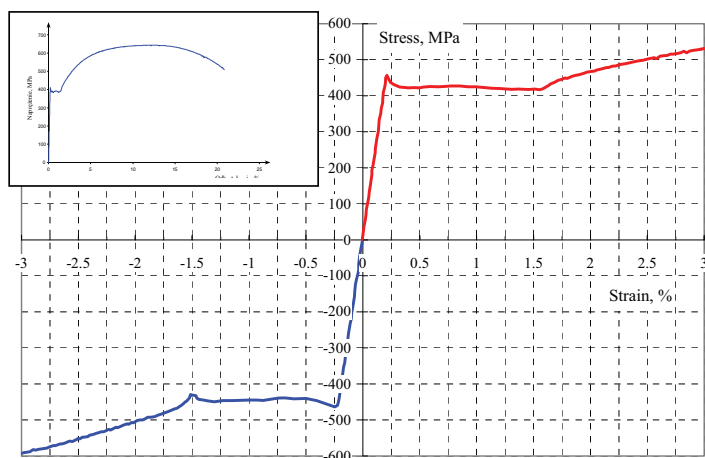


Fig. 2 Tension and compression test of C45 steel in condition of static loading

Table 2. Static properties of steel C45

	Static properties of steel C45					
	R _e	R _m	R _u	E	Z	A ₅
	MPa	MPa	MPa	MPa	%	%
<i>Average value</i>	446.3	713.3	1098.0	215000	44.3	24.3
<i>Standard deviation</i>	12.3	21.7	46.6	10000	4.7	3.5

2.3. Test results in cyclic loading conditions

a) Determination of Ramberg-Osgood ($\sigma - \epsilon$) cyclic strain curve

The rule of determination of individual points of the curve ($\sigma - \epsilon$) was described in the paper [2]. Point of the curve means the top of hysteresis loop (point A) in the phase of stabilization of cyclic properties. Because the phase, as it was shown in the paper [3], does not appear significantly in in whole fatigue life of the specimen, there was assumed a loop from a half of fatigue life. Cyclic strain curve determined in the range of controlled stress conditions (3) and the cyclic strain curve determined in the range of controlled strain conditions (2) were shown on the background of the static tensile curve (1) in fig. 3 .

Curves from the fig. 3 were described with following formulas:

- for the case of controlled stress

$$\varepsilon = \frac{\sigma}{215000} + \left(\frac{\sigma}{1121}\right)^{5,5} \quad (1)$$

- for the case of controlled strain

$$\varepsilon = \frac{\sigma}{215000} + \left(\frac{\sigma}{1232}\right)^{5,06} \quad (2)$$

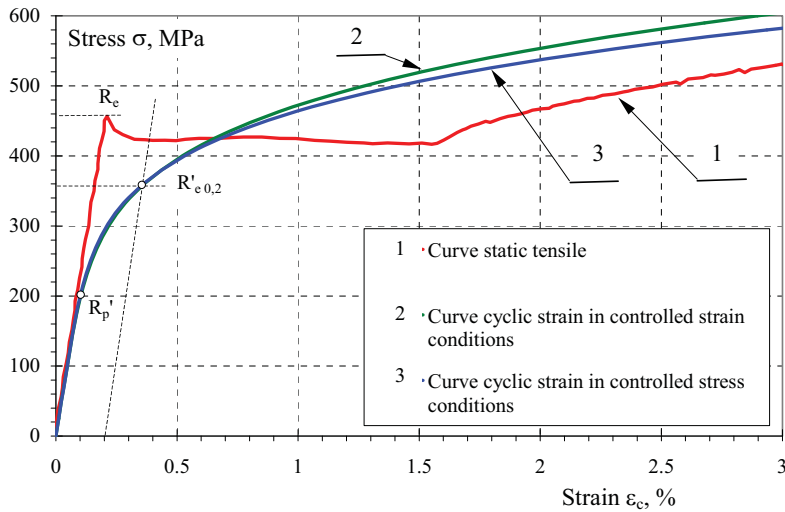


Fig. 3 Curves: static tensile (1), cyclic strain in stress controlled conditions (3) and cyclic strain in controlled strain conditions (2) of steel C45

b) $(\sigma - N)$ curve

Performing tests in conditions of sinusoidal stress with constant amplitude σ_a the N number of cycles leading to fatigue cracking is determined. These data lead to a point of the fatigue curve. Repeating test for different values of σ_a we obtain set of points that enables to determine the curve $(\sigma - N)$ with a method of linear regression. In fig. 4 there was shown the curve $(\sigma - N)$ determined on the base of 15 test results.

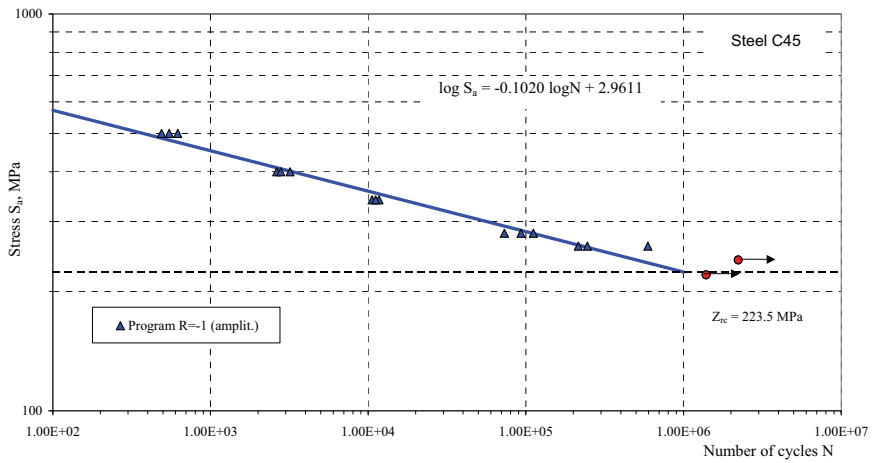


Fig. 4 Wohler curve for C45 steel

The curve is described by the formula (3)

$$\log \sigma_a = -0,1020 \log N + 2,9611 \quad (3)$$

c) $(\epsilon_{ac} - 2N_f)$ curve

Curves $(\epsilon_{ac} - 2N_f)$ are determined in tests in total strain conditions with constant amplitude. The number of $2N_f$ refers to each value of ϵ_{ac} amplitude in these tests. These data give the set of points that enable to determine the curve $(\epsilon_{ac} - 2N_f)$ which was shown in

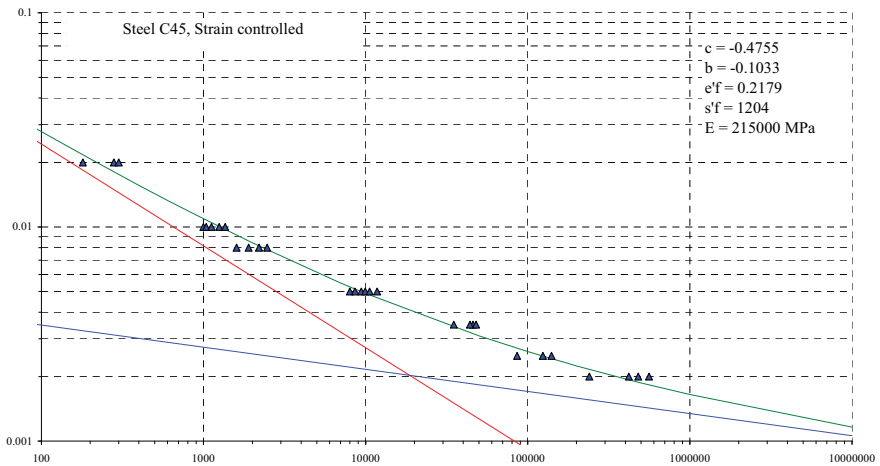


Fig. 5. Mason-Coffin $(\epsilon_{ac} - 2N_f)$ curve for C 45 steel

and the formula describing the curve is:

$$\varepsilon_{ac} = \frac{1204}{E} (2N_f)^{-0,1033} + 0,2179 (2N_f)^{-0,4755} \quad (4)$$

3. Analysis of test results

With reference to the aim of the paper the analysis of the test results will be based on comparison of fatigue life curves obtained in different conditions of loading. The comparison needs a proper transformation of test results with an application of the cyclic strain curve.

In the first case there will be performed transformation of the curve $(\varepsilon_{ac} - 2N_f)$ into the $(\sigma_a - N)$ system. For each strain ε_{ac} from the curve $(\varepsilon_{ac} - 2N_f)$ – fig. 5 there is a proper value of stress amplitude σ_a read from the $(\sigma - \varepsilon)$ curve – fig. 3. The set of points from fig. 5 transferred into the system $(\sigma_a - N)$ was marked green and shown in fig. 6 on the background from fig. 4,

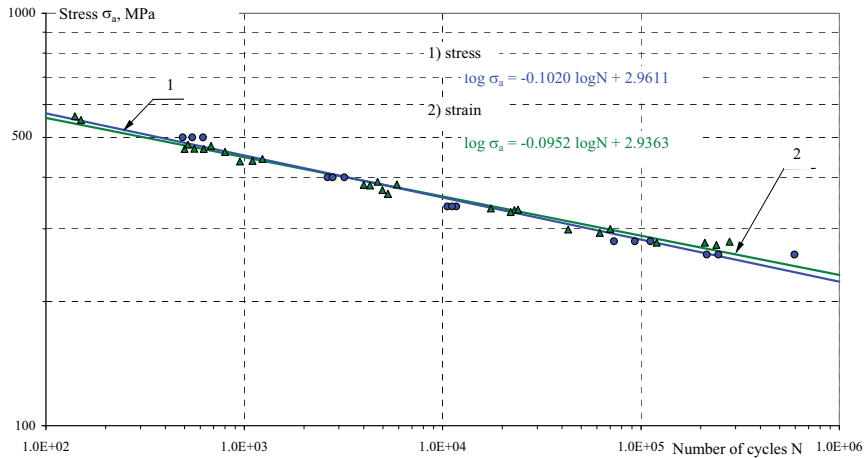


Fig. 6. Comparison of Wöhler curves determined in conditions of „controlled” stress (blue colour) and „controlled” strain (green colour) for C45 steel.

and the formula describing the curve for the set is:

$$\log \sigma_a = -0,0952 \log N + 2,9363 \quad (5)$$

Comparing differences in fatigue life on the ends of the test range for $\sigma_a=550$ MPa and 250 MPa their relative values are obtained on the level:

$$\delta_{550} = \frac{N_{\sigma} - N_{\varepsilon}}{N_{\sigma}} \cdot 100 = 21,64\% \quad (6)$$

and

$$\delta_{250} = \frac{N_{\sigma} - N_{\varepsilon}}{N_{\sigma}} \cdot 100 = -36,1\% \quad (7)$$

where: N_{σ} – number of cycles to fatigue crack for the „controlled” stress amplitude,
 N_{ε} – number of cycles to fatigue crack for the „controlled” strain amplitude.

Similar transformation was performed converting suitable data from the curve $(\sigma - \varepsilon)$ – fig. 4 into the coordinate system $(\varepsilon_{ac} - 2N_f)$ applying the curve $(\sigma - \varepsilon)$.

Results of the trasformation were shown in fig. 7, where on the background of the curve ($\varepsilon_{ac} - 2N_f$) from fig. 5 suitable data were applied that give another curve described by the formula:

$$\varepsilon_{ac} = \frac{1411}{E} (2N_f)^{-0,1246} + 0,4991 (2N_f)^{-0,5699} \quad (8)$$

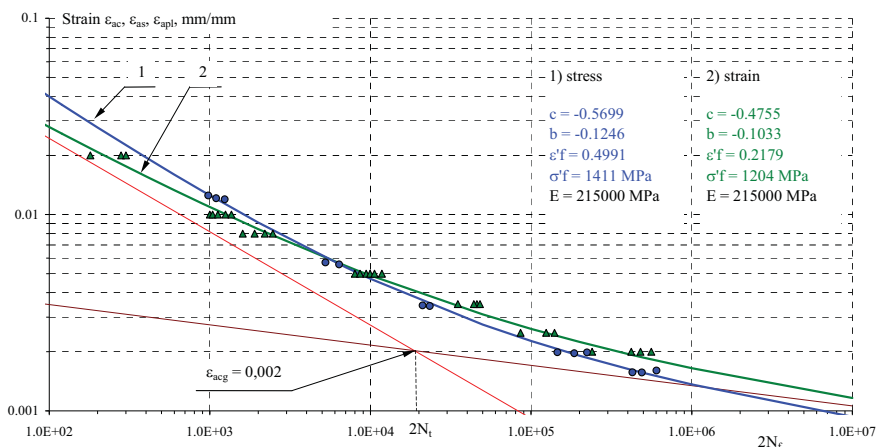


Fig. 7. Comparison of Manson-Coffin ($\varepsilon_{ac} - 2N_f$) curves determined in conditions of: „controlled” stress (blue colour) and „controlled” strain” (green colour) for C 45 steel

Comparing differences of fatigue life on the ends of the test range for $\varepsilon_{ac} = 0,03$ and $0,0015$ their relative values are obtained as follows:

$$\delta_{0,03} = \frac{2N_{\sigma} - 2N_{\varepsilon}}{2N_{\sigma}} \cdot 100 = 51,36\% \quad (9)$$

and

$$\delta_{0,0015} = \frac{2N_{\sigma} - 2N_{\varepsilon}}{2N_{\sigma}} \cdot 100 = -190,1\% \quad (10)$$

Relative differences in fatigue life described by formulas (6), (7) and (9), (10). Their influence on fatigue life calculations in variable amplitude loading is essential. To confirm its importance it is necessary to perform suitable calculations what will be an essence of the other paper.

4. Summary

There are essential insights resulting from the presented test results. They have crucial value for the choice of the proper calculation method of fatigue life of contructional elements.

From fig. 3 it results that constructional C45 steel after hardening and tempering is subjected to cyclic weakening in the range of minor values of amplitudes $\sigma_a \leq 420 \text{ MPa}$, and then it is subjected to cyclic hardening for higher values of stress amplitudes $\sigma_a > 420 \text{ MPa}$. Cyclic yield stress $R'_{e0,2}$ is significantly lower then yield stress R_e determined in conditions of static loading. The fact states about the weakness of assumptions of yield stress R_e as a criterion of ranges of LCF and HCF that decide on assumptions of suitable fatigue curves ($\sigma - N$) or ($\varepsilon_{ac} - 2N_f$) in fatigue life calculations. The above statement finds its confirmation also in course of the curve ($\sigma - N$) in the range of

stresses $\sigma_a > R_e$ (the curve does not change its character) what states that the curve ($\sigma - N$) can be also applied in the range of low cycle fatigue (LCF).

Relatively small differences between curves determined in conditions of „controlled” stress amplitude and the „controlled” total strain one point on the possibility of their interchangeable application in fatigue life calculations.

Generally there is a set rule that for dynamic operating loading the ($\sigma - N$) curves are applied whereas for kinematic loading the ($\epsilon_{ac} - 2N_f$) curves are applied [3] .

References

- [1] Mroziński S., Szala J.: *Problem of cycling hardening or softening in metals under programmed loading*, Proceedings of the VI-th International Symposium on Mechanics of Materials and structures, Augustów, Mah 30 – June 2, 2011.
- [2] Kocańda S., Szala J.: *Podstawy obliczeń zmęczenia*, Wydawnictwa naukowe PWN, Warszawa 1997.
- [3] Mroziński S.: *Stabilization of cyclic properties in metals and its influence on fatigue life*, Wydawnictwa Uczelniane Uniwersytetu Technologiczno-Przyrodniczego w Bydgoszczy, 2008.

Note : This work has been elaborated in the frame of the project No.NN 503 222 139 financed by Polish Ministry of Sciences and Higher Education



COMPUTER AIDED LABORATORY ACCREDITATION PROCESS. MEASUREMENT DATABASE AS AN INITIAL STAGE OF SOFTWARE APPLICATION

Marek Szczutkowski

*University of Technology and Life Sciences in Bydgoszcz
ul. Prof. Kaliskiego 7 85-789 Bydgoszcz, Poland
tel.: +48 52 340 82 55, fax: +48 52 340 82 55
e-mail: m.szczutkowski@utp.edu.pl*

Abstract

The problem of quality of laboratory test results is essential in the context of their future application for example in machine design. Usually quality of test results means their reliability. To achieve it laboratories often tend to accredit their tests in national accreditation bodies. For example in Poland PCA (Polish Centre for Accreditation) is the national governmental body that controls the process and states that a laboratory fulfills the requirements of the PN-ISO/IEC 17025 standard. To fulfill the requirements means to introduce a lot of effort in technical and organizational areas of activity. In order to help and support such activities the attempt of elaboration of computer aided accreditation software is being developed. One of the key issues of the problem is to maintain measurement processes on the proper level. Measurement database can be a useful tool at the initial stage of accreditation activities. The paper presents its assumptions with reference to the management system.

Keywords: *quality, accreditation, reliability of tests, measurement data base*

1. Introduction

Testing laboratory is a place that connects worlds of science and engineering. Performance and conclusions obtained from research activities are a base for descriptions created by science and innovations implemented in engineering. Without dividing customers into categories with reference to a branch a laboratory has to deliver service characterized by the best quality. It was assumed, basing on own experience and references, that creation of customer's satisfaction in laboratories is possible by the usage of ISO/IEC 17025:2005 standard [4]. According to [2] the practical benefits of technical and management quality improvements are seen on a daily basis in the laboratory. Faster identification and resolution of issues regarding methods, personnel or equipment, improved customer satisfaction, meeting quality requirements of specialized customers, and overall increased laboratory business are all the result of implementing an effective quality system.

As it was mentioned the problem of accreditation based on the consists of two parts: technical and management. While the second one is usually referred to well known ISO/IEC 9000 standard series and it is possible to find a lot of information on the issue so the first one has not been described sufficiently enough. As a result an author of the paper, supported by scientists working

in the environment of strength and fatigue testing laboratories, decided to elaborate and develop software tools to implement, maintain and manage the quality system in accredited testing laboratories with a special reference to strength laboratories. The main aim of the work is to develop the methodology of implementation of quality system with accordance to ISO/IEC 17025:2005 standard on the base of propose software. Additionally, the aim of software is to face the most often problems connected usually with documentation, both traditional and electronic. Moreover the system will help in exchanging experience of laboratory specialists by communication with authors.

What is more important in the context that modern generations communicate and work usually with usage of IT tools. While in the 1960s computers started to be implemented step by step in industry systems of files started to remove traditionally gathered and processed data. Since then database systems have started to become a standard tool [5][6].

The goal of this paper is to present the basic assumptions for computer aided laboratory accreditation process with a special reference to measurement database as its initial stage.

2. Basic assumptions for designed software

Designed software consists of 7 modules that are able to work independently. They can be a part of the management system (8th application – as in the algorithm) built in a different way what can increase the number of potential users. On the other hand the efficient working of individual modules can lead to implementation of all modules that support the system in the whole.

System based on the proposed software can eliminate present problems, especially in the area of traditional and electronic documentation, facilitate the fulfilling of accreditation requirements, and enhance exchange of experience [5].

Software, referring to requirements of ISO/IEC 17025:2005 standard, was divided into two groups:

- 1) Requirements referring to management system (documentation, internal audits, corrective and preventive actions, management system reviews).
- 2) Requirements referring to technical area (testing method, measurement database, personnel)

To facilitate the programming process (especially in the context of application of object-oriented programming) the above division was presented in fig. 1.

There are a lot of available applications connected with the management area but with reference to the designed software they have a number of disadvantages. First of all such applications are usually connected with ISO 9000 quality standard series. Second of all, as a consequence, they are not focused on technical requirements. Moreover, both areas are not connected so such applications are not efficient from the point of view of successful accreditation process [5].

Proposed system fully reflects requirements specific for electronic systems, i.e.:

- digital signature,
- backup copies,
- data integrity.

Fig. 1 shows also relations among individual modules.

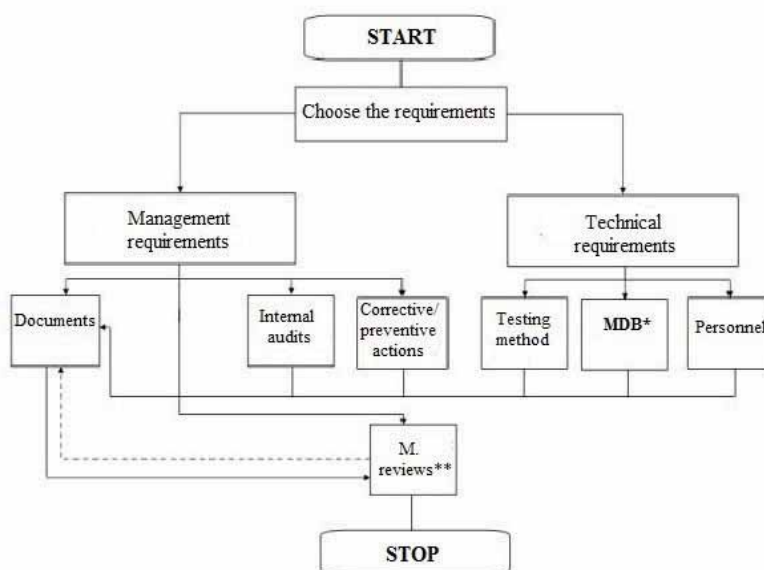


Fig. 1. Algorithm of computer aided accreditation software in testing laboratories, *MDB – measurement database, ** M. reviews – management reviews [5]

3. Measurement database as a part of designed software

3.1. Goal of the database design

Databases are likewise found at the core of many scientific investigations. They represent the data gathered by astronomers, by investigators of the human genome, and by bio-chemists exploring the medicinal properties of proteins, along with many other scientists [5].

The power of databases comes from a body of knowledge and technology that has developed over several decades and is embodied in specialized software called a database management system, or DBMS, or more colloquially a „database system.“ DBMS is a powerful tool for creating and managing large amounts of data efficiently and allowing it to persist over long periods of time safely. These systems are among the most complex types of software available. The capabilities that a DBMS provides the user are [1]:

- a) Persistent storage. Like a file system, a DBMS supports the storage of very large amounts of data that exists independently of any processes that are using the data. However, the DBMS goes far beyond the file system in providing flexibility such as data structures that support efficient access to very large amounts of data.
- b) Programming interface. DBMS allows the user or an application program to access and modify data through a powerful query language. Again, the advantage of a DBMS over a file system is the flexibility to manipulate stored data in much more complex ways than the reading and writing of files.

c) Transaction management. A DBMS supports concurrent access to data, i.e.: simultaneous access by many distinct processes (called "transactions") at once. To avoid some of the undesirable consequences of simultaneous access, the DBMS supports isolation, the appearance that transactions execute one-at-a-time, and atomicity, the requirement that transactions execute either completely or not at all. A DBMS also supports durability, the ability to recover from failures or errors of many types.

Having in mind the above definitions the main goal of the designed database has to be fulfillment of direct requirements of the standard [4] with the special emphasis put on the chapter 5. Moreover a manager of a laboratory has to have in mind such documents as ISO 10012:2004 „Measurement management systems — Requirements for measurement processes and measuring equipment” and proper documents of governmental accreditation bodies on the topic. They have to be associated with documentation of laboratory management system (quality manual, procedures etc.). It is essential for the laboratory to describe the process of hardware and software maintenance.

At this stage it is worth to add that the standard [3] defines measuring equipment as „measuring instrument, software, measurement standard, reference material or auxiliary apparatus, or a combination thereof, necessary to realize a measurement process”.

Measuring equipment should be properly identified and consequently followed by certain information that can be processed. One can not divide metrological processes from other activities so measurement database seems to be an essential part of the whole computer aided accreditation software [5].

3.2. Measurement database in the management system

With accordance to the proper levels of management, taking into consideration information transformed with the usage of the database, on individual levels of management following actions are taken:

- a) laboratory manager – decisions on purchasing of measuring equipment and usage of reference/calibration equipment,
- b) quality manager – management on proper maintenance, service and proper usage of measuring equipment as well as issues connected with metrological confirmation,
- c) each laboratory technician – realization of individual activities resulting from suitable documentation on measuring equipment with reference to own scope of responsibilities.

Assuming that one of the issues in the measuring process is calibration different people are responsible for different actions. Laboratory manager decides if one can use for example gauge blocks or a calibrating thermometer in individual cases, but the quality manager makes a decision about time intervals between calibrations. He or she also decides about service activities while action can be taken directly by a laboratory technician.

In the process of calibration the above mentioned people, everyone in a different range, have to deal, at least, with following documents of the management system:

- a) measuring system maintenance procedure,
- b) calibration procedure,
- c) lists of measuring equipment,
- d) charts of calibrations,
- e) equipment card,
- f) unit list,

- g) equipment labels,
- h) schedule of calibrations,
- i) calibration reports.

Working on example on the base of instruction on calibration of thermometers as an output information one will receive a report.

In the context of creating of the database it is essential to build connections and interactions among suitable data i.e.:

- a) block gages and Vernier caliper, calibrating and calibrated thermometers etc.,
- b) assignment of responsibilities directly for equipment in the context of people/ places/ functions/ rooms, ,
- c) customer's requirements and measurement ranges and time intervals of calibrations,
- d) customer's requirements and information obtained from measurement maintenance and service (i.e. Analysis of trends with reference to previous calibrations) ,
- e) choice of subcontractors in the range of calibration services.

4. Summary

In the paper basic assumptions or initial works connected with design of the database of measurement equipment working as a one of the modules of computer aided accreditation software were presented.

Information connected with individual measuring tools and relations among them, depending on a laboratory unit, can be different. But even in the case of a small laboratory it is impossible to analyse data gathered within years of activity without an influence on realization of other activities and responsibilities. Application of databases gives more possibilities in the context of making strategical decisions. If, in the context, one considers an accreditation of testing laboratories it seems as an efficient step not to ignore any experience in the range of database systems.

Complete software, basing on the knowledge and experience in the range of accreditation of testing laboratories should be an essential support for scientific and industrial organizations that will to increase reliability of performed tests.

References

- [1] Hector Garcia-Molina H., Ullman J.D., Widom J., *Database Systems: The Complete Book*, Prentice Hall, 2000.
- [2] Honsa J.D., McIntyre D.A., *ISO 17025: Practical Benefits of Implementing a Quality System*, Journal of AOAC International vol. 86, no. 5, 2003.
- [3] ISO 10012:2004: *Measurement management systems — Requirements for measurement processes and measuring equipment*.
- [4] PN-EN ISO/IEC 17025:2005: *Ogólne wymagania dotyczące kompetencji laboratoriów badawczych i wzorcujących*.
- [5] Szczutkowski M., *Narzędzia informatyczne wspomagające proces akredytacji laboratoriów wytrzymałościowych. Projekt bazy danych przyrządów pomiarowo – badawczych cz. 1 Etap wstępny projektu-podstawowe założenia*, Logistyka, Instytut Logistyki i Magazynowania, no. 6, 2010.
- [6] Szczutkowski M., *Narzędzia informatyczne wspomagające proces akredytacji laboratoriów wytrzymałościowych. Projekt bazy danych przyrządów pomiarowo – badawczych cz. 2 Specyfika języka baz danych*, Logistyka, Instytut Logistyki i Magazynowania, no. 6, 2010.



SURFACE HARDENING OF PLAIN DUCTILE CAST IRON

Tadeusz Szykowny, Krzysztof Ciechacki*

*University of Technology and Life Sciences
al. Prof. S. Kaliskiego 7, 85-789 Bydgoszcz, Poland
tel.: +48 52 3408719, fax: +48 52 3408796
e-mail: krzysztof.ciechacki@utp.edu.pl

Abstract

The GTAW method was used to surface remelt samples of plain (unalloyed) ductile cast iron with ferritic/pearlitic structure. The cold remelting, hot remelting and multiple remelting techniques were used. Samples underwent penetrant tests, macro- and microscopic tests, x-ray diffraction tests and hardness tests.

Keywords: *ferritic/pearlitic plain ductile cast iron, surface hardening, GTAW method*

1. Introduction

Service conditions of cast iron castings very often require high abrasion resistance and resistance to wear caused by flaking and pitting of selected surfaces. Typical examples include surfaces of cast iron sliding or rolling guides, surfaces of cams, followers etc. High abrasive and contact wear resistance can be obtained through surface hardening. Hardness of surface hardened cast iron guides of machine tools should be within 48÷53HRC [10].

The required hardness of cast iron can be obtained with the same heat treatment methods as those used for steel, i.e. induction or flame surface hardening or heat/chemical treatment, e.g. nitriding [6].

Authors of article [3] present results of surface hardening of plain ductile cast iron based on the casting method, i.e. with the use of chills in moulds. Hardness of the white layer obtained, up to 12mm thick, is within 40÷50HRC, which extends life of the casting many times.

Hardness and tribological properties of cast iron surfaces can be further improved by modern methods based on a concentrated heat stream. The heat source may be either electric arc plasma (GTAW method) or a laser beam [2].

Comprehensive and extensive research into those promising methods have been conducted by authors of [4,5,7]. Depending on parameters of GTAW-based remelting of plain ductile cast iron, surface hardness of the remelted layer is within 54÷60HRC and the layer thickness – 2.5mm [3].

The research into the influence of current intensity and scanning rate on micro-hardness $\mu\text{HV}0.1$ of the partial melting area showed that depending on the process parameters, micro-hardness is within 773÷902 μHV . Abrasive wear, depending on micro-hardness, is approximated with very high correlation coefficient by a decreasing linear function [4]. In the remelted zone, there is a cementitic fibrous eutectic or plate eutectic cementite [5]. The author of [7] found out that a diffusionless transformation of austenite occurs in the remelted zone and heat affected zone.

Hardness of cast iron and consequently its abrasive wear resistance may also be improved by cold plastic forming [8].

The research described in [9] shows that macro- and micro-cracks of various intensity, depending on the cast iron grade and remelting parameters, occur in the remelted layer. Their presence, particularly in case of contact stresses, may cause faster wear of the hardened layer.

Induction or flame surface hardening is a method commonly used for surface hardening of cast iron. In case of predominance of ferrite in the cast iron matrix, the hardening effect is not sufficient [6], and results of surface remelting should not depend on the matrix structure.

This research is aimed at producing and analysing layers hardened with the surface remelting process in the ferritic/pearlitic cast iron using the GTAW method.

2. Material, programme and research object

Ferritic/pearlitic ductile cast iron with chemical composition given in table 1 was used for the tests.

Table 1. Chemical composition of cast iron, % mass

C	Si	Mn	P	S	Cr	Cu	Ti	Mg
3.82	3.41	0.19	0.057	0.02	0.04	0.04	0.019	0.05

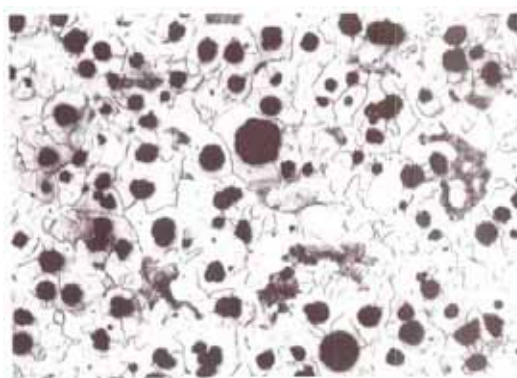


Fig.1. Structure of cast iron, as-cast state, microscope magnification 200x, etching with 2% HNO₃

Cast iron shown in figure 1 in as-cast state has a ferritic/pearlitic structure (approx. 15% pearlite content). Based on a tensile test, it has been classified as EN-GJS-400-15 grade.

YII samples were cast in green-sand moulds. From the bottom part of YII wedge, 30x75x16mm cuboidal samples were cut out for remelting.

The GTAW method was applied for surface remelting of cast iron. A 2.4mm diameter tungsten electrode was used. Argon 4.0 was used as shielding gas. Travel speed of a nonconsumable electrode was 200mm/min and current intensity – 80; 120; 160 or 200A.

The following three methods of GTAW-based surface hardening were applied:

- remelting of samples of room temperature (cold),
- remelting of cast iron pre-heated to 450°C (hot),
- multiple (repeated) remelting of samples of room temperature with 160A current.

The phase composition of the remelted layer was determined by x-ray diffraction. Measurements of hardness on the remelted surface were performed using the Rockwell method, C scale. The structure of remelted layers was evaluated and distribution of HV3 hardness by layer depth was determined on lateral metallographic microsections etched with nital. Penetrant tests were conducted to reveal micro-cracks.

3. The results of the research and their analysis

In „cold” remelting, the remelted layer consists of two phases: cementite and martensite. Regardless of current parameters of the remelting process, the phase composition remains the same. As an example, a diffractogram for the surface of cast iron remelted with 160A current is shown in figure 2. The average hardness for nine measurements made on the remelted surface of cast iron is $66 \div 68\text{HRC}$.

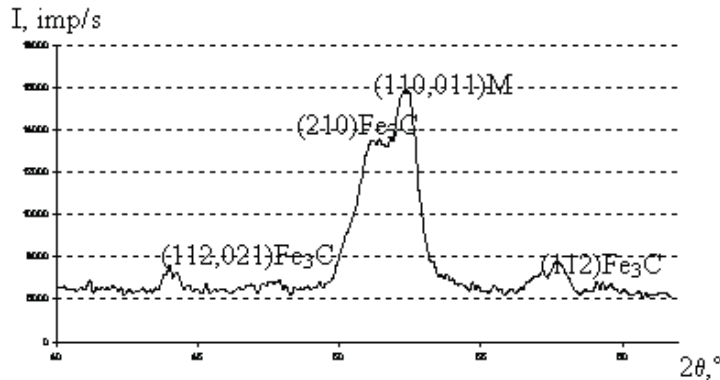


Fig.2. Diffractogram of melted surface

A distribution of hardness of the hardened layer depending on the depth and current is shown in figure 3. Based on the distribution of hardness, thickness of the remelted zone and thickness of heat affected zone can be determined. As the current increases from $80 \div 200\text{A}$, so is thickness of the remelted zone from $0,7 \div 2,0\text{mm}$, while thickness of the heat affected zone is within $0,5 \div 1,0\text{mm}$.

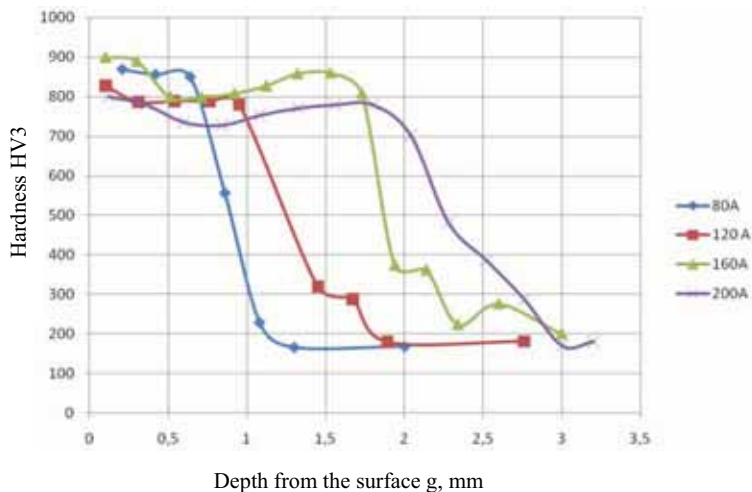


Fig.3. Distribution of hardness in the hardened zone

Figure 4 shows results of penetrant tests. The tests revealed micro-cracks positioned across the remelted layer. The number of cracks increased with an increase of current.



Fig.4. Macro-structure of remelted layers depending on current

Macro-cracks occur in the remelted layer as a result of stresses caused by the martensitic transformation. An example of the remelted layer structure with macro-cracks is shown in figure 5.

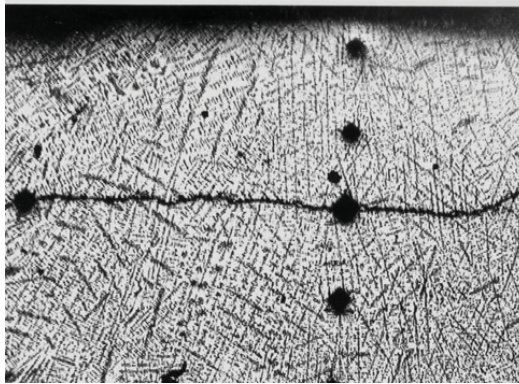


Fig.5. Macro-cracks in melted layer, current intensity 160A, magnification 70x

Micro-cracks in the transitional layer, between the remelted layer and the base material usually occur along the boundaries of eutectic grains (fig. 6).

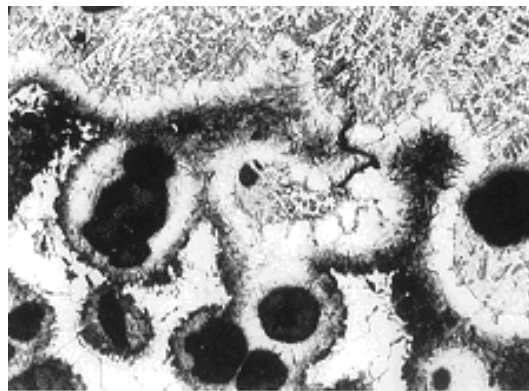


Fig.6. Micro-structure of transitional layer, melted layer-base material, magnification 175x

In order to eliminate cracks caused by the martensitic transformation, “hot” remelting was used. The phase composition of the remelted layer includes ferrite and cementite. Regardless of the remelting conditions, the phase composition is the same. A diffractogram for the surface of the layer “hot” remelted with 160A current and travel speed of a nonconsumable electrode of 200mm/min is shown in figure 7.

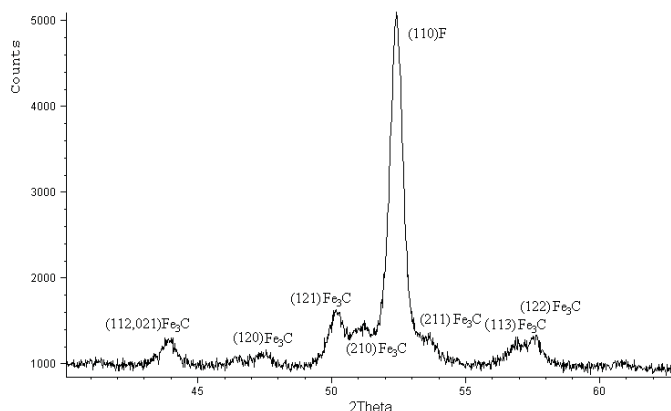


Fig.7. Diffractogram for surface of hot remelted layer, current intensity 160A

Pre-heating has completely eliminated micro- and macro-cracks, however, hardness measured on the surface decreased by approx. $8 \div 10$ HRC as compared to „cold” remelting. Cast iron pre-heating increases the costs of the hardening technology based on surface remelting.

In this article, it was proposed to harden the surface by multiple remelting of the layer using the GTAW method. The purpose of multiple remelting is to reduce the temperature gradient between the remelted layer and the hardened cast iron. It was assumed that multiple remelting would prevent the martensitic transformation that causes cracks.

The phase composition of surface layers subjected to multiple remelting, where no macro-cracks were observed, include ferrite and cementite, which is shown in diffractogram in figure 8.

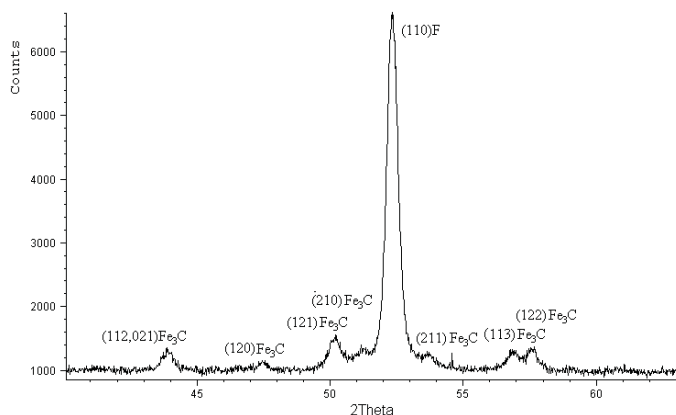


Fig.8. Diffractogram for surface of hot remelted layer, current intensity 160A

Results of penetrant tests are shown in figure 9, where: a – cast iron remelted 4 times, b – cast iron remelted 6 times.

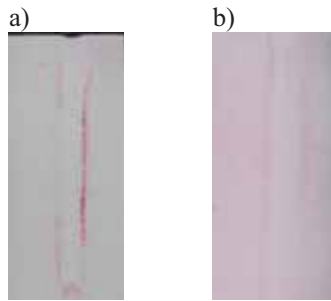


Fig.9. Penetrant tests of repeatedly remelted layers

The structure of layer remelted 6 times is transformed ledeburite. Under the remelted layer, there is a normalization zone consisting of dense pearlite with grid cementite shown in figure 10.

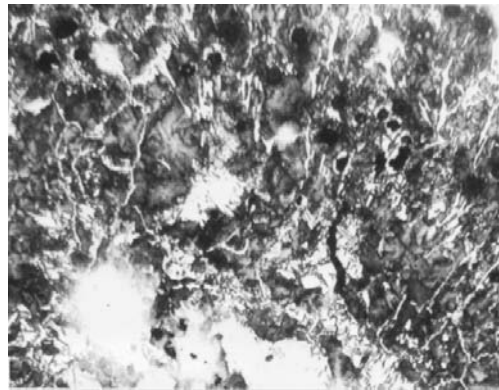


Fig. 10. Structure of normalization zone, magnification 170x

Hardness of ferritic cast iron remelted 6 times is approximately 60HRC.

4. Conclusion

The GTAW remelting method is an effective means of increasing the surface hardness of ferritic/pearlitic plain ductile cast iron. Macro and micro-cracks occur in the hardened surface as an adverse effect of the remelting process, with reference to usage and in particular with regard to contact loads. The frequency of crack occurrence depends on both the remelting process parameters and cast iron matrix structure. The best way to eliminate cracks in the hardened surface is to remelt cast iron preheated to a temperature higher than the martensitic transformation temperature, as the sources of cracks originate from the martensitic transformation of austenite being a component of ledeburite.

The remelted layer of cast iron that was preheated above the M_s temperature has the structure of transformed ledeburite and hardness approximately $8\div 10$ HRC lower than cold remelted cast iron. For technical and economic reasons preheating cast iron makes the surface remelting method without equal when compared with alternative hardening methods. Using standard welding equipment it is possible to obtain hardened layers by multiple remelting of the same layer. The purpose of multiple remelting is to reduce the temperature gradient and avoid martensitic transformation. In case of cast iron with ferritic structure, application of the multiple remelting

method entirely eliminates the occurrence of macro-cracks, with an insignificant number of micro-cracks still occurring within the remelted material/base material transitional zone. Further research on surface hardening processes employing the GTAW method ought to concentrate on the selection of current parameters, nonconsumable electrode feed rate, as well as the manner of moving the nonconsumable electrode during remelting. Until now, the electrode has only been moved longitudinally, at the same rate. The possibility of reducing the temperature gradient between the remelted layer and the base material would allow transverse movements to the remelting direction.

References

- [1] Greń J., *Models and tasks of mathematical statistics*, PWN, Warsaw 1970.
- [2] Klimpel A., *Metal welding and cutting – technologies*, WNT, Warsaw 1999.
- [3] Orłowicz W. et al.: *Surface hardening of cast iron*, 8th International Conference „Development trends in manufacturing processes”, Section III, p. 65, Zielona Góra 1997.
- [4] Orłowicz W., Trytek A., *Performance aspects of quick crystallization of the outer layer of ductile cast iron castings*, R8, p. 301, 2002.
- [5] Orłowicz W., Trytek A., *Application of GTAW process for surfacing of cast iron castings*, Acta Metallurgica Slovaca, R7, p. 9, 2001.
- [6] Piaskowski J., Jankowski A., *Ductile cast iron*, WNT, Warsaw 1974.
- [7] Trytek A., *Ductile cast iron castings surface hardened with electric arc plasma*, Foundry Review, no. 12, p. 431, 1998.
- [8] Szykowny T., Ciechacki K., *Improving properties of cast iron as tool material through plastic forming and heat treatment*, 7th National Conference, Tool issues in plastic treatment, Bydgoszcz-Venice. p. 145, 2001.
- [9] Szykowny T., Ciechacki K., *Structure and hardness of layers remelted with the GTAW method of ductile cast iron*, Foundry Archives, annual volume 6, no. 18 (2/2), p 195, 2006.
- [10] Wrotny L., *Machining tool design basics*, WNT, Warsaw 1973



MODIFICATION OF GRINDERS OF BIOMATERIALS USED FOR ENERGY PURPOSES

Andrzej Tomporowski, Adam Mroziński

University of Technology and Life Sciences
ul. Prof. S. Kaliskiego 7, 85-789 Bydgoszcz
Tel./fax: +48 52 3408255
a.tomporowski@utp.edu.pl

Abstract

Grinding of biological materials is an energy-consuming process. During grain decohesion, complex strain state occurs induced by compressing, twisting, bending, tearing, cracking, grinding or shearing. The work attempts to find structural solutions of the grinding and process control system enabling to increase rice grinding functionality: efficiency, energy-saving and regularity. The practical aim was to develop the methodology for innovative research on grain grinding which supports development of grinders.

Based on theoretical discussions and earlier scientific research, it can be concluded that it is possible to obtain optimal quality of material being ground and satisfactory functionality of the rice grain grinding process within a permissible range of values of the multi-disc grinder structural features. The exceeding of these values will result in the worsening of the process effectiveness and the quality of a grinding product. Finding relations between functionality, operation regularity, selected movement and energy related characteristics of the grinding process and structural features of the biomaterial grinding unit justifies the need for carrying out an analysis, studies and experiments with quasi-shearing in order to determine the indexes of the research object model variables.

Key words: structure; grinding; optimisation

1. Introduction

The analysis of the transformations and states of operational efficiency of biomaterial grinders aims to solve the issue of the momentary conversion of the biological medium into a structural element subjected to the complex load state. This conversion is connected with a transfer of grinding loads and maintaining, or even increasing, its natural properties, e.g. energy value – as the basic objectives of grinding, e.g. environmental objectives of processing effected by machines [2,3,4].

The aim of the work is to analyse energy effectiveness, efficiency and grinding regularity of rice grains with the aim of optimising and developing the structure of multi-disc grinders. The practical aim was to develop the methodology for innovative research into grain grinding which facilitates the designing of grinders.

2. Research issue

The research issue was formulated in the form of a question: what structural conditions (W_k), parameters and structural features of tools (C_{KN}) in used and analysed grinders (ZR_{BMZ}) and rice grain property variables (W_{RR}) are necessary for optimal realisation of the grinding process ($PR_{optimum}$).

$$\{[W_k(C_{KN})? \cap W_{RR} ?] ZR_{BMZ} \} \Rightarrow PR_{optimum} . \quad (1)$$

Structural conditions (W_k) are determined by structural features (C_k) of the multi-disc and multi-edge unit in terms of: geometrical form (Π_k), number of discs (l_t), number of movable blade edges (l_k), number of tool holes in discs (l_{otw}), number of hole rows (l_{tz}), hole diameters (d_{otw}), angles of edge blades or holes (β_{ij}) and other material and dynamics related features (C_{k-m-d}) of grinding elements.

As the solution estimators, the postulated states (SP_u) of the grinding process were taken: minimum power consumption (N_u), rational productivity (W_u), high energy effectiveness of the process (E_u) and product quality (Q_R).

The hypothesis was proposed that obtaining optimal quality (J_{proc}) of the grinding process is possible within a certain range of structural parameters of the multi-disc grinder and the exceeding of these parameters or changes of the form or dimensions results in the worsening of the product quality and process effectiveness.

$$For \vdash \{ [\rightarrow P, \rightarrow Q, \uparrow \eta, \uparrow e_r, \uparrow J_p] \cap [f_{dz}(x_i), f_u(x_j)] \} \Leftrightarrow [(C_k^* \in \langle X_n, X_m \rangle \Rightarrow \uparrow J_{proc}) \cup (C_k^* \notin \langle X_n, X_m \rangle \Rightarrow \downarrow J_{proc})], \quad (2)$$

where:

P – power,

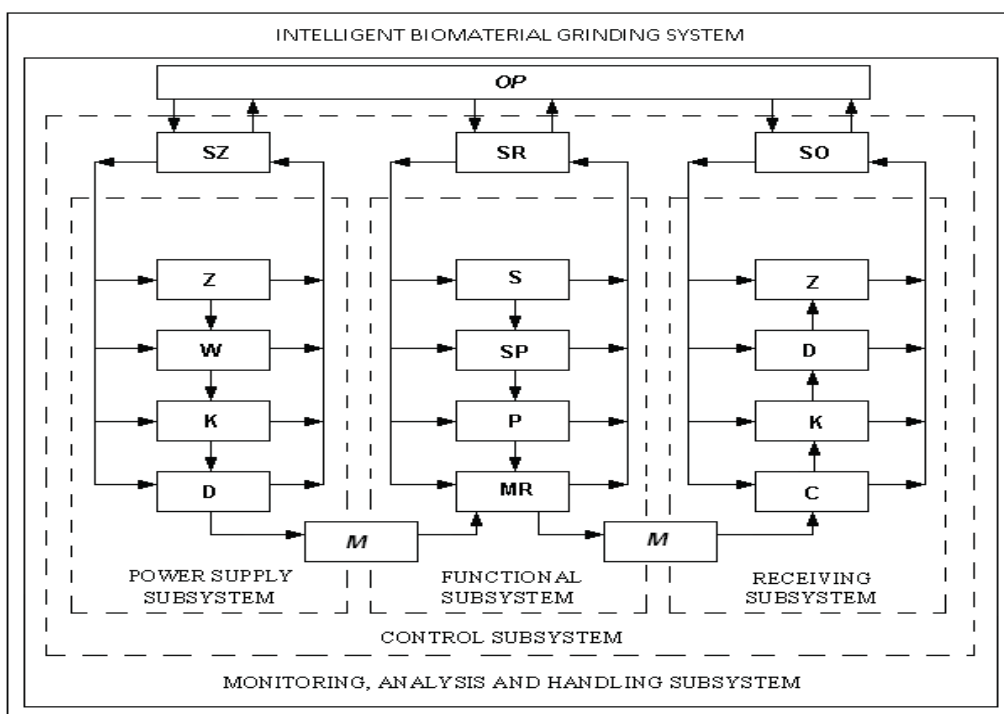
Q – productivity,

η – efficiency,

e_r – process energy consumption,

J_p – product quality,

X_m, X_n – boundary values of structural parameters.



INTELLIGENT BIOMATERIAL GRINDING SYSTEM

Fig. 1: Intelligent biomaterial grinding system; OP – process handling, SZ – power supply control, SR – grinding control, SO – handling control, min: Z – tanks, W – selectors, K – conveyors, D – feeders, MR – grinding machines, P – gears, SP – couplings, S – motors; M – magnetic separators, C – cyclones

If the intelligent grinding system (figure 1) does not have postulated operating characteristics desired by the operator (e.g. it is characterised by low effectiveness of operation, insufficient product quality, adverse effect on the environment), the causes for this may be the following:

1. Respective system constituents; cause: deformed elements or erroneous relations between them,
2. Control system; cause: incorrect control effect,
3. Biomaterial grinding process; cause: incorrect concept of process realisation and incorrect control effect.

The expected functional status of an operational grinding system comprises the following process development models [5,6]:

1. Effectiveness of operation – data on product structure and operating system characteristics are available,
2. Product quality – data on product quality (e.g. grinding fineness and percentage content of the expected fraction) are available,
3. Mutual effects, lives, safety – data are available on the effects of system operation and product.

In search of desired solutions aimed at development of the rice grain grinder structure, an optimisation procedure should be conducted, e.g. analytical or enumerative (notional) methods, random search for solutions or genetic algorithms.

3. Model of the subject of research

Instantaneous values of angular velocities and torque allow determination of the following grinding process parameters:

- kinematic grinder gear ratio, (i_k),
- dynamic grinder gear ratio, (i_d),
- power at the gear entry equal to the power at the exit from the drive motor, (N_1),
- power at the exit from the gear equal to the power at the grinder shaft, (N_2),
- drive efficiency (η_p).

Finding the relation between functionality, operational regularity, selected movement and energy related characteristics of the grinding process (H_u) and structural features of the rice grinding unit (C_k) justifies the need for carrying out analyses, studies and experiments with quasi-shearing in order to determine the indexes of model variables. The following constructional criteria were adopted:

- optimal loads, (M_{op}, P_{op}),
- optimal material, (C_{km}),
- optimal stability, (C_k, Δ_e),
- optimal relations between related values, ($E_R, \delta_d, \eta_o, Q_s, Q_j$).

Design process (innovation and development) should be guided in such a way so that the conditions of the grinder usefulness meet structural features [9]:

- maximisation of the function of regularity, efficiency, productivity, fineness for:

$$\left\{ C_k^* \in \phi \right\} : \left\{ \bigwedge_{c_k \in \phi} H_u(c_k) < H_u(c_k^*) \right\} \text{ dla: } H_u: e_R \uparrow, W_u \uparrow, \eta \uparrow, \lambda \uparrow, \quad (3)$$

- minimisation of power demand, energy consumption per unit, energy dispersion:

$$\left\{ C_k^* \in \phi \right\} : \left\{ \bigwedge_{c_k \in \phi} H_u(c_k) > H_u(c_k^*) \right\} \text{ dla: } H_u: N_u \downarrow, E_T \downarrow, M \downarrow, \omega \downarrow, v \downarrow, n \downarrow, \quad (4)$$

where:

C_k^* - solution to the task,

Φ – permissible area of the structural features vector,

H_u – performance characteristics of the structural features vector.

Dynamic irregularities (fig. 2) of grinder operation can be described mathematically as per the following formalisation [9]:

- exponential:

$$M(t) = M_1 e^{j\omega t} + M_2 e^{j\omega t} + \dots + M_n e^{j\omega t}, \quad (5)$$

- trigonometric:

$$M(t) = a_0 + c_1 \cos(n\omega t + \phi_1) + c_2 \cos(n\omega t + \phi_2) + \dots + c_n \cos(n\omega t + \phi_n). \quad (6)$$

Diagrams of random variable cumulative distribution function $E(M, \omega)$;

- dynamic:

$$E_t(M) = P [M(t) < x] \quad \text{and} \quad E_{t+\Delta t}(M) = P [M(t+\Delta t) < x], \quad (7)$$

- kinematic:

$$E_t(\omega) = P [\omega(t) < \omega] \quad \text{and} \quad E_{t+\Delta t}(\omega) = P [\omega(t+\Delta t) < \omega]. \quad (8)$$

where:

M – torque at the grinder shaft,

ω – angular velocity of the grinder shaft.

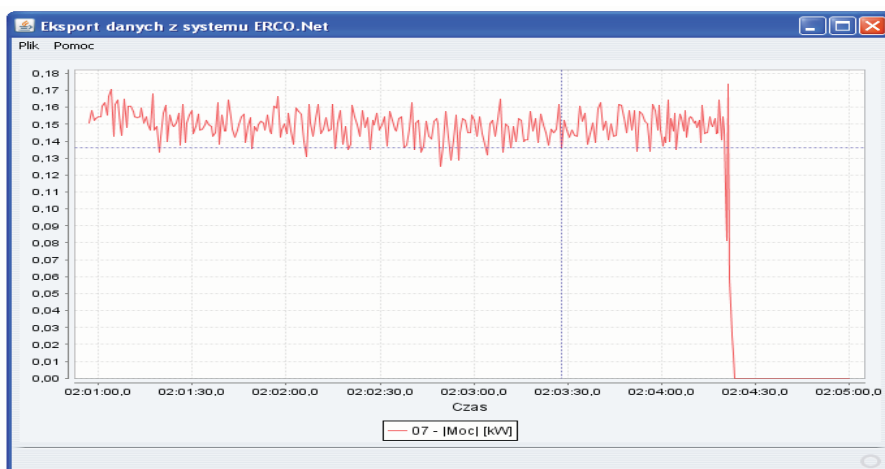


Fig. 2: Instantaneous power demand (irregularities) during grinding of rice grains using a multi-disc grinder RWT-5

Statistically presented grinding process is constant if obtained cumulative distribution functions are equal;

$$E_t(M, \omega) = E_{t+\Delta t}(M, \omega). \quad (9)$$

4. Model discussion

Expected structural features from the field of possible solutions to the design and structural task for the model of the subject of research are a function of many variables (maximised and minimised indexes) and therefore:

$$C_k = f(\eta \uparrow, W \uparrow, N_e \downarrow, E_T \downarrow, \omega \downarrow, M \downarrow, v \downarrow, n \downarrow), \quad (10)$$

where:

C_k – solution to the design and structural task.

The effectiveness model assumed is the dependence defining the increase in the grinding energy effectiveness

$$\Delta e_R = \frac{K_E}{E_R} = \frac{(\Delta)E_{pp}}{(\Delta)E_{R\lambda(F)}}, \quad (11)$$

where:

K_E – energy benefits, $J \cdot g^{-1}$,

E_E – energy input, $J \cdot g^{-1}$,

E_{pp} – processability energy, $J \cdot g^{-1}$,

$E_{R\lambda(F)}$ – grinding energy (phenomenon), e.g. for obtaining a product with desired fraction and postulated weight share expressed in percents, $J \cdot g^{-1}$.

The grinding process effectiveness can be defined by determining energetic, economic and ecological effectiveness.

Power demand required to achieve efficient and expected biomaterial grinding can be determined by using one of the known grinding theories. According to Rittinger, grinding energy equals:

$$E_R = K_R \frac{6}{d\rho} \left(1 - \frac{1}{n_i}\right), \quad (12)$$

where:

K_R – energy required to generate a surface increase unit as per Rittinger, $\text{Jg}\cdot\text{m}^{-2}$,
 ρ – material density $\text{Mg}\cdot\text{m}^{-3}$.

The efficiency of the grinding process is determined by specifying the following: bioenergy material acquisition efficiency, processing (production) efficiency, use (utilisation) efficiency [1]. A calculation model supplemented with detailed relation for effectiveness and grinding regularity. To assess energy specific consumption for multi-edge grinding of rice grains, the following mathematical formula [8]:

$$E_R = \frac{P_R v_R t}{\eta_S \eta_P}, \quad (13)$$

where:

E_R - unit consumption of energy for machine grinding, J/g ,
 P_R - grinding force load, $\text{N}\cdot\text{g}^{-1}$,
 v_R – grinding speed, $\text{m}\cdot\text{s}^{-1}$,
 t – cycle duration, s ,
 η_S – motor efficiency, -,
 η_P – transmission efficiency, -.

That dependence does not take into account specificity of grinding for energy purposes; therefore, a general model of energy effectiveness of the machine-based multi-disc grinding process has been formulated as follows:

$$e_R = \frac{\Delta E_{bio}}{E_R} = \frac{(\eta_{bio} - \eta_z) \cdot E_{gross} \eta_S \cdot \eta_P}{(k_j v_R + \sigma_{max} F_R + \varepsilon F_R v_R^2) v_R t M_k}, \quad (14)$$

where:

ΔE_{bio} – index of an increase of energy benefits (for further tasks) resulting from the grinding process, kJ/g , $(0.40-0.48)E_{gross}$,
 η_{bio} – efficiency of ground product incineration, $(0.50-0.98)$,
 η_z – efficiency of whole rice grain incineration, $(0-0.49)$,
 E_{gross} – gross energy of grains, $\text{kJ}\cdot\text{g}^{-1}$, (rice $E_{gross} = 14.1 \text{ kJ}\cdot\text{g}^{-1}$),
 k_j – resistance coefficient for lost motion, Nsm^{-1} ,
 σ_{max} – stresses related to permanent deformation, Nm^{-2} ,
 ε – dynamic resistance coefficient, Ns^2m^{-4} ,
 M_k – ratio of the analyzed mass to 1 g,
 F_R, F_R' – grinding section, m^2 .

A model described with the above dependence is very useful in evaluating the incineration process, energy effectiveness of operation, efficiency and functionality. However, it is not very useful in analysing instantaneous irregularity of grinder run and operation. The basic problem is that the variability of mass characteristics of biomaterials, functional working, driving and process units has to be taken into account each time. For the purpose of describing, modelling and evaluating the functionality of work of the analysed grinders it is more convenient to use special motion models and in particular – dynamic irregularity dependence. For the purpose of detailed analysis of dynamic irregularity, modification of moment relation was used and the average value of torque transformed into the following form:

$$\delta_d = \frac{M_{c\max} - M_{c\min}}{M_{csr}} = \frac{2\pi[p_c \Delta_{\max} r \cos\tau(1 + \mu tg\tau) - p_c \Delta_{\min} r \cos\tau(1 + \mu tg\tau)]}{z \int_{\varphi_p}^{\varphi_k} M_c(\Psi) d\Psi} = \frac{A(\Delta_{\max} - \Delta_{\min})}{M_{csr}}, \quad (15)$$

When invariability of unit grinding resistance and friction conditions are taken into account, the dependence takes a convenient form that may be used for measuring procedure. The degree of dynamic irregularity, measured for instantaneous settings of knife unit, is determined on the basis of measurement of instantaneous cutting length Δl_i – with determination of extreme values; and instantaneous torque M_i and determination of the average value. Under test conditions, the value of A constant is also determined for design of the multi-edge system design, rice grains and parameters of the disintegration process defined in the research programme.

5. Research results

Research has been conducted on the basis of the research plan and programme, (Fig.1, Fig.3).

EXPERIMENT PROGRAMME			
Properties of ground material [7]:		Working parameters of grinder	Technological parameters
1. humidity 2. bulk density 3. angle of repose 4. viscosity 5. structure of biological material 6. strength values		1. number of holes in discs 2. number of hole rows in first and subsequent discs 3. gap between discs 4. hole diameters 5. diameters of hole distribution on disc 6. angle of cutting edges 7. number of discs	1. angular speed 2. direction of disc rotation 3. rotational speed of feeder screw
MULTI-DISC GRINDING			
Result relations:			
Mass productivity	Calorimetric indexes	Fineness	Power demand

Fig. 3. Experiment programme

The simulation tests were conducted to determine sections and loads. Computer-based TEST-4 procedure was applied (Fig.4).

The machine-based tests were conducted using a multi-disc multi-hole grinder RWT-5:KZ owned by Engineering Systems and Environmental Protection Unit of the University of Technology and Life Sciences in Bydgoszcz. Rice grains with stabilized humidity parameter were used as the feed material. Figure 5 shows comparison between experimental and calculation-based results, figure 6 shows the influence of rice grain humidity on energy demand of 5-disc RWT-5KZ grinder, and figure 7 – influence of grain batch feed on demand of the analysed grinder. Fig. 8 shows instantaneous values of torque (M_{01} - M_{05}) for five discs of the grinding unit.

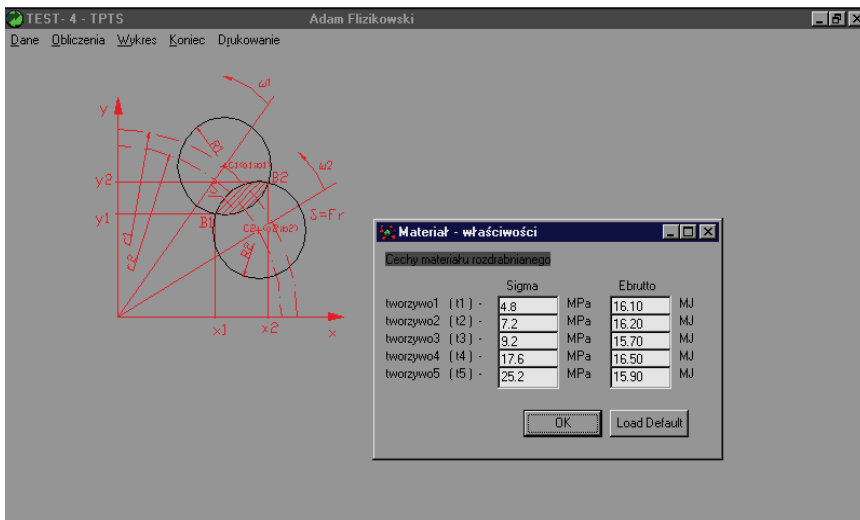


Fig. 4. Results of grinding load simulation

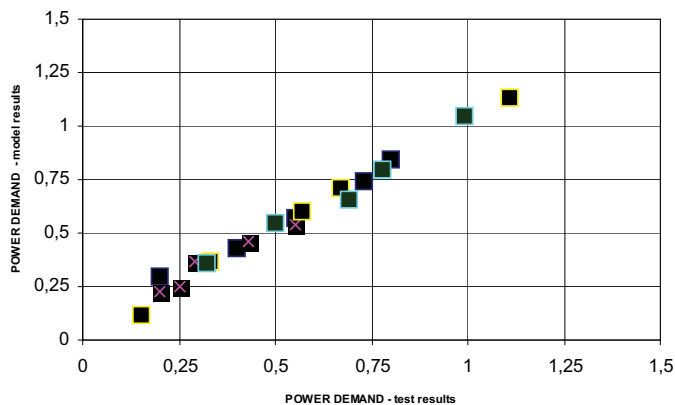


Fig. 5. Comparison between test results and mathematical model results $P=f(Z, W)$

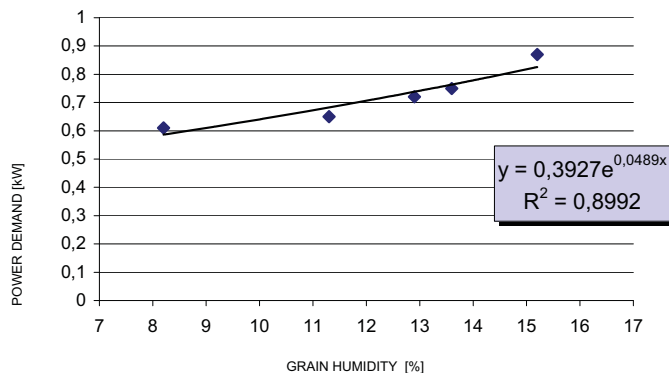


Fig. 6. Influence of rice grain humidity on power demand of the RWT-5:KZ multi-hole grinder

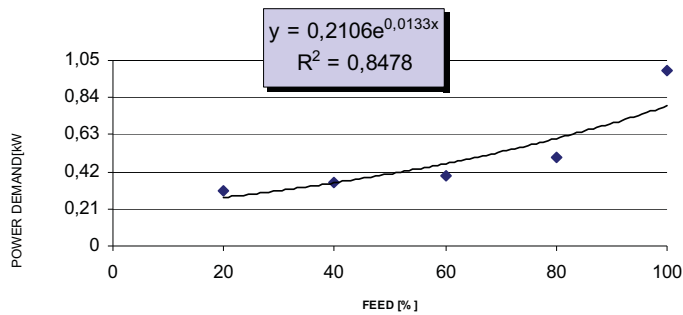


Fig. 7. Influence of the rice grain feed on power demand of the RWT-5;KZ multi-hole grinder, digitally controlled loose material feeder: Hydrapres DSK07/10I

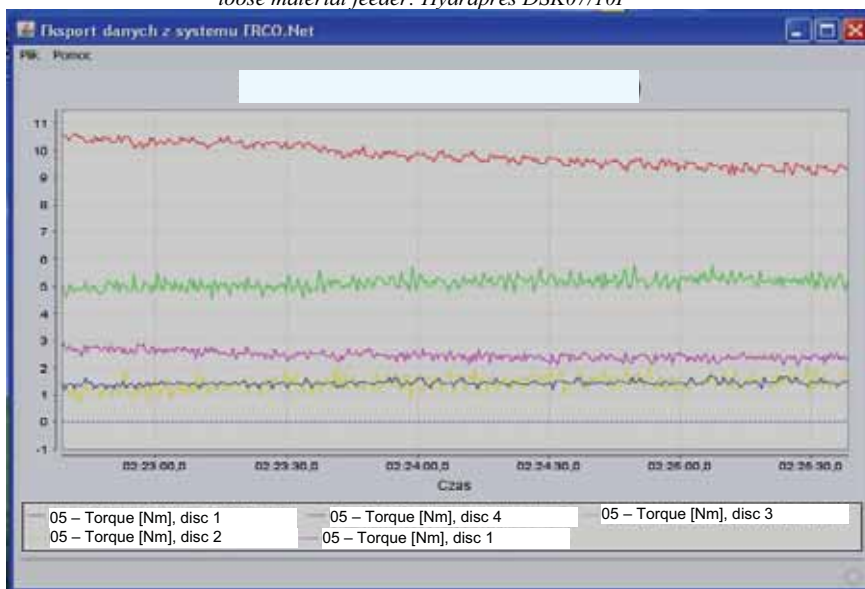


Fig. 8. Instantaneous values (irregularities) of power demand, all disc

When looking for design (structural) features of the working unit that fulfil solution of the task and additionally condition of maximum incineration heat Q_s , structural features of the working unit of RWT-5;KZ multi-hole, multi-edge grinder (table 1);

$$[(C_k^* \in \langle X_n, X_m \rangle \Rightarrow \uparrow J_{proc}) \cup (C_k^* \notin \langle X_n, X_m \rangle \Rightarrow \downarrow J_{proc})] \quad (16)$$

Tab. 1. Changes of incineration energy of ground size fractions of rice, kJ/g,

Sample	Fraction	Wire weight	Sample weight	W'_{ex} [%]	A^a [%]	H^a [%]	Q_s [kJ/kg]	Q_j [kJ/kg]
1	0.2 ÷ 0	0.006	1.014	13.5	4.6	4.427027	16740	15443.844
2		0.007	1.022	13.5	4.6	4.427027	16650	15353.844
3		0.005	1.013	13.5	4.6	4.427027	16630	15333.844
4		0.005	1.018	13.5	4.6	4.427027	16690	15393.844
5	0.45÷0.2	0.006	1.013	13.5	4.6	4.427027	16340	15043.844
6		0.005	1.016	13.5	4.6	4.427027	16070	14773.844
7		0.006	1.009	13.5	4.6	4.427027	16410	15113.844

8		0.005	1.01	13.5	4.6	4.427027	16420	15123.844
9	0.8÷0.45	0.006	1.008	13.5	4.6	4.427027	15570	14273.844
10		0.006	1.01	13.5	4.6	4.427027	15700	14403.844
11		0.005	1.008	13.5	4.6	4.427027	15650	14353.844
12		0.005	1.01	13.5	4.6	4.427027	15770	14473.844
13	1÷0.8	0.005	1.013	13.5	4.6	4.427027	16030	14733.844
14		0.005	1.008	13.5	4.6	4.427027	15930	14633.844
15		0.005	1.015	13.5	4.6	4.427027	15580	14283.844
16		0.005	1.011	13.5	4.6	4.427027	16030	14733.844
17	1.4÷1	0.006	1.019	13.5	4.6	4.427027	15800	14503.844
18		0.005	1.01	13.5	4.6	4.427027	15380	14083.844
19		0.007	1.007	13.5	4.6	4.427027	15520	14223.844
20		0.006	1.008	13.5	4.6	4.427027	15490	14193.844

The ground rice has been subjected to calorimetric incineration tests taking into account size fractions and fineness. The results obtained are shown in table 1.

6. Summary

In the light of results of mathematical and experimental study, formalization of irregularities, with rice grain grinding used as an example, for selected parameters of determined functions and random function shows that the assumptions made are correct. The analysis should, however, include detailed verification of assumptions related to ergodicity and constancy of characteristics of torque, angular speed and power at shaft (shafts) of the grinder.

For the uniform operation of multi-edge grinders it is necessary, within the given area of assumptions, to propose modified models of irregularity of machine runs, taking into consideration: unit shearing resistance p_c , friction μ and other conditions of quasi-shearing of heterogeneous materials, for determination of specific value describing the material and selected conditions of the grinding process.

On the basis of the presented model and research programme, structural features of the unit that evenly grinds rice grain has been selected, with the operational irregularity within ($\delta d \leq 10$) %.

Energy effectiveness, regularity, energy consumption, rice grinding efficiency, working resistance for the gain in specific surface area, increases in incineration energy and temperature, power consumption and stream of the grinding process productivity, depend on motion of elements and therefore on properties of ground materials and design of the machine used.

„ The research financed by the funds of the National Centre for Research and Development in 2010/2013 as a development project”

Reference

- [1] Detyna, J., *Analysis of nonequilibrium states in the sieve separation process*, Maintenance and Reliability 1(49)2011: 78-85.
- [2] Flizikowski, J., *Konstrukcja rozdrabniaczy żywności*, Wydawnictwo Uczelniane Akademii Techniczno – Rolniczej w Bydgoszczy, Bydgoszcz 2005.
- [3] Flizikowski, J., Bieliński, K., Bieliński, M., *Podwyższenie energetycznej efektywności wielotarczowego rozdrabniania nasion zbóż na paszę*, Wydawnictwo ATR-OPO, Bydgoszcz 1994.
- [4] Flizikowski, J., Bieliński, M., *Rozdrabniacz wielotarczowy zwłaszcza do materiałów ziarnistych*, Patent RP.
- [5] Mroziński, A., *Modelling of waste-paper stock treatment process in disc refiners*, Journal of POLISH CIMAC nr 3/2010, Vol. 5, str. 113-119.

- [6] Mroziński, A., *Podstawy rozwoju przetwarzania mas makulaturowych w młynach*, Ekologia i Technika, Vol. 101, nr 4 (2009), str. 151-158.
- [7] Razavi, S.M.A., Farahmandrar, R., *Effect of hulling and milling on the physical properties of rice grains*, International Agrophysics, 2008, 22, 353-359.
- [8] Tomporowski, A., *Testing the power of multi - disc shrebing grains of rice*, Ekologia i Technika nr 3, s. 161-164.
- [9] Tomporowski, A., *Assumptions to the formalization of the courses of grinding irregularities by means of the random function*,. Ekologia i Technika nr 6 (2009), s. 317-320.



THE PROCESS OF MODELING CURVE OF AN INEQUALITY GRINDING RICE GRAINS

Andrzej Tomporowski

University of Technology and Life Sciences
ul. Prof. S. Kaliskiego 7, 85-789 Bydgoszcz
Tel./fax: +48 52 3408255
a.tomporowski@utp.edu.pl

Abstract

There has been the modelling of regularity of weights of multiedge biological material mincers conducted at work. The record of irregularity, registered in the time interval, is called the execution of stochastic irregularity of the grinding process. The construction features of the grinding tool, parameters of the process and individual features of ground and biological material of anisotropic structure influence their shape. For adopted assumptions, there has been proposed the psychical model to be published in trigonometric and exponential function. The suggested methodology to mathematically model the curve of the machine run non-uniformity and the grinding process itself fulfils the expectations concerning the development aimed at: high process effectiveness and product usable quality.

With the conformity of the above model for real course, the evaluated function ($Q=||y-y^||$) was determined at the level of 6-12% depending on ice properties.*

The necessary condition to increase uniformity and efficiency as well as further development of grinding biological and fibrous materials is to elaborate an effective method to model and describe the grinding non-uniformity curve.

Keywords: non-uniformity, grinding, biological materials, multi-edge grinders

1. Introduction

The process of angular velocity of the torque and grinding power is of impulse character. It is associated with the periodical operation of the grinding edges and determined operation of biological material, its function of biological materials cannot be definitely predicted, it is a stochastic phenomenon. The registered parameter in the function, for example time, of which values all the time change at random, is called the record of stochastic starting signal. However, one can depict the shape, structure and operating elements of the machine. The course of the grinding irregularity and state the range (t_1, t_2) defined by time or angle of rotation (α_n, α_k) and approximated moment value of measured parameter. The very important feature of stochastic register of irregularity of grinders' operation is the independence of the registered parameter (power or angular velocity) of the property, from the freely chosen time intervals, in which one makes the analysis of the objective course of the starting signal.

In the real course of grinding materials of the farm and food industry, one finds it difficult to predict, occurring one after the other, states of changes and stresses. On these grounds we deal with, from the point of view of work regularity, the stochastic process. The basic difference that

distinguishes this type of processes from the determined processes is that: the stochastic process is an accumulation of different executions, and the executions last relatively long.

The research problem was formulated in the form of a question: What are the formalization possibilities of real processes of dynamic (M) irregularity and kinematic one (ω), with the use of parameters and properties of random function?

2. Assumptions

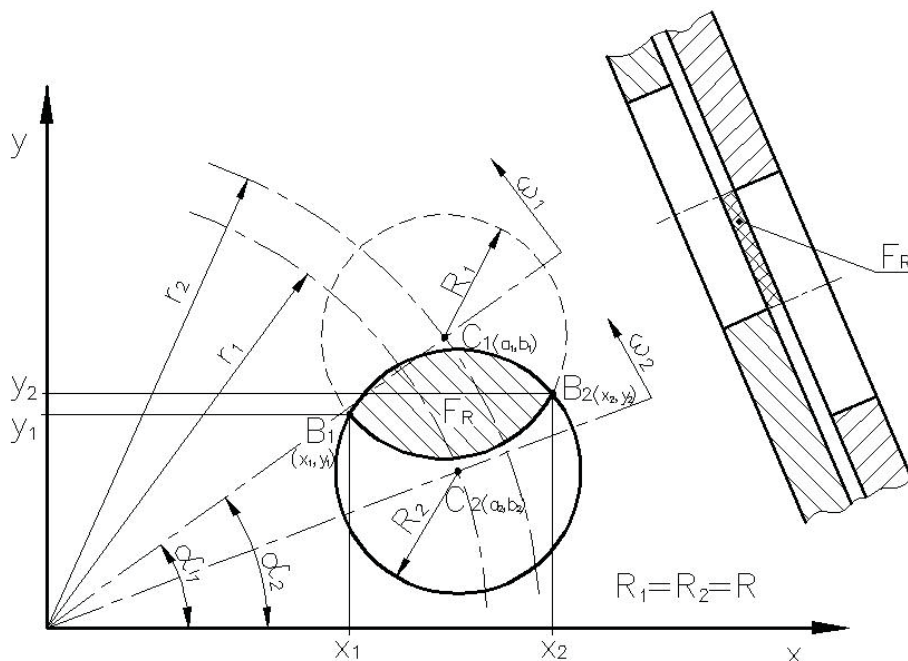


Fig. 1. Sectional area and effective grinding surface for two grinding discs between edges of the grinding holes [1,2]

During the time a single blade goes through the material being ground (Fig. 1), the grinder shaft torque increases from zero (start of cutting) up to the maximum value, and then it gradually goes down to zero (at the moment when the cutting operation is finished). The torque value inside a multi-hole grinder depends on the design parameters of the quasi-shearing assembly

In turn great changeability of torque makes alternate variations of the angular velocity. The changes in the angular velocity are of a pulsing nature. The measure of uniformity of work of the grinders is inaccuracy of realization of the preset motion function, it means non-uniformity of run, loads, and even efficiency [1, 2].

The power requirement to drive a blade is very unstable (Fig. 2), since there is a period of the machine idle run between cutting the consecutive pieces of material. Therefore significant changes in power consumption may occur.

The changing difference of the active torque and the torque of driving forces is a reason for changeability of the angular velocity of the grinder shaft. The active torque M_{cz} is considered to be the torque which occurs when cutting. While the torque of driving forces M_{sn} is used to denote the torque taken from an electric motor. If the shaft makes n revolutions, then the average angular velocity being equal to the nominal velocity is

$$\omega_{ir} = \omega_{nom} \approx \frac{\omega_{max} + \omega_{min}}{2}. \quad (1)$$

The variations of the shaft angular velocity during the steady motion take place between ω_{\max} and ω_{\min} . The aforementioned changes are included in the coefficient of the non-uniformity of the machine run [6], which is determined by

$$\delta_k = \frac{\omega_{\max} - \omega_{\min}}{\omega_{sr}} \quad (2)$$

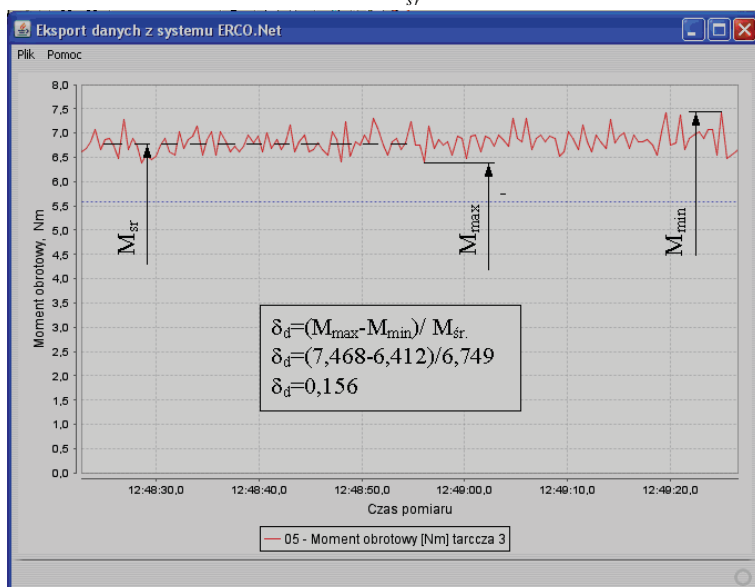


Fig. 2. Fragment of torque sequence and evaluation of non-uniformity of loads of the five-shielded grinder RWT-5KZ, while grinding a rice grain

2. Approximation of the grinding non-uniformity curve to obtain its mathematical form

The recorded courses of kinematic and dynamic non-uniformity (Fig. 4) of the grinder work may be described in a mathematical form by applying essential elementary function systems:

- exponential,

$$M(t) = M_1 e^{j\omega t} + M_2 e^{j\omega t} + \dots + M_n e^{j\omega t}, \quad (3)$$

- trigonometric,

$$M(t) = a_0 + c_1 \cos(n\omega t + \phi_1) + c_2 \cos(n\omega t + \phi_2) + \dots + c_n \cos(n\omega t + \phi_n). \quad (4)$$

For the needs of transformation of the measurement curve (e.g. stochastic one) to obtain its mathematical form, it is advantageous to select the relationships which shall assure representation of a real course at the minimum level of the acceptable deviation error [4]. This is a characteristic feature of trigonometric and polynomial functions. A periodic function describing the investigated non-uniformity courses, which meets the necessary conditions may be set as the Fourier series, made of the sum of the individual trigonometric functions, with various amplitudes, and a constant component. The physical form of the period course of grinding non-uniformity is a sufficient condition for existence of a real mathematical function.

The periodic function of non-uniformity function developed to the Fourier series has many theoretical and strictly practical applications. It facilitates presentation of the course of non-uniformity of grinding operation when presenting frequency analysis for sinusoidally changing

courses. Each component of a pulse, an increase or a decrease in load may be investigated separately for the linear representations.

Presentation of the course of non-uniformity of the grinding machine course as the Fourier series is equivalent to decomposition of the essential function into its components; a constant component and individual components (respective answers to loads). The investigated non-uniformity curve may be approximated by means of a finite number of harmonic courses so that after adding next sequential harmonic components an image showing more and more precise approximation of the real course can be obtained.

The essential, graphic mathematical models describing the courses of non-uniformity of the grinding machine work are affected by some error – a deviation from the real values. They may be presented as a regular wave with a typical geometrical configuration by means of an infinite trigonometric series, with the functions having the form of the dominant course:

- with an isosceles triangle outline

$$M(t) = 8 \frac{A}{\pi^2} \left(\frac{\sin \omega t}{1} - \frac{\sin 3\omega t}{9} + \frac{\sin 5\omega t}{25} - \dots \right), \quad (5)$$

- with a right-angled triangle outline;

$$M(t) = 2 \frac{A}{\pi} \left(\frac{\sin \omega t}{1} - \frac{\sin 2\omega t}{2} + \frac{\sin 3\omega t}{3} - \dots \right), \quad (6)$$

- with a trapezoidal outline;

$$M(t) = 4 \frac{A}{\alpha \pi^2} \left(\frac{\sin \pi \alpha \sin \omega t}{1} + \frac{\sin 3\pi \alpha \sin 3\omega t}{9} + \frac{\sin 5\pi \alpha \sin 5\omega t}{25} + \dots \right). \quad (7)$$

In the analysed courses of non-uniformity of work of the multi-edge grinders the amplitudes of individual components are inversely proportional to frequency, therefore the components with smaller frequency have greater amplitude than the components with higher frequency.

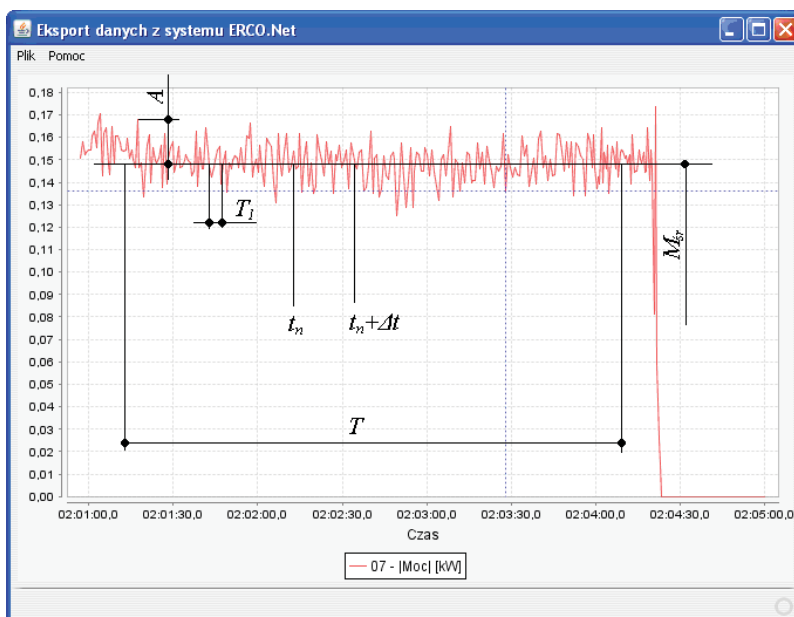


Fig. 3. The examination power of the stochastic process values of one-shield grinder during grinding grinder RWT-5KZ, while grinding a rice grain

Approximation of a real course to obtain the corresponding model curve is simplified or it becomes more general after applying the exponential Fourier series.

$$M(t) = A_0 + A_1 e^{j\omega t} + A_2 e^{j2\omega t} + A_3 e^{j3\omega t} + \dots + A_n e^{jn\omega t}, \quad (8)$$

where:

$M(t)$ — approximated function - torque,

$n = 1, 2, 3, \dots$,

$\omega = 2\pi/T$,

T - period.

The coefficient A_n facilitates to determine a set of harmonic components which when summed up make the course of the function $M(t)$.

Exemplary presentation of the sequence of the rectangular pulses (velocity or torque) by means of the trigonometric series is formulated as:

$$M(t) = \frac{\alpha A}{T} \left[1 + 2 \left(\sin \frac{1\alpha\pi}{T} \cos 1\omega t + \sin \frac{2\alpha\pi}{T} \cos 2\omega t + \dots \right) \right]. \quad (9)$$

With the conformity of the above model for real course, the evaluated function ($Q = \|y - y^*\|$) was determined at the level of 6-12% depending on the rice properties.

3. The statistic characteristics of irregularities processes

Making average of the obtained values of the torque or rotational speed of the grinder's shaft, as a random value in relation to the time, one can make the average of one of the execution in relation to the time parameter or rotational angle of the operational shaft.

It is essential, in the analysis of the stochastic process, to check whether in the tested process of irregularity of the grinding machine operation do not occur the statistic regularities which indicated the process at least partially determined. It may be performed using the non-complicated examination procedure. One needs to register repeatedly the process of irregularity of the machine process. The achieved results one needs to compare with one another in a few, and even several, similar time intervals from t_1 to t_n (or whether depending on the kept register, rotational angle of the operational shaft from α_1 to α_n). Compare and make the analysis, read in the chosen ranges the values of the registered parameter: of torque for the dynamic register and angular velocity for the kinematic one, from $M_1(t_1)$ to $M_1(t_n)$, and in turn all ones, till to the value from $M_n(t_n)$. In order to exclude the dependence of the achieved function on the accepted time values, the checking procedure should be repeated for the moved times. As a consequence one should make the diagrams of cumulative frequency of the random variable $E(M, \omega)$, in the form of:

- for the dynamic irregularity

$$E_t(M) = P [M(t) < x] \quad \text{and} \quad E_{t+\Delta t}(M) = P [M(t+\Delta t) < x], \quad (10)$$

- for the kinematic irregularity

$$E_t(\omega) = P [\omega(t) < \omega] \quad \text{and} \quad E_{t+\Delta t}(\omega) = P [\omega(t+\Delta t) < \omega], \quad (11)$$

where:

M –the torque on the grinder's shaft,

ω - the angular velocity of the grinder's shaft.

The process is stationary, if the achieved cumulative frequencies are equal, which means

$$E_t(M, \omega) = E_{t=\Delta t}(M, \omega). \quad (12)$$

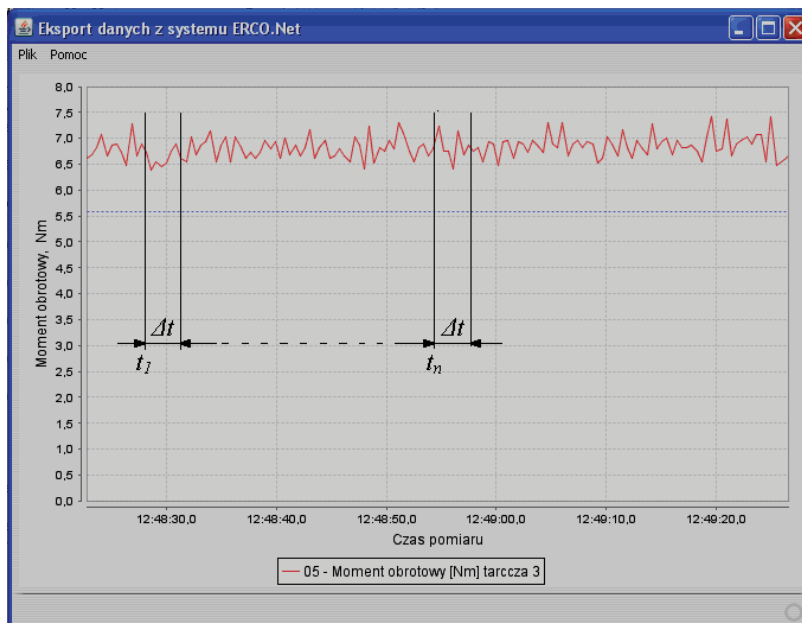


Fig.4. The examination of the stochastic process values of one-shield grinder during grinding grinder RWT-5KZ, while grinding a rice grain

One cannot predict the course of the irregularities of grinding the biological materials, it is completely stochastic phenomenon. Correctly designed process of multi-edged grinding technology let us predict some properties of statistical registered record of irregularities.

The record of the process of grinder's work irregularity may be read in double ways:

- reading of the record data – statistic feature of the model, record,
- reading of the changes speed, registered staring point – describes statistically the variability of the objective record.

The analysis of irregularities as of the stochastic phenomenon defines in the statistic sense the process of multi-edged grinding. Practically, for a correct description of the grinding process one should register the irregularities of the stochastic record in a very long time interval [5].

4. Static characteristics of irregularities course

The average value (Fig. 3) of the random form of irregularity of the grinding machine process $M(t)$ and $\omega(t)$ defines the static component, one which is not accidental. As a result of its subtracting from the irregularity value, we receive the value including only the random variable component.

The random mean value may be presented in the form:

- for the dynamic irregularity:

$$M_{sr}(t) = \lim_{T \rightarrow \infty} \frac{1}{T} \int_0^T M(t) dt, \quad (13)$$

– for the kinematic irregularity:

$$\omega_{sr}(t) = \lim_{T \rightarrow \infty} \frac{1}{T} \int_0^T \omega(t) dt. \quad (14)$$

For the description of the statistical properties of the irregularity register of the grinding machine course, one may use its mean-square value, as a measure characterizing the irregularity course, both the dynamic and kinetic one, of the course of the biological materials of grinders;

$$M_{sr}^2(t) = \lim_{T \rightarrow \infty} \frac{1}{T} \int_0^T M^2(t) dt, \quad (15)$$

where:

T – time interval.

The likelihood that the temporary value of the irregularity M(t) shall be included in the range (M_A, M_B) is expressed by the formula;

$$P[M(t) \in \langle M_A; M_B \rangle] = \lim_{T \rightarrow \infty} \frac{1}{T} (t_1 + t_2 + \dots + t_k), \quad (16)$$

where:

t_k - times of which the temporary values of the signal M(t).

The density of likelihood of the temporary values of the multi-openings grinder's irregularity course may be written in the form of the formula;

$$p(M) = \lim_{\Delta x \rightarrow \infty} \frac{P[M(t) \in \langle M_A; M_B \rangle]}{t_1 + t_2 + t_3 + \dots}. \quad (17)$$

The arrangement of the likelihood of the continuous random variable M (moment) or ω (the angular speed) in the time is the dependence of the likelihood density p(x) from the independent variable x.

$$p(M) = \text{const} \Leftrightarrow M \in \langle M_{\min}; M_{\max} \rangle,$$

and

$$p(M) = 0 \Leftrightarrow M \notin \langle M_{\min}; M_{\max} \rangle. \quad (18)$$

The density of the likelihood of the irregularity (dynamic) function of the grinder's course of the model approximated to the form of described with the formula;

$$M(t) = 2M_i \frac{1 - 2\left(\frac{\cos \omega t}{3} + \frac{\cos 2\omega t}{15} + \frac{\cos 3\omega t}{35} + \dots\right)}{\pi}, \quad (19)$$

is:

$$P(M) = \pi \sqrt{M_{\max}^2 - M_i^2}, \quad (20)$$

where:

M_i – temporary values.

For the description variation of the irregularities course of the biological materials grinding, one may use the function of autocorrelation as a measure of the dependence of the function values M(t) or ω(t) distant to each other of the difference value of their measurement. It may be depicted with the formula:

$$S(\Delta t) = \lim_{T \rightarrow \infty} \frac{1}{T} \int_0^T M(t_i) M(t_i + \Delta t) dt. \quad (21)$$

5. Summary

The necessary condition to increase uniformity and efficiency as well as further development of grinding biological and fibrous materials is to elaborate an effective method to model and describe the grinding non-uniformity curve [6]. At each stage such a design solution of the tool and grinding unit is sought which shall guarantee, during the preset time, extreme function of: effectiveness, quality and uniformity.

The up to present examinations of the irregularity course [1, 2, 3], directed at the experimental cognition of the course values and characteristics, prove the formalization need. The formalization of the grinding irregularities courses carried out on the example of biomaterials, for the chosen random function parameters prove the soundness of the accepted assumptions. Such a proceedings should cover the detailed verification of the ergodicity assumptions and the stationarity of the characteristics of the torque, angular speed, and the power on the grinder's shaft.

References

- [1] Flizikowski, J., *Konstrukcja rozdrabniaczy żywności*, Wydawnictwo Uczelniane Akademii Techniczno – Rolniczej w Bydgoszczy, Bydgoszcz 2005.
- [2] Flizikowski, J., Bieliński, M., *Rozdrabniacz wielotarczowy zwłaszcza do materiałów ziarnistych*, Patent RP.
- [3] Flizikowski, J., Tomporowski, A., *Mechanical processing of elastic – plastics corns*, 12-th International Conference on Developments in Machinery Design and Control, Nowogród 2008.
- [4] Mroziński, A., *Modelling of waste-paper stock treatment process in disc refiners*, Journal of POLISH CIMAC nr 3/2010, Vol. 5, str. 113-119.
- [5] Tomporowski, A., *Testing thy power of multi - disc shrebing grains of rice*, Ekologia i Technika nr 3, s. 161-164.
- [6] Tomporowski, A., *Nierównomierność obciążeń przy rozdrabnianiu drewna*, Recykulacja, Bydgoszcz 2008.
- [7] Tomporowski, A., *Rozdrabniacz do wilgotnych ziaren zbóż*, Inżynieria maszyn 22/2004, Bydgoszcz 2004.



DESIGN CONSIDERATIONS FOR SHREDDER FEED CONVEYORS USED IN FARM AND FOOD INDUSTRY

Andrzej Tomporowski

*University of Technology and Life Sciences
ul. Prof. S. Kaliskiego 7, 85-789 Bydgoszcz
Tel./fax: +48 52 3408255
e-mail: a.tomporowski@wp.ptl*

Abstract

The purpose of conveyors, designed depending on the type of raw material and requirements with regard to the comminuted materials is to ensure smooth and efficient comminution procedure. Scientific literature provides detailed descriptions and studies focusing on the functionality and operational characteristics of systems used for feeding long (continuous) materials; corn stems, plastics, branches (wood) and other similar materials. These descriptions usually refer to the design features of shredders in connection with applicable operational characteristics. Nonetheless, despite the existence of various types of conveyors intended for feeding long materials, it is still a pertinent issue to ensure high effectiveness, including consistent feed, and efficiency of the feeding equipment. Based on both own research and the studies by other academics, it has been proven that the design of the working units applied in the analysed equipment, aside from the properties of the fed material and the applicable process parameters, has a significant influence on consistent and efficient energy consumption.

1. Introduction

The production and processing of specific materials used in the farm and food industry depend largely on the development of modern engineering and technological solutions. The key element in the production and processing of this type of materials is the process generally referred to as comminution of raw and base materials used in the farm and food industry.

Primary processing of these materials develops equally dynamically as engineering solutions focused on the management and recovery of waste from these materials. Comminution is an essential stage of each production and subsequent recirculation process, both in the initial as well as the final phase of a full cycle. The purpose of conveyors, designed depending on the type of raw material and requirements with regard to the comminuted materials is to ensure smooth and efficient comminution procedure. Scientific literature provides detailed descriptions and studies focusing on the functionality and operational characteristics of systems used for feeding long (continuous) materials; corn stems, plastics, branches (wood) and other similar materials. These descriptions usually refer to the design features of shredders in connection with applicable operational characteristics. Nonetheless, despite the existence of various types of conveyors intended for feeding long materials, it is still a pertinent issue to ensure high effectiveness, including consistent feed, and efficiency of the feeding equipment. Based on both own research and the studies by other academics, it has been proven that the design of the working units applied

in the analysed equipment, aside from the properties of the fed material and the applicable process parameters, has a significant influence on consistent and efficient energy consumption [1,2,4,5].

The purpose of this study was to systematize models which support of designing roll feeders for long, continuous materials intended for use in farm and food industry. The study was conducted based on a prototypical shredding unit provided by Jamox company.

2. Roll feeder design principles

Roll feeders are commonly utilized in comminution equipment used for shredding continuous (long and fibrous) materials. Porous, continuous materials which, when leaving the roller gap, are much more compacted, displaced and deformed, due to external forces, than the originally fed material, are transferred into the working gap of the feeder.

The process of compacting continuous material within the inter-roll area may be divided into two stages (Fig.1): drawing stage and compacting stage.

By analogy to raw material in the form of uniform and continuous material, it is possible to use existing models based on the principle of continuity, in order to determine relative speed as the difference between the speed of the raw material v_s and the peripheral speed of the feeding roll surface v_r :

$$v = v_s - v_r, \quad (1)$$

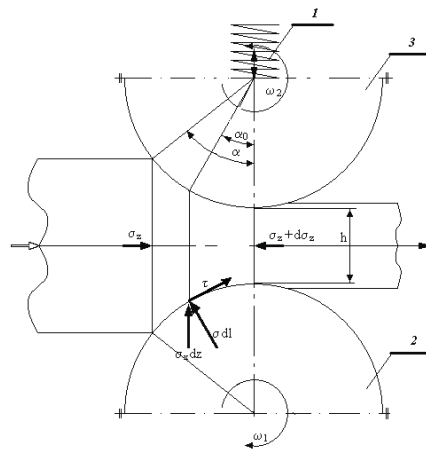


Fig. 1. Functional diagram of a roll feeder; 1) pressure spring, 2) fixed roll, 3) pressure roll

When the material is fed into the inter-roll area the peripheral speed on the surface of the feeding rolls is larger than the linear speed of the raw material. Thus, the relative speed v_{rel} compared to the roll surface is the smallest and is bound to increase due to the locally decreasing height of the gap $h(z)$. The state of balance for an average stress σ and friction angle φ_w between the material and roll surface is defined by the following relationship:

$$h(z) \frac{d\sigma_z}{dz} + 2\sigma_z \tan \alpha = 2\sigma_x \tan(\alpha + \varphi_w) \quad (2)$$

Therefore:

$$\frac{d\sigma_z}{dz} + f(z)\sigma_z(z) + g(z) = 0 \quad (3)$$

From the moment the material is captured by the rolls the surface pressure increases from zero to the maximum value occurring at the point where the relative speed $v = 0$. According to these assumptions, this is where the maximum pressure may be observed. The following stages may be identified during spatial compaction of continuous material within the working area of a roll feeder [5]:

1. Initial volume reduction, mutual displacement of individual units of the raw material.
2. Further volume reduction caused by elastic deformations and plastic strains.
3. Burnishing, breaking and fracturing of the fed material.

The first stresses occur within the inter-roll area, in the slip zone. Individual constituents of the raw material meant for comminution come into contact with one another and the fibres begin touching the surface of the walls and rolls. This phenomenon may be described using the principles of mechanics. If the shearing stresses of the wall are sufficient for the given raw material to be drawn without any slip, that point signifies the beginning of an adhesion zone. This is where the material is further compacted, depending on the geometrical conditions. The properties of the continuous material are a reliable basis with regard to the stress pattern.

The stresses occurring within the slip zone are substantially influenced by the pressures generated on the material feeding plane, since these pressure values determine the shearing stresses acting on the walls, towards the roll gap. The higher the pressure of the rolls on the material fed on the roll grip plane z_G is, the higher the resulting stress with suitably stronger compacted material. The total pressure force may be derived from the integral of the roll perimeter pressure curve.

3. Design guidelines

Figure 2 shows the slip zone and adhesion zone in the inter-roll gap. The roll surface exhibits certain lead/advance above the roll grip angle θ_G due to as yet insignificant friction stress. The so-called slip state occurs in this area. Below the roll grip angle, the nonslip material drawing causes a certain compaction, correspondingly to the geometrical conditions within the inter-roll gap. At the $\alpha = 0$ point, the compressed material leaves the roll gap without elastic deformation.

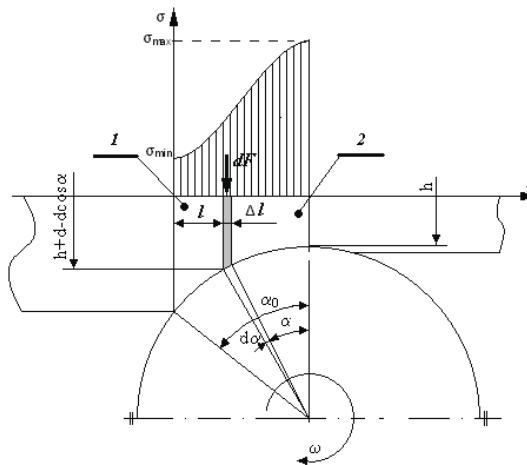


Fig. 2. Slip zone and adhesion zone within a roll area; 1- slip zone, 2- adhesion zone

The analysis of the stress pattern within the working area of the roll feeder (in the roll gap) involves determining:

1. stresses within the slip zone,
2. stresses within the adhesion zone,
3. roll grip angle α_G .

4. Stresses within the slip zone

The following consideration are based on the assumption that the slip processes, occurring between individual constituents of the fed material and between the fed material itself and the walls of the feeder, are decisive within this area. The material behaviour may be characterized based on, e.g. the effective slip point or the point of slip on the mouth and roll wall. The state of stress within an element of the fed material is described assuming a coexistence of the main stress directions and main deformation directions (unit elongations) with material isotropy acc. Mohr's circle of stresses.

Shear and normal stresses for a given plane are represented as points on the circle of stresses. This way of representation enables determination of stresses on various planes of the analysed fed material volume. Relationships between normal stresses σ_x and σ_z and relatively identical shear stresses τ_{xz} and τ_{zx} are following:

$$\left\{ \begin{array}{l} \sigma_x = \frac{\sigma_1(1 + \cos \beta) + \sigma_2(1 - \cos \beta)}{2} \\ \sigma_z = \frac{\sigma_1(1 - \cos \beta) + \sigma_2(1 + \cos \beta)}{2} \\ \tau_{xz} = \frac{\sigma_1 \sin \beta - \sigma_2 \sin \beta}{2} \\ \tau_{zx} = \frac{\sigma_1 \sin \beta - \sigma_2 \sin \beta}{2} = \tau_{xz} \end{array} \right. \quad (4)$$

The largest principal stresses σ_1 are exerted, in accordance with definition, on the plane free of shear stresses and are turned by a $\beta/2$ angle in a mathematically negative direction in relation to the direction of normal stress σ_x .

Both stresses on the σ - τ plane form a β angle in a mathematically positive direction, while the stresses σ_x and σ_z , as well as σ_1 and σ_2 form a right angle. That is why the line connecting these stresses on the σ - τ plane runs straight through the central point of the Mohr's circle of stresses.

The notion of relative slip between elements of the fed material is understood as plastic strain of its element subject to pressure generated by the feeder rolls. By applying the criterion of inter-material slip, based on the theory of Mohr's circle of stresses, it is possible to determine the plane on which this displacement between the constituents of the fed material occurs, including the related maximum shear stress of this plane.

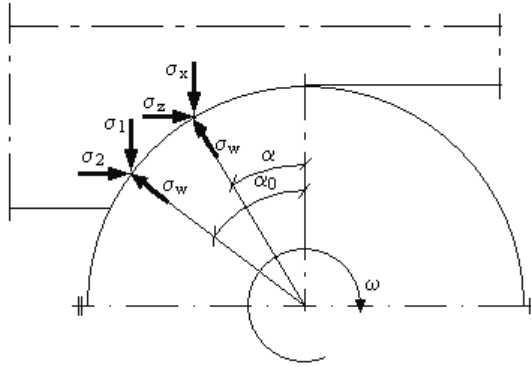


Fig. 3 The stresses that occur on the feeder roll surface

Figure 3 shows the states of stress for two continuous elements of the fed material on the surface of the roll. The elements of the fed material are in a state of elasto-plastic balance with a slip in its volume and on the wall of the feeder mouth. The largest principal stress σ_1 forms an angle α with direction x , while the stress σ_w forms an angle α with the negative direction x . The sum of angles $\beta + \alpha$ is always present between the stresses σ_1 and σ_w on the σ - τ plane.

Since: $x = 0$, $\beta = 0$ on the symmetry plane as well, the direction of principal stresses has been established along the whole plane $z = \text{const}$, defined by α_0 . On this plane lies the beginning of the coordinate system applied herein. Therefore:

$$\alpha_0 = \frac{1}{2} \left[\varphi_\omega + \arcsin \frac{\sin \varphi_\omega}{\sin \varphi_e} \right] \quad (5)$$

This plane is referred to as the material feeding plane.

$$\omega = \alpha_0 - \alpha \quad (6)$$

It enables, with identified properties of flow from the coordinate α determination of direction ω of the largest principal strain σ_1 on the surfaces of the feeding rolls.

The analysis performed as part of this study did not cover gravitational forces of the fed material exerted on the surface of the bottom feeder roll and the guiding trough. Owing to a relatively small weight and considerably high pressures generated by feeder rolls, these forces were considered irrelevant for the subject matter of this study and were thus omitted. The balance of stresses in the z and x direction lead to the following system of equations:

$$\begin{cases} \frac{\partial \sigma_z}{\partial z} + \frac{\partial \tau_{xz}}{\partial x} = 0 \\ \frac{\partial \sigma_z}{\partial x} + \frac{\partial \tau_{zx}}{\partial z} = 0 \end{cases} \quad (7)$$

Therefore:

$$\left\{ \begin{array}{l} (1 + \sin \varphi \cos \beta) \frac{\partial \sigma}{\partial z} - \sin \varphi \sin \beta \frac{\partial \frac{\beta}{2}}{\partial z} + \sin \varphi \cos \beta \frac{\partial \sigma}{\partial x} + \sin \varphi \sin \beta \frac{\partial \frac{\beta}{2}}{\partial x} = 0 \\ (1 + \sin \varphi \cos \beta) \frac{\partial \sigma}{\partial x} + 2 \sigma \sin \varphi \cos \beta \frac{\partial \frac{\beta}{2}}{\partial x} + \sin \varphi \sin \beta \frac{\partial \sigma}{\partial z} + 2 \sigma \sin \varphi \cos \beta \frac{\partial \frac{\beta}{2}}{\partial z} = 0 \end{array} \right. \quad (8)$$

The increase of stresses in the symmetry axis of the roll gap was identified as an approximate solution, by the application of the integral calculus average value theorem, and it amounts to:

$$\frac{1}{\sigma} \frac{d\sigma}{dz} = \frac{8\alpha_0 - 8\alpha \operatorname{tg} \varphi_e}{\left[\frac{s}{2} + \frac{d}{2}(1 - \cos \alpha) \right] \left[\operatorname{tg} \left(\frac{\alpha_u - \alpha}{2} - \frac{\varphi_c}{2} + \frac{\pi}{4} \right) - \operatorname{tg} \left(\frac{\alpha_u - \alpha}{2} + \frac{\varphi_c}{2} - \frac{\pi}{4} \right) \right]} \quad (9)$$

$$\text{where:} \quad z = \frac{d}{2} \cos(\alpha) \quad (10)$$

therefore, the stresses amount to:

$$\sigma = \sigma_0 \exp \int_0^\alpha f(z) dz \quad (11)$$

5. Stresses within the adhesion zone of the feeder

The postulated compression of the fed material in a roll feeder of shredder takes place within the adhesion zone where there are no slips on the smooth surface of the roll. The stress pattern was established based on the volume reduction value in the inter-roll gap of the feeder (Fig. 2). The volume of material in the mouth of the feeder amounts to:

$$V_\theta = [(h + d(1 - \cos \alpha)) \cos \alpha - H] b \Delta l, \quad (12)$$

calculated for width of the rolls which equals b . The teeth that help drawing the material onto the surface of the rolls were included by introduction of the H value which stands for an averaged reduction of the substitute gap, which is connected with the volume of a single tooth V_R and the number of these teeth n_R , determined by the following equation:

$$\pi d b \frac{H}{2} = n_R V_R \quad (13)$$

The decrease in volume, derived based on the roll grip angle α_G , results in an increase in compressed material density ρ_K . The density ratio is as follows:

$$\frac{\rho_K \alpha}{\rho_{K_1} \alpha_G} = \frac{V_{\alpha_G}}{V_\alpha} = \frac{H + (h + d(1 - \cos \alpha_G)) \cos \alpha_G}{H + (h + d(1 - \cos \alpha)) \cos \alpha} \quad (14)$$

The following approximate relationship occurs between density and compressive stress:

$$\sigma \approx \rho_K^K \quad (15)$$

stress pattern in the adhesion zone:

$$\sigma_{\alpha} = \sigma_{\alpha_G} \left[\frac{H + (h + d(1 - \cos \alpha_G)) \cos \alpha_G}{H + (H + d(1 - \cos \alpha)) \cos \alpha} \right]^K \quad (16)$$

The roll grip angle was derived based on the above equation, therefore:

$$\left. \frac{d\sigma}{dz} \right|_{\alpha} = K\sigma_{\theta} \left[\frac{d(2\cos \alpha - 1) - s}{H + [h + d(1 - \cos \alpha) \cos \alpha]} \right] \frac{2tg \alpha}{d} \quad (17)$$

where:

$$\alpha = \arcsin \frac{2(h_0 - z)}{d} \quad (18)$$

6. Determination of the feeder roll grip angle

The equation (17) contains the output stress on the $z = 0$ plane as boundary condition. Based on both stress gradients in the adhesion zone and slip zone, it is possible to determine the feeder roll grip angle. The compaction is conditional upon continuity in the inter-roll gap of the feeder and results in smaller increase in surface pressure due to the compaction that has already occurred. Equal stress gradients are therefore necessary prerequisite for the unknown roll grip angle.

$$\left. \frac{d\sigma_1}{ds} \right|_{\alpha_G} = \left. \frac{d\sigma_2}{ds} \right|_{\alpha_G} \quad (19)$$

The largest principal stress for the roll grip angle amounts to:

$$\sigma_1 = \sigma + \sigma \sin \varphi_e \quad (20)$$

7. Pressure and driving power forces

In accordance with figure 2, the pressure force F was determined by integration of the field below the curve of the surface pressures occurring in the roll gap:

$$F = \frac{bd}{2} \int \sigma_1 \cos \alpha d\alpha \quad (21)$$

Depending on the pressure force, only the surface pressures occurring in the adhesion zone are taken into consideration. The pressures in the slip zone are negligibly low.

$$F = \frac{bd\sigma}{2} \int_0^{\alpha} \left(\frac{h + H}{H[h + d \cos \alpha - d \cos^2 \alpha]} \right) \cos \alpha d\alpha \quad (22)$$

where the maximum stress at the narrowest point of the roll gap amounts to $\sigma_{1 \max}$.

The torque was determined through integration of the pressure force on the roll surface in the adhesion zone:

$$M = 0,25 F d t g \alpha \quad (23)$$

The driving power was derived from the relationship between torque and roll revolutions n_r .

$$P = 2\pi M n_r \quad (24)$$

8. Conclusions

The phenomena, processes and relationships between feeding continuous materials such as tree branches or plant stems and multi-edge grinding are relatively easy to describe formally, despite their complexity and multifaceted nature. Arriving at the answer to the question about process factors (actions and methods), design features (means, devices and systems), operational conditions pertaining to roll feeders and their influence on the dynamics and efficiency of the whole comminution process (tree branches), with a multi-edge shredder used as an example, was possible with an assumption that quasi-cutting stresses will propagate at an infinite rate [3,4,5].

It seems appropriate to continue the research focusing on optimising the design features of the analysed prototypical shredding unit.

I would like to thank the owners of Jamox Company for making the prototype and required technical resources available for the purpose of this study.

References

- [1] Flizikowski, J., *Konstrukcja rozdrabniaczy żywności*, Wydawnictwo Uczelniane Akademii Techniczno – Rolniczej w Bydgoszczy, Bydgoszcz 2005.
- [2] Flizikowski, J., Bieliński, M., *Rozdrabniacz wielotarczowy zwłaszcza do materiałów ziarnistych*, Patent RP.
- [3] Mroziński, A., *Modelling of waste-paper stock treatment process in disc refiners*, Journal of POLISH CIMAC nr 3/2010, Vol. 5, str. 113-119.
- [4] Tomporowski, A., *Testing the power of multi - disc shrebing grains of rice*, Ekologia i Technika nr 3, s. 161-164.
- [5] Tomporowski, A., *Nierównomierność obciążeń przy rozdrabnianiu drewna*, Recykulacja, Bydgoszcz 2008.



METHODOLOGY OF FATIGUE TESTS FOR GLUED DENTAL SAMPLES

Tomasz Topoliński, Mateusz Wirwicki

*University of Technology and Live Sciences in Bydgoszcz
ul. Kaliskiego 7, 85-796 Bydgoszcz, Poland
tel.: +48 52 3408497, fax: +48 52 3408245
e-mail: wirwicki@utp.edu.pl*

Abstract

In human teeth, depending on the age at which it is located, there are two types of teeth: milk and solid. During the consumption of various food groups of teeth meet their unique tasks. During Eating teeth are exposed to cyclic loading resulting in microcracks in the structure of the tooth. Using special preparations of dental enamel can be broken by bind to the tooth. The article presents the strength tests for determination of different bonding characteristics of the tooth. Also presents a literature review was divided into groups: the test material and methods of researchers. Of all disguised literature describes and compares the two close to each endurance test methods for tissue tooth blade in tempered. Methods of Testing was conducted under conditions of low and high cyklowych. Summarizes the methods shown and described as would appear the author's own research.

Keywords: strength tests, human dentition, molar teeth, dentin

1. Introduction

Human dentition is divided into two categories depending on the stage of life: primary teeth and permanent teeth. Primary dentition appears in children at the age between 2 and 6. Altogether, there are 20 teeth, 10 in the lower jaw and 10 in the upper jaw. Permanent teeth replace the primary ones in children aged between 6 to 14. There are 32 permanent teeth in total and they are categorised into several groups: incisor teeth, canine teeth, premolar teeth and molar teeth [pic. 1]. During consumption of various foods, these groups play different and vital functions. The basic role of incisors is to chop bits of food, facilitate proper pronunciation and construct the external mouth profile. Next type of teeth, canine teeth, support lip muscles, chop and smash food and protect premolar teeth from chewing pressure. Then, premolar and molar teeth, together called molars, are necessary for grinding and chewing of food to make it easy for further assimilation in the body [23]. Picture [2] presents anatomical construction of a tooth. Four main tissues can be distinguished. Enamel, dentine, root cement and pulp. Mineralised elements include dentine and cement. The pulp is vascularised and innervated. The solid tissue located on the surface protects it from external factors [23].

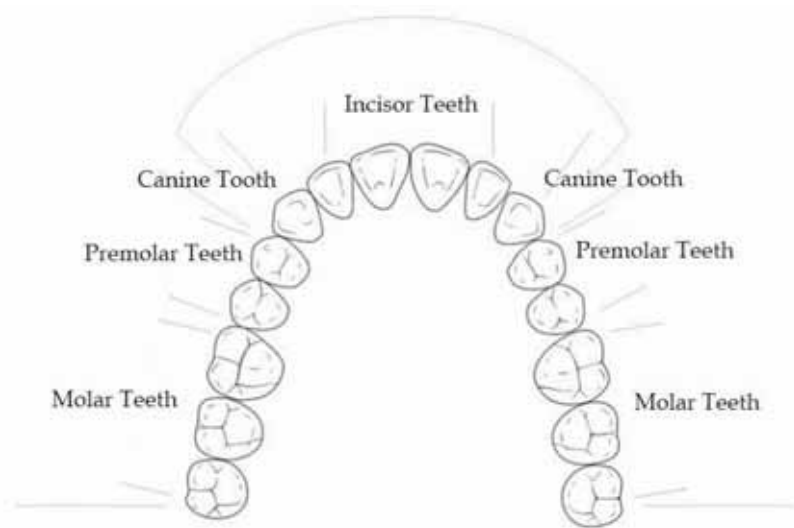


Fig. 1 Permanent teeth - occlusion view [23]

During food consumption, teeth can be affected by cyclical load which causes micro cracks in the tooth structure. Deepening of cracks in the tooth tissue may lead to damage or partial chipping of the material. Tooth construction analysis confirms that the damage occurs mainly at the dentine – enamel junction, enamel as such gets fractured more rarely. In some instances, the pulp cavity gets open and tooth nerves become destroyed.

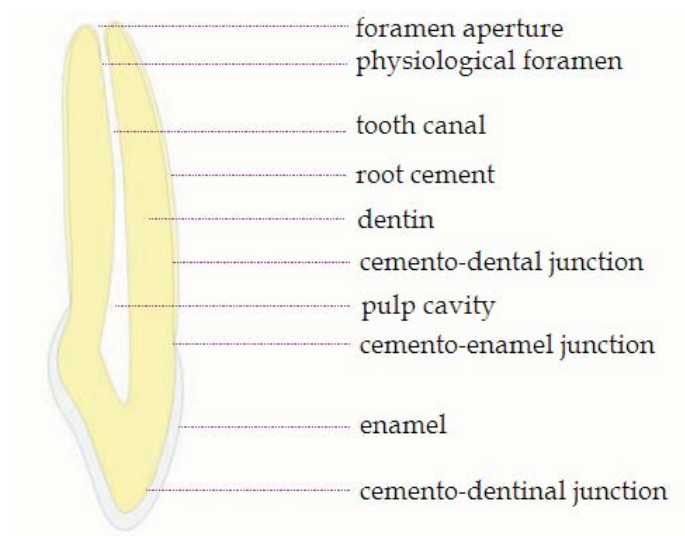


Fig. 2 Tooth anatomy layout [23]

Fatigue – endurance tests are classified on the basis of the analysed material or on the basis of the analysis method and are grouped in two categories. The first group includes the analysis of:

- natural teeth, especially human, e.g.: [1], [2], [3], [4], [6], [7], [9], [10], [12], [14], [16], [17], [18], [19], [20], [28], which is further divided into the analysis of incisor teeth, e.g.: [12], [14], [16], premolar teeth: [1], [6] and molar teeth: [2], [10]
- false teeth, e.g.: [13], [15], [31]
- bovine teeth, e.g.: [5], [28],
- dental materials, e.g.: polymer resin [21], [22], [30], cement: [21], junction technologies [7], [21].

The second category comprises various analysis methods. It can be divided into:

- static tests, e.g.: [2], [5], [15], [18], [19], [21], [26], [30], [31],
- dynamic tests, e.g.: [1], [2], [4], [6], [7], [9], [10], [12], [13], [14], [15], [16], [17], [21], [22], [30], [31], high-cycle: [1], [10], [13], [16], [17], [22], and low-cycle: [1], [3], [4], [12], [14], [17], [20], [28],

Static testing helps to determine pressure and deformations which the material undergoes due to high, higher than average, load. In article [18] authors analyse the endurance of metacrylan dental glues exposed to wet and dry conditions.

Test were conducted for cylinder shaped samples (beams), bent at 3 points. Article [26] presents fatigue tests of a stretched bovine sample. After trimming, the samples were stored in salt solution and at the end of the test their structure was scanned. In article [19], authors selected carefully researched material and attempted to test by damaging samples statically at the angle of 45°. Damaged points were analysed thoroughly. The article concludes that teeth which were additionally filled up with composite glue demonstrated better endurance than those which underwent tests right after gluing. In article [5] authors used as test material molar bovine teeth. They compared 3 composite types of glue hardened by light. Their results indicate that there is a huge range for a tooth fracture resistance, which can reach even up to 60%.

Dynamic testing constitutes the second category of analysis method. It can be divided into high-cycle and low-cycle. Paper [28] belongs to the former group. Authors present a new view on fatigue testing for glued junctions during teeth mineralisation. They also mention the analysis environment – wet and dry conditions. Samples are tested in 40.000 cycles at the frequency of 0.25Hz. Article [3] describes tests in which 4 “all in one” glues were used in 5×10^4 cycles at the frequency of 0.2Hz. Article [4] presents two methods of sample preparation for tests in a material testing machine. In the first method, similar to the above mentioned, the analysed element is trimmed to match the size of testing machine jaws. In the second method, the sample is fixed in metal attachment point (2mm in height) which is fixed to the material testing machine. Article [20] presents low-cycle dynamic tests. By the selection of modern glues and modified resin, samples are destroyed in 10^4 cycles. Concluding from authors work [20], “all in one glues” and self etching glues do not provide any substantial resistance to fatigue.

This paper will focus on low-cycle tests. Similar analysis samples were user for the two methods described below.

2. Materials and methods

2.1. Dynamic and static bond-strength [24]

Tests were conducted on healthy and selected molar teeth. Before the analysis, samples were kept in water and chloramine 0,5% solution at the temperature of 4°C. Teeth were fixed in a gypsum block and trimmed by a saw ISOMET 1000. The cut surface was checked under a microscope for any remaining residue or enamel.

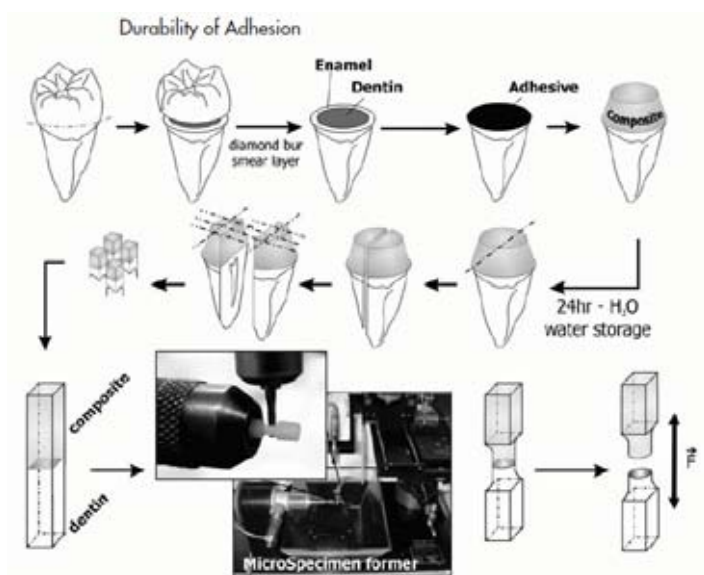


Fig 3. Layout of sample preparation and the conduction of endurance tests [8]

The samples were analysed for glue 3-E & Ra: OptiBond FL. The producer's procedure was applied by gluing. After gluing, surfaces were complemented with composite resin Z100. Each of the applied resins had to be hardened by the light from Optilux 500 machine for 40s. After 7 days the samples were trimmed down to 6mm in height, which enables static stretch and fatigue analysis. Materials were placed in a testing machine INSTRON 5848 and stretched with 500N where the speed of relocation for upper jaw equalled 1mm/min. μ TBS index – static stretching – was introduced in the analysis. Dynamic – cyclical load was indexed as μ TFR for samples which were tested at the frequency of 2Hz and for which 10Hz frequency caused destruction or when cycles reached the value of 10^4 , which equalled 3 months of constant food chewing in the oral cavity. Samples were divided into 3 groups: samples analysed directly after gluing, samples stored in the solution for one week and samples stored in the solution for one month.

2.2. Fatigue of dentin-composite [27]

Samples for analysis were extracted from human molar teeth which were sterilised with gamma radiation [4]. The samples were trimmed to the dimension 1.1mm x 1.1mm x 6mm. The surface was polished with 600 thick sand paper. Gluing point was located in the middle of the dental crown height. The junction of composite with the remaining part of the tooth was created of 3 layers. Firstly, the glued surface had to be prepared. Etching liquid (SE Bond Primer) was used to this purpose and spread on the glued surface. Then, resin glue (SE Bond), previously hardened by light for 20sec., was placed. Finally, the composite was applied. It was formed to the shape of the analysed beam. After initial polymerisation, samples were placed in a water container for 24 hours.

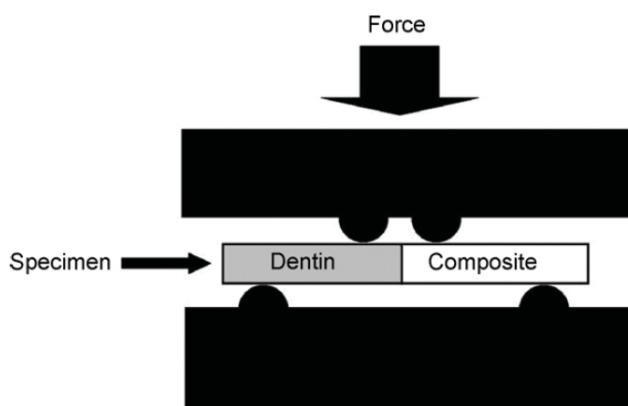


Fig. 4. Four points of sample bent layout[27]

In the first stage of the experiment, a test of static bent of elements until destruction was carried out. Upper jaw relocation grew linearly every 0.001mm/sec. The second group of samples was put to cyclical load test until destruction point or 10^6 cycles.

3. Results

3.1. Method 1 [2]

The results of static and dynamic load for the samples glued with the OptiBond FL glue are presented in table 1. It is noticeable that highest scores are found in tests for μ TFR at 2Hz for samples stored 1 week. Analysing the chart presented in picture 5, which demonstrates loads for the sample glued at various cycles and loads, one can see that at low pressure values (up to 21MPa) the tested material does not become destroyed. It was only the sample which underwent cyclical loads of 2Hz and was previously stored for 3 months in the solution that was damaged quickest. The sample showed material fatigue already at 19.7MPa. Picture 6 presents the percentage of surface fracture for different fatigue tests (glue OptiBond FL).

Tabele 1. Static and dynamic stretching divided according to storage period[24]

Glue	μ TBS [MPa]	μ TFR 10 Hz after first week [MPa]	μ TFR 2 Hz po after first week [MPa]	μ TFR 2 Hz after 3 months
-E & Ra: OptiBond FL	51. \pm 17.6	20.5 \pm 16	21.3 \pm 17.4	19.7 \pm 16.6

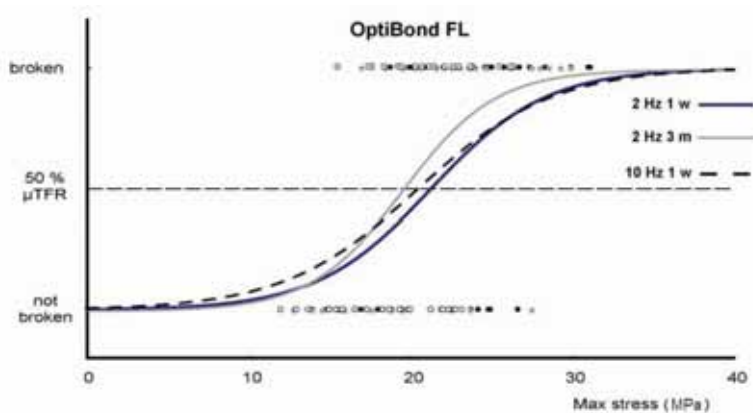


Fig 5. Chart for cyclical load of a sample glued with OptiBond FL glue, including 3 storage periods [24]

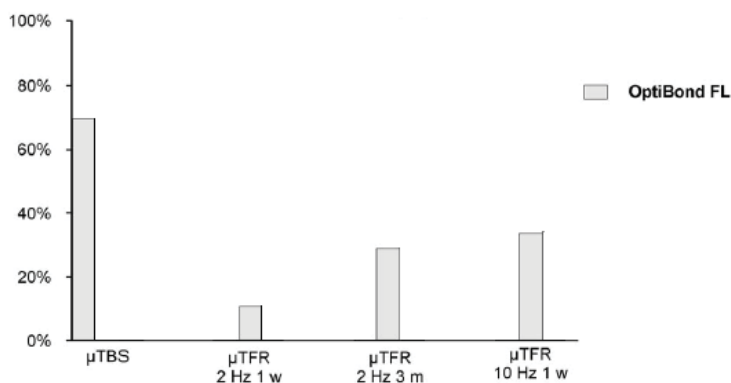


Fig 6. Percentage of surface destruction for particular test method[24]

The highest percentage of fractures occurs in static load of the tested element. The results reach even up to 70%. Cyclical fatigue tests for 2Hz and 10Hz display relatively little damage of the analysed teeth enamel surface. The range falls between 17% to 40%.

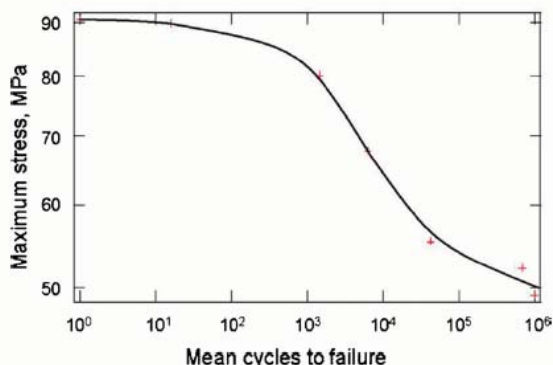
3.2. Method 2 [27]

Results for samples which were bent statically are very similar and they amount to: 164.4 ± 9.1 and 164 ± 2.4 MPa (table 1).

Tabela 2. Dental samples endurance to four-point bending [27]

Type of sample	Mean fracture stress in MPa	Statistical grouping
Solid dentin	$164,4 \pm 9,1$	A
Solid composite	$164,6 \pm 2,4$	A
Bonded beam	$90,6 \pm 2,5$	B

Among samples that underwent cyclical load, all samples endured the maximum number of cycles which equalled 10^6 at the maximum pressure – 49.2MPa. Picture 7 indicates that along the increase of cycle number, the maximum pressure for the sample decreases.



Pic. 7. Scheme representing an average number of cycles for the maximum pressure [27]

4. Summary

The purpose of this paper was to present the endurance and fatigue tests methodology for human and bovine dental samples. The article describes two methods which help to determine properties of analysed glue. The first testing method for glued junctions in molar teeth is much more time consuming as it includes methods of static stretching of the analysed sample and cyclical – dynamic stretching at the frequency of 2Hz and 10Hz. The obtained results confirm there is a difference in the range of endurance depending on the method and period of sample storage in the solution. Table 2 lists results of analysis methodology for the two above described methods. In this article only one glue type is mentioned as the aim of the paper was to present the method for properties determination of glued tooth – composite junctions. Similarly to the above mentioned, method 1 will be used by the author for own analysis. A difference will be introduced by altering the mode of storage – right after extraction, dental samples will be frozen down to -32°C and later cleansed of any remaining soft tissue. Samples will be disinfected with gamma rays just as in method no 2. The ISOMET 4000 machine will be used for the analysis. It will be applied for trimming the samples into beams into the dimension: 1.5mm x 1.5mm x 15mm. Samples will undergo tests in a material testing machine of a load 500N.

Table 2. List of methods

Methods	1	2	3[3]
Load	dynamic	dynamic and static	dynamic
Frequency	2 Hz and 10 Hz	10^6 cycles	0,25Hz 4×10^4 cycles
Storage period	0,5% chloroamine in 4°C	Sterilisation with γ rays Hanks salt solution (HBSS) in 25°C	24h in distilled water at 37°C
Range of testing (pressure)	500 N; 0 – 40 MPa	165 N; 0 – 90 MPa	24 – 54 MPa
Problem type	Measurement of dynamic and static tensions for results comparison	Determination of junction properties for tooth- composite junction during static and dynamic tests	Shear fatigue limit testing coupled with shear bond strength measurements

5. References

- [1] Attia A., Abdelaziz K.M., Freitag S., Kern M.: Fracture load of composite resin and feldspathic all-ceramic CAD/CAM crowns, *J Prosthet Dent*, 2006, Vol. 95, No. 2, ss. 117 – 123
- [2] Bajaj D., Nazari A., Eidelman N., Arola D.D.: A comparison of fatigue crack growth in human enamel and hydroxyapatite, *Biomaterials*, 2008, Vol. 29, ss. 4847 – 4854
- [3] Barkmeier WW, Erickson RL, Latta MA. : Fatigue limits of enamel bonds with moist and dry techniques, *Dental materials journal* Vol 25(12) ss. 1527 – 1531
- [4] Belli S, Ozçopur B, Yeşilyurt C, Bulut G, Ding X, Dorsman G. : The effect of loading on microTBS of four all-in-one adhesives on bonding to dentin, *J Biomed Mater Res B Appl Biomater*, Vol 91(2) ss. 948 – 956
- [5] Bijelic J, Garoushi S, Vallittu PK, Lassila LV. : Fracture load of tooth restored with fiber post and experimental short fiber composite, *The open dentistry journal*, Vol 5 ss. 58 – 65
- [6] Bolhuis P., de Gee A., Feilzer A.: Influence of fatigue loading on four post-and-core systems in maxillary premolars, *Quintessence Int.*, 2004, Vol. 35, No. 8, ss. 657 – 667
- [7] Braem M.: Microshear Fatigue Testing of Tooth/Adhesive Interfaces, *J Adhes Dent.*, 2007, Vol. 9, Supplement 2, ss. 249 – 253
- [8] De Munck J., Van Landuyt K., Peumans M., Poitevin A., Lambrechts P., Braem M. and Van Meerbeek B.: A Critical Review of the Durability of Adhesion to Tooth Tissue: Methods and Results, *Journal of Dental Research* 2005, Vol. 84 ss. 118 - 133
- [9] Drummond J.L.: Degradation, fatigue and failure of resin dental composite materials, *J Dent Res.*, 2008, Vol. 87, No. 8, ss. 710-719
- [10] El-Mowafy O., Rubo M.: Retention of a Posterior Resin-Bonded Fixed Partial Denture with a Modified Design: An In Vitro Study, *The International Journal of Prosthodontics*, 2000, Vol. 13, No. 9, ss. 425-431
- [11] Garcia Eugenio J., Gomes Osnara M.M., Gomes Joao C.: In vitro analysis of bond strength of self – etching adhesives applied on superficial and deep dentin, *Acta Odontol*, Vol. 22 ss. 57-62
- [12] Garoushi S.K., Lassila L.V.J., Vallittu P.K.: Fatigue Strength of Fragmented Incisal Edges Restored with a Fiber Reinforced Restorative Material, *The Journal of Contemporary Dental Practice*, 2007, Vol. 8, No. 2, ss. 1-10
- [13] Gateau P., Sabek M., Dailey B.: Fatigue testing and microscopic evaluation of post and core restorations under artificial crowns, *J Prosthet Dent.*, 1999, Vol. 82, No. 3, ss. 341-347
- [14] Goto Y., Nicholls J.I., Phillips K.M., Junge T.: Fatigue resistance of endodontically treated teeth restored with three dowel-and-core systems, *J Prosthet Dent.*, 2005, Vol. 93, No. 1, ss. 45-50
- [15] Herion T., Ferracane J.L., Covell D.A.Jr.: Three Cements Used for Orthodontic Banding of Porcelain Molars, *Angle Orthod.*, 2007, Vol. 77, No.1, ss. 94-99

- [16] Heydecke G., Butz F., Hussein A., Strub J.R.: Fracture strength after dynamic loading endodontically treated teeth restored with different post- and-core systems, *J Prosthet Dent*, 2002, Vol. 87, No. 4, ss. 438-445
- [17] Hsu Y.B., Nicholls J.I., Phillips K.M., Libman W.J.: Effect of Core Bonding on Fatigue Failure of Compromised Teeth, *The International Journal of Prosthodontics*, 2002, Vol. 15, No. 2, ss. 175-178
- [18] Huang H.H., Lin M.C., Lin C.C., Hsu C.C., Chen F.L., Lee S.Y., Hung C.C.: Effects of welding pulse energy and fluoride ion on the cracking susceptibility and fatigue behavior of Nd: YAG laser-welded cast titanium joints, *Dent Mater J.*, 2006, Vol. 25, No. 3, ss. 632-640
- [19] Inoue T, Nishimura F, Debari K, Kou K, Miyazaki T. : Fatigue and tensile properties of radicular dentin substrate, *Journal of Biomechanics* 2011, Vol 44(4) ss. 586 – 592
- [20] Li BH, Zhao X, Bao Y, Ai HJ. : Resistance to cyclic fatigue of pulpless teeth with flared root canals restored with three kinds of post-and-cores, *Shanghai Kou Qiang Yi Xue* Vol. 18 ss. 69 - 72
- [21] Lohrer H., Behr M., Hintereder M., Rosentritt M., Handel G.: The impact of cement mixing and storage errors on the risk of failure of glass-ceramic crowns, *Clin Oral Invest*, 2009, Vol. 13, No. 2, ss. 217-222
- [22] Minami H., Suzuki Sh., Minesaki Y., Kurashige H., Tanaka T.: In Vitro Evaluation of the Effect of Thermal and Mechanical Fatigues on the Bonding of an Autopolymerizing Soft Denture Liner to Denture Base Materials Using Different Primers, *Journal of Prosthodontics*, 2008, Vol. 17, ss. 392-400
- [23] Piątowska D., Jarosław Cynkier, Małgorzata Paul-Stalmaszczyk: *Stomatologia Zachowawcza, współczesne metody opracowania i wypełniania ubytków próchnicowych*. Bestom DENTOnet.pl, Łódź 2009
- [24] Poitevin A., Jan De Munck, Marcio Vivan Cardoso, Atsushi Mine, Marleen Peumans, Paul Lambrechts, Bart Van Meerbeek :Dynamic versus static bond-strength testing of adhesive interfaces, *Dental Matherials* 2010 Vol. 26, ss. 1068–1076
- [25] Shono Y., Ogawa T., Terashita M., Carvalho R.M., Pashley E.L. and Pashley D.H.: regional measurement of resin – dentin bonding as an array, *Journal of Dental Research*, Vol. 78, ss. 699 – 705
- [26] Singh V, Misra A, Marangos O, Park J, Ye Q, Kieweg SL, Spencer P. : Viscoelastic and fatigue properties of model methacrylate-based dentin adhesives, *Journal of Biomedical materials research* 2010, Vol 95(2), ss. 283 – 290
- [27] Staninec M., Kim P., Marshall G. W., Ritchie R.O., Marshall S. J.: Fatigue of dentin–composite interfaces with four-point bend, *Dental Materials* 2008, Vol. 24, ss. 799 - 803
- [28] Stellini E, Stomaci D, Zuccon A, Bressan E, Ferro R, Petrone N, Favero L, Mazzoleni S. : Tooth fragment reattachment through the use of a nanofilled composite resin, *European journal of paediatric dentistry*, Vol 11(2), ss. 77 – 81
- [29] Topoliński T.: Problemy wytrzymałości i trwałości zmęczeniowej w materiałach i konstrukcjach inżynierii biomedycznej, WNITiE, Bydgoszcz 2009

[30] Yamamoto M., Takahashi H.: Tensile Fatigue Strength of Light Cure Composite Resins for Posterior Teeth, Dental Materials Journal, 1995, Vol. 14, No. 2, ss.175-184

[31] Zahran M., El-Mowafy O., Tam L., Watson P.A., Finer Y.: Fracture Strength and Fatigue Resistance of All-Ceramic Molar Crowns Manufactured with CAD/ CAM Technology, Journal of Prosthodontics, 2008, Vol. 17, ss. 370-377